Molecular mechanisms of cognitive impairment in a maternal immune activation model for schizophrenia in the rat

A thesis submitted to The University of Manchester for the Degree of Doctor of Philosophy in the Faculty of Biology, Medicine and Health

2023

Rebecca M. Woods

School of Biological Sciences, Division of Evolution, Infection and Genomics

Contents

Word Count: 99,992

List of Figures

CHAPTER 1

CHAPTER 2

CHAPTER 3

CHAPTER 4

CHAPTER 5

CHAPTER 6

CHAPTER 7

List of Tables

CHAPTER 1

CHAPTER 2

CHAPTER 3

CHAPTER 4

CHAPTER 5

CHAPTER 6

Abbreviations

1C	1-carbon
4-PL	Four parameter logistic regression
5caC	5-carboxyl-cytosine
5fC	5-formyl-cytosine
5hmC	5-hydroxymethyl-cytosine
5mC	5-methyl-cytosine
5-MTHF	5-methyltetrahydrofolate
AMPA	α-amino-3-hydroxy-5-methyl-4-isoxazolepropionic acid
APOBEC	Apolipoprotein B mRNA editing catalytic polypeptide-like
ASD	Autism spectrum disorder
ASPA	Animals (Scientific Procedures) Act
ASST	Attentional set shifting task
ATP	Adenosine triphosphate
AUC	Area under the curve
AV	Average
AWERB	Animal Welfare and Ethical Review Body
BBB	Blood brain barrier
BER	Base excision repair
bis-DNA	Bisulphite-converted DNA
bis-PCR	Bisulphite PCR
bis-seq	Bisulphite-sequencing
BMPs	Bone morphogenetic proteins
bp	Base pairs
BPD	Bipolar disorder
BSA	Bovine serum albumin
BSF	Biological Services Facility
CANTAB	Cambridge Neuropsychological Test Automated Battery
CBT	Cognitive behavioural therapy
cDNA	Complementary DNA
CFD	Cerebral folate deficiency
CGI	CpG island
Ch-ABC	Chondroitinase ABC
CI	Confidence interval
CNS	Central nervous system
CNV	Copy number variants

CpG	Cytosine-guanine dinucleotide
CpH	Cytosine adjacent to a base other than guanine
CSF	Cerebral spinal fluid
CSPG	Chondroitin sulphate proteoglycan
Ct	Cycle threshold
CV	Co-efficient of variation
DALYs	Disability-adjusted life years
dH_2O	Distilled water
DHF	Dihydrofolate
DMC	Differentially methylated CpG
DMR	Differentially methylated region
DNA	Deoxyribonucleic acid
DNAhm	DNA hydroxymethylation
DNAm	DNA methylation
DNMT	DNA methyltransferase
DOHaD	Developmental origins of health and disease
DSM	Diagnostic and Statistical Manual of Mental Disorders
DTI	Diffusion tensor imaging
ECM	Extracellular matrix
ED	Extradimensional
EDTA	Ethylenediaminetetraacetic acid
EI	Excitatory/Inhibitory
ELISA	Enzyme-linked immunosorbent assay
ELS	Early-life stress
EPM	Elevated plus maze
ESC	Embryonic stem cell
F	Female
FC	Frontal cortex
FDR	False discovery rate
FGF	Fibroblast growth factor
FST	Forced swim test
GABA	Gamma-aminobutyric acid
GAD	Glutamate decarboxylase
GD	Gestational day
gDNA	Genomic DNA
GLM	General linear model
GLMM	General linear mixed model
GOF	Gain of function

GR	Glucocorticoid receptor
GWAS	Genome wide association study
HAPLN	Hyaluronan and proteoglycan link protein
HAT	Histone acetyltransferase
HDAC	Histone deacetylase
HDM	Histone demethylase
HDR	High dynamic range
hiPSC	Human induced pluripotent stem cells
HMT	Histone methyltransferase
HPA	Hypothalamus-pituitary-adrenal axis
HPLC	High performance liquid chromatography
i.p.	Intraperitoneal
ICD	International Statistical Classification of Diseases and Related Health Problems
ID	Intradimensional
IF	Immunofluorescence
IHC	Immunohistochemistry
iNF	Insoluble nuclear fraction
IVC	Individually ventilated cage
JZ	Junctional zone
kb	Kilobases
kDa	Kilodaltons
KEGG	Kyoto encyclopaedia of genes and genomes
KO	Knock-out
LEV	Local exhaust ventilation
LI	Latent inhibition
LMW	Low molecular weight
LOF	Loss of function
LPS	Lipopolysaccharide
LTP	Long-term potentiation
LZ	Labyrinth zone
M	Male
MATRICS	Measurement and Treatment Research to Improve Cognition in Schizophrenia
MCB	Maternal care behaviours
MCCB	MATRICS Consensus Cognitive Battery
MIA	Maternal immune activation
miRNA	Micro RNA
MMP	Matrix metalloproteinase
MRI	Magnetic resonance imaging

mRNA	Messenger RNA
MWM	Morris water maze
N	Dam n-number
n	Offspring/foetal/placenta n-number
ncRNA	Non-coding RNA
ND	Not detected
NDD	Neurodevelopmental disorder
NHP	Non-human primate
NMDA	N-methyl-D-aspartate
NOR	Novel object recognition
NPC	Neural progenitor cell
ns	Non-significant
NSP	No significant effects of any predictors
NTC	No template control
OCT	Optimal cutting temperature compound
OD	Optical density
OF	Open field
OPC	Oligodendrocyte progenitor cell
OR	Odds ratio
PBS	Phosphate buffered saline
PC	Positive control
PCP	Phencyclidine
PCR	Polymerase chain reaction
PD	Postnatal day
PFA	Paraformaldehyde
PFC	Prefrontal cortex
PIC	Poly(I:C)
piRNA	P-element induced wimpy testis-interacting RNA
PMSF	Phenylmethylsulfonyl fluoride
PN1	Postnatal cohort 1
PN2	Postnatal cohort 2
PN2A	Postnatal cohort 2A
PN2B	Postnatal cohort 2B
PNN	Perineuronal net
Poly(I:C)	Polyinosinic:polycytidylic acid
PPI	Prepulse inhibition
PPL	Procedural Project Licence
PR1	Prenatal cohort 1

PTM	Post-translational modification
PVI	Parvalbumin interneuron
QC	Quality control
qPCR	Quantitative PCR
r	Pearson's correlation coefficient
RAM	Radial arm maze
rho	Spearman's correlation coefficient
RM-GLM	Repeated measure GLM
RNA	Ribonucleic acid
RRBS	Reduced representation bisulphite sequencing
RT-	Reverse transcriptase negative
SAH	S-adenosyl homocysteine
SAM	S-adenosyl methionine
SD	Standard deviation
SDS	Sodium dodecyl sulphate
SEM	Standard error of the mean
SI	Social interaction
siRNA	Short interfering RNA
SLIM	Sliding window model
SN	Social novelty
sNF	Soluble nuclear fraction
SNPs	Small nucleotide polymorphisms
SVZ	Subventricular zone
TAE	Tris-acetate-EDTA
TET	Ten-eleven translocation methylcytosine dioxygenase
TGX	Tris-glycine extended
THF	Tetrahydrofolate
TLR	Toll-like receptor
tNF	Total nuclear fraction
Tnsc	Tenascin
TSS	Transcription start site
VEH	Vehicle
VZ	Ventricular zone
WES	ProteinSimple Western
WFA	Wisteria floribunda agglutinin
WGBS	Whole genome bisulphite sequencing

Abstract

Schizophrenia is a debilitating neuropsychiatric disorder with heterogenous symptoms across three key domains: positive, negative and cognitive symptoms. Current therapeutic interventions rely primarily on psychopharmaceuticals (e.g., antipsychotics) in combination with psychotherapy. While these approaches have been successful at managing positive and more recently negative, symptom domains, they provide limited benefit for cognitive symptoms. Lack of efficacious therapeutic approaches owes particularly to the complex aetiology of schizophrenia, comprising both genetic and environmental risk factors. Critically, schizophrenia is hypothesised to arise from perturbed neurodevelopment, with maternal infection, resulting in maternal immune activation (MIA), recognised as a crucial risk factor for schizophrenia in MIA-exposed foetuses. Preclinical models of this paradigm are essential for identification of causal mechanisms underscoring this risk and therefore identification of novel therapeutic targets. This thesis aimed to explore the developmental molecular mechanisms which mediate the relationship between MIA *in utero* and later-life cognitive deficits in a rat model for MIA.

The model used here induced MIA on gestational day (GD) 15 via administration of the viral mimetic, poly(I:C), in pregnant Wistar rats, with acute MIA measured by changes in plasma cytokine concentrations and weight in the 24h period post-exposure. Adolescent and adult offspring cognitive performances were measured through various behavioural tasks to identify phenotypes of relevance for schizophrenia. Placental and foetal brain samples were collected at GD15, 16 and 21 and postnatal cortex samples collected across a longitudinal timeline: at postnatal day 1 (infancy), 21 (juvenile), 35 (adolescence), 100-175 (adulthood) to assess ongoing neurodevelopmental alterations in response to MIA. Accordingly, molecular measurements included: metabolite quantification, DNA methylation profiling, relative gene and protein expression, enzymatic activity assays and cell density/morphology changes.

Poly(I:C) administration induced acute MIA, with elevations in plasma pro-inflammatory cytokines IL-6 and TNFα 3h post-exposure and subsequent weight loss 6-24h post-exposure. MIA-exposure *in utero* induced a distinct prenatal phenotype consisting of foetal neuroinflammatory dysregulation coincident with disturbances in placental and foetal brain one carbon metabolism pathways. Prenatal perturbations to these processes appear to alter glial cell differentiation and development, seemingly driven by altered DNA methylation of glial-specific genes. Critically, altered epigenetic patterns at glial-specific genes persist throughout the postnatal period, resulting in altered transcriptomic and proteomic profiles of these cells across postnatal neurodevelopment, alongside altered cell densities and morphologies. Dysfunctional glia, in turn, associate with malformed myelin and extracellular matrices which precipitate loss of synaptic plasticity and early closure of the prefrontal cortex (PFC) critical period, an essential developmental period for correct development of higher cognitive functions. Reduced plasticity in this period precedes excitatory/inhibitory imbalance and inflammatory dysregulation in adulthood, manifesting alongside a robust PFC-mediated cognitive deficit in the attentional set-shifting task, indicative of executive function deficits, of relevance to schizophrenia. Notably, the characterised PFC molecular phenotype in MIA-exposed adults demonstrates key similarities to findings from schizophrenia patients, including: parvalbumin interneuron dysfunction, glutamatergic receptor imbalance, inflammatory dysregulation and demyelination. Likewise, differentially methylated genes in the adult PFC were significantly enriched for schizophrenia-risk genes; together supporting the relevance of the model for schizophrenia. Critically, the results postulate a window between adolescence and adulthood, where neuro-molecular abnormalities are present alongside preliminary evidence for elevated systemic IL-6 protein as a biomarker, prior to the development of cognitive deficits, which could be utilised to target interventions which prevent development of, or ameliorate, schizophrenia-like behaviours in MIA-offspring. Overall, the findings demonstrate a robust MIA model, with molecular and behavioural phenotypes that offers promise as a preclinical schizophrenia model.

Declaration

The following portions of the work referred to in this thesis have been submitted in support of an application for another degree or qualification at this University but are included here as reference data.

- Behavioural data (Chapter 2, Figure 2.18) and PD35 and PD100 %5mC data (Results Chapter 4, Figure 4.12) were submitted as part of a PhD thesis by Dr Harry Potter (2021).
- qPCR data for placental genes *Slc7a5* and *Slc7a8* (Chapter 3, Figure 3.5) were submitted as part of a PhD thesis by Dr Hager Kowash (2019).

Note that all work outlined above has been acknowledged in full both in the contributions section and also appropriately in the text.

Copyright statement

Contributions from collaborators

All experiments other than the following were performed by the author:

CHAPTER 2. Animal procedures/husbandry and maternal cytokine ELISAs and tissue collection were performed jointly by Dr Hager Kowash, Dr Harry Potter and the author. Foetal sex-typing was performed by Dr Hager Kowash. Animal behavioural assessment was performed by Dr Harry Potter. PN1/PN2A tissue processing was performed jointly by the author and Dr Harry Potter. Foetal brain cytokine ELISAs were performed jointly by undergraduate students Melody Maxell and Ines Jimenez Pulido, MSc student Isabella Harris and PhD students Francesca McEwan, Jarred Lorusso and the author.

CHAPTER 3. Dr Hager Kowash performed placental RNA extractions and qPCR for *Slc7a5* and *Slc7a6* in the placenta.

CHAPTER 4. PN1 RNA/DNA extractions were performed jointly by the author and Dr Harry Potter. Dr Harry Potter performed %5mC ELISA on PD35 and PD175 samples.

CHAPTER 5. *Qk* and *Myrf* qPCR were performed jointly by undergraduate students Melody Maxell and Ines Jimenez Pulido and the author. Checking of automated cell counts was performed jointly by the author and Ines Jimenez Pulido.

CAPTER 6. Dr Jennifer Fletcher performed qPCR assays for *Acan, Bcan, Ncan* and *Vcan*. IHC for PNN/PV and WES experiments for NR2A/2B and PV were performed jointly by Dr Jennifer Fletcher and the author. DAB1 Westerns, *Dab1* qPCR and bisulphite PCR and PSD95 WES were performed jointly by Isabella Harris and the author.

Acknowledgements

I would like to thank my supervisory team, Dr Reinmar Hager, Dr Jocelyn Glazier and Prof Joanna Neill, for their continued support and guidance throughout the PhD as well as their tireless support throughout the many COVID lockdowns. I would also like to thank my external supervisor Dr Christopher Murgatroyd for making me feel welcome at MMU and for his insights into epigenetics which formed a key part of the hypothesis for this thesis.

To my fellow MIA PhD students: Hager Kowash, Harry Potter, Jarred Lorusso, Jennifer Fletcher and Francesca McEwan and to other PhD students in the wider group: Zhe Yang Yim, Hawa Jahan and Stephanie Cahill. Whether it was for all the years, some late nights or a few hours, you all joined me on this journey and contributed significantly to my everyday research life – I honestly would not have made it to the end without you, so thank you for your continuous support and for all the laughs.

To my students, Isabella Harris, Melody Maxwell and Ines Jimenez Pulido, I want to thank you for all your hard work and enthusiasm in the final stages of my PhD, you all contributed to the final thesis in one way or another and without your effort it would not be the story that it is – I know you will all go on to do great things.

Finally, to my family, you were my rocks throughout the experience. I want to thank my sisters for the support you gave and the effort you put into the final thesis, from making my figures better to checking my references, those contributions really helped. For my parents, I thank you for putting up with me throughout the PhD and for always being an ear even when you didn't always know what I was talking about. And to my dog, who has always lent her ears for a stroke when writing was tough.

Dedication

This thesis is dedicated to all the people who told me I could do it…and all the people who told me I couldn't.

The Author

I. Peer reviewed publications

Woods, R. M., Lorusso, J. M., Fletcher, J., ElTaher, H., McEwan, F., Harris, I., Kowash, H. M., D'Souza, S., Harte, M., Hager, R., Glazier, J. D., (2023). Maternal immune activation and role of placenta in the prenatal programming of neurodevelopmental disorders. *Neuronal Signalling,* 7, NS20220064.

Woods, R. M., Lorusso, J. M., Harris, I., Kowash, H. M., Murgatroyd, C., Neill, J. C., Glazier, J. D., Harte, M., Hager, R., (2023). Maternal immune activation induces adolescent cognitive deficits preceded by developmental perturbations in cortical reelin signalling. *Biomolecules*, *13,* 489.

Potter, H. G., Kowash, H. M., **Woods, R. M.**, Revill, G., Grime, A., Deeney, B., Burgess, M. A., Aarons, T., Glazier, J. D., Neill, J. C., Hager, R., (2023). Maternal behaviours and adult offspring behavioural deficits are predicted by maternal TNFα concentration in a rat model of neurodevelopmental disorders. *Brain, Behaviour and Immunity*, 108, 162-175.

Lorusso, J. M., **Woods, R. M**., McEwan, F., Glazier, J. D., Neill, J. C., Harte, M., Hager, R., (2022). Clustering of cognitive phenotypes identifies susceptible and resilient offspring in a rat model of maternal immune activation and early-life stress. *Brain, Behaviour and Immunity – Health*, 25, 100514.

Kowash, H. M., Potter, H. G., **Woods, R. M**., Ashton, N., Hager, R., Neill, J. C., Glazier, J. D., (2022). Maternal immune activation in rats induces dysfunction of placental leucine transport and alters foetal brain growth. *Clinical Science*, 136, 1117-1137

Woods, R. M., Lorusso, J. M., Potter, H. G., Neill, J. C., Glazier, J. D., Hager, R., (2021). Maternal immune activation in rodent models: A systematic review of neurodevelopmental changes in gene expression and epigenetic modulation in the offspring brain. *Neuroscience and Biobehavioural Reviews*, 129, 389-421.

II. National and international conference and meeting presentations

Woods *et al.* 2022 'Maternal immune activation induces foetal epigenetic dysfunction, developmental perturbations in glutamatergic signalling and adult cognitive deficit in a rodent model for schizophrenia.' SFN, Neuroscience 2022, San Diego. Poster presentation.

Woods *et al*. 2022. 'Can an animal model translate to an inflammatory phenotype in schizophrenia?' Journal of Psychopharmacology, Supplement to Issue 36. Symposia Oral Presentation, BAP 2022.

Woods *et al*. 2022. Maternal immune activation induces offspring glial cell dysfunction and aberrant perineuronal net formation, with implications for cognitive deficits in schizophrenia. FENS 2022, Paris. Poster presentation.

Woods *et al.* 2021. 'Mechanisms of cognitive impairment in a neurodevelopmental model for schizophrenia.' PIMS annual away day 2021, Virtual. Oral presentation.

Woods *et al*. 2021. 'Altered cortical DNA methylation in a rodent model for schizophrenia suggests programmed changes in neurodevelopment and neuronal signalling processes.' BNA 2021 Festival of Neuroscience Poster abstracts, Brain and Neuroscience Advances, 1-201. BNA 2021. Poster presentation.

Woods *et al*. 2020. 'Cognitive impairment associates with altered brain methylation and gene expression in a neurodevelopmental rodent model for schizophrenia induced by maternal immune activation.' FENS 2020. Poster presentation.

III. Academic awards and travel grants

University of Manchester Doctoral Academy conference support fund, August 2022.

BNA Travel Bursary to attend FENS 2022, May 2022.

Traditional Student poster prize, BNA 2021, June 2021

Ian Massey Prize, Stage 3 Biomedical Genetics Prize, Newcastle University, July 2018

John Corran Book Prize, Newcastle University, July 2016.

CHAPTER 1. INTRODUCTION

1.1. Schizophrenia

Neuropsychiatric disorders, including schizophrenia, represent a collection of disorders associated with various complex pathological brain and behavioural phenotypes (Taber et al., 2010). Schizophrenia is estimated to impact ~1% of the population (Castillejos et al., 2018; Charlson et al., 2018) with a slight increased incidence in males, calculated as a male-to-female incidence risk ratio of 1.31-1.42 (Aleman et al., 2003; McGrath et al., 2004). Schizophrenia is rated among the top 20 disability-adjusted life years (DALYs) in the global burden of disease analyses, owing to the significant impact of schizophrenia on quality of life, with patients' incapable of self-care and independence, with a resulting burden on healthcare systems (He et al., 2020; Institute for Health Metrics and Evaluation, 2018; Janoutova et al., 2016; Kaur and Cadenhead, 2010). Schizophrenia patients are estimated to have up to a 25-year lower life expectancy than the general population, owing to high rates of suicide, somatic/metabolic illness, side-effects of antipsychotics and substance abuse (Bobes et al., 2010; Laursen et al., 2013, 2014; Newcomer, 2007; Saha et al., 2007).

1.1.1. Symptoms and diagnosis

Diagnosis of schizophrenia is dependent on criteria outlined in the Diagnostic and Statistical Manual of Mental Disorders (DSM; 5th Edition, American Psychiatric Association, 2022) and International Statistical Classification of Diseases and Related Health Problems (ICD; 11th Edition, World Health Organisation, 2019), generally based on the presence and duration of symptoms and how symptoms affect quality of life. Schizophrenia symptoms are broadly divided into three main groups: positive, negative and cognitive symptoms (Figure 1.1; Mihaljević-Peleš et al., 2019; Tamminga, 2008). Positive symptoms consist of 'additive' traits, including: disorganised speech, delusions, hallucinations (auditory and visual), paranoia and psychosis; while negative symptoms consist of 'reduced' traits, such as anhedonia, lack of motivation, depression and social withdrawal (Figure 1.1; American Psychiatric Association, 2022). Cognitive symptoms, by contrast, consist of cognitive deficits across seven key domains: social cognition, verbal, visual and working memory, vigilance, processing speed and problem solving, clinically defined by the Measurement and Treatment Research to Improve Cognition in Schizophrenia (MATRICS; August et al., 2012; Green et al., 2008; Kern et al., 2008; Young et al., 2009). While patients often experience periods of remission for positive symptoms, negative and cognitive symptoms are chronic and are arguably the larger contributors to loss of life quality (Kahn et al., 2015). Further, delineation of symptoms into distinct domains does not mean they are separate with negative symptoms significantly perpetuated by positive symptoms (e.g., paranoia and disturbing hallucinations), stress of diagnosis and the disruption to normal life. Such secondary negative symptoms can be incredibly debilitating and contribute to worse patient outcomes (Correll and Schooler, 2020). Schizophrenia onset usually occurs between 15-30 years of age and, while individual symptom progression varies, clinical staging includes a prodromal stage followed by acute and chronic phases of psychosis (Janoutova et al., 2016;

Lieberman, 1999; Niendam et al., 2006). The prodrome is usually a period of weeks/months of non-specific symptoms, usually comprising cognitive and emotional deficits, such as isolation and deficits in memory and attention (George et al., 2017). The prodromal stage ends with the onset of acute psychosis, including psychotic episodes with onset and remission, with such symptoms resolving in ~30% of patients (Janoutova et al., 2016; Yung et al., 2007). In patients where symptoms do not resolve, individuals deteriorate into a symptomatically stable psychosis (the chronic phase) during which patients are often incapable of independence or self-care (Janoutova et al., 2016; Kaur and Cadenhead, 2010).

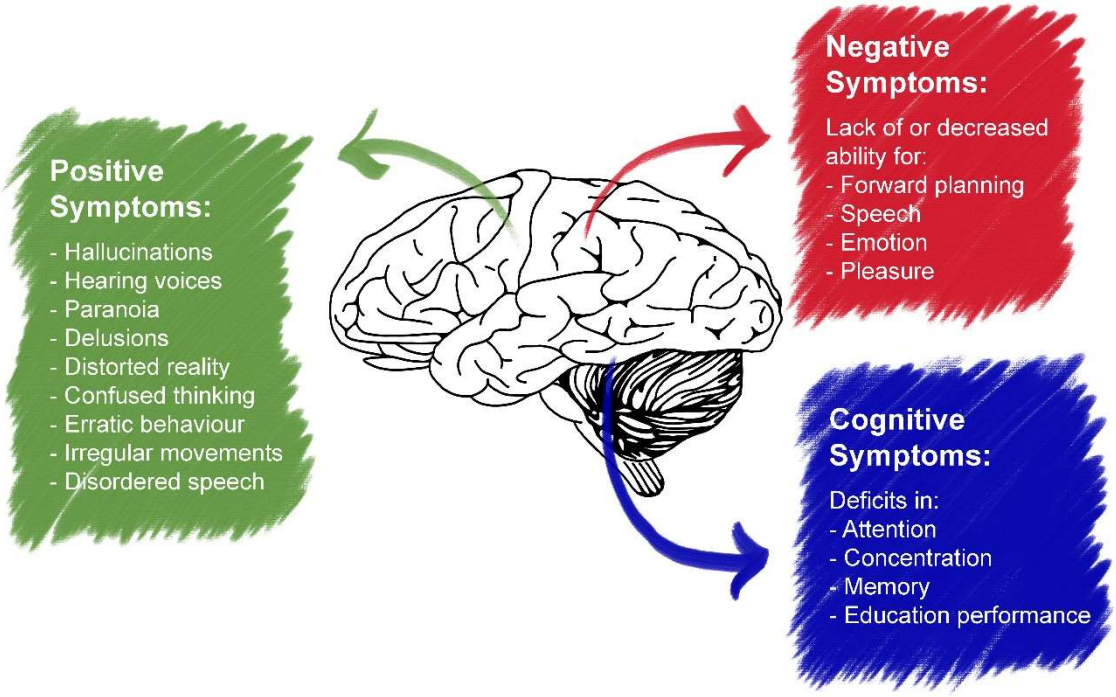

Figure 1.1. Schizophrenia symptom domains
Summary of the positive, negative and cognitive symptoms arising in schizophrenic patients as outlined by the American Psychiatric Association (2022).

Despite extensive efforts to standardise the schizophrenia diagnostic processes, it is not without its shortfalls. Schizophrenia is often used as an umbrella term for schizophrenia, schizoaffective disorder and psychosis, which can cause issues with correct diagnosis, with significant overlap between symptoms outlined in the DSM (American Psychiatric Association, 2022). Given the similar risk factors and symptom presentations across neurological disorders, current research suggests that inclusion of both transdiagnostic and disorder-specific trait evaluation could improve diagnostic accuracy (Dalgleish et al., 2020; Reininghaus et al., 2019). Further, the current diagnostic rubric is also suggested to introduce inherent bias into the diagnostic process. Historically, there is an increased schizophrenia risk in men (Aleman et al., 2003; McGrath et al., 2004). This has been suggested to owe to delayed symptom onset in females who tend to present with more affective symptoms (e.g., depression and anxiety) and thereby bias diagnosis

to schizoaffective disorders, leading to sub-optimal care (Brand et al., 2022; Reininghaus et al., 2019). Likewise, there are historically high rates of schizophrenia diagnosis among black individuals (Barnes, 2004). However, lack of genetic risk evidence has led to the more recent implication that this increased risk owes to symptom presentation divergences between races which bias diagnosis (Reininghaus et al., 2019; Schwartz and Blakenship, 2014, Schwartz et al., 2019b). Finally, early detection and subsequent intervention is beneficial for schizophrenia patients, by preventing the development of chronic psychosis (George et al., 2017; Kulhara et al., 2008). Early intervention for schizophrenia has been historically challenging, as it is the acute and chronic phases of schizophrenia where symptoms become readily diagnosable under standard diagnostic processes, whereas more subtle early prodromal symptoms are usually missed (George et al., 2017; Kulhara et al., 2008; Taber et al., 2010). That said, improvements to early diagnosis are being made, through the development of approaches to recognising high risk individuals, enabling early intervention and reduced psychiatric admissions, particularly involuntary admissions (Malda et al., 2019; Sizer et al., 2022).

1.1.2. Treatment

1.1.2.1. Psychopharmacology and drug-based strategies

The field of neuropsychopharmacology was established in the 1950s following the development of the first antipsychotic, chlorpromazine, which was found to possess adrenolytic, gangliolytic and antiemetic properties (Anton-Stephens, 1954; Ban, 2007; Ramachandraiah et al., 2009). Subsequently, various chlorpromazine-like compounds, including phenothiazines and butyrophenones, constitute ‘first-generation’ antipsychotics (Ban, 2007; Ramachandraiah et al., 2009), acting through antagonism of dopaminergic receptors (Carlsson and Lindqvist, 1963; Seeman et al., 1975). Later tricyclic compounds, including clozapine and risperidone, were found to have antipsychotic properties with less extrapyramidal side-effects (e.g., tremors, dyskinesia and slurred speech) experienced with first-generation antipsychotics (Ramachandraiah et al., 2009). These ‘second-generation’ antipsychotics were found to act as potent antagonists at serotonin receptors, as well as dopamine receptors (Meltzer et al., 1989, 2003). While first and second-generation antipsychotics remain the mainstay of schizophrenia therapy, they are not without challenges. Most patients show an incomplete response to antipsychotics, with psychosis resolving in only ~70-75% of patients, with limited effect on auditory hallucinations (Ibrahim and Tamminga, 2011; Keefe et al., 2007; Lieberman et al., 2005; Spark et al., 2022; Swartz et al., 2007). Further, while second-generation antipsychotics have been indicated to ameliorate some negative symptoms (Meltzer et al., 2003), this was found to be primarily attributable to secondary negative symptoms (Căpățînă et al., 2021; Correll and Schooler, 2020), with antipsychotic compounds ineffective for cognitive symptoms (Ibrahim and Tamminga, 2011; Jaaskelainen et al., 2013; Spark et al., 2022). Further, antipsychotics are associated with severe side-effects including metabolic syndromes, hormonal and neurological symptoms (Muench and Hamer, 2010; Ucok and Gaebel, 2008). The side-effects and lack of

efficacy of antipsychotics can provoke lack of patient compliance. Indeed, since their advent and clinical introduction, patients were found to have poor adherence to oral dosing of antipsychotics (Rubio et al., 2021), with a recent systematic review estimating noncompliance to medication in schizophrenia patients to be as high as 50% (Semahegn et al., 2020). This prompted the development of long-acting injectables, however, these have not always been well-received by patients and have been less favoured by clinicians than oral antipsychotics (Brissos et al., 2014; Correll et al., 2021).

It is notable that the challenges associated with antipsychotics do not discriminate between first and second-generation antipsychotics. Indeed, comparative clinical trials between first- and second-generation antipsychotics (e.g., CATIE and CUtLASS trials) showed little difference between them in terms of patient compliance, effectiveness and quality of life (Naber and Lambert, 2012; Spark et al., 2022).

More recent drug treatments aim to overcome many of the limitations of current antipsychotics. For example, novel atypical antipsychotics such as asenapine (Căpățînă et al., 2021) and cariprazine (Fleischhacker et al., 2019) have been found to show improvements to negative symptoms with better affinity than earlier compounds. That said, despite promising clinical trials for novel compounds targeting alternative neurotransmitter systems, none have been successful, with high attrition in late-stage clinical trials relating to lack of efficacy and safety profiles (Spark et al., 2022). Alternatively, adjuvant therapies have been employed in an attempt to manage negative and cognitive symptom domains, in combination with antipsychotics. Such adjuvant therapies have included antidepressants which attempt to manage negative symptoms, including selective serotonin reuptake inhibitors, tricyclic and tetracyclic antidepressants and have in general shown promising results, though it remains unclear if they improve primary or secondary negative symptoms (Căpățînă et al., 2021; Correll and Schooler, 2020). Likewise, anti-inflammatories have also been suggested as adjuvant therapies, hypothesised to improve schizophrenia symptoms domains (Section 1.1.3.4) though with mixed success (Çakici et al., 2019; Cho et al., 2019; Hashimoto, 2019; Jeppesen et al., 2020).

1.1.2.2. Psychotherapy and alternative strategies

More recent research suggests that integration of psychopharmacology and psychotherapy/psychosocial interventions may be better practice for schizophrenia management than drug-based strategies alone (Mueller, 2023). Psychosocial interventions, include: cognitive behavioural and remediation therapies, psychoeducation programs, family intervention programs and social skills training and assertive community treatment. Such methods have been shown to improve patient symptom outcomes and reduce patient drug noncompliance (Chien et al., 2013; Cooper et al., 2020). Cognitive behavioural therapy (CBT) has been a prevalent approach, showing extensive benefits in social function, psychosis and secondary negative symptoms (Moritz et al., 2019; Sitko et al., 2020). CBT is recommended at all stages of schizophrenia progression and in particular has proven efficacious in treatment-

resistant schizophrenia where antipsychotics have proven ineffective (Moritz et al., 2019; Polese et al., 2019). Other beneficial alternative treatment strategies for schizophrenia include increased physical exercise (Tew et al., 2023) and creative pursuits (Shukla et al., 2022) which have been suggested to improve overall patient well-being.

1.1.3. Etiopathogenesis

1.1.3.1. Brain morphological changes

Various brain changes have been identified in schizophrenia and are suggested to be progressive into the chronic stages of the disease course (DeLisi et al., 2006; Liloia et al., 2021). Magnetic resonance imaging (MRI) and computed tomography scan studies in schizophrenia patients have consistently shown enlargement of lateral ventricle volume and subarachnoid space (Elkis et al., 1995; Gaser et al., 2004; Kanahara et al., 2022; Kempton et al., 2010), concomitant with volume reduction in several other brain regions including: the amygdala, hippocampus, striatum, thalamus and overall cortical thinning (Dabiri et al., 2022; Gaser et al., 2004; Kuo and Pogue-Geile, 2019; Lawrie and Abukmeil, 1998; Nelson et al., 1998; Pina-Camacho et al., 2022; Velakoulis et al., 1999). These volume reductions owe primarily to overall loss of grey matter (Kuo and Pogue-Geile, 2019; Pantelis et al., 2003; Stegmayer et al., 2014; Vita et al., 2012), arising due to reductions in synapse and dendritic density (Dabiri et al., 2022). White matter changes are usually measured by diffusion tensor imaging (DTI) for measuring white matter integrity. Various studies have evidenced reduced white matter integrity in schizophrenia (Arnone et al., 2008; Koshiyama et al., 2020; Zong et al., 2021), particularly associated with cognitive deficits (Holleran et al., 2020; Zong et al., 2021).

1.1.3.2. Neurotransmitter signalling

Dopamine and serotonin were among the first neurotransmitter systems associated with schizophrenia, owing to the discovery that first- and second-generation antipsychotics acted via antagonism of these pathways (Carlsson and Lindqvist, 1963; Meltzer et al., 1989; Seeman et al., 1975), with early hypotheses (i.e., the dopamine hypothesis) suggesting serotonin-dopamine interactions were critical in schizophrenia pathophysiology (Kapur and Remington, 1996; Meltzer et al., 2003). However, while the so-called dopamine hypothesis has been one of the most enduring theories in schizophrenia research, it is not alone sufficient to explain the disease symptomatology (Gomes and Grace, 2021; Yang and Tsai, 2017). Indeed, while likely playing roles in the development of positive symptoms (e.g., psychosis; Howes and Kapur, 2009) dopamine dysfunction cannot explain the severe cognitive symptoms experienced by schizophrenia patients. Likewise, despite ongoing interest in serotonin pathways, few studies have provided direct evidence for serotonergic dysfunction in schizophrenia (De Deurwaerdère and Di Giovanni, 2020; Yang and Tsai, 2017). Accordingly, more recent research has turned to alternative neurotransmitter systems, notably, glutamatergic and GABAergic systems. Early studies implicated deficient glutamate signalling (the major excitatory neurotransmitter; Niciu et

al., 2012), in the pathology of schizophrenia, through observations that glutamatergic *N*-methyl D-aspartate (NMDA) receptor antagonists, such as phencyclidine (PCP) and ketamine, promote psychosis development and cognitive dysfunction in humans and rodents (Cadinu et al., 2018; Javitt and Zukin, 1991; Krystal et al., 1994; Meltzer et al., 2013). Indeed, PCP administration remains a common method for preclinical animal models for schizophrenia (Cadinu et al., 2018; Lee and Zhou, 2019; Meltzer et al., 2013). Dysfunctional glutamate signalling is further supported by analysis of schizophrenia post-mortem brains which demonstrate reduced expression and hypofunction of hippocampal and prefrontal NMDA receptors (Harrison et al., 2003; Olney and Farber, 1995; Yang and Tsai, 2017). By contrast, gamma-aminobutyric acid (GABA) is the main inhibitory neurotransmitter, synthesized from glutamate by glutamate decarboxylase (GAD) enzymes (e.g., GAD65 and GAD67; Watanabe et al., 2002), enriched in GABAergic interneurons (Llorca and Deogracias, 2022). It has been suggested through live imaging studies that GABA signalling or concentrations are reduced in distinct brain regions and cerebral spinal fluid (CSF) in schizophrenia and are associated with symptom severity (Chiapponi et al., 2016; Orhan et al., 2018) aligning with post-mortem studies which support reduced GABAergic output in schizophrenia (Curley et al., 2011; Hyde et al., 2011; Lewis et al., 2005, 2012).

1.1.3.3. Neuroendocrine signalling

Neuroendocrine signalling occurs at the juncture of neuronal and peripheral hormone signalling (Gore, 2013). Within the brain, the hypothalamus is the major regulator for neuroendocrine signalling, circadian rhythms and stress responses, as part of the hypothalamic-pituitary-adrenal (HPA) axis (Figure 1.2; Stephens and Wand, 2012). Under stress conditions, the hypothalamus is triggered to release cortisol-releasing hormone (CRH) which induces the anterior pituitary gland to stimulate adrenocorticotrophic hormone (ACTH) which in turn acts on the adrenal glands atop the kidneys, concluding with the release of the stress hormone, cortisol (Figure 1.2; Stephens and Wand, 2012). Cortisol (or corticosterone in rodents) is a glucocorticoid hormone, which binds to and activates glucocorticoid receptors (GRs). Upon activation, GRs translocate to the nucleus and promote the transcription of various downstream target genes (Oakley and Cidlowski, 2013).

Elevated circulating cortisol in schizophrenia patients has been correlated with poorer symptoms and increased mortality (Bradley and Dinan, 2010; Sachar et al., 1970; Walder et al., 2000). Meanwhile, altered expression of genes/proteins involved in the normal stress response signalling pathways have also been identified in the brains and blood of schizophrenia patients (Liu et al., 2020b; Sinclair et al., 2013; Webster et al., 2002). However, systematic reviews of cortisol response after stress have suggested a blunted cortisol response in schizophrenia, associated with poor stress adaptivity, though this does appear to differ between disease stage (e.g., acute vs chronic; Dauvermann and Donohoe, 2019; Lange et al., 2017). Taken together, these results postulate dysregulated HPA-axis signalling and stress responses in schizophrenia patients.

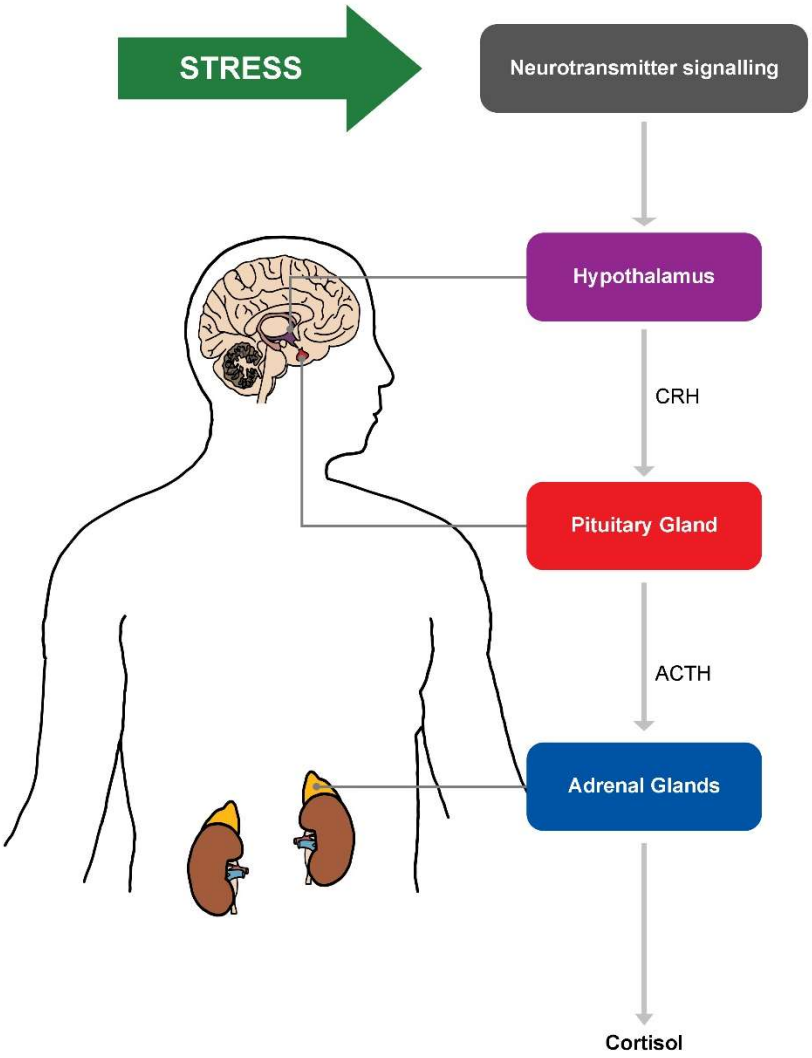

Figure 1.2. Hypothalamus-pituitary-adrenal (HPA) axis signalling
Following stress, neurotransmitter signalling induces the hypothalamus to release cortisol-releasing hormone (CRH) which acts on the anterior pituitary gland to stimulate adrenocorticotrophic hormone (ACTH) which in turn acts on the adrenal glands atop the kidneys, thereby stimulating release of the stress hormone, cortisol.

1.1.3.4. Inflammation

There is growing evidence for the involvement of inflammation in the aetiology of schizophrenia. Population studies have shown that infections increase risk of schizophrenia outcome (Khandaker et al., 2012; Moccia et al., 2023) and it is hypothesised that infection-mediated inflammatory pathways contribute to this risk. Inflammation can influence multiple body sites, including the central nervous system (CNS; Choudhury and Lennox, 2021; Müller et al., 2015). Microglial cells are the critical CNS immune cells (Dawson et al., 2003; Dos Santos et al., 2020) becoming activated in response to infection, generating an inflammatory signalling cascade and secretion of cytokines (Fernández-Arjona et al., 2017). In the past 10 years, there has been particular interest in the function and role of microglia in schizophrenia pathology, with active microglia hypothesised to drive neuroinflammatory disturbances in schizophrenia brains (Laskaris et al., 2016; Trovão et al., 2019). However, results from post-mortem studies have been mixed, with some demonstrating increased active microglial density or activity (Bernstein

et al., 2015; De Picker et al., 2021; Frick et al., 2013) while others have observed no effect (Conen et al., 2021; Di Biase et al., 2017). Likewise, several studies have associated cytokine functions with schizophrenia symptoms and progression, including increased serum/plasma and CSF protein concentrations for TNF-α, IL-1β, IL-6, IL-8, IL-12 and decreased for IL-17 and IFN-γ (Gallego et al., 2018; Kalmady et al., 2018; King et al., 2021; Kogan et al., 2018; Trovão et al., 2019; Upthegrove et al., 2014) though inter-study variability remains for individual cytokines. Furthering the possible role of inflammation in schizophrenia, as mentioned previously, anti-inflammatory agents have been suggested as early-stage adjuvant therapies (Hashimoto, 2019). However, recent meta-analyses have indicated a general lack of efficacy of anti-inflammatories in schizophrenia (Çakici et al., 2019; Cho et al., 2019; Jeppesen et al., 2020). These inter-study discrepancies likely owe to the more recent speculation that an individual subgroup of schizophrenia patients present with a high basal inflammatory state and hence lack of patient stratification in clinical trials and large-scale studies could confound these findings (Hameete et al., 2020; Di Biase et al., 2017).

1.1.3.5. Genetics

Twin studies can be used to assess heritability of complex disorders. Monozygotic twins have no differences in DNA sequence while dizygotic twins are genetically dissimilar (Verweij et al., 2012). However, the shared environments of twins allow control over environmental risk factors, enabling the calculation of the relative contribution of genetics and environment to the basis of a disease (Riley, 2004). Accordingly, if all the variance of a disease phenotype were genetic, heritability estimates of 100% for monozygotic twins and 50% for dizygotic twins would be calculated (Verweij et al., 2012). Twin studies in schizophrenia have shown greater concordance in monozygotic twins relative to dizygotic twins, with an estimated heritability of ~80% (Hilker et al., 2018; Sullivan et al., 2003) suggesting a high contribution of genetic risk. This was supported by the finding that schizophrenia risk is ten times greater for relatives of a schizophrenia patient (Riley, 2004).

Early studies investigating the genetic variants which contributed to schizophrenia risk used gene linkage studies. These were typically performed within family pedigrees, identifying genetic markers within chromosomes (e.g., microsatellites), which co-segregated with the schizophrenia phenotype (Riley, 2004). Early linkage studies identified several chromosome regions of interest, including 3p, 5q, 6p, 8p, 20p and 22q (Curtis et al., 1996; Daniels et al., 1997; Hovatta et al., 1998). However, a crucial disadvantage to these early studies was the size of the genomic regions, which included hundreds of genes and hence it was not clear which were functional candidates. Later studies investigated smaller copy number variants (CNVs), comprising genomic insertions/deletions usually ≥1000 base pairs (bp), which often alter gene expression dosage (Gamazon and Stranger, 2015). In contrast to linkage studies, CNVs are usually identified using microarray technologies in large case-control cohorts. Multiple studies have shown a contribution of CNVs to schizophrenia risk, including the consistent finding of *NRXN1* exon-disrupting CNVs (Howrigan, 2017; Kirov et al., 2009; Lee et al., 2010; Marshall et al., 2017;

Rees et al., 2014). Critically, pathogenic CNVs, while rare within the schizophrenia population, are thought to be highly penetrant in particular patient subgroups (Foley et al., 2020; Marshall et al., 2017). Moreover, next-generation sequencing technologies have also enabled genome-wide evaluation of single bp variants or small nucleotide polymorphisms (SNPs) within the DNA sequence. SNPs are usually analysed as part of genome wide association studies (GWAS) which assess SNP differences between disease cases and controls. These studies have primarily been performed by collaborations, such as the Schizophrenia Psychiatric GWAS Consortium (Dennison et al., 2020) with numerous GWAS conducted for schizophrenia in various human cohorts (Bigdeli et al., 2021; Pardiñas et al., 2018; Ripke et al., 2011, 2013, 2014), together identifying hundreds of genes. It has been suggested that schizophrenia risk variants are present at high rates in the general population and that these variants likely combine additively or under epistasis, combining with environmental risks to result in schizophrenia (Andreasen et al., 2011; Dennison et al., 2020; Riley, 2004). However, functional validation of genome-wide significant SNPs has proven challenging (Pardiñas et al., 2018). That said, more recently, SNPs have been shown to associate with distinct symptom domains, such as neurocognitive and psychotic symptoms and symptom severity in schizophrenia (Gennarelli et al., 2022; Greenwood et al., 2019; Wan et al., 2021), with some variants shown to increase schizophrenia risk in a single sex (Sozuguzel et al., 2019), supporting a functional role for SNPs in schizophrenia pathology. In line with this, more recent studies have shown that schizophrenia risk genes functionally converge in inhibitory GABAergic interneurons and excitatory glutamatergic neurons and synaptic function (Liu et al., 2022; Schmidt-Kastner et al., 2020; Trubetskoy et al., 2022), in support of a role in the disease etiopathogenesis.

1.1.3.6. Environment

Several environmental factors have been shown to contribute to increased risk of schizophrenia development. These include substance abuse, particularly cannabis, alcohol and tobacco which have been demonstrated to exacerbate psychotic symptoms (Janoutova et al., 2016; Khokhar et al., 2018). General environmental conditions have a relationship with schizophrenia. Urban living has been significantly associated with schizophrenia risk (Murray, 2003; Paksarian et al., 2018; Szoke et al., 2014). It has been shown that urban lifestyle factors such as stress, excess noise (Wright et al., 2016), pollution (Lei et al., 2023; Newbury et al., 2021), lack of sunshine (Liu et al., 2023) and drug availability (Janoutova et al., 2016; Khokhar et al., 2018) all contribute to schizophrenia development, symptom severity and relapse. Exposure to multiple environmental insults has also been demonstrated to result in earlier age of onset and worse prognosis, suggesting a cumulative effect of environmental factors on schizophrenia pathogenesis (Brown, 2011; Stepniak et al., 2014). Additionally, various prenatal and early-life events have been suggested to contribute to schizophrenia risk, underscoring the neurodevelopmental hypothesis for schizophrenia (Section 1.2).

1.1.3.7. Patient biotypes and clinical stratification

A significant amount of variability exists in the literature regarding schizophrenia etiopathogenesis and in part this likely owes to a lack of patient stratification into different subgroups. Schizophrenia is a highly heterogenous disorder with recent work suggesting that, within schizophrenia, there are divergent patient biotypes (Clementz et al., 2016, 2022), distinct from the DSM criteria. Indeed, Clementz et al. (2022) have suggested three patient biotypes, distinguished by severity of symptoms (notably cognitive ability) and functional brain changes. Validation work has suggested stratification using these biotypes to provide better predictability for biological changes, including regional volumetric changes and white matter integrity changes (Guimond et al., 2021; Kelly et al., 2021). Distinct patient biotypes are also hypothesised to underscore disparate genetic and environmental risk factors (Choudhury and Lennox, 2021). With this in mind, standard medication is unlikely to be universally beneficial across these biotypes (Clementz et al., 2022). This speculation is consistent with lack of efficacy of current treatments such as antipsychotics. Recognition of these subgroups is hence critical for clinical testing of new therapies, with a personalised medicine approach likely to be more efficacious. Accordingly, it has been postulated that the lack of anti-inflammatory efficacy is due to a lack of patient stratification based on individual basal inflammatory state, with more recent clinical trials aiming to overcome this (UK Research and Innovation, 2023).

1.2. Neurodevelopmental hypothesis for schizophrenia

The Barker hypothesis originated with the concept that a sub-optimal maternal environment could predispose offspring to later-life diseases (Barker, 1990). This idea was supported by early studies demonstrating that undernutrition during pregnancy produced foetal growth restriction and increased offspring propensity for metabolic syndromes, deemed the ‘thrifty phenotype’ (Barker, 2002; Hales and Barker, 1992, 2001). Much of the supportive epidemiological research for this hypothesis was performed in the Dutch Winter Cohort, a population which experienced famine in 1944-1945, with exposed offspring shown to have higher rates of obesity, glucose intolerance and cardiovascular diseases (Ravelli et al., 1976; Roseboom et al., 2006). This research is now commonly referred to as the developmental origins of health and disease (DOHaD), proposing that early-life environments (prenatally and postnatally) induce developmental changes which predispose individuals to disease (Gillman, 2005). Historically, schizophrenia was considered a neurodegenerative disorder, until the neurodevelopmental hypothesis of schizophrenia emerged. This hypothesis proposed that schizophrenia results from perturbed brain development (Weinberger, 1987). The mammalian brain develops over a protracted period, beginning at early post-conception and advancing into adulthood. This creates a large window of vulnerability during which neurodevelopmental trajectory can be altered by environmental factors, in line with the DOHaD hypothesis. Early events thought to impact neurodevelopment and predispose individuals to schizophrenia include pregnancy

complications, maternal infection, placental dysfunction and early-life adversity (Murray and Lewis, 1988; Owen et al., 2011; Rapoport et al., 2005).

1.2.1. Neurodevelopment: a brief overview

The mammalian CNS is a complex structure, composed of both neuronal and non-neuronal cells, which together form networks which transmit signals via synapses and signalling circuits to form the complete CNS (Azevedo et al., 2009; Jiang and Nardelli, 2016; Stiles and Jernigan, 2010). Brain development is a lengthy process, beginning relatively early in foetal development (~gestational week three in humans and gestational day (GD) 5 in rodents) and continuing into postnatal adolescence (Jiang and Nardelli, 2016; Stiles and Jernigan, 2010).

Early stages of brain development occur with neural tube convergence and patterning followed by proliferation of neuroepithelial cells, which transition into radial glial cells, the essential neural progenitor cells (NPCs) of the CNS (Gotz and Huttner, 2005). NPC proliferation and differentiation occurs in the ventricular zone (VZ) and subventricular zone (SVZ) to give rise firstly to neurons (i.e., neurogenesis; McEwan et al., 2023). Newly generated neurons then migrate outwards into the layers of the cortex (Gotz and Huttner, 2005; Marin et al., 2010). Of note, GABAergic interneurons are among the last neurons to be specified in the SVZ (~GD15 in rodents) before migrating to the cortical layers postnatally (Hu et al., 2017; Llorca and Deogracias, 2022). Neurogenesis is followed by gliogenesis, the production of astrocytes and oligodendrocytes from SVZ NPCs (Baydyuk et al., 2020; Gotz and Huttner, 2005; Tong and Vidyadaran, 2016; Zheng et al 2022). The switch from neurogenesis to gliogenesis (i.e., the gliogenic switch) is regulated both temporally and spatially by various signalling pathways (Miller and Gauthier et al., 2007; Naik et al., 2017; Sarkar et al., 2019). Finally, myelination, synaptic sculpting/pruning and maturation of cells and circuitry networks occurs in the postnatal period (Guirado et al., 2020; Larsen and Luna, 2018; Stadelmann et al., 2019; Tau and Peterson, 2010). Other key postnatal neurodevelopmental events include the GABAergic inhibitory switch and glutamatergic NMDA receptor switch, both important for the establishment of the normal excitatory/inhibitory (EI) balance in the postnatal brain (Ganguly et al., 2001; Groc et al., 2007; Liu et al., 2021). Also important in brain development are microglial cells which originate from monocyte precursors in the yolk sac, from which they migrate to the CNS in early foetal development (Ginhoux et al., 2013; Menassa and Gomez-Nicola, 2018; Tong and Vidyadaran, 2016). The entry of microglia into the foetal brain coincides with the formation of radial glial cells from neuroepithelial cells. Microglia first cluster in the SVZ and then later populate the rest of the cortex, remaining throughout life (Tong and Vidyadaran, 2016). It is thought that microglial invasion influences normal neuronal migration and differentiation patterns and modulates neuronal circuity formation. Indeed, microglia have been shown to regulate the NPC pool, neuronal positioning, synaptic pruning and myelination (Menassa and Gomez-Nicola, 2018; Reemst et al., 2016; Tong and Vidyadaran, 2016). Overall, this protracted period of brain development (Figure 1.3) leaves it highly vulnerable to prenatal and postnatal stressors, which

can disturb these processes and thereby alter neurodevelopmental trajectory (Giussani, 2011; Sarkar et al., 2019).

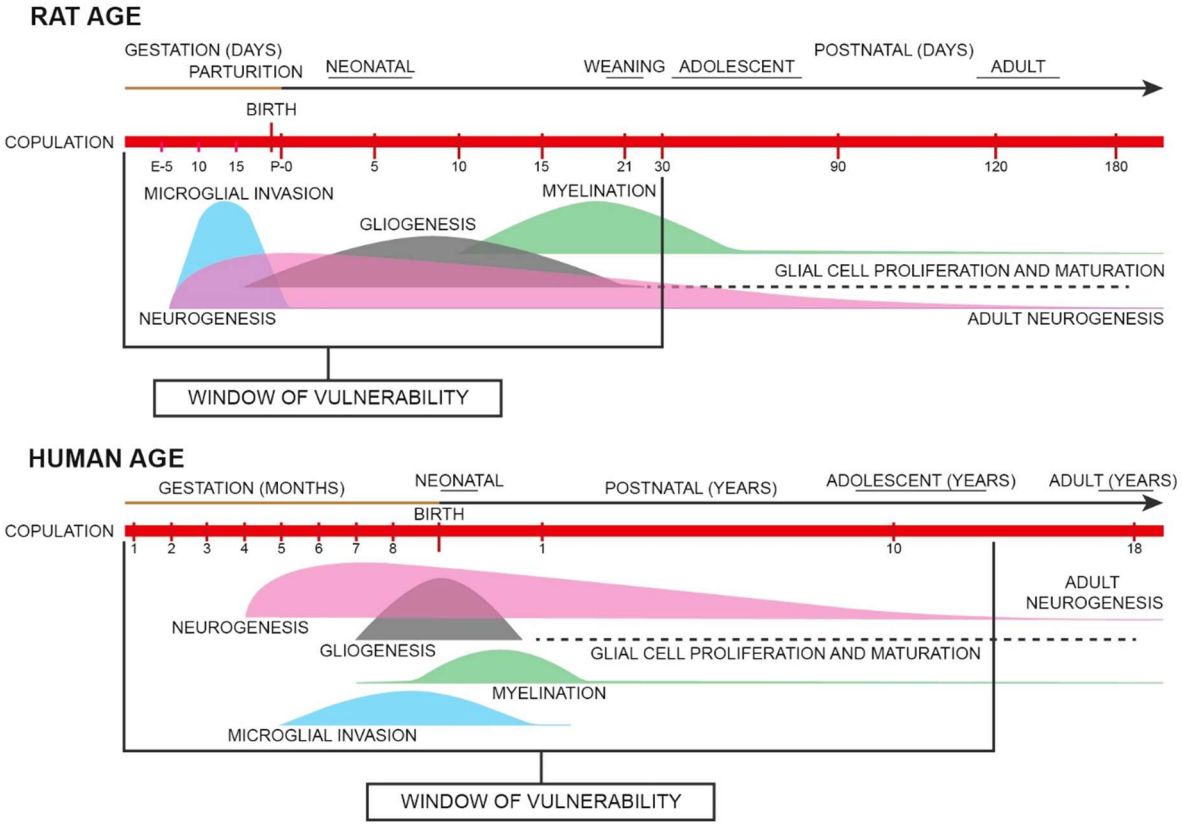

Figure 1.3. Overview of rat and human neurodevelopment
Figure illustrates neurodevelopmental timelines in both rats and humans, beginning from conception through to adulthood as indicated by the red timelines. Critical developmental stages and vulnerability windows are shown encompassing prenatal, neonatal, adolescence and adulthood periods. Key developmental events have been indicated in event peaks, beginning at the initiation of a process and peaking when the process is most dominant and then tailing off when the event ends/or is diminishing in later life. Key events detailed include neurogenesis (pink), gliogenesis (grey), microglial cell invasion (blue) and myelination (green). Windows of vulnerability denote the time period where stress and environment can critically influence these developmental processes. Adapted from Sarkar et al. (2019).

1.2.2. Neurodevelopmental risk factors for schizophrenia

1.2.2.1. Early-life stress (ELS) and adversity

Early-life trauma/adversity, ELS and altered care have all been associated with schizophrenia development. Indeed, abuse and neglect in childhood have been linked to poorer intellectual and social cognition and outcomes in schizophrenia patients (Kilian et al., 2018; Loewy et al., 2011; Rokita et al., 2018; Schalinski et al., 2018). The effect of early-life events has been theorised to work through the 'traumagenic neurodevelopmental' model of schizophrenia in which ELS alters the normal HPA-axis function in children, altering their stress response and ultimately predisposing children to psychosis (Read et al., 2001). *In vivo*, it has been shown that rodent pups receiving reduced maternal care behaviours (MCB) demonstrate increased anxiety and fear alongside decreased cognition (Caldji et al., 1998; Lehmann et al., 1999; Lovic and Fleming, 2004). Molecular changes were also noted following MCB deficits, including robust support for dysregulated HPA-axis response in affected offspring (Caldji et al., 1998; Liu et al.,

1997; Plotsky and Meaney, 1993; Plotsky et al., 2005; van Bodegom et al., 2017). Further studies have also shown altered neurotransmitter signalling pathways (Liu et al., 2000; Vicentic et al., 2006) and immune dysregulation (Catale et al., 2020; Dutcher et al., 2020). Of note, the latter has also been demonstrated in human studies, which have shown a role for systemic cytokine dysregulation, notably elevated IL-6 following ELS, as a biomarker for psychosis development (Khandaker et al., 2014; King et al., 2021; Perry et al., 2021).

1.2.2.2. Pregnancy complications and undernutrition

Several studies have associated low birthweight, premature birth and preeclampsia with increased risk of schizophrenia in offspring (Boksa, 2004; Cannon et al., 2002; Eide et al., 2013; Kunugi et al., 2001). Likewise, prenatal undernutrition, as a result of placental dysfunction or maternal diet, has also been shown to increase schizophrenia risk (Brown and Susser, 2008; He et al., 2018). *In vivo* studies have suggested that one of the primary mechanisms of action is hypoxia and resulting oxidative stress, with perinatal hypoxia in rodents shown to produce schizophrenia-associated behavioural traits (Boksa, 2004; Nicodemus et al., 2008). Prenatal undernutrition in rats has accordingly been shown to associate with similar behavioural deficits and cortical oxidative stress (Allgäuer et al., 2023; Xu et al., 2019). That said, nutrient supply during pregnancy is critical for a range of developmental processes, with restrictive or unbalanced nutrient supply to the developing foetus shown to have marked developmental impacts. One of the most well-studied impacts of nutrient inadequacy relates to folate provision, where folate insufficiency has been robustly associated with neural tube defects, cognitive deficits and psychosis (Brown and Susser, 2008; Irvine et al., 2022; Rubini et al., 2021).

1.2.2.3. Maternal immune activation (MIA)

Early evidence supporting the contribution of maternal infection to schizophrenia came from epidemiological studies demonstrating that schizophrenia incidence increased following influenza epidemics (Adams et al., 1993; Mednick et al., 1988). The key methodological issue for these studies was that the calculated schizophrenia risk was underscored by the timing of an infectious outbreak, rather than corroborated evidence of true maternal infection (Brown and Derkits, 2010). That said, later studies successfully correlated serological maternal antibodies for influenza with up to a three-fold offspring risk of schizophrenia (Brown et al., 2004). Subsequently, several other infectious agents have also been associated with schizophrenia risk, with supporting serological evidence, including *Toxoplasma gondii* (Bo Mortensen et al., 2007) and *herpes simplex virus* (Buka et al., 2008). Additionally, multiple neurodevelopmental disorders (NDDs) have been associated with MIA, including autism spectrum disorder (ASD) and bipolar disorder (BPD), both NDDs with a similar genetic risk profiles to schizophrenia (Atladottir et al., 2010; Canetta et al., 2014). Accordingly, there is now a general consensus for the role of prenatal infection in the development of schizophrenia, though individual infectious agents are still debated (Cheslack-Postava and Brown, 2022) and hence it is proposed that it is the maternal immune response or MIA as opposed to the infectious agent itself that promotes

schizophrenia risk (Akbarian, 2014). The prevailing hypothesis is that maternal infection indirectly affects offspring neurodevelopment through MIA-mediated mechanisms which in turn promote schizophrenia development (Estes and McAllister, 2016; Labouesse et al., 2015b). This concept has been supported in animal models of MIA which report no evidence that administered immune agents (e.g., virus/bacteria) reach the developing foetus (Ashdown et al., 2006; Fatemi et al., 2012) and that infectious mimetics also produce behavioural deficits consistent with NDDs (Ashdown et al., 2006; Harvey and Boksa, 2012; Meyer, 2014). With this in mind, it is thought that cytokines are key in mediating the effect of MIA (Meyer et al., 2009b).

I. The cytokine hypothesis

Infection in pregnant women generates elevated cytokine concentrations in both maternal serum and amniotic fluid (Romero et al., 1989, 1990). Further studies in humans have associated elevated maternal cytokines with impaired cognitive development, anxiety, depression and psychosis risk in exposed children (Allswede et al., 2020; Giollabhui et al., 2019; Nazzari et al., 2020). Such maternally-derived cytokines, notably IL-6 and TNFα, have been demonstrated to cross the placenta, enter the foetal blood circulation and cross the foetal blood brain barrier (BBB; Banks et al., 1991, 1994; Dahlgren et al., 2006; Zaretsky et al., 2004). Cytokines and their receptors are expressed constitutively throughout foetal brain development (Mehler and Kessler, 1997; Mousa et al., 1999) with cytokines shown to function in a range of neurodevelopmental pathways (Deverman and Patterson, 2009). Taken together, these data support a hypothesis whereby MIA induces disturbed cytokine expression which impacts placental and foetal development to induce neuroinflammation, ultimately converging in altered brain developmental trajectory, predisposing affected individuals to pathology (Meyer et al., 2009b).

II. The SARS-CoV-2 pandemic

SARS-CoV-2 infections have been shown to generate a systemic immune response, including the production of pro-inflammatory cytokines IL-6 and TNFα (Pedersen and Ho, 2020). Pregnant women are among the high-risk category for SARS-CoV-2 infection, demonstrating elevated cytokine responses even with asymptomatic presentation (Garcia-Flores et al., 2022; Wastnedge et al., 2021) with limited evidence of vertical SARS-CoV-2 transmission (Dube and Kar, 2020). However, placentas from exposed pregnancies have demonstrated inflammatory properties (Argueta et al., 2022; Garcia-Flores et al., 2022) aligning with the cytokine hypothesis for MIA. It is estimated that up to 20 million babies per year could have been exposed globally to maternal SARS-CoV-2 infection *in utero* (Dubey et al., 2022; Shook et al., 2022) with emerging evidence already suggesting that exposed children have increased risk of neurodevelopmental impairment (Shook et al., 2022; Shuffrey et al., 2022). These data therefore suggest a population-wide increased risk of MIA-associated NDDs, including schizophrenia, in the coming years. Hence our understanding of the mechanisms which link MIA and altered neurodevelopment are critical.

1.2.3. The role of the placenta

The placenta forms during pregnancy through interactions between both embryonic (from the chorionic sac) and maternal (from the endometrium) derived cells and is essential for normal foetal development (Gude et al., 2004). A placental exchange barrier consisting of distinct cellular layers separates foetal and maternal blood flows of the fetoplacental and uteroplacental circulations respectively (Bryant-Greenwood, 1998). The placenta performs several functions required to support foetal growth and development including the transport of essential nutrients and oxygen, protection from infection and xenobiotics, removal of foetal waste products and hormone secretion. Placental function also adapts during gestation to meet foetal developmental and growth demand and hence perturbations to placental development and function can be detrimental to the foetus (Gude et al., 2004). The placenta also protects the foetus against the transfer of microbial infections and provides the foetus with maternal immunoglobulin antibodies (Palmeira et al., 2012).

The placenta has a unique structure comprising distinct structural zones. Considering first the rodent placenta, there are three clear morphological zones, each with different functions, including: the maternal decidua, across which the spiral arteries deliver maternal blood flow, the junctional zone (JZ), important in endocrine functions throughout pregnancy and the labyrinth zone (LZ) containing the placental villi and the site of transfer of nutrients between maternal and foetal blood flows (Figure 1.4A; Rai and Cross, 2014; Soares et al., 2012). The human placenta, by contrast, has three analogous structural zones comprising an outer decidua layer, containing the maternal spiral arteries which deliver the maternal blood flow; the basal plate (considered similar to the JZ in rodents) and a collection of chorionic villi, which, though less intricately dense than the rodent LZ, also functions in nutrient transfer between maternal and foetal blood flows to mediate maternofoetal nutrient exchange (Figure 1.4B; Gude et al., 2004; Rai and Cross, 2014; Soares et al., 2012). Classification of placentation is based on the number of cellular layers separating the maternal and foetal blood circulations (Dilworth and Sibley, 2013; Gude et al., 2004). Human and rodent placentas are both classified as haemochorial, with maternal blood in direct contact with the foetal trophoblast cell layer (Enders and Blankenship, 1998; Soares et al., 2012). However, while in humans a single trophoblast layer (haemomonochorial) separates the maternal and foetal blood flows, in rodents, by contrast, there are three (layers I, II and III) distinct trophoblast layers (haemotrichorial) between the two circulations (Figure 1.5; Gude et al., 2004; Rai and Cross, 2014; Soares et al., 2012). Layer I is composed of mononuclear sinusoidal trophoblast giant cells in direct contact with the maternal blood flow with large fenestrations between these cells, thought to allow unrestrictive transport of nutrients through this layer (Figure 1.5; Dilworth and Sibley 2013). By contrast, layers II and III are composed of syncytiotrophoblast cells, constituting the main, selective barrier to nutrient transfer between maternal and foetal blood flows in the rodent (Figure 1.5; Dilworth and Sibley 2013; Soares et al., 2012).

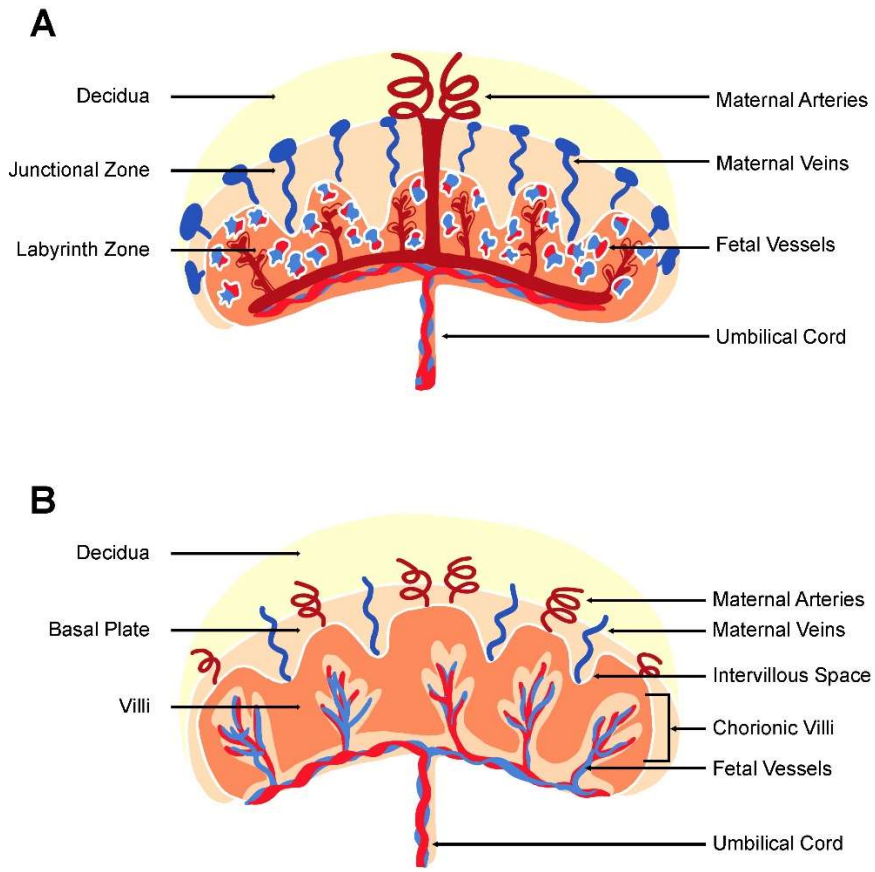

Figure 1.4. Schematic comparison of rodent and human placental structure
A. Schematic of rodent placenta depicting the three structural zones, from top (maternal side) to bottom (foetal side): decidua, junctional zone (JZ) and labyrinth zone (LZ). The spiral arteries can be seen entering the placenta at the decidua, filling the maternal blood spaces surrounding the placental villi of the LZ containing the foetal capillaries. **B.** Schematic of human placenta, from top (maternal side) to bottom (foetal side): decidua, basal plate, villi. The spiral arteries can be seen entering the placenta via the decidua to fill the intervillous space with maternal blood in direct contact with the placental villi containing the foetal capillaries. Adapted from Rai and Cross (2014).

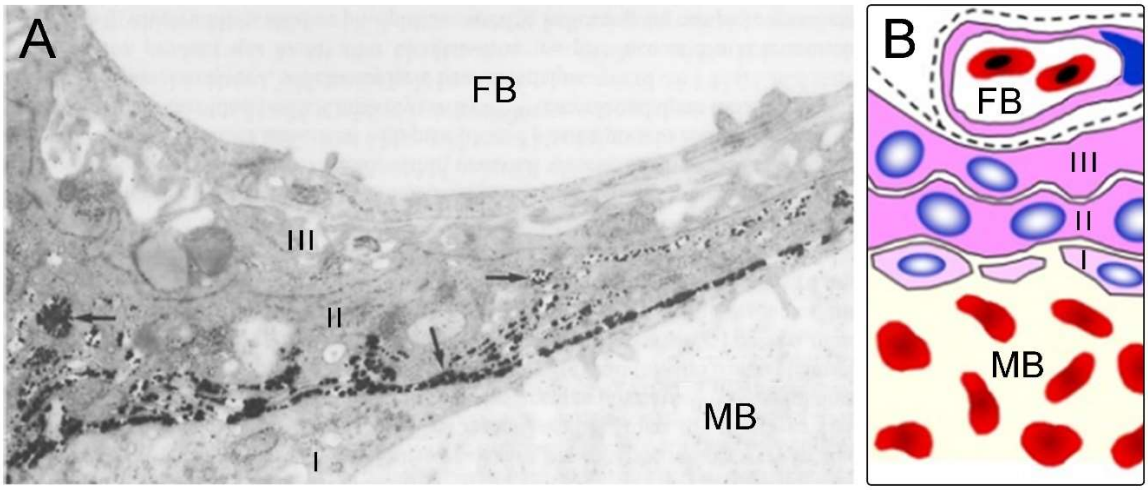

Figure 1.5. Haemotrichorial placenta
A. Electron microscopy image of fixed rat haemotrichorial placenta. I, II and III indicate the three trophoblast layers. Staining of alkaline phosphatase in the rat placenta, showing localisation product (arrows) between trophoblast layers I and II, indicating the first main barrier for maternofoetal nutrient transport resides at the maternal-facing plasma membrane of layer II. Adapted from Glazier et al. (1990). **B.** Schematic representation of rat haemotrichorial placenta showing three trophoblast layers I, II and III. As depicted, layer I is composed of sinusoidal trophoblast giant cells with intercellular spaces, whereas layers II and III are syncytiotrophoblast layers (syncytial multinuclear cellular layers with no lateral boundaries). Adapted from Furukawa et al. (2014). Abbreviations: FB, foetal blood within the foetal capillary; MB, maternal blood space containing maternal blood.

Despite some structural differences between rodent and human placentas, there are significant similarities, including mechanistic physiology (Enders and Blankenship 1998), transport capabilities (Cramer et al., 2002; Glazier et al., 1996; Novak and Beveridge 1997) and conservation of genes involved in regulating placentation (Soares et al., 2012).

The placenta is a complex and essential organ for normal foetal development, critical for the provision of nutrients to support normal growth. With this in mind, it has been suggested that stress and MIA can impact on the placenta in such a way, most likely through alteration of its transport and metabolic functions, to disrupt foetal neurodevelopment. There is supportive evidence for this mechanistic framework. MIA has been shown to induce placental morphological changes, including increased inflammatory cells and loss of LZ morphology (Fatemi et al., 2012) and elevated cytokine concentrations (Mueller et al., 2019). Further, it has been shown that cytokines, particularly IL-6, can transverse the placenta to the foetus (Dahlgren et al., 2006; Zaretsky et al., 2004) thereby suggesting one mechanism by which MIA can impact directly on foetal neurodevelopment. Further, we and others have shown that MIA induces significant changes in expression and function of critical amino acid transporters (Kowash et al., 2022; McColl and Piquette-Miller, 2019). Likewise, transcriptomic profiling of the placenta following influenza-induced MIA has demonstrated changes in placental gene expression related to functions in apoptosis, hypoxia, inflammation/immune response and psychosis (Fatemi et al., 2012). Together, these studies suggest functional changes to the placenta in the context of MIA which could impact on the developing foetal brain. Critically, several schizophrenia risk genes have been suggested to be related to normal placental function (Ursini et al., 2017). These risk loci also appear to associate with pregnancy complications and hypoxia, supporting the role of the placenta as a mediator of prenatal challenges that increase risk of NDDs (Ursini et al., 2017). Of note, there is also evidence that these placental changes act in a sex-specific way (Bronson and Bale, 2016). In normal pregnancies there are clear sex differences in the placenta, with transcriptomic profiling showing differences in expression of several genes between male and female offspring (Buckberry et al., 2014). Particularly, the placental enzyme 11β-HSD, which works to protect the foetus from the majority of maternal cortisol and protect offspring from maternal stress, is expressed more highly in male placentae than female placentae (Hirasawa et al., 2000). Reduction in the placental expression of this enzyme affects normal foetal development and is seen in both growth restriction and preeclampsia pregnancies, two prenatal risk factors for schizophrenia (Schoof et al., 2001; Shams et al., 1998). Finally, placental transport function will also be crucial for the provision of foetal biosynthetic precursors and foetal methylation capacity and hence foetal epigenetic patterning. The essential nutrient folate, as well as methionine, required for cellular methylation pathways, are actively transported to the foetus by the placenta (Antony, 2007; Solanky et al., 2010; Tsitsiou et al., 2009) and deficiencies in folate transport to the foetus are associated with birth defects and brain malformations (Refsum, 2001) and impaired amino acid transport is associated with foetal growth restriction (Glazier et al., 1997).

1.2.4. The role of epigenetics

Waddington (1956, 2012) first proposed the concept of epigenetics, suggesting a mechanism through which environmental factors might induce heritable phenotypic alterations. Epigenetics is now commonly defined as mitotically/meiotically heritable mechanisms which regulate changes in gene expression that do not entail changes to the DNA sequence (Holliday, 1994; Wu and Morris, 2001). Epigenetic mechanisms can be broadly divided into three categories: DNA modifications, histone modifications and non-coding RNA (ncRNA), which collaboratively regulate gene expression (Figure 1.6). Epigenetic mechanisms are particularly important for regulating tissue-specific transcriptomes (Roadmap Epigenomics Consortium et al., 2015). Eukaryotic DNA is packaged into a nucleoprotein structure called chromatin, the basic unit of which is the nucleosome, constructed from DNA (~147bp) wrapped around a core histone octamer. The regulation of chromatin structure effects gene expression by enabling or inhibiting access of transcription factors to regulatory elements, forming repressive heterochromatin (in which gene expression is inhibited) and active euchromatin (in which gene expression is enabled or potentially enabled; Lawrence et al., 2016; Quina et al., 2006).

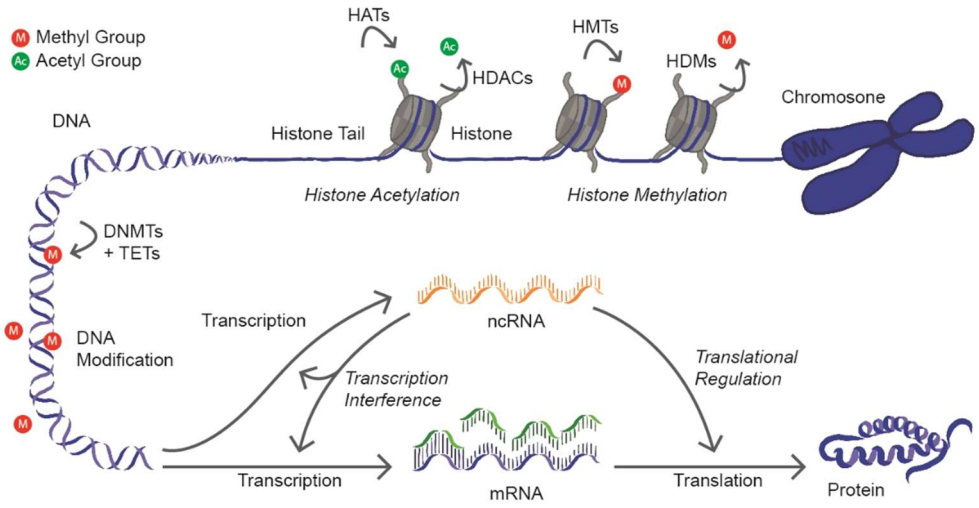

Figure 1.6. Chromatin structure and epigenetic regulatory mechanisms
The chromosome is formed from repeating nucleosome units (DNA wrapped around histone octamers). Histone modifications occur on the histone protein tails, most commonly on lysine residues. The most prevalent modifications are histone methylation and acetylation, established by histone acetyl (HATs) and methyl transferases (HMTs) and removed by histone deacetylases (HDACs) and demethylases (HDMs). DNA modifications are direct modifications, typically on cytosine bases, within the double stranded DNA helix, established by DNA methyltransferases (DNMTs) and removed by ten-eleven translocation (TET) enzymes. The final epigenetic mechanisms is non-coding RNA (ncRNA). ncRNA is transcribed from DNA alongside messenger RNA (mRNA). ncRNA regulates gene expression primarily post-transcriptionally through transcriptional interference and regulation of translation. Adapted from Joosten et al. (2018).

1.2.4.1. Overview of epigenetic mechanisms

I. DNA methylation (DNAm)

DNAm is achieved through addition of a methyl residue to the 5th position of cytosine bases usually located adjacent to a guanine (Roy and Weissbach, 1975), referred to as cytosine-guanine dinucleotides (CpGs). It is estimated that 70-80% of all CpG sites are methylated in

human tissues with the brain being one of the most highly methylated tissues (Ehrlich et al., 1982; Illingworth et al., 2010; Meissner et al., 2008). The majority of CpG sites are located in a clustered fashion within so-called CpG islands (CGIs), usually ~1 kilobase (kb) long (Bird et al., 1985). These islands are normally hypomethylated and lie outside nucleosome structures, associated with transcription start sites (TSS) and promoters which regulate nearby genes. Hence CGIs are available for interaction with regulatory proteins and thereby modulate gene expression (Bird et al., 1985; Saxonov et al., 2006; Tazi and Bird, 1990) with CGI and promoter methylation usually leading to inhibition of gene expression (Mohn et al., 2008). Multiple mechanisms enable this, including inhibition of transcription factor binding, recruitment of repressive methyl-binding proteins and chromatin compaction (Moore et al., 2013). Of note, while DNAm was initially believed to occur only at CpG sites, genome-wide mapping studies have demonstrated that methylated cytosines can also occur at non-CpG sites, where the methyl-cytosine is adjacent to a base other than guanine (CpH-sites; Lister and Ecker, 2009). CpH methylation is highly tissue-specific but is present at high levels in the brain and is enriched in promoters and gene bodies (Christopher et al., 2017; Guo et al., 2014). DNAm patterns are established by a family of enzymes known as DNA methyltransferases (DNMTs) which catalyse the transfer of a methyl group, from the donor S-adenosyl methionine (SAM), onto cytosine residues (Christopher et al., 2017; Moore et al., 2013). DNMTs comprise two groups. The first group, *de novo* DNMTs, establish methylation patterns in previously non-methylated DNA (DNMT3a and DNMT3b; Figure 1.7A) while the second group, maintenance DNMT, accurately copies DNAm patters within hemi-methylated DNA during cellular divisions (DNMT1; Figure 1.7B). A final DNMT, DNMT3L, lacks the typical catalytic domain and is thought to instead direct the activity of *de novo* DNMTs (Aapola et al., 2000; Cedar and Bergman, 2009).

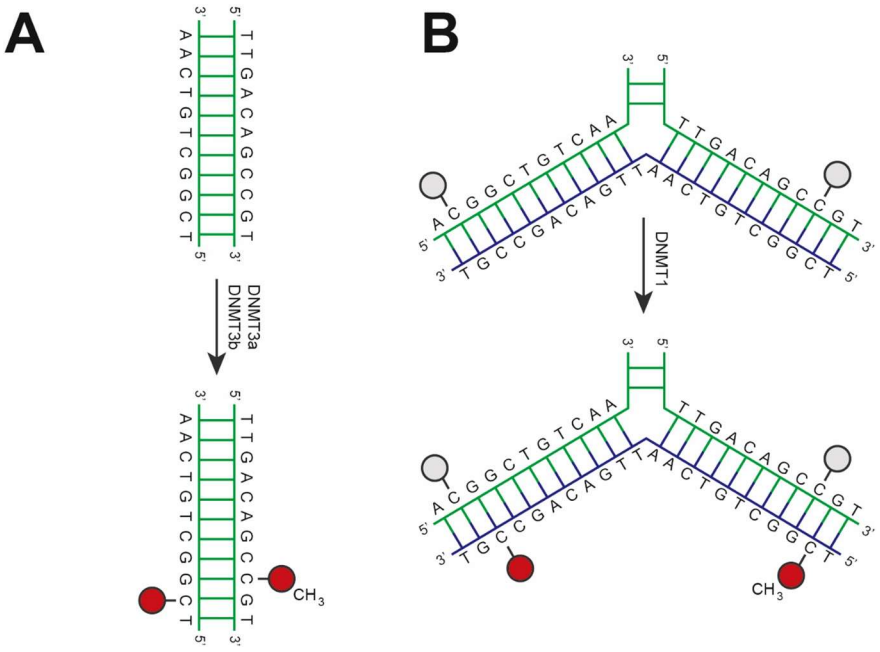

Figure 1.7. DNA methylation (DNAm) by DNA methyltransferases (DNMTs)
A. DNMT3a and DNMT3b add a methyl group to the 5th position of previously non-methylated cytosine bases to establish *de novo* methylation. **B.** DNMT1 copies previous DNAm patterns during DNA replication and favours hemi methylated DNA. Adapted from Moore et al. (2013).

DNA demethylation can either be active, using enzymes that catalyse the removal of methyl groups, or passive, through loss of fidelity of DNMT1 activity (Bhutani et al., 2011; Monk et al., 1991). Active DNA demethylation proceeds through several enzymatic processes whereby 5-methyl-cytosine (5mC) is deaminated and oxidised to regenerate an unmodified cytosine base (Bhutani et al., 2011; He et al., 2011; Ito et al., 2011).

II. Histone modifications

Histone protein post-translational modifications (PTMs), primarily within the N-terminal tails, affect the structure and function of chromatin and thus gene expression (Jenuwein and Allis, 2001). To date >30 residues exist within each of the four histone tails that are known have PTMs (Figure 1.8) including: phosphorylation, ubiquitination, carbonylation and ADP-ribosylation (Bannister and Kouzarides, 2011; Jenuwein and Allis, 2001; Lawrence et al., 2016). Arguably the most studied PTMs are histone methylation and acetylation, the latter of which is catalysed by histone acetyl transferases (HATs) and histone deacetylases (HDACs) and the former by histone methyltransferases (HMTs; Bannister and Kouzarides, 2011; Rice and Allis, 2001). The mechanism by which histone PTMs act are twofold; through electrostatic interactions between the histone PTMs and DNA to alter chromatin compaction and through interaction with regulatory proteins which in turn influence chromatin structure/gene expression (Figure 1.6; Bannister and Kouzarides, 2011; Lawrence et al., 2016; Rice and Allis, 2001). Of note, it has also been shown that histone tail PTMs can directly influence the establishment of DNAm patterns through interaction with and modulation of the DNMT enzymes (Cedar and Bergman, 2009; Fu et al., 2020).

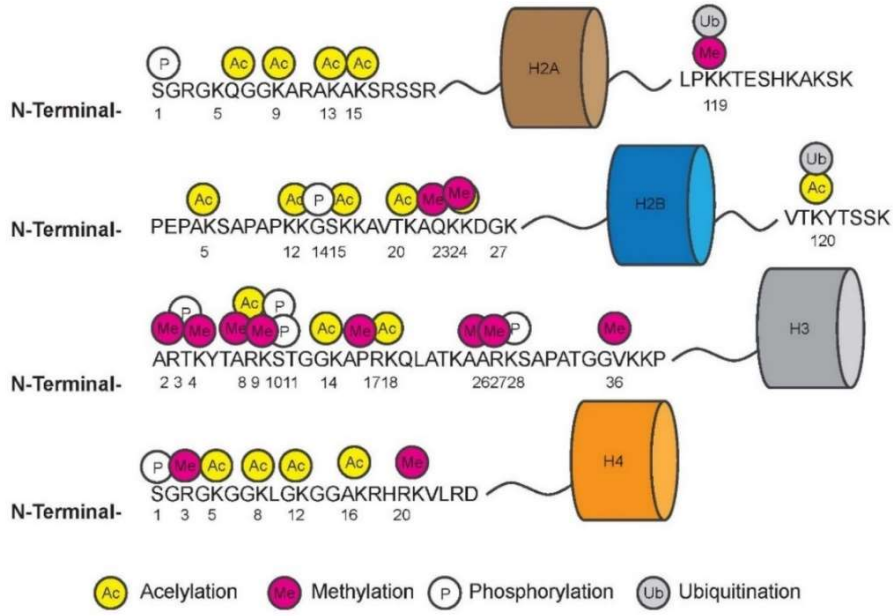

Figure 1.8. Histone post-translational modifications (PTMs)
Histone PTMs are added to amino acid residues in the N-terminal tail of histone proteins in the nucleosome. Marks can co-ordinate active or repressed transcription. Several modifications are found in each histone tail. Shown in the figure are acetylation, methylation, phosphorylation and ubiquitination.

III. Non-coding RNA (ncRNA)

ncRNAs are divided into two groups: long ncRNA and short ncRNA (Huang et al., 2013). Short ncRNAs can further be subdivided into short interfering RNA (siRNA), P-element induced wimpy testis-interacting RNAs (piRNA) and microRNA (miRNA; Huang et al., 2013). Within these groups, miRNAs are perhaps the most well categorised and most widely expressed in mammalian tissues, comprising nucleotide structures of ~22bp. They function by binding to complementary messenger RNA (mRNA) transcripts and regulating gene expression by impacting transcript and translation interference, usually via promoting transcript cleavage and degradation (Figure 1.6; Bartel, 2004; Catalanotto et al., 2016; Huang et al., 2013). Studies evaluating miRNA function in human tissues have estimated that >50% of the total human transcriptome is regulated by miRNAs (Brennecke et al., 2005; Catalanotto et al., 2016; Krek et al., 2005; Xie et al., 2005). Further, DNAm and histone modifications also, in turn, regulate ncRNA expression much as they do mRNA (Barski et al., 2009; Han et al., 2007), while ncRNA molecules directly influence DNA and histone modification patterns via recruitment of DNMTs and histone modifier proteins to distinct genomic regions (Holz-Schietinger and Reich, 2012; Peschansky and Wahlestedt, 2014).

1.2.4.2. The environment and epigenetic programming of disease

Epigenetic mechanisms have become of particular interest in recent years owing to the fact that they mediate interactions between environmental stressors and changes in gene expression (Fraga et al., 2005; Wong et al., 2010). Epigenetic programming describes the erasure and re-establishment of epigenetic marks (Messerschmidt et al., 2014; Morgan et al., 2005). Accordingly, it has been suggested that epigenetic programming plays a role in the DOHaD hypothesis, underscored by the idea that prenatal and early-life environment induces adaptive epigenetic programming events which predispose individuals to later-life disease (Bianco-Miotto et al., 2017). Initial proof of concept for this hypothesis in NDDs arose from *in vivo* ELS models with pivotal work demonstrating that deficient MCB correlates with altered promoter methylation and histone modifications of critical genes in offspring brains, alongside concomitant changes in gene expression and NDD-like behavioural traits. These genes included *Bdnf* and *Nr3c1* (encoding the GR), involved in neuron survival and stress responses, respectively (Meaney, 2001; Weaver et al., 2004). These early studies were followed by numerous *in vivo* studies supporting the impact of prenatal or ELS on epigenetic changes in the brain, particularly at stress-response genes (Catale et al., 2020; Fitzgerald et al., 2021; Mueller and Bale, 2008; Murgatroyd et al., 2009; Wu et al., 2014). Such findings have since been corroborated in human studies evaluating methylation changes following early-life adversity or trauma (Essex et al., 2011; Houtepen et al., 2016; Suderman et al., 2012; Wiegand et al., 2021).

1.2.4.3. Epigenetics in the brain

Epigenetic mechanisms are known to be essential for normal brain development and function. A number of human disorders, with perturbed brain function, originate from mutations in genes critical for normal epigenetic regulation (Table 1.1; Jakovcevski and Akbarian, 2012). These findings have been supported by *in vivo* genetic manipulation of epigenetic modifiers which produce deficits in learning and memory consistent with human diseases (Table 1.1). Likewise, pharmacological inhibition of DNMTs and HDACs have been shown to be detrimental and beneficial respectively, for normal learning and memory processes (Miller et al., 2010; Morris et al., 2010).

There are key epigenetic differences between the brain and other organs. Indeed, the brain shows distinct epigenetic patterns compared to other tissues, including overall hypermethylated DNA and high ncRNA expression (Ehrlich et al., 1982; Guo et al., 2014; Qureshi and Mehler, 2012). Rather uniquely, mature neurons lack mitotic activity and, as a result, fail to maintain stringent regulation of epigenetic marks creating vulnerability to epigenetic dysfunction (Christopher et al., 2017). Likewise, expression of epigenetic modifying enzymes (e.g., DNMTs) persist in adult neurons whereas they are usually downregulated in other tissues, implying a maintained functional role for epigenetics in the brain (Feng et al., 2005; Inano et al., 2000; Sendžikaitė et al., 2019; Watanabe et al., 2006). There is also critical evidence for the ongoing role of epigenetics in neurodevelopment. Longitudinal genome-wide methylation profiling in both human and mouse corticies demonstrated distinct differences between foetal and young adult stages of development (Lister et al., 2013) with brain methylation patterns, as with other tissues, predictive of age (Grodstein et al., 2021). Likewise, profiling mouse brain miRNA expression across development has suggested 20% of miRNAs undergo significant changes of expression (both down and up-regulation) over the developmental time-course (Krichevsky et al., 2003). There are also key cell-type specific epigenetic patterns in the brain (Kadriu et al., 2012), with thousands of differentially methylated genes between neuronal and non-neuronal cells and notably higher DNAm in oligodendrocytes than GABAergic or glutamatergic neurons (Kozlenkov et al., 2014, 2018; Lister et al., 2013).

In line with the distinctive epigenetic patterns in the brain throughout development, there are also functional roles for epigenetics throughout neurodevelopment. During early neurodevelopment, epigenetic modifications regulate cell fate decisions, including neurogenesis and gliogenesis (Jobe and Zhao, 2017; Park et al., 2022; Shirvani-Farsani et al., 2021), while later in neurodevelopment, DNAm and histone remodelling occurs in line with synaptogenesis and ongoing synaptic plasticity. It has been suggested this attributes a role for epigenetics in memory formation and long-term potentiation (LTP) by inducing synaptic transcriptome changes (Creighton et al., 2020; Levenson et al., 2006; Lister et al., 2013).

Table 1.1. Gene mutations of epigenetic modifiers and resulting neurological phenotypes

Epigenetic modifier	Associated Epigenetic Mechanism	Human disease	Rodent phenotype	References
DNMT1	DNAm enzyme	Heterozygous mutation in the *DNMT1* gene causes autosomal dominant cerebellar ataxia, deafness and narcolepsy (ADCADN) characterised by narcolepsy/cataplexy, sensorineural deafness and dementia, optic atrophy, sensory neuropathy, psychosis and depression.	KO was anti-depressive and anxiolytic in mice.	Moghadam et al., 2014; Morris et al., 2016.
DNMT3A	DNAm enzyme	Heterozygous mutation causes Tatton-Brown-Rahman syndrome, characterised by macrocephaly, overgrowth and impaired intellectual development.	KO consistently demonstrates learning and memory deficits.	Morris et al., 2016; Tatton-Brown et al., 2018.
MECP2	Major DNAm binding protein	LOF mutations result in the NDD, Rett syndrome, characterised by impairments in language and coordination and repetitive movements.	KO mice display a phenotype comparable to that observed in Rett syndrome patients.	Amir et al., 1999; Guy et al., 2001.
HDAC2	Histone de-acetylating enzyme	-	KO in mice causes enhanced fear and distress. Overexpression causes reduced performance in cognition/working memory.	Guan et al., 2009; Morris et al., 2013.
HDAC4	Histone de-acetylating enzyme	Heterozygous mutation results in Neurodevelopmental disorder with central hypotonia and dysmorphic facies (NEDCHF), characterised by global developmental delay, impaired intellectual development, seizures.	KO mice show increased anxiety, deficient learning and memory.	Kim et al., 2012; Wakeling et al., 2021.
DICER1	Enzyme, critical in miRNA biosynthesis	-	KO disrupts brain development, promoting microcephaly and delayed myelination with neurodevelopmental phenotypes.	Davis et al., 2008; Dugas et al., 2010.
DGCR8	Microprocessor complex subunit, involved in miRNA biosynthesis	-	Heterozygotic mice have disrupted cortical miRNA expression correlated with decreased postnatal excitatory signalling with neurodevelopmental phenotypes.	Schofield et al., 2011.

Abbreviations: LOF, loss of function; KO, knock-out

1.2.4.4. Epigenetics and schizophrenia

Studies in the epigenetics of schizophrenia have supported dysregulated epigenetic patterns in the brain (Akbarian et al., 2005; Beveridge and Cairns, 2012; Chen et al., 2021a; Pries et al., 2017; van Dongen and Boomsma, 2013), however DNAm is perhaps the most studied mechanism (Villicaña and Bell, 2021). The first study in DNAm patterns in schizophrenia (Mill et al., 2008), was followed by an exponential increase in subsequent studies which have broadly supported genomic hypomethylation in schizophrenia patients (Li et al., 2018a; Pries et al., 2017; Wan et al., 2019). Genome-wide methylation studies in schizophrenia have collectively identified thousands of differentially methylated loci, both genic and intergenic. Of note, findings from these studies are often sex-specific (Adanty et al., 2022; Wan et al., 2019). While meta-analyses have shown lack of replication between studies, there have been some inter-study overlapping genes, including *GAD1, RELN, BDNF* and *COMT* (Chen et al., 2021a; Pries et al., 2017). When trying to unravel the function of epigenetic variants in schizophrenia, one study mapping prefrontal cortex (PFC) DNAm changes in schizophrenia patients discovered that schizophrenia-associated CpG sites were found at loci which function in prenatal-postnatal developmental transition (Jaffe et al., 2016), suggesting a role for DNAm patterns in the genesis of neurodevelopmental abnormalities in schizophrenia. In line with this, several studies have evidenced disturbed epigenetic aging in schizophrenia brains (Akbarian, 2020), although with mixed outcomes as to whether there is accelerated (Higgins-Chen et al., 2020; Jeremian et al., 2022b; Zhang et al., 2020b), delayed (Wu et al., 2021), or no changes (Hannon et al., 2021) found. However, some of these differences may be explained by the effect of antipsychotics on DNAm patterns (Burghardt et al., 2020; Higgins-Chen et al., 2020). Moreover, genetic variants, particularly SNPs have been shown to induce changes in the normal epigenetic patterns, with genome and epigenome variants thought to play an interactive role in predisposition to disease (Do et al., 2017; Mangnier et al., 2022; Zhi et al., 2013).

DNAm changes in schizophrenia have also been associated with particular symptoms, such as cognitive performance and psychosis (Hannon et al., 2022; Ho et al., 2020) alongside other factors such as suicide risk (Jeremian et al., 2022a) and treatment resistance (Hannon et al., 2021; Lu et al., 2023). Overall, these data suggest that DNAm contributes causally to schizophrenia pathogenesis. Accordingly, individual candidate genes have begun to be functionally validated. For example, *RELN*, one of the most robust epigenetically associated genes in schizophrenia, has shown promoter hypermethylation significantly reduced Reelin expression (Abdolmaleky et al., 2005; Guidotti et al., 2016; Nabil Fikri et al., 2017).

1.3. Preclinical modelling for schizophrenia

The current lack of efficacious therapeutic approaches, which manage all symptom domains, owes for the most part to the complex and multifactorial nature of schizophrenia aetiology (Taber et al., 2010; Thapar et al., 2017). Understanding the molecular mechanisms that promote

schizophrenia pathology are critical in the development of effective therapeutic strategies. Preclinical models for schizophrenia are hence an invaluable tool for the discovery of such neuropathological changes and identification of novel therapeutic targets and biomarkers (Bale et al., 2019; Białoń and Wąsik, 2022; Cadinu et al., 2018; Jones et al., 2011; Winship et al., 2019). Several preclinical models for schizophrenia exist, including genetic knock-out (KO) models (e.g., *Disc1* KO), pharmacological models (e.g., PCP models) and neurodevelopmental models (e.g., MIA models). That said, to be considered effective for application to preclinical research, the model needs to be translatable to the human disease, often requiring extensive validation. Indeed, there are distinct validity criteria that should be considered, historically divided into three groups: face, construct and predictive validity (Figure 1.9; Mattei et al., 2015; Meyer and Feldon, 2010, 2012; Willner, 1986). However, a particular caveat of these validation criteria is that animal models are often designed to recapitulate a narrow spectrum of the disease which can restrict the advancement of novel drugs targets (Garner, 2014). Hence, the 'construct' validity should consider both 'pathogenic' (does the model mimic the developmental progression of the disease) and 'mechanistic' (does the design of the model produce biological changes comparable to those seen in the disease) validity.

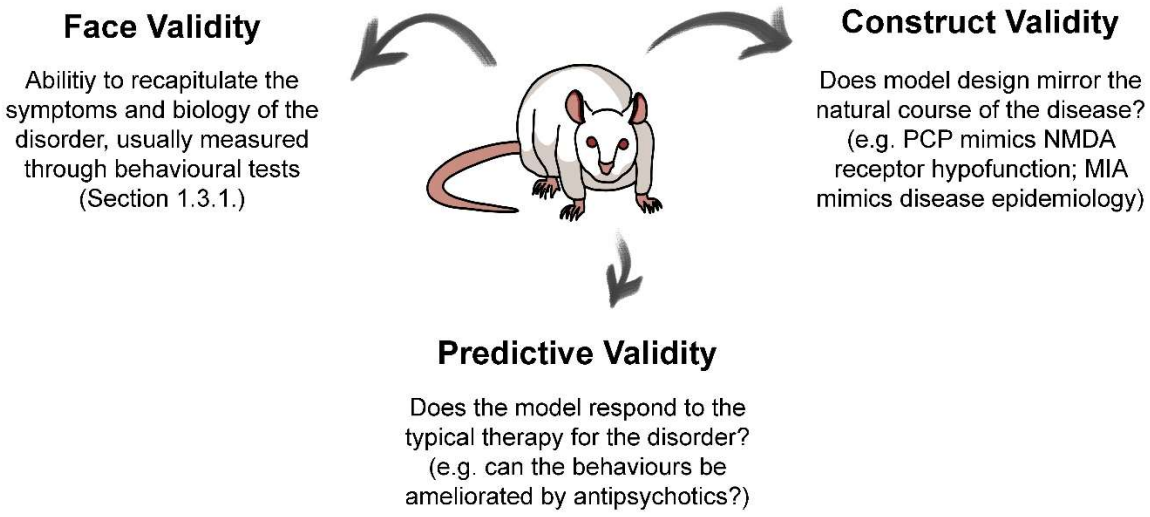

Figure 1.9. Preclinical model validity
Figure summarises the three domains of preclinical model validity: face, construct and predictive validity.

1.3.1. Key considerations

1.3.1.1. Rodent behaviours and their clinical relevance

Despite their preclinical necessity, rodent models are unable to demonstrate an exhaustive set of symptoms for psychiatric disorders, in particular traits such as hallucinations/psychosis (Low and Hardy, 2007). Accordingly, preclinical rodent models for schizophrenia typically aim to model a restricted spectrum of symptoms, measured through behavioural tests (Bergdolt and Dunaevsky, 2019; Meyer and Feldon, 2010). Various behavioural tests exist to measure deficits

comparable to discrete symptom domains (Table 1.2). Of note, while many preclinical studies favour the use of mice, rats are larger and show less conspecific aggression and hence are usually better for use in cognitively-demanding and social tasks (Ellenbroek and Youn, 2016; Netser et al., 2020).

Table 1.2. Selected rodent behaviour tests used in preclinical schizophrenia models

Behavioural Task(s)	Behavioural measure	Schizophrenia symptom domain
Amphetamine-induced locomotion	Substance dependence	Positive
Attentional set-shifting task (ASST)	Cognitive flexibility, learning and memory, executive function	Cognitive
Elevated plus maze (EPM) **Zero maze**	Anxiety, avoidance	Negative
Forced swim test (FST)	Depressive behaviour	Negative
Latent inhibition (LI)	Sensory information processing, attention	Cognitive/Positive
Light-dark box	Anxiety	Negative
Morris water maze (MWM)	Spatial learning and memory	Cognitive
Novel object recognition (NOR)	Learning and memory, episodic memory	Cognitive
Open field (OF)	Anxiety, locomotion	Positive/Negative
Prepulse inhibition (PPI)	Sensory information processing, attention	Cognitive/Positive
Radial arm maze (RAM) **T-maze/Y-maze**	Spatial learning and memory, working memory	Cognitive
Social interaction (SI) **Social preference** **Social novelty (SN)**	Social memory, social preference, anxiety	Cognitive/Negative
Sucrose preference	Depression, anhedonia	Negative
5-choice task	Attention	Cognition

Task summaries extracted from Hånell and Marklund, 2014; Lezak et al., 2017; Sousa et al., 2006; Tanila, 2018; Tanimizu et al., 2017; van den Buuse, 2010.

1.3.1.2. Extrapolating developmental timelines

Rodent models are particularly useful in NDD research by enabling longitudinal analysis across a developmental time course (Meyer and Feldon, 2010). However, it is important to consider extrapolating neurodevelopmental timelines between rodents and humans. For example, rodent gestation is estimated to contribute only to human trimesters one and two, with the third trimester relative to the first rodent postnatal week (Figure 1.3; Bayer et al., 1993; Clancy et al., 2001, 2007; Sarkar et al., 2019). Further, there are also temporal differences between rodent species, with developmental events in mice occurring ~2 days earlier than rats (Clancy et al., 2001, 2007). These differences should hence be considered when designing neurodevelopmental preclinical models for schizophrenia. Indeed, developmental models (e.g., MIA and ELS models) have shown that the timing of insults produce differences in behavioural and molecular phenotypes which can make extrapolating data between rodents and humans challenging (Meyer et al., 2007).

1.3.2. Preclinical modelling for MIA: an overview of current findings

Despite growing support for a role of MIA in schizophrenia aetiology and the emerging evidence following the SARS-CoV-2 pandemic, our ability to study the impact of MIA in humans remains limited, due to the protracted timeline of the disease, ethical considerations and methodological challenges (Bale et al., 2019; Dubey et al., 2022; Massrali et al., 2022). This prevents clear understanding of mechanisms which mediate risk between MIA and offspring outcomes. Hence, rodent models of MIA are invaluable for the investigation of this paradigm and, ultimately, for identifying mechanisms and loci of dysfunction for potential new therapies (Meyer and Feldon, 2010). Accordingly, the past 30 years have seen a dramatic increase in MIA model research.

1.3.2.1. Rodent models for MIA

MIA models are designed to mimic epidemiological studies in humans, hence, common models induce MIA via influenza, lipopolysaccharide (LPS) and polyinosinic:polycytidylic acid (poly(I:C)) at a prespecified window during rodent gestation (Meyer and Feldon, 2010, 2012; Reisinger et al., 2015). Offspring from these pregnancies are then assessed for behavioural (Table 1.2) and biological changes, including morphological and molecular changes (Woods et al., 2021).

I. Influenza models

The first MIA model was created by infecting pregnant mice with active influenza virus, with the objective of inducing a suitable immune response (Mattei et al., 2015; Meyer, 2013; Reisinger et al., 2015). Alongside behavioural alterations (Table 1.3), several biological changes were observed in the offspring, representative of those seen in schizophrenia patients (Fatemi et al., 1998a, 1998b, 2012), demonstrating the validity of the model. However, while the use of the influenza virus has the positive attribute of directly recapitulating human infection, it requires use of a live pathogen and hence warrants rigorous health and safety considerations and limits control over length and potency of the generated immune response (Reisinger et al., 2015). Consequently, the use of alternative immune stimulants with better immuno-safety have become popular amongst laboratories, commonly applying LPS and poly(I:C) to mimic bacterial and viral infections, respectively. A main advantage these mimetics is that they produce distinct but short-lived immune responses, allowing for precise control of temporal immune activation and dose-dependency (Cunningham et al., 2007; Meyer et al., 2005). However, as they elicit a restricted immune response, they may not completely recapitulate the entirety of the MIA phenotype (Reisinger et al., 2015). That said, the demonstration of a range of behavioural and biological phenotypes displayed by exposed offspring supports their utility as MIA model alternatives (Meyer et al., 2009a).

II. Lipopolysaccharide (LPS)

LPS is a naturally occurring gram-negative bacterial endotoxin which elicits an immune response via toll-like receptor (TLR) 4, mimicking bacterial infection (Hao et al., 2010; Reisinger et al., 2015). TLR4 signalling induces distinct immune responses, notably, the TLR4-MyD88-dependent pathway produces inflammatory cytokines via activation of NF-κB while the TLR4-MyD88-independent path stimulates the interferon regulatory factor which in turn promotes activation of inteferon-responsive genes (Akira and Takeda, 2004; Kawai and Akira, 2007). These pathways promote downstream activation of both pro- and anti-inflammatory cytokines, including IL-1, IL-6 and TNFα (Boksa, 2010). Several studies using LPS-induced MIA models, have confirmed a sufficient maternal immune response, including systemically elevated IL-1β, IL-2, IL-6 and TNFα (Arsenault et al., 2014; Borrell et al., 2002; Gilmore et al., 2003; Núñez-Estevez et al., 2020; Oskvig et al., 2012). However, a key issue with the use of LPS is high inter-batch variability and serotype, which produce variable immune profiles, challenging direct comparisons between studies (Boksa, 2010; Migale et al., 2015).

III. Poly(I:C)

Poly(I:C) is a commercially available, synthetic double-stranded RNA which mimics viral infection (Meyer, 2014; Reisinger et al., 2015) through TLR3 (Alexopoulou et al., 2001; Tatematsu et al., 2014). Importantly, TLR3 expression is detected across a range of tissues including the placenta and the brain (Matsumoto et al., 2011). TLR3 triggers upregulation of cytokines and chemokines that induce downstream immune response systems (Alexopoulou et al., 2001; Leonard et al., 2008; Matsumoto and Seya, 2008; Matsumoto et al., 2011). Cytokine profiles in MIA models which use poly(I:C) have consistently demonstrated dam systemic elevations in IL-1β, IL-6 and TNF-α (Arrode-Brusés and Brusés, 2012; Kowash et al., 2022; Meyer et al., 2006b; Mueller et al., 2019, 2021; Murray et al., 2019; Potter et al., 2023; Smith et al., 2007). However, supplier of poly(I:C) and molecular weight have been shown to induce disparate immune profiles and hence these methodological criteria need to be considered when comparing results across studies (Careaga et al., 2018; Kowash et al., 2019; Mueller et al., 2019). A notable benefit of poly(I:C)-induced MIA is that few changes to litter survival have been documented, suggesting a better safety margin regarding foetal viability when compared to LPS-induced MIA (Arsenault et al., 2014).

1.3.2.2. Behavioural changes

To date, it has been well validated that MIA induces a range of behavioural deficits of relevance to all three schizophrenia symptom domains, including locomotor-based tasks, analogous to positive symptoms, anhedonia and anxiety tasks for negative symptoms and several learning and memory tasks, for cognitive symptoms (Table 1.3). Further, many offspring behavioural changes have post-pubertal emergence, suggesting the relevance of these phenotypes to the clinical progression of schizophrenia (Lorusso et al., 2022; Fernández de Cossío et al., 2021; Meyer et al., 2008a; Potter et al., 2023; Zuckerman and Weiner, 2005; Zuckerman et al., 2003).

Additionally, studies have produced mixed results on sex-specific behaviours, with some indicating no difference (Meyer et al., 2005; Zuckerman et al., 2003) while others demonstrate clear sex-specific phenotypes (Bronson and Bale, 2014; Gogos et al., 2020; Schwendener et al., 2009). These studies together begin to demonstrate face validity of the MIA model. Further studies have begun to investigate predictive validity of MIA models, demonstrating that first- and second-generation antipsychotics alleviate offspring behavioural and molecular deficits in both rats and mice in LPS and poly(I:C) paradigms (Borrell et al., 2002; Farrelly et al., 2015; MacDowell et al., 2021; Meyer et al., 2010; Piontkewitz et al., 2009; Zuckerman et al., 2003). Of note, following on from recent hypotheses that cannabidiol could improve cognitive deficits in schizophrenia (Osborne et al., 2017b), cannabidiol has been shown to induce improvements in cognitive ability in a poly(I:C)-rat model for MIA (Osborne et al., 2017a, 2019). That said, findings for the beneficial effects of cannabidiol in schizophrenia remain mixed (Ahmed et al., 2021; Dyck et al., 2022). Following these extensive and well-validated behavioural outcomes, work has now begun to focus on the mechanisms which mediate these outcomes.

1.3.2.3. Brain morphometric and cell density changes

MIA models have shown several morphological brain changes comparable to those seen in schizophrenia, including region-specific volume and grey matter reductions and white matter alterations, with the latter including both increases and decreases in white matter (Casquero-Veiga et al., 2023; Crum et al., 2017; Fatemi et al., 2008; Paintlia et al., 2008; Richetto et al., 2017a; Wood et al., 2019). Cell changes have been evaluated to explain these morphometric changes. Findings have included reduced prenatal and postnatal neurogenesis and disturbed gliogenesis (Couch et al., 2021; Khan et al., 2014; Paintlia et al., 2008) with postnatal brains, as a result, shown to have altered cell densities. For glial cells, astrocyte and oligodendrocyte (responsible for myelination and white matter integrity) densities have been found to be both increased and decreased, (Anderson et al., 2022; de Souza et al., 2015; Ding et al., 2019; Makinodan et al., 2008; Paintlia et al., 2008; Paylor et al., 2016; Ratnayake et al., 2012; Xia et al., 2020). This discordance is most likely attributable to timing of immune insult and brain region analysed. Of note, more recent studies have shown altered astrocyte morphology and function in the brains of MIA-offspring in the absence of density changes (Hayes et al., 2022; Saavedra et al., 2021). Likewise results from microglial changes have been variable, reviewed recently by Carloni et al., (2021). However emphasis is now, as with astrocytes, placed on evaluation of microglial activity rather than density, with general support for pro-inflammatory microglia. For neurons, one of the more robust findings has been reductions in GABAergic interneuron densities, particularly parvalbumin and somatostatin interneurons (Casquero-Veiga et al., 2023; Mao et al., 2022; Nakamura et al., 2021; Paylor et al., 2016; Vasistha et al., 2019; Wegrzyn et al., 2021).

Table 1.3. Summary of offspring behaviours identified in MIA models

Immunogen	Species	GD of MIA	Behavioural phenotype	Reference(s)
Influenza	Mouse	GD9	↓PPI ↓OF exploration ↓NOR performance ↓SI performance	Fatemi et al., 2008; Patterson, 2005; Shi et al., 2003.
LPS	Mouse	GD8 GD17	↓NOR performance ↓SI performance	Borrell et al., 2002; Coyle et al., 2009; Fortier et al., 2004, 2007; Golan et al., 2005.
	Rat	GD15 GD18	↓PPI ↓PPI	
Poly(I:C)	Mouse	GD9	↓PPI ↑Despair in FST ↑Amphetamine locomotion	Connor et al., 2012; Guma et al., 2021; Khan et al., 2014; Labouesse et al., 2015a; Lorusso et al., 2022; Meyer et al., 2008a, 2008b; Morais et al, 2018; Mueller et al., 2021; Ozawa et al., 2006; Piontkewitz et al., 2009, 2012; Potter et al., 2023; Ratnayake et al., 2012; Richetto et al., 2013; Shi et al., 2003; Vorhees et al., 2015; Vuillermot et al., 2010; Zuckerman and Weiner, 2003; Zuckerman et al., 2003.
		GD12	↓PPI ↓OF performance ↓MWM performance ↓NOR performance ↑Despair in FST ↓SI performance ↓EPM exploration ↓SN performance ↓Sucrose preference	
		GD17	↓Y-maze performance ↓OF performance ↓T-maze performance ↓NOR performance ↓SN performance ↓SN performance	
		GD18	↓SI performance ↓MWM performance	
		GD20	↓OF exploration ↓NOR performance	
	Rat	GD15	↓LI ↓PPI ↓NOR performance ↓ASST performance	
		GD18	↓T-maze performance ↓MWM performance ↓LI	

Abbreviations: GD, gestational day of injection; AD, alternate days; ↓Decrease; ↑ Increase; ASST, attentional set-shifting task; FST, forced swim test; LI, latent inhibition; MWM, Morris water maze; OF, open field; PPI, prepulse inhibition; NOR, novel object recognition; SI, social interaction; SN, social novelty.

1.3.2.4. Molecular changes

A recent systematic review was performed by this author (Woods et al., 2021), of molecular changes in the brains of offspring exposed to all paradigms of MIA. The key findings were that the genes which demonstrated greatest magnitude of change in response to MIA could be clustered into three main functional groups: immune/stress response genes, neurotransmission/neuronal signalling genes and neurodevelopmental genes (Woods et al., 2021). Of note, an additional systematic review of MIA models, focusing on immune changes in exposed offspring (Hameete et al., 2020) similarly identified generally dysregulated immune profiles in the brains of MIA-offspring. Meanwhile, a recent meta-analysis in poly(I:C)-models only corroborated the key changes in pathways associated with neurodevelopment and neuronal signalling (Laighneach et al., 2021), supporting further the findings from our review (Woods et al., 2021). These processes are all postulated to be critical in the etiopathogenesis of schizophrenia (Section 1.1.3), including notable changes in glutamatergic, GABAergic and dopaminergic pathways (Figure 1.10; Woods et al., 2021), supporting the pathogenic and mechanistic validity of the MIA model in schizophrenia research. That said, methodological heterogeneity and lack of reporting and validation prevented thorough comparisons between studies. Likewise, changes were often developmental- and sex-specific, supporting the need for future studies to perform longitudinal analysis of brain changes in both sexes. Further, of surprise, few studies were found to have evaluated epigenetic changes in MIA models, however, where evaluated epigenetic changes were found to frequently correlate with gene expression changes, providing preliminary evidence that changes in gene expression as a result of MIA, may derive from perturbed epigenetic programming (Woods et al., 2021). Taken together, the findings support ongoing neuropathology as a result of MIA, with direct relevance for schizophrenia. However, further investigations to corroborate previous findings and establish a robust framework of alterations will be essential for identification of novel therapeutic targets.

1.3.2.5. The cytokine hypothesis in MIA models

One of the key hypotheses following human epidemiology studies, is that maternally-derived cytokines, as a result of an activated immune response to a virus or pathogen, mediate the risk of MIA in promoting schizophrenia development (Meyer et al., 2009b). Rodent models of MIA have provided substantial evidence for this hypothesis. We and others have shown that MIA disturbs the normal cytokine profile in the foetal environment (including the placenta and amniotic fluid) and foetal brain (Hameete et al., 2020; Kowash, 2019; Meyer et al., 2006a; Urakubo et al., 2001; Woods et al., 2021). Further to this, pivotal work by Smith et al. (2007) demonstrated that IL-6 is a key mediator in MIA-induced phenotypes. By injecting pregnant mice with recombinant IL-6, they were able to effectively demonstrate similar offspring behavioural phenotypes as those seen for poly(I:C). They also demonstrated that injection of poly(I:C) in IL-6 KO mouse dams, or indeed the application of an anti-IL6 antibody in conjunction with poly(I:C) treatment in wild-type dams, was sufficient to abolish poly(I:C)-induced traits in the offspring.

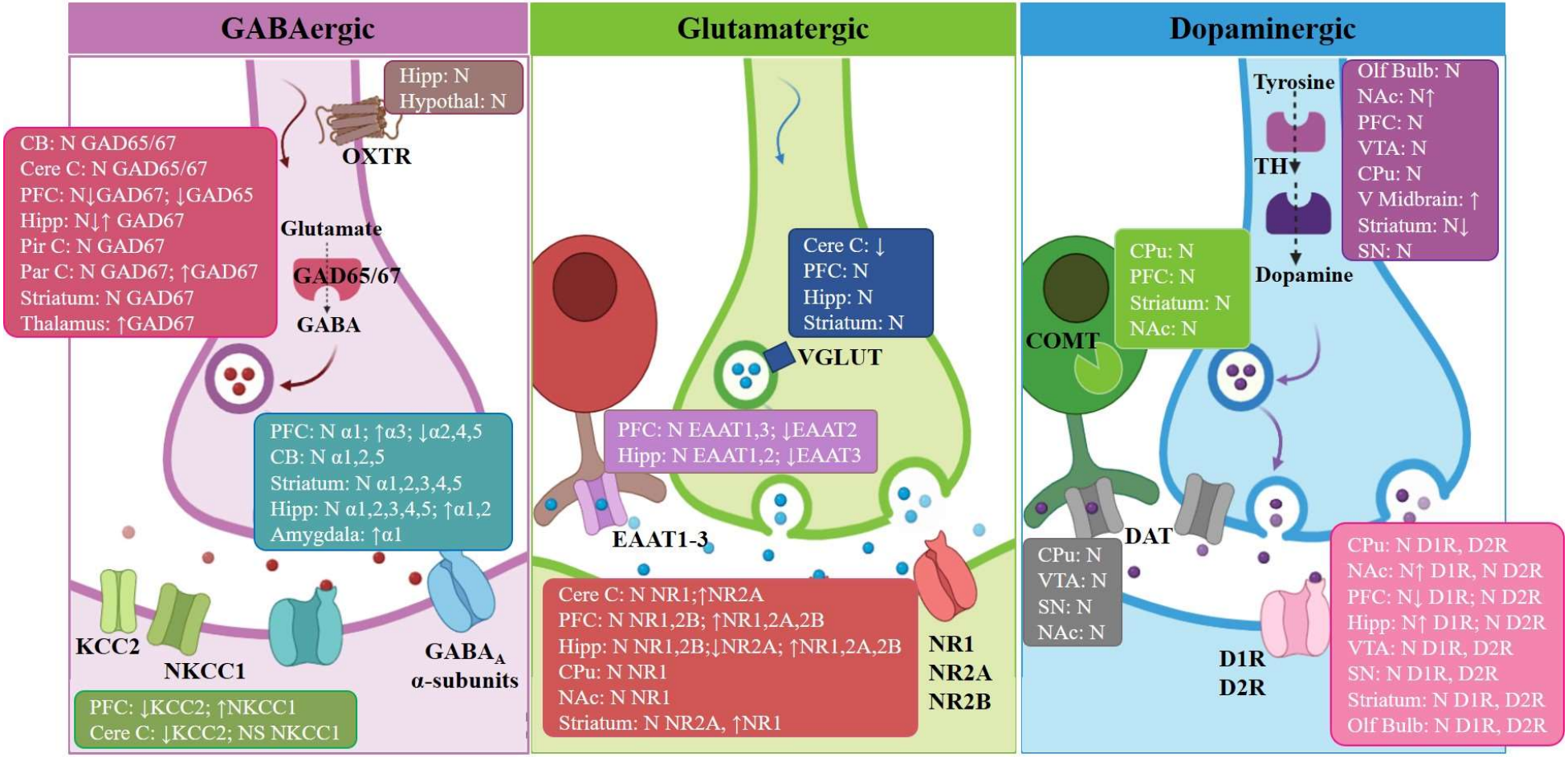

Figure 1.10. Summary of key MIA-induced changes in neuronal signalling pathways

Figure summarises the changes in neurotransmitter genes in adult offspring brain tissues, as identified in the systematic review (Woods et al., 2021). Abbreviations: N, no change in expression; ↑ increased expression; ↓ decreased expression; CB, Cerebellum; Cere C, Cerebral Cortex; CPu, Caudate Putamen; Hipp, Hippocampus; Hypothal, Hypothalamus; NAc, Nucleus Accumbens; Olf Bulb, Olfactory Bulb; Par C, Parietal Cortex; Pir C, Piriform Cortex; PFC, Prefrontal Cortex; SN, Substantia Nigra; V Midbrain, Ventral Midbrain; VTA, Ventral Tegmental Area.

This work was corroborated by Samuelsson et al. (2006) who injected rat dams with recombinant IL-6 and observed similar changes in offspring behavioural and brain molecular changes as with a traditional MIA model**.** More recent work has also postulated a role for IL-17a. Similar to the aforementioned studies, it was shown that injection of an IL-17a blocking antibody in conjunction with poly(I:C) was sufficient to abolish offspring brain and behavioural phenotypes (Choi et al., 2016). Notably, IL-6 and IL-17a are suggested to have a synergistic relationship, with upregulation of one inducing upregulation of the other during response to viral infection (Velazquez-Salinas et al., 2019). In line with these studies, neuroinflammatory pathways and IL-6, remain among the most robustly investigated molecular changes in MIA models (Hameete et al., 2020; Woods et al., 2021). Further, a recent study demonstrated plasma cytokine disturbances, including IL-6, in behaviourally affected MIA-offspring (Mueller et al., 2021). Likewise, anti-inflammatories have been shown to ameliorate behavioural and molecular deficits in MIA and similar models (Aria et al., 2020; Ferreira et al., 2020; Han et al., 2019). These results, together, broadly establish the role of cytokines in the genesis of the MIA phenotype, with a particular role for the IL-6 pathway and suggest an ongoing role for disturbed inflammatory signalling in MIA-offspring, which may precipitate behavioural deficits (Meyer et al., 2009a; Mueller et al., 2021).

1.3.2.6. Challenges for MIA model validation

MIA models are not without challenges. First, it is difficult to integrate data between different research groups (Harvey and Boksa, 2012; Woods et al., 2021). The main reason for this owes to methodological heterogeneity in choice of rodent (e.g., mouse/rat) and strains within this (e.g., Wistar/Sprague Dawley rats), which have different developmental timelines and genetics which may result in different phenotypes (Bayer et al., 1993; Clancy et al., 2001, 2007). There are also differences in methods of immune induction between models (influenza/LPS/poly(I:C)) which, while producing similar phenotypes, have different pathways of action (Meyer and Feldon, 2010, 2012; Meyer, 2014). Furthermore, batches and origins of immunogens (notably LPS and poly(I:C)) have also been shown to produce variability in immune response (Boksa, 2010; Careaga et al., 2018; Kowash et al., 2019; Mueller et al., 2019). There will also be the added irregularities in dose and timings at which these immunogens are given (Harvey and Boksa, 2012), with timing (early/late gestation) of MIA, in particular, shown to produce disparate behavioural and molecular phenotypes (Guma et al., 2021; Meyer et al., 2006b). Animal housing has also been shown to impact on MIA outcomes, with environmental enrichment abolishing MIA-induced behavioural deficits (Schander et al., 2021; Zhao et al., 2021) and use of individually ventilated cages (IVCs) shown to attenuate MIA-induced behaviours (Mueller et al., 2018). A final key challenge is single-sex bias (Coiro and Pollak, 2019), despite evidenced sex effects in MIA behavioural and molecular phenotypes (Bronson and Bale, 2014; Gogos et al., 2020; Schwendener et al., 2009; Woods et al., 2021).

With these challenges in mind, there is the call for proper validation and characterisation of MIA models, alongside rigorous reporting guidelines, in an effort to reduce model variability and consolidate results (Kentner et al., 2019; Roderick and Kentner, 2019). Accordingly, our in-house model of MIA has been extensively characterised, validating the use of an intraperitoneal (i.p.) injection of 10mg/kg bodyweight low molecular weight (LMW) poly(I:C) on GD15 in Wistar rat dams. These methodological conditions were selected as they resulted in the least variable immune response, producing a consistent and robust elevation in maternal plasma pro-inflammatory cytokines, IL-6 and TNFα, on day of administration (Kowash et al., 2019, 2022; Murray et al., 2019; Potter et al., 2023). This characterisation work created a robust platform and paradigm model which can be used efficiently and effectively to study mechanisms which underpin the role of MIA in schizophrenia.

1.3.3. Non-human primate (NHP) models for MIA

Beyond preclinical rodent modelling, NHP models of MIA have been used to further explore the role of MIA in schizophrenia development. While more expensive and time-intensive, NHP-models are closer to the human paradigm, better able to mimic human behavioural traits, brain developmental trajectory and structure (Hanson et al., 2022). Work in NHP models for MIA, including influenza and poly(I:C)-models have, critically, validated findings from rodents. NHP MIA-exposed offspring have robustly demonstrated behavioural deficits, notably social and cognitive deficits (Bauman et al., 2014; Hanson et al., 2022; Vlasova et al., 2021). Findings include, morphological changes, such as reduced grey matter and enlarged lateral ventricles (Short et al., 2011), altered immune responses (Rose et al., 2017), neuro-molecular changes, including altered dendrite morphology and transcriptomic profiles representative of altered synaptic and oligodendrocyte function (Page et al., 2021; Weir et al., 2015) and metabolic changes, including altered amino acid metabolism (Boktor et al., 2022).

1.3.4. *In vitro* MIA modelling

A key drawback of both rodent and NHP models is the inability to functionally validate the mechanisms of action in real-time, with brains generally collected post-mortem for *ex vivo* analysis. Further, animal models cannot completely recapitulate human brain function and development. Hence, a combination on *in vivo* and *in vitro* methods will ultimately be required to preclinically evaluate novel therapeutic approaches for schizophrenia (Couch et al., 2021; Koszła et al., 2020), with *in vitro* models providing functional mechanistic validations in complement to *in vivo* disease modelling. *In vitro* modelling in the context of MIA has utilised human and animal-derived cells and has provided some critical insights into the mechanism of MIA, particularly in regard to the impacts of MIA on neurogenesis and microglial function. Such studies have demonstrated that cytokines induce transcriptomic changes in patient-derived human induced pluripotent stem cells (hiPSC), associated with immune dysregulation and synaptic dysfunction and enriched for NDD risk genes (Bhat et al., 2022; Warre-Cornish et al.,

2020). Likewise, hiPSC-derived microglia, show increased motility and immune responses following acute IL-6 exposure (Couch et al., 2023), while microglia derived from a mouse MIA-model show dampened immune reactivity upon LPS-stimulation (Hayes et al., 2022). Further while single-cell findings are incredibly useful, more complex cell cultures such as organoids are suggested to be better representative of the human brain (Couch et al., 2021). Indeed, a recent human organoid model of MIA validated responses to IL-6 identified in rodent models, including transcriptomic changes, immune dysregulation and altered cell differentiation, while also identifying novel human-specific mechanisms for future investigation (Sarieva et al., 2023).

1.4. Summary

Schizophrenia is a neuropsychiatric disorder, with a severe health burden and impact on patient quality of life (Castillejos et al., 2018; Charlson et al., 2018). To date, the mainstay of schizophrenia therapy is antipsychotics, which primarily ameliorate positive symptoms, with little impact on negative and cognitive symptom domains (Naber and Lambert, 2012; Spark et al., 2022). Further, antipsychotics face several challenges, including patient non-compliance, severe side-effects and lack of efficacy (Ibrahim and Tamminga, 2011; Muench and Hamer, 2010; Semahegn et al., 2020). With this in mind, there is critical need for novel therapeutic strategies. This is hindered by the complex and multifactorial nature of the disease, comprising both genetic and environmental risk factors. Indeed, schizophrenia is hypothesised to arise following disturbed neurodevelopment, arising due to environmental stress, including infection. Epidemiology studies have identified that MIA, following maternal infection, accounts for a significant proportion of schizophrenia cases (Brown and Derkits, 2010; Weinberger, 1987). However, the longitudinal investigation of this paradigm is challenging in humans and hence the past 30 years has seen the development of several preclinical animal models of MIA (Meyer and Feldon, 2010). One of the most common MIA models uses exposure to the viral mimetic, poly(I:C), during mid-late gestation. This has been shown to induce an acute MIA and result in behavioural deficits in offspring with relevance to all domains of schizophrenia symptoms (Table 1.3). In line we this, we have recently characterised a rat model for MIA which administers poly(I:C) on GD15 in Wistar rat dams (Murray et al., 2019; Kowash et al., 2019), to use as a platform to investigate the critical mechanisms which underscore the relationship between MIA and the development of these phenotypes.

1.4.1. Hypothesis

MIA, induced by poly(I:C), induces adaptive epigenetic changes in the developing brain, which in turn promote changes in gene/protein expression which dysregulate normal cell development and function, leading to the development of behavioural deficits relevant for schizophrenia.

1.4.2. Thesis aims

The principal aim of this thesis was to investigate the molecular mechanisms which predispose offspring to behavioural deficits as a consequence of MIA. To achieve this, a pre-characterised rat model for MIA was used, administering an i.p. injection of poly(I:C) to pregnant Wister rats on GD15. To confirm an acute dam immune response had been achieved, plasma pro-inflammatory cytokines, IL-6 and TNFα, were measured alongside changes in dam bodyweight. Molecular mechanisms were then analysed in the offspring brains, using a developmental longitudinal approach, inclusive of foetal, infant (postnatal day (PD) 1), juvenile (PD21), adolescent (PD35) and adult (PD100-175) stages of development, in an effort to identify when pathological changes occur. Various molecular mechanisms were explored in the offspring brains, including changes in: metabolite concentrations, DNAm patterns, gene and protein expression and cell morphologies and density. To improve the clinical relevance of the study peripheral inflammatory biomarkers were also assessed.

The overarching aim of this thesis was hence to establish translatable molecular mechanisms which contribute to schizophrenia risk following MIA and ultimately add to the understanding of schizophrenia aetiology, with the long-term aim of identifying novel targets for drug development.

CHAPTER 2. MIA model validation: maternal and offspring outcomes

2.1. INTRODUCTION

2.1.1. Schizophrenia: a brief overview

Symptoms of schizophrenia are broadly divided into three groups: positive, negative and cognitive symptoms (Figure 1.1; Mihaljević-Peleš et al., 2019; Tamminga, 2008) with clinical staging including a prodrome of non-specific symptoms followed by acute and chronic phases of psychosis (Janoutova et al., 2016; Kaur and Cadenhead, 2010; Lieberman, 1999; Niendam et al., 2006). Schizophrenia is rated among the top 20 DALYs in the global burden of disease analyses, owing to the significant impact of schizophrenia on quality of life, with patients' incapable of self-care and independence, with a resulting burden on healthcare systems (He et al., 2020; Institute for Health Metrics and Evaluation, 2018; Janoutova et al., 2016; Kaur and Cadenhead, 2010). Early detection and subsequent intervention could be beneficial for schizophrenia patients through preventing the development of chronic psychosis (Kulhara et al., 2008), however, this depends on: i) early diagnosis and ii) effective therapeutics. While much progress has been made in early diagnostic strategies for schizophrenia patients, the mainstay of schizophrenia treatment relies on antipsychotics which target dopaminergic/serotonergic neurotransmitter systems (Spark et al., 2022; Taly, 2013). However, antipsychotics lack efficacy with little impact on cognitive and/or negative symptoms and are associated with multiple adverse side effects which can contribute to lack of patient compliance (Ibrahim and Tamminga, 2011; Jaaskelainen et al., 2013; Keefe et al., 2007; Lieberman et al., 2005; Stroup and Gray, 2018; Swartz et al., 2007). Given these limitations, novel therapeutic strategies are necessary to improve the management of schizophrenia symptoms and quality of life. Current lack of efficacious therapeutics is partly due to a limited understanding of the complex disease aetiology. Indeed, while a clear genetic component exists for schizophrenia (Avramopoulos, 2018), there is also extensive evidence of environmental risk factors (Gianfrancesco et al., 2019; Janoutova et al., 2016). Notably, prenatal and early-life environments are thought to be critical in mediating schizophrenia risk.

2.1.2. Schizophrenia and neurodevelopment

The Barker hypothesis originated in the 1990s with the postulate that sub-optimal maternal nutrition during foetal development could pre-dispose offspring to metabolic diseases later in life (Barker, 1990). This hypothesis has since been well-validated (Barker, 2002; Roseboom et al., 2006) and is now commonly referred to as the DOHaD hypothesis (Gillman, 2005). Historically, schizophrenia was considered a neurodegenerative disorder, until the 1980s when the neurodevelopmental hypothesis of schizophrenia emerged, proposing that schizophrenia results from perturbed brain development (Weinberger, 1987). The mammalian brain develops over a protracted period, beginning early post-conception and extending into adulthood. This creates a large window of vulnerability where neurodevelopment can be altered by environmental factors. Environmental events thought to impact brain development and thereby

predispose individuals to schizophrenia include pregnancy complications, maternal infection and placental dysfunction (Murray and Lewis, 1988; Rapoport et al., 2005).

2.1.2.1. Infection and MIA

Early evidence supporting the contribution of maternal infection to schizophrenia came from epidemiological studies demonstrating that schizophrenia prevalence increased in the population following influenza epidemics (Adams et al., 1993; Mednick et al., 1988). A key limitation of these studies was that calculated schizophrenia risk was underscored by the timing of an infectious outbreak, rather than evidence of true maternal infection (Brown and Derkits, 2010). Accordingly, later studies investigating the serum of infected mothers, successfully correlated presence of maternal antibodies for influenza with up to a three-fold offspring risk of developing schizophrenia (Brown et al., 2004). This work proposed that it is maternal immune responses as opposed to the infectious agent itself that promotes schizophrenia risk, a concept supported by influenza-induced animal models of MIA, which produced offspring behavioural deficits, without evidence for virus particles reaching the developing foetus (Ashdown et al., 2006; Fatemi et al., 2012). The prevailing hypothesis is that maternal infection indirectly affects offspring neurodevelopment through MIA-mediated mechanisms which, in turn, promote schizophrenia development (Labouesse et al., 2015b). Accordingly, it is hypothesised that maternal-derived cytokines are important in mediating the effect of MIA (Meyer et al., 2009b).

I. The cytokine hypothesis

Studies in humans have associated elevated maternal cytokines with impaired cognitive development, anxiety, depression and psychosis risk in exposed children (Allswede et al., 2020; Giollabhui et al., 2019; Mevorach et al., 2021; Nazzari et al., 2020). Maternal-derived cytokines have been demonstrated to enter the foetal blood circulation and cross the foetal BBB (Banks et al., 1991, 1994; Dahlgren et al., 2006; Zaretsky et al., 2004). Cytokines and their receptors are expressed constitutively throughout foetal neurodevelopment (Mehler and Kessler, 1997; Mousa et al., 1999) and function in a range of neurodevelopmental pathways (Deverman and Patterson, 2009). These data hence formulate a hypothesis whereby maternal infection induces MIA and cytokine elevation, which could induce foetal neuroinflammation and ultimately converge in altered neurodevelopment (Meyer et al., 2009b). Further, it has been suggested that such foetal cytokine dysregulation may persist postnatally in affected offspring and be a predictive risk factor for schizophrenia development (Choudhury and Lennox, 2021; Khandaker et al., 2014; Meyer et al., 2009b). Indeed, several studies have associated cytokine dysregulation with schizophrenia symptoms, including genetic variants (Penninck et al., 2021; Shivakumar et al., 2020) and increased serum and CSF pro-inflammatory cytokine concentrations (Gallego et al., 2018; Kalmady et al., 2018; Kogan et al., 2018; Miller et al., 2011; Upthegrove et al., 2014). Taken together, these data imply a key role for cytokines and immune dysregulation in the aetiology of schizophrenia (Choudhury and Lennox, 2021). Accordingly, anti-inflammatory drugs have been suggested as adjuvant therapies in schizophrenia

(Hashimoto, 2019). However, recent meta-analyses have debated their efficacy (Çakici et al., 2019; Cho et al., 2019; Jeppesen et al., 2020) though this likely owes to lack of patient stratification in clinical trials with respect to individual basal inflammatory state.

II. Placental dysfunction

The placenta is required for transport of essential nutrients to the developing foetus, including the provision of folate and methionine, essential for methylation capacity and nucleotide biosynthesis in the foetal compartment, delivered to the foetus through active placental transport (Antony, 2007; Gude et al., 2004; Solanky et al., 2010; Tsitsiou et al., 2009). Further, placental function adapts during gestation to meet foetal developmental and growth demand and hence perturbations to placental development and function can be detrimental to the foetus (Gude et al., 2004; Tsukada et al., 2019). It has been suggested that maternal stress and MIA can impact on the placenta in such a way, most likely through altered transport and metabolic functions, to disrupt foetal brain development (Kowash et al., 2022). The brain is an energetically costly organ and hence is particularly vulnerable to placental dysfunction (Shallie and Naicker, 2019). Moreover, it has been shown that cytokines, particularly IL-6, can transverse the placenta to the foetus (Dahlgren et al., 2006; Zaretsky et al., 2004) thereby suggesting a mechanism by which MIA can impact directly on foetal neurodevelopmental trajectory. Further, it is well-established that physiological perturbations in the maternal environment are sensed by the placenta, eliciting placental functional changes. This can result in disturbed foetal homeostatic balance and therefore influence foetal growth and development (Myatt, 2006; Sferruzzi-Perri and Camm, 2016). Taken together, these data support the role of the placenta as a key mediator of prenatal stressor-induced challenges that increase risk of schizophrenia.

2.1.3. Rodent models for MIA and the role of cytokines

Despite growing support for a role of MIA in schizophrenia, our ability to study this in humans remains limited due to the protracted timeline of the disease, ethical considerations and methodological challenges (Bale et al., 2019; Massrali et al., 2022). This prevents clear understanding of the mechanisms which mediate the risk between MIA and offspring outcomes. Hence, rodent MIA models are valuable for preclinical validation of this paradigm and to ultimately identify mechanisms for potential new therapies (Meyer and Feldon, 2010). Rodent models for studying MIA in the context of schizophrenia are based on human epidemiological studies, which demonstrated an association between influenza infection during pregnancy and subsequent schizophrenia risk in exposed offspring (Meyer and Feldon, 2010; Reisinger et al., 2015). The most common MIA model uses gestational exposure to the viral mimetic, poly(I:C), with exposed offspring assessed for behavioural and biological changes (Meyer and Feldon, 2010, 2012; Woods et al., 2021). Indeed, it has been well validated that MIA induces a range of behavioural deficits of relevance across schizophrenia symptom domains (Table 1.3). Beyond extensive behavioural validations, work has now begun to focus on neuro-molecular mechanisms which mediate offspring outcomes. Particularly, in line with the cytokine hypothesis

(Section 1.2.2.3), pivotal work has identified maternal IL-6 is a key mediator of MIA-induced schizophrenia phenotypes in offspring, in both mice (Smith et al., 2007) and rats (Samuelsson et al., 2006), broadly establishing the role of cytokines in the genesis of the MIA phenotype, with a particular role for IL-6 (Meyer et al., 2009b). Several reviews on neuro-molecular changes in MIA models have been performed, three comprising systematic analyses (Hameete et al., 2020; Laighneach et al., 2021; Woods et al., 2021). Many identified changes were involved in neurotransmission and neurodevelopment, as might be expected in models for NDDs. However, there were multiple analyses of cytokines and immune-related pathways. Woods et al. (2021) identified the four most extensively studied cytokines as IL-10, IL-1β, IL-6 and TNFα, with particular support for altered foetal profiles of pro-inflammatory cytokines in the first 24h post-exposure to MIA (Figure 2.1; Woods et al., 2021).

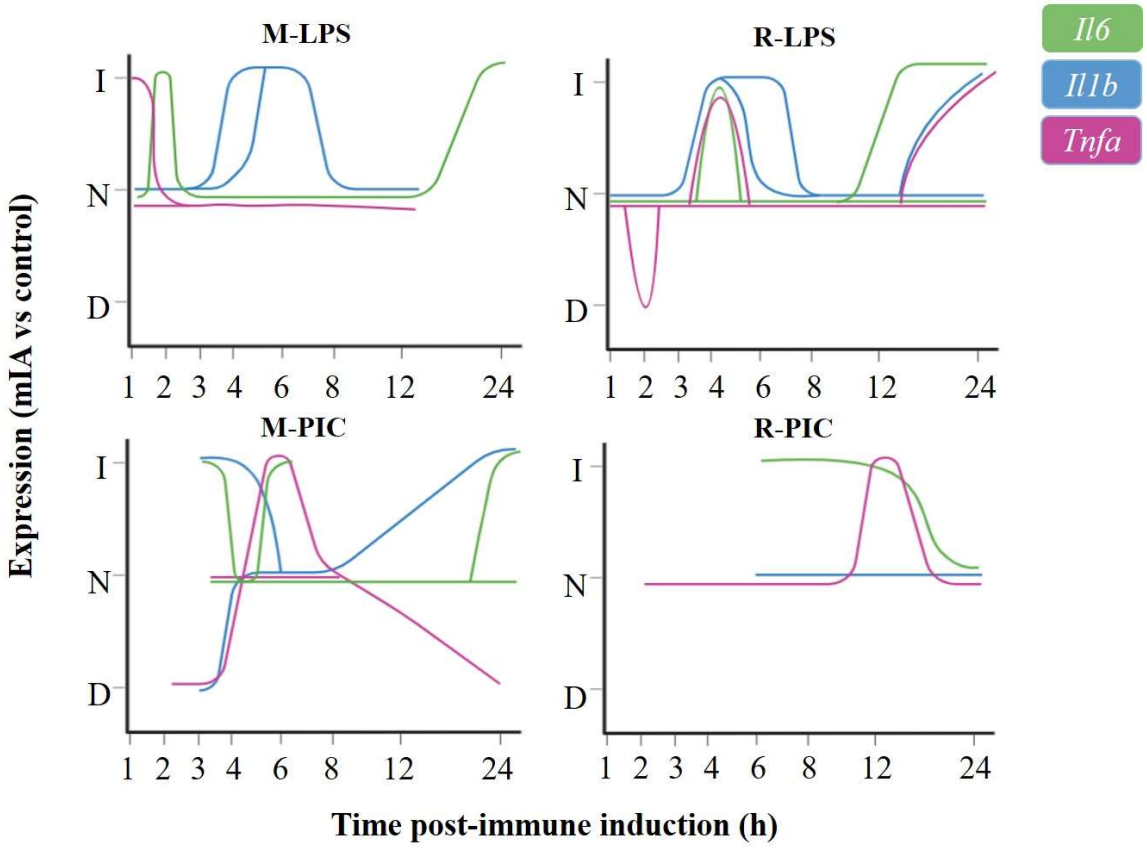

Figure 2.1. Pro-inflammatory foetal brain cytokine changes 24h post-MIA
Summary of temporal changes of *Il1b* (IL-1β; Blue), *Il6* (IL-6; Green) and *Tnfa* (TNFα; Purple) expression in the foetal brain over the first 24h post-immune induction in MIA models using LPS or poly(I:C) as immunostimulants. Where a line diverges, this indicates that there is conflicting data for the expression of that gene/protein at that time post-induction, often associated with methodological differences between studies. Abbreviations: M-PIC, mouse-poly(I:C); models, M-LPS, mouse-LPS; R-LPS, rat-LPS; R-PIC, rat-poly(I:C); I, increase; D, decrease; N, no change. Adapted from Woods et al. (2021).

Accordingly, neuroinflammatory pathways remain among the most robustly investigated neuro-molecular changes in MIA models (Hameete et al., 2020; Woods et al., 2021). Ongoing systemic inflammatory disturbances have been less documented, though a recent study effectively demonstrated plasma cytokine disturbances in behaviourally affected MIA-offspring, suggesting systemic cytokines may function in determining susceptibility to MIA (Mueller et al., 2021).

Likewise, anti-inflammatory therapies have been shown to ameliorate behavioural and molecular deficits in MIA and similar models (Aria et al., 2020; Ferreira et al., 2020; Han et al., 2019), suggesting a causal role for inflammation in MIA-induced behavioural phenotypes.

2.1.4. Chapter aims

Several studies have emphasised the difficulty comparing MIA model data between research groups (Harvey and Boksa, 2012; Kentner et al., 2019; Woods et al., 2021). A key reason for this owes to methodological heterogeneity, including differences in: rodent species/strain used (Bayer et al., 1993; Clancy et al., 2001, 2007); methods of immune induction (e.g., influenza, LPS, poly(I:C)) (Meyer, 2014; Meyer and Feldon, 2010, 2012); immunogen batches (Boksa, 2010; Careaga et al., 2018; Kowash et al., 2019; Mueller et al., 2019); dose and timings at which immunogens are given (Harvey and Boksa, 2012; Meyer et al., 2006b), which together have been shown to induce different immune profiles and behaviours. With these factors in mind and with the long-term goal of using MIA models for preclinical drug discovery, there is need for proper validation/characterisation of MIA models (Kentner et al., 2019; Woods et al., 2021).

In this Chapter, extensive validation of the robustness of our model, building on previous broad characterisation (Murray et al., 2019; Kowash et al., 2019), is performed, in particular across cohorts which will be used for molecular analyses in subsequent chapters. Further, to support the primary hypothesis that cytokines play role in mediating the outcomes of MIA (Meyer et al., 2009b), a major aim of this Chapter was to investigate specific cytokine changes in the developing brain as a possible causal mechanism in our model. Accordingly, the aims of this Chapter were:

i) Validate reproducibility of maternal response to poly(I:C) in our model (Murray et al., 2019; Kowash et al., 2019) across cohorts, including plasma cytokine response, weight changes and litter sizes.
ii) Validate offspring outcomes following MIA, including, foetal and postnatal offspring body/brain weights.
iii) Validate the role of cytokines in offspring outcomes, including changes in foetal brain cytokines and ongoing postnatal cytokine pathology following MIA.
iv) To place these findings in the context of previous behavioural phenotyping (Potter, 2021).

2.2. MATERIALS AND METHODS

2.2.1. Animal procedures, husbandry and tissue collection

Adult Wistar rats were obtained from Charles River Laboratories (Females: 200-300g; Males: 400-500g) and maintained in the Biological Services Facility (BSF) at the University of Manchester within two-level IVCs (Double-Decker Cage; Tecniplast, London, UK), with up to five animals per cage. Throughout experiments, animals were maintained in a 12h light:dark cycle (07:00-19:00) at a temperature of 21±2°C and humidity 55±5% with *ad libitum* access to standard rat chow (Special Diet Services, Essex, UK) and water. Sizzle nest, wood chipping, cardboard tubes and wooden blocks formed the only environmental enrichment, to minimise impacts of enrichment on behavioural outcomes (Schander et al., 2021; Zhao et al., 2021). All animals were acclimatised to the BSF for one week prior to starting procedures. Animal procedures were performed under the authority of the procedural project licence (PPL) P473EC3B1. Procedures adhered to the Animals (Scientific Procedures) Act (ASPA) 1986 and were approved by the University of Manchester Animal Welfare and Ethical Review Body (AWERB). Given the timeframe of the animal cohorts (~6 months/cohort), technical requirements (e.g., two experimenters needed for injection/blood sampling) and financial challenges of maintaining large cohorts demanded to achieve sufficient n-numbers (see Section 2.2.1.1), cohorts were required to be collaborative between PhD researchers. Likewise, every effort was made to adhere to the 3Rs of animal research (Tannenbaum and Bennett, 2015) with animals shared for both behavioural studies and various downstream molecular projects. Where cohorts have been contributed to/used by multiple PhD researchers, this will be clearly outlined.

2.2.1.1. Sample size calculations

Sample size was calculated using the G*Power statistical software package (v3.1.9.2. Düsseldorf, Germany; Faul et al., 2007) using a sensitivity analysis, assuming a medium to large effect size (f=0.25-0.4), as based on previous effect size estimates from our and other molecular/behavioural studies in MIA models (Dickerson et al., 2014; Giovanoli et al., 2015, 2016; Hao et al., 2019; Kowash et al., 2022; Labouesse et al., 2015a; Potter et al., 2023; Richetto et al., 2017a, 2017b; Weber-Stadlbauer et al., 2021). This predicted a minimum of 5-6 offspring/sex/group/age required for molecular analysis and a minimum of 8 offspring/sex/group/age required for behavioural assessments, to be sufficiently powered (1-β=0.8), with a type I error rate (α) of 0.05. Thus, a minimum of 6 or 8 dams/group/cohort would be needed to provide a sufficient number of offspring for molecular and behavioural analyses, respectively; assuming one male and one female per litter used for each analysis to minimise maternal effects (Meyer et al., 2008a). For all analyses both sexes were considered to account for sex-differences in neurodevelopment, immune functions and behaviours (Giollabhui et al., 2019; Gogos et al., 2020; Wheelock et al., 2019) and to overcome traditional sex-bias in neuroscience research (Coiro and Pollak, 2019).

2.2.1.2. Mating procedures

Nulliparous female rats were time-mated with one randomly assigned male for up to three days. Evidence of a copulation plug in the base of the cage was checked daily and taken as confirmation of conception (GD1). Mating was performed under standard BSF conditions, in designated mating cages constructed from IVCs with the upper level and all bedding material removed. Black paper underneath a raised metal grate lined the cage base to aid in copulation plug identification.

Following successful mating, pregnant females were pair-housed until GD15. All pregnant rats were weighed daily to track pregnancy progress and acclimatise to handling. Unmated females were returned to their home cages for at least one week before reattempting a mating procedure. Breeding males were returned to home cages for at least 48h before being remated with a new female.

2.2.1.3. Induction of MIA

I. Preparation of solutions for injection

Endotoxin-free LMW poly(I:C) (tlrc-picw; InvivoGen, London, UK,) was reconstituted to a 10mg/mL solution in physiological saline (0.9% NaCl) as per manufacturer's instructions. 0.5mL aliquots of poly(I:C) or saline only (vehicle control, hereafter referred to as 'vehicle') were prepared in sterile, endotoxin-free Eppendorf's by an independent experimenter and labelled solutions 'A' or 'B' to henceforth blind experimenters to treatment group (hereafter referred to as 'group'). Prepared solutions were stored at -20°C until use. The lot-numbers of each poly(I:C) batch were assessed using agarose gel electrophoresis as described previously (Kowash et al., 2019). A single clear band without distortion was taken as indication of good quality poly(I:C) for use in *in vivo* injections (Appendix 1, Supplementary Figure S1.1).

II. Procedure for induction of MIA

MIA was induced on GD15, a timepoint shown previously to induce developmental and cognitive deficits relevant to schizophrenia (Kowash, 2019; Kowash et al., 2019, 2022; Murray et al., 2019; Potter, 2021; Potter et al., 2023). On GD15, dams were pseudo-randomly assigned to group A or B using a random number generator. Assigned solution was removed from the freezer and allowed to thaw at room temperature. Dams were weighed and the dose of their designated solution calculated as 1mL/kg bodyweight, corresponding to 10mg/kg bodyweight poly(I:C). Solutions were delivered via a single i.p. injection, using a 23G needle and sterile, single use 1mL syringe. All injections were performed between 08:00-10:00 to minimise circadian influence on immune outcomes (Scheiermann et al., 2013). Injected dams were monitored regularly for 24h post-treatment to ensure no adverse effects as per the PPL, in particular: spontaneous abortions and severe abdominal contractions, which precluded them from further use in the study. Weight measurements were taken at 3h, 6h and 24h post-treatment (for prenatal GD15

harvests, performed between 3-4h post-injection, only 3h weights were taken). On GD16, dams not assigned to GD15/GD16 harvests were housed individually with adequate access to nesting material and weights monitored daily until GD22 (term is GD23), but otherwise pregnant dams were left undisturbed.

III. Collection of dam plasma samples

3h post-injection lateral tail vein blood samples were collected for downstream inflammatory marker analysis to confirm MIA. This timeframe was selected for representing the peak pro-inflammatory response in our model (Kowash et al., 2019; Murray et al., 2019). Dams were placed in hotbox (40°C) for 10min to promote vasodilation, then carefully restrained under a surgical blanket. A second experimenter collected a lateral tail vein blood sample using a 25G butterfly needle. Blood samples were collected in heparinised tubes and centrifuged (10,000xg for 1min) within 5min to collect plasma, which was removed and stored in 60µL aliquots at -80°C.

2.2.1.4. Prenatal harvest procedures

Dams assigned to prenatal cohorts (GD15, GD16 or GD21) were anaesthetised with 5L/min isoflurane (Abbott, Maidenhead, UK) in 2L/min O_2 until cessation of breathing. The dams were then sacrificed by cardiac puncture and removal of the heart. Their abdominal cavity was opened, the uterine horn exposed and the fetoplacental unit rapidly removed. The whole foetus and the placenta were isolated and weighed. Harvested placentas were randomly assigned to be stored (at -80°C) in RNAlater stabilisation solution (Sigma-Aldrich, Gillingham, UK) or flash-frozen for downstream nucleic acid and protein analysis, respectively. Foetal tail tips were taken and stored at -80°C for sex-typing using the KAPA Express Extract and KAPA2G Robust HotStart® ReadyMix™ (Sigma-Aldrich, Gillingham, UK) as described previously, using the male *Sry* gene to identify male sex (performed by Dr Hager Kowash, see Kowash, 2019; Kowash et al., 2022).

Foetal whole brains were then rapidly harvested and weighed. For early prenatal samples (GD15, GD16) it was not possible to reliably dissect brain areas by hand and thus for these timepoints, whole brains were taken for downstream analysis. Harvested whole brains were randomly assigned to be stored (at -80°C) in RNAlater (Sigma-Aldrich, Gillingham, UK) or flash-frozen for nucleic acid and protein analysis, respectively. For GD21, where more complex brain structures have begun to form, it was possible to dissect distinct brain regions and hence these brains underwent further processing procedures (see Section 2.2.2)

2.2.1.5. Postnatal offspring husbandry and tissue collection

For dams assigned to postnatal cohorts, dams were allowed to birth naturally with presence of pups in the nest considered PD0. On PD1 (between 16:00-17:00) the dam was removed from the nest and placed in a holding cage. All pups from the litter were removed from the nest and

placed on a heat mat (40°C) to maintain body temperature. Each pup was then quickly weighed and sexed based on ano-genital distance (Schwartz et al., 2019a). To ensure even distribution of maternal care resources across litters (Suvorov and Vandenberg 2016), significantly small litters were excluded (>2 standard deviations (SD) from the mean, given the normal distribution of litter sizes; Section 2.3.1), while litters >10 pups were culled to 10 to match more closely litter sizes in wild Norway rat populations. Pups were randomly selected for culling using a random number generator, with equal sex ratios maintained where possible to minimise sex-biased maternal care. PD1 pups selected for culling were sacrificed by overdose anaesthetic 5L/min isoflurane (Abbott, Maidenhead, UK) in 2L/min O_2. Pups were then rapidly decapitated and checked for cessation of bleeding. Trunk blood was collected in heparinised tubes and centrifuged (10,000xg for 1min) within 5min of collection, with resulting plasma stored in 100µL aliquots at -80°C. PD1 brains were isolated, weighed and processed for downstream molecular analysis (see Section 2.2.2). Remaining pups were marked with a distinguishing pattern on their back (Potter, 2021) using a non-toxic marker to identify them and returned to the nest, along with the dam. It is worth noting that for experiments in which cross-fostering was employed (postnatal cohort 2A (PN2A)), half the remaining PD1 pups were randomly cross-fostered, following marking, to a reciprocal treatment dam (Potter, 2021) such that half the litter was hereafter referred to as cross-fostered and half remained in the home cage with their birth dam (non-cross-fostered). Cross-fostered animals were not used in any of the downstream molecular experiments in subsequent chapters. Pups were marked daily until weaning, to counter their rapid removal due to dam licking behaviours. On PD6, PD10 and PD14, dams were removed into a holding cage for 1h to enable ultra-sonic vocalisation and MCB scoring (Potter, 2021). During this time, pups were weighed to track developmental growth. On PD21, all pups were weighed, marked and one male and one female from each litter randomly selected for sample collection. These animals were asphyxiated by 2L/min CO_2, followed by cervical dislocation. Animals were then decapitated and trunk blood collected in heparinised tubes and centrifuged (10,000xg for 1min), with resulting plasma stored in 100µL aliquots at -80°C. PD21 brains were also isolated, weighed and processed for downstream molecular analysis (Section 2.2.2)

Offspring were weaned on PD28 and dams subsequently sacrificed by 2L/min CO_2, followed by cervical dislocation. Weaned offspring were randomly assigned to female (5/cage) or male (2-3/cage) cages irrespective of group, with weekly tail-marking to maintain identification. New IDs were provided to re-blind experimenters prior to behavioural testing. At this stage offspring were randomly assigned to adolescent (PD35) or adult (PD100-175) behavioural analysis. Post-behavioural profiling, animals were culled by either:

i) Asphyxiation by 2L/min CO_2 until cessation of breathing, followed by cervical dislocation for nucleic acid/protein analysis. Following asphyxiation/cervical dislocation, animals were subsequently decapitated and trunk blood collected in heparinised tubes. Blood samples were centrifuged (10,000xg for 1min), with resulting plasma stored in 100µL aliquots at -

80°C. Whole brains were isolated and weighed prior to downstream processing (Section 2.2.2).

ii) Overdose of anaesthetic followed by trans-cardial perfusion with paraformaldehyde (PFA), for immunohistochemical analysis. Animals were anesthetised with 5% isoflurane (Abbott, Maidenhead, UK) in 2L/min O_2. Once they were unresponsive to physical stimuli, an abdominal incision was made, below the xiphoid cartilage. The diaphragm was then severed and the heart exposed. A 15G perfusion needle, attached to a perfusion pump (20mL/min flow rate), was inserted into the left ventricle and clamped into position. An incision was then made in the right atrium to permit outflow from the circulatory system. The first flush was performed with ice-cold 1XPBS (Oxoid, Basingstoke, UK) for approximately 10min until the outflow was clear, followed by ice-cold 4%PFA (Sigma-Aldrich, Gillingham, UK) in 1XPBS for a further 10min. The brains were then removed for downstream processing (Section 2.2.2).

Postnatal timepoints correspond to infant (PD1), juvenile (PD21), adolescent (PD35) and adult (PD100-175) developmental periods (Spear, 2000; Woods et al., 2021)

2.2.1.6. Offspring behavioural assessments

Behavioural experiments were performed in adolescence (PD35) and adulthood (PD100-175). Cognitive tasks were selected (Table 2.1) based on their clinical relevance, measured according to the MATRICS Consensus Cognitive Battery (MCCB; August et al., 2012) to best represent schizophrenia cognitive symptoms (Mihaljević-Peleš et al., 2019). Behavioural tasks were performed by Dr Harry Potter (see Potter, 2021; Potter et al., 2023). Behavioural phenotypes of offspring will be discussed only as they relate to the downstream molecular analyses.

Table 2.1. Cognitive behavioural assessments

Task	Cognitive Measure	Brain region	Ages
NOR	Visual recognition memory	Hippocampus	Adolescent, Adult
SI	Social cognition	PFC	Adolescent, Adult
RAM	Spatial working memory	Hippocampus	Adolescent, Adult
ASST	Cognitive flexibility Reversal learning	PFC	Adult

2.2.2. Preparation of harvested brains for downstream analysis

For nucleic acid and protein analysis, whole brains collected at GD21, PD1, PD21, PD35 and PD100/PD175 were bisected into left and right hemispheres and stored in RNAlater (Sigma-Aldrich, Gillingham, UK) for nucleic acid isolation or flash-frozen using dry ice for protein isolation, respectively. Samples were then stored at -80°C in sterile Bijou tubes for later use. Hemispheric dissections were subsequently performed on ice by hand to isolate brain regions of interest as directed by the Rat Brain Stereotaxic Co-ordinates (6th Edition, Paxinos and Watson, 2006; Figure 2.2). For GD21 and PD1 where the PFC has not yet formed (Kolk and Rakic, 2022), left or right hemisphere frontal cortex (FC) only were dissected, whereas from

later postnatal samples (PD21, PD35, PD100/175) both FC and PFC were dissected. All dissected brain tissues were stored in individual clean Eppendorf tubes containing 200µL RNAlater (left hemisphere for nucleic acid isolation) or frozen without buffer (right hemisphere for protein isolation) at -80°C. The PFC was selected for its involvement in cognition and schizophrenia pathophysiology and, particularly, its role in the ASST (Miller, 2000; Salgado-Pineda et al., 2009).

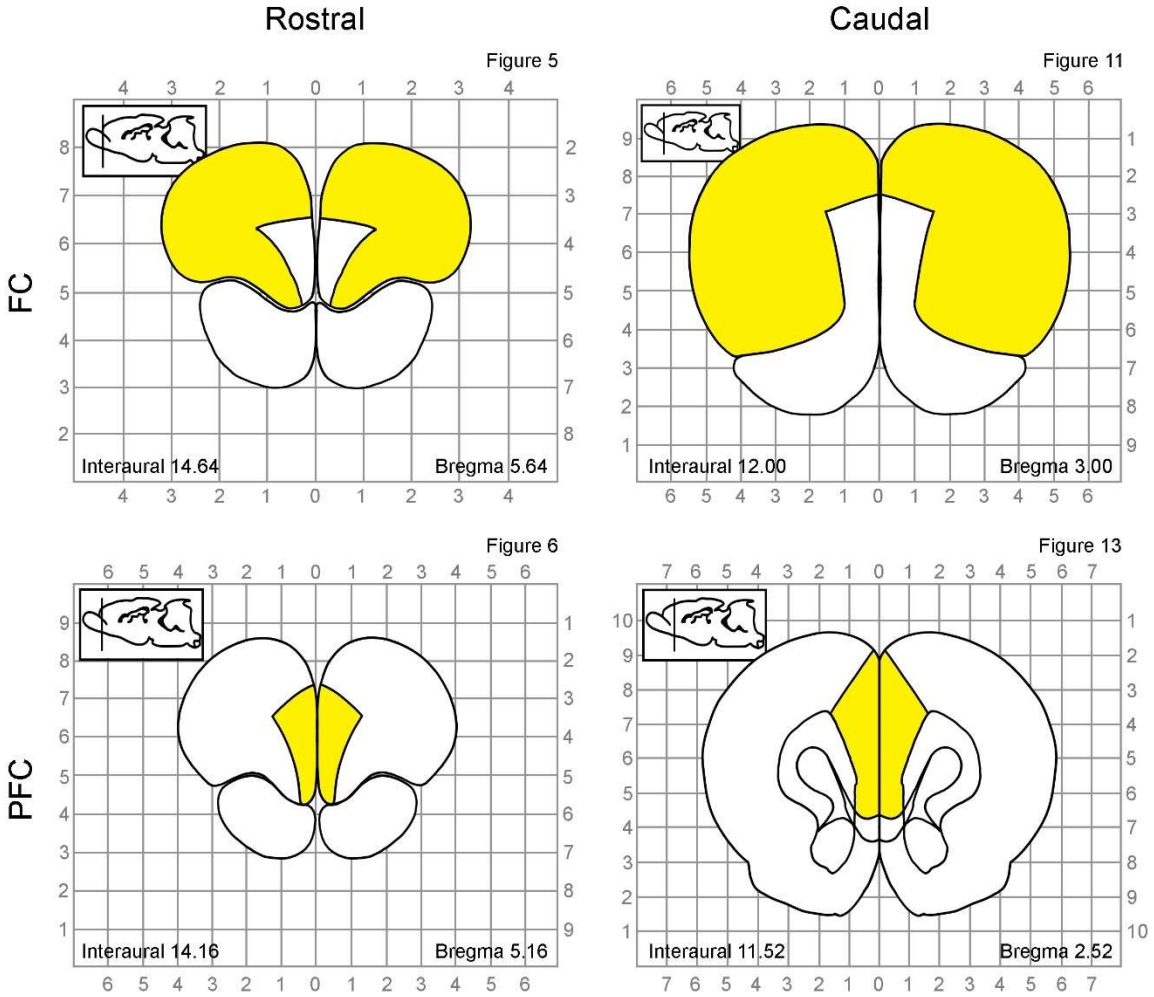

Figure 2.2. Stereotaxic co-ordinates for rat brain dissections
Offspring brains were dissected for corticol regions of interest: the frontal cortex (FC) and prefrontal cortex (PFC) as directed by the Rat Brain Sterotaxic Co-ordinates (6th Edition, Paxinos and Watson, 2007). Co-ordinates are shown by the furthest rostral and caudal identifiers for each region, with figure number references, bregma and interaural co-ordinates provided. The FC and PFC have been highlighted in yellow.

For immunohistochemical (IHC) and immunofluorescence (IF) analysis, perfused brains were placed in 10mL ice-cold 4%PFA (Sigma-Aldrich, Gillingham, UK) in 1XPBS and incubated overnight at 4°C to post-fix. Brains were then transferred into 10mL 30% sucrose (Sigma-Aldrich, Gillingham, UK) solution for 24-48h at 4°C until the brain sank, indicating complete infiltration. The brain was then snap frozen in isopentane (Fisher Scientific, Loughborough, UK) and stored at -80°C until sectioning. For sectioning, frozen brains were coated in optimal cutting temperature (OCT) compound (Scigen, Gardena, USA) and mounted onto a cryostat (Leica

Biosystems, Newcastle, UK), with the rostral face of the brain aligned to the blade. Using the Rat Brain Stereotaxic Co-ordinates as a guide (6th Edition, Paxinos and Watson, 2006; Figure 2.2), 30µM coronal sections were sliced through the PFC. Once cut, sections were rapidly submerged in cryoprotectant (prepared from 30% ethylene glycol (Sigma-Aldrich, Gillingham, UK), 30% glycerol (Sigma-Aldrich, Gillingham, UK), in 1XPBS (Oxoid, Basingstoke, UK)), in a 12-well culture plate. Moving from rostral to caudal, every 8th section was pooled (creating 8 samples/animal). Section pools were stored at -20°C.

2.2.3. Preparation of protein lysates from brain samples

Stock homogenisation buffer was prepared as per Table 2.2, divided into 10mL aliquots and stored at -20°C until use, with stock solutions of phosphatase and protease inhibitors prepared as per Table 2.3 on day of use. Briefly, one 10mL homogenisation buffer aliquot was removed from the freezer and thawed at room temperature. Once thawed, 400µL 25X cOmplete protease inhibitor cocktail, 100µL 0.1M PMSF and 100µL 0.1M sodium orthovanadate were added to activate the buffer.

Table 2.2. Homogenisation buffer composition for protein lysates

Reagent	Weight or volume	Final concentration
Trizma base (Sigma-Aldrich, UK)	242.28mg	10mM
Sucrose (Sigma-Aldrich, UK)	21.9mg	0.32mM
Ethylenediaminetetraacetic acid (EDTA; Sigma-Aldrich, UK)	148.9mg	2.5mM
dH_2O	Up to 200mL	-

Samples were thawed on ice and activated homogenisation buffer added to the samples at 10µL/mg frozen tissue weight. The samples were then homogenised on ice using a pestle until no visible tissue remained. For whole tissue lysates, samples at this stage were stored at -80°C.

Table 2.3. Preparation of protease/phosphatase inhibitors for whole tissue lysates

Compound	Role	Preparation	Concentration
Phenylmethylsulfonyl fluoride (PMSF; Sigma-Aldrich, UK)	Protease inhibitor	87.1mg in 5mL 100% ethanol	0.1M
Sodium Orthovanodate (Sigma-Aldrich, UK)	Phosphatase inhibitor	91.96mg in 5mL dH_2O	0.1M
cOmplete protease inhibitor (Roche, UK)	Protease inhibitor	1 tablet cOmplete protease inhibitor in 2mL dH_2O	25X

2.2.3.1. Bradford assay for quantifying protein concentrations

Protein concentration was quantified using a Bradford Protein Assay (Bio-Rad, Watford, UK), according to the manufacturer's instructions. Briefly, samples were diluted (whole tissue lysate, 1:100) in distilled water (dH_2O) in a total of 50µL volume. Bovine serum albumin (BSA; A2153;

Sigma-Aldrich, Gillingham, UK) was used to create a standard curve. BSA was dissolved in dH_2O to a 1mg/mL BSA stock solution, aliquoted and stored at -20°C. An 8-point standard ranging from 0.01-1mg/mL BSA, including a dH_2O blank (0mg/mL), was prepared fresh from the frozen BSA stock solution on day of use. 20µL of prepared samples/standards were loaded into a clear, flat-bottomed microplate in duplicate. 90µL 0.3M NaOH (Sigma-Aldrich, Gillingham, UK) was added to each well and incubated for 5min to solubilise protein, followed by addition of 90µL 0.3M HCl (Sigma-Aldrich, Gillingham, UK), incubated for 5min to neutralise. 50µL Bradford reagent was then added and mixed thoroughly by repeated pipetting, with a colour change of brown to blue indicative of high protein concentration.

Absorbance was read at 595nm on the Biotek synergy H1 plate reader (Agilent, Cheadle, UK). Data was exported and input into GraphPad Prism (v9.0; San Diego, USA) and a linear regression standard curve used to interpolate sample values. Interpolated sample values were corrected for their initial dilution factor to give final protein concentration (mg/mL). Pass criteria for Bradford assays included a standard $R^2 \geq 0.99$ and replicate percentage co-efficient of variation (%CV) ≤10%. A representative curve can be found in Figure 2.3.

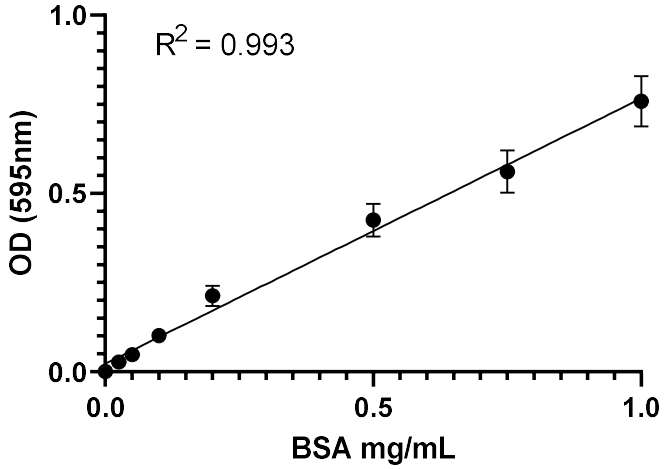

Figure 2.3. Representative Bradford protein assay standard curve
Linear regression with R^2-value indicated ($p<0.0001$). Data shown as mean ±SEM.

2.2.4. Quantification of maternal and offspring cytokines

2.2.4.1. Measurement of maternal plasma TNFα and IL-6 concentration

Abcam (Cambridge, UK) TNFα (ab100784) and IL-6 (ab100772) ELISA kits were used to measure maternal plasma cytokines, as per manufacturer's instructions. Reagents/buffers from both kits were prepared to their working dilutions as per kit guidelines. 400µL Assay Diluent A (TNFα) or 500µL Assay Diluent C (IL-6) were added to the supplied stock standard vials. From these stock standards, 8-point serial dilution standards were prepared as directed: 41.15-

20,000pg/mL TNFα and 40.96-10,000pg/mL IL-6. For both standard curves a 0pg/mL (Assay Diluent only) standard point was included.

50µL standards were added to the provided pre-coated plates in duplicate. 50µL neat plasma sample was added per single well (or duplicate wells where volume was available). Plates were then incubated at room temperature for 2.5h on an orbital shaker (100rpm; S1500 Stuart™; Cole-Parmer, Illinois, USA). The solutions were then discarded and wells washed 4 times with 300µL 1XWash solution before addition of 50µL 1XBiotinylated detection antibody. The plate was then incubated for 1h at room temperature on an orbital shaker (100rpm). The solutions were discarded and wells washed as previously. 50µL 1XHRP-Streptavidin solution was added to each well and the plate incubated for 1h at room temperature on an orbital shaker (100rpm). The solutions were then discarded and wells washed as previously. 100µL TMB solution was added to each well and incubated in the dark for 30min at room temperature on an orbital shaker (100rpm). 50µL Stop Solution was added to each well and plate absorbance read at 450nm on a FLUOstar Omega microplate reader (BMG Labtech, Aylesbury, UK) within 5min. Raw Data was imported into GraphPad Prism (v9.0) and analysed by generating a 4-parameter logistic regression (4-PL) curve to interpolate sample values (pg/mL). %CV values were calculated for all standards/sample duplicates and accepted at CV≤10%. Standard curve values consistently had R^2≥0.99 indicating goodness of fit. A representative standard curve for IL-6 and TNFα can be seen in Figure 2.4.

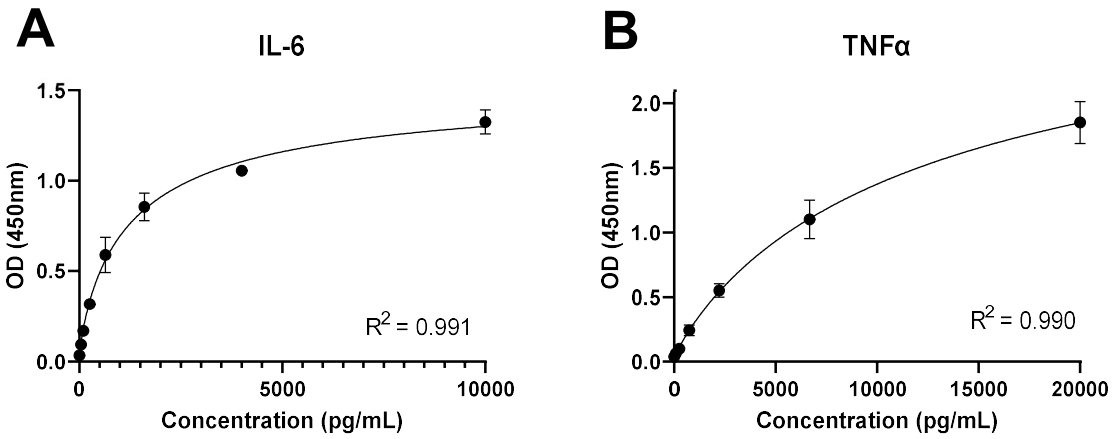

Figure 2.4. Representative standard curves for maternal plasma cytokine ELISAs
A. IL-6, 0-1,000pg/mL; **B.** TNFα, 0-2,000pg/mL. Standard curves were fitted with 4-PL analysis, with R^2-values indicated. Data shown as mean ±SEM.

2.2.4.2. Quantification of cytokines from foetal brain tissue

To assess changes in the brain neuroinflammatory profiles, the Abcam ELISA kits were trialled using foetal (GD15, GD16) whole brain lysates, alongside a well containing the homogenisation buffer only. It was found that the homogenisation buffer interfered with the assay, resulting in high background, over which the sample concentrations were not interpretable (data not shown).

Hence it was determined that these were not suitable for the quantification of cytokines from tissue lysates and instead alternative ELISAs were selected for these analyses.

I. TNFα, IL-1β and IL-10

TNFα, IL-1β and IL-10 ELISAs were obtained from Proteintech (Manchester, UK) and performed as per kit specifications. In brief, standard concentrates were reconstituted in 1mL sample diluent PT1-dc (IL-1β) or 2mL PT1-ef (TNFα and IL-10). For each analyte a 1:2 serial dilution standard was prepared: 31.25-2,000pg/mL (IL-1β), 15.125-1,000pg/mL (TNFα), 31.25-4,000pg/mL (IL-10). All standard curves included a 0pg/mL (sample diluent only) standard point.

Onto the supplied pre-coated microplate 100µL standards were loaded in duplicate along with a single 100µL neat foetal whole brain tissue lysate (duplicate where feasible). The plate was incubated for 2h at 37°C and 100rpm on the Mini Shaking Incubator (N-Biotek, Gyeonggi-do, Korea). The wells were then washed four times with 1XWash buffer. 100µL Detection Antibody (prepared from 100XDetection Antibody diluted 1:100 in Detection Diluent) was added to each well and incubated for 1h at 37°C and 100rpm on the Mini Shaking Incubator. The wells were then washed as previously and 100µL HRP-conjugated antibody (prepared from 100XHRP-conjugated antibody diluted 1:100 in Detection Diluent) added to each well and incubated for 40min at 37°C and 100rpm on the Mini Shaking Incubator. The wells were then washed as previously. 100µL TMB substrate was added to each well and incubated for 20min at 37°C in the dark before addition of 100µL Stop Solution. Absorbance was then read on a Biotek synergy H1 plate reader (Agilent, Cheadle, UK) at a primary wavelength of 450nm and reference wavelength of 630nm.

To analyse, the reference wavelength absorbance reading was subtracted from the primary wavelength to generate a normalised optical density (OD). GraphPad Prism (v9.0) was used to generate a 4-PL standard curve, with representative standard curves shown in Figure 2.5A-C. %CV of standard values ranged from 0-12%, with an $R^2 \geq 0.99$. Interpolated sample values (pg/mL) were normalised to protein concentration (mg/mL) to generate tissue concentration (pg cytokine/mg protein) for each sample.

II. IL-6

R&D systems (Abingdon, UK) Duoset IL-6 rat ELISA and ancillary kit were used as per manufacturer's instructions. Briefly, from the ancillary kit, 25XWash buffer concentrate was diluted 1:25, 10XReagent diluent concentrate diluted 1:10, both in dH_2O to produce 1XWorking solutions. IL-6 lyophilised reagents were reconstituted as per Lot-specific instructions to create stock solutions of the following concentrations: Mouse Anti-Rat IL-6 Capture Antibody (480µg/mL) in 1XPBS, Biotinylated Goat Anti-Rat IL-6 Detection Antibody (9µg/mL) in 1XReagent diluent, Recombinant Rat IL-6 Standard (230ng/mL) in 1XReagent diluent.

Reconstituted Capture Antibody was diluted to 4µg/mL (1:120 dilution) in 1XPBS. 100µL diluted Capture Antibody was added to each well of the microplate and incubated overnight at room

temperature (25°C). The solution was discarded and each well washed three times with 200µL 1XWash buffer. 300µL 1XReagent diluent was added to each well and incubated at room temperature for 1h. Solution was discarded and wells washed three times with 400µL 1XWash buffer. 34.8µL reconstituted Recombinant Rat IL-6 Standard was diluted in 965.2µL 1XReagent diluent to produce an 8,000pg/mL starting solution. A 1:2 serial dilution was prepared from the starting standard solution to produce a 31.25-4,000pg/mL standard curve. Prepared standard curves also included a 0pg/mL (1XReagent diluent only) standard point. 100µL neat foetal brain protein lysate (single) and prepared standards (duplicate) were added to the wells of the prepared microplate and incubated for 2h at 25°C. The Detection Antibody was diluted 15min prior to use to working dilution of 150ng/mL in 1XReagent diluent containing 2% (v/v) normal goat serum (Vector Laboratories, UK). Samples and standards were discarded and wells washed three times with 200µL 1XWash buffer before addition of 100µL Detection Antibody solution, incubated for 2h at 25°C. Detection antibody was discarded and wells washed three times with 200µL 1XWash buffer. 100µL streptavidin-HRP (diluted 40-fold with 1XReagent diluent) was added to each well and incubated for 20min at 25°C. The substrate solution was prepared 5min before use by mixing equal volumes reagent A and B. Streptavidin-HRP solution was discarded and wells washed three times with 200µL 1XWash buffer. 100µL prepared substrate solution was added to each well and incubated for 20min at 25°C, followed by addition of 50µL Stop Solution. Plate absorbance was read on Biotek Synergy H1 plate reader (Agilent, Cheadle, UK) at a primary wavelength of 450nm and reference wavelength of 570nm. The reference wavelength values were deducted from the primary absorbance values prior to analysis. These corrected OD values were then input into GraphPad prism (v9.0), a 4-PL standard curve generated and sample values interpolated. %CV of standard duplicates ranged from 0-6%, with $R^2 \geq 0.99$. A representative standard curve for IL-6 can be seen in Figure 2.5D. Interpolated sample IL-6 values (pg/mL) were then divided by the protein concentration (mg/mL) to give a tissue IL-6 concentration (pg/mg protein).

2.2.4.3. Quantification of cytokines from offspring tissues

To investigate ongoing inflammatory disturbances in postnatal offspring, multiplexes were firstly trailed owing to their ability to assay several analytes in low sample volumes with high sensitivity. Two multiplex platforms: BioTechne Luminex and Merck Millipore Milliplex rat cytokine panels were trialled. However, results from these studies showed high background signal from tissue samples which prevented accurate quantification of cytokines (data not shown). As a contingency, owing to limited sample availability and large volumes required for ELISA-based methods (outlined above), only a single cytokine could be analysed from matched plasma and brain lysates in postnatal offspring. IL-6 was selected for analysis as the only cytokine showing significant changes in both maternal plasma and foetal whole brain in response to MIA. Further, IL-6 is thought to be critical in mediating the outcomes of MIA (Samuelsson et al., 2006; Smith et al., 2007) and has been identified as a marker for increased psychosis-risk following ELS

(Khandaker et al., 2014; King et al., 2021; Perry et al., 2021). For this, the pre-optimised R&D systems Duoset IL-6 rat ELISA (Section 2.2.4.2) assay was used, analysing matched plasma and whole tissue lysate samples from GD21-PD100. The only alteration to the outlined methodology was that standards and samples were loaded at 50µL due to the limited lysate volume obtained from postnatal PFC samples. This lower sample input did not affect the standard curve, with similar R^2-values and %CVs between replicates.

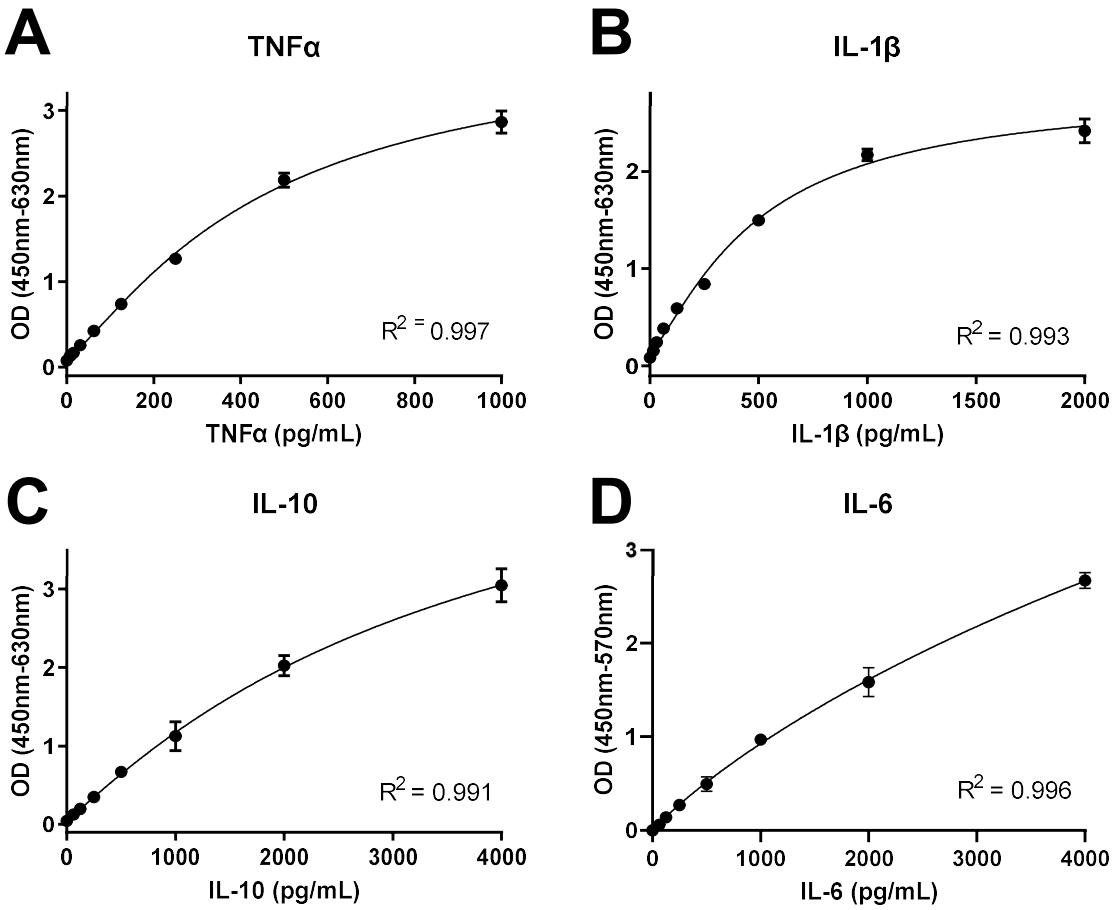

Figure 2.5. Representative standard curves for foetal cytokine ELISAs
A. TNFα, 0-1,000pg/mL; **B**. IL-1β, 0-2,000pg/mL; **C**. IL-10, 0-4,000pg/mL; **D**. IL-6, 0-4,000pg/mL. Standard curves are fitted by 4-PL with R^2-values indicated. Data are shown as mean ±SEM.

2.2.5. Statistics

All statistical analysis was performed in SPSS v28.0 (IBM, Armonk, USA). Within-group outliers were identified and excluded using SPSS extreme outlier function, calculated as datapoints >3X interquartile range. For all statistical models the least significant predictors were sequentially removed to find a minimal model, which included significant and/or trending to significant predictor variables only (Grafen and Hails, 2002). P-values≤0.05 were considered statistically significant, while 0.05<p≤0.08 were considered trending towards significant.

Maternal plasma cytokine concentrations (IL-6 or TNFα pg/mL) were analysed by general linear modelling (GLM), while for dam percentage weight change across pregnancy, a repeated

measures GLM (RM-GLM) was used to assess pre- and post-treatment growth rates, both using group as a fixed factor. Maternal measures were first assessed across all cohorts, including cohort as a fixed factor in the model and then, where cohort had a significant main effect, data was analysed within each cohort individually. For dam weight changes, maternal 3h plasma TNFα and IL-6 (pg/mL) were also included in the model as covariates to evaluate if the magnitude of MIA influenced dam weights.

For foetal/offspring measures (including the following dependent variables in this Chapter: litter size, weights and brain/plasma cytokine concentrations), general linear mixed modelling (GLMM) was used, with the degrees of freedom estimated using the Satterthwaite approximation and with normality of error assumptions assessed. Dam was included as a random factor in each GLMM to account for variability induced by shared maternal environments and group and sex were used as fixed factors. Maternal 3h plasma TNFα and IL-6 (pg/mL) were also included as co-variants because it is hypothesized that maternal-derived cytokines drive pathological changes in MIA-exposed offspring (Meyer et al., 2009b). Where effects of all four predictors (sex, group, maternal TNFα and IL-6) were insignificant, the phrase ‘there were no significant effects of any predictors’ will be used. For all GLMMs, where sex or group*sex interactions were significant or trending toward significance, a further GLMM was performed within a single sex with Dam as a random factor, group as a fixed factor and maternal cytokines as covariates. As each timepoint or molecular analyses comprised different animals no multiple testing correction was applied to any GLMM analysis in this thesis.

Where appropriate, correlations were used to evaluate the relationship between quantitative dependent variables and covariates. Normality of raw data distribution was determined using the Shapiro-Wilk Test, with $p \geq 0.05$ indicating normal distribution. When both variables were normally distributed, post-hoc Pearson’s (r) correlations were used, where one or more variables were non-normally distributed, Spearman’s (rho) correlations were used.

All graphs were generated using GraphPad prism (v9.0), with n-numbers for dam per group (N) and foetuses/pups/placentas per sex per group (n) indicated in the figure legends. For bar charts, data are represented as mean ±SEM. Plotted points on graphs indicate individual samples.

2.3. RESULTS

PR1 dam/foetal weights/dam cytokine quantification was performed by Dr Hager Kowash (Kowash, 2019), with author support for GD21. PN1/PN2A dam cytokine quantification was performed by Dr Harry Potter (Potter, 2021), with author support for weight data. PN2B data and foetal/offspring cytokine data was collected by the author.

2.3.1. Cohort summaries

A total of three cohorts of animals were used for the molecular studies in this thesis. The first two cohorts, prenatal cohort 1 (PN1, comprising dams harvested on GD15, 16 and 21; Kowash, 2019) and postnatal cohort 1 (PN1, the first postnatal cohort; Potter, 2021; Potter et al., 2023), were performed from 2017-2018 and used poly(I:C) Lot PIW-38-04. The third was a second postnatal cohort (PN2) which used poly(I:C) Lot PIW-39-01. This cohort was performed in two parts from 2019-2020: the first a primary cohort with a split-litter cross fostering design (PN2A; Potter, 2021), the second a satellite cohort of animals which did not undergo a cross-fostering procedure (PN2B) but underwent the same husbandry procedures as PN1/PN2A to induce the same adult cognitive phenotypes. Offspring from the latter cohort were used exclusively for molecular analysis. A summary of the cohorts can be found in Table 2.4. Of the outlined cohorts, all litters were included in downstream analysis, except for two dams in PN2B: one vehicle-dam and one poly(I:C)-dam, with litters of three pups, falling outside the pre-specified mean ±2SD inclusion criterion, indicating these were abnormal litter sizes. Hence, these litters were excluded from all downstream analyses, resulting in seven vehicle-dams and eight poly(I:C)-dams in PN2B.

Table 2.4. Summary of animal cohorts

Cohort		Poly(I:C) Lot	Dam number	Litter size (mean ±SD)	Offspring sex/litter (mean ±SD)	Adolescent behaviour	Adult behaviour
PR1*	**GD15**	PIW-38-04	6 VEH 8 PIC	VEH: 15±3 PIC: 14±3	VEH: 8±3 (M); 7±2 (F) PIC: 7±2 (M); 7±2 (F)	NA	NA
	GD16		6 VEH 6 PIC	VEH: 14±4 PIC: 14±1	VEH: 6±1 (M); 8±3 (F) PIC: 7±3 (M); 7±3 (F)	NA	NA
	GD21		6 VEH 6 PIC	VEH: 14±3 PIC: 13±3	VEH: 7±2 (M); 7±2 (F) PIC: 7±2 (M); 7±1 (F)	NA	NA
PN1**			9 VEH 9 PIC	VEH: 14±2 PIC: 12±3	VEH: 6±2 (M); 8±3 (F) PIC: 7±2 (M); 5±2 (F)	PD35	PD175
PN2**	**A**	PIW-39-01	11 VEH 11 PIC	VEH: 13±2 PIC: 12±3	VEH: 6±3 (M); 7±2 (F) PIC: 6±2 (M); 6±2 (F)	PD35	PD100
	B		8 VEH 9 PIC	VEH: 12±3 PIC: 11±3	VEH: 6±2 (M); 6±3 (F) PIC: 5±3 (M); 5±4 (F)	-	-

*PR1 designed and performed by Dr Hager Kowash, with author support for mating, procedures and GD21 litter culls.
**PN1/PN2A designed and performed by Dr Harry Potter, with author support for PN2A mating, MIA induction and plasma collection, offspring weighing and culling. PN2B was performed by the author. Abbreviations: VEH, vehicle-dams, PIC, poly(I:C)-dams; F, female; M, male; NA, not applicable. Data are represented as mean ±SD owing to the SD-based exclusion criteria applied to litter sizes (Section 2.2.1.5)

2.3.2. Dam response to poly(I:C)

2.3.2.1. Dam plasma cytokines

Two pro-inflammatory cytokines, IL-6 and TNFα, were selected for plasma cytokine analysis 3h post-treatment based on previous studies showing the relevance of these cytokines in MIA outcomes (Kowash et al., 2019; Potter et al., 2023; Smith et al., 2007).

I. IL-6

There was a significant main effect of group (GLM: $F_{1,60}$=9.75, p=0.003), with increased plasma IL-6 concentration in poly(I:C)-dams relative to vehicle-dams and a main effect of cohort (GLM: $F_{2,60}$=39.69, p<0.001). When cohorts were considered individually there was a significant main effect of group in each of the cohorts, with poly(I:C) consistently inducing elevated plasma IL-6 at the 3h timepoint. However, the concentration values (pg/mL) for IL-6 varied across cohorts (Table 2.5; Figure 2.6A), with a high variance seen in poly(I:C)-groups, especially for PR1 and PN1 cohorts.

Table 2.5. Summary of dam plasma IL-6 concentrations across cohorts

Cohort	Vehicle IL-6 (mean ±SEM)	Poly(I:C) IL-6 (mean ±SEM)	Main effect of group (GLM)
PR1	82.43±5.24	133.66±18.38	$F_{1,30}$=6.43, p=0.017
PN1	1.38±0.98	23.20±11.39	$F_{1,14}$=5.18, p=0.039
PN2A	ND	ND	-
PN2B	12.09±0.31	21.32±2.5	$F_{1,13}$=11.54, p=0.005

Abbreviations: ND, not detected.

II. TNFα

As with IL-6, there was a significant main effect of group (GLM: $F_{1,74}$=49.07, p<0.001), with increased plasma TNFα in poly(I:C)-dams relative to vehicle-dams and a main effect of cohort (GLM: $F_{3,74}$=9.46, p<0.001). When cohorts were considered individually there was a main effect of group in each of the cohorts, with poly(I:C) consistently inducing elevated plasma TNFα at the 3h timepoint, with the effect seeming more robust than observed for IL-6, though again the TNFα concentration (pg/mL) varied between cohorts, with greatest variability in poly(I:C)-groups (Table 2.6; Figure 2.6B).

Table 2.6. Summary of dam plasma TNFα concentrations across cohorts

Cohort	Vehicle IL-6 (Mean ±SEM)	Poly(I:C) IL-6 (Mean ±SEM)	Main effect of group (GLM)
PR1	315.38±44.33	1128.12±181.06	$F_{1,29}$=17.83, p<0.001
PN1	109.26±34.74	842.28±180.20	$F_{1,15}$=17.92, p<0.001
PN2	40.88±5.45	398.93±53.78	$F_{1,31}$=36.48, p<0.001
PN2A	32.87±9.37	471.69±69.44	$F_{1,16}$=31.20, p<0.001
PN2B	50.01±2.28	307.98±76.99	$F_{1,13}$=9.72, p=0.008

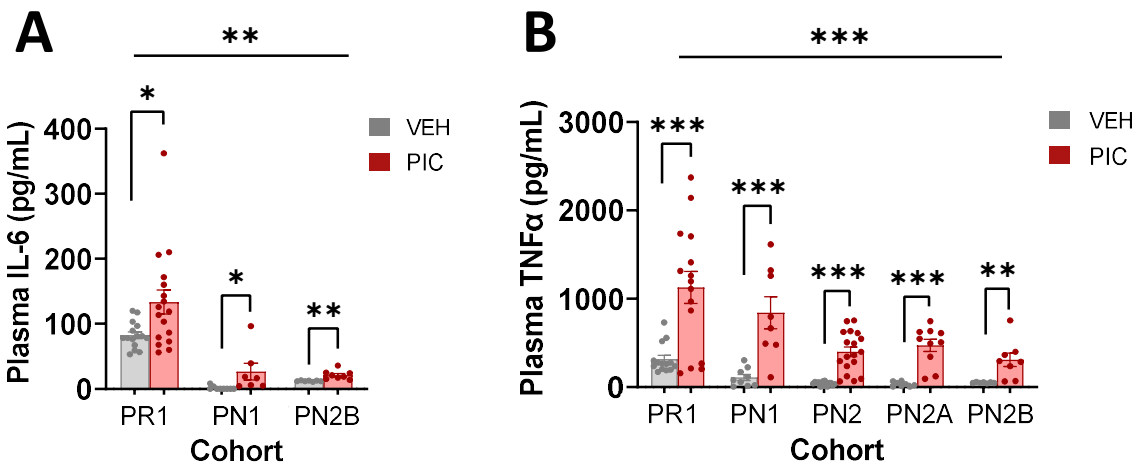

Figure 2.6. Dam plasma cytokine concentrations
A. Maternal plasma IL-6 pg/mL (N=7-17) **B.** Maternal plasma TNFα pg/mL (N=7-15). – shaped significance bars show GLM result across all cohorts, Π-shaped significance bars indicate GLM result within a single cohort. Symbols indicate significant main effects of: group *p<0.05, **p<0.01, ***p<0.001. Abbreviations: PR, prenatal cohort; PN, postnatal cohort; VEH, vehicle-dams; PIC, poly(I:C)-dams. Data show mean ±SEM, dots represent individual dams.

2.3.2.2. Dam weight changes

Pre-pregnancy weight (mean ±SEM) of all dams included in the study (N=95) was 260.45g ±1.94, with no significant differences between cohorts/groups. A summary of percentage weight gain across pregnancy can be found in Figure 2.7. Dams showed an average percentage weight gain of 21.52% ±4.22 up to GD14, with no significant difference between groups (RM-GLM: $F_{13,689}$=0.430, p=0.959; Figure 2.7). By comparison, weight gain post-treatment (GD15-22) was significantly different between groups (RM-GLMM: $F_{7,301}$=4.472, p<0.001) with poly(I:C)-dams having a lower weight gain increment rate than vehicle-dams (Figure 2.7).

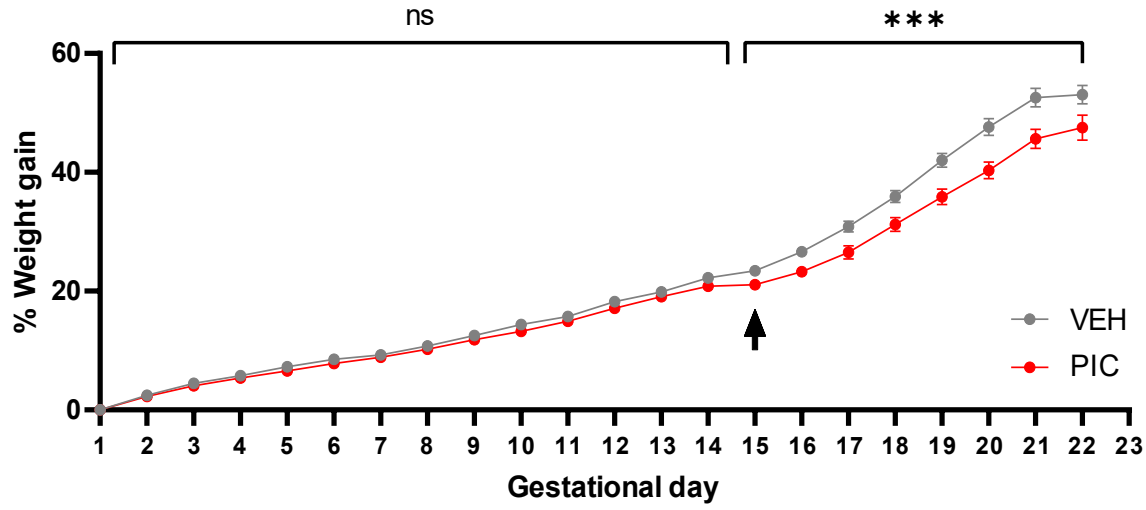

Figure 2.7. Dam weight gain through pregnancy
Percentage weight gain of vehicle (VEH; N=46) and poly(I:C) (PIC; N=49) dams throughout pregnancy, relative to GD1. Arrow indicates GD15, treatment. Rate of growth (%weight gain) was compared pre-(GD1-14) and post-(GD15-22) treatment: ns, non-significant; ***p<0.001 (RM-GLM). Data show mean ±SEM.

The initial weight change between groups could be attributed to a greater weight loss in the poly(I:C)-dams relative to vehicle-dams across 3h, 6h and 24h post-treatment on GD15 (RM-GLM: $F_{2,104}$=9.00, p<0.001; Figure 2.8A).

I. 3h weight change

There was no main effect of cohort on 3h weight loss. However, there was a trend toward main effects of both group (GLM: $F_{1,56}$=2.48, p=0.063; Figure 2.8A) and plasma IL-6 (GLM: $F_{1,56}$=2.51, p=0061; Figure 2.8A), the latter corresponding to a negative correlation between plasma IL-6 and weight loss (r=-0.235, p=0.066; Figure 2.8B), suggesting a relationship between magnitude of MIA and acute weight loss.

II. 6h weight change

6h weight change analysis included 3h weight change as a covariate to account for any effects of MIA on the 3h weight change. Here, there was a significant main effect of 3h weight change (GLM: $F_{1,71}$=39.84, p<0.001; Figure 2.8A), with a positive correlation between 3h and 6h weight changes (r=0.443, p=0.006; Figure 2.8D) and a main effect of group (GLM: $F_{1,71}$=31.70, p<0.001; Figure 2.8A), with greater 6h weight loss in poly(I:C)-dams relative to vehicle-dams and a main effect of cohort (GLM: $F_{3,71}$=4.90, p=0.004). The addition of plasma cytokines as covariates had no impact on the minimal model, although there was a negative correlation between 6h weight change and plasma TNFα (r=-0.355, p=0.042; Figure 2.8C), indicating high plasma TNFα induces weight loss at 6h.

Given the significant main effect of cohort, 6h weight change was re-analysed within each individual cohort. These results showed that across all cohorts, 3h weight change predicted 6h weight change (Table 2.7). However, there was a main effect of group in cohorts PR1/PN2, with greater weight loss at 6h in poly(I:C)-dams relative to vehicle-dams (Table 2.7), but a main effect of plasma IL-6 in PN1, with a negative correlation between plasma IL-6 and 6h weight changes (r=-0.571, p=0.021). Nevertheless, these data support a robust MIA-induced weight loss at 6h post-treatment that associates with maternal cytokine concentrations.

Table 2.7. Summary of 6h dam weight changes within each cohort

Cohort	GLM results
PR1	Group: $F_{1,19}$=17.06, p<0.001; 3h weight change: $F_{1,19}$=8.52, p=0.009
PN1	Plasma IL-6: $F_{1,13}$=14.94, p=0.002; 3h weight change: $F_{1,13}$=19.58, p<0.001
PN2	Group: $F_{1,30}$=5.27, p=0.029; 3h weight change: $F_{1,30}$=54.93, p<0.001
PN2A	Group: $F_{1,30}$ =5.27, p=0.029; 3h weight change: $F_{1,30}$=54.93, p<0.001
PN2B	Group: $F_{1,12}$=9.91, p=0.008; 3h weight change: $F_{1,12}$=6.09, p=0.030

III. 24h weight change

Similar to the 6h weight change, 24h weight change analysis included both 3h and 6h weight changes as covariates in the GLM. There was a significant main effect of 6h weight change

(GLM: $F_{1,50}$=35.29, p<0.001; Figure 2.8A) and cohort (GLM: $F_{2,50}$=10.66, p<0.001). Accordingly, there was a significant correlation between 24h weight change and both 6h (r=0.500, p<0.001; Figure 2.8E) and 3h (r=0.369 p=0.006; Figure 2.8F) weight changes. Of note, there was a negative correlation between plasma IL-6 (r=-0.361, p=0.046; Figure 2.8B) and a trend to a significant negative correlation between plasma TNFα (r=-0.264, p=0.067; Figure 2.8C) and weight changes at 24h, suggesting a relationship between magnitude of MIA and 24h weight loss.

Given the main effect of cohort, 24h weight changes were re-analysed within each cohort separately (Table 2.8). Here, there was main effect of 6h weight change in cohorts PN1/PN2B, but a main effect of 3h weight change and a main effect of group in PN2A.

Table 2.8. Summary of 24h dam weight changes within each cohort

Cohort	GLM results
PN1	6h weight change: $F_{1,16}$=29.58, p<0.001
PN2	Group: $F_{1,29}$=3.57, p=0.069; 6h weight change: $F_{1,29}$=8.34, p=0.007
PN2A	Group: $F_{1,14}$=8.32, p=0.012; 3 h weight change: $F_{1,14}$=6.74, p=0.021
PN2B	6h weight change: $F_{1,13}$=7.34, p=0.018

Taken together the results indicate a poly(I:C)-induced weight loss 6h post-treatment, with this weight loss appearing to remain in effect at 24h. Notably, the observed weight changes can be directly attributed to the magnitude of the elicited immune response, evidenced by the negative correlations between maternal plasma pro-inflammatory cytokines and dam weight change. Further, the poly(I:C)-dams do not recuperate from this loss and remain lagging in percentage weight gain for the remainder of pregnancy (Figure 2.7). It is worth noting that vehicle-dams displayed weight loss from 0-6h post-treatment, which may be attributed to normal circadian weight loss and food intake during the light cycle for laboratory rats (Kawamura et al., 2020).

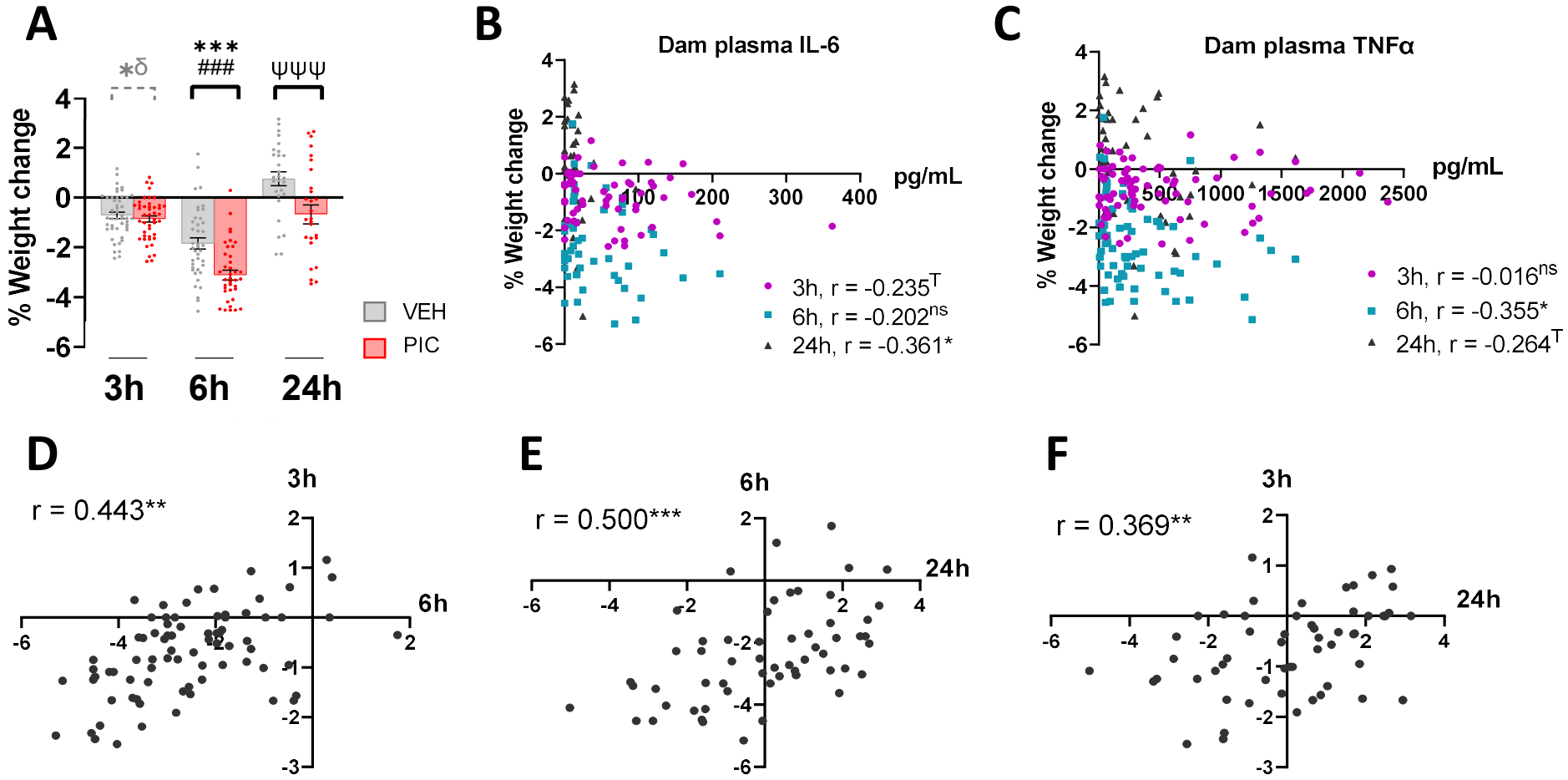

Figure 2.8. Dam weight changes in the 24h post-treatment

A. %weight change at 3h, 6h and 24h post-treatment (mean ±SEM; N=46-49). Black Π-shaped bars show significant GLM results. Black symbols show significant main effects of: group, ***p<0.001; 3h weight change, ###p<0.001; 6h weight change, ψψψp<0.001. Grey dashed Π-shaped bars and symbols show trending main effects of: group, *p=0.063; plasma IL-6, δp=0.061. **B-C**: Pearson's r correlations between dam 3h plasma cytokines and dam weight changes at 3h, 6h and 24h post-treatment. Two-tailed significance is indicated: *p<0.05, T, trending (p<0.07); ns, non-significant. **D-E**. Pearson's r correlations between weight changes. Axis represent %weight change at the timepoint indicated on the axis. Two-tailed significance is indicated: **p<0.01, ***p<0.001.

2.3.2.3. Litter sizes and demographics

When litter size was analysed, dam plasma TNFα almost reached statistical significance (GLM: $F_{1,47}$=3.97, p=0.052; Figure 2.9A), with a negative correlation between litter size and dam plasma TNFα in postnatal cohorts only (r=-0.268, p=0.060). This suggests that high plasma TNFα, resulting from poly(I:C)-elicited MIA, leads to smaller live-birthed litters, but does not appear to impact the number of viable foetuses prenatally, although Kowash et al. (2022) report a litter size reduction at GD21. For litter sex demographics, there were no differences in number of males, however, there were reduced number of females in poly(I:C)-litters relative to vehicle-litters (GLM: $F_{1,52}$=6.24, p=0.016; Figure 2.9C), suggesting that reduced poly(I:C)-litter size is due to a reduced number of females.

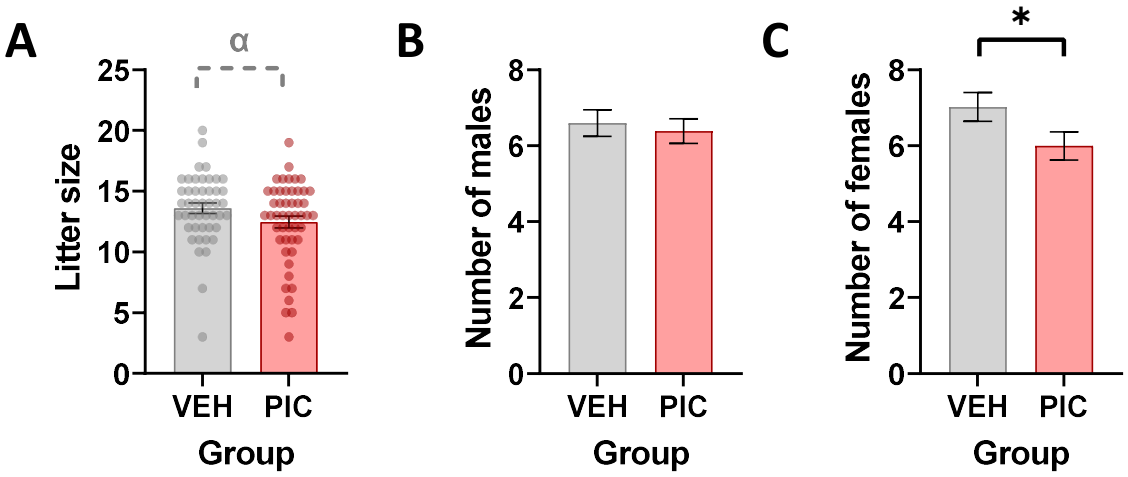

Figure 2.9. Litter sizes and demographics
A. Litter size (mean ±SEM; N=46-49; dots represent individual litters). **B.** Number of males within each litter (mean ±SEM; N=46-49). **C**. Number of females within each litter (mean ±SEM; N=45-48). Black Π-shaped bar shows significant GLM results. Black symbols show significant main effects of: group, *p<0.05. Grey dashed Π-shaped bar shows trending GLM results for: maternal TNFα, αp=0.052. Abbreviations: VEH, vehicle; PIC, poly(I:C).

2.3.3. Foetal and offspring weights

2.3.3.1. Prenatal cohort

Foetal weight increased as expected with advancing gestational age, with the largest increase in weight observed between GD16-GD21 (Figure 2.10).

I. GD15

There was a significant main effect of sex (GLMM: $F_{1,197.98}$=9.57, p=0.002) on foetal weight, with male-foetuses being heavier than female-foetuses (Figure 2.10A; as expected, Kalisch-Smith et al., 2017) and seen at the other gestational ages (Figure 2.10). There were no significant differences for brain weight, brain:bodyweight ratio (Figure 2.10B&C), placental weight or placental:bodyweight ratio (data not shown).

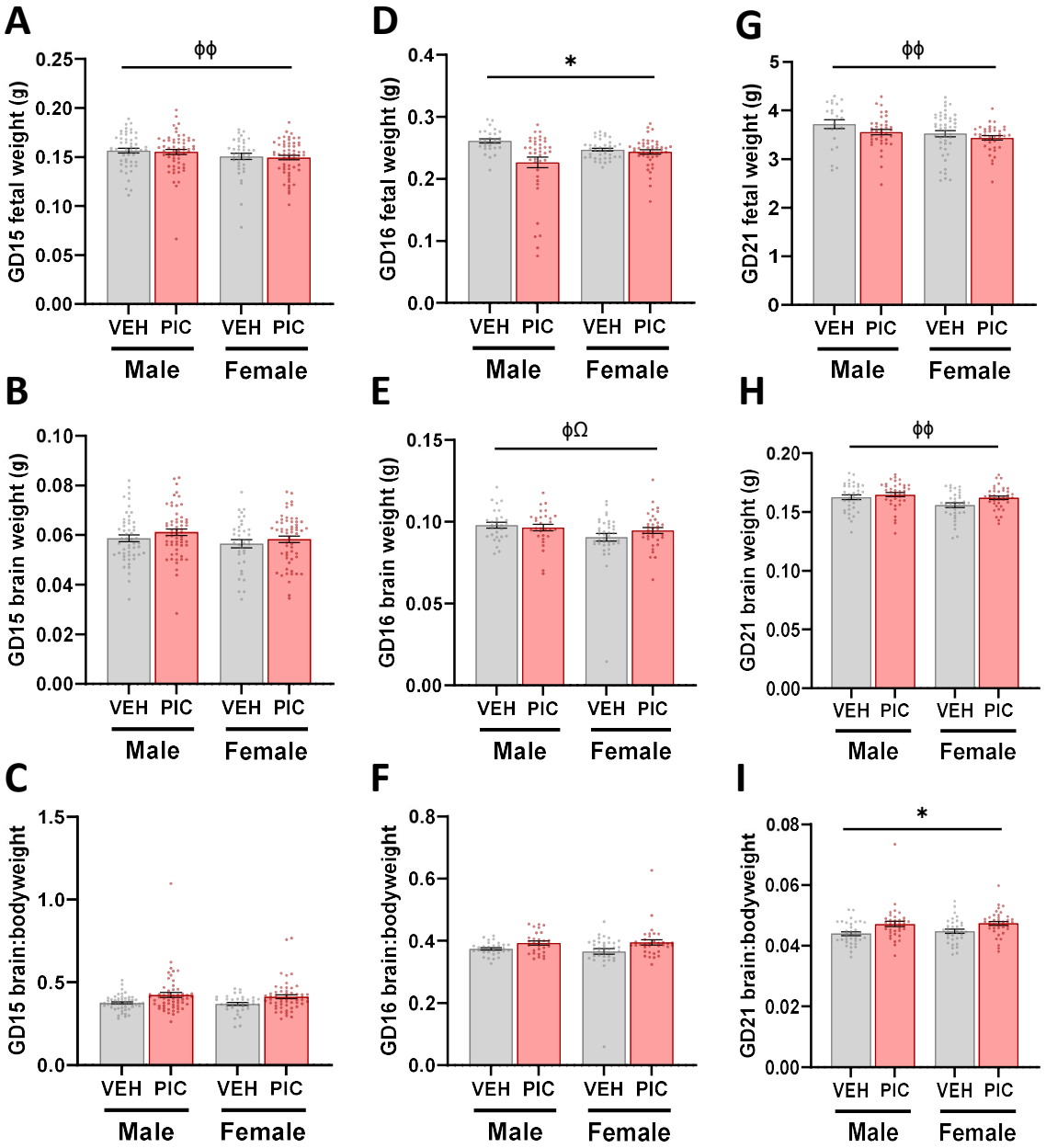

Figure 2.10. Foetal body and brain weights and brain:bodyweight ratios
A. GD15 foetal weight; **B**. GD15 brain weight; **C.** GD15 brain:bodyweight ratio; **D.** GD16 foetal weight; **E**. GD16 brain weight; **F.** GD16 brain:bodyweight ratio; **G.** GD21 foetal weight; **H.** GD21 brain weight; **I.** GD21 brain:bodyweight ratio. Bars represent mean ±SEM (N=6-9, n=25-59). Significance bars indicate GLMM results. Symbols show significant main effects of: sex, ϕp<0.05, ϕϕp<0.01, group, *p<0.05; litter size, Ωp<0.05. Abbreviations: VEH, vehicle; PIC, poly(I:C).

II. GD16

There was a significant main effect of group (GLMM: $F_{1,8.95}$=5.91, p=0.038; Figure 2.10D) on foetal weight, with poly(I:C)-foetuses being lighter relative to vehicle-foetuses. There was also a significant main effect of sex (GLMM: $F_{1,130.76}$=5.40, p=0.022) and litter (GLMM: $F_{1,12.028}$=4.83, p=0.048) on GD16 brain weight (Figure 2.10E), with males having heavier brain weight than females. There were no significant differences for brain:bodyweight ratio (Figure 2.10F), placental weight or placenta:bodyweight ratio (data not shown).

III. GD21

There was a significant main effect of sex (GLMM: $F_{1,139.91}$=8.36, p=0.004) on foetal weight (Figure 2.10G), with male-foetuses being heavier than females, this was also found for brain weight (GLMM: $F_{1,140.86}$=7.18, p=0.008; Figure 2.10H). However, when brain:bodyweight was compared, there was a main effect of group (GLMM: $F_{1,9.77}$=5.56, p=0.041; Figure 2.10I), with poly(I:C)-foetuses having increased brain:bodyweight ratios compared to vehicle-foetuses. There were no significant differences for placental weight or placenta:bodyweight ratio (data not shown).

2.3.3.2. Postnatal cohorts

A summary of offspring growth trajectory can be found in Figure 2.11. Offspring weight increased as expected with advancing age. Likewise, males were typically heavier than females throughout development, with the largest divergence in weight between sexes observed in adulthood (PD100-175).

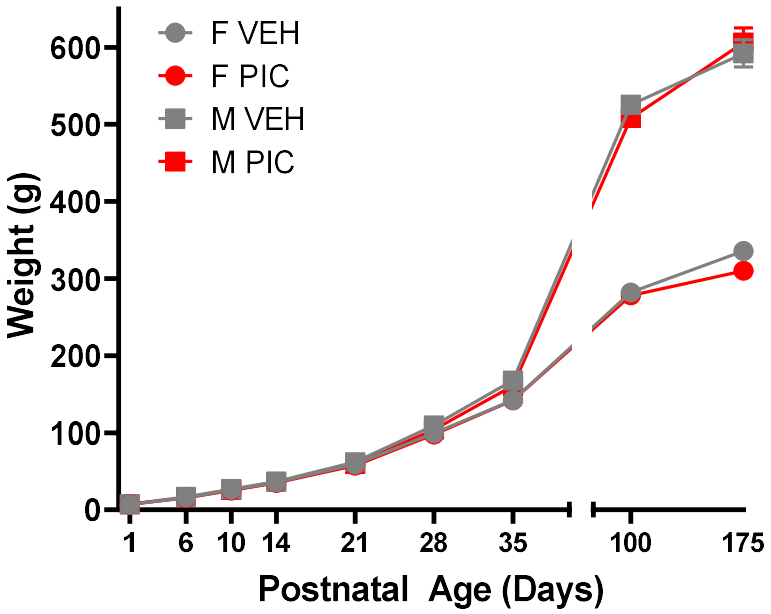

Figure 2.11. Offspring developmental growth trajectory
The developmental increase in offspring (N=28-29, n=139-160) weight from all postnatal cohorts. Data at each timepoint is presented as mean ±SEM. Abbreviations: F, female; M, male; PIC, poly(I:C); VEH, vehicle.

I. Birthweight (PD1)

For PD1 weight, there were significant main effects of both sex (GLMM: $F_{1,523.12}$=33.025, p<0.001; Figure 2.12A), with males being heavier than females (as expected; Slob et al., 1975) and litter size (GLMM: $F_{1,285.64}$=76.99, p<0.001; Figure 2.12A), with a negative correlation between litter size and PD1 weight (r=-0.405, p=0.01; Figure 2.12C; as expected, Russell, 1980). Post-hoc analysis by sex showed only a significant main effect of litter size for males (GLMM: $F_{1,96.69}$=31.60, p<0.001), while for females, there were significant main effects of litter size (GLMM: $F_{1,113.23}$=35.141, p<0.001) and group (GLMM: $F_{1,111.06}$=7.83, p=0.006), with poly(I:C)-females heavier than vehicle-females. To illustrate these latter findings, PD1 weights were plotted relative to litter size (Figure 2.12B). For PD1 brain weight, there was a main effect of maternal TNFα (GLMM: $F_{1,64.67}$=5.61, p=0.021; Figure 2.12D), corresponding to a negative correlation between the two (r=-0.306, p=0.003; Figure 2.12F). However, for brain:bodyweight ratio, there was only a trending main effect of litter size (GLMM: $F_{1,54.39}$=3.99, p=0.051; Figure 2.12E).

Note PD1 weight was included as a covariate when analysing all subsequent postnatal offspring weights to account for birthweight effects on growth trajectory. To illustrate the significant effects of PD1 weight, postnatal weights at each age are plotted relative to their respective PD1 weight.

II. Early developmental weight changes (PD6, PD10 and PD14)

Across all three timepoints there was a main effect of PD1 weight: PD6 (GLMM: $F_{1,406.94}$=538.02, p<0.001), PD10 (GLMM: $F_{1,488.29}$=305.77, p<0.001) and PD14 (GLMM: $F_{1,510.59}$=260.34, p<0.001) implying a significant relationship between birthweight an early developmental weight change. There was also a continued main effect of group: PD6 (GLMM: $F_{1,180.32}$=19.23, p<0.001), PD10 (GLMM: $F_{1,201.77}$=11.22, p<0.001) and PD14 (GLMM: $F_{1,\ 195.14}$=9.31, p=0.003) with poly(I:C)-offspring being consistently lighter than vehicle-offspring (Figure 2.13A-C)

III. Juvenile weight changes (PD21-28)

At both timepoints there was a continued main effect of PD1 weight: PD21 (GLMM: $F_{1,405.50}$=175.09, p<0.001), PD28 (weaning; GLMM: $F_{1,267.34}$=132.43, p<0.001) suggesting a continued relationship between birthweight and developmental weight change. Likewise, there remained a main effect of group: at PD21 (GLMM: $F_{1,108.42}$=13.96, p<0.001) and PD28 (GLMM: $F_{1,94.89}$=14.61, p<0.001) with poly(I:C)-offspring being lighter than vehicle-offspring (Figure 2.13D-E). However, there was also a main effect of sex: PD21 (GLMM: $F_{1,356.45}$=9.19, p=0.003) and PD28 (GLMM: $F_{1,311.26}$=98.53, p<0.001), with males being heavier than females (Figure 2.13D-E), suggesting a notable increase in male-offspring weight gain in the juvenile period, compared to females.

When PD21 brain weight was analysed, there was a significant main effect of sex (GLMM: $F_{1,42.72}$=5.48, p=0.021; Figure 2.14A), with male brains being heavier than female brains and a group*sex interaction (GLMM: $F_{2,41.74}$=3.90, p=0.028; Figure 2.14A). Post-hoc analyses showed

there was a significant main effect of group in females, with reduced brain weight in poly(I:C)-females relative to vehicle-females (GLMM: $F_{1,22.59}$=7.27, p=0.013). For brain:bodyweight ratio, there was only a main effect of litter (GLMM: $F_{1,55.49}$=11.38, p=0.01; Figure 2.14B).

IV. Adolescent weight changes (PD35)

Again, there was a main effect of PD1 weight (GLMM: $F_{1,195.51}$=120.82, p<0.001) but no main effect of group as seen in earlier development, suggesting that any influences of MIA on offspring weight is abolished post-weaning. However, there was a main effect of sex (GLMM: $F_{1,318.30}$=434.21, p<0.001) with males being heavier than females (Figure 2.13F).

When PD35 brain weight was compared there was a significant main effect of sex (GLMM: $F_{1,42.17}$=26.89, p<0.001; Figure 2.14C), with males having heavier brain weights than females. For brain:bodyweight ratio, there was also a main effect of sex (GLMM: $F_{1,85}$=51.44, p<0.001; Figure 2.14D), revealing that female-offspring, while having lighter brain weights, have a much higher brain:bodyweight ratio, a phenomenon not observed in the juvenile time period. This change likely represents the large and rapid male bodyweight gain post-weaning (Figure 2.11).

V. Adult weight changes (PD100/175)

At both adult timepoints (PD100 and PD175), there was no main effect of PD1 weight, suggesting the relationship between birthweight and developmental weight change is abolished by adulthood. There was a significant main effect of sex: PD100 (GLMM: $F_{1,73.27}$=1877.54, p<0.001) PD175 (GLMM: $F_{1,36.99}$=186.09, p<0.001), with males being significantly heavier than females (data not shown).

Brain weights were only available for PD100 offspring, showing a main effect of sex (GLMM: $F_{1,29}$=308.28, p<0.001; Figure 2.14E), with reduced brain weight in females relative to males. For brain:bodyweight ratio, there was a main effect of sex (GLMM: $F_{1,61.32}$=41.71, p<0.001; Figure 2.14F), showing again that females, while having lighter brain weights, have higher brain:bodyweight ratios than males.

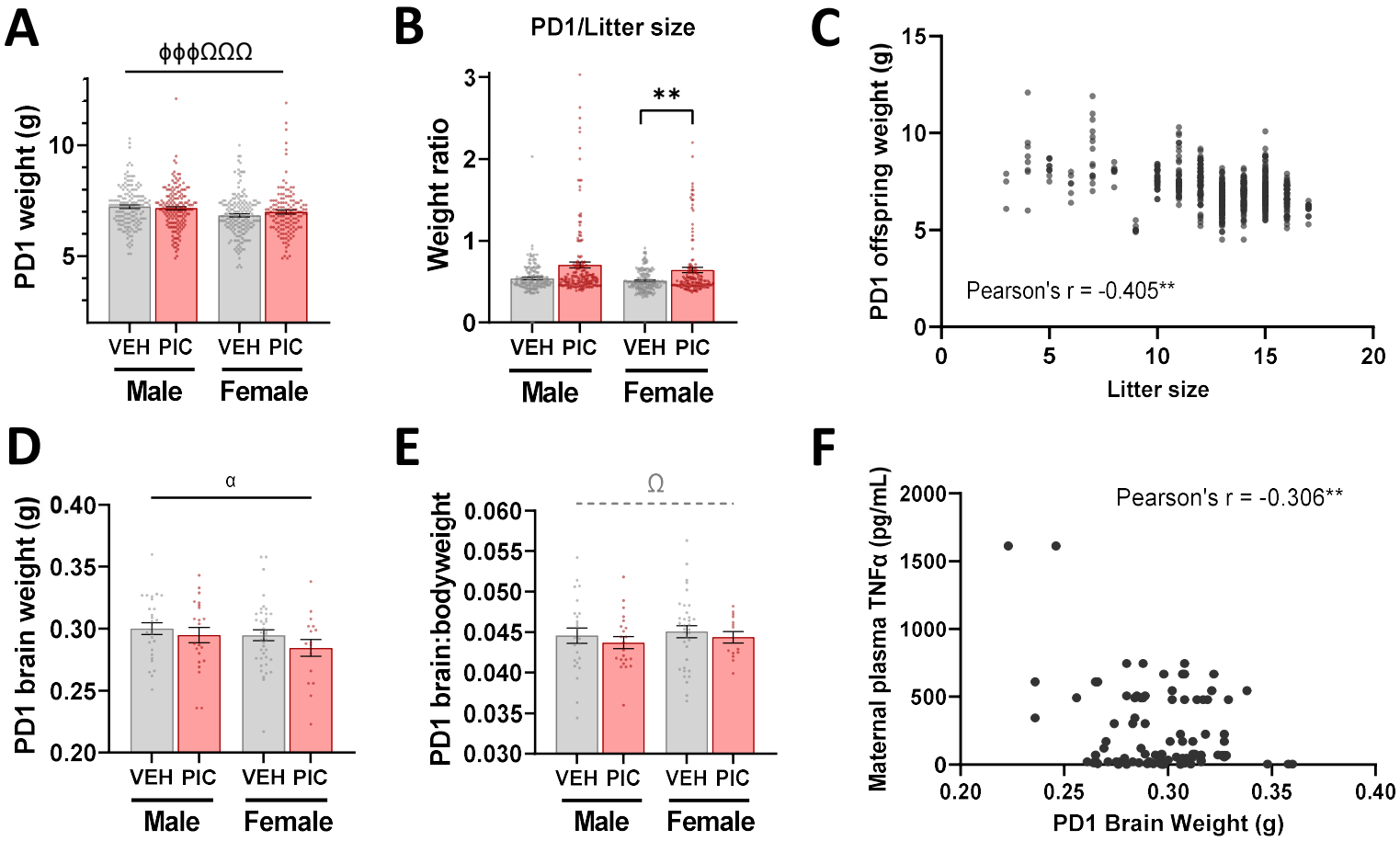

Figure 2.12. PD1 pup weights

A. PD1 pup weights. **B.** PD1 pup weight:litter size ratio. **C**. Pearson's r correlation between PD1 pup weight and litter size, two-tailed significance indicated, **p≤0.01. **D**. PD1 brain weights. **E.** PD1 brain:bodyweight ratio. **F**. Pearson's r correlation between PD1 brain weight and maternal TNFα, two-tailed significance indicted **p<0.01. Bars represent mean ±SEM (N=28-29, n=139-160), dots show individual animals. Significance bars indicate GLMM results: black bars, significant results; grey-dashed bars, trending results. – shaped significance bars show changes across both sexes, Π-shaped significance bars indicate post-hoc GLMM within a single sex. Black symbols show significant main effects of: sex, ϕϕϕp<0.001; litter size, ΩΩΩp<0.001; group, **p<0.01; maternal TNFα αp<0.05. Grey symbols indicate trending main effects of: litter, Ωp<0.06. Abbreviations: VEH, vehicle; PIC, poly(I:C).

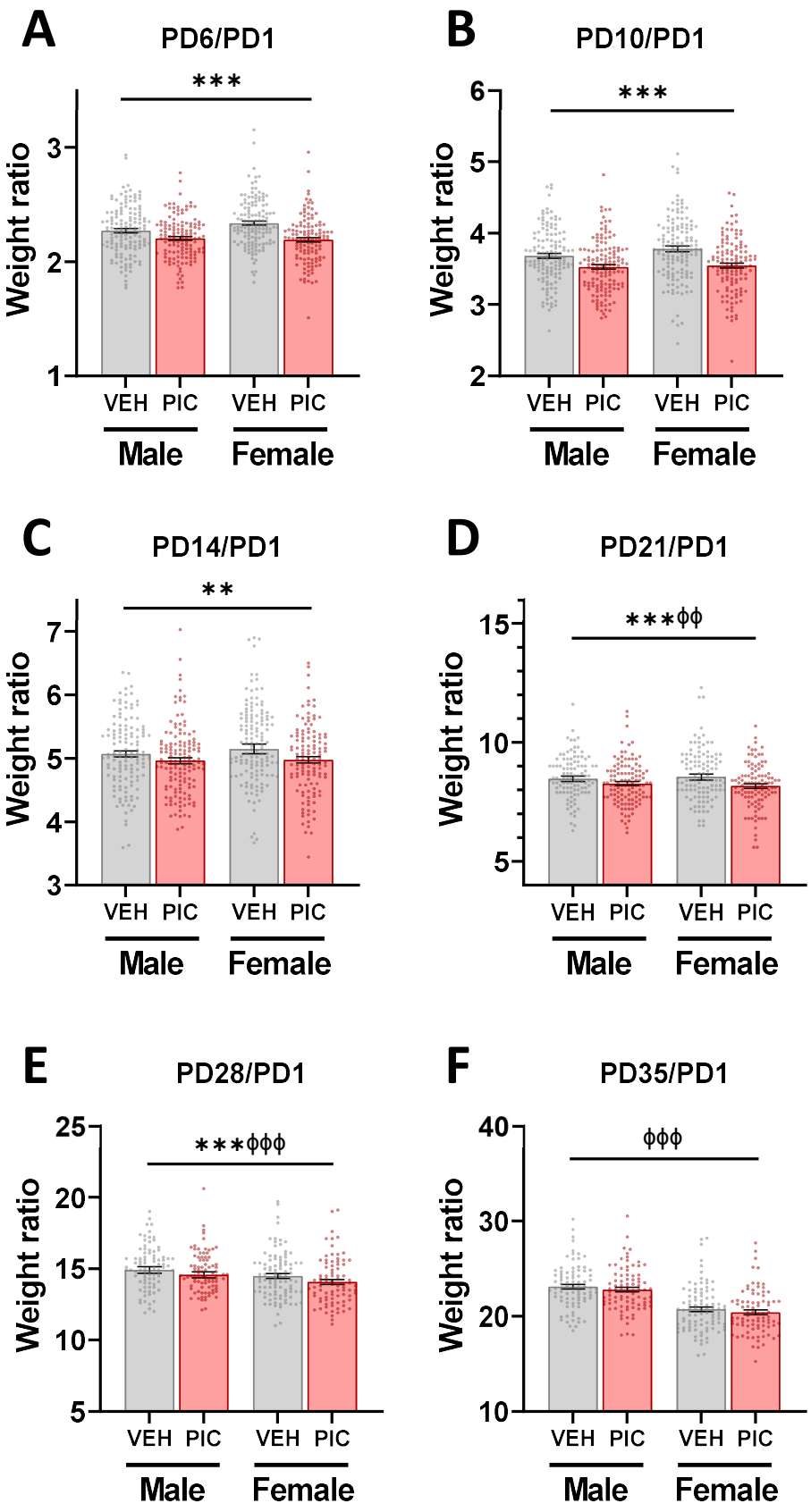

Figure 2.13. Developmental weight:birthweight ratios
Figure shows developmental weights (g) from PD6-PD35 normalised to birthweight (PD1 weight, g). Bars represent mean ±SEM. **A**. PD6 (n=124-145); **B.** PD10 (n=124-145); **C**. PD14 (n=124-145); **D.** PD21 (n=124-145); **E.** PD28 (n=86-98); **F.** PD35 (n=86-98). Significance bars show GLMM results across both sexes. Symbols show significant main effects of: group, **p<0.01, ***p<0.001; sex, ϕϕp<0.01, ϕϕϕp<0.001. Abbreviations: VEH, vehicle; PIC, poly(I:C).

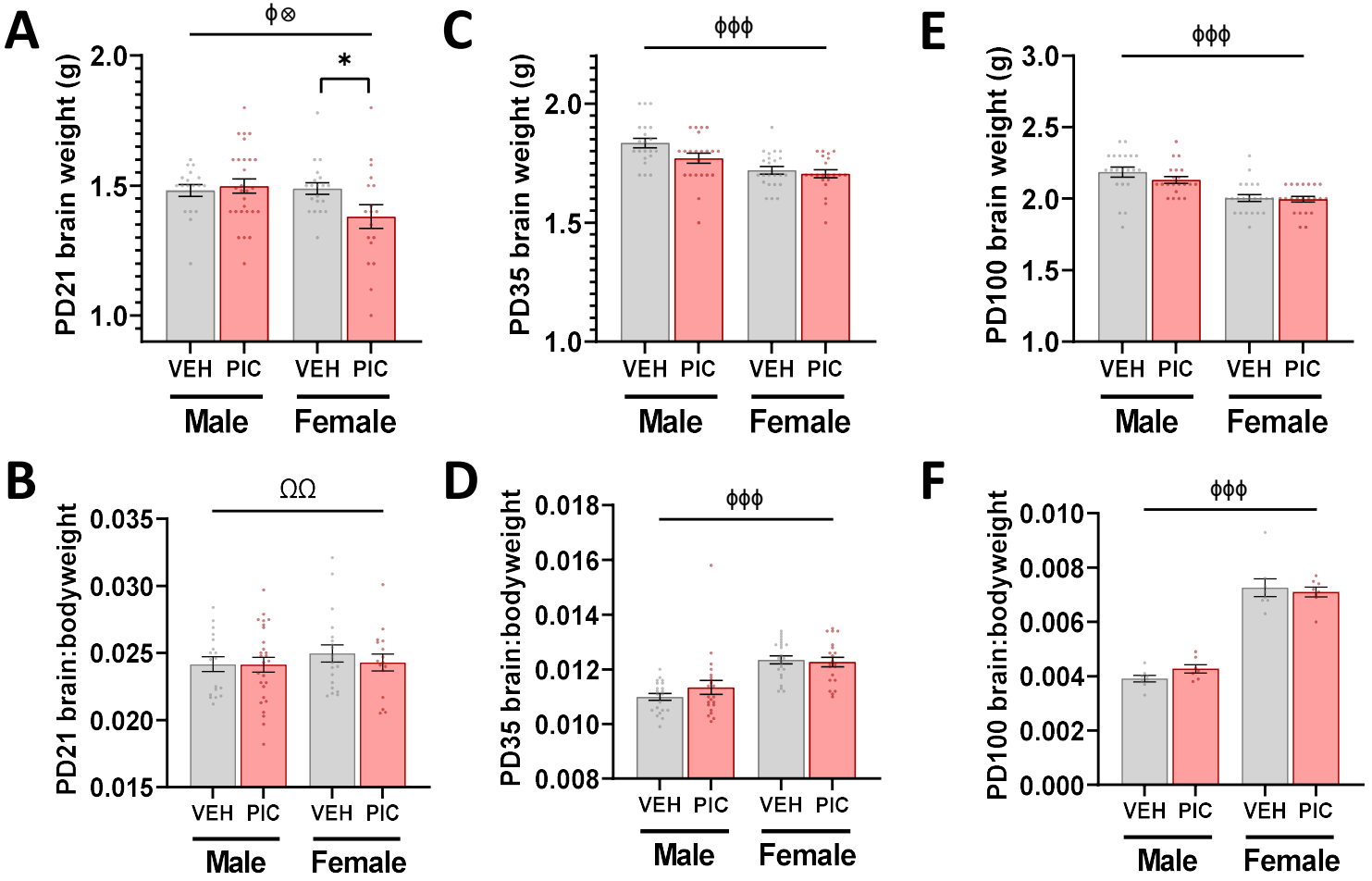

Figure 2.14. Postnatal offspring brain weights

A. PD21 brain weight (n=18-28); **B.** PD21 brain:bodyweight ratio (n=18-28); **C.** PD35 brain weight (n=21-23); **D.** PD35 brain:bodyweight ratio (n=21-23); **E.** PD100 brain weight (n=21-22); **F.** PD100 brain:bodyweight ratio (n=21-22). Bars represent mean ±SEM. — shaped significance bars show GLMM results across the whole dataset, Π-shaped significance bars show post-hoc GLMM within a single sex. Symbols show significant main effects of: sex, ϕp<0.05, ϕϕϕp<0.001; litter size, ΩΩp≤0.01; group, *p<0.05; group*sex interaction, ⊗p<0.05. Abbreviations: VEH, vehicle; PIC, poly(I:C).

2.3.4. Acute foetal brain cytokine concentrations (GD15-16)

Four cytokines were measured at 3h and 24h post-treatment in the foetal whole brain: the anti-inflammatory IL-10 and pro-inflammatory IL-1β, IL-6 and TNFα, selected as the most consistently investigated cytokines in the foetal brain in MIA models (Woods et al., 2021).

At GD15 (3h post-treatment; corresponding to peak pro-inflammatory response in the dam) there was only a significant difference in IL-10, with a main effect of maternal TNFα (GLMM: $F_{1,8.55}$=8.22, p=0.020; Figure 2.15A), corresponding to a positive correlation between maternal plasma TNFα concentration and foetal brain IL-10 concentration (rho=0.655, p<0.001). There were no significant effects of any predictors on pro-inflammatory cytokine concentration.

At GD16 (24h post-treatment; Figure 2.15B) there were no significant effects of any predictors on IL-10 or TNFα concentrations. However, for IL-1β there was a main effect of both sex (GLMM: $F_{1,10.34}$=7.63, p=0.020), with males having higher IL-1β concentrations than females and maternal plasma TNFα (GLMM: $F_{1,3.3}$=22.35, p=0.014), corresponding to a positive correlation between 3h maternal plasma TNFα concentration and 24h foetal brain IL-1β concentration (rho=0.697, p=0.002). For IL-6 there was a significant main effect of group (GLMM: $F_{1,14}$=18.48, p<0.001), with higher IL-6 concentrations in poly(I:C)-foetuses relative to vehicle-foetuses.

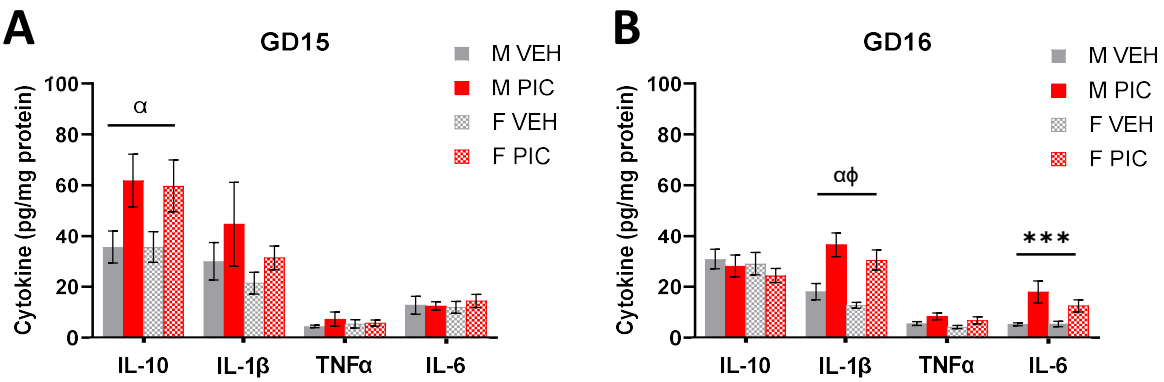

Figure 2.15. Foetal brain tissue cytokine concentration
A. GD15 (N=5, n=5-6); **B.** GD16 (N=5, n=5-7). Bars represent mean ±SEM. Significance bars show GLMM results, symbols show significant main effect of: sex, ϕp<0.05; maternal TNFα, αp<0.05; group, ***p<0.001. Abbreviations: M, male; F, female; VEH, vehicle; PIC, poly(I:C).

2.3.5. Systemic and cortical IL-6 across development (GD21-PD100)

In the GD21 FC there was increased IL-6 concentration in the pol(I:C)-foetuses relative to vehicle-foetuses, with a trend to a main effect of group (GLMM: $F_{1,7.27}$=4.92, p=0.061; Figure 2.16A).

Postnatally, at both PD1 (Figure 2.16B&F) and PD21 (Figure 2.16C&G) there were no significant effects of any predictors on cortical or plasma IL-6 concentrations. However, at PD35 there was a trend to a main effect of group for both cortical (GLMM: $F_{1,25}$=3.41, p=0.077; Figure 2.16D)

and plasma (GLMM: $F_{1,25}$=3.85, p=0.071; Figure 2.16H) IL-6 concentrations, with both showing increased IL-6 in poly(I:C)-offspring relative to vehicle-offspring. By PD100 this increase became significant with main effects of group for both cortical (GLMM: $F_{1,13.30}$=8.98, p=0.015; Figure 2.16E) and plasma (GLMM: $F_{1,11.87}$=5.36, p=0.039; Figure 2.16I) IL-6 concentrations.

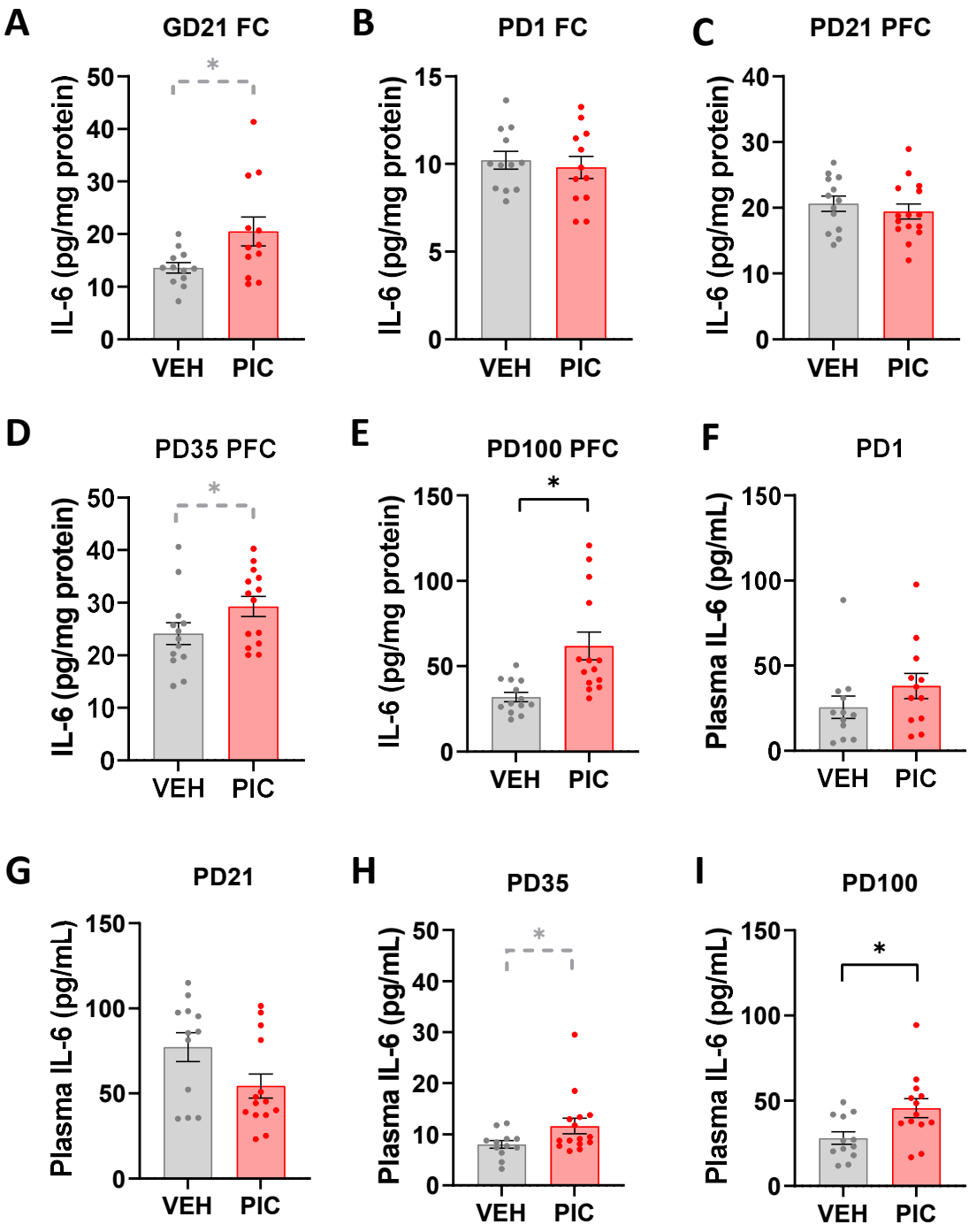

Figure 2.16. Cortical and plasma IL-6 concentrations
Cortical tissue IL-6 concentration at **A.** GD21 FC; **B.** PD1 FC; **C.** PD21 PFC; **D.** PD35 PFC; **E.** PD100 PFC; and offspring plasma concentration at **F.** PD1; **G.** PD21; **H.** PD35; **I.** PD100. Bars represent mean ±SEM (N=5-7; n=6-7), dots show individual animals. Black significant bars and symbols show significant GLMM results with main effects of: group, *p<0.05. Grey dashed bars and symbols show trending (0.05<p<0.08) GLMM results. Abbreviations: VEH, vehicle; PIC, poly(I:C).

These findings translate to a direct correlation between plasma and cortical IL-6 concentrations at both PD35 (r=0.412, p=0.041; Figure 2.17C) and PD100 (r=0.426, p=0.034; Figure 2.17D). These correlations are not observed at PD1 (r=0.329, p=0.116; Figure 2.17A) or PD21 (r=-0.021, p=0.918; Figure 2.17B).

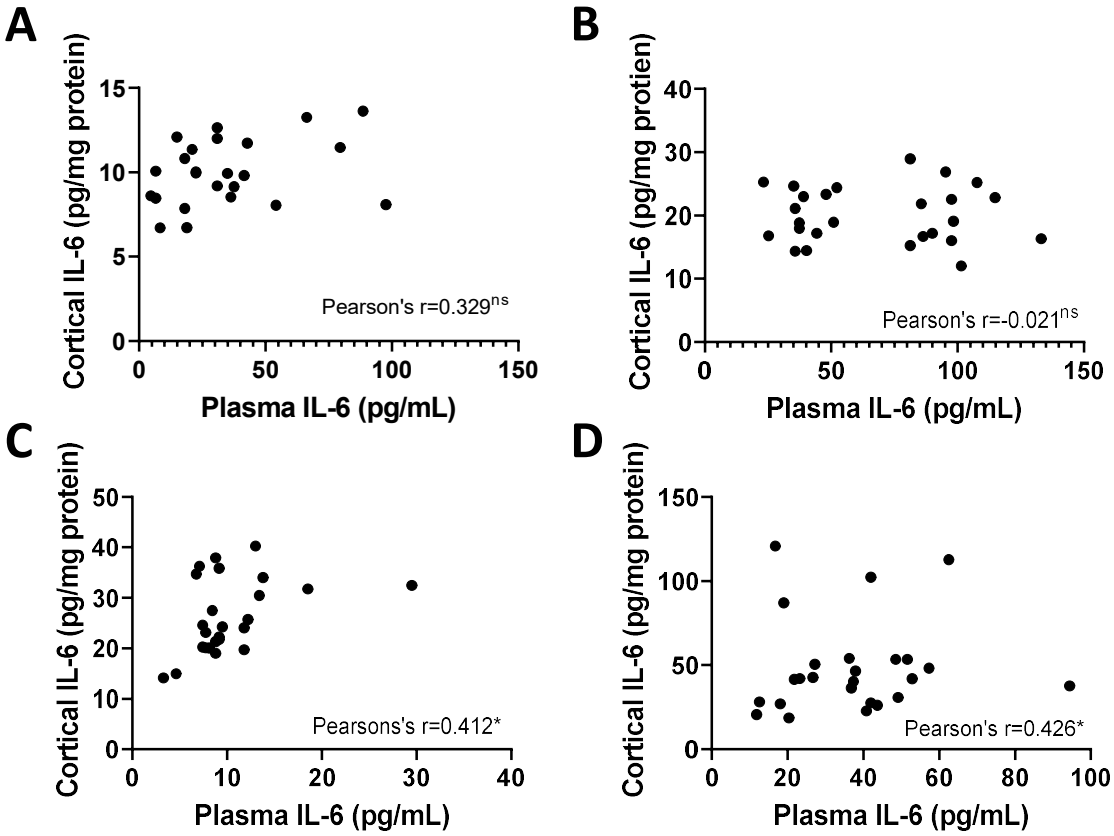

Figure 2.17. Correlations between plasma and cortical IL-6 concentrations in offspring
A. PD1; **B.** PD21; **C.** PD35; **D.** PD100. Plasma IL-6 concentration plotted against matched cortical IL-6 concentration. Dots represent individual samples. Pearson's r correlation co-efficient indicated alongside two-tailed significance: ns, non-significant; *p<0.05.

2.3.6. Offspring behaviour

This work was designed and performed by Dr Harry Potter (Potter, 2021). It will be outlined here solely for the context of future work and to confirm validity of the model.

2.3.6.1. Cognitive behavioural assessments in adolescence

In PD35 poly(I:C)-offspring from both PN1 and PN2A we found inconsistent deficits in the NOR discrimination index (Potter, 2021, Chapter 4, Section 4.2.9 and Chapter 5, Section 5.3.9.). In PN1 there was indication of increased pro-social behaviours in SI and working memory deficits on day three of the RAM task (Potter, 2021, Chapter 4, Section 4.2.9) but these changes were not robust across cohorts, with no evidence of these in PN2A (Potter, 2021, Chapter 5, Section 5.3.9.). These tests broadly establish no overt cognitive phenotypic traits in PD35 poly(I:C)-offspring.

2.3.6.2. Cognitive behavioural assessments in adulthood

In PN1 and PN2A cohorts, there were no deficits in the NOR discrimination index, SI behaviours or RAM performance (Potter, 2021, Chapter 4, Section 4.2.9 and Chapter 5, Section 5.3.9). However, in the ASST (Table 2.1) there was an increased number of trials and errors in the extra-dimensional (ED) shift phases of the task, translating to an increased intradimensional (ID)/ED shift in adult poly(I:C)-offspring across cohorts; with group significantly predicting ID/ED shift increase in adult females (adult males were not assessed) in PN1 (GLMM: $F_{1,13}$=7.20, p=0.019; Figure 2.18A) and both adult females (GLMM: $F_{1,48}$=22.06, p<0.001; Figure 2.18B) and males (GLMM: $F_{1,21}$=5.57, p=0.028; Figure 2.18C) in PN2A. Importantly, the latter was not affected by cross-fostering, indicating this deficit is driven by MIA and not influenced by MCB.

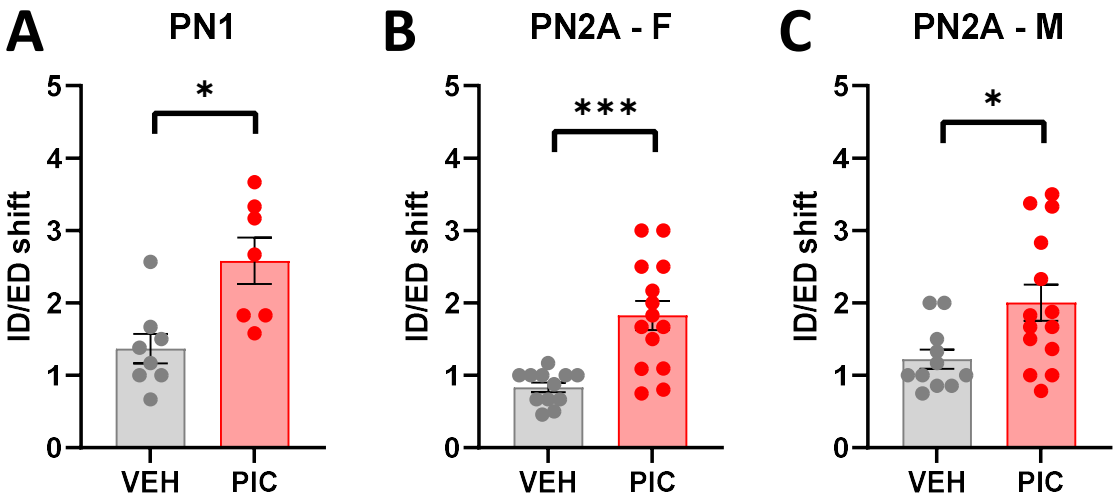

Figure 2.18. Adult offspring ID/ED shift
A. PN1 (females only). **B.** PN2A Females (F). **C.** PN2A Males (M). The intradimensional (ID)/extradimensional (ED) shift in the attentional set shifting task (ASST) across cohorts (N=8-12; n=8-14). Bars represent mean ±SEM, dots show individual animals. Significant bars and symbols indicate GLMM results, with main effect of: group, *p<0.05, ***p<0.001. Abbreviations: VEH, vehicle; PIC, poly(I:C). Data taken from Potter (2021).

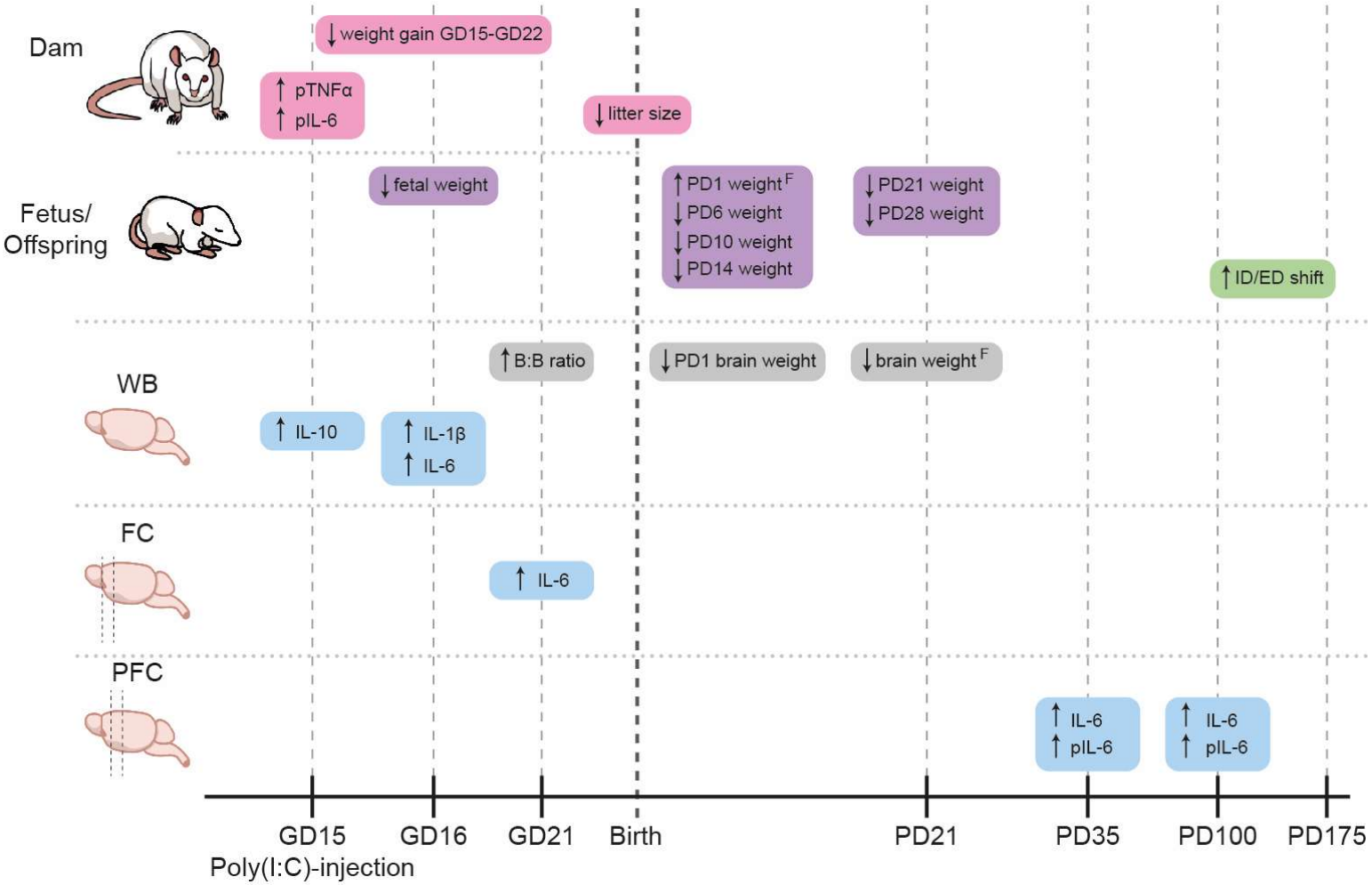

Figure 2.19. Summary of significant findings in Chapter 2

Summary of MIA-induced maternal and offspring changes identified in Chapter 2. Timeline (bottom) indicates the developmental age. Live measurements in dam/foetus/offspring or tissue analysed (whole brain (WB), frontal cortex (FC) or prefrontal cortex (PFC)) are indicated on the left. Pink: dam measurements; Purple: foetal/offspring weights; Green: offspring behaviours; Grey: brain weights; Blue: foetal/offspring cytokine changes. Abbreviations: GD, gestational day; PD, postnatal day; ↓Decrease; ↑Increase; F, female-specific result; p, plasma cytokine; B:B, brain:bodyweight ratio

2.4. DISCUSSION

The key aim of this Chapter was to perform extensive validation of the robustness of our MIA model, building on previous broad characterisation (Kowash et al., 2019; Murray et al., 2019). The analysis included the maternal response to poly(I:C) (e.g., plasma cytokines and weight changes) and offspring outcomes (e.g., foetal/postnatal offspring body and brain weights). Further, to support the primary hypothesis that cytokines act as mediators of offspring outcomes in the MIA paradigm, a major aim was to investigate cytokine changes, both cortical and systemic, as a possible causal mechanism in our model. Finally, this Chapter aimed to summarise previous offspring behavioural phenotyping (Potter, 2021), as a validation of the effect of MIA in predisposing offspring to later-life cognitive deficits. Critically, this validation was performed across cohorts which will be used for molecular analyses in subsequent chapters. The results from this Chapter achieved these aims, demonstrating in-depth validation of a viral-mediated acute MIA model which produces a robust PFC-mediated cognitive deficit in adult MIA-exposed offspring, particularly relevant for schizophrenia. Of note, this Chapter also provides preliminary evidence for inflammatory disturbances in MIA-exposed foetuses and offspring which precede the onset of cognitive deficits in adulthood, suggesting a possible role for ongoing inflammatory signalling in the development of schizophrenia-like traits in MIA-exposed offspring. A summary of the findings from this Chapter are outlined in Figure 2.19 and will be discussed in detail below.

2.4.1. Poly(I:C) induces an acute MIA

Across all cohorts there were significant increases in maternal plasma cytokines IL-6 and TNFα, at 3h post-exposure to poly(I:C), indicative of an acute inflammatory response (Figure 2.6). Of note, there were significant differences in the baseline (vehicle) plasma concentrations between cohorts, driving a significant main effect of cohort in the model. This difference likely owes to storage differences, with plasma cytokine stability known to alter across time (Vincent et al., 2019). Plasma cytokine analysis was typically performed at the completion of a cohort, for prenatal cohorts, analysis was performed within 1month of sample collection, while for postnatal cohorts this was often 6months after sample collections, with PN2 impacted by COVID lockdown, hence prolonging analysis of cytokines from collected plasma. Further, ELISA kit Lot-numbers varied across cohorts and could have further influenced readouts across cohorts. Irrespective of differences in baseline cytokine values, the data clearly demonstrate a robust acute inflammatory response to viral mimetic, poly(I:C), validating a robust MIA response in the model.

2.4.2. MIA induces maternal and early developmental weight changes

As another validation of MIA, maternal weight was monitored across the 24h post-treatment (Figure 2.8). Dams exposed to poly(I:C) showed acute weight loss 6h post-treatment which predicted a sustained weight loss at 24h. Further, dams which received poly(I:C) on GD15 show reduced weight gain for the reminder of pregnancy (Figure 2.7). This weight loss further represents an acute MIA in response to poly(I:C), in line with elevated plasma cytokines. Given that there were no statistically significant treatment effects on litter size (Figure 2.9), it appears this observed weight loss cannot be attributed to a loss in foetus number. This infers that the observed 24h post-treatment weight loss in poly(I:C)-dams likely reflects reduced foetal weight gain over this time, indicated by reduced GD16 foetal weight (Figure 2.10D). This scenario would imply reduced placental transfer of nutrients required for efficient foetal growth in the 24h post-exposure to poly(I:C). Of note, a reduction in transplacental transport of leucine, an essential amino acid required for foetal growth, in the poly(I:C)-dams has been previously demonstrated over this timeframe within the prenatal cohort (Kowash et al., 2022), lending weight to this hypothesis. Importantly, the GD16 foetal weight loss appears to be recovered by GD21 (Figure 2.10G), likely due to compensatory increases of transplacental transport in later pregnancy (Kowash et al., 2022). However, these observed weight changes during pregnancy appear to have limited impact on foetal viability, with no differences seen in prenatal litter sizes. That said, there was a trend to a relationship between maternal plasma TNFα and litter size (Figure 2.9A), primarily driven by postnatal cohorts. This suggests that any differences in litter sizes are due to a reduction in live-birthed pups, perhaps due to changes in normal cannibalism rates in Wistar rat dams (Tarôco et al., 2015). In particular, there was a reduction in the number of live-birthed female poly(I:C)-offspring (Figure 2.9C).

The observed effects of MIA on offspring weight appear to persist throughout early development. Litter size is one of the most common factors predicting birthweight (PD1 weight). This is not surprising as a fewer number of pups receive greater maternal resource allocation to each individual pup (Russell, 1980; Suvorov and Vandenberg, 2016). However, when litter size is accounted for, PD1 poly(I:C)-pups appeared heavier than vehicle-pups (Figure 2.12), perhaps driven by the increased transplacental nutrient transport in later pregnancy (Kowash et al., 2022). From PD6 up until PD28 weaning (accounting for birthweight), there was a significant main effect of group (Figure 2.13), with poly(I:C)-offspring being lighter than vehicle-offspring. It could be hypothesised that the reduced postnatal weight gain of poly(I:C)-offspring, despite an increased birthweight, owes to altered metabolism in these animals, primed as a result of dysregulated nutrient availability during pregnancy, in line with the DOHaD hypothesis (Gillman, 2005). However, given that this group effect only persists until weaning, after which sex becomes the most significant predictor of offspring weight, due to a rapid and pronounced weight gain in male offspring from weaning to adulthood (Figure 2.11), it is more likely that early developmental weight reductions in poly(I:C)-offspring is due to an effect of poly(I:C)-dam

resources. It could be that poly(I:C)-dam milk is insufficient or of lower quality, or that their care behaviours are somehow altered, which could be investigated in future research.

Brain weights were rarely different between groups, with the exception of an increased brain:bodyweight ratio at GD21 and a negative correlation between brain weight and 3h maternal TNFα at PD1 and reduced brain weight in PD21 poly(I:C)-females, though neither of the latter were significant when ratioed to bodyweight. These findings suggest very limited gross brain anatomical changes following MIA. This finding is at odds with observed volumetric reductions in the brains of schizophrenia patients (Haijma et al., 2013), though it should be acknowledged that weight here does not necessarily correspond to brain volume.

Taken together, the weight data show that adolescent and adult offspring from MIA dams appear, for the most part, largely identical to their vehicle counterparts. This raises the interesting possibility that more covert molecular abnormalities occur in the poly(I:C)-offspring brains, a postulate which is investigated further in subsequent chapters.

2.4.3. MIA stimulates foetal and offspring inflammatory dysregulation

In the 24h after poly(I:C)-exposure, there was a pronounced change in the foetal neuroinflammatory profile. Initially, 3h post-exposure to poly(I:C), where we observe the peak maternal inflammatory response (Figure 2.6; Kowash et al., 2019, 2022; Potter, 2021), there was a concurrent increase in the anti-inflammatory cytokine IL-10 in the foetal brain. Of note, this was directly proportional to the dam TNFα plasma concentration. It is suggested that this is an acute attempt by the foetal brain to counteract the inflammatory response in the maternal circulation. However, at 24h post-exposure, when the peak dam inflammatory response has subsided (Kowash et al., 2019), there was an increase in pro-inflammatory IL-1β and IL-6 in the foetal brain. This could be attributable to i) foetal-driven pro-inflammatory responses following the initial, acute anti-inflammatory phenotype; ii) a maternal-driven pro-inflammatory foetal response, owing to maternal-derived pro-inflammatory cytokines reaching the foetal compartment; iii) a foetal pro-inflammatory response to placental inflammation which may be temporally shifted relative to the peak maternal inflammatory response. Taken together, all these factors may account for the observed change in foetal neuroinflammatory profiles. To better understand the relationship between the maternal and foetal inflammatory responses it would be interesting to consider how placental changes fit temporally with observed maternal and foetal inflammatory changes. Nonetheless, the observed changes in the foetal brain cytokine profile in the 24h post-MIA, are in line with the current literature in MIA models (Woods et al., 2021). Indeed, while exact temporal results in cytokine concentrations vary between models, often dependent on methodology, there is a general consensus between our and other studies, in that the foetal brain experiences neuroinflammatory disturbances during the 24h period post-treatment (Figure 2.1). Notably, the data also shows that the observed elevation in

foetal IL-6 at GD16 is likely sustained throughout foetal brain development post-MIA, with a trend towards elevated IL-6 in the GD21 FC (Figure 2.16A).

Such neuroinflammatory disturbances could have critical impacts on the developing foetal brain. The timing of MIA in our model corresponds to the peak period of foetal neurogenesis, microglia proliferation and the specification of interneurons and glial progenitors (Figure 1.3; Sarkar et al., 2019; van Tilborg et al., 2018), all processes for which cytokines are important regulators (Bilbo and Schwarz, 2009; Dziegielewska et al., 2000; Favrais et al., 2011; Park et al., 2018; Taylor et al., 2010). Accordingly, it could be suggested that the observed foetal cytokine profiles may lead to dysregulated cellular development, including altered microglia priming, which may lead to long-term immune dysregulation and neuroinflammation, while perturbations in neurogenesis and gliogenesis could lead to altered proliferative capacity within the foetal brain, perhaps represented in the increased GD21 brain:bodyweight ratio. In addition to altered cellular development, the observed cytokine disturbances could have important epigenetic consequences. The analysed cytokines and their downstream inflammatory signalling pathways are known to induce the expression and activity of DNMTs, important for establishing normal DNAm patterns (Guarnieri et al., 2020; Ibrahim et al., 2018; Komanda and Nishimura, 2022; Li et al., 2012; Morisawa et al., 2017; Mourtzi et al., 2021; Seutter et al., 2020). Hence, dysregulation of cytokines in the foetal brain could lead to an altered epigenetic landscape which would induce long-term dysregulation of cellular gene expression and programmed changes in cell development.

Following this, it was of interest to determine whether this foetal neuroinflammatory disturbance is sustained postnatally. Due to methodological constraints which allowed quantification of only a single cytokine, IL-6 was selected for analysis (Figure 2.16). IL-6 is thought to be a critical mediator in the MIA model and in predicting child cognitive outcomes and psychosis in response to ELS (Khandaker et al., 2014; Perry et al., 2021; Samuelsson et al., 2006; Smith et al., 2007). Interestingly, the sustained foetal neuroinflammatory response at GD21 was abolished by birth (Figure 2.16). Indeed, postnatally, there were no differences in IL-6 measurements during early development. However, from PD35-100 there was an increase in both plasma and cortical IL-6, indicative of general inflammatory dysregulation in adolescent and adult MIA-offspring, with the significant correlations between plasma and cortical IL-6 indicative of a direct relationship between systemic inflammation and neuroinflammation which are known to be inherently linked (Sun et al., 2022). The observed increase in plasma IL-6 at both PD35 and PD100 and concurrent elevation in the PFC, highlights a possible role for systemic IL-6 as a biomarker for MIA-driven neuroinflammation. While neuroinflammation has been observed in a range of NDDs, including schizophrenia (Comer et al., 2020), systemic inflammatory biomarkers have shown relatively inconsistent results, though elevated IL-6 has been among one of the more robust (Borovcanin et al., 2017; Miller and Goldsmith, 2020; Miller et al., 2011; Zhou et al., 2021). Biomarker studies in schizophrenia are inherently challenging, with a lack of control over patient age, disease stage or treatment status (Lleó, 2021). Likewise, schizophrenia is a highly

heterogenous disorder with recent work suggesting different patient biotypes may exist (Clementz et al., 2022). These biotypes are hence likely to reflect different biomarker subgroups, not yet evaluated in clinical settings. It could therefore be proposed that systemic inflammatory disturbance is more likely to be observed in specific patient subgroups, such as those impacted by MIA or ELS, with a neuroinflammatory phenotype as observed here.

2.4.4. Adult MIA-offspring possess cognitive deficits relevant for schizophrenia

A key validation for preclinical models is their face validity and for MIA models they must demonstrate behaviours relevant to schizophrenia. Our group has focussed on cognitive symptoms (due to b-neuro group interests and the establishment of the scPCP model for schizophrenia-associated cognitive impairment). Accordingly, several cognitive tasks were selected, in accordance with the MCCB, for their relevance to schizophrenia (Table 2.1). Very few behavioural changes were observed in adolescent (PD35) offspring (Potter, 2021). This is perhaps surprising given that prodromal states of schizophrenia are thought to be present in adolescent individuals with schizophrenia (Janoutova et al., 2016; Kaur and Cadenhead, 2010). That said, this finding does not negate the possibility of molecular neuropathology preceding presentation of cognitive deficits. Indeed, these possibilities will be explored in subsequent results chapters. Further, our behavioural testing was not exhaustive and it could be that other subtle behavioural deficits may be detected in these animals. In adult offspring there was a robust deficit in ASST performance, resulting in an increased ID/ED shift in MIA offspring (Figure 2.18). The ASST mimics the Cambridge Neuropsychological Test Automated Battery's (CANTAB) ID/ED task, analogous to the Wisconsin card sorting task (Sharma, 2013), utilised in the schizophrenia diagnostic process. Patients with early-stage schizophrenia demonstrate difficulty with the ED shift phases of the task, while patients with chronic schizophrenia struggle in both the ID and ED phases of the task (Orellana and Slachevsky, 2013). Our results therefore suggest that our model is particularly translatable to early-phase schizophrenia, as would be expected in young adults. This robust cognitive deficit is highly representative of executive function deficits, mediated by the PFC (Orellana and Slachevsky, 2013). Taken together, these findings support the hypothesis that that MIA induces a PFC-mediated cognitive deficit in adult offspring, particularly relevant for schizophrenia.

2.5. SUMMARY

This Chapter has demonstrated the validation of a viral-mediated acute MIA model. Indeed, exposure to the viral mimetic, poly(I:C), induced a robust elevation in 3h plasma pro-inflammatory cytokines IL-6 and TNFα (Figure 2.6) and 24h maternal weight loss (Figure 2.8), indicative of acute MIA, across four separate animal cohorts. In turn, MIA was shown to induce foetal neuroinflammatory disturbances 24h after poly(I:C)-exposure (Figure 2.15). This foetal neuroinflammatory disturbance has the capacity to affect various neurodevelopmental processes including epigenetic programming, cellular development and brain connectivity (Bilbo and Schwarz, 2009; Dziegielewska et al., 2000; Favrais et al., 2011; Park et al., 2018; Taylor et al., 2010). Acute MIA and subsequent foetal neuroinflammatory disturbance was shown to produce a reliably increased ID/ED shift in the ASST in adult MIA-offspring (Figure 2.18). This behavioural phenotype is indicative of a PFC-mediated cognitive deficit, relevant to schizophrenia (Orellana and Slachevsky, 2013; Sharma, 2013). Given the lack of overt physical (brain/bodyweight) phenotypes post-weaning (Figure 2.12-14), it can be postulated that more subtle neuro-molecular mechanisms underscore the observed cognitive deficit, as is hypothesised in schizophrenia patients. Of note, there were inflammatory disturbances in adolescence and adult offspring, shown here by elevated plasma and cortical IL-6 (Figure 2.16), highlighting there are enduring changes in offspring inflammatory status following MIA-exposure *in utero*. These inflammatory changes appear to precede the onset of cognitive deficits in adulthood, suggesting a possible role for ongoing inflammatory disturbances in the development of schizophrenia-like traits. How these prenatal and postnatal inflammatory changes contribute to the development of cognitive deficits will be explored in subsequent chapters, focusing on molecular changes in the developing cortex.

CHAPTER 3. MIA-induced developmental changes to one carbon metabolism transport and cortical methylation capacity

3.1. INTRODUCTION

As outlined in the previous Chapter, there was evidence of MIA-induced weight loss in both the dam and the foetus in the 24h period post-injection (Figure 2.8&10). In line with this, we have previously shown reduced amino acid transport in the placentas of MIA-exposed dams across this time, followed by a, perhaps compensatory, increase in later gestation and provided preliminary evidence for MIA-induced alterations in foetal brain amino acid profiles (Kowash et al., 2022). Altered metabolite availability during neurodevelopment is known to have detrimental consequences for cell development and growth, as well as epigenetic patterning (Antony, 2007; Solanky et al., 2010; Tsitsiou et al., 2009), supporting a link between MIA-induced changes in metabolite transport and altered neurodevelopment. That said, we have yet to determine if the observed prenatal transport changes are enduring postnatally and how/whether they impact on metabolite availability during key stages of brain development and therefore this formed the focus of this Chapter.

3.1.1. One carbon (1C) metabolism

The 1C metabolism pathway is a universal metabolic pathway which catalyses the transfer of 1C for use in various biosynthetic processes (Ducker and Rabinowitz, 2017; Mentch and Locasale, 2016). Central to the 1C pathway, are the integrated activities of the folate and methionine cycles (Figure 3.1) which are particularly important for DNA and protein methylation pathways through the production of the methyl donor, SAM.

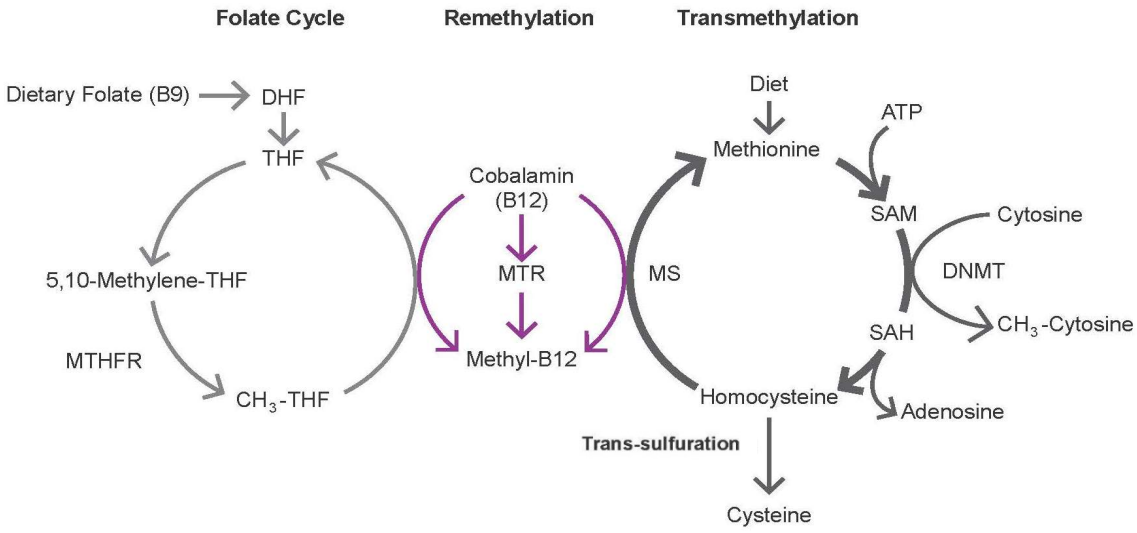

Figure 3.1. One carbon (1C) metabolism
1C metabolism pathway. In the transmethylation pathway, dietary methionine is metabolised to S-adenosyl methionine (SAM), through the transfer of an adenosyl group from adenosyl triphosphate (ATP). SAM is used as a methyl donor to methylate cytosine residues by DNA methyltransferases (DNMTs), resulting in S-adenosyl homocysteine (SAH). SAH is hydrolysed to homocysteine and adenosine. Homocysteine can be re-methylated to methionine by methionine synthase (MS). This reaction is dependent on B12 and the donation of a methyl group from 5-methyltetrahydrofolate (CH_3-THF; 5-MTHF) which is converted to THF. 5-MTHF is produced from dietary folate in the folate cycle, with dietary folate converted to dihydrofolate (DHF), then THF and 5,10-methylene-THF which is finally converted to 5-MTHF by the enzyme MTHF reductase (MTHFR).

SAM is produced from the transfer of adenosine onto the amino acid, methionine, a reaction catalysed by methionine adenosyltransferase. During the donation of a methyl group in methyltransferase reactions, SAM is converted to S-adenosyl homocysteine (SAH; Caudill et al., 2001; Ducker and Rabinowitz, 2017). SAH is hydrolysed to homocysteine and adenosine by SAH hydrolase. However, under physiological conditions this reaction equilibrium favours SAH synthesis over hydrolysis. To limit SAH accumulation effective removal of homocysteine is required (Caudill et al., 2001; Mentch and Locasale, 2016), primarily achieved by re-methylation of homocysteine to methionine (Caudill et al., 2001; Ducker and Rabinowitz, 2017). Direct re-methylation of homocysteine is catalysed by methionine synthase, a reaction dependent on 5-methyltetrahydrofolate (5-MTHF) and vitamin B_{12}, the former of which is generated from dietary folate by methyltetrahydrofolate reductase (MTHFR; Tisato et al., 2021). Thus, there is a metabolic interface and interdependency between the folate and methionine cycles, whereby reduced folate availability provokes reduced homocysteine re-methylation and hence reduced SAM synthesis and increased SAH accumulation (Caudill et al., 2001; Ducker and Rabinowitz, 2017). These interconnected cycles are heavily dependent on key metabolite availability. Importantly, folate and methionine cannot be produced through mammalian cellular pathways and must be obtained in the diet and subsequently transported into cells (Crider et al., 2012; Mentch and Locasale, 2016).

3.1.2. Transport of 1C metabolites

There are various membrane transport proteins involved in cellular uptake of folate and methionine, explored in detail below. Disturbances in cellular expression/activity of these transport systems could lead to dysregulated intracellular folate and methionine availability and 1C metabolism and hence affect cellular methylation capacity.

3.1.2.1. Transport of folates

Folates are transported by folate transporters, comprising the reduced folate carrier (RFC; encoded by *Slc19a1*), the protein-coupled folate transporter (PCFT; encoded by *Slc46a1*) and folate receptors, alpha (FRα; encoded by *Folr1*) and beta (FRβ; encoded by *Folr2*). The RFC is an anionic exchanger and major transporter for systemic folate delivery at physiological pH, while the PCFT, a proton-folate–symporter, transports folates most effectively at low pH (Zhao et al., 2009). The folate receptors, by contrast, are located in plasma membranes and transport folates into cells by receptor-mediated-endocytosis, although this occurs at a much slower rate (Tisato et al., 2021; Zhao et al., 2009). These transporters and receptors therefore work collaboratively to transport dietary folates to systemic tissues/cells, with folate transporters primarily shuttling dietary folate to organs, while folate receptors function in cellular folate uptake (Tisato et al., 2021; Zhao et al., 2011). The expression of these folate transport systems tend to be tissue-specific depending on demand. In the brain, FRα is the primary folate receptor, while the transporters show specific locality, with PCFT critical in folate transport through the choroid

plexus (Zhao et al., 2011), while recent studies suggest crucial roles for RFC in BBB-mediated folate uptake (Frigerio et al., 2019).

3.1.2.2. Transport of methionine

Amino acids, on the other hand, are transported into cells by multiple amino acid transport mechanisms. The transport mechanisms for methionine include system L (Na+-independent, large and branched chain neutral amino acid transporters), system A (Na+-dependent neutral amino acid transporters) and system y+L (transport of neutral amino acids like system L but in a Na+-coupled manner and also transports cationic amino acids in a Na+-independent manner; Kandasamy et al., 2018). Of note, system L and system y+L, are heterodimers of CD98 (heavy chain) and system L or y+L subunit (light chain), the latter of which confers catalytic activity (Tsitsiou et al., 2009). Methionine can be transported by subtypes of system A (SNAT1, *Slc38a1*; SNAT2, *Slc38a2;* SNAT4, *Slc38a4)*, system L (LAT1, *Slc7a5*; LAT2, *Slc7a8*) and system y+L (y+LAT1, *Slc7a7*; y+LAT2, *Slc7a6*) amino acid transporters (Cleal and Lewis, 2008; McColl and Piquette-Miller, 2019; Tsitsiou et al., 2009). As with folate transport mechanisms, the expression of individual transport systems is tissue-specific. Methionine has high uptake into the brain, primarily due to system L transport mechanisms, notably LAT1 (Young and Shalchi, 20005; Zaragozá, 2020). Indeed, LAT1 demonstrates high affinity for methionine and is expressed at the BBB and throughout various brain regions, including the cortex and hippocampus (Singh and Ecker, 2018; Zhang et al., 2020a). Further, while primarily studied for their roles in glutamate transport, system A transporters also possesses high affinity methionine transport capacity (Mackenzie et al., 2003). Notably, SNAT1 is highly expressed in the rat brain (Varoqui et al., 2000) and exhibits development-related changes in its expression (Weiss et al., 2003). Importantly, SNAT1 protein is expressed prenatally, identified as early as GD17, localised to the neocortex, hippocampus and neuroepithelium (Weiss et al., 2003).

3.1.2.3. The role of the placenta

The role of folate and methionine transport has particular significance when considering prenatal development where maternal provision and delivery of essential nutrients by transplacental transport is crucial for normal foetal growth and development (Bordeleau et al., 2021; Irvine et al., 2022). Inappropriate nutrient supply to the developing foetus, including both deficiency and excess, can have important consequences for development. This has been particularly well documented in the cases of deficits in both maternal folate supply to the developing foetus, which can result in neural tube defects (Irvine et al., 2022) and amino acid transport deficits, associated with foetal growth restriction (Aiko et al., 2014; Glazier et al., 1997; Jansson and Powell, 2007).

The placenta forms during pregnancy via interactions between both embryonic and maternal-derived cells and is essential for normal foetal development, with folate and methionine delivered to the foetus through active placental transport (Gude et al., 2004; Solanky et al., 2010;

Tsitsiou et al., 2009). Placental transport function adapts during gestation to meet foetal developmental and growth demand and hence perturbations to placental development and function can be detrimental to foetal development (Gude et al., 2004). It has been suggested that stress and inflammation in the mother can impact the placenta in such a way, likely through alteration of its transport and metabolic functions, to disrupt foetal brain development. Indeed, we have shown that MIA can alter transplacental transport of amino acids, with temporal reductions and increases in system L expression and function throughout gestation (Kowash et al., 2022). Changes in placental function have critically been suggested to mediate foetal programming of disease, supporting a mechanistic role for disturbed placental function following MIA and long-acting consequences for the developing brain (Jansson and Powell, 2007).

3.1.3. 1C metabolism in neurodevelopment and neuropathology

The brain is a metabolically demanding tissue during foetal development and hence is especially sensitive to perturbations in nutrient supply (Shallie and Naicker, 2019). 1C metabolism is essential for methylation pathways (e.g., methylation of various cellular substrates and regeneration of nucleotides for DNA synthesis), which are indispensable for normal cellular proliferation and differentiation (Ducker and Rabinowitz, 2017; Mentch and Locasale, 2016; Newman and Maddocks, 2017). Neurodevelopment consists of peak periods of neurogenesis and gliogenesis, comprising large waves of cellular differentiation and proliferation, generating large demand for 1C metabolism-driven biosynthetic processes (Ducker and Rabinowitz, 2017; Sarkar et al., 2019). Alterations to the transplacental and foetal cerebral transport of folate/methionine could disturb these normal neurodevelopmental processes, with consequences for normal cellular development (Fawal et al., 2018). In later postnatal neurodevelopment, 1C metabolism has been linked to ongoing neural plasticity and connectivity and establishment of normal myelin patterns. Particularly, system A transporters have been associated with normal GABAergic-glutamatergic circuitry, through biosynthesis of neurotransmitters, glutamate and GABA (Qureshi et al., 2019, 2020; Varoqui et al., 2000). Likewise, folate is essential for gliogenesis and establishment of normal myelination (McFarland, 2012; Weng et al., 2017).

Considering the key role for 1C metabolism throughout neurodevelopment and brain function, it is unsurprising that perturbations to 1C metabolism have been associated with a range of neurological disorders. Indeed, elevated serum homocysteine has been implicated in schizophrenia patients, particularly males (Kinoshita et al., 2013; Levine et al., 2002; Moustafa et al., 2014) while elevated SAM has been found in the cortex of schizophrenia patients (Guidotti et al., 2007). Likewise, *MTHFR* gene polymorphisms, leading to altered 1C metabolism and metabolite clearance rates, have been associated with schizophrenia and ASD (Li et al., 2020a; Wan et al., 2021; Wan and Wei, 2021). Further, altered expression/function of proteins which transport folate and methionine have been identified in several neurological disorders. Notably, dysfunction of folate transport proteins, FRα, RFC and PCFT have been associated with

cerebral folate deficiency (CFD; Frigerio et al., 2019; McFarland, 2012). CFD is defined as decreased CSF folate availability, relative to systemic folate, due to deficient cerebral folate transport, classified by neuropsychiatric and cognitive phenotypes and has been associated with ASD and schizophrenia (Ramaekers and Quadros, 2022; Rubini et al., 2021). Likewise, reduced BBB LAT1 expression has been identified in Parkinson's disease patients, owing to the role of LAT1 in dopamine precursor transport (Ohtsuki et al., 2010), while functional LAT1 gene variants have been associated with increased risk for ASD (Smith et al., 2019). Similarly, *Slc38a1* (SNAT1) regulates synaptic vesicles and GABA synthesis within parvalbumin GABAergic interneurons (PVIs; Qureshi et al., 2019, 2020). Given that PVIs are implicated in a range of neurological disorders, including schizophrenia (Lewis et al., 2012), it has been suggested that dysfunctional SNAT1 contributes to these disorders through dysfunctional PVIs (Qureshi et al., 2019, 2020).

3.1.4. Chapter aims

Taken together, these studies highlight the critical importance of 1C metabolism in neurodevelopment and therefore MIA-induced 1C metabolism alterations could disturb neurodevelopmental trajectories and predispose offspring to behavioural abnormalities. Indeed, several studies have implicated a role for disturbed 1C metabolism/transport in the pathogenesis of neurological diseases, including schizophrenia. Accordingly, we have previously shown altered system L transport in the placentas of MIA-exposed dams, with reduced transplacental transport of the essential amino acid leucine, 24h post-MIA, followed by increased, perhaps compensatory, transport at GD21 (Kowash et al., 2022). This functional transport change was associated with a trend towards reduced placental LAT2 expression at GD16 and upregulated system L transporter gene expression at GD21. As leucine and methionine are both transported by system L in the placenta (Cleal and Lewis 2008; Tsitsiou et al., 2009), it could be postulated that there are corresponding disturbances in transplacental transport of methionine, which would have critical impacts on foetal brain DNAm capacity. However, we have yet to determine if i) there are changes in other methionine transport systems; ii) these changes are enduring postnatally; iii) these influence methylation capacity. Therefore, it was hypothesised that observed foetal neuroinflammation (Chapter 2), together with placental transport disturbances of 1C metabolites folate and methionine (Kowash et al., 2022), would provoke altered foetal/offspring brain methylation capacity.

The aims of this Chapter were therefore to determine:

i) If MIA altered placental and cortical expression of genes important in methionine/folate transport.
ii) Whether transport alterations coincided with altered 1C metabolite availability in the developing cortex.

3.2. MATERIALS AND METHODS

Note: methods in this Chapter were performed on samples collected from PR1 and PN1.

3.2.1. Nucleic acid isolation

3.2.1.1. Simultaneous DNA and RNA extraction

Genomic DNA (gDNA) and RNA were extracted from tissue samples using the DNeasy Blood and Tissue kit (Qiagen, Manchester, UK) and RNeasy Plus Mini Kit (Qiagen, Manchester, UK) according to the manufacturer's instructions. Briefly, dissected tissues (frozen in RNAlater) were allowed to thaw on ice, followed by aspiration of RNAlater. The lysis reaction buffer was prepared in a local exhaust ventilation (LEV) cabinet by adding β-mercaptoethanol (Sigma, Gillingham, UK) diluted 1:100 in RLT Plus buffer. Placental samples were homogenised in 1.5mL lysis buffer using a Dounce homogeniser, while cortex samples were homogenised in 600µL lysis buffer using a pestle, until the tissue was completely lysed. Homogenates were then centrifuged at 18,800xg for 3min. Following centrifugation, 300µL cortex supernatant was used for RNA extraction and 300µL for gDNA extraction, while placental supernatant was proceeded through RNA extraction only.

For RNA extraction, supernatant was transferred to gDNA elimination column and centrifuged at 9,600xg for 30s to remove gDNA. An equal volume of 70% ethanol was then added to flow-through and the resulting solution added to an RNeasy Spin column and centrifuged at 9,600xg for 15s. 700µL RW1 buffer was added to the column and centrifuged at 9,600xg for 15s. Subsequently, 500µL RPE buffer was added to the column and centrifuged at 9,600xg for 15s, followed by a second addition of 500µL RPE buffer, centrifuged at 21,100xg for 2min. 50µL RNase-free water was then added to the column and incubated for 1min at room temperature before centrifuging at 9,600xg for 1min to elute RNA.

For gDNA extraction, to the corresponding 300µL supernatant, 300µL 100% ethanol was added. Solutions were then immediately centrifuged at 9,600xg for 10min and resulting supernatant discarded. The resultant pellet was reconstituted in 180µL ATL buffer with 20µL proteinase K for 2h at 56°C. 200µL AL buffer was then added, followed by a further 10min incubation at 56°C. 200µL 100% ethanol was added and the resulting solution transferred to a DNeasy Mini Spin Column and centrifuged at 6,200xg for 1min. 500µL AW1 buffer was then added to the column and centrifuged at 6,200xg for 1min, followed by 500µL AW2 buffer and centrifuged at 18,800xg for 3min. 200µL AE Buffer was then added to the column, incubated for 1min at room temperature and centrifuged at 6,200xg for 1min to elute gDNA.

gDNA/RNA samples were stored at -80°C until use.

3.2.1.2. RNA quantification and RNA quality control (QC)

RNA concentration was measured using the ThermoFisher NanoDrop® (Waltham, USA), with 2µL sample loading volume and RNAase-free water (Qiagen, Manchester, UK) as the blanking solution. Nanodrop purity ratios 260/280 and 260/230 were assessed for protein and chemical contamination, respectively, with values of 1.8-2.2 considered suitable.

Quality of RNA samples were assessed by agarose gel electrophoresis using several representative samples. 1% (w/v) agarose (Bioline, London, UK) gel in 1XTris-Acetate-EDTA (TAE) was prepared with a 1:10,000 addition of Gel Red stain (VWR, Lutterworth, UK). 1XTAE solution was prepared from a 1:50 dilution of 50XTAE stock (Cleaver Scientific, Rugby, UK) in dH_2O. Samples were diluted in nuclease-free water with 800ng RNA/15µL, mixed with 3µL 5XDNA loading buffer (Bioline, London, UK). Electrophoresis was performed in 1XTAE buffer at 120V for 1h. Gels were imaged on Syngene InGenius using the GeneSnap software (Cambridge, UK) and UV fluorescence, with automatic exposure time. Two clear RNA bands (representing 28S and 18S ribosomal RNA) with no visual smearing, were taken as evidence of good RNA integrity with no contamination/degradation. A representative gel can be found in Appendix 2, Supplementary Figure S2.1.

3.2.2. mRNA expression analysis

3.2.2.1. Reverse transcription

RNA was reverse transcribed to complementary DNA (cDNA) using the QuantiTect Reverse Transcription Kit (Qiagen, Manchester, UK) with RNA inputs of 1700ng/24µL (FC/PFC) or 2µg/24µL (placenta). Samples were diluted as appropriate in RNase-free water. Samples with low RNA yields, which precluded cDNA preparation at these inputs, were excluded from gene expression analysis. Each cDNA reaction was prepared according to the manufacturer's instructions. Briefly, 4µL gDNA wipe-out buffer was added to each 24µL RNA solution. Samples were then incubated at 42°C for 2min, to degrade gDNA contamination and then placed on ice. 8µL Quantiscript RT buffer, 2µL RT primer mix and 2µL Quantiscript Reverse Transcriptase were added to each sample. Samples were then incubated at 42°C for 15min followed by 95°C for 3min using the ^{3}Prime thermal cycler (Techne, London, UK). Negative controls were also performed in parallel, including a reverse transcriptase negative (RT-), where 2µL Quantiscript reverse transcriptase was replaced with RNase-free water and a no template control (NTC), where the sample contained RNase-free water only. All cDNA reactions were stored at -20°C for later use.

3.2.2.2. Quantitative PCR (qPCR)

Gene expression was quantified by real-time quantitative PCR (qPCR) using Qiagen QuantiTect Primers, accessed through Gene Globe software (https://www.qiagen.com/gb/shop/ genes-and-pathways/, Qiagen, Manchester, UK). The Gene Globe software for the rat genome (*Rattus*

norvegicus) was searched for each of the candidate genes of interest. Selected candidates included system L subtypes (*Slc7a5* (LAT1) and *Slc7a8* (LAT2)) which transport methionine and for which we have previously observed altered placental transport capacity following poly(I:C)-exposure (Kowash et al., 2022) and a system A transporter subtype (*Slc38a1* (SNAT1)), which also transports methionine. While both system A subtypes SNAT1 and SNAT2 have shown changes in placental and foetal brain expression *in vivo* following MIA (McColl and Piquette-Miller, 2019; Tsivion-Visbord et al., 2020) and *in vitro*, following exposure to pro-inflammatory cytokines IL-6 and TNFα (Jones et al., 2009; McColl et al., 2022), SNAT1 was chosen for its high enrichment in the rat brain (Varoqui et al., 2000; Weiss et al., 2003). Folate transporters *Folr1* (FRα) and *Slc19a1* (RFC), were chosen as these are important for cerebral folate transport (Tisato et al., 2021; Zhao et al., 2009), while the 1C metabolism enzyme *Mthfr*, was selected, as *MTHFR* mutations are associated with schizophrenia risk (Wan and Wei, 2021; Wan et al., 2021). Exon-spanning primers were selected where possible with QuantiTect primer details provided in Table 3.1. Lyophilised primers were reconstituted in 1.1mL Tris-EDTA pH8.0 (Invitrogen, Loughborough, UK) and stored at -20°C. QuantiTect primer assays were used in conjunction with QuantiFast SYBR Green RT-PCR Kit (Qiagen, Manchester, UK). Each reaction included 12.5µL QuantiFast SYBR Master Mix, 2.5µL QuantiTect primer mix and 10µL diluted cDNA sample/standard/control. A 1:50 dilution was found to be optimal for all candidate genes following a dilution trial, which tested 1:25, 1:50 and 1:100 dilutions of pooled sample in each tissue/timepoint, selecting the dilution which consistently produced a cycle threshold (Ct) value of 15-30 across development. All real-time qPCR reactions were performed on the AriaMx System (Agilent, Cheadle, UK) under the following cycling conditions: 95°C for 5min (1 cycle), 95°C for 10s and 60°C for 30s (40 cycles). SYBR dye fluorescence was measured at the end of each cycle to generate amplification curves, with ROX as a reference dye. Following this, a dissociation curve was generated using the following conditions: 95°C for 1min, 55°C for 30s, a ramp stage up to 95°C (0.5°C increments) and a final 95°C for 30s. SYBR fluorescence was measured at each temperature increment. A dissociation curve with a single peak was taken to infer generation of a single, specific PCR product.

Table 3.1. QuantiTect primer assays (Chapter 3)

Gene	QuantiTect primer assay (Cat no.)	Amplicon size (bp)	Exons spanned
***Slc38a1* (SNAT1)**	Rn_Slc38a1_1_SG (QT00187586)	97	4/5
***Slc7a5* (LAT1)**	Rn_Slc7a5_1_SG (QT00188090)	124	1/2
***Slc7a8* (LAT2)**	Rn_Slc7a8_1_SG (QT00193116)	131	6/7
***Folr1* (FRα)**	Rn_Folr1_1_SG (QT01080128)	70	-
***Slc19a1* (RFC)**	RN_Slc19a1_1_SG (QT00182231)	95	4/5
Mthfr	Rn_Mthfr_2_SG (QT00371280)	68	-

Abbreviations: bp = base pair

For each 96-well qPCR plate, a standard curve was prepared from a pooled cDNA reference sample (1µL pooled from each cDNA sample). The concentration of the pool was calculated from RNA input for cDNA conversion (cortex: 42.5ng/µL; placenta 50ng/µL), assuming a 100%

cDNA conversion rate. An eight-point 1:2 serial dilution standard curve was created with a top standard concentration of 4ng/uL (40ng/well). The standard curve (cDNA input vs fluorescence fitted by linear regression) on each plate was used to determine qPCR reaction efficiency and to interpolate sample expression values (ng/well). Negative controls, including RT-, NTC and buffer only (water replacement of cDNA) were included on each plate. All samples, standards and negative controls were loaded in duplicate and %CV calculated from Ct-values. All qPCR standard curves met the following acceptance criteria: 90-110% qPCR efficiency, conformance to linearity (R^2>0.98), CV≤1% between replicates, with no Ct-values detectable for negative controls. If these criteria were not met, the assay was repeated. Sample Ct-values passed when duplicate %CV was ≤1%. Samples not meeting this criterion were repeated.

3.2.2.3. GeNorm analysis

Accurate qPCR analysis of candidate gene expression is dependent on selection of stable reference genes for normalisation (Ramhøj et al., 2019). With this in mind the stability of expression for six common reference genes: *Gapdh, Ubc*, *Ywhaz*, *B2m*, *Actb*, *Mdh1* (GeNorm primer panel, Z-HK-SY-RA-600; PrimerDesign Ltd., Chandler's Ford, UK; reconstituted in 330µL RNase-free water) were analysed using a random selection of males (n=2) and females (n=2) from each vehicle and poly(I:C) group for each tissue/timepoint, generating a pool of eight representative samples from any given tissue, comprising both groups and sexes. Each sample was analysed in duplicate for each of the six reference genes. All qPCR reactions were performed as outlined previously (Section 3.2.2.2) and raw data exported to Excel and then uploaded into QBase+ (Biogazelle, Ghent, Belgium) GeNorm analysis software. GeNorm analysis was performed within each tissue type to identify a reference gene which was stable across the developmental timeline as described by Vandesompele et al. (2002). The analysis software calculates the average expression stability of examined reference genes, displayed as geNorm M, as an indication of reference gene stability, while the geNorm V plot is used to determine the optimal reference gene number (Appendix 3). Based on this analysis, it was determined that three reference genes (*Gapdh, Ubc* and *Mdh1*) would be used for expression normalisation in the cortex (Supplementary Figure S3.1), while two (*Actb* and *Gapdh)* would be used for the placenta (Supplementary Figure S3.2). Notably in the developing cortex, *Actb* was the least stable reference gene, in line with previous studies (Ramhøj et al., 2019).

Following appropriate reference gene selection, expression of each reference gene in each sample was quantified as outlined above (Section 3.2.2.2). Normalised candidate gene expression was calculated within each sample by dividing the interpolated candidate gene value by the geometric mean of the interpolated reference gene values.

3.2.2.4. qPCR gels

Following qPCR, 20µL qPCR product from a random selection of samples were assessed by agarose gel electrophoresis. Gels were prepared at 2% (w/v) agarose (Bioline, London, UK) in

1XTAE and a 1:10,000 dilution of GelRed (VWR, Lutterworth, UK). 1XTAE solution was prepared from a 1:50 dilution of 50XTAE stock (Cleaver Scientific, Rugby, UK). A 25bp HyperLadder™ (Bioline, London, UK) was loaded to assess qPCR product size. Gel electrophoresis was performed in 1XTAE at 100V for 2.5h. Gels were visualised on a GelDoc XR (Bio-rad, Watford, UK) on automatic exposure. A clear amplicon of predicted size (Table 3.1) was observed for all genes. Representative qPCR gels for each gene can be found in Appendix 4, Section 1.

3.2.3. Isolation of nuclear and cytosolic cellular fractions

Nuclear and cytosolic lysates were prepared using the Nuclear Extract kit (Active Motif, Waterloo, Belgium). All buffers were prepared as per kit specifications (Table 3.2) while flash frozen brain samples thawed on ice.

Table 3.2. Nuclear extract kit buffer preparations

Buffer	Reagents per sample
1XHypotonic Homogenisation Buffer	20µL 10XHypotonic Buffer 2µL Protease Inhibitor Cocktail 20µL Phosphatase Inhibitors 0.2µL 1M DTT 0.2µL Detergent 158µL dH_2O
1XHypotonic Cytoplasmic Buffer	2.5µL 10XHypotonic Buffer 22.5µL dH_2O
Complete Lysis Buffer	0.25µL 10mM DTT* 2.22µL Lysis Buffer AM1 0.025µL Protease Inhibitor Cocktail

*1M DTT diluted 1:100 in dH_2O to produce 10mM DTT solution

150µL 1XHypotonic Homogenisation Buffer was added to each tissue sample and tissue homogenised using a pestle until visibly lysed. The whole tissue lysate was incubated on ice for 15min before centrifuging at 850xg at 4°C for 10min to pellet cells (Note: 2µL of the whole tissue lysate was collected prior to centrifuging for western blotting validation experiments). Following centrifugation, the supernatant (extracellular fraction) was removed and the pellet was resuspended in 25µL 1XHypotonic Cytoplasmic Buffer and then incubated for 15min on ice before adding 1.25µL detergent. The sample was centrifuged for 30s at 14,000xg at 4°C and the supernatant (cytosolic fraction) transferred to a new tube. The pellet, containing the total nuclear fraction (tNF), was resuspended in 2.5µL Complete Lysis Buffer and 0.15µL detergent and then incubated on ice for 30min with regular vortexing to disrupt the nuclear membrane. This tNF could be divided into soluble (sNF) and insoluble (iNF) nuclear fractions by centrifugation at 14,000xg at 4°C for 10min. The supernatant (sNF) was removed and the pellet (iNF) reconstituted in 5µL 1XPBS. Samples were stored at -80°C for later use.

3.2.3.1. Protein concentration of individual fractions

Protein concentrations were determined using a Bradford assay (Chapter 2, Section 2.2.3.1). Sample fractions were diluted in dH_2O (matrix fraction 1:50; whole tissue lysate, cytosolic and nuclear fractions 1:100) in a total of 50µL and assayed in duplicate.

3.2.3.2. Validation of fractions by Western blotting

Western blots were used to validate the nuclear and cytoplasmic fractions using the nuclear-specific protein Histone 3 (rabbit monoclonal anti-H3, ab176842; 0.495mg/mL; Abcam, Cambridge, UK) and the primarily cytosolic protein, GAPDH (mouse monoclonal anti-GAPDH, 60004-1-Ig; Proteintech, Manchester, UK; Tristan et al., 2011).

For all Western blotting experiments, a standard protocol was used and optimised for each antibody. Where changes were made to the standard protocol these have been indicated in each section. All Western blots were performed using the Mini-PROTEAN® Tetra Cell Electrophoresis unit, Mini Trans-Blot® Module and PowerPac™ Basic Power Supply (Bio-rad, Watford, UK) using precast Mini-PROTEAN Tris-Glycine eXtended (TGX) Gels (4-15% polyacrylamide, 50µL, 10 wells; Bio-rad) with 5µL Precision Pus Protein™ All Blue Prestained Protein Standards (10–250kDa; Bio-rad) for molecular weight determination. Secondary IRDye® antibodies (Li-Cor, Cambridge, UK) were used for infrared detection including: IRDye® 800CW donkey anti-rabbit IgG(H+L) and IRDye® 680RD donkey anti-mouse IgG(H+L). Lyophilised IRDye® antibodies were reconstituted with 100µL dH_2O and stored at 4°C until use. Prior to starting, 5XElectrode and 10XTransfer buffers were prepared (Table 3.3). These stock solutions were made to 1X when required: for 1XElectrode buffer 200mL 5XStock solution was added to 800mL dH_2O; for 1XTransfer buffer 100mL 10XStock solution was added to 700mL dH_2O and 200mL methanol (Fisher Scientific, Leicestershire, UK). For the validation of nuclear fractions, all fraction samples were diluted in dH_2O to a concentration of 20µg protein/18µL. 6µL boil reducing buffer (Table 3.3) was added to 18µL sample (1:3 buffer:sample ratio).

Samples were incubated at 95°C for 5min on an AccuBlock Digital Dry Bath (Labnet, Windsor, UK), followed by an incubation on ice for 5min. Mini-PROTEAN TGX Gels were removed from packaging and their base strip and comb removed. Precast gels were placed in Mini-PROTEAN® Tetra Cell Electrophoresis units and wells washed with 1XElectrode buffer. Excess electrode buffer was removed with a needle and syringe. 5µL Precision Plus Protein™ Standards and 24µL samples were loaded into wells and overlayed with 1XElectrode buffer. The unit was placed in the electrophoresis tank, filled with 1XElectrode buffer. Gel electrophoresis was performed at 200V for 30min using the PowerPac™ Basic Power Supply. Following electrophoresis, the precast gel cassettes were opened and the gel washed 3x5min with 1XTransfer buffer. 8.5cmx7cm Immobilon®-FL PVDF membranes (Sigma-Aldrich, Gillingham, UK) were activated by successive incubations as follows: 100% methanol (1min), dH_2O (1min); 1XTransfer buffer for 20min to equilibrate. For each gel, two foam pads (Bio-rad,

Watford, UK) and four 8.5cmx7cm filter papers were also equilibrated in 1XTransfer buffer for 20min. The gel holder cassettes were then prepared, placing the pre-soaked items onto the transparent cassette base in the following order: 1 sponge, 2 filter papers, 1 activated PVDF membrane, 1 gel, 2 filter papers and 1 sponge. The cassette was then closed and placed into the Mini Trans-Blot® Module which was inserted in the electrophoresis tank with the membrane aligned to the positive electrode. The tank was filled with 1XTransfer buffer and ice blocks to dissipate generated heat during transfer. Transfer was performed at 100V for 30min using the PowerPac™ Basic Power Supply. Once transfer was complete, membranes were rinsed for 5min in 1XPBS (Table 3.3) before leaving to dry at room temperature for 1h. Following drying, membranes were inserted into 50mL falcon tubes (protein side facing inwards). 15mL 5%BLOTTO (Table 3.3) was added to the membrane-containing falcon and the falcon placed on an Analogue Tube Roller (Stuart™; Cole-Parmer, Illinois, USA) for 1h at room temperature to block non-specific binding.

Table 3.3. Western blotting buffers

Buffer	Reagent	Weight/volume
10XTransfer buffer	Trizma base (Sigma-Aldrich) Glycine (Fisher Scientific) dH_2O	60.6g (250mM) 288g (1.92M) In 2L
5XElectrode buffer	Trizma base (Sigma-Aldrich) Glyciene (Fisher Scientific) SDS (Sigma-Aldrich) dH_2O	60.6g (250mM) 288g (1.92M) 20g (34.7mM) In 2L
Boil reducing buffer	4XLaemmli buffer (Bio-rad) β-mercaptoethanol (Sigma-Aldrich)	0.4mL 0.1mL
1XPBS	PBS tablets (Oxoid™) dH_2O	10 tablets In 1L
1XPBS/0.1%Tween	1XPBS (As above) Tween®20 (Sigma-Aldrich)	999mL 1mL
LI-COR secondary diluent (PBS/0.2%Tween/0.01%SDS)	Tween®20 (Sigma-Aldrich) 0.01% SDS (Sigma-Aldrich) 1XPBS (As above)	0.2mL 0.01g In 100mL
5%BLOTTO	Milk powder (Marvel) 1XPBS (As above)	5g In 100mL
5%BLOTTO/0.05%Tween	5%BLOTTO (as above) Tween®20 (Sigma-Aldrich)	99.5mL 0.5mL

Primary antibodies were diluted as specified (Table 3.4) in 5%BLOTTO/0.05%Tween (Table 3.3). 5mL diluted primary antibody solution was added to each blot and left on the Analogue Tube Roller overnight at 4°C. The following morning, blots were equilibrated to room temperature for 1h. Membranes were then washed 4x5min with 15mL 1XPBS/0.1%Tween (Table 3.3). If a second target/reference antibody (e.g., anti-GAPDH antibody) was to be used it was diluted as specified (Table 3.4) in 5%BLOTTO/0.05%Tween (Table 3.3). 5mL diluted second target/reference antibody solution was added to each blot and left on the Analogue Tube Roller for 2h at room temperature. The membranes were then washed 4x5min with 15mL 1XPBS/0.1%Tween (Table 3.3).

Table 3.4. Antibody dilutions

Antibody	Supplier	Dilution (Titre)
Anti-H3	Abcam, Cambridge, UK	1:1,000 (0.495µg/mL)
Anti-GAPDH	Proteintech, Manchester, UK	1:4,000 (0.25µg/mL)

Following completion of target/reference antibody incubation(s), the falcon tubes were wrapped in foil to protect them from light. The IRDye® 800CW (800nm; green) was diluted 1:20,000, while the IRDye® 680RD (700nm; red) was diluted 1:40,000, in 10mL Li-Cor secondary diluent (Table 3.3). 10mL diluted secondary antibody (of appropriate anti-host species) was added to each blot and incubated for 1.5h at room temperature on the Analogue Tube Roller. The membranes were washed 4x5min with 15mL 1XPBS/0.1%Tween followed by a final wash in 1XPBS (Table 3.3) to remove residual Tween. The blots were imaged under 700nm and 800nm wavelengths using the Li-Cor Odyssey CLX (Cambridge, UK) under default conditions.

The initial validation confirmed that the nuclear-specific protein H3 was present only in iNF and sNF and absent from cytosolic and matrix fractions (Figure 3.2), indicating a clear enrichment in the nuclear-designated fractions. Comparatively, GAPDH showed greatest enrichment in the cytosolic fraction. However, GAPDH expression was still present in the nuclear and matrix fractions, not unsurprising given the literature supporting presence of GAPDH across several cellular fractions (Tristan et al., 2011).

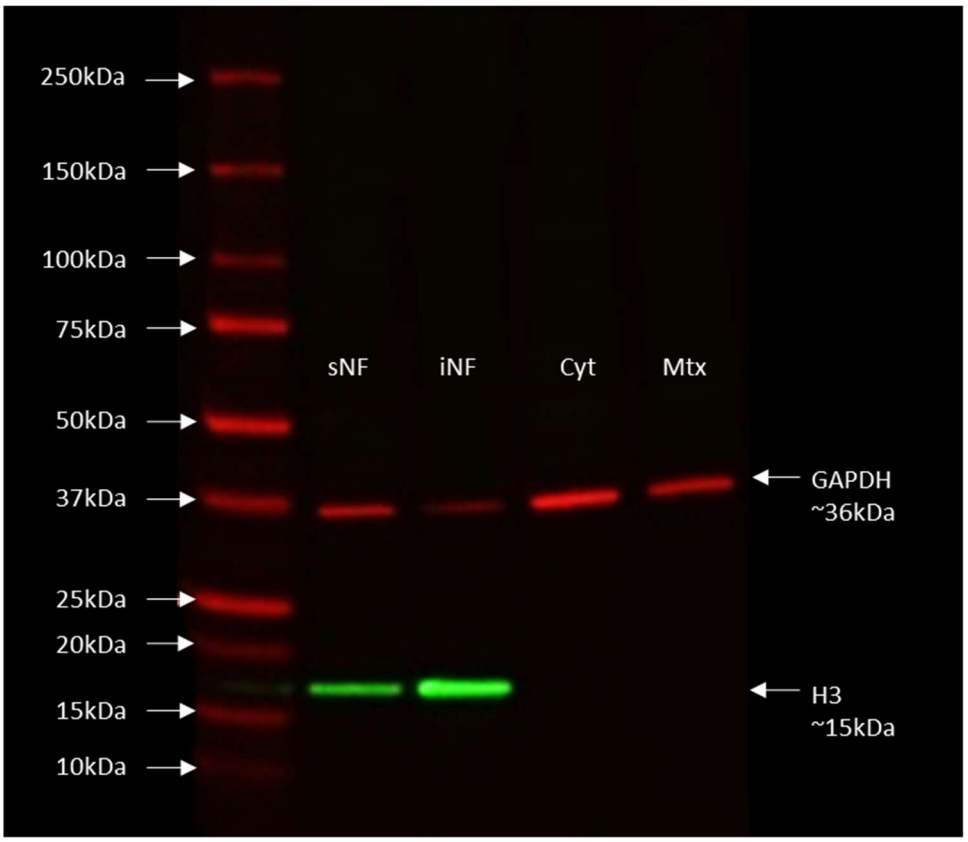

Figure 3.2. Nuclear and cytosolic fraction validation
Western blot image for Histone 3 (H3, Green; ~15kDa) and GAPDH (Red; ~37kDa) using the Li-Cor Odyssey CLX system. Molecular weight ladders are shown on the left. 20µg of lysate was loaded/well. Abbreviations: sNF, soluble nuclear fraction; iNF, insoluble nuclear fraction; tNF, total nuclear fraction; Cyt, cytosolic fraction; Mtx, matrix fraction.

3.2.4. SAH quantification

SAH was quantified from cytosolic fractions (Section 3.2.3) using the S-adenosyl homocysteine (SAH) ELISA (Cell Biolabs, San Diego, USA) as per kit instructions. Prior to starting, the following reagents were prepared: 1XPBS prepared from 10XPBS (pH7.4; Invitrogen, Waltham, USA) diluted 1:10 in dH_2O; 1XWash Buffer prepared by diluting 10XWash Buffer 1:10 in dH_2O, both stored at 4°C. The SAH Conjugate Coated Plate was prepared by adding 100µL 1XSAH conjugate (prepared by diluting 100XSAH conjugate 1:100 in 1XPBS) to each well of the 96-well Protein Binding Plate and incubated overnight at 4°C. The diluted SAH conjugate was discarded and wells washed three times with 200µL 1XPBS. 200µL Assay Diluent was added to each well and the plate blocked for 1h at room temperature (25°C) at 50rpm on a Mini Shaking Incubator (N-Biotek, Gyeonggi-do, Korea).

While the plate was blocking, a seven-point 1:2 serial dilution of SAH standard was prepared in Assay Diluent with a top concentration of 12.5nmol/mL, using the provided kit stock standard (1,250nmol/mL SAH). An eighth standard point containing assay diluent only (0nmol/mL SAH) was also prepared. Cytosolic fraction samples were thawed on ice and diluted in 1XPBS to a concentration of 250µg protein/50µL, determined to be the input at which maximal signal was achieved while maintaining assay linearity.

The Assay Diluent was discarded from the plate and 50µL samples/standards added to the SAH Conjugate Coated wells. Each cytosolic sample (250µg protein/well), SAH standard and absolute blank (containing no solutions) was assayed in duplicate. The plate was incubated at 25°C for 10min at 50rpm on a Mini Shaking Incubator, before addition of 50µL diluted anti-SAH antibody (prepared by diluting the anti-SAH antibody 1:500 with Assay Diluent). The plate was then incubated at 25°C for 1h at 50rpm on a Mini Shaking Incubator. The solutions were discarded and wells washed three times with 200µL 1XWash Buffer. 100µL diluted Secondary Antibody HRP Conjugate (prepared by diluting the Secondary Antibody HRP Conjugate 1:1,000 with Assay Diluent) was added to each well and incubated at 25°C for 1h at 50rpm on a Mini Shaking Incubator. During this incubation, the Substrate Solution was equilibrated to room temperature. The Antibody HRP Conjugate Solution was discarded and wells washed three times with 200µL 1XWash Buffer. 100µL Substrate Solution was added to each well, including the absolute blank wells and incubated at 25°C for 5min at 50rpm on a Mini Shaking Incubator. 100µL Stop Solution was added to each well, including the absolute blank and mixed thoroughly.

The plate absorbance was read at 450nm as the primary wavelength and 620nm as the reference wavelength on the Biotek synergy H1 plate reader (Agilent, Cheadle, UK). The correction wavelength was deducted from the primary wavelength reading within each well, to give a normalised OD reading for each well. The average of the absolute blanks was deducted from all wells. The data was imported into GraphPad Prism (v9.0) and a standard curve constructed as a semi-log line (Figure 3.3). Sample concentrations were interpolated using the built-in interpolation function. Standard and sample duplicates showed a %CV 0-15% across

plates and standard R^2-values were calculated for goodness of fit and ranged from 0.985-0.991. The sample values were calculated as nmol/mg cytosolic protein lysate.

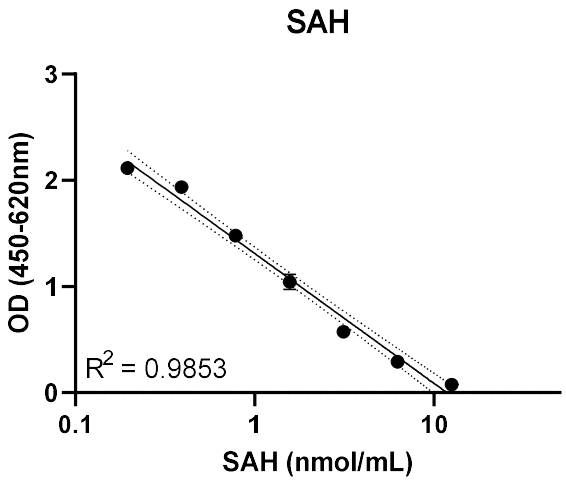

Figure 3.3. Representative SAH standard curve
Semi-log fit of standard curve, with SAH input concentration of 0.195-12.5nmol/mL. R-squared and 95% CI (dashed lines) indicated.

3.2.5. SAM quantification

SAM was quantified from cytosolic fractions (Section 3.2.3.) using a SAM ELISA Kit (Aviva Systems Biology, San Diego, USA) as per kit instructions. Prior to starting, 1XWash Buffer was prepared by adding 30mL 25XWash Buffer to 720mL dH_2O and stored at 4°C until use. Standards were prepared by addition of 1mL Sample Diluent to the 100nmol Lyophilized SAM Standard and mixed gently until dissolved. The reconstituted standard was left at ambient temperature for 15min before preparing a seven-point 1:2 serial dilution in Sample Diluent, with 100nmol/mL top concentration. An eighth standard point containing Sample Diluent only (0nmol/mL SAM) was also prepared. Cytosolic fractions (Section 3.2.3) were thawed on ice and diluted to 250µg protein/50µL in sample diluent, the input at which maximal signal was achieved while maintaining assay linearity.

50µL standards/samples were added into the wells of the pre-coated SAM microplate in duplicate followed by addition of 50µL 1XSAM-Biotin Complex (prepared by diluting 100XSAM-Biotin Complex 1:100 with Complex Diluent) to each well (excluding absolute blank wells which contained no solutions). The plate was incubated for 1h at 37°C at 50rpm on a Mini Shaking Incubator (N-Biotek, Gyeonggi-do, Korea). The liquid was discarded and the wells washed three times with 200µL 1XWash Buffer. 100µL 1XAvidin-HRP Conjugate (prepared by diluting the 100XAvidin-HRP Conjugate 1:100 with Conjugate Diluent) was added to each well and incubated for 45min at 37°C at 50rpm on a Mini Shaking Incubator. The liquid was discarded and the wells washed three times with 200µL 1XWash Buffer. 90µL TMB Substrate was added to each well, including absolute blanks and incubated at 37°C in the dark for 20min at 50rpm on a Mini Shaking Incubator. 50µL of Stop Solution was added to each well and mixed thoroughly. Absorbance at the primary 450nm wavelength was read alongside a correction wavelength of

570nm on the Biotek synergy H1 plate reader (Agilent, Cheadle, UK). The correction wavelength values were deducted from the primary wavelength reading within each well and the average of the absolute blanks deducted from all wells. The data was imported into GraphPad Prism (v9.0) and a standard curve constructed as a semi-log line (Figure 3.4). Sample concentrations (nmol/mL) were interpolated using the built-in function. Standard and sample duplicates showed a %CV 0-12% across plates and standard R^2-values were calculated for goodness of fit ranging 0.975-0.982. The sample values were subsequently calculated as nmol/mg cytosolic protein lysate

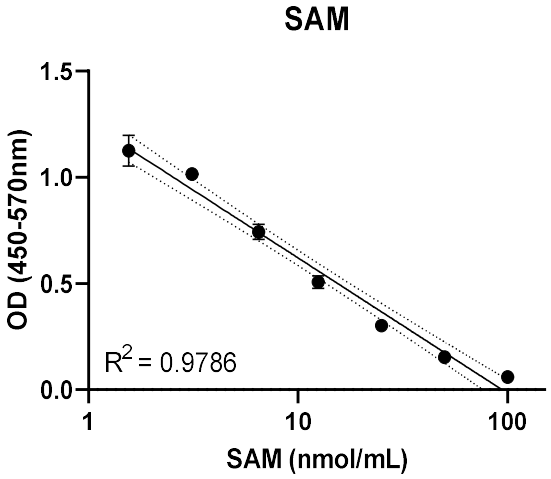

Figure 3.4. Representative SAM standard curve
Semi-log line standard curve fit for SAM assay, with SAM concentrations 1.5625-100nmol/mL. R-squared and 95% CI (dashed lines) indicated.

3.2.6. Statistics

Statistical analysis of foetal/offspring molecular outputs (including the following dependent variables in this Chapter: relative gene expression, SAM concentration, SAH concentration, SAM/SAH ratio) were performed as described in Chapter 2, Section 2.2.5 using SPSS v28.0 (IBM). Briefly, within-group outliers were identified and excluded using SPSS extreme outlier function. Between-group and post-hoc sex comparisons were analysed by GLMM including dam as a random factor and the following predictors: fixed factors (sex, group) and covariates (maternal IL-6 and TNFα), with p-values≤0.05 considered statistically significant and 0.05<p≤0.08 highlighted as trending towards significance. Where effects for all four predictors were insignificant the phrase 'there were no significant effects of any predictors' will be used. Post-hoc correlations (Pearson's (r) or Spearman's (rho)) were used to evaluate directionality of relationship between numerical dependent variables and covariates.

Graphs were generated using GraphPad Prism (v9.0), with n-numbers for dam per group (N) and foetuses/pups/placentas per sex per group (n) indicated in figure legends. For bar charts, data are represented as mean ±SEM. Note that group*sex interactions are not indicated on graphs, instead post-hoc analyses by sex have been outlined where significant.

3.3. RESULTS

3.3.1. Gene expression changes

3.3.1.1. Placental expression of genes involved in 1C metabolite transport

I. Genes involved in folate transport

In the GD15 placenta there was a trend to a main effect of sex for both *Folr1* (GLMM: $F_{1,20}$=3.92, p=0.062) and *Slc19a1* (GLMM: $F_{1,14.17}$=3.57, p=0.08), with reduced mRNA expression in female-placentae relative to male-placentae (Figure 3.5A).

In the GD21 placenta there were no significant effects of any predictors on *Folr1* mRNA expression (Figure 3.5B), while for *Slc19a1*, there was a significant main effect of maternal TNFα (GLMM: $F_{1,12}$=6.76, p=0.023; Figure 3.5B), corresponding to a positive correlation between maternal TNFα and placental *Slc19a1* expression (r=0.600, p=0.023).

II. Genes involved in methionine transport

In the GD15 placenta there was a main effect of sex for *Slc7a5* (GLMM: $F_{1,26.60}$=5.30, p=0.029), with increased mRNA expression in female-placentae relative to male-placentae (Figure 3.5A). Comparatively, for *Slc7a8,* there was a main effect of sex (GLMM: $F_{1,26.31}$=11.17, p=0.002; Figure 3.5A) and a group*sex interaction (GLMM: $F_{1,12.0}$=3.63, p=0.05). Post-hoc analysis revealed a main effect of maternal IL-6 in the males (GLMM: $F_{1,18}$=5.233, p=0.034; Figure 3.5A), corresponding to a negative correlation between maternal IL-6 and *Slc7a8* mRNA expression in male-placentae (r=-0.475, p=0.034). For *Slc38a1* there was a significant main effect of group (GLMM: $F_{1,19}$=35.95, p<0.001; Figure 3.5A) with increased *Slc38a1* mRNA expression in the poly(I:C)-placentae relative to vehicle-placentae.

In the GD21 placenta there were no significant effects of any predictors on *Slc7a8* expression. However, for *Slc7a5,* there was a main effect of group (GLMM: $F_{1,8.90}$=5.35, p=0.046; Figure 3.5B), with increased *Slc7a5* mRNA expression in the poly(I:C)-placentae relative to vehicle-placentae. Likewise, for *Slc38a1,* there was a main effect of maternal IL-6 (GLMM: $F_{1,12}$=25.69, p<0.001; Figure 3.5B) corresponding to a positive correlation between maternal IL-6 and *Slc38a1* mRNA expression (r=0.639, p=0.003).

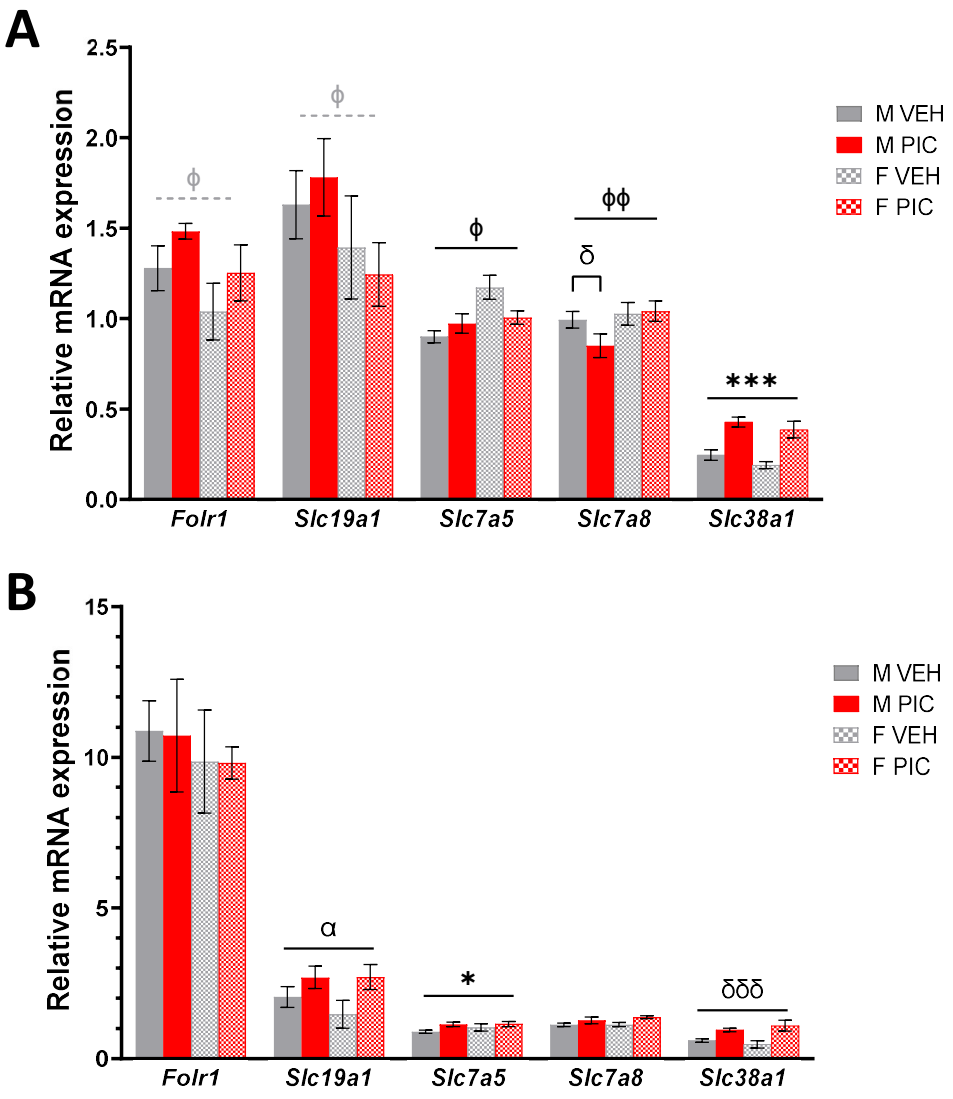

Figure 3.5. Placental transport gene expression
Relative placental mRNA expression (normalised to the geometric mean of two reference genes as described in methods). **A.** GD15. **B.** GD21. Bars represent mean ±SEM (N=5-7; n=5-10). Black significance bars show GLMM results, – shaped bars represent results across the gene they overlap, Π-shaped bars represent post-hoc results within a single sex. Black symbols show significant main effects of: sex, ϕp<0.05, ϕϕp<0.01; group, *p<0.05, ***p<0.001; maternal IL-6, δp<0.05, δδδp<0.001; maternal TNFα, αp<0.05. Grey dashed bars and symbols show trending (0.05<p≤0.08) significant GLMM results. Abbreviations: GD, gestational day; M, male; F, female; VEH, vehicle; PIC, poly(I:C).

3.3.1.2. Cortical expression of genes involved in folate transport and metabolism

I. *Folr1*

GD21

There were no significant effects of any predictors on *Folr1* expression (Figure 3.6A).

PD21

In the FC there was a significant main effect of group (GLMM: $F_{1,19}$=6.48, p=0.02; Figure 3.6A) with reduced *Folr1* expression in poly(I:C)-offspring relative to vehicle-offspring, but no significant effects of any predictors on *Folr1* expression in the PFC.

PD35

In the FC there was a significant main effect of sex (GLMM: $F_{1,16}$=5.11, p=0.038; Figure 3.6A), with reduced *Folr1* mRNA expression in females relative to males, whereas in the PFC there was a significant main effect of sex (GLMM: $F_{1,16.26}$=10.78, p=0.005; Figure 3.6A), also indicating reduced *Folr1* mRNA expression in females relative to males and a trend to a group*sex interaction (GLMM: $F_{2,17}$=3.45, p=0.055). Post-hoc analysis showed a significant main effect of maternal TNFα in the male offspring (GLMM: $F_{1,9}$=6.54, p=0.031; Figure 3.6A), corresponding to a negative correlation between maternal TNFα and *Folr1* mRNA expression (rho=-0.806, p=0.003).

PD175

In the FC there was a significant main effect of sex (GLMM: $F_{1,16}$=5.11, p=0.038; Figure 3.6A), with reduced *Folr1* expression in females relative to males and group (GLMM: $F_{1,16}$=6.31, p=0.023; Figure 3.6A), with reduced *Folr1* expression in poly(I:C)-offspring relative to vehicle-offspring. In the PFC, there was a significant main effect of group (GLMM: $F_{1,17}$=9.11, p=0.008; Figure 3.6A), with reduced *Folr1* expression in poly(I:C)-offspring relative to vehicle and maternal TNFα (GLMM: $F_{1,17}$=6.70, p=0.019; Figure 3.6A), though this did not correspond to a significant post-hoc correlation.

II. *Slc19a1*

GD21

There was a significant main effect of group (GLMM: $F_{1,11}$=5.37, p=0.041; Figure 3.6B) with elevated *Slc19a1* expression in poly(I:C)-foetuses relative to vehicle-foetuses.

PD21

In the FC there was a significant main effect of sex (GLMM: $F_{1,10.85}$=6.06, p=0.032; Figure 3.6B), with elevated *Slc19a1* expression in females relative to males. There were no significant effects of any predictors on *Slc19a1* expression in the PFC.

PD35

In the FC there was a trend to a significant main effect of sex (GLMM: $F_{1,14.60}$=4.51, p=0.051; Figure 3.6B), with reduced *Slc19a1* expression in females relative to males. In the PFC there was a significant main effect of sex (GLMM: $F_{1,6.51}$=25.34, p<0.001; Figure 3.6B), with elevated *Slc19a1* expression in females relative to males and a group*sex interaction (GLMM: $F_{2,8.86}$=4.43, p=0.046). Post-hoc analysis showed a significant main effect of group in the female offspring (GLMM: $F_{1,7}$=6.67, p=0.036; Figure 3.6B), with elevated *Slc19a1* expression in poly(I:C)-females relative to vehicle-females and a significant main effect of maternal IL-6 in male offspring (GLMM: $F_{1,9}$=6.45, p=0.032; Figure 3.6B) corresponding to a positive correlation (rho=0.736, p=0.015) between maternal IL-6 and male PFC *Slc19a1* expression.

PD175

There were no significant effects of any predictors, in the FC or PFC, on *Slc19a1* expression.

III. *Mthfr*

GD21

There were no significant effects of any predictors on *Mthfr* expression (Figure 3.6C).

PD21

In the PFC there was a significant group*sex interaction (GLMM: $F_{2,12.55}$=5.78, p=0.017) and a trend towards a main effect of sex (GLMM: $F_{1,11.90}$=4.35, p=0.059; Figure 3.6C). Post-hoc analysis showed a trend to significant main effect of group in the males (GLMM: $F_{1,10}$=4.03, p=0.075; Figure 3.6C), with a reduction in *Mthfr* expression in poly(I:C)-males relative to vehicle-males and a trend to a significant main effect of group in the females (GLMM: $F_{1,8}$=4.86, p=0.059; Figure 3.6C), with increased *Mthfr* expression in poly(I:C)-females relative to vehicle-females. There were no significant effects of any predictors on *Mthfr* expression in the FC.

PD35

In the FC there was a significant main effect of sex (GLMM: $F_{1,12.98}$=5.52, p=0.035; Figure 3.6C) with reduced *Mthfr* expression in females relative to males, whereas in the PFC there was a significant main effect of sex (GLMM: $F_{1,18}$=5.35, p=0.033; Figure 3.6C), with males having reduced *Mthfr* expression relative to females and group (GLMM: $F_{1,\ 18}$=5.99, p=0.025; Figure 3.6C) with higher *Mthfr* expression in poly(I:C)-offspring compared to vehicle-offspring.

PD175

There was a main effect of sex in both the FC (GLMM: $F_{1,18}$=7.61, p=0.013; Figure 3.6C), with reduced *Mthfr* expression in females compared to males and PFC (GLMM: $F_{1,20}$=5.14, p=0.035; Figure 3.6C), with reduced *Mthfr* in the males relative to the females.

3.3.1.3. Cortical expression of genes involved in methionine transport

I. *Slc7a5*

GD21

There was a significant group*sex interaction in the FC (GLMM: $F_{3,8}$=7.21, p=0.012). Post-hoc analysis showed a main effect of group in the males (GLMM: $F_{1,3}$=32.52, p=0.011; Figure 3.7A), with increased *Slc7a5* expression in poly(I:C)-males compared to vehicle-males and maternal IL-6 (GLMM: $F_{1,3}$=15.51, p=0.029; Figure 3.7A), corresponding to a positive correlation between maternal IL-6 and *Slc7a5* mRNA expression in male-foetuses (r=0.793, p=0.019).

PD21

In the FC there was a significant main effect of sex (GLMM: $F_{1,19}$=4.83, p=0.041; Figure 3.7A), with elevated *Slc7a5* expression in females relative to males. Post-hoc analyses showed a significant main effect of maternal IL-6 in the females (GLMM: $F_{1,8}$=13.92, p=0.006; Figure 3.7A) corresponding to a positive correlation between *Slc7a5* expression and maternal IL-6

(rho=0.769, p=0.009). In the PFC there was significant main effect of group (GLMM: $F_{1,8.40}$=5.27, p=0.049; Figure 3.7A), with increased *Slc7a5* expression in the poly(I:C)-offspring relative to vehicle-offspring, maternal TNFα (GLMM: $F_{1,7.69}$=11.23, p=0.011; Figure 3.7A) and a trend to a main effect of maternal IL-6 (GLMM: $F_{1,7.33}$=3.91, p=0.08; Figure 3.7A), though the latter two did not correspond to significant post-hoc correlations.

PD35

In the PFC, there was a significant main effect of maternal IL-6 (GLMM: $F_{1,17}$=6.35, p=0.022; Figure 3.7A) and a trend to a main effect of group (GLMM: $F_{1,17}$=3.54, p=0.077; Figure 3.7A), with increased *Slc7a5* expression in the poly(I:C)-offspring relative to vehicle-offspring and maternal TNFα (GLMM: $F_{1,17}$=3.87, p=0.066; Figure 3.7A). However, post-hoc correlation analysis showed no significance. In the FC there were no significant effects of any predictors on *Slc7a5* expression.

PD175

There was a main effect of sex for both FC (GLMM: $F_{1,18}$=6.35, p=0.023; Figure 3.7A) and PFC (GLMM: $F_{1,18}$=7.37, p=0.014; Figure 3.7A) with reduced *Slc7a5* expression in females relative to males.

II. *Slc7a8*

There were no significant effects of any predictors on *Slc7a8* expression at GD21 or PD35 (Figure 3.7B).

PD21

In the PFC there was a main effect of maternal TNFα (GLMM: $F_{1,9.7}$=7.12, p=0.024; Figure 3.7B) and a trend to a main effect of group (GLMM: $F_{1,10.41}$=3.99, p=0.073; Figure 3.7B), with increased *Slc7a8* expression in poly(I:C)-offspring relative to vehicle-offspring. In the FC were no significant effects of any predictors on *Slc7a8* expression.

PD175

In the PFC there was a main effect of sex (GLMM: $F_{1,18}$=9.71, p=0.006; Figure 3.7B), with reduced *Slc7a8* expression in females relative to males. There were no significant effects of any predictors on *Slc7a8* expression in the FC.

III. *Slc38a1*

The only significant effects of any predictors identified were in PD175, with a significant main effect of sex in the FC (GLMM: $F_{1,18}$=6.18, p=0.023; Figure 3.7C), with reduced *Slc38a1* expression in females relative to males and a trend towards a main effect of group (GLMM: $F_{1,12.11}$=4.14, p=0.064; Figure 3.7C) in the PFC, with elevated *Slc38a1* expression in poly(I:C)-offspring relative to vehicle-offspring.

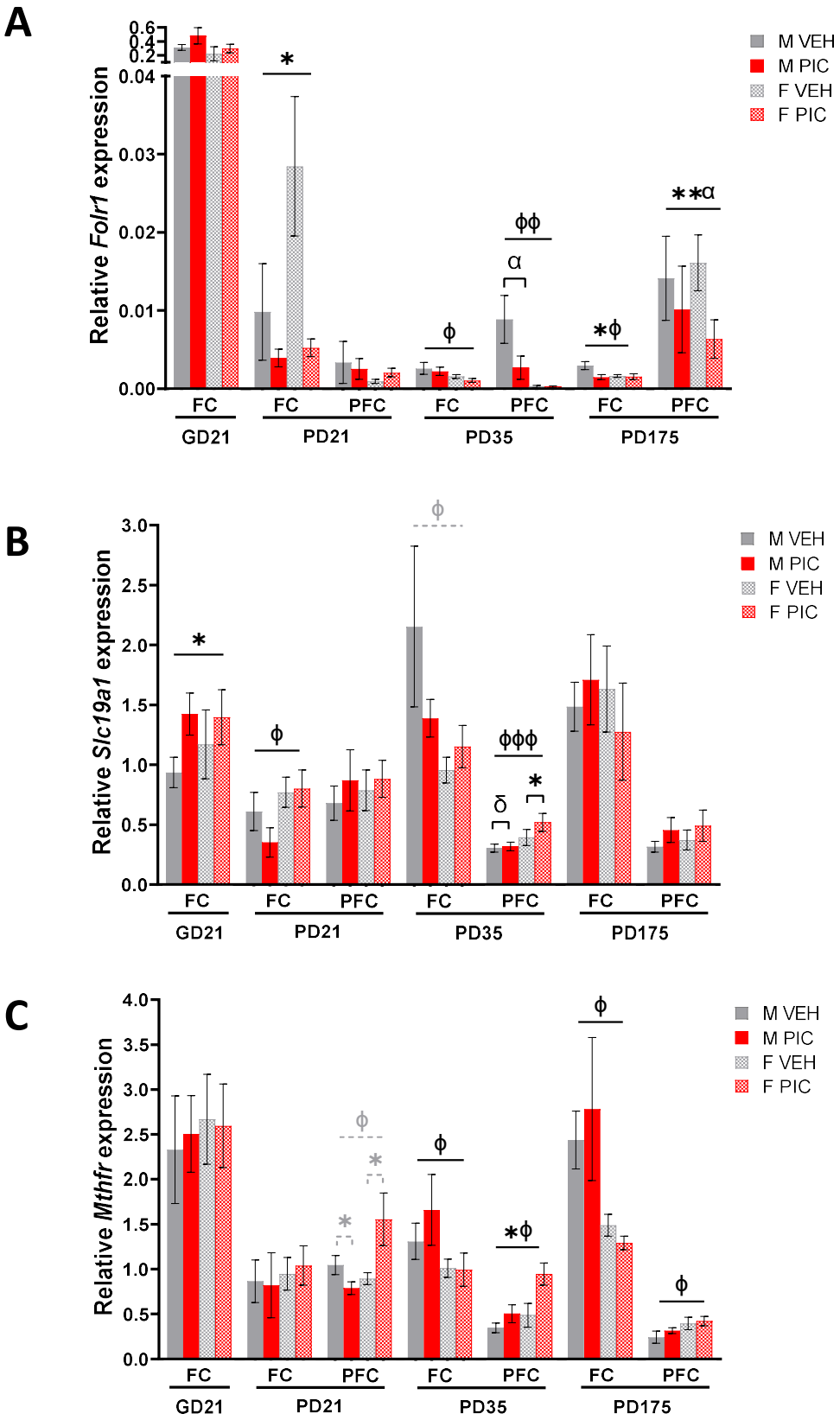

Figure 3.6. Folate transport and metabolism gene expression in the developing cortex
Relative mRNA expression (normalised to the geometric mean of three reference genes as detailed in methods) across the developmental timeline **A.** *Folr1* expression. **B.** *Slc19a1* expression **C.** *Mthfr* expression. Bars represent mean ±SEM (N=5-7; n=5-8). Black significance bars show significant GLMM results, – shaped bars represent results across the developmental age they overlap, Π-shaped bars represent post-hoc results within a single sex. Black symbols indicate significant main effects of: sex: ϕp<0.05, ϕϕp<0.01, ϕϕϕp<0.001; group, *p<0.05, **p<0.01; maternal IL-6, δp<0.05; maternal TNFα, αp<0.05. Grey dashed bars and symbols show trending (0.05<p<0.08) GLMM results. Abbreviations: GD, gestational day; PD, postnatal day; FC, frontal cortex; PFC, prefrontal cortex; M, male; F, female; VEH, vehicle; PIC, poly(I:C).

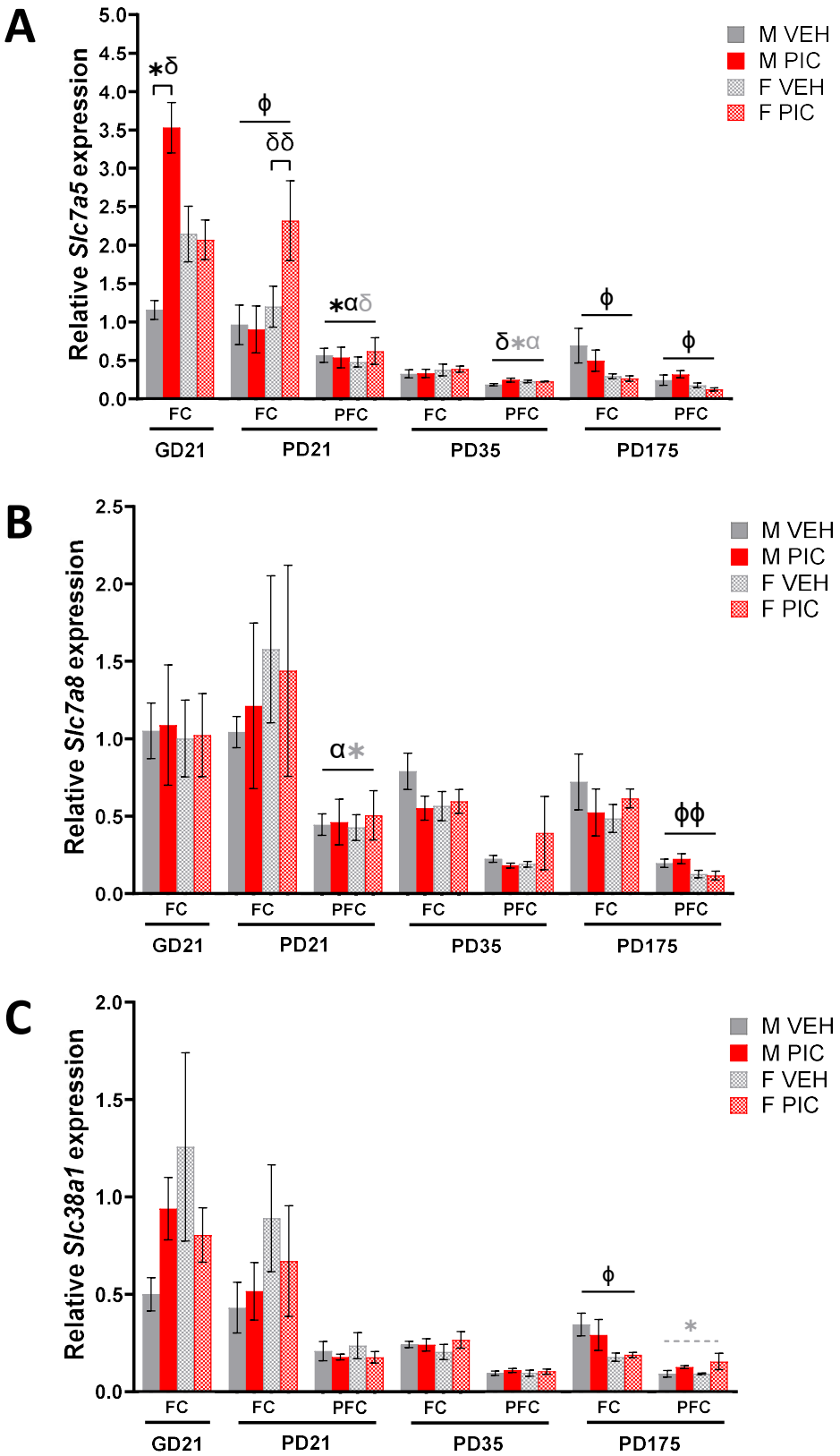

Figure 3.7. Expression of genes involved in methionine transport in the developing cortex
Relative mRNA expression (normalised to the geometric mean of three reference genes as described in methods) across development. **A.** *Slc7a5* expression. **B.** *Slc7a8* expression **C.** *Slc38a1* expression. Bars represent mean ±SEM (N=5-7; n=5-8). Black significance bars show significant GLMM results, – shaped bars show results across the age they overlap, Π-shaped bars represent post-hoc results within a single sex. Black symbols show significant main effects of: sex: ϕp<0.05, ϕϕp<0.01; group, *p<0.05; maternal IL-6, δp<0.05, δδp<0.01; maternal TNFα, αp<0.05. Grey dashed bars and/or symbols show trending (0.05<p≤0.08) GLMM results. Abbreviations: GD, gestational day; PD, postnatal day; FC, frontal cortex; PFC, prefrontal cortex; M, male; F, female; VEH, vehicle; PIC, poly(I:C).

3.3.2. Changes to SAH and SAM concentrations in the cytosol

3.3.2.1. SAH

GD21

There was a trend to a main effect of sex (GLMM: $F_{1,19}$=3.47, p=0.078; Figure 3.8A) with female-foetuses having higher cytosolic SAH than male-foetuses.

PD21

In the PFC there was a main effect of maternal TNFα (GLMM: $F_{1,17}$=10.43, p=0.005; Figure 3.8A), with a positive correlation between maternal TNFα and cytosolic SAH (r=0.589, p=0.006) and a trend to a main effect of sex (GLMM: $F_{1,17}$=3.57, p=0.076; Figure 3.8A), with males having higher cytosolic SAH relative to females. There were no significant effects of any predictors on cytosolic SAH in the FC.

PD35

In the PFC there was a main effect of sex (GLMM: $F_{1,3.48}$=16.83, p=0.020; Figure 3.8A), with females having higher cytosolic SAH than males. There were no significant effects of any predictors on cytosolic SAH in the FC.

PD175

In the PFC there was a trend to a group*sex interaction (GLMM: $F_{1,4.72}$=4.84, p=0.072). Post-hoc analysis showed a main effect of maternal IL-6 (GLMM: $F_{1,6}$=25.23, p=0.002; Figure 3.8A) and TNFα (GLMM: $F_{1,6}$=19.46, p=0.005; Figure 3.8A) in the males, however there were no significant post-hoc correlations. In the FC there was a significant main effect of sex (GLMM: $F_{1,10.22}$=10.95, p=0.008; Figure 3.8A), with elevated cytosolic SAH in females relative to males and maternal IL-6 (GLMM: $F_{1,11.61}$=6.41, p=0.027; Figure 3.8A), with a positive correlation between maternal IL-6 and cytosolic SAH (rho=0.659, p=0.003). There was also a trend to a main effect of maternal TNFα (GLMM: $F_{1,11.34}$=4.62, p=0.054; Figure 3.8A), but post-hoc correlations for the latter did not reach significance.

3.3.2.2. SAM

GD21

There was a significant main effect of group (GLMM: $F_{1,9.08}$=8.87, p=0.015; Figure 3.8B), with higher cytosolic SAM in the poly(I:C)-foetuses compared to vehicle-foetuses.

PD21

In the FC there was a significant main effect of maternal TNFα (GLMM: $F_{1,7.64}$=7.05, p=0.030; Figure 3.8B) and a trend towards a main effect of maternal IL-6 (GLMM: $F_{1,7.47}$=4.30, p=0.074; Figure 3.8B) corresponding to a negative correlation between cytosolic SAM and maternal TNFα (rho=-0.462, p=0.046). In the PFC there was a main effect of sex (GLMM: $F_{1,18}$=4.46, p=0.049; Figure 3.8B) with elevated cytosolic SAM in males relative to females.

PD35

There were no significant effects of any predictors on SAM concentration in the FC or PFC.

PD175

In the FC there were significant effects of several predictors in the model, including: a significant main effect of group (GLMM: $F_{1,12}$=4.71, p=0.050; Figure 3.8B), with higher cytosolic SAM in poly(I:C)-offspring relative to vehicle-offspring; sex (GLMM: $F_{1,12}$=4.77, p=0.050; Figure 3.8B), with higher cytosolic SAM in females relative to males; maternal IL-6 (GLMM: $F_{1,12}$=9.09, p=0.011; Figure 3.8B); maternal TNFα (GLMM: $F_{1,12}$=9.19, p=0.011; Figure 3.8B); and a group*sex interaction (GLMM: $F_{1,12}$=8.26, p=0.014). Post-hoc analysis revealed a significant main effect of maternal IL-6 in the females (GLMM: $F_{1,7}$=25.25, p=0.002; Figure 3.8B) with a positive correlation between maternal IL-6 and cytosolic SAM (rho=0.885, p=0.002). In the PFC there was a trend to a main effect of group (GLMM: $F_{1,16}$=3.52, p=0.079; Figure 3.8B) with increased cytosolic SAM in the poly(I:C)-offspring relative to vehicle-offspring.

3.3.2.3. SAM/SAH ratio

GD21

There was a significant main effect of group (GLMM: $F_{1,10}$=7.98, p=0.018; Figure 3.8C), with increased SAM/SAH ratio in the poly(I:C)-foetuses relative to vehicle-foetuses and sex (GLMM: $F_{1,10}$=5.72, p=0.038; Figure 3.8C), with higher SAM/SAH ratios in males relative to females and a group*sex interaction (GLMM: $F_{1,10}$=11.35, p=0.007). Post-hoc analysis revealed that in the females there were significant main effects of maternal IL-6 (GLMM $F_{1,4}$=95.24, p<0.001; Figure 3.8C) and TNFα (GLMM: $F_{1,4}$=79.47, p<0.001; Figure 3.8C), with positive correlations between female cytosolic SAM/SAH ratio and maternal TNFα (rho=0.976, p<0.001) and IL-6 (rho=0.980, p<0.001), while in the males there was a significant main effect of group (GLMM: $F_{1,5}$=12.34, p=0.017; Figure 3.8C), with increased SAM/SAH ratio in the poly(I:C)-males relative to vehicle-males.

PD21

In the FC and PFC there were no significant effects of any predictors on SAM/SAH ratio.

PD35

In the FC there was a significant group*sex interaction (GLMM: $F_{3,14}$ =6.71, p=0.005), but there were no significant effects of any predictors in the post-hoc analysis by sex. In the PFC there were no significant effects of any predictors on SAM/SAH ratio.

PD175

In the FC there were no significant effects of any predictors on SAM/SAH ratio but in the PFC there was a main effect of maternal TNFα (GLMM $F_{1,14}$=4.54, p=0.050; Figure 3.8C), with a positive correlation between maternal TNFα and SAM/SAH ratio (rho=0.594, p=0.009). There was also a trend to a main effect of sex (GLMM: $F_{1,14}$=3.79, p=0.072; Figure 3.8C), with females having lower SAM/SAH ratios than males and maternal IL-6 (GLMM: $F_{1,14}$=3.19, p=0.08; Figure

3.8C). Post-hoc analysis showed a main effect of group in females (GLMM: $F_{1,7}$=10.20, p=0.015; Figure 3.8C) with increased SAM/SAH ratio in poly(I:C)-females relative to vehicle-females, while in the males there were significant main effects of maternal TNFα (GLMM: $F_{1,6}$=13.35, p=0.011; Figure 3.8C) and maternal IL-6 (GLMM: $F_{1,6}$=14.38, p=0.009; Figure 3.8C), though these did not demonstrate any significant correlations with SAM/SAH ratio.

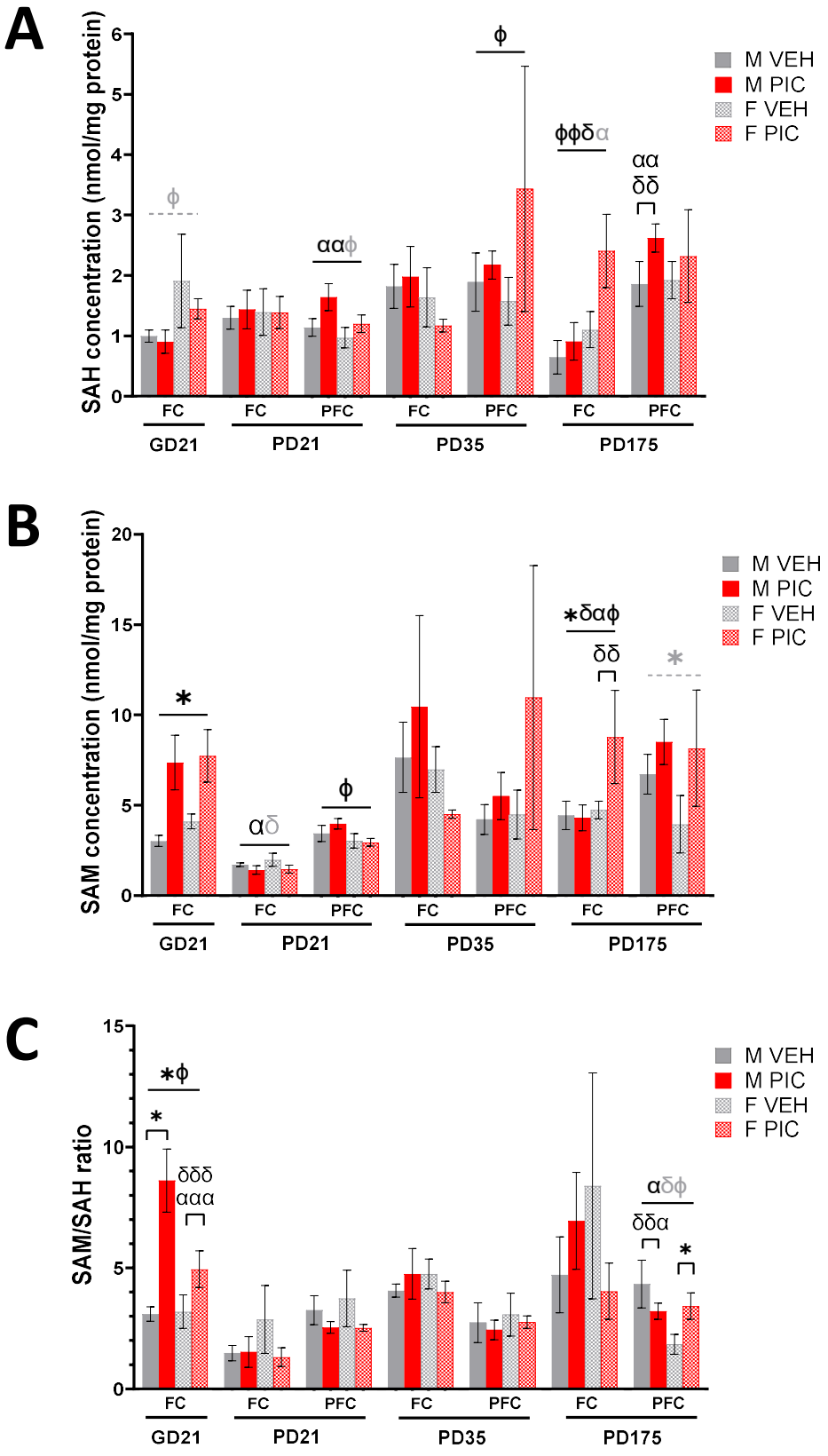

Figure 3.8. Cytosolic SAM and SAH ratio

A. Cytosolic SAH concentration (nmol/mg protein) in the FC and PFC across development. **B.** Cytosolic SAM concentration (nmol/mg protein) in the FC and PFC across development. **C.** SAM/SAH ratio in the FC and PFC across development. Bars represent mean ±SEM (N=5; n=5-6). Black significance bars show significant GLMM results, — shaped bars show results across the age they overlap, Π-shaped bars represent post-hoc results within a single sex. Black symbols show significant main effects of: sex, ϕp≤0.05, ϕϕp<0.01; group, *p≤0.05; maternal IL-6, δp<0.05, δδp<0.01, δδδp<0.001; maternal TNFα, αp≤0.05, ααp<0.01, αααp<0.001. Grey dashed lines and/or symbols show trending (0.05<p≤0.08) GLMM results. Abbreviations: GD, gestational day; PD, postnatal day; FC, frontal cortex; PFC, prefrontal cortex; M, male; F, female; VEH, vehicle; PIC, poly(I:C).

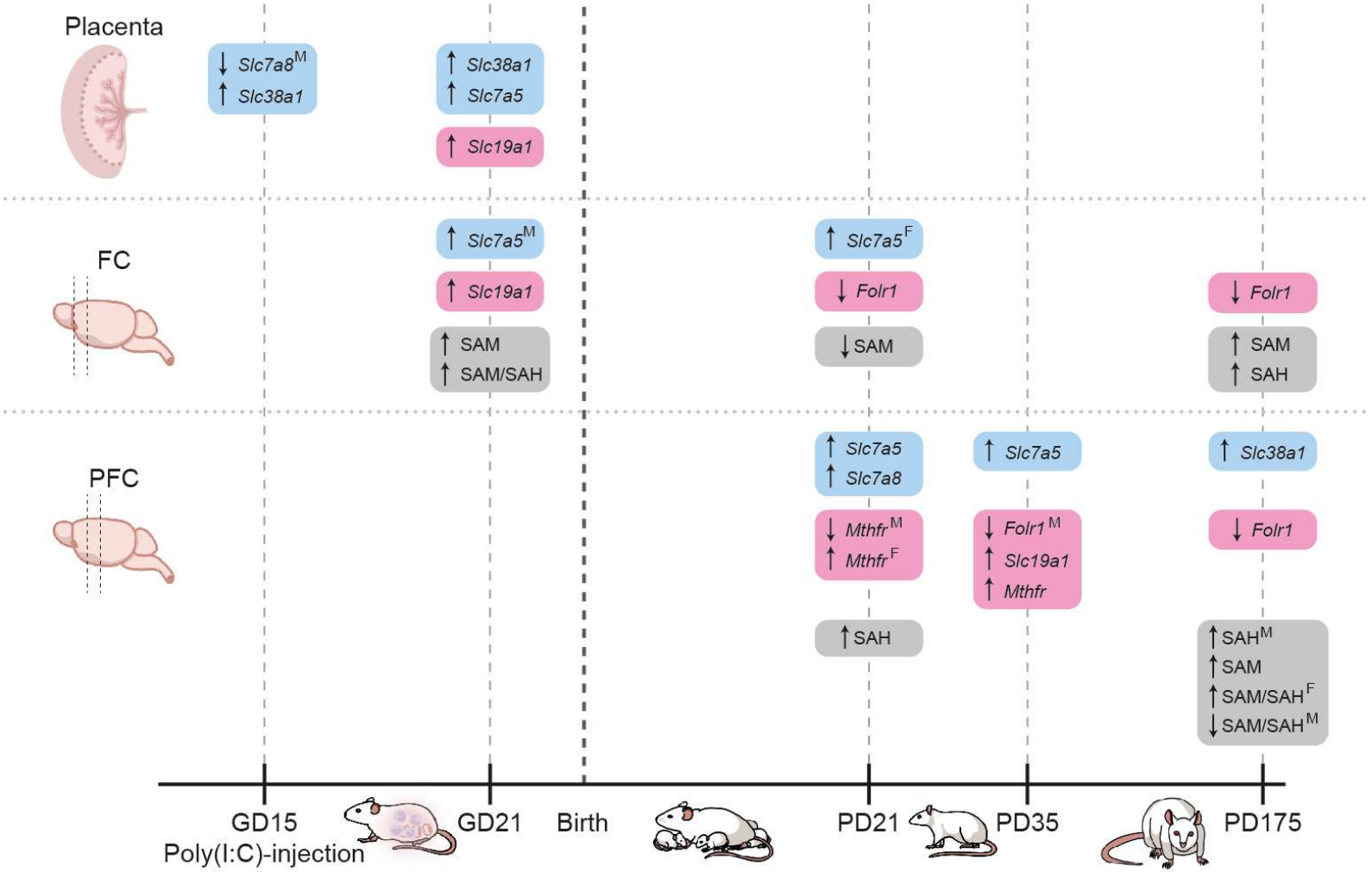

Figure 3.9. Summary of significant findings in Chapter 3

Summary of the MIA-induced molecular changes. Timeline (bottom) indicates the developmental age, tissue analysed: placenta, frontal cortex (FC) or prefrontal cortex (PFC) are indicated on the left. Blue: changes in amino acid transporter gene mRNA expression; Pink: changes to folate transporter/metabolism gene mRNA expression; Grey: changes to cytosolic SAM and SAH concentrations. Abbreviations: ↓Decrease; ↑Increase; F, female-specific result; M, male-specific result.

3.4. DISCUSSION

A key hypothesis of this Chapter was that foetal neuroinflammation (Chapter 2), together with placental transport disturbances (Kowash et al., 2022), would potentiate altered 1C metabolism and transport in the foetal/offspring brain and therefore impact methylation capacity. The aims of this Chapter were to assess MIA-induced changes in placental and cortical expression of genes important in methionine/folate transport and metabolism and whether such alterations result in altered 1C-metabolite availability in the developing cortex. The data reported in this Chapter establish that these aims were achieved with evidence of MIA-induced developmental changes in folate and methionine transporter expression, in both the placenta and cortex, alongside changes in cytosolic SAM and SAH availability in the developing cortex. A summary of the findings in this Chapter can be found in Figure 3.9 and will be discussed in-depth below.

3.4.1. MIA induces disturbances to folate transport but not metabolism

The expression of two folate transporters, RFC (encoded by *Slc19a1*) and FRα (encoded by *Folr1*) and the folate metabolism enzyme, *Mthfr* were conducted in parallel and, bearing in mind the importance of folate metabolic cycling, all three genes were co-expressed in all tissues. Limited changes in expression of *Mthfr* were identified, with the only noted statistically significant effects of MIA seen as an elevation in *Mthfr* expression in the PD35 PFC (Figure 3.6C), perhaps suggesting increased folate metabolism requirement at this particular timepoint. Adolescence forms a critical period for synaptic plasticity associated with higher cognitive development in the PFC (Morishita et al., 2015) and hence this may suggest elevated metabolism demand. While there were limited treatment-driven changes in *Mthfr* expression, there were many sex and regional differences across development. Notably, across PD35-PD175 females display elevated *Mthfr* expression relative to males in the PFC, while in the FC males display elevated *Mthfr* expression relative to females (Figure 3.6C), indicating sex-specific regulation of *Mthfr*. Accordingly, in humans, SNPs in the *MTHFR* gene have been shown to produce sex-specific effects on disease phenotypes (Wan et al., 2019) while animal models with *Mthfr* gene mutations show sex-specific behavioural phenotypes (Levav-Rabkin et al., 2011). Further, such mutations, driving *Mthfr* deficiency, differentially regulate GABAergic and glutamatergic system development in the cortex, with many of the changes more notable in females (Blumkin et al., 2011; Mossa and Manzini, 2021). Taken together, these results support sex-specific regulation of *Mthfr* in the developing cortex which could underscore the observed sex-specific expression of this gene.

By comparison, there were a greater number of changes in the expression of the folate transporter genes *Slc19a1* and *Folr1*. There was an initial increase in *Slc19a1* expression in the GD21 placenta, indicative of MIA-induced increases in placental folate transport. In this context, it is worth noting that folate transport increases across the rat placenta as gestation advances, to meet foetal demand, accompanied by upregulated expression of genes encoding FRα, PCFT

and RFC (Yasuda et al., 2008). Hence, it could be postulated that MIA induces an advancement of the normal placental upregulation of *Slc19a1* expression. Likewise, folate demand in the developing brain increases during foetal and early postnatal life, supporting large volumes of cellular proliferation and remains high throughout life to support ongoing methylation pathways, important in normal brain function (McGarel et al., 2015). In the developing cortex, there was MIA-induced increased *Slc19a1* expression in the GD21 FC, mirroring the change observed in the placenta and in the PD35 FC (females only) and PFC (Figure 3.6B). By contrast, *Folr1* showed MIA-induced reductions in expression in the PD21 FC, PD35 PFC (males only) and PD175 FC and PFC (Figure 3.6A). This divergence between the directionality of change in folate transporter expression in response to MIA in adolescence, may suggest an upregulation of folate delivery by *Slc19a1* (RFC), a rapid, high capacity folate exchanger (Solanky et al., 2010), in the setting of a reduced cellular uptake through *Folr1* (FRα)-mediated endocytosis. That said, the lack of protein data limits functional interpretation of these findings. Various post-transcriptional and post-translational regulatory events mean there is not always direct correspondence between mRNA and protein expression. Studies estimate ~40% correspondence (de Sousa Abreu et al., 2009), hence functional interpretations here should be taken with caution. Likewise, the gene expression of other proteins involved in the cellular uptake of folate such as PCFT (encoded by *Slc46a1*), required to transport released folate from the FRα internalised into endosomes (Solanky et al., 2010) was not measured in this study, but may offer further insights into folate transport changes in the developing cortex following MIA. Nonetheless, the data supports developmental alterations in normal folate transport throughout cortical development, with initial increased transport capacity during early development, followed by reduced transport in adulthood. Folate supplementation during prenatal and early development has been shown to improve cognitive performance (Irvine et al., 2022; Rubini et al., 2021). However, high cerebral folate, such as might be hypothesised by the observed upregulation in *Slc19a1* expression, has also been associated with memory impairments and reduced neurotrophic factors in the PFC (Garcez et al., 2021). Indeed, research suggests that both deficient and excess folate and subsequent disturbance of 1C metabolism is detrimental to various neurodevelopmental processes (Naninck et al., 2019). Further, dysfunction of folate transport proteins, FRα, RFC and PCFT promotes CFD (Frigerio et al., 2019; McFarland, 2012), which has been associated with neuropsychiatric and cognitive phenotypes. Hence, the observed transport disturbances, particularly the reductions in transport in adulthood, may precipitate the observed adult cognitive deficits.

These findings together signify that appropriate regulation of folate transport and normal folate balance is important throughout neurodevelopment and either inadequate or excess folate availability, leading to perturbed allied metabolism, could have detrimental consequences for the developing cortex and predisposition to disease. Folate and its derivatives in tissues are usually quantified by high-performance liquid chromatography (HPLC) and mass spectrometry-based methods (Liu et al., 2011; Schittmayer et al., 2018) and unfortunately, sample availability precluded this analysis, but it does open possible avenues for future investigation.

3.4.2. Amino acid transporter expression changes in the placenta and developing cortex

mRNA expression of three amino acid transporters, *Slc7a5* (LAT1), *Slc7a5* (LAT2) and *Slc38a1* (SNAT1) was measured. All three genes were found to be expressed in all tissues examined and showed MIA-induced changes in expression in the foetal brain and/or placenta, in line with previous literature (Kowash et al., 2022; McColl and Piquette-Miller, 2019). In the (GD15-21) placenta, there were MIA-induced increases in *Slc7a5* (LAT1) and *Slc38a1* (SNAT1) expression (Figure 3.5). Of note, we have previously shown significant reductions in *Slc7a5* (males) and *Slc7a8* (females) expression at GD15 (Kowash et al., 2022), with the latter corroborated here. This supports sex-specific differences in MIA-induced placental transcriptional responses, in support of previous findings (Bale, 2016; Barke et al., 2019) as well as highlighting both acute (3h post-treatment) and more enduring (GD21) transcriptional regulation of these genes in the placenta. In this context, the observed upregulation in expression of amino acid transporters at GD21 may serve as an adaptive, compensatory mechanism to promote foetal growth and development. However, others have failed to show a changes in placental *Slc7a5* or *Slc7a8* expression in response to MIA, although they did show significant transcriptional changes of several transporters across different gene families with time-dependency (McColl and Piquette-Miller, 2019; McColl et al., 2022). As observed in the GD21 placenta, in the foetal GD21 FC, *Slc7a5* was increased (males), but interestingly, postnatal offspring also exhibited changes, with PD21 FC (females), PD21 PFC and PD35 PFC also demonstrating altered *Slc7a5* expression in response to MIA, while *Slc7a8* only showed an increase only in the PD21 PFC (Figure 3.7A-C). These results suggest the genes encoding LAT1 and LAT2 may have long-lasting differential pattern of regulation in response to MIA. Conversely, *Slc38a1* had far fewer changes, with only a trending MIA-induced increase in expression in the PD175 PFC. Overall, the results support MIA-induced developmental dysregulation of amino acid transport in the cortex, beginning prenatally and persisting into adulthood. The driving causes for these changes in expression remain to be fully determined, but *in vitro* studies have shown that pro-inflammatory cytokines induce upregulation of amino acid transporters and hence it could be suggested that maternal (Chapter 2, Figure 2.6), placental (Kowash et al., 2022) and foetal inflammatory responses (Chapter 2, Figure 2.15) following poly(I:C)-exposure provoke the observed increased amino acid transporter expression by GD21, as supported by others (Hsiao and Patterson 2011; McColl and Piquette-Miller, 2019).

The amino acid transporter gene expression changes are likely to have critical consequences for brain development. It is worth commenting that transcriptional changes found previously in the placenta for amino acid transporters were accompanied by derangements in foetal brain amino acid concentrations, including the concentration of LAT1 and LAT2 substrates leucine and isoleucine (Kowash et al., 2022), important for neurotransmitter glutamate synthesis (McColl and Piquette-Miller, 2019). Hence, altered expression of amino acid transporters in the brain could affect neurotransmission and neuromodulation, impacting on brain development and

function (Yudkoff, 1997). Moreover, adequate amino acid provision to meet foetal protein demand is critical, particularly during second and third trimesters (mid-late gestation in rats), when foetal growth is rapid. Hence, temporal disturbances observed over GD15-21 could have detrimental impacts on neurodevelopment (Bordeleau et al., 2021). Further, amino acids have key roles throughout postnatal development. Disturbances in plasma amino acid concentrations have been observed in schizophrenia (Saleem et al., 2017), accordingly, a study in rhesus macaques using poly(I:C)-induced MIA showed disturbed amino acid concentrations in the plasma and CSF of exposed adolescent offspring, with methionine among the top 10 in both sample types (Boktor et al., 2022). Increased maternal methionine supplementation from mid-pregnancy has been shown to induce schizophrenia-like behaviours in offspring (Alachkar et al., 2018), with similar traits found for postnatal methionine over-supplementation (Wang et al., 2015). Excess methionine also induces increases in global DNAm (Chen et al., 2021b), supporting a link between methionine, SAM and epigenetic dysregulation. Against the background of an altered expression of system L and A subtypes, which transport methionine, it could be hypothesised that inflammation-induced upregulation of amino acid transporters results in enhanced methionine transport in the brain, increased SAM and thereby increased DNAm, which could induce behavioural deficits relevant to schizophrenia. To better evaluate this, SAM and SAH concentrations were quantified.

3.4.3. MIA and amino acid transport changes influence cortical SAM and SAH availability

As expected, this study confirmed a higher tissue cytosolic SAM concentration, relative to SAH, with a mean SAM/SAH ratio of 2.41-3.47, confirming positive methylation capacity. It should be noted that these metabolites were quantified using competitive ELISAs. Traditionally these metabolites, along with their amino acid derivatives, methionine and homocysteine, are quantified by HPLC-based techniques. However, comparative assessment of assay outputs to published literature values in the rodent brain (Table 3.5), showed good agreement. Importantly, SAH and SAM concentrations measured in this study fit within the identified literature range, with good concordance to the calculated SAM/SAH ratios, providing validity of assay approach.

Interestingly, there were MIA-induced temporal changes in the cytosolic SAH and SAM concentrations in the developing cortex. SAH concentrations were increased in PD21 PFC, PD175 FC (females only) and PD175 PFC (males only), while SAM was reduced in the PD21 FC, but increased in the GD21 FC and PD175 FC (Figure 3.8A&B). There were elevated SAM/SAH ratios in the GD21 FC following MIA and reduced SAM/SAH ratios in the PD175 PFC (Figure 3.8C). This would suggest these developmental timepoints have the greatest MIA-induced disturbances in cellular methylation capacity. Changes in SAM/SAH ratios in this form have been shown to induce crucial changes in brain methylation pathways, resulting in altered DNAm and are associated with behavioural phenotypes, relevant to NDDs (Caudill et al., 2001;

Devlin et al., 2004; Young and Shalchi, 2005), supporting a possible role for the observed SAM/SAH ratio changes in the MIA-associated cognitive phenotype.

Table 3.5. Cerebral SAH and SAM concentrations in rodent brain

Study	Metabolite	nmol/100mg tissue*	Rodent
Caudill et al., 2001	SAH	1.51	MOUSE
	SAM	3.49	
	SAM:SAH	2.3	
Devlin et al., 2004	SAH	0.17	MOUSE
	SAM	1.3	
	SAM:SAH	8.73	
Da Silva et al., 2014	SAH	4-5.5	MOUSE
	SAM	5-11.8	
	SAM:SAH	2.3	
Witham et al., 2013	SAH	1-1.2	MOUSE
	SAM	2-4	
	SAM:SAH	2-3.5	
Trolin et al., 1994	SAH	0.178-0.267	RAT
	SAM	1.9-2.1	
	SAM:SAH	9-10	
Dyer and Greenwood, 1988	SAH	0.197	RAT
	SAM	2.24	
	SAM:SAH	10	
Li et al., 2016	SAH	0.5-1	MOUSE
	SAM	1.5-2	
	SAM:SAH	2-3	
Young and Shalchi, 2005	SAH	0.33-0.54	RAT
	SAM	2.6-3.0	
	SAM:SAH	4.5-8	
This study	SAH	1.31-1.96	RAT
	SAM	2.49-6.84	
	SAM:SAH	2.41-3.47	

*All results were standardised to nmol/100mg tissue to allow inter-study comparison.

As already outlined (Figure 3.1), SAM and SAH concentration are dependent on the intricate relationship between the methionine and folate cycles. Accordingly, the observed disturbances in SAM, SAH and SAM/SAH ratio could be due to: i) disturbed methionine/folate transport; ii) disturbed activity/expression of 1C metabolism enzymes. While no overt changes in expression of *Mthfr* mRNA were noted across development, this does not necessarily reflect enzymatic activity. However, the changes in the expression of folate and amino acid transporters shown here would be consistent with transport dysfunction which could impact SAM and SAH metabolism. Given that methionine is a key mediator of SAM availability and disturbed methylation is associated with schizophrenia (Higgins-Chen et al., 2020; Jeremian et al., 2022b; Pries et al., 2017; Zhang et al., 2020b), it would be of interest to examine the relationship between amino acid transporter expression and cytosolic SAM and SAH concentration. While this cannot be achieved functionally here, correlation analysis shows no significant correlations between mRNA expression of amino acid transporters and cytosolic SAH while, in most tissues, there was a significant correlation between cytosolic SAM and expression of at least one amino acid transporter (Table 3.6). This is perhaps not surprising as cytosolic SAH concentration is more likely dependent on homocysteine metabolic disposal by enzymatic pathways, including re-methylation to methionine, or trans-sulphuration to cysteine (Figure 3.1), rather than the transport of homocysteine *per se*, although system L-mediated activity could be one mechanism

of homocysteine transport (Tsitsiou et al, 2009). However, SAM is dependent on cellular methionine availability, either from re-methylation of homocysteine and/or methionine transport. Notably, the relationship between cytosolic SAM and amino acid transporter expression appears driven primarily by the LAT system, with direct correlations between cytosolic SAM and *Slc7a5* expression prenatally and *Slc7a8* in later development. This could suggest a developmental switch between LAT-subtype transport dependency. Accordingly, it is worth commenting that LAT1 exhibits higher substrate affinity across a relatively narrow profile of larger neutral amino acids (Rossier et al., 1999), where LAT2 has broader substrate selectivity and transports smaller neutral amino acids (Pineda et al., 1999), although both accept methionine as a substrate (Cleal and Lewis, 2008).

Table 3.6. Correlations between cytosolic SAM and amino acid transport gene expression

Tissue	*Slc7a5*	*Slc7a8*	*Slc38a1*
GD21 FC	**rho=0.514, p=0.024***	rho=0.165, p=0.486	rho=0.391, p=0.089
PD21 FC	rho=0.186, p=0.491	rho=0.304, p=0.207	**rho=0.451, p=0.050***
PD21 PFC	rho=0.015, p=0.950	**rho=0.480, p=0.032***	rho=0.217, p=0.359
PD35 FC	rho=0.038, p=0.878	**rho=0.473, p=0.041***	rho=0.183, p=0.454
PD35 PFC	rho=0.135, p=0.593	**rho=0.560, p=0.016***	rho=0.358, p=0.145
PD175 FC	rho=0.068, p=0.777	rho=0.194, p=0.413	rho=0.132, p=0.578
PD175 PFC	rho=0.242, p=0.304	**rho=0.666, p=0.001***	rho=0.284, p=0.225

All correlations are Spearman's rho, alongside two-tailed significance. *p≤0.05

Overall, the data suggests that MIA-driven changes in methionine transport contribute to disturbed SAM/SAH ratios in the developing cortex.

Evidence that the maintenance of normal physiological methionine balance is crucial to cerebral function comes from studies showing that early-life methionine over-supplementation induces behavioural alterations consistent with schizophrenia (Alachkar et al., 2018; Chen et al., 2021b; Wang et al., 2015). In line with this, a recent study demonstrated that increased SAM supplementation prenatally induced changes in DNAm in a sex-specific pattern, occurring at genes involved in neuroinflammation and neurodevelopment (Weinstein-Fudim et al., 2020). This postulates that the observed prenatal elevations in SAM may induce long-term DNAm changes, resulting in altered transcriptomic regulation. Conversely, later-life SAM supplementation in Alzheimer's models have shown improved cognitive performance (Montgomery et al., 2014). This would align with the concept that the here observed adult reduction in SAM/SAH ratio, may contribute to the observed cognitive deficits in MIA-offspring. Hence, the reduction in cytosolic SAM and concomitant increase in SAH observed by PD21 may reflect an attempt to correct the prenatal disturbance in methylation patterning, causing aberrant methylation capacity persisting in adulthood, which could impact normal epigenetic mechanisms.

3.4.4. Sexual dimorphism in MIA-induced developmental changes to 1C metabolism

Irrespective of MIA, various molecular outputs were sex-specific. The adult male cortex appears to have higher amino acid transporter gene expression than females for *Slc38a1* in the FC and *Slc7a5* and *Slc7a8* in the PFC. While in the adolescent (PD35) FC and PFC sex influenced expression of *Folr1* (male increase relative to females), *Slc19a1* (males increased in FC, females in PFC) and *Mthfr* (males increased in FC, females in PFC). Accordingly, SAM/SAH availability also demonstrated sexual dimorphisms at these timepoints. Sexual dimorphism in brain transcriptomes across development are well documented (Berchtold et al., 2008; Shi et al., 2016; Trabzuni et al., 2013). Of note, the sex-specific effects on gene expression here arise in adolescence. This coincides with the critical sexual dimorphism in body growth and brain:bodyweight ratios between male and female offspring (Chapter 2, Section 2.3.3.2). Given that sexual maturity occurs during this developmental period for rats (Sengupta, 2013), it could be that sex hormones drive these normal sex differences in the developing brain. Indeed, sex hormones and receptors are known to play crucial roles in brain development (McEwen and Milner, 2017). Given the normal sexual dimorphism in the developing brain, the brain response to stress and inflammation has been shown to be sex-specific (McEwen and Milner, 2017; Murtaj et al., 2019). Hence, it is unsurprising that MIA induces sex-specific effects in the developing brain. Further, given the key roles for 1C metabolism in methylation pathways that establish epigenetic patterns, these results may also reflect differential demands for programming in male and female brains following MIA. Indeed, sex-specific methylomes are well-established in the normal brain (McCarthy et al., 2009) and in schizophrenia (Adanty et al., 2022). However, despite these apparent sex-specific differences, both male and female MIA-offspring demonstrated the same cognitive phenotype (Chapter 2, Figure 2.18). This may suggest sexual convergence, in that sex-differences are observed in the molecular mechanisms in response to MIA, but result in the same phenotypic endpoint (McCarthy et al., 2012; McEwen and Milner, 2017)

3.5. SUMMARY

The data reported indicate that MIA induces developmental changes in 1C-metabolite transporter expression, which in turn promote changes in cytosolic SAM and SAH availability. This is particularly evident prenatally, when the foetus is dependent on transplacental transfer of maternal nutrients. Here, increased system L and A amino acid transporter expression, in the foetal brain and placenta, correlates with increased cytosolic SAM in the GD21 FC, promoting increased SAM/SAH ratio. This highlights the foetal provision of amino acid precursors as key mechanistic pathways of interest for future investigation. Further, these observed changes persist through juvenile and adolescent timepoints (PD21-35) before showing the opposing patterns by adulthood. These ongoing disturbances will have critical consequences in processes dependent on 1C metabolism (Moore et al., 2013). Notably, the cellular SAM/SAH ratio is often considered to represent the cellular methylation capacity, with increased SAM/SAH ratio indicative of increased cellular methylation capacity (Caudill et al., 2001). Hence, the function of 1C metabolism is critically important for normal DNAm and dysregulations in 1C metabolism can alter DNAm patterns (Mentch and Locasale, 2016), with increased cerebral folate/methionine availability in prenatal and early development associated with increased global DNAm (Chen et al., 2021b; Wang et al., 2021b). DNAm is critical for normal brain development and function, with DNAm disturbances known to induce behavioural phenotypes analogous to those seen in this model (Jakovcevski and Akbarian, 2012). With this in mind, the next Chapter aims to explore the impact of disturbed 1C metabolism, identified here, on developmental DNAm profiles and identify which genes/pathways are affected by such epigenetic dysregulation.

CHAPTER 4. MIA-induced changes in genomic DNA methylation patterns across development

4.1. INTRODUCTION

Epigenetics is broadly defined as mitotically/meiotically heritable mechanisms which regulate changes in gene expression that do not entail changes to the DNA sequence (Holliday, 1994; Wu and Morris, 2001). Epigenetic mechanisms can be divided into three categories: DNA modifications, histone modifications and ncRNA which work together to regulate cell-, tissue- and developmental-specific transcriptomes (Figure 1.6; Roadmap Epigenomics Consortium et al., 2015). Epigenetic mechanisms are of particular interest owing to their ability to mediate interactions between environmental stressors and changes in gene expression (Bianco-Miotto et al., 2017; Fraga et al., 2005; Wong et al., 2010). It is therefore hypothesised that epigenetic mechanisms are critically important in predisposing individuals to diseases following environmental stressors, such as MIA.

4.1.1. DNAm and DNA hydroxymethylation (DNAhm)

DNAm is perhaps the most extensively studied epigenetic modification, most likely due to its stability which makes it amenable to downstream analysis (Villicaña and Bell, 2021). DNAm is achieved through addition of a methyl group to the 5th position of cytosine bases, to produce 5mC residues, within CpG sites (Roy and Weissbach, 1975). Mammalian DNAm patterns are highly tissue-specific, with the brain being one of the most highly methylated tissues and the placenta one of the least (Ehrlich et al., 1982; Illingworth et al., 2010; Meissner et al., 2008). The majority of CpG sites are clustered within CGIs, which are typically associated with TSS/promoters that regulate nearby gene transcription (Bird et al., 1985; Saxonov et al., 2006; Tazi and Bird, 1990) with methylation of these regions (CGIs/promoters) inhibiting gene expression (Mohn et al., 2008). Similarly, methylation of cytosine residues within the first exon and intron of a gene, downstream of the TSS, are also correlated with reduced gene expression (Anastasiadi et al., 2018; Brenet et al., 2011). The mechanism through which DNAm represses transcription in these regions is multi-fold, including inhibition of transcription factor binding, recruitment of repressive methyl-binding proteins and chromatin compaction (Moore et al., 2013). By comparison, gene-body CpG methylation has more complex functions and has been shown both to repress gene expression, usually in rapidly dividing cells (Brenet et al., 2011) and increase gene expression, usually in slowly dividing/non-dividing cells (Aran et al., 2011), although the mechanisms which determine these outcomes are less clear. Gene-body methylation can also regulate splicing. Over 90% of mammalian genes undergo alternative splicing (Maor et al., 2015). Studies have demonstrated that exonic methylation is significantly higher than intronic methylation and enriched at intron-exon boundaries, with these patterns shown to regulate exon splicing/retention (Li et al., 2018b; Maor et al., 2015; Shayevitch et al., 2018).

DNAm patterns are established by DNMTs which catalyse the transfer of a methyl group, from the methyl-donor, SAM, onto cytosine residues, producing SAH (Moore et al., 2013). SAH, in

turn, inhibits DNMT activity in a negative feedback loop. Accordingly, an increased SAM/SAH ratio is indicative of increased cellular methylation capacity (Caudill et al., 2001). In this context, the function of 1C metabolism (Chapter 3, Figure 3.1) is critically important for normal DNAm (Mentch and Locasale, 2016). DNMTs comprise two groups: i) *de novo* DNMTs (DNMT3a/DNMT3b) which establish methylation patterns in previously non-methylated DNA; ii) maintenance DNMTs (DNMT1) which accurately copy DNAm patterns within hemi-methylated DNA during cellular divisions. DNMTs are hence critically important during cell differentiation/development for establishing and maintaining cell-specific DNAm patterns, but are usually less active in differentiated cells (Moore et al., 2013).

DNA demethylation can be active, using enzymes that catalyse the removal of methyl groups, or passive, through loss of DNMT1 fidelity (Bhutani et al., 2011; Monk et al., 1991). Active DNA demethylation is thought to be energetically costly, proceeding through several stages whereby 5mC is oxidised by the ten-eleven translocation (TET) methylcytosine dioxygenases and deaminated by the APOBEC (Apolipoprotein B mRNA Editing Catalytic Polypeptide-like) family of enzymes to 5-hydroxymethyl-cytosine (5hmC) and then to other modified cytosines, 5-formyl-cytosine (5fC) and 5-carboxyl-cytosine (5caC; He et al., 2011; Ito et al., 2011), until finally the base excision repair (BER) pathway returns the base to an unmodified cytosine (Figure 4.1; Bhutani et al., 2011). It was originally thought that 5hmC was simply an intermediate in the DNA demethylation process (Hahn et al., 2014; Ito et al., 2010; Tahiliani et al., 2009). However, studies have shown that DNAhm is abundant in many human tissues, with the brain having the highest %5hmC (at ~40% the level of 5mC) compared to any other organ (Jin et al., 2011; Kriaucionis and Heintz, 2009; Munzel et al., 2010). Critically, several genomic loci have been shown to maintain the 5hmC modification throughout development (Hahn et al., 2013; Hashimoto et al., 2012; Szulwach et al., 2011; Valinluck and Sowers, 2007). Taken together, the data suggests that 5hmC is a stable DNA modification, independent of 5mC, likely to have functional importance. Indeed, the MECP2 methyl-binding protein and transcriptional regulator can bind 5hmC. Likewise, methyl-CpG binding domain 3 (MBD3) and several other transcription factors have also been shown to localise to and interact with 5hmC sites with greater affinity than 5mC, thereby regulating 5hmC-driven transcription (Kaas et al., 2013; Mellen et al., 2012; Spruijt et al., 2013; Williams et al., 2011; Yildirim et al., 2011). Moreover and contrary to methylation, hydroxymethylation of gene promoters correlates with open chromatin and actively expressed genes (Cheng et al., 2015; Mendonca et al., 2014). TET1, in particular, seems to modulate promoter hydroxymethylation patterns, while TET2 localises to gene bodies, both correlating with active gene expression (Antunes et al., 2019). Further, 5hmC is enriched at intron-exon boundaries and constitutively expressed exons, suggesting roles for 5hmC in splice regulation (Khare et al., 2012).

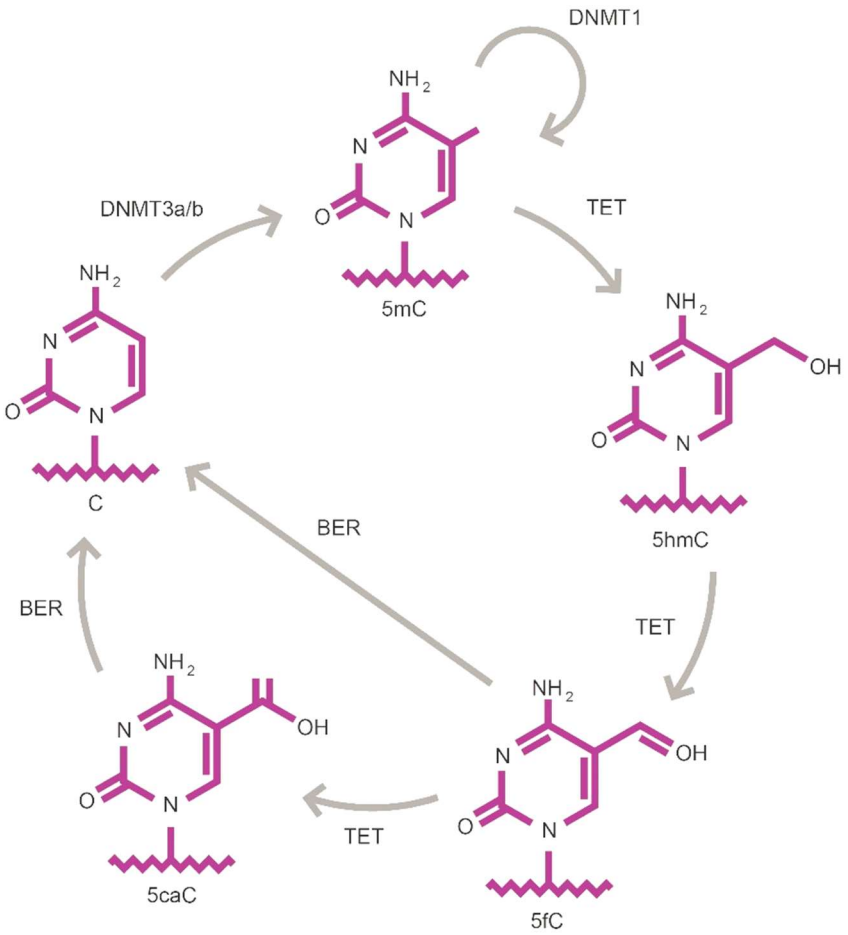

Figure 4.1. Establishment of DNA methylation (DNAm) and hydroxymethylation (DNAhm)
Diagram showing the pathways of DNAm and demethylation. *De novo* methylation of cytosine (5-methylcytosine, 5mC) is established by DNMT3a/b and maintained by DNMT1 through cellular divisions. Without methylation maintenance by DNMT1, 5mC undergoes passive demethylation to cytosine. Active DNA demethylation requires oxidation of 5mC to 5-hydroxymethyl-cytosine (5hmC) by the TET family of enzymes. This modification can be stable or removed by further oxidation to 5-formyl-cytosine (5fC) and 5-carboxyl-cytosine (5caC), both of which are removed by the base-excision repair (BER) pathway to re-establish non-modified cytosines.

4.1.2. Role of DNA modifications during neurodevelopment

4.1.2.1. DNAm

The brain shows distinct patterns of DNAm, including overall hypermethylated DNA (Ehrlich et al., 1982; Guo et al., 2014; Jin et al., 2011). A longitudinal genome-wide DNAm profiling in both human and mouse cortices demonstrated distinct DNAm differences between foetal and adult stages of development (Lister et al., 2013). Indeed, age-related DNAm patterns are highly specific and as such can be used to predict biological brain age, both pre- and postnatally (Grodstein et al., 2021; Steg et al., 2021). While individual DNMT expression patterns in the brain vary temporally, they persist in adult neurons whereas they are usually downregulated in other tissues (Feng et al., 2005; Inano et al., 2000). *DNMT1* mRNA expression is elevated in both the developing nervous system and post-mitotic brain cells, including neurons and glia (Feng et al., 2007, 2010). Meanwhile for *de novo* DNMTs, *DNMT3B* expression is highest in early neurons, with limited expression in adulthood, while *DNMT3A* expression is upregulated later in development, peaking during postnatal neuron maturation and remaining present in all

adult neuronal cells and oligodendrocytes, thought to be critical for establishing postnatal brain methylation patterns (Feng et al., 2007, 2010; Sendžikaitė et al., 2019; Watanabe et al., 2006). DNMT expression and DNAm patterns are also dynamic between cell subtypes, with higher expression of *DNMT1* and *DNMT3A* in GABAergic relative to glutamatergic neurons (Kadriu et al., 2012) while studies investigating DNAm differences between neuronal and non-neuronal cells found thousands of differentially methylated genes and notably higher DNAm in oligodendrocytes than GABAergic or glutamatergic neurons (Kozlenkov et al., 2014, 2018; Lister et al., 2013). In general, studies support a key role for DNAm throughout neurodevelopment: DNAm and DNMTs have been shown to regulate brain cell fate decisions, neurogenesis, gliogenesis, cell proliferation, differentiation and survival along with extracellular matrix (ECM) formation (Jobe and Zhao, 2017; Shirvani-Farsani et al., 2021), while later in neurodevelopment DNAm remodelling occurs in line with synaptogenesis and ongoing synaptic plasticity (Levenson et al., 2006; Lister et al., 2013).

4.1.2.2. DNAhm

DNAhm and, in particular, TET3 expression, is enriched in the brain (Antunes et al., 2019). DNAhm first appears at relatively low levels in the foetal brain (~10-fold lower than the adult brain) before rapidly increasing postnatally around the time of synaptogenesis (Grayson and Guidotti, 2018; Szulwach et al., 2011) where it localises to euchromatin, alongside RNA polymerase, promoting gene expression (Chen et al., 2014). Accordingly, longitudinal DNAhm profiling in both human and mice cortices demonstrated that DNAhm clusters in putative regulatory elements in foetal brains which became hypomethylated and actively expressed in the adult brain (Lister et al., 2013; Shi et al., 2017; Wen et al., 2014), supporting a continued role for 5hmC across neurodevelopment. It has also been shown that TET2 is required for embryonic stem cells (ESCs) to develop into NPCs, while TET3 is needed for further NPC differentiation (Hon et al., 2014; Lister et al., 2013; MacArthur and Dawlaty, 2021). Moreover, as with DNAm, DNAhm and TET expression patterns are highly cell-type specific, enriched in neurons compared to glia, with particularly dynamic DNAhm patterns found in GABAergic interneurons (Antunes et al., 2019; Kozlenkov et al., 2014, 2018).

4.1.3. DNA modifications in schizophrenia

Genetic studies have failed to unravel the entirety of the heritability estimate for schizophrenia and epigenetic mechanisms are proposed to be one of the processes which might explain this (van Dongen and Boomsma, 2013). Consistent with this, studies have shown that both DNAm and DNAhm are likely to have functional importance in the genesis of schizophrenia.

When focusing on the enzymes that regulate DNAm/DNAhm patterns, studies have identified increased *TET1* mRNA and protein expression alongside a reduction of *APOBEC3A/APOBEC3C* mRNA expression in schizophrenia cortex samples (Dong et al., 2012). Additionally, elevated *DNMT1* and *DNMT3A* mRNA has been shown in cortical

GABAergic interneurons in schizophrenia patients (Guidotti et al., 2007; Veldic et al., 2004; Zhubi et al., 2009) while inhibition of the DNMT enzymes has been shown to change promoter methylation of schizophrenia-risk genes including *BDNF*, *RELN* and *GAD1* (Kundakovic et al., 2009; Lubin et al., 2008). The advent of genome-wide sequencing methods has enabled genome-wide DNAm/DNAhm profiling of schizophrenia traits. Following the first study evaluating changes in DNAm patterns in schizophrenia patient brain samples (Mill et al., 2008), subsequent studies have broadly supported genomic hypomethylation in schizophrenia patients (Li et al., 2018a; Wan et al., 2019), though findings are often sex-specific (Adanty et al., 2022). These studies have collectively identified thousands of differentially methylated loci in schizophrenia patients, both genic and intergenic. While meta-analyses have shown lack of replication between studies, there have been some overlapping genes between studies, including *GAD1, RELN, BDNF* and *COMT* (Chen et al., 2021a; Pries et al., 2017). Furthermore, it has been suggested that schizophrenia-associated CpG sites are found at loci which function in prenatal-postnatal developmental transition (Jaffe et al., 2016), suggesting a role for DNAm patterns in the genesis of neurodevelopmental abnormalities in schizophrenia. In line with this, several studies have evidenced disturbed epigenetic aging in schizophrenia, although with mixed outcomes as to whether there is accelerated or delayed epigenetic aging in patient brains (Akbarian, 2020; Hannon et al., 2021; Jeremian et al., 2022a, 2022b; Wu et al., 2021; Zhang et al., 2020b). While less studied, DNAhm patterns are also becoming of interest in schizophrenia. Genome-wide DNAhm profiles have shown region-specific increases in schizophrenia brain samples (Akbarian, 2014). Similarly, PFC DNAhm changes in schizophrenia are cell-specific, with highest levels of DNAhm changes found in GABAergic interneurons (Kozlenkov et al., 2018).

4.1.4. Chapter aims

Despite the recognition that adverse prenatal events can disturb neuro-epigenetic patterning and induce behavioural abnormalities (Bermick and Schaller, 2022) a systematic review (Woods et al., 2021) showed an under-representation of studies into disturbed epigenetic mechanisms in MIA models. With this in mind and given the evident importance of epigenetic mechanisms in regulating neurodevelopment, it was of interest to examine this further in our model. The strategy adopted was to focus on epigenetic dysfunction throughout the developmental timeline, from the foetal period to adulthood, to define how this may associate with MIA-induced behavioural phenotypes. It has previously been demonstrated that inflammatory signalling pathways can induce DNAm changes, with cytokines, including IL-6, IL-1β, TNFα and IL-10, analysed in the foetal brain (Chapter 2, Figure 2.15) and glucocorticoid signalling, shown to induce changes in DNMT and TET enzyme expression and thereby modulate DNAm patterns (Guarnieri et al., 2020; Ibrahim et al., 2018; Komanda and Nishimura, 2022; Li et al., 2012; Morisawa et al., 2017; Mourtzi et al., 2021; Seutter et al., 2020). Given the evident foetal neuroinflammatory disturbance in the 24h period post-MIA (Chapter 2, Figure 2.15), it is plausible that normal neuro-epigenetic patterns could be disturbed, by cytokine-induced changes in DNMT

expression/activity. Alongside cytokine-mediated DNMT expression disturbances, DNMT activity would also be inherently dependent on cellular SAM/SAH availability. As outlined in Chapter 3, MIA altered expression of genes involved in 1C metabolism and provoked developmentally disturbed SAM/SAH ratios. Therefore, it was hypothesised that the observed foetal neuroinflammation, together with placental transport disturbances and SAM/SAH availability, would support functional increases in DNMT enzyme expression/activity prenatally and therefore changes to genomic DNAm patterns in the developing cortex.

The aims of this Chapter were therefore to determine:

i) The impact of MIA on developmental expression/activity of DNMT enzymes, important for establishment of normal DNAm.
ii) How MIA-induced alterations in methylation pathways influence genomic DNAm patterns across the developmental timeline.
iii) Which cellular pathways and biological processes are enriched for MIA-induced DNAm changes.

4.2. MATERIALS AND METHODS

Note: the methods in this chapter were performed on samples collected from cohorts PR1 and PN1.

4.2.1. Nucleic acid isolation and quantification

Nucleic acid isolation was performed as described in Chapter 3, Section 3.2.1.1.

RNA concentration and purity was measured by the ThermoFisher NanoDrop® as described in Chapter 3, Section 3.2.1.2.

gDNA concentration was determined using the QuantiFluor® ONE dsDNA System (Promega, Southampton, UK) according to the manufacturer's instructions. Briefly, 20XTris-EDTA (pH7.5) buffer was diluted 1:20 in dH_2O to prepare a 1XTris-EDTA solution. Promega QuantiFluor® ONE dye was diluted 1:100 with 1XTris-EDTA buffer and 200µL pipetted into each well of a black opaque 96-well microplate. A serially diluted standard curve was prepared from commercially available rat brain gDNA (1110ng/µL; AMSBIO, Abington, UK), diluted in 1XTris-EDTA buffer, consisting of the following concentrations (ng/µL): 0(buffer only), 1, 2, 5, 10, 20, 50, 100, 150, 200. All standards/samples were performed in duplicate with 1µL/well. Endpoint fluorescence was read on a FLUOstar Omega plate reader (BMG Labtech, Aylesbury, UK) at excitation/emission wavelengths of 485/520nm. Raw data was imported into GraphPad Prism v9.0 and a standard curve (ng/well) fitted with linear regression (Figure 4.2), with typical R^2-values≥0.99. The standard was used to interpolate sample DNA concentration ng/well (equating to ng/µL).

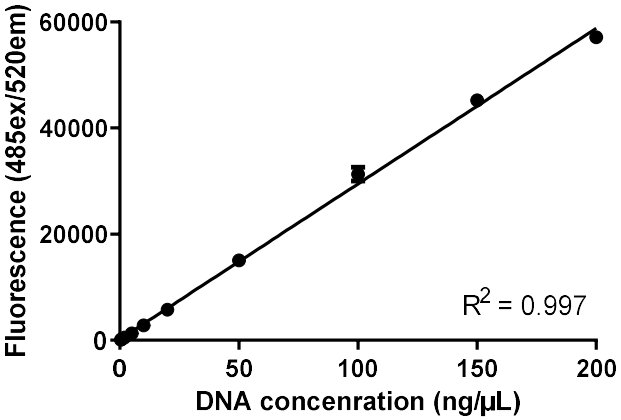

Figure 4.2. Representative QuantiFluor standard curve
Representative standard curve of rat genomic DNA 0-200ng/µL by the QuantiFluor® ONE dsDNA System (Promega, Southampton, UK).

The quality of extracted RNA/DNA samples was assessed by agarose gel electrophoresis as described in Chapter 3, Section 3.2.1.2. Samples were diluted in nuclease-free water with 800ng RNA and 50ng DNA contained in 15µL, mixed with 3µL 5XDNA loading buffer (Bioline, London, UK). A high molecular weight single band for genomic DNA and two bands for RNA

(representing 28S and 18S ribosomal RNA) with no visual smearing, was taken as evidence of good nucleic acid integrity with no contamination or degradation. Representative gels can be found in Appendix 2, Supplementary Figure S2.1.

4.2.2. mRNA expression analysis

All reverse transcription and qPCR reactions were performed as previously described (Chapter 3, Section 3.2.2). Again, the Gene Globe software (Qiagen, Manchester, UK) was searched for each of the *Dnmt* genes of interest with a full list of QuantiTect primer assays used shown in Table 4.1. As found previously a 1:50 dilution was optimal for all candidate genes following a dilution trial, consistently producing Ct values 15-30 across development (Chapter 3, Section 3.2.2.2). These gene expression analyses were performed in the same samples as Chapter 3, hence the reference genes *Gapdh, Ubc* and *Mdh1* were used for normalisation of candidate *Dnmt* gene expression in the developing cortex (Appendix 3, Figure S3.1; Vandesompele et al., 2002). Agarose gel electrophoresis was performed to assess correct amplicon size (Table 4.1), as described previously (Chapter 3, Section 3.2.2.4). Representative qPCR gels for each gene can be found in Appendix 4, Section 2.

Table 4.1. QuantiTect primer assays (Chapter 4)

Gene	QuantiTect primer assay (Cat no.)	Amplicon size (bp)	Exons spanned
Dnmt1	Rn_RGD:620979_1_SG (QT00493577)	81	10/11/12
Dnmt3a	Rn_Dnmt3a_1_SG (QT01567083)	61	11/12
Dnmt3b	Rn_Dnmt3b_1_SG (QT01584625)	144	3/4

Abbreviations: bp, base pair

4.2.3. Isolation and validation of nuclear and cytosolic cellular fractions

Nuclear lysates were prepared using the Nuclear Extract kit (Active Motif, Waterloo, Belgium) as described in Chapter 3, Section 3.2.3. Initial validation of these fractions by Western blotting confirmed that the nuclear-specific protein H3 was present only in the nuclear fractions, while GAPDH showed greatest enrichment in the cytosolic fraction (Chapter 3, Figure 3.2). Here, as further validation for use in the DNMT activity assay, it was confirmed that DNMTs were enriched with intact protein integrity in the nuclear fraction. For this, the standard Western blotting protocol was used (Chapter 3, Section 3.2.3.2). The effectiveness of several anti-DNMT antibodies were evaluated using Nuclear Extract whole tissue lysates (Appendix 5) and it was determined that the rabbit polyclonal anti-DNMT3a antibody (GTX129126; GeneTex, California, USA), diluted 1:500 (2µg/mL) for the primary antibody incubation was optimal for confirming fractional enrichment of DNMTs. This validation showed that DNMT3a was expressed in the tNF, sNF and iNF but absent from the cytosolic and matrix fractions (Figure 4.3). Based on the highest DNMT3a expression observed in the tNF, this fraction was used for measurement of nuclear DNMT activity.

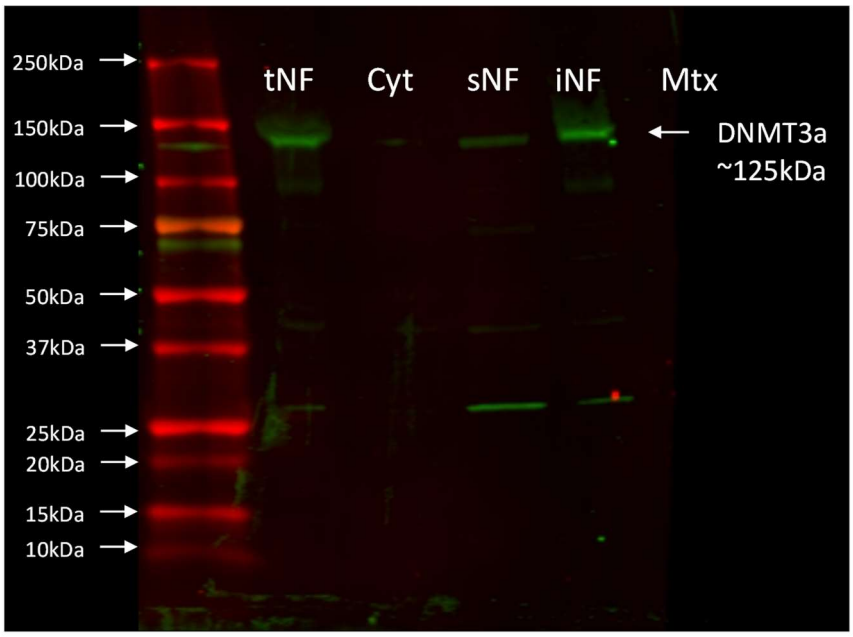

Figure 4.3. Western blot image for DNMT3a enrichment in cellular fractions
Western blot image for DNMT3a (~125 kilodaltans, kDa) using the Li-Cor Odyssey CLX system. Molecular weight ladders are shown on left. 20µg of fraction lysate was loaded/well. Abbreviations: sNF, soluble nuclear fraction; iNF, insoluble nuclear fraction; tNF, total nuclear fraction; Cyt, cytosolic fraction; Mtx, matrix fraction.

4.2.4. DNMT activity assay

The Epiquick DNMT Activity/Inhibition Assay Ultra kit (Epigentek, Farmingdale, USA) was used to quantify total DNMT activity (comprising both *de novo* and maintenance DNMT activity) in tNF isolated from cortex samples (Chapter 3, Section 3.2.3). An active control enzyme (50ng/µL; MU4), with the activity of both maintenance and *de novo* DNMTs, was used to ensure assay performance, used at a concentration of 25ng/well (positive control 1) and 12.5ng/well (positive control 2) on each plate. A negative control without enzyme/sample was also performed on each plate. tNF samples were analysed at 10µg protein/well, determined to be the input at which maximal signal was achieved while maintaining assay linearity.

The protocol was performed as follows: MU1 Wash Buffer concentrate was diluted 1:10 with dH_2O and MU3 Adomet concentrate was diluted 1:50 with MU2 Assay Buffer to produce the Adomet working solution. Samples and controls were added in duplicate to the provided microplate as follows:

- Negative control (blank) wells: 50µL Adomet working solution.
- Positive controls: 49.5µL (positive control 1) or 49.75µL (positive control 2) Adomet working solution and 0.5µL and 0.25µL MU4 active enzyme control, respectively.
- Samples: ≤5µL tNF, comprising 10µg protein, made up to 50µL with Adomet working solution.

The plate was sealed and incubated for 2h at 37°C at 50rpm on a Mini Shaking Incubator (N-Biotek, Gyeonggi-do, Korea). The solution was then discarded and the wells washed three times

with 150µL diluted MU1 Wash Buffer. MU5 (Capture Antibody) was diluted 1:1,000 with MU1 Wash Buffer and 50µL added to each well. The plate was incubated at room temperature (25°C) for 1h at 50rpm on the Mini Shaking Incubator and then solutions discarded. Wells were washed three times with 150µL diluted MU1 Wash Buffer. MU6 (Detection Antibody) was diluted 1:2,000 in MU1 wash buffer and 50µL added to each well and incubated at 25°C for 30min at 50rpm on a Mini Shaking Incubator. The solutions were discarded and wells washed four times with 150µL MU1 Wash Buffer. MU7 (Enhancer Solution) was diluted 1:5,000 with MU1 Wash Buffer and 50µL added to each well. The plate was incubated at 25°C for 30min at 50rpm on a Mini Shaking Incubator. The solution was discarded and wells washed five times with 150µL MU1 Wash Buffer. 100µL MU8 (TMB) was added to each well and incubated for 20min at 25°C at 50rpm on a Mini Shaking Incubator. 100µL MU9 (STOP solution) was added to each well.

Absorbance was read on the Biotek Synergy H1 (Agilent, Cheadle, UK) microplate reader within 5min at 450nm primary wavelength with a reference wavelength of 655nm. The reference wavelength reading was deducted from the primary wavelength reading within each well to give a normalised OD reading. DNMT activity was calculated as per kit equation:

$$\text{DNMT Activity (OD/µg/h)} = \left(\frac{\text{Sample OD} - \text{Blank OD}}{\text{µg input} \times \text{h incubation}}\right) \times 1000$$

The average (mean ±SEM) activity of the control enzyme across plates was calculated as 35.88 ±2.32 (OD/ng/h), indicating high inter-plate consistency in assay efficiency. %CV were calculated between sample duplicates as 2.3-10.1%, indicating low intra-plate variability.

4.2.5. DNAm ELISA

An initial, rapid estimation of total genomic DNAm (Kurdyukov and Bullock, 2016) was performed using a %5mC ELISA kit (ENZO, Exeter, UK) as per manufacturer's instructions. A standard curve of 0-100% CpG methylation was prepared using ratios of positive (100% methylated DNA) and negative (0% methylated DNA) controls provided at 100ng/µL. 1µL prepared standards were brought to 100µL by the addition of 99µL coating buffer. The assay required that sample volume did not exceed 20µL/well (i.e., 20µL sample made up to 100µL by addition of 80µL coating buffer) and that standard and sample DNA concentration (ng/well) be equal. Accordingly, for any given plate, standards were prepared at a concentration (ng/µL) to allow an equivalent sample concentration in a volume of ≤20µL. Therefore, samples with gDNA concentrations ≥50 ng/µL were analysed at a concentration of 100ng/well while samples of gDNA concentration which fell within the range of 5-50ng/µL were analysed at 50ng/well and samples ≤5ng/µL were analysed at a concentration of 25ng/well, with three standard curves prepared accordingly.

Prepared standards and samples were denatured at 98°C for 5min (Dry block; IKA, Staufen, Germany) and then incubated on ice for 10min. Solutions were then transferred to wells of the provided microplate and incubated at 37°C for 1h at 50rpm on a shaking incubator (S1500 Stuart™; Cole-Parmer, Illinois, USA). Each well was washed three times with 200µL ELISA buffer. 200µL ELISA buffer was then added to each well and incubated for 10min at 37°C at 50rpm on a shaking incubator. ELISA buffer was then discarded from wells and 100µL antibody solution (prepared from 998.5µL ELISA buffer, 0.5µL anti-5mC antibody and 1µL conjugate HRP-antibody) was added to each well. The plate was then incubated for 1h at 37°C at 50rpm on a shaking incubator. Each well was subsequently washed three times with 200µL ELISA buffer. 100µL HRP developer solution was added to each well and incubated for 10min at room temperature.

Absorbance was read on a FLOUstar Omega plate reader (BMG Labtech, Aylesbury, UK) at 410nm. %CV values were calculated for all standard and sample duplicates and accepted at ≤10%. Standard values were entered into GraphPad prism (v9.0) to generate a standard curve (Figure 4.4). A 4-PL fit was applied and R^2-values calculated for goodness of fit, with $R^2 \geq 0.98$ accepted. Samples were then interpolated from the standard curve using the built-in interpolate function.

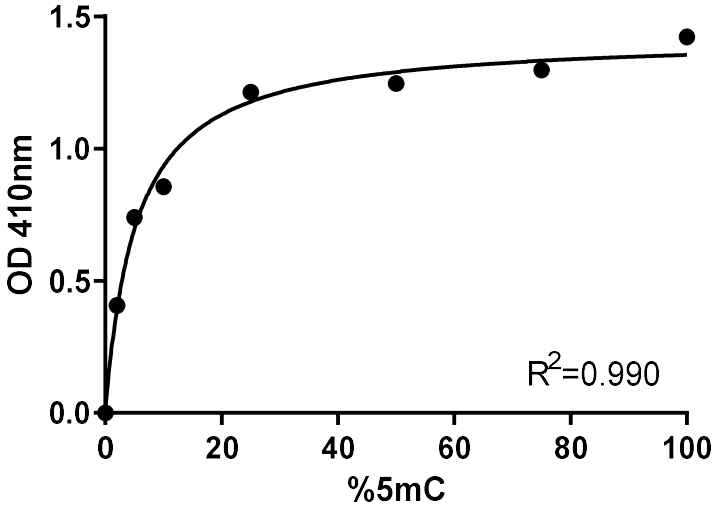

Figure 4.4. Representative %5mC standard curve
Standard curve from 0-100% 5mC was fitted by 4-PL analysis, with R^2 value indicated.

As described by the kit, rat gDNA CpG density per genome length (0.0089) is less than that for *E. Coli* DNA (0.075; kit standard material) and hence interpolated sample %5mC values need to be corrected (Figure 4.5). With this in mind, sample interpolated values were multiplied by the fold difference between *E. Coli* and rat CpG density per genome length, as identified by Su et al. (2009) and recommended by ENZO technical support.

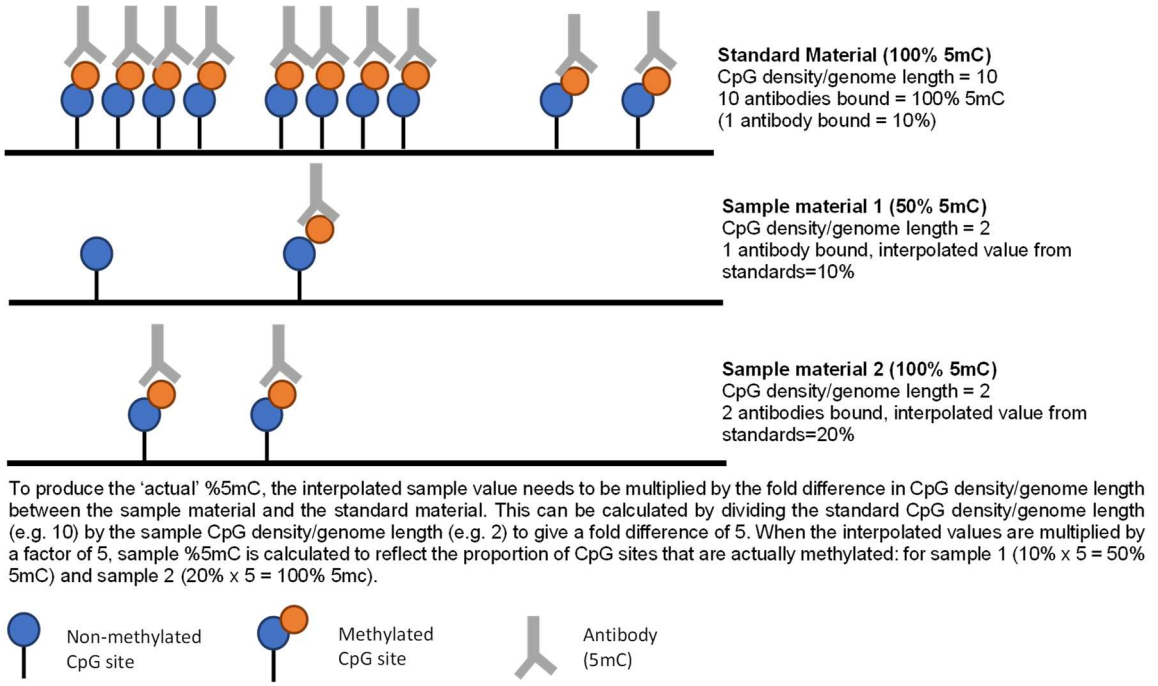

Figure 4.5: Scheme outlining %5mC interpolated value corrections
Figure to explain the methodology for correcting interpolated sample values. As the standard material, derived from *E. Coli,* has a greater CpG density per genome length relative to sample rat genome, interpolated sample values need to be multiplied by the fold difference in CpG density per genome length to correct for this relative difference.

4.2.6. Statistics

Foetal/offspring molecular outputs (including the following dependent variables in this Chapter: relative gene expression, DNMT activity, %5mC) were analysed as described in Chapter 2, Section 2.2.5 and Chapter 3, Section 3.2.6, in SPSS v28.0 (IBM). Briefly, within-group outliers were excluded using SPSS extreme outlier function. Between-group and post-hoc sex comparisons were analysed by GLMM including dam as a random factor and the following predictors: fixed factors (sex, group) and covariates (maternal IL-6 and TNFα), with p-values≤0.05 considered statistically significant and 0.05<p≤0.08 highlighted as trending towards significant. Where the effects of all four predictors were insignificant, the phrase 'there were no significant effects of any predictors' will be used. Post-hoc Pearson's (r) or Spearman's (rho) correlations were used to evaluate directionality of relationship between numerical dependent variables and covariates.

Graphs were generated using GraphPad Prism (v9.0), with n-numbers for dam per group (N) and foetuses/pups per sex per group (n) indicated in figure legends. Data is represented as mean ±SEM and dots represent individual samples. Note: group*sex interactions are not indicated on graphs, instead post-hoc analyses by sex are outlined where significant.

4.2.7. Reduced representation bisulphite sequencing (RRBS)

DNAm ELISAs, while valuable for rapid DNAm screening, only provide a rough estimate, without information on the genomic location of DNAm changes and often produce variable results

(Kurdyukov and Bullock, 2016). To assess gene-specific methylation changes in the PFC of adult behaviourally-assessed animals, bisulphite sequencing (bis-seq) was performed as the gold-standard method for DNAm analysis, providing single-base resolution of DNAm (Beck et al., 2022; Kurdyukov and Bullock, 2016). RRBS in particular was selected as it enriches for CpG dense regions, which are more likely to provide functional regulation of gene expression. RRBS was performed in partnership with Diagenode (Liège, Belgium). Methods performed in-house or by Diagenode are indicated.

4.2.7.1. In-house QC and sample selection

As whole genome sequencing required intact, minimally fragmented gDNA, samples underwent additional QC assessment using the D1000 Tapestation Fragment Analyser kit (Agilent, Cheadle, UK) using the manufacturer's instructions. Reagents were equilibrated to room temperature prior to use and DNA samples thawed on ice. The D1000 ScreenTape device and loading tips were inserted into the 2200 TapeStation instrument (Agilent, Cheadle, UK). The size ladder was prepared by mixing 3µL D1000 Sample Buffer with 1µL D1000 Ladder. Samples were prepared by mixing 3µL D1000 Sample Buffer with 1µL gDNA sample in PCR tubes. PCR tubes containing ladder/sample were loaded onto the 2200 Tapestation device. The Tapestation was run as per standard settings, analysing for fragments of DNA between 25–1000bp, indicative of fragmented DNA. A representative output can be seen in Figure 4.6.

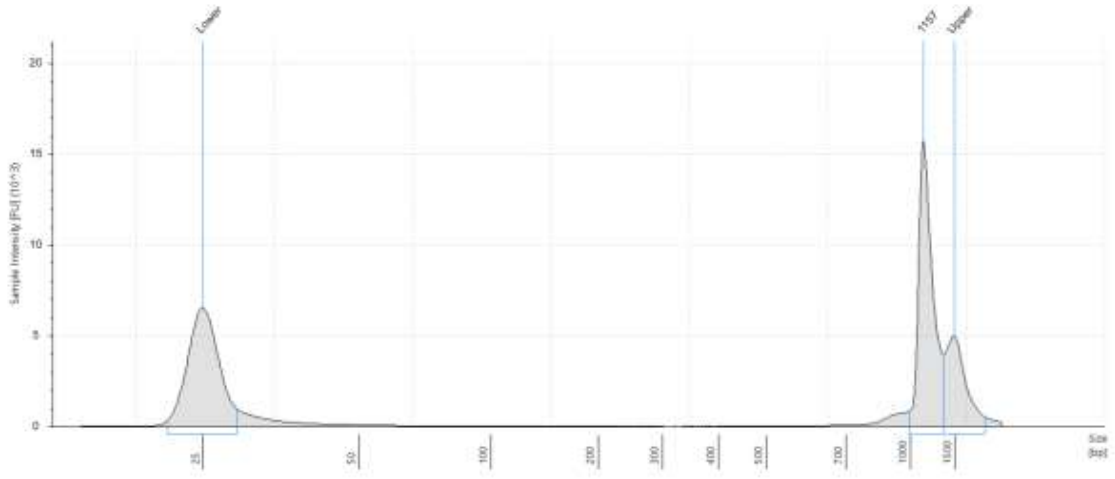

Sample Table

Well	Conc. [ng/µl]	Sample Description	Alert	Observations
B1	14.3	FK3.6		

Figure 4.6. Representative Agilent TapeStation Fragment Analyser sample output
Electropherogram of representative DNA sample, absence of peaks between 25-1000bp indicates good quality DNA with limited fragments.

Changes in genomic DNAm have been linked with cognitive performance in schizophrenia (Ho et al., 2020) hence female-offspring samples were selected as in the PN1 cohort cognitive deficits in the ASST were only conclusively shown in adult females (Chapter 2; Potter et al., 2023). The PFC was chosen as the region of interest for its key role in higher cognitive function,

particularly executive functions measured in the ASST. Eight adult female PFC gDNA samples were selected as having the highest concentration with minimal fragmentation.

4.2.7.2. Sample QC and quantification by Diagenode

DNA concentration was measured using the Qubit® dsDNA BR Assay Kit (ThermoFisher, Waltham, USA) with a minimum 5ng/µL concentration required for sequencing. DNA quality was assessed with the Fragment Analyzer™ and the DNF-488 High Sensitivity Genomic DNA Analysis Kit (Agilent, Cheadle, UK). Figure 4.7 shows a representative sample QC result, passing with no/minimal fragments indicated between 5-1000bp. All eight adult female PFC DNA samples passed Diagenode QC and were used for library preparation.

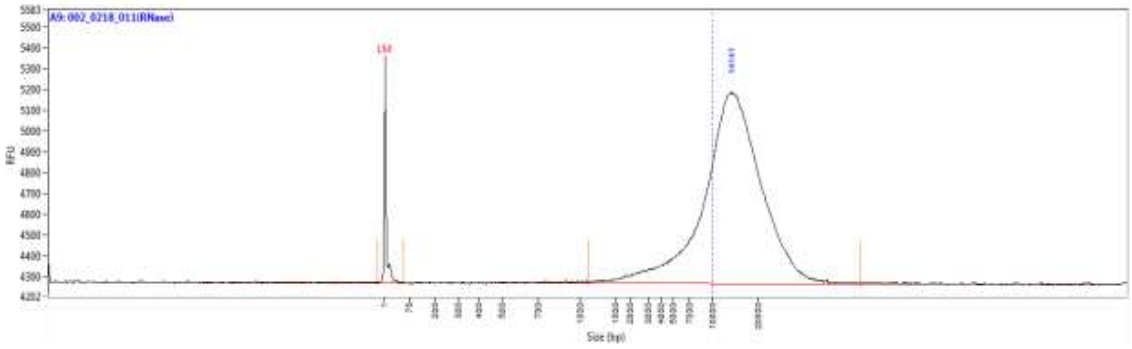

Figure 4.7. Representative DNF-488 High Sensitivity genomic DNA analysis result
Electropherogram of representative DNA sample, where absence of peaks 5-1000bp is required for sequencing.

4.2.7.3. RRBS library preparation and sequencing by Diagenode

RRBS libraries were prepared using the Premium Reduced Representation Bisulphite Sequencing Kit (Diagenode, Liège, Belgium) as per manufacturer's instructions and published workflow (Veillard et al., 2016). A full outline of the methodology is provided in Appendix 6, Section 1. The final prepared RRBS library pool was sequenced in paired-end mode on an Illumina NovaSeq 3000/4000 (Illumina, San Diego, USA), generating 50 base reads (SE50).

Following sequencing, standard bioinformatics were performed by Diagenode (see Appendix 6, Section 2 for full details). Briefly, this included: QC checks and sequence read alignment to the rat reference genome Rn5.0 (Andrews, 2010; Krueger and Andrews, 2011; Krueger, 2012). Mapping efficiency was also calculated and spike-in control sequences (methylated and non-methylated) used to assess the bisulphite conversion rates, validating the efficiency of the bisulphite treatment, with ≤2% and ≥98% conversion rates considered acceptable, respectively. R/Bioconductor packages, were subsequently used for differential methylation analysis between the two sample groups with pairwise comparison performed for 'Poly(I:C)' versus 'Vehicle' to identify differentially methylated CpGs (DMCs) and regions (DMRs), the latter comprising sequence stretches of 1000bp. Logistic regression was used to compare methylation percentages between groups at each given DMC/DMR and the sliding window model (SLIM)

used to correct p-values to q-values, accounting for multiple comparison tests. Statistically significant DMCs and DMRs were identified with a pre-determined q-value cut-off ≤0.01 and a methylation difference ≥25%. These stringent cut-offs are typically used in RRBS studies to account for the false discovery rate (FDR) of DMCs as a result of technical variability (e.g., coverage, read depth) and inherent heteroscedasticity of raw methylation values (Singer, 2019; Veillard et al., 2016; Wreczycka et al., 2017). Significant DMCs/DMRs were annotated to genomic location within the UCSC Rat reference genome Rn5.0 (Cavalcante and Sartor, 2017; Lee et al., 2022). The annotation comprising two categories: (i) distance to a CGI including: overlapping a known CGI; within the 2000bp flanking region of a CGI (CpG shore); within 2000bp of the CpG shore (CpG shelves) or outside these regions (open sea); (ii) genic annotation (intergenic, exonic, intronic or promoter). Using these genic locations, DMCs/DMRs were mapped to genes in which they were located. Gene ontology was then performed to determine the enriched biological processes, molecular functions and cellular components of the DMC-containing genes (Alexa and Rahnenführer, 2022). Reactome pathway enrichment analysis was also carried out (Yu and He, 2016) using Kyoto Encyclopedia of Genes and Genomes (KEGG) terms. Enrichment analyses was performed using a hypergeometric model with FDR used to correct p-values.

4.2.7.4. In-house bioinformatics and candidate gene selection

The dataset was entered into Tissue Enrichment analysis (Jain and Tuteja, 2019; https://tissueenrich.gdcb.iastate.edu/). Both the Human Protein Atlas and the mouse ENCODE datasets were used, with a hypergeometric model to assess enrichment. Next, the Enrichr database (Kuleshov et al., 2016; https://maayanlab.cloud/Enrichr/) was used to assess enrichment of disease risk genes in the RRBS dataset, using Fishers exact test for significance of enrichment. To assess the validity of the RRBS dataset for schizophrenia research, schizophrenia-risk gene lists were collated from genetic and epigenetic studies, alongside an additional similar study evaluating whole genome methylation in the PFC of adult male mice from a poly(I:C)-model (Table 4.2). Gene identifiers were converted to rat orthologues using the BioMart database (Durinck et al., 2009; Kinsella et al., 2011). A hypergeometric test was used to assess enrichment of the RRBS genes within these additional compiled lists.

Table 4.2. Gene lists associated with schizophrenia

Gene list ID	Summary of gene list	References
SZ_GENE	Genes with a genetic link to schizophrenia from GWAS, CNV and Linkage studies	Wu et al., 2020; Butler et al., 2016.
SZ_EXP	Genes differentially expressed in schizophrenia	Wu et al., 2020.
SZ_ME	Genes differentially methylated in schizophrenia	Wu et al., 2020; Pries et al., 2017.
SZ_EXOME	Genes associated with schizophrenia through whole exome sequencing	Wu et al., 2020.
MIA_DMC	Differentially methylated CpG sites identified in the adult male PFC following poly(I:C)-exposure in mice on GD9 or GD17	Richetto et al., 2017b.
MIA_DMR	Differentially methylated regions identified in the adult male PFC following poly(I:C)-exposure in mice on GD9 or GD17	Richetto et al., 2017b.

To select candidate genes/pathways for future analysis, the following criteria were applied to the RRBS dataset:

i) Genes were selected for being present in at least two previous datasets, either a MIA model (Richetto et al., 2017b; Woods et al., 2021) and/or a schizophrenia-risk gene (Table 4.2).
ii) Selected for genes with differential methylation in regions with known regulatory functions: CGI (Deaton and Bird, 2011), promoter (Moore et al., 2013), exon 1 (Brenet et al., 2011), intron 1 (Anastasiadi et al., 2018) or at a spliced exon/intron (Shayevitch et al., 2018; Li et al., 2018b).
iii) Genes were required to have expression in the brain, determined using the Protein Atlas database (Sjöstedt et al., 2020)
iv) Genes were required to have comparable expression patterns between rodents and humans such that functions were similar, determined by single cell RNA-seq databases (Keil et al., 2018).

The final candidate genes were entered into STRING network analysis (Szklarczyk et al., 2021) to assess for gene ontology/pathway enrichments.

4.3. RESULTS

4.3.1. *Dnmt* mRNA expression changes in the cortex

I. *Dnmt1*

There were no significant effects of any predictors on *Dnmt1* expression at GD21 or PD21 (Figure 4.8A).

PD35

In the FC there was a significant main effect of maternal IL-6 (GLMM: $F_{1,19}$=5.93, p=0.025; Figure 4.8A), corresponding to a negative correlation between maternal IL-6 and *Dnmt1* expression in the PD35 FC (r=-0.489, p=0.024). There were no significant effects of any predictors on *Dnmt1* expression in the PFC.

PD175

In the FC there was a significant main effect of sex (GLMM: $F_{1,5.97}$=11.61, p=0.014; Figure 4.8A), with reduced *Dnmt1* expression in females relative to males. Post-hoc analysis resulted in a significant main effect of group in males (GLMM: $F_{1,7}$=11.15, p=0.012; Figure 4.8A), with reduced *Dnmt1* expression in poly(I:C)-males relative to vehicle-males. There were no significant effects of any predictors on *Dnmt1* expression in the PFC.

II. *Dnmt3a*

GD21

There was a significant main effect of maternal IL-6 (GLMM: $F_{1,11}$=9.80, p=0.011; Figure 4.8B), corresponding to a positive correlation between foetal *Dnmt3a* expression and maternal IL-6 (rho=0.617, p=0.006).

PD21

In the FC there was a significant main effect of sex (GLMM: $F_{1,7.39}$=6.65, p=0.035; Figure 4.8B), with females having higher *Dnmt3a* expression than males. Post-hoc analysis showed a significant main effect of group in the males (GLMM: $F_{1,9}$=5.41, p=0.045; Figure 4.8B), with reduced *Dnmt3a* expression in the poly(I:C)-males relative to vehicle-males. There were no significant effects of any predictors on *Dnmt3a* expression in the PFC.

PD35

In the FC there was a significant main effect of sex (GLMM: $F_{1,19}$=5.12, p=0.036; Figure 4.8B), with females having higher *Dnmt3a* expression compared to males. In the PFC there was a significant main effect of sex (GLMM: $F_{1,5.16}$=7.91, p=0.036; Figure 4.8B), with females again having higher *Dnmt3a* expression compared to males and a trend to a main effect of group (GLMM: $F_{1,11.12}$=3.59, p =0.080; Figure 4.8B), with increased *Dnmt3a* expression in poly(I:C)-offspring relative to vehicle-offspring.

PD175

In the FC there was a significant main effect of sex (GLMM: $F_{1,18}$=14.89, p=0.001; Figure 4.8B), with lower *Dnmt3a* expression in the females relative to males, while in the PFC there was a trend to a main effect of group (GLMM: $F_{1,18}$=4.26, p=0.054; Figure 4.8B) with reduced *Dnmt3a* expression in poly(I:C)-offspring compared to vehicle-offspring.

III. *Dnmt3b*

GD21

There was a significant main effect of group (GLMM: $F_{1,8.55}$=8.16, p=0.02; Figure 4.8C) with elevated *Dnmt3b* expression in the poly(I:C)-foetuses compared to vehicle-foetuses.

PD21

In the FC there was a significant main effect of sex (GLMM: $F_{1,9.32}$=5.74, p=0.039; Figure 4.8C) with elevated *Dnmt3b* expression in the females relative to the males. There were no significant effects of any predictors on *Dnmt3b* expression in the PFC.

PD35

In the FC there was a significant main effect of group (GLMM: $F_{1,17}$=4.54, p=0.048; Figure 4.8C), with increased *Dnmt3b* expression in the poly(I:C)-offspring relative to vehicle-offspring. There was also trends towards main effects of sex (GLMM: $F_{1,17}$=4.28, p=0.054; Figure 4.8C), with elevated *Dnmt3b* expression in females relative to males and maternal TNFα (GLMM: $F_{1,17}$=4.07, p=0.06; Figure 4.8C) though the latter did not correspond to a significant correlation. In the PFC there was a significant main effect of sex (GLMM: $F_{1,5.16}$=7.91, p=0.036; Figure 4.8C), with females having elevated *Dnmt3b* expression relative to males and a trend to a main effect of group (GLMM: $F_{1,11.12}$=3.59, p=0.08; Figure 4.8C), with poly(I:C)-offspring having higher *Dnmt3b* expression than vehicle-offspring. Post-hoc analysis revealed a significant main effect of maternal TNFα in the males (GLMM: $F_{1,9}$=5.23, p=0.048; Figure 4.8C), corresponding to a trending positive correlation between *Dnmt3b* expression and maternal TNFα (rho=0.564, p=0.071).

PD175

In the FC there was a significant main effect of sex (GLMM: $F_{1,16}$=428.63, p<0.001; Figure 4.8C), with elevated *Dnmt3b* expression in males relative to females and group (GLMM: $F_{1,16}$=6.31, p=0.023; Figure 4.8C), with reduced *Dnmt3b* expression in poly(I:C)-offspring relative to vehicle-offspring and a trending main effect of maternal IL-6 (GLMM: $F_{1,16}$=3.91, p=0.06; Figure 4.8C), though no post-hoc correlations were significant. In the PFC there were significant main effects of group (GLMM: $F_{1,13}$=8.42, p=0.012; Figure 4.8C), with reduced *Dnmt3b* expression in the poly(I:C)-offspring relative to vehicle-offspring, maternal TNFα (GLMM: $F_{1,13}$=9.27, p=0.009; Figure 4.8C) and maternal IL-6 (GLMM: $F_{1,13}$=6.19, p=0.027; Figure 4.8C) though no post-hoc correlations were significant.

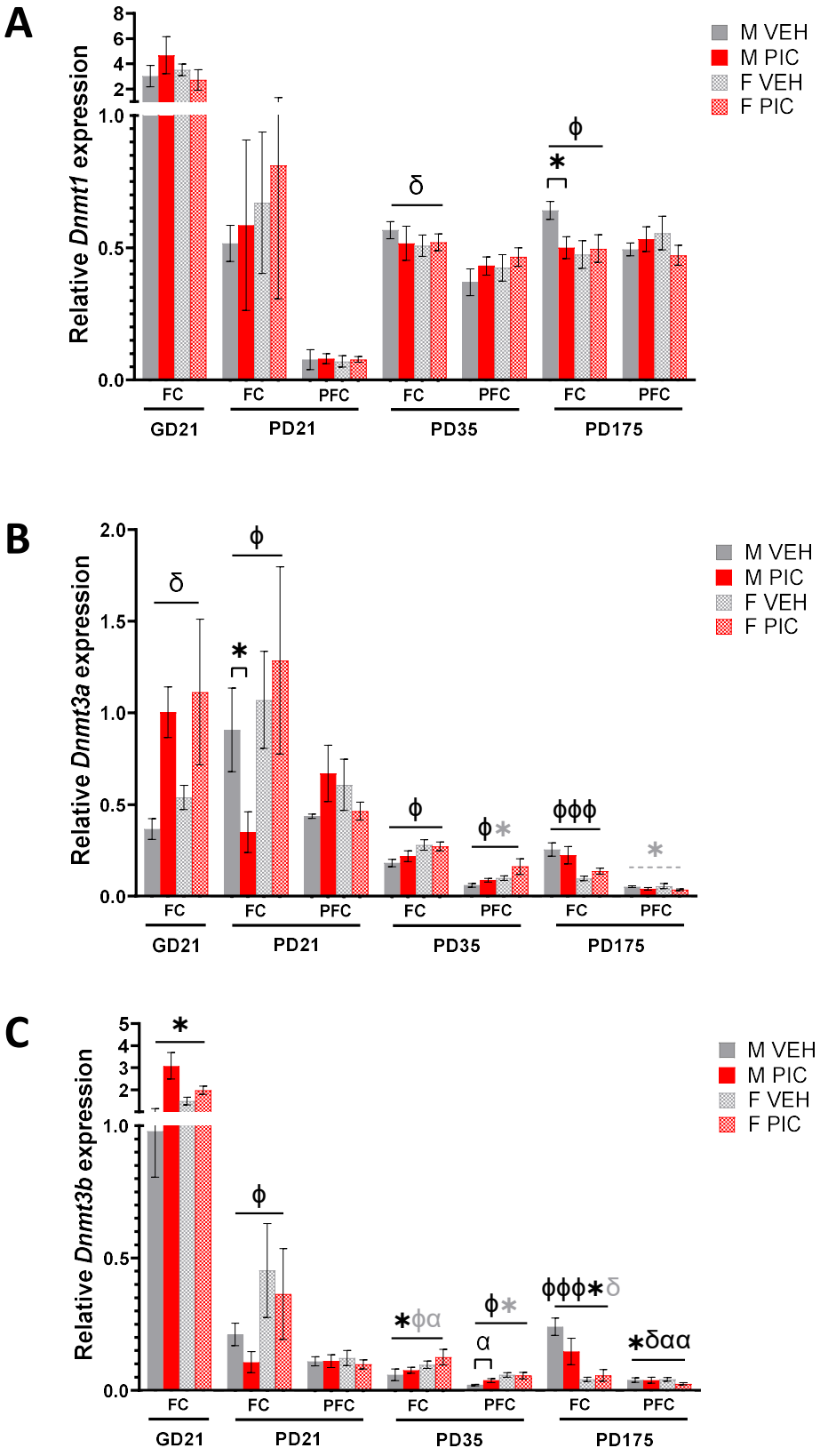

Figure 4.8. *Dnmt* mRNA expression
Relative *Dnmt* mRNA expression (normalised to the geometric mean of three reference genes as described in methods) across development. **A.** *Dnmt1* expression. **B.** *Dnmt3a* expression **C.** *Dnmt3b* expression. Bars represent mean ±SEM (N=5-7; n=5-8). Back significance bars show significant GLMM results, — shaped bars represent results within the tissue/age they overlap, Π-shaped bars represent post-hoc within a single sex. Black symbols show significant main effects of: sex, ϕp<0.05, ϕϕϕp≤0.001; group, *p<0.05; maternal IL-6, δp<0.05; maternal TNFα, αp<0.05, ααp<0.01. Grey dashed lines and/or symbols represent trending (0.05<p≤0.08) GLMM results. Abbreviations: GD, gestational day; PD, postnatal day; FC, frontal cortex; PFC, prefrontal cortex; M, male; F, female; VEH, vehicle; PIC, poly(I:C).

4.3.2. DNMT activity changes in the developing cortex

The below analyses outline the standard GLMM analyses (Section 4.2.6) within each age/tissue to identify influences of MIA and sex on developmental DNMT activity. However, total nuclear DNMT activity is driven by the amount of DNMTs present (e.g., DNMT expression) and SAM/SAH bioavailability (Caudill et al., 2001). Hence, whether these molecular factors influenced DNMT activity was investigated, by performing a second analysis, including these measurements as covariates in the GLMM and using post-hoc correlation analysis, to examine the relationship between DNMT activity and the following molecular predictors: *Dnmt* expression (Figure 4.8) and cytosolic SAH/SAM availability and ratio (Chapter 3, Figure 3.8).

GD21 FC

There was a significant main effect of group (GLMM: $F_{1,12}$=15.22, p=0.002; Figure 4.9) with increased DNMT activity in the poly(I:C)-foetuses relative to vehicle-foetuses.

Molecular covariates also significantly influenced variability in DNMT activity, including a main effect of *Dnmt3b* expression (GLMM: $F_{1,16}$=11.92, p=0.003) and cytosolic SAH (GLMM: $F_{1,16}$=10.64, p=0.005). Post-hoc correlations showed a significant negative correlation between cytosolic SAH and DNMT activity (rho=-0.445, p=0.043; Figure 4.10A) and trends to positive correlations between cytosolic SAM (rho=0.392, p=0.073; Figure 4.10A) and SAM/SAH ratio (rho=0.414, p=0.062; Figure 4.10A) and DNMT activity. Establishing a relationship between metabolite availability and DNMT activity in the GD21 FC. However, there were no significant correlations between *Dnmt* mRNA expression and DNMT activity (Figure 4.11A).

PD21 FC

There were significant main effects of both maternal IL-6 (GLMM: $F_{1,6.78}$=12.69, p=0.011; Figure 4.9) and maternal TNFα (GLMM: $F_{1,7.32}$=5.72, p=0.047; Figure 4.9), though there was only a positive correlation between maternal TNFα and DNMT activity (rho=0.461, p=0.041). There was also a main effect of sex (GLMM: $F_{1,7.30}$=8.31, p=0.023; Figure 4.9) and a group*sex interaction (GLMM: $F_{2,7.78}$=5.58, p=0.031). Accordingly, post-hoc analysis by sex showed a main effect of maternal IL-6 (FLMM: $F_{1,7}$=8.97, p=0.020; Figure 4.9) and maternal TNFα (GLMM: $F_{1,7}$=18.22, p=0.004; Figure 4.9) in the females, corresponding to a positive correlation between maternal cytokines and DNMT activity, although only maternal TNFα was significant (rho=0.636, p=0.048), while in the males there was a main effect of maternal IL-6 (GLMM: $F_{1,7}$=15.89, p=0.005; Figure 4.9) and maternal TNFα (GLMM: $F_{1,7}$=9.12 p=0.016; Figure 4.9); though no post-hoc correlations reached statistical significance.

Dnmt3a expression was the only significant molecular predictor of DNMT activity (GLMM: $F_{1,14.96}$=7.49, p=0.015). However, post-hoc correlation analysis showed a negative correlation between *Dnmt1* expression and DNMT activity (rho=-0.545, p = 0.016; Figure 4.11B) and a significant positive correlation between DNMT activity and *Dnmt3a* expression (rho=0.557, p=0.020; Figure 4.11B).

PD21 PFC

There were no significant effects of group, sex or maternal cytokines on DNMT activity (Figure 4.9).

Analysis of molecular predictors showed significant main effects of cytosolic SAM (GLMM: $F_{1,11.92}$=5.15, p=0.043) and SAM/SAH ratio (GLMM: $F_{1,\ 11.91}$=6.13, p=0.029) and a trend to a main effect of cytosolic SAH (GLMM: $F_{1,11.60}$=3.44, p=0.080), although no significant correlations were observed (Figure 4.10C&Figure 4.11C), indicating a co-dependent relationship of these covariates.

PD35 FC

There were no significant effects of group, sex or maternal cytokines on DNMT activity (Figure 4.9).

Analysis of molecular predictors showed a main effect of *Dnmt1* expression on DNMT activity (GLMM: $F_{1,13}$=4.78, p=0.048), corresponding to a positive correlation between nuclear DNMT activity and *Dnmt1* expression (rho=0.518, p=0.048; Figure 4.11D).

PD35 PFC

There was a significant main effect of sex (GLMM: $F_{1,11.42}$=5.37, p=0.040; Figure 4.9), with reduced DNMT activity in females relative to males. Post-hoc analysis showed a trend to a significant effect of maternal TNFα (GLMM: $F_{1,6}$=5.74, p=0.054; Figure 4.9) and group (GLMM: $F_{1,6}$=5.46, p=0.059; Figure 4.9) in the males, corresponding to a trending negative correlation between maternal TNFα and DNMT activity (r=-0.623, p=0.071).

There were no significant effects of molecular predictors on DNMT activity.

PD175 FC

There were no significant effects of group, sex or maternal cytokines on DNMT activity (Figure 4.9).

Analysis of molecular predictors showed main effects of cytosolic SAM (GLMM: $F_{1,10.93}$=37.22, p<0.001) and SAM/SAH ratio (GLMM: $F_{1,4.36}$=46.36, p=0.002) on DNMT activity and a positive correlation between DNMT activity and SAM/SAH ratio (rho=0.511, p=0.043; Figure 4.10F).

PD175 PFC

There was a main effect of group (GLMM: $F_{1,18}$=7.26, p=0.015; Figure 4.9) with reduced DNMT activity in poly(I:C)-offspring relative to vehicle-offspring.

Analysis of molecular predictors showed main effects of: *Dnmt3b* expression (GLMM: $F_{1,11}$=8.49, p=0.014), cytosolic SAM (GLMM: $F_{1,11}$=7.87, p=0.017), cytosolic SAH (GLMM: $F_{1,11}$=9.56, p=0.010) and SAM/SAH ratio (GLMM: $F_{1,11}$=10.68, p=0.007). However, there were no significant correlations (Figure 4.10G&Figure 4.11G), likely owing to the co-dependent relationship of these covariates.

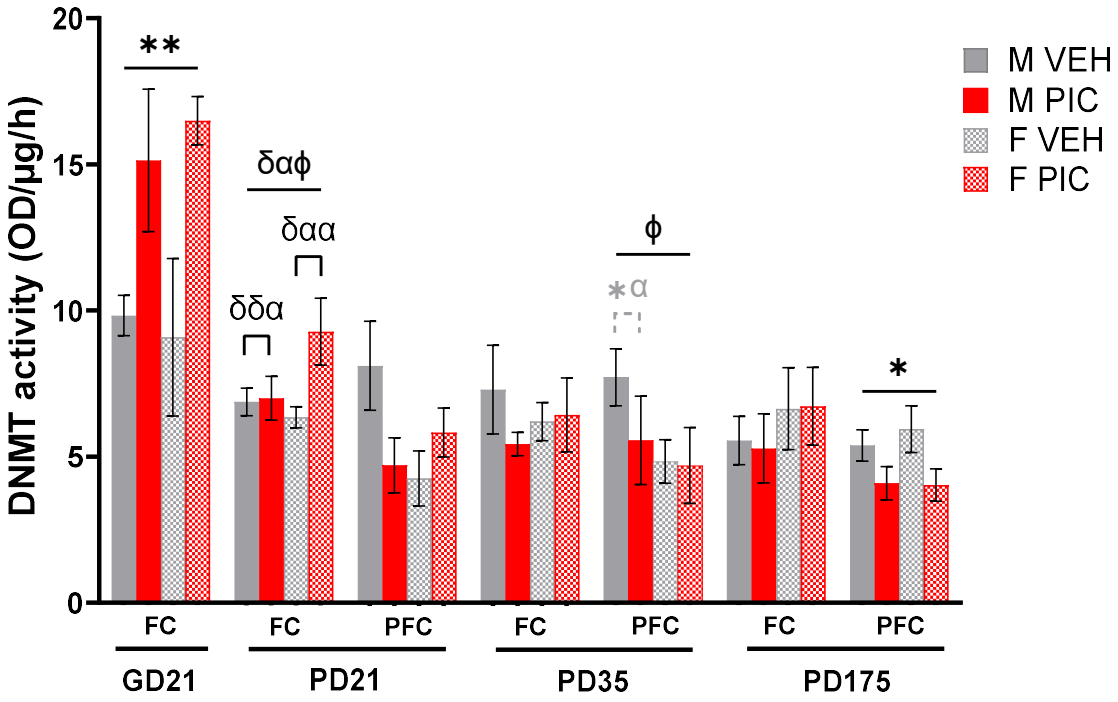

Figure 4.9. Nuclear DNMT activity
Nuclear DNMT activity across development. Bars represent mean ±SEM (N=5; n=5-6). Black significance bars show significant GLMM results, — shaped bars represent results within the tissue/age they overlap, Π-shaped bars represent post-hoc results within a single sex. Black symbols indicate significant main effects of: sex, ϕp<0.05; group, *p<0.05, **p<0.01; maternal IL-6, δp<0.05, δδp<0.01; maternal TNFα, αp<0.05, ααp<0.01. Grey dashed lines and symbols show trending (0.05<p<0.08) GLMM results. Abbreviations: GD, gestational day; PD, postnatal day; FC, frontal cortex; PFC, prefrontal cortex; M, male; F, female; VEH, vehicle; PIC, poly(I:C).

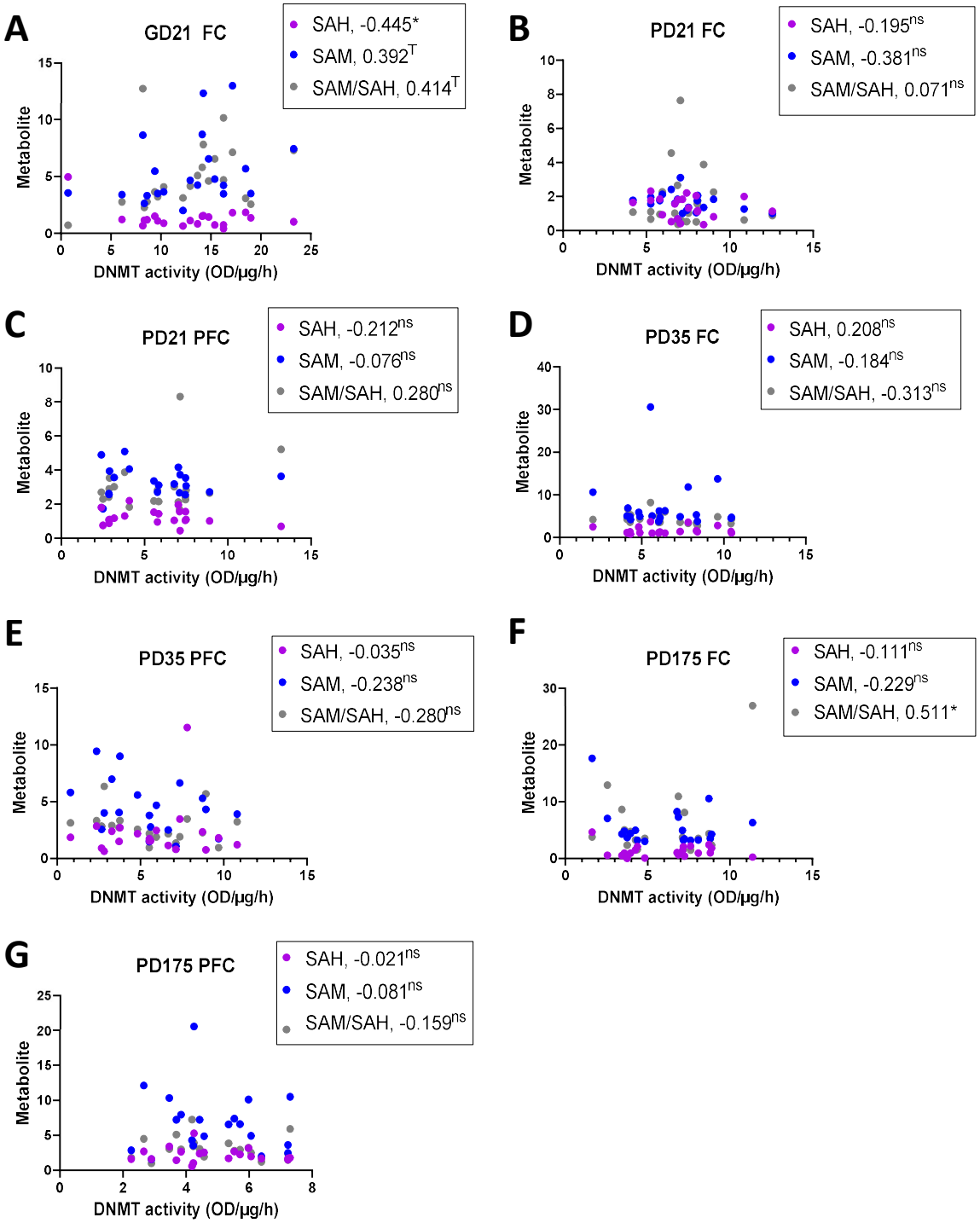

Figure 4.10. DNMT activity and metabolite correlations
Nuclear DNMT activity (OD/µg protein/h) correlated with cytosolic SAM and SAH concentrations (nmol/mg protein) and the SAM/SAH ratio. Graphs indicate correlation co-efficient (Spearman's rho) alongside two-tailed significance: $^{ns}p>0.08$; $^{T}p\leq0.08$; $^{*}p\leq0.05$. **A.** GD21 FC **B.** PD21 FC. **C.** PD21 PFC. **D.** PD35 FC. **E.** PD35 PFC. **F.** PD175 FC. **G.** PD175 PFC.

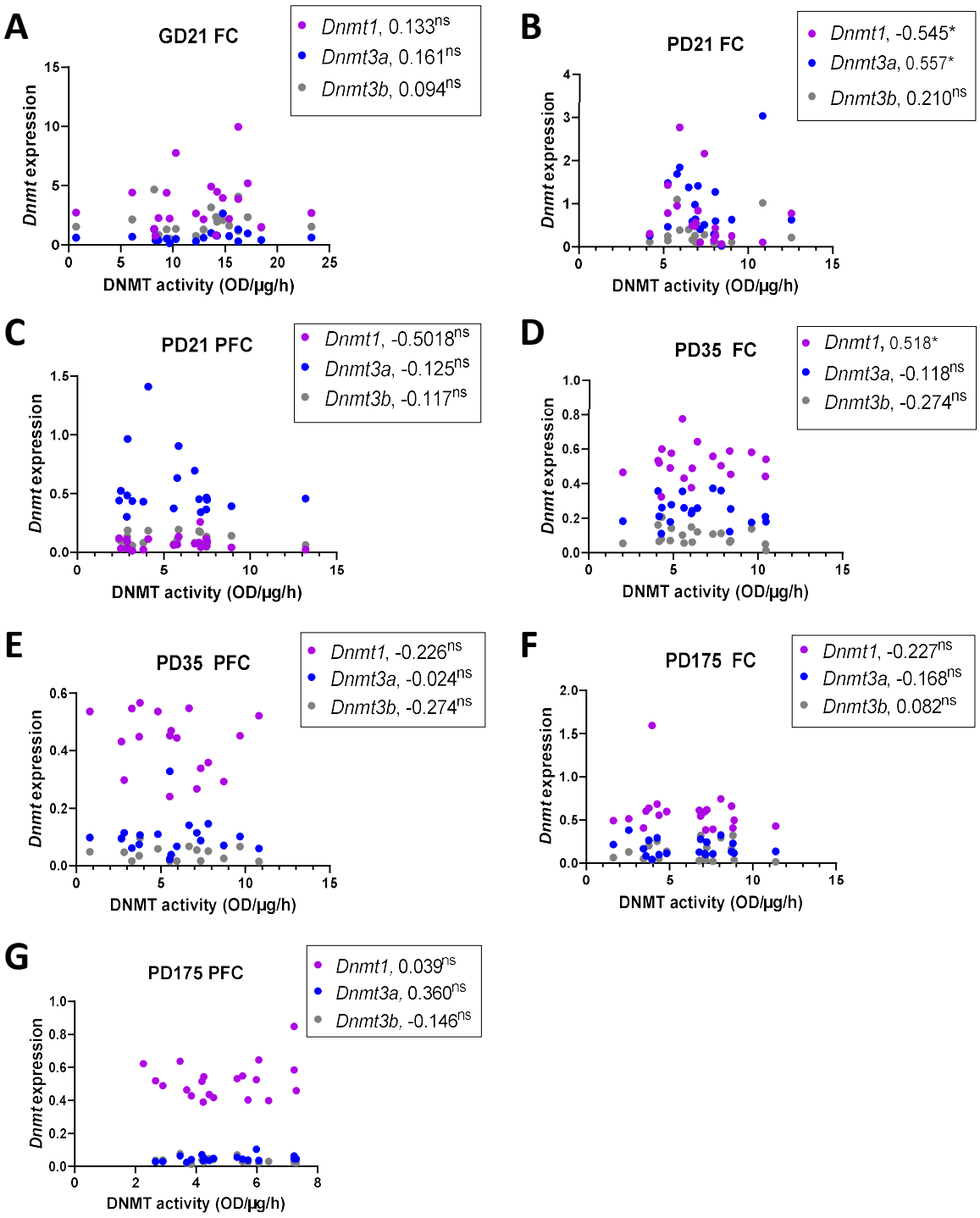

Figure 4.11. DNMT activity and *Dnmt* mRNA expression correlations
Nuclear DNMT activity (OD/µg protein/h) correlated with relative *Dnmt* mRNA expression. Graphs show correlation co-efficient (Spearman's rho) alongside two-tailed significance: $^{ns}p>0.08$; *p≤0.05. **A.** GD21 FC **B.** PD21 FC. **C.** PD21 PFC. **D.** PD35 FC. **E** PD35 PFC. **F.** PD175 FC. **G.** PD175 PFC.

4.3.3. Total genomic DNAm changes in the developing cortex

The below analyses outline the standard GLMM analyses (Section 4.2.6) within each age/tissue to identify the influence of MIA and sex on DNAm throughout development. However, DNAm patterns are established by both *de novo* and maintenance DNMT activity (which, as outlined previously, are dependent on *Dnmt* expression and SAM/SAH availability). Hence, a second GLMM analysis was also performed, including these measurements as covariates and using post-hoc correlation analysis, to examine the relationship between %5mC and the following molecular predictors: DNMT activity (Figure 4.9), *Dnmt* mRNA expression (Figure 4.8) and cytosolic SAM and SAH availability (Chapter 3, Figure 3.8).

GD21 FC

There was a significant group*sex interaction (GLMM: $F_{1,16}$=6.42, p=0.047) and a main effect of both sex (GLMM: $F_{1,16}$=4.49, p=0.05; Figure 4.12) and group (GLMM: $F_{1,16}$=9.73, p=0.007; Figure 4.12). Post-hoc analysis revealed a significant main effect of group (GLMM: $F_{1,4}$=34.61, p=0.004; Figure 4.12) and maternal IL-6 (GLMM: $F_{1,4}$=8.35, p=0.045; Figure 4.12) in male-foetuses, while in female-foetuses there was a trend to a main effect of maternal TNFα (GLMM: $F_{1,3}$=8.28, p=0.064; Figure 4.12) and group (GLMM: $F_{1,3}$=7.51, p=0.071; Figure 4.12). In both cases the effect of group indicated increased %5mC in poly(I:C)-foetuses relative to vehicle-foetuses.

Analysis of molecular predictors showed main effects of DNMT activity (GLMM: $F_{1,6.20}$ =11.19, p=0.015) and cytosolic SAH (GLMM: $F_{1,6.58}$=11.10, p=0.014) and a trend to main effect of *Dnmt1* (GLMM: $F_{1,10.10}$=4.48, p=0.060) and *Dnmt3a* expression (GLMM: $F_{1,7.91}$=4.43, p=0.069). Post-hoc correlation analysis showed significant positive correlations between %5mC, expression of each of the three *Dnmt* genes, cytosolic SAM and SAM/SAH ratio (Table 4.3; Figure 4.13A; Figure 4.14A) and a trend to a positive correlation with DNMT activity (r=0.411, p = 0.071; Figure 4.15A), supporting a relationship between global DNAm and rate-limiting molecular factors.

Table 4.3. GD21 FC Spearman's correlations for global DNAm covariates

Covariate	rho	p-value
Dnmt1 expression	0.493	0.027
Dnmt3a expression	0.627	0.003
Dnmt3b expression	0.538	0.014
Cytosolic SAH	-0.030	0.900
Cytosolic SAM	0.439	0.051
SAM/SAH ratio	0.516	0.020

PD21 FC

There was a significant main effect of maternal TNFα (GLMM: $F_{1,19}$=5.04, p=0.037; Figure 4.12) and a trend towards a main effect of maternal IL-6 (GLMM: $F_{1, 19}$=4.04, p = 0.059; Figure 4.12), corresponding to a positive correlation between maternal TNFα and %5mC (rho=0.458, p=0.045).

Analysis of molecular predictors showed main effects of cytosolic SAM (GLMM: $F_{1,\ 11}$=4.86, p=0.050), SAM/SAH ratio (GLMM: $F_{1,11}$=6.28, p =0.029) and DNMT activity (GLMM: $F_{1,11}$=23.91, p<0.001), with the latter corresponding to a positive correlation between DNMT activity and %5mC (rho=0.539, p=0.014; Figure 4.15B).

PD21 PFC

There was a significant group*sex interaction (GLMM: $F_{3,15}$=4.06, p=0.027). Post-hoc analysis by sex revealed a significant main effect of group in the males (GLMM: $F_{1,9}$=11.28, p=0.008; Figure 4.12), with elevated %5mC in poly(I:C)-males relative to vehicle-males.

Analysis of molecular predictors showed main effects of *Dnmt3b* expression (GLMM: $F_{1,5.61}$=14.36, p=0.010), cytosolic SAH (GLMM: $F_{1,5.24}$=15.49, p=0.010) and DNMT activity (GLMM: $F_{1,10.21}$=6.98, p=0.024). However post-hoc correlations were non-significant (Figure 4.13C; Figure 4.14C; Figure 4.15C), likely owing to the highly co-dependent nature of these covariates.

PD35 FC

There were no significant effects of group, sex or maternal cytokines on %5mC (Figure 4.12).

Likewise, analysis of molecular predictors showed only a trend to a main effect of *Dnmt3a* expression (GLMM: $F_{1,11.03}$=85.69, p=0.064), while a post-hoc positive correlation was observed between DNMT activity and DNAm (rho=0.498, p=0.026; Figure 4.15D).

PD35 PFC

There were no significant effects of group, sex or maternal cytokines on %5mC (Figure 4.12).

Likewise, analysis of molecular predictors showed only a trend to a main effect of *Dnmt3b* expression (GLMM: $F_{1,12}$=3.57, p=0.080), with no significant post-hoc correlations (Figure 4.13E; Figure 4.14E; Figure 4.15E).

PD175 FC

There was a trend towards a group*sex interaction (GLMM: $F_{3,16}$=2.78, p=0.075), however post-hoc analysis showed no significant effects of any predictors of %5mC within either sex.

Analysis of molecular predictors showed main effects of DNMT activity (GLMM: $F_{1,13.98}$=5.80, p=0.030), *Dnmt3a* expression (GLMM: $F_{1,4.07}$=24.80, p=0.007) and cytosolic SAM (GLMM: $F_{1,6.85}$=8.51, p=0.023) and SAM/SAH ratio (GLMM: $F_{1,4.04}$=121.61, p<0.001), although only the latter corresponded to a positive post-hoc correlation with %5mC (rho=0.451, p=0.045; Figure 4.13F).

PD175 PFC

There were no significant effects of group, sex or maternal cytokines on %5mC (Figure 4.12).

Analysis of molecular predictors showed main effects cytosolic SAM (GLMM: $F_{1,11.88}$=21.69, p<0.001), cytosolic SAH (GLMM: $F_{1,12.0}$=20.73, p<0.001) and SAM/SAH ratio (GLMM:

$F_{1,11.59}$=12.55, p=0.004). However, there were no significant post-hoc correlations detected, probably due to the highly co-dependent nature of these covariates.

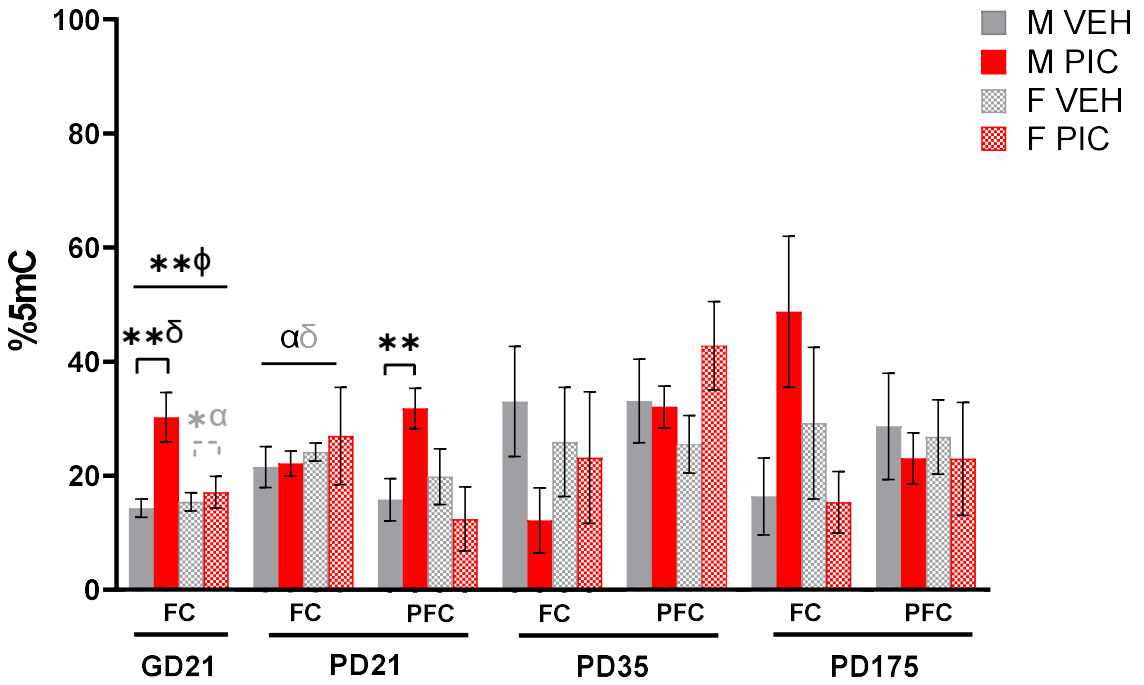

Figure 4.12. Global DNAm changes
%5mC across the developmental timeline. Bars represent mean ±SEM (N=5-6; n=5-7). Black significance bars show significant GLMM results, — shaped bars represent results within the timepoint they overlap, Π-shaped bars represent post-hoc results within a single sex. Black symbols indicate significant main effects of: sex, ϕp≤0.05; group, *p<0.05, **p<0.01; maternal IL-6, δp<0.05; maternal TNFα, αp<0.05. Grey dashed lines and/or symbols show trending (0.05<p<0.08) GLMM results. Abbreviations: GD, gestational day; PD, postnatal day; FC, frontal cortex; PFC, prefrontal cortex; M, male; F, female; VEH, vehicle; PIC, poly(I:C).

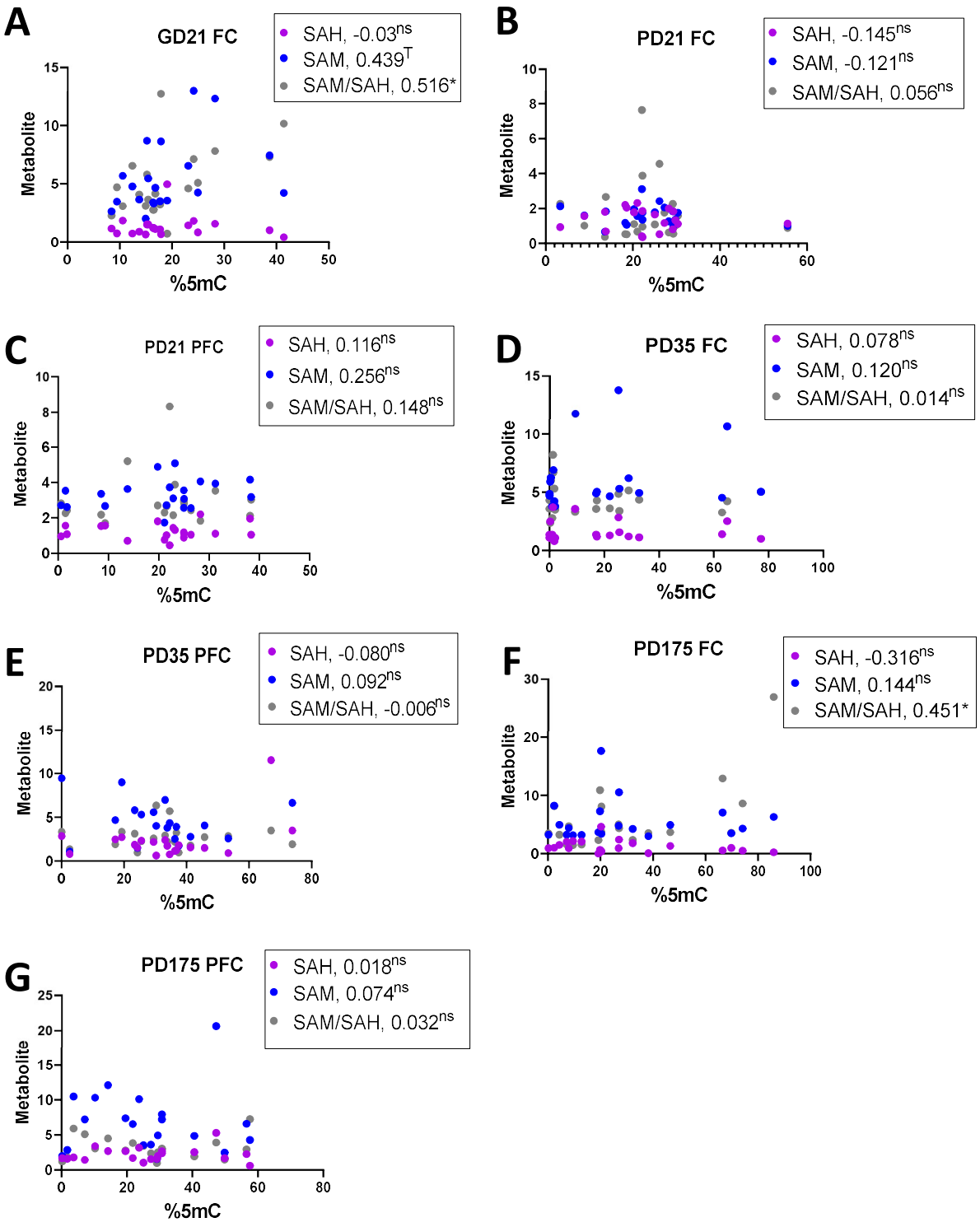

Figure 4.13. %5mC and metabolite correlations
Global DNA methylation (%5mC) correlated with cytosolic SAM and SAH concentrations (nmol/mg protein) or SAM/SAH concentration ratio. Graphs show correlation co-efficient (Spearman's rho) alongside two-tailed significance: $^{ns}p>0.08$; $^{T}p\leq0.08$; $^{*}p\leq0.05$. **A.** GD21 FC **B.** PD21 FC. **C.** PD21 PFC. **D.** PD35 FC. **E.** PD35 PFC. **F.** PD175 FC. **G.** PD175 PFC.

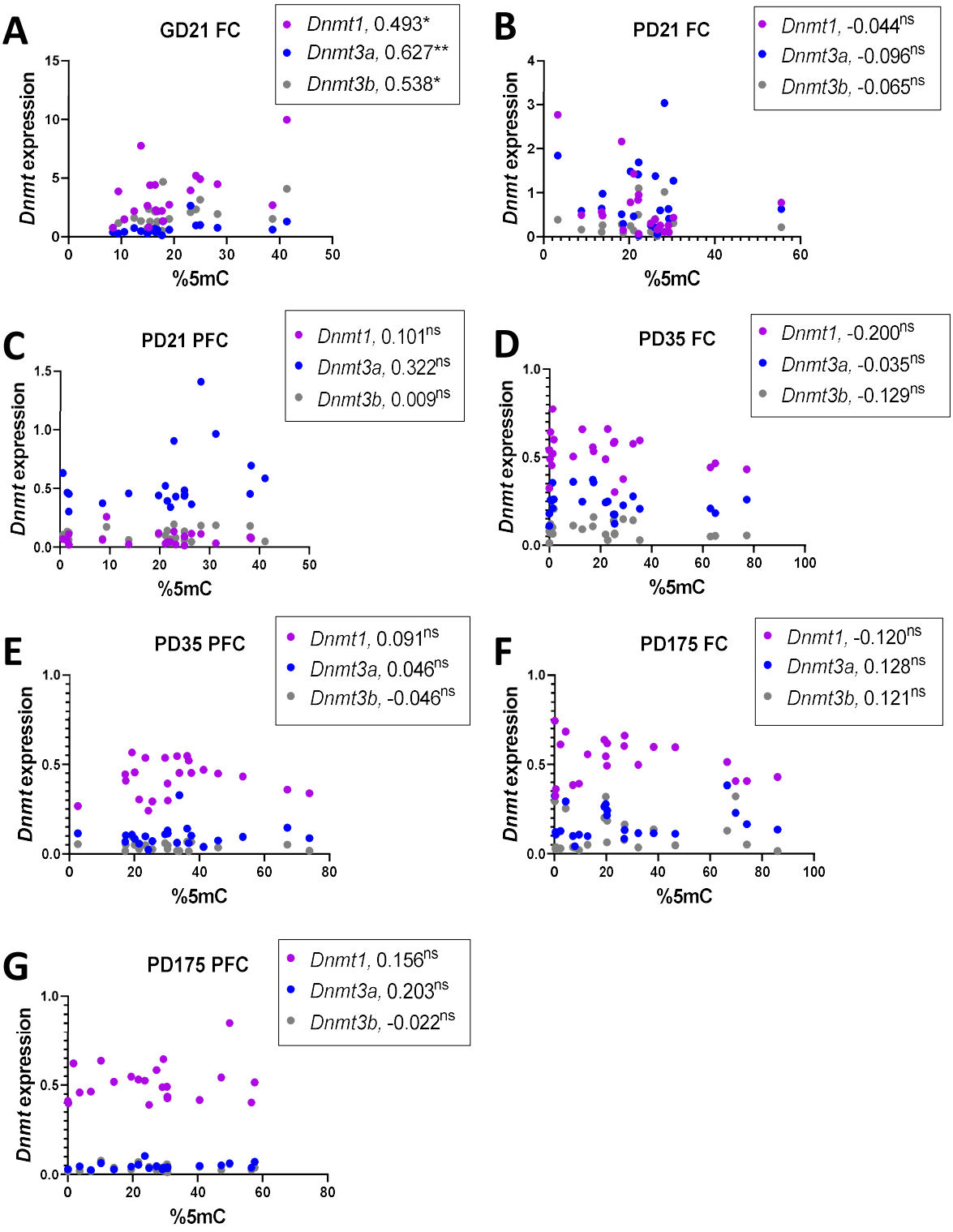

Figure 4.14. %5mC and *Dnmt* expression correlations
Global DNA methylation (%5mC) correlated with relative *Dnmt* mRNA expression. Graphs show correlation co-efficient (Spearman's rho) alongside with two-tailed significance: ^{ns}p>0.08; ^{T}P≤0.08 *p≤0.05; **p≤0.01. **A.** GD21 FC **B.** PD21 FC. **C.** PD21 PFC. **D.** PD35 FC. **E.** PD35 PFC. **F**. PD175 FC. **G**. PD175 PFC.

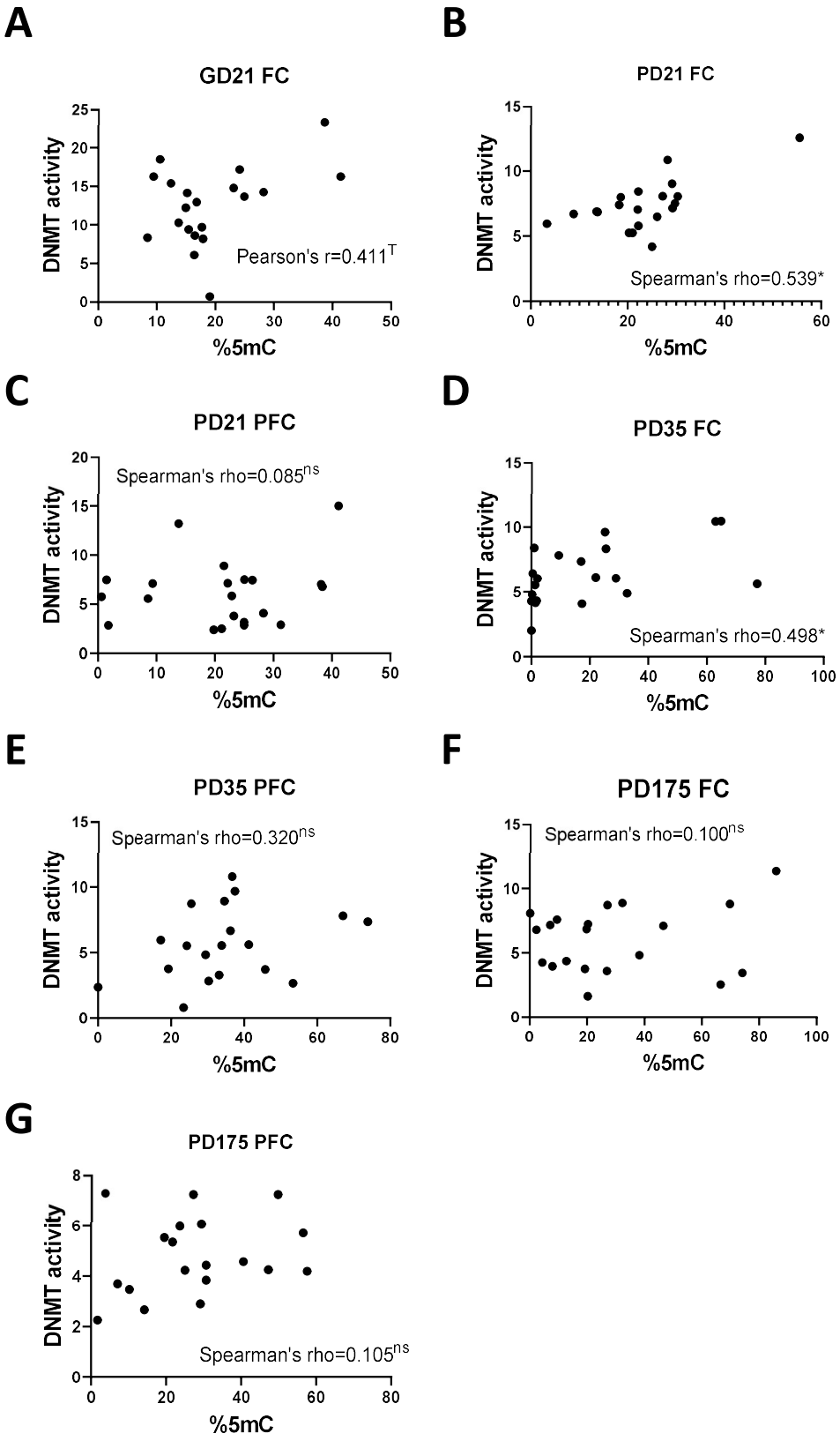

Figure 4.15. %5mC and DNMT activity correlations
Global DNA methylation (%5mC) correlated with nuclear DNMT activity (OD/µg protein/h). Graphs show correlation co-efficient (Spearman's rho or Pearson's r) indicated alongside two-tailed significance: $^{ns}p>0.08$; $^{T}p\leq0.08$ *$p\leq0.05$. **A**. GD21 FC **B**. PD21 FC. **C.** PD21 PFC. **D**. PD35 FC. **E** PD35 PFC. **F**. PD175 FC. **G**. PD175 PFC.

4.3.4. Gene-specific DNAm changes in the developing cortex

4.3.4.1. Summary of sequencing outputs and genomic mapping

Initial RRBS statistics are shown in Table 4.4. These results show that the sequencing reads are within the expected ranges: mapping efficiency of 65.7-67.09%, with ≥75% of detected CpGs covered more than 10X such that they could be included for differential analysis, resulting in 721,189 detected CpGs common to all eight samples. Spike-in controls passed within acceptable limits: ≤1.93% (methylated) and ≥99.31% (non-methylated) conversion rates.

Table 4.4. Sequencing sample overview

Sample ID	Total Read Pairs	Uniquely aligned Reads	Mapping efficiency (%)	CpGs detected	CpG Covered >10	Average Coverage	Conversion rate of methylated spike (%)	Conversion rate of non-methylated spike (%)
FA1	27,930,930	18,646,038	66.76	2,182,574	1,645,383	30.06X	1.71	99.96
FA2	35,757,041	23,494,127	65.70	2,439,341	1,880,602	34.09X	1.53	99.83
FA3	34,382,801	22,883,318	66.55	2,428,545	1,842,391	31.72X	1.72	99.77
FA4	37,528,364	24,718,122	65.87	2,415,256	1,876,946	36.70X	1.71	99.74
FB1	42,555,265	28,047,116	65.91	2,482,566	1,973,325	40.86X	1.71	99.31
FB2	39,047,620	26,106,922	66.86	2,440,463	1,926,744	38.34X	1.87	99.75
FB3	37,643,426	25,254,916	67.09	2,346,579	1,888,549	39.06X	1.93	99.83
FB4	33,718,054	22,356,976	66.31	2,394,051	1,831,638	32.05X	1.77	99.62

Using the cut-off of a q-value≤0.01 and ≥25% methylation difference (Singer, 2019; Veillard et al., 2016; Wreczycka et al., 2017, see Section 4.2.7.3), 22,096 DMCs and 3,227 DMRs were identified (Figure 4.16A&B). Of the DMCs 12,985 (58.77%) were hypomethylated and 9,111 (41.23%) were hypermethylated, while for DMRs 2,025 (62.75%) were hypomethylated and 1,202 (37.25%) were hypermethylated. Both hypomethylated and hypermethylated DMCs and DMRs were present across all chromosomes, with highest proportionate amount of hypermethylation identified on chromosome 18 for both DMCs and DMRs, while the highest proportionate amount of hypomethylation was identified on chromosome 14 for DMCs but on chromosome 13 for DMRs (Figure 4.16C&D). Genomic mapping (Figure 4.16E&G) for identified DMCs/DMRs were considered next. The majority of DMCs/DMRs were mapped to open sea regions, 76.92% and 85.3%, respectively. For DMRs, the fewest proportion were mapped to CGIs (1.5%) with identical numbers mapped to shelves and shores (6.6%). By comparison, for DMCs, the second highest mapping was to CGIs (9.75%), then shores (9.06%) with shelves having the least DMCs (4.28%). Next DMCs and DMRs were mapped to genic location (Figure 4.16F&H), with the least number mapped to promoters (3.07% and 2.14% respectively), then exons (12.63% and 11.35% respectively), introns (28.97% and 33.35% respectively) and most mapped to intergenic regions (55.33% and 53.16% respectively).

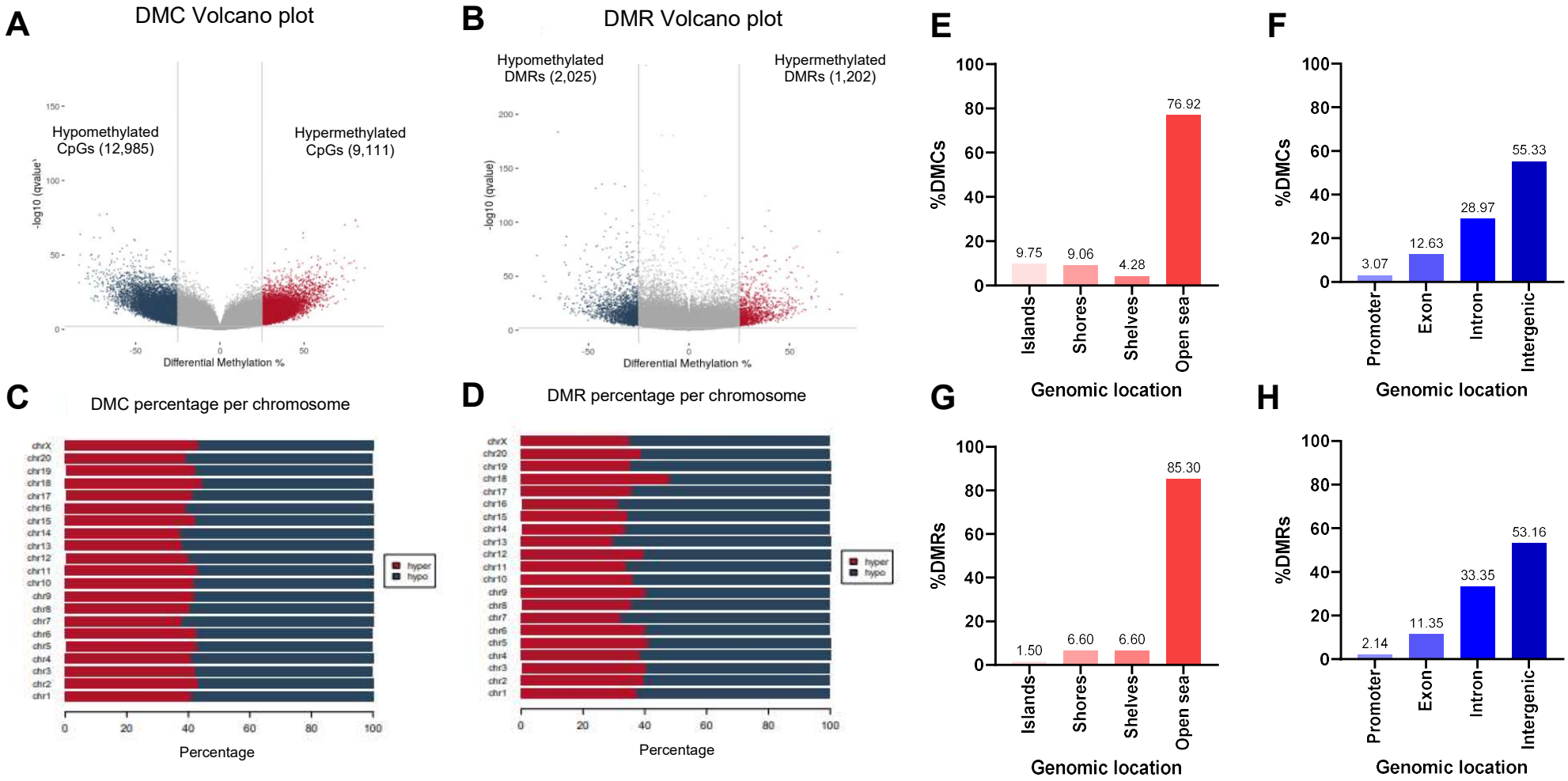

Figure 4.16. RRBS DMC and DMR identification and genomic mapping
Volcano plots show the number of DMCs (**A**) and DMRs (**B**) with changed patterns of methylation between “Poly(I:C)” and ”Vehicle” with ±25% difference and a q-value≤0.01. The difference in methylation (%) is reflected in the x-axis while the y-axis represents the significance (q-value) of the difference. The chromosomal location of hypo and hypermethylated DMCs (**C**) and DMRs (**D**). Genomic mapping of DMCs to CGIs (**E**) and genic location (**F**). Genomic mapping of DMRs to CGIs (**G**) and genic location (**H**).

These promoters, exons and introns (Figure 4.16F&H) were used to interpret the genes in which the DMCs and DMRs were located. This resulted in a total of 4,029 differentially methylated genes (Appendix 7; Supplementary Table S7.1). The number of DMCs mapped to different genes showed a range of 1-86 (Mean=6.9), likewise, for DMRs, the range was 1-30 (Mean=1.5). Genes with the greatest number of DMCs (top 25) and DMRs (top 20) are in Table 4.5.

Table 4.5. Genes containing the greatest number of DMCs/DMRs

DMC		**DMR**	
Number	**Gene symbol**	**Number**	**Gene symbol**
86	*Gnas*	**30**	*Ndrg4*
47	*Pcdhga1*		
43	*Pcdhga3, Pcdhga2*	**18**	*Grk6*
36	*Slc8a1*		
33	*Muc19, Camta1*	**16**	*Sgk1*
31	*Pcdhga5, Nfasc*		
30	*Pde11a, Camk2b*	**12**	*Camk2b, Tpm1*
29	*Ctdspl*		
28	*Pcdhga7, Adgrl2*	**11**	*Sipa1*
27	*Txndc15, Pcdhga8*		
26	*Bcl11b*	**10**	*Egfl7, Map7*
24	*Pcdhga9, Ndrg4*		
23	*Chat*	**9**	*Cdc20, Cngb1, Khsrp, Lrrc45, Naca, Plcb2*
22	*Ppil*		
21	*Gbr10, Celf4, Ank3*	**8**	*Ank3, Apc2, Arhgef1, Lama5, Slc26a6, Snurf*

Along with range in number of DMCs/DMRs mapped to any given gene, the observed percentage change in methylation of DMCs ranged from -78.44% to +85.95% and for DMRs this was -75.69% to +75.93%. The top ten greatest changes in %methylation for DMCs/DMRs are shown in Table 4.6.

Table 4.6. DMCs/DMRs with greatest percentage change in methylation

DMC				**DMR**			
% Increase	**Gene symbol**	**% Decrease**	**Gene symbol**	**% Increase**	**Gene symbol**	**% Decrease**	**Gene symbol**
+85.95	*Ano6*	-78.43	*Ank3*	+75.93	*Agap1*	-75.69	*Ank3*
+81.12	*Crtac1*	-75.88	*Myom1*	+63.53	*Klhl29*	-74.04	*Gfra2*
+79.70	*Stau2*	-75.70	*Plpp3*	+63.20	*Fam126b*	-71.37	*Etv5*
+79.44	*Fam217a*	-74.77	*Gal3st3*	+61.05	*Dlgap2*	-64.93	*Peli2*
+75.93	*Agap1*	-74.04	*Gfra2*	+61.04	*Chst8*	-63.90	*Sox13*
+73.56	*Ffar1*	-73.27	*Tfga*	+58.08	*Miat*	-61.81	*Svil*
+73.48	*Ift46*	-72.95	*Ank3*	+57.07	*Agbl4*	-60.95	*Tmem178a*
+71.98	*Slc38a8*	-72.19	*Hpd*	*+56.31*	*Ptn*	-59.76	*Slc4a1*
+70.05	*Pax7*	-71.96	*Iqsec2*	*+55.89*	*Rai1*	-58.97	*N4bp1*
+69.15	*Pard3*	-71.79	*Dpp4*	+55.15	Rgs5	-58.47	*Acvr1b*

4.3.4.2. Gene function analysis

I. Tissue enrichment

To validate the tissue enrichment of the RRBS-identified genes, tissue gene enrichment analysis was conducted. This showed that the differentially methylated genes were significantly enriched

for expression in the human cortex (Figure 4.17A) and mouse cortex, cerebellum, olfactory bulb and foetal brain (Figure 4.17B). Taken together, these findings support the functional relevance of the RRBS for the brain region of interest (i.e., PFC).

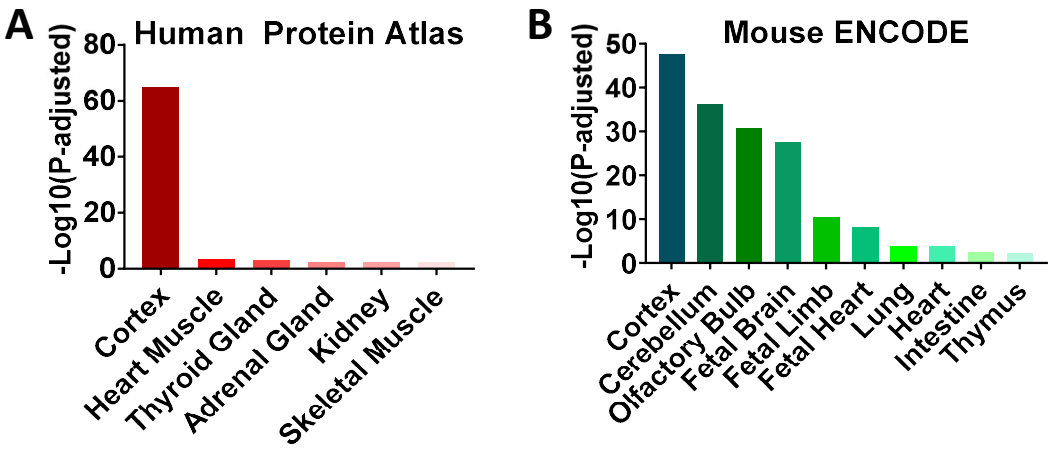

Figure 4.17. Tissue enrichment of RRBS genes
The RRBS gene set was input into Tissue Enrichment analysis (Jain and Tuteja, 2019) to assess the normal expression patterns of the differentially methylated genes. Both the Human Protein Atlas (**A**) and the mouse ENCODE (**B**) dataset were used. A hypergeometric model was used to assess enrichment.

II. Gene family enrichment

The 4,029 genes identified as differentially methylated belonged to several gene families, ranging from membrane proteins to transcription factors. Of note, there were several gene families where there were ≥10 genes within the dataset, including:

- G-protein coupled receptor signalling: G-protein coupled receptors (*Gpr* gene family, n=12), Rho GTPase activating proteins (*Arhgap* gene family, n=13), Rho guanidine nucleotide exchange factors (*Arhgef* gene family, n=11) and protein kinases (*Prk* gene family; n=17).
- Phosphatase proteins: protein tyrosine phosphatases (*Ptp* gene family; n=22) and protein phosphatase regulatory subunits (*Ppp1r* gene family; n=11).
- Transmembrane channel proteins: voltage gated calcium channel superfamily (*Cacna* genes; n=13, *Cacnb* genes; n=3, *Cacng* genes; n=5), potassium ion channels (*Kcn* gene family, n=46), kinesin superfamily (*Kif* gene family, n=14), ATP transporters (*Atp* gene family; n=21), solute carriers (*Slc* gene family; n=92) and transmembrane protein family (*Tmem* genes, n=33).
- Structurally-related proteins: coiled-coil domain-containing (CCDC) (*Ccdc* gene family, n=24), family with sequence similarity members (FAM) (*Fam* gene family, n=28), leucine-rich repeat containing (*Lrrc* gene family, n=14), ring finger (*Rnf* gene family, n=15), zinc finger (*Zfp* gene family, n=35), tripartite motif (TRIM) family (*Trim* gene family, n=10) and WD-repeat domain (*Wdr* gene family, n=10).
- Cell adhesion/extracellular proteins: cell surface (CD) antigens (*Cd* gene family, n=13), collagens (*Col* gene family, n=16), cadherins (*Cdh* gene family, n=11) and protocadherins (*Pcd* gene family, n=33).
- non-coding genes: miRNAs (*Mir* gene family, n=28).

III. Gene Ontology and pathway analysis

Gene Ontology analysis was performed on the gene set inclusive of biological process (Appendix 8; Supplementary Table S8.1), molecular function (Appendix 8; Supplementary Table S8.2) and cell component (Appendix 8, Supplementary Table S8.3). The top ten biological processes (Figure 4.18) demonstrate an enrichment for functions in neuronal development, including synapse/axon generation and cell differentiation. Of note, within the top 20 biological processes (Appendix 8; Supplementary Table S8.1) there was also a significant enrichment for genes involved in behaviours relevant to schizophrenia, including locomotor behaviour, memory, learning and cognition.

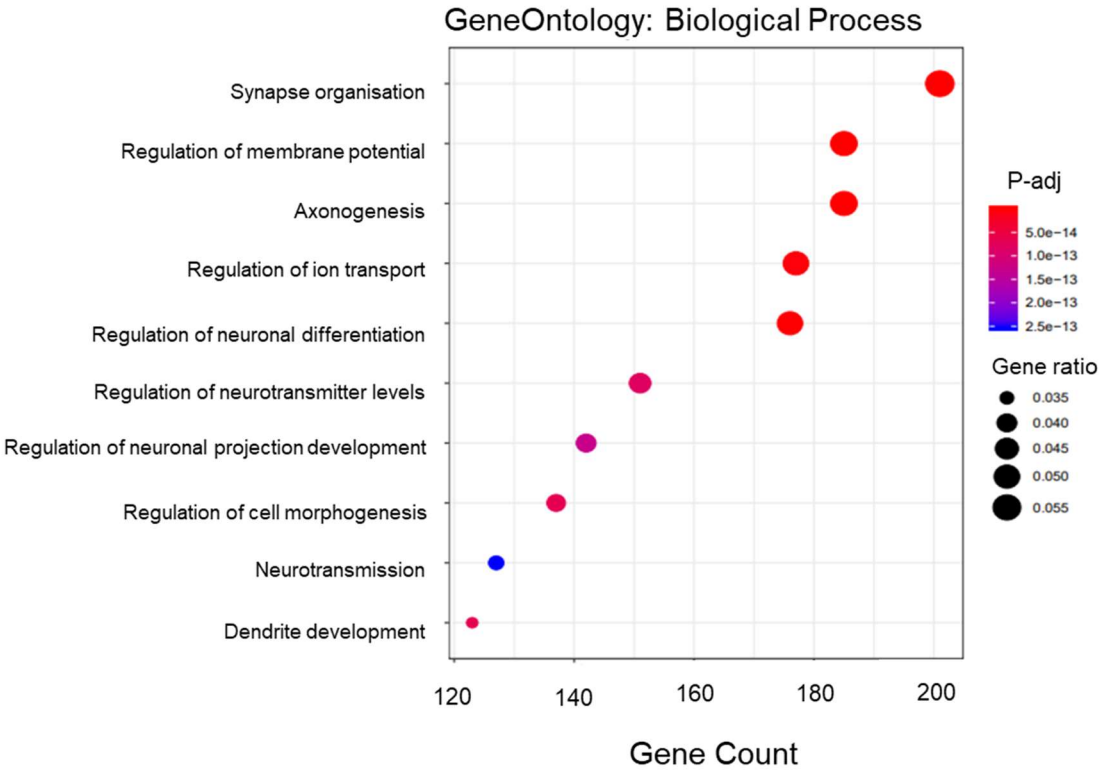

Figure 4.18. GeneOntology: Biological Processes
Gene ontology identifying biological processes for the 4,029 differentially methylated genes determined from the R/Bioconductor topGO package. Left lists the top ten biological processes. Size of the circle represents gene ratio (calculated as number of genes enriched/total number of genes in the dataset), while significance (adjusted p-value) is indicated by the colour, with red being the most significant. Enrichment analysis was performed using a hypergeometric model with Bonferroni correction.

For molecular functions, many of the top ten were associated with transmembrane transport/signalling (Figure 4.19), including those involved with ion transport by transmembrane channels. Of note, in the top 20 molecular functions (Appendix 8; Supplementary Table S8.2) there was also DNA-binding transcription factor activity, actin binding, kinase activity and cell adhesion. These aligned with the major gene family enrichments outlined previously (Table 4.5&6). The top ten cell components (Figure 4.20) were primarily enriched for synaptic membranes and within the top 20 (Appendix 8, Supplementary Table S8.3), there were also enrichments for cell-cell junctions and main/distal axon functions. This supports a role for the differentially methylated genes in normal neuronal function.

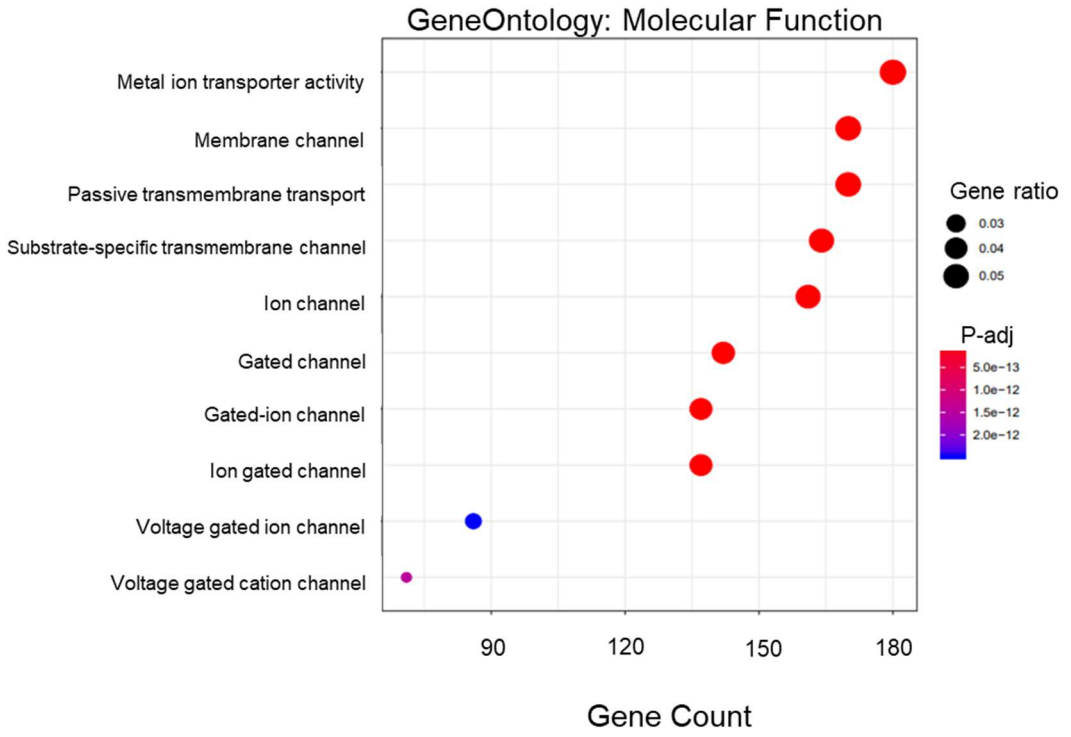

Figure 4.19. GeneOntology: Molecular Function
Gene ontology identifying molecular function for the 4,029 differentially methylated genes determined from the R/Bioconductor topGO package. Left lists the top ten molecular functions. Size of the circle represent the gene ratio (calculated as number of genes enriched/total number of genes in the dataset), while significance (adjusted p-value) is indicated by the colour, with red being the most significant. Enrichment analysis was performed using a hypergeometric model with Bonferroni correction.

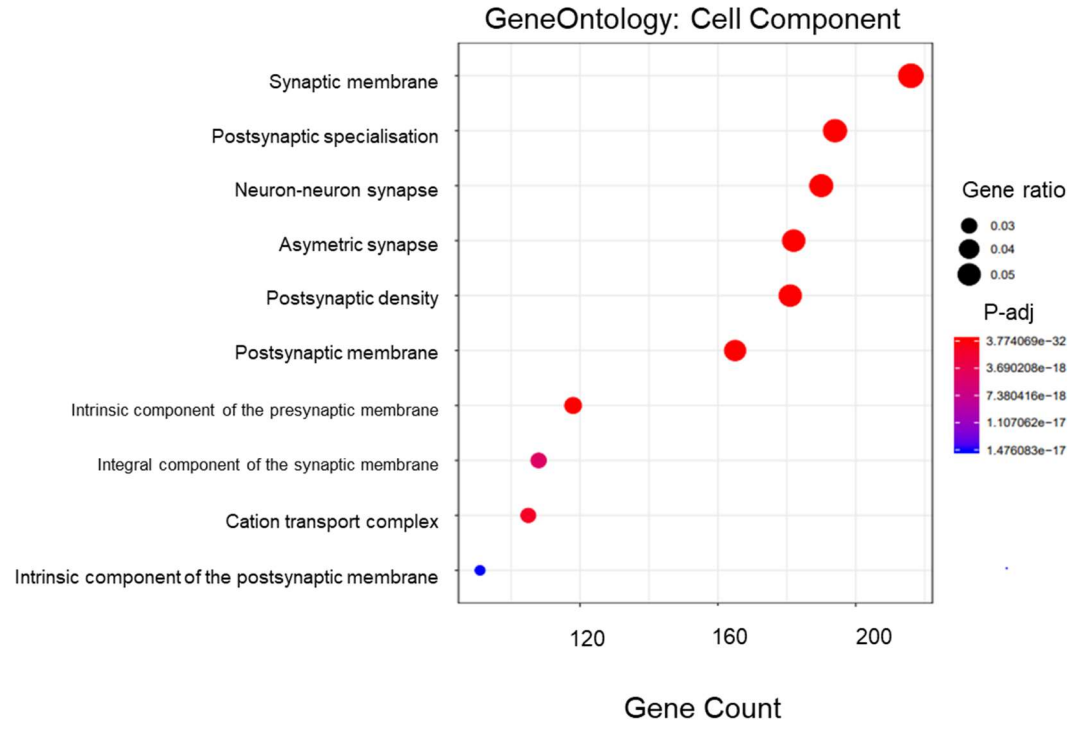

Figure 4.20. GeneOntology: Cell Component
Gene ontology identifying cell components for the 4,029 differentially methylated genes determined from the R/Bioconductor topGO package. Left lists the top ten cell components. Size of the circle represent the gene ratio (calculated as number of genes enriched/total number of genes in the dataset), while significance (adjusted p-value) is indicated by the colour, with red being the most significant. Enrichment analysis was performed using a hypergeometric model with Bonferroni correction.

Taken together, the Gene Ontology assessments support an enrichment of the differentially methylated genes in neurodevelopmental processes and neuronal signalling, both implicated in the pathogenesis of NDDs.

Finally, the RRBS dataset was assessed via KEGG pathway analysis (Appendix 8, Supplementary Table S8.4). In support of the Gene Ontology findings, the KEGG pathway analysis showed that the top ten enriched pathways (Figure 4.21) were those involved in normal neuronal functional and neuronal signalling pathways and therefore further support disturbed neurodevelopmental processes.

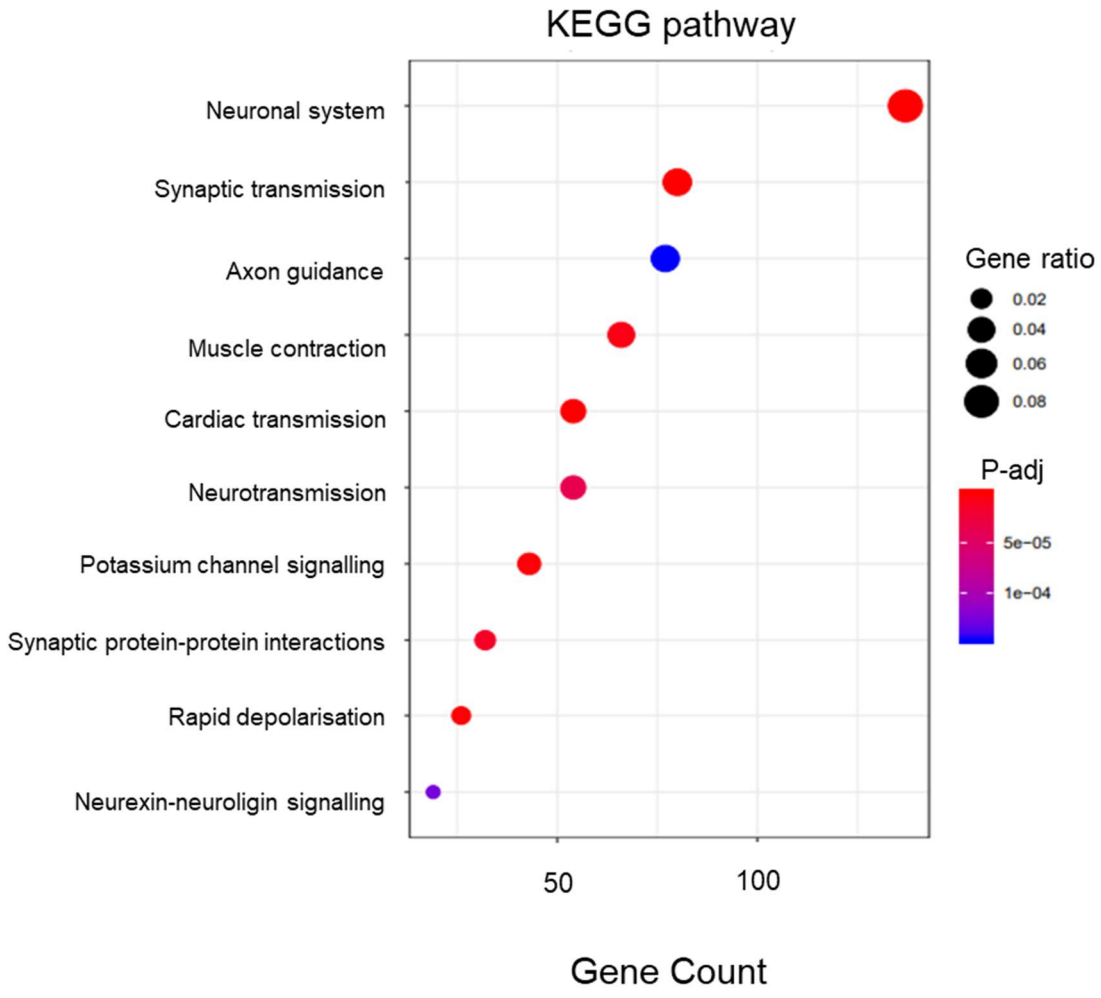

Figure 4.21. KEGG pathway analysis
KEGG pathway analysis for the 4,029 differentially methylated genes determined from the R/Bioconductor ReactomePA package. Left lists the tope ten KEGG pathways. Size of the circle represent the gene ratio (calculated as number of genes enriched/total number of genes in the dataset), while significance (adjusted p-value) is indicated by the colour, with red being the most significant. Enrichment analysis was performed using a hypergeometric model with Bonferroni correction.

IV. Disease enrichments

To determine whether the RRBS gene-set contained any known disease-risk genes, an analysis for DisGeNet genes was performed via Enrichr. The top five enriched diseases were all neurological disorders known to be at risk following MIA (Table 4.7).

Table 4.7. DisGeNet disease enrichment

Disease/Condition	P-value	Odds Ratio
ASD	$5.905e^{-22}$	1.77
Attention deficit hyperactivity disorder	$2.492e^{-18}$	1.92
BPD	$1.481e^{-18}$	1.63
Intellectual Disability	$1.152e^{-20}$	1.36
Schizophrenia	$1.233e^{-19}$	1.40

Behavioural phenotyping demonstrated a robust cognitive deficit in the ASST for MIA-exposed adult offspring, a task particularly relevant for schizophrenia. Likewise, schizophrenia was amongst the top five diseases with which the RRBS genes were associated. Accordingly, the RRBS gene-set was compared to distinct gene lists compiled from studies in schizophrenia, including expression studies (SZ_EXP), DNAm studies (SZ_ME), genome variant studies (Including GWAS and CNV; SZ_GENE) and whole exome sequencing studies (SZ_EXOME). In addition, to investigate the robustness of the observed findings, the dataset was compared to a whole genome bisulphite sequencing (WGBS) study performed in the PFC of adult male MIA-exposed mice (Richetto et al., 2017b), comparing against their DMC-genes (MIA_DMC) and DMR-genes (MIA_DMR). These analyses (Table 4.8) showed the RRBS gene-set significantly overlapped with all schizophrenia gene-sets. Notably, the RRBS gene-set demonstrated a highly significant, >50% overlap with genes identified from the MIA mouse-model with >2,000 genes differentially methylated in both studies. Individual gene overlaps are detailed in the RRBS summary dataset (Appendix 7).

Table 4.8. Gene list overlaps

LIST	OVERLAP	OR	CI	P-VALUE
MIA_DMC	2190	2.556591	2.407246-Inf	$\leq 2.2e^{-16}$
MIA_DMR	579	2.299769	2.102335-Inf	$\leq 2.2e^{-16}$
SZDB_EXP	133	1.445073	1.21642-Inf	$2.311e^{-4}$
SZ_GENE	299	1.937763	1.719449-Inf	$\leq 2.2e^{-16}$
SZ_ME	420	1.558069	1.410706-Inf	$2.219e^{-13}$
SZ_EXOME	1235	1.648668	1.545252-Inf	$\leq 2.2e^{-16}$

Abbreviations: OR, odds ratio; CI, confidence interval.

To focus on the most robust candidate pathways the RRBS gene-set was narrowed using a non-biased pre-defined method (see Section 4.2.7.4). 78 genes withstood the pre-defined acceptance criteria and were subsequently entered into STRING (Figure 4.22A). This analysis showed interactions between 54 of the 78 proteins. Gene ontologies of these proteins could be broadly divided into: neurodevelopment (red nodes); neuronal signalling, glutamatergic (yellow nodes); neurogenesis/gliogenesis (purple nodes); inflammation/stress responses (turquoise nodes); cell adhesion (green nodes). These pathways were interpreted as those pathways epigenetically altered by MIA and disturbed in schizophrenia and hence these pathways form the focus of subsequent chapters. These 54 interconnected genes can be found in Appendix 9, along with information on their selection criteria. Of note, single-cell expression analysis showed that many of these 54 interconnected genes are enriched for expression in glial cells (n=35; including oligodendrocytes (n=9), microglia (n=9) and astrocytes (n=25)), relative to neurons (n=25; Appendix 9, Supplementary Table S9.1; Figure 4.22B).

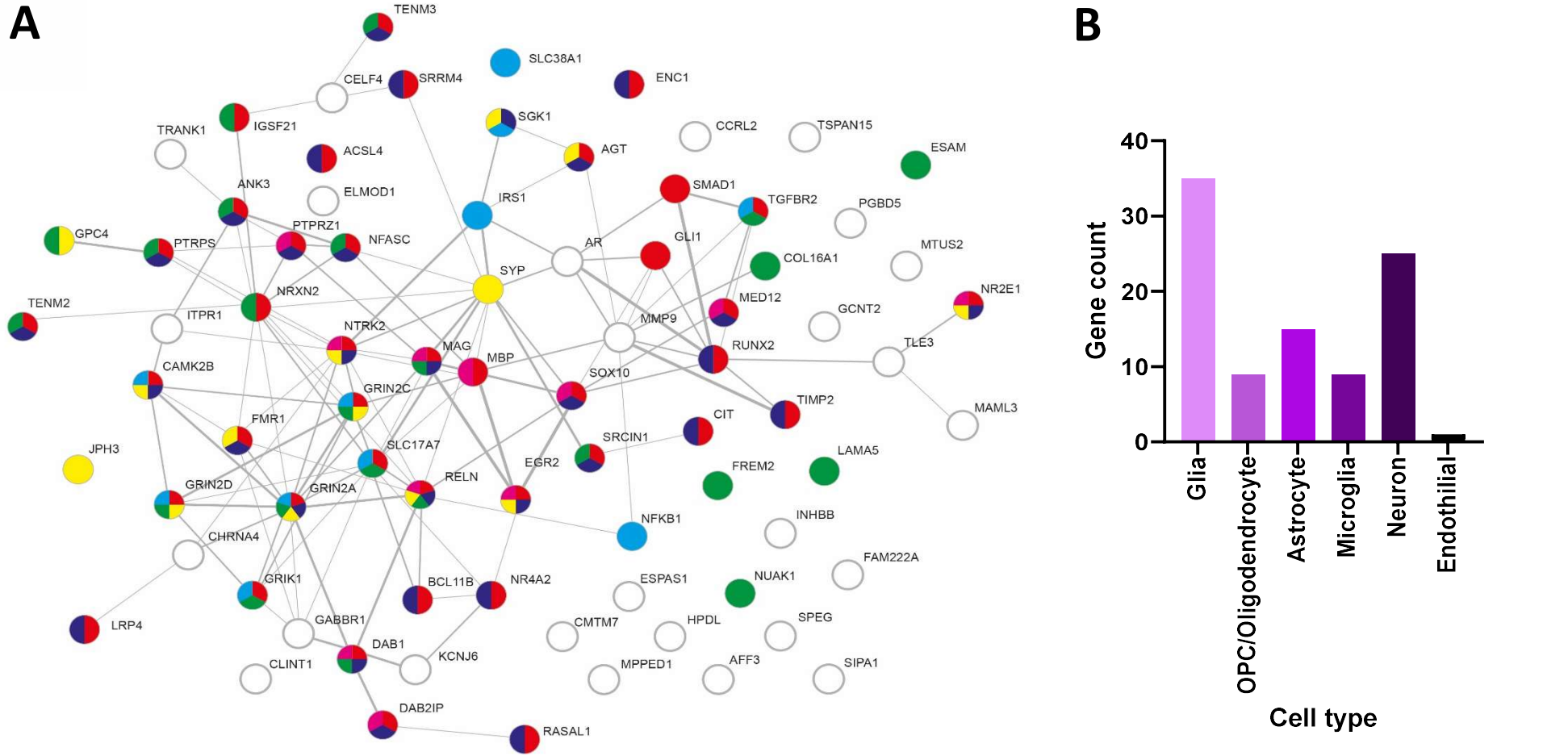

Figure 4.22. STRING network analyses

A. STRING analysis of the 78 genes which withstood the pre-defined acceptance criteria. Each node represents a protein, with lines showing protein interactions, either direct or within a signalling pathway. The thicker the line the higher confidence of the interaction. Outlying nodes showed no known interactions with the rest of the dataset. Coloured nodes indicate gene ontologies: red: general neurodevelopment; purple/pink: regulation of neurogenesis/gliogenesis; green: cellular adhesion; blue: inflammation/stress responses; yellow: glutamatergic signalling. **B.** Graph depicts the single cell expression enrichment (BrainRNAseq.org) for the 54 interconnected nodes from the STRING analysis. Where a gene showed enrichment in two cell types this was counted twice.

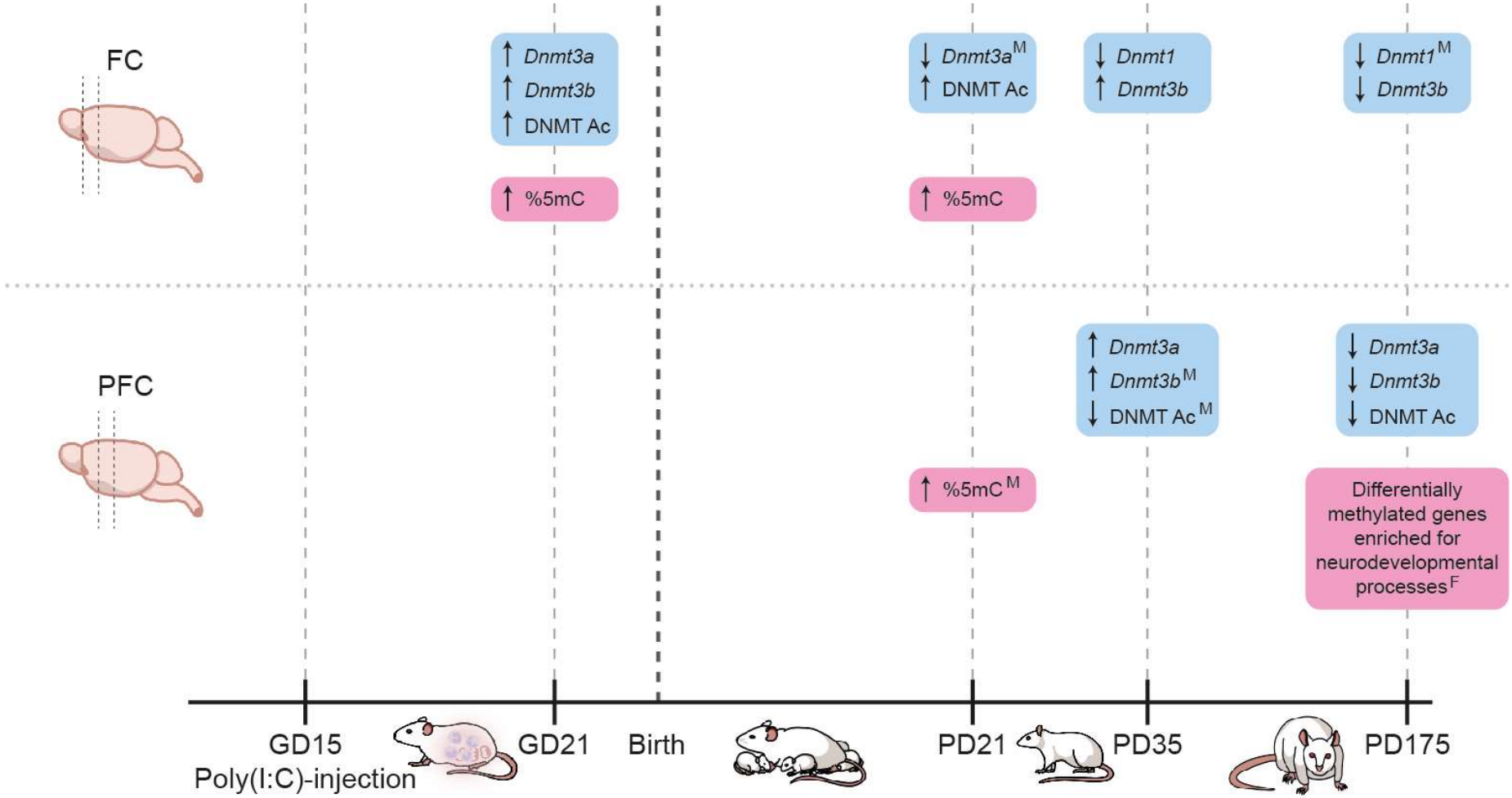

Figure 4.23. Summary of significant findings from Chapter 4
Summary of the MIA-induced molecular changes in the developing cortex. Timeline (bottom) indicates the developmental age; tissue analysed: frontal cortex (FC) or prefrontal cortex (PFC) are indicated on the left. Blue: DNMT changes, including individual *Dnmt* gene mRNA expression and DNMT activity (DNMT Ac); Pink: changes to DNAm, including global changes (%5mC) and gene-specific changes. Abbreviations: ↓Decrease; ↑Increase; F, female-specific result; M, male-specific result.

4.4. DISCUSSION

The key hypothesis of this Chapter was that foetal neuroinflammation (Chapter 2), together with placental transport disturbances and SAM/SAH availability (Chapter 3), would lead to functional changes in DNMT enzyme expression/activity and thereby genomic DNAm patterns in the developing cortex. Hence this Chapter aimed to determine the impact of MIA on developmental expression/activity of DNMT enzymes and how MIA-induced alterations in methylation pathways influence genomic DNAm patterns across the developmental period alongside which cellular pathways are impacted by such MIA-induced DNAm changes. These aims have been achieved, with key data demonstrating MIA-induced developmental changes in cortical *de novo* DNMT expression and concurrent dysregulation of DNMT activity. DNMT activity also appears, in part, driven by MIA-induced dysregulation of SAM/SAH availability (Chapter 3). These MIA-induced changes in cortical methylation pathways converge in altered DNAm. Critically, gene-specific DNAm analysis in the adult PFC demonstrated significant changes at pathways and genes with functional relevance for schizophrenia. The findings in this Chapter are summarised in Figure 4.23 and will be discussed in more detail below.

4.4.1. MIA induced developmental changes in *de novo* DNMT expression

The individual *Dnmt* gene expression patterns were distinct from each other. Expression of all *Dnmt* enzymes was higher prenatally, adhering to the understanding that prenatal brain development comprises large volumes of cellular differentiation and proliferation, which require radical DNAm changes (Moore et al., 2013). In line with the literature, *Dnmt1* expression was stably expressed across development (Figure 4.8A; Cisternas et al., 2019; Feng et al., 2007, 2010) while *de novo* DNMT expression demonstrated temporal changes at distinct developmental ages. *Dnmt3b* expression was highest prenatally, but displayed the lowest expression of the three genes postnatally (Figure 4.8C), while *Dnmt3a* expression peaked at PD21 (Figure 4.8B), during postnatal neuron maturation, remaining expressed throughout development at relatively higher levels than *Dnmt3b*, both patterns consistent with previous findings (Cisternas et al., 2019; Feng et al., 2007, 2010; Sendžikaitė et al., 2019; Watanabe et al., 2006). Despite this agreement, previous evidence has shown that expression of these enzymes and their functions, are highly cell-type specific in the cortex (Kadriu et al., 2012; Kozlenkov et al., 2014, 2018; Lister et al., 2013), hence full interpretation of the findings here are limited.

When assessing the impact of MIA on developmental changes in *Dnmt* expression, *Dnmt1* expression showed limited MIA-induced changes. This is unsurprising given that DNMT1 is the maintenance DNMT, hence large tissue-wide changes in expression would be anticipated as less likely to occur. That said, investigations into the role of DNMT1 in schizophrenia have suggested highly tissue- and cell-specific functions, with a particular role for its elevation in GABAergic interneurons where *Dnmt1* expression is notably enriched (Guidotti et al., 2007;

Veldic et al., 2004; Zhubi et al., 2009). Such changes would not be detectable here. By comparison, there were notable changes in expression of the *de novo* DNMTs. Expression of both *Dnmt3a* and *Dnmt3b* were increased in the GD21 FC in response to MIA (Figure 4.8B&C), with *Dnmt3a* increases correlating directly with maternal plasma IL-6 and TNFα concentrations. Chapter 2 demonstrated MIA-induced increases in foetal brain pro-inflammatory cytokines, including IL-6 and IL-1β, at 24h post-exposure. Studies have shown that cytokine signalling pathways induce increased DNMT expression (Guarnieri et al., 2020; Ibrahim et al., 2018; Komanda and Nishimura, 2022; Li et al., 2012; Morisawa et al., 2017; Mourtzi et al., 2021; Seutter et al., 2020) and hence it is speculated that foetal neuroinflammation following MIA increases expression of *de novo* DNMTs in the prenatal cortex. This response initially seems short lasting, with no evident changes in *de novo* DNMT expression at PD21. However, there was increased *Dnmt3b* expression once again in the PD35 FC and PFC (Figure 4.8C). This may imply altered DNAm patterns in adolescence, a critical period for cognitive development and synaptic plasticity (Morishita et al., 2015). Interestingly, there was then reduced *de novo* DNMT expression by PD175, significant in the PFC (Figure 4.8B&C). This may suggest an attenuated ability to establish dynamic DNAm patterns by adulthood, perhaps leading to reduced plasticity and memory formation, for which these enzymes have been suggested to be critical (Feng et al., 2010; Miller et al., 2010). Of note, there were often sex-specific changes in expression of these enzymes, with males showing elevated *Dnmt3a* and *Dnmt3b* expression relative to females in the PD175 FC and PFC, while in the PD35 FC and PFC, the inverse was true, with females having elevated *de novo* DNMT expression. These sexual dimorphisms may underscore normal sex differences in the developing brain methylome (Adanty et al., 2022; McCarthy et al., 2009).

Overall, the broader changes in the expression of *de novo* DNMTs relative to the maintenance DNMT1 implies a greater role for these enzymes in mediating adaptive DNAm responses to MIA. This is perhaps not surprising as any new DNAm patterns are firstly established by these enzymes and then maintained by DNMT1. Hence, ongoing alterations to DNAm patterns in response to MIA will be highly dependent on the function of the *de novo* enzymes. However, the analysis performed here was of *Dnmt* mRNA expression and, as outlined in Chapter 3, post-transcriptional and post-translational regulatory events mean there is not always direct correspondence between mRNA and protein expression (de Sousa Abreu et al., 2009). Hence, functional interpretations here should be taken with caution.

4.4.2. *Dnmt* expression and SAM/SAH ratios influence nuclear DNMT activity

Total nuclear DNMT activity was demonstrated to be higher prenatally than postnatally (Figure 4.9A), in agreement with previous studies (Moore et al., 2013) and the observed developmental expression of individual *Dnmt* genes (Figure 4.8A-C). There was a MIA-induced increase in total nuclear DNMT activity in in the GD21 and PD21 FC, with reduced activity in the PD175 PFC

(Figure 4.9). Patterns of DNMT activity, both prenatally and in adulthood, appeared to correspond to MIA-induced changes in SAM/SAH ratios and altered expression of *Dnmt3a* and *Dnmt3b*. However, it is important to note that DNMT activity measured here reflects total nuclear DNMT activity and hence which of the three DNMTs contribute to the activity changes cannot be delineated. Of note, only one previous study evaluated DNMT activity in a MIA model, identifying no differences in adult mice exposed to poly(I:C) *in utero* (Pujol Lopez et al., 2016). However, this study analysed whole brain samples, when there is likely marked regional differences, as observed here between the adult FC and PFC (Figure 4.9) and hence such granularity was likely missed in this previous study.

Total DNMT activity is driven by DNMT expression and the availability of metabolic precursors for the donation of methyl groups. In this regard, SAM and SAH increase and inhibit DNMT activity, respectively (Caudill et al., 2001). Given this understanding, these covariates were factored into the statistical modelling at each developmental age. Notably, the SAM/SAH ratio displayed a positive correlation broadly with DNMT activity across development (Figure 4.10), as would be expected. Likewise, there were mostly positive corelations with *Dnmt* expression and total nuclear DNMT activity. However, this was less consistent than observed for metabolites (Figure 4.11). This may imply that i) SAM/SAH availability has a greater influence on nuclear DNMT activity than *Dnmt* expression (as these enzymes are inherently rate-limited by SAM/SAH ratio (Caudill et al., 2001)); ii) in cases where DNMT mRNA expression and enzymatic activity do not correlate, mRNA expression may not represent protein expression; iii) other factors not measured here may be influencing the observed DNMT activity. It is likely that there are relationships between all three, acting as modulatory factors to DNMT activity. Indeed, often both *Dnmt* expression and cytosolic SAM/SAH had significant effects on DNMT activity in the majority of timepoints analysed. Notably, this is evident in the GD21 FC and PD175 PFC where the greatest changes in DNMT activity were observed. It could therefore be suggested that the increased SAM/SAH ratio (Chapter 3, Figure 3.8C) and *de novo* DNMT expression (Figure 4.8) observed in GD21 FC promotes increased DNMT activity, while in the PD175 PFC, reduced SAM/SAH availability (Chapter 3, Figure 3.8C) and *Dnmt* expression (Figure 4.8) results in reduced DNMT activity. Given that changes in *Dnmt* expression and cytosolic SAM/SAH ratios are driven by MIA, it can be postulated that MIA-induced disturbances in SAM/SAH ratios (as a result of altered amino acid transport or 1C metabolism) and *Dnmt* expression, leads to developmentally disturbed DNMT activity, which influences DNAm patterns and thus developmental gene regulation.

4.4.3. Altered cellular methylation pathways and MIA lead to global DNAm disturbances

As there were clear disturbances in the mechanisms which are necessary for normal DNAm, changes to global DNAm patterns were investigated using a %5mC ELISA. This showed that global methylation increased accordingly with age from prenatal to postnatal timepoints,

stabilising between adolescence and adulthood. This developmental pattern and percentage is in line with previous studies (Grodstein et al., 2021; Jin et al., 2023; Steg et al., 2021). There were significant MIA-associated increases in global DNAm in early cortical development in the GD21 FC, PD21 FC and PFC (males only). Interestingly, the magnitude of increase is most notable in the prenatal cortex. This is perhaps not surprising given that DNAm is highly dynamic in the foetal cortex with cells undergoing large waves of methylation changes during cellular differentiation/proliferation (Jobe and Zhao, 2017; Shirvani-Farsani et al., 2021), leaving these processes particularly vulnerable to inflammatory-induced epigenetic disturbances. Further, the global methylation changes observed across development were often sex-specific in response to MIA. This is a finding that has been noted in schizophrenia previously, with highly different cortical methylomes described between male and female patients (Adanty et al., 2022).

When investigating the relationship between global DNAm and cellular methylation mechanisms (comprising SAM/SAH availability (Chapter 3, Figure 3.8C), DNMT mRNA expression (Figure 4.8) and activity (Figure 4.9)) across development, there were primarily positive correlations between both cytosolic SAM/SAH ratios and DNMT activity and global DNAm. Accordingly, these molecular predictors often had significant effects on global DNAm in the GLMM, particularly at timepoints where MIA-induced increases in global DNAm were observed. Hence, as already postulated, elevated DNMT activity and 1C-metabolite availability appear to drive MIA-mediated changes in global DNAm in early development. Indeed, it has been shown that excess methionine induces increased global DNAm (Chen et al., 2021b), supporting a link between excess methionine, SAM and epigenetic dysregulation. The early upregulation of amino acid transporters (Chapter 3, Figure 3.7) and concordant increased SAM/SAH ratios (Chapter 3, Figure 3.8C), would enable increased DNMT activity and DNAm. This global hypermethylation in early development could have critical neurodevelopmental consequences and lead to behavioural deficits of relevance to schizophrenia. It is well documented that LOF mutations in MECP2, a key functional mediator of DNAm, causes the neurodevelopmental disorder, Rett Syndrome, characterised by severe cognitive deficits. However, MECP2 gain of function (GOF) mutations (e.g., MECP2 duplication syndrome) present with mental retardation, stunted development, epilepsy and spasticity, along with ASD-like symptoms, depression and anxiety, suggesting that increased DNAm-driven gene repression also leads to neurodevelopmental deficits (van Esch, 2012). Hence, global hypermethylation is likely to promote similar phenotypes. Indeed, the methionine-induced animal model for schizophrenia, which results in DNA hypermethylation, is characterised by schizophrenia-like deficits (Wang et al., 2015). The key role of epigenetics in regulating development through cell-specific gene expression is likely to underpin such phenotypes. DNAm is critical for cell specification/differentiation during neurodevelopment and for ongoing cellular function and plasticity. The latter is important during adolescence for synaptic plasticity and learning during the critical period (Morishita et al., 2015) and hence could effect cognitive development. Collectively, these observations therefore support a hypothesis whereby MIA-induced changes in early cellular methylation mechanisms and, consequently, global DNAm, lead to ongoing

alterations in cellular signalling pathways causing disturbed neurodevelopment and adult cognitive deficit (Chapter 2, Figure 2.18). In line with this, a study in neuronal DNAm changes in schizophrenia, suggested that schizophrenia-associated differential methylation changes accounted for up to 40% of schizophrenia-associated differentially expressed genes (Jin et al., 2023), suggesting that the observed DNAm changes likely have functional consequences for the cortical transcriptome and the observed cognitive deficits. However, there were no significant differences in global DNAm in adulthood found here, although there were MIA-associated changes to *Dnmt* expression, DNMT activity and metabolite ratios, indicative of disturbed cellular methylation mechanisms in adulthood. Indeed, analysis demonstrated significant associations between these molecular covariates and global DNAm patterns in adulthood, indicating perhaps a more complex relationship between cellular epigenetic mechanisms and DNAm that does not manifest in a global DNAm phenotype. This could be attributable to demethylation pathways which have not been investigated here, or because the changes mediated by these mechanisms are more subtle. Nonetheless, if specific genes are epigenetically dysregulated, this could drive functional disturbances of particular pathways.

4.4.4. Gene-specific methylation changes in the PFC of adult MIA-offspring of relevance to schizophrenia

When assessing global DNAm changes at a gene-specific level, the adult female PFC was studied. The PFC was chosen, as this brain region is known to underpin higher cognitive function, in particular executive function, critical for the ASST. Changes in global DNAm have been linked to cognitive performance in schizophrenia (Ho et al., 2020) and hence evaluation of gene-specific DNAm changes in the adult female PFC would likely identify pathways important for the observed cognitive phenotype. However, this does present some limitations as sex-specific methylomes in schizophrenia have been documented (Adanty et al., 2022) and hence future work should also consider the male offspring PFC. Another methodological limitation here is that the sequencing technique used (RRBS) is inherently reliant on bisulphite-treatment and hence is unable to distinguish 5mC from 5hmC. In this respect, the analysis represented here is perhaps better described as a reflection of global DNA modifications rather than methylation. A future consideration would be the application of oxidative bis-seq which would allow for identification of 5hmC vs 5mC at each individual CpG (Booth et al., 2013). Nonetheless, as proof of concept, the data still supports large MIA-induced genomic differences in DNA modifications. Indeed, the RRBS identified >4,000 differentially methylated genes in the adult PFC following MIA. These genes were enriched for expression in the mammalian cortex, suggesting that these methylation changes likely result in changes in the PFC transcriptome. The differentially methylated genes were involved in neurodevelopmental processes, including synapse and axon generation and cellular differentiation and also involved in schizophrenia-associated behaviours, including anxiety, learning, memory and cognition, supporting a functional role for the differentially methylated genes in the genesis of the observed cognitive behaviours (Chapter 2, Figure 2.18; Potter et al., 2023). Of the genes identified, ion channels/receptors and G-

protein/calcium signalling families and adhesion molecules were among the largest families, by gene count. Interestingly, total DNAm analysis in schizophrenia blood samples across multiple studies showed notable changes in ECM and adhesion molecule genes (Hannon et al., 2021), consistent with the RRBS analyses presented here. Further, the observed changes in protocadherin methylation may be linked to the observed postnatal *Dnmt3b* disturbances as DNMT3b is known to regulate the methylation of this gene family during brain development (Shirvani-Farsani et al., 2021).

Notably, the RRBS gene-set was compared to disease datasets, showing a significant enrichment for NDD risk genes and a significant overlap between the RRBS gene-set and schizophrenia-risk genes (Table 4.7&8). Further, there was a significant >50% overlap observed with the study by Richetto and colleagues (Richetto et al., 2017b), which analysed MIA-induced DNAm changes in the adult male PFC in a mouse poly(I:C)-model. A recent re-analysis of the Richetto dataset demonstrated, as here, a significant enrichment for schizophrenia-risk genes (Johnson et al., 2022), supporting the relevance of the findings from these models for the disease phenotype. The overlap between these studies also suggests that the genes identified show robust changes in methylation in response to MIA across sexes and species and are likely functionally relevant in the development of the adult behavioural phenotypes.

Finally, unbiased criteria (Section 4.2.7.4) were used to narrow the 4,029 genes to candidate genes associated with both schizophrenia and MIA. Following this process, the top five gene ontologies were: general neurodevelopment, neurogenesis/gliogenesis, ECM, immune/stress responses and glutamatergic signalling (Figure 4.22A). Of interest, within this reduced gene list, several of the top differentially methylated genes (Table 4.5&6) were included: *Ank3, Bcl11b, Camk2b, Nfasc* and *Sgk1*, supporting the strength of the unbiased selection criteria. Further, *Slc38a1* (SNAT1) was also present in the final list, suggesting this gene may also be regulated by DNAm. Hence, the observed increase in *Slc38a1* expression in the adult PFC (Chapter 3, Figure 3.7C) supports DNAm-driven gene expression changes in this brain region.

4.5. SUMMARY

The data reported in this Chapter indicate that MIA induces developmental changes in *de novo* DNMT expression alongside a concurrent dysregulation of nuclear DNMT activity. Changes in DNMT activity also appear, in part, driven by MIA-induced dysregulation of SAM/SAH availability (Chapter 3) in the developing cortex. This postulates a link between altered 1C metabolism and altered epigenetic mechanisms in the developing brain. Notably, the most significant changes in these pathways were observed in the GD21 FC. Indeed, the results suggest that increased foetal SAM/SAH ratios (perhaps resulting from dysregulated folate and methionine transport; Chapter 3) and increased *de novo* DNMT expression, perhaps driven by foetal neuroinflammation (Chapter 2, Figure 2.15) promotes increased nuclear DNMT activity, which together could underscore the observed increases in genomic DNAm in the GD21 FC. These observed changes appear to persist through juvenile and adolescent timepoints (PD21-35) before showing the opposing patterns by adulthood (PD175). Notably, in the adult PFC there were MIA-induced disturbances in cytosolic SAM/SAH ratios (Chapter 3, Figure 3.8) and *de novo* DNMT expression, leading to reduced DNMT activity but no differences in total genomic DNAm. However, gene-specific DNAm analysis in the adult PFC demonstrated that, while there is no overt genomic hypermethylation or hypomethylation, there are significant specific differences in individual gene DNAm with functional relevance for schizophrenia. Epigenetic dysregulation of PFC development could have critical consequences, importantly, this study poses the question of how these DNAm changes contribute to observed adult cognitive deficits, a question which will be explored in subsequent chapters. In particular, future chapters will focus on specific schizophrenia-risk candidate genes, identified by the RRBS analyses and explore how these are epigenetically and transcriptionally dysregulated throughout development as a result of MIA. Further, it will be critical to identify if such changes precede the onset of cognitive deficits such that they could be ameliorated.

CHAPTER 5. MIA-induced changes to glial cell development

5.1. INTRODUCTION

Chapter 4 demonstrated profound epigenetic changes in the developing brain following MIA, showing that differentially methylated genes in the PFC of adult females with a cognitive deficit were enriched for pathways involved in neurodevelopment and brain function. DNAm patterns, in both healthy and disease states, are known to be highly cell-type specific (Kozlenkov et al., 2014, 2018; Mendizabal et al., 2019; Quina et al., 2006) and hence the observed differential DNAm patterns (Chapter 4) were likely driven by distinct changes within individual cell types. Indeed, a cell-type analysis of the differentially methylated genes showed an enrichment for genes specifically expressed from glial cells (Chapter 4, Figure 4.22A). This suggests particular alterations to the function of glial cells as a result of MIA, which will form the focus of this Chapter.

5.1.1. Neurodevelopment: a glial cell perspective

The brain is an incredibly complex organ, composed from billions of neurons and glia organised into intricate signalling networks (Azevedo et al., 2009). As previously outlined, a key hypothesis of MIA is that maternal inflammation disturbs offspring neurodevelopment, likely mediated through cytokine imbalances in the developing foetal brain, which alter cell developmental trajectories and thereby disturb postnatal brain maturation (Meyer et al., 2009b). Glial cells are abundant in the brain and can be subdivided into ‘microglia’ and ‘macroglia’ (Dietz et al., 2020).

5.1.1.1. Microglia

Microglia are considered the resident immune cells of the brain, believed to comprise ~10% of non-neuronal cells in the CNS (Dawson et al., 2003; Dos Santos et al., 2020). Microglia originate from monocyte precursors in the yolk sac, from which they migrate to the CNS in early foetal development, coinciding with the transition of neuro-epithelial cells to radial glial cells (Figure 1.3; Menassa and Gomez-Nicola, 2018; Tong and Vidyadaran, 2016). Migrating microglia first cluster in the SVZ, where NPCs form and then later populate the rest of the cortex during late prenatal development, remaining present throughout life through self-renewal (Tong and Vidyadaran, 2016). Under homeostatic conditions, microglia exist in a resting or ramified state, however, as the critical CNS immune cells, microglia are responsible for responding to injury and infection through phagocytosis of cellular debris and secretion of inflammatory mediators, notably cytokines and chemokines. Under these conditions, microglia transition to an activated state, including an ameboid “phagocytic” morphology or a hypertrophic “hyper-ramified” state (Fernández-Arjona et al., 2017; see Figure 5.2). Activated microglial states are typically triggered by stress (e.g., glucocorticoid signalling) and neuroinflammation (Frank et al., 2007; Perry, 2007). Beyond their role in neuroinflammation, microglia have crucial roles during neurodevelopment: influencing neuronal/glial cell differentiation through secretion of signalling molecules (e.g., cytokines) and phagocytosis of progenitor cell pools; synapse and

neurocircuitry formation through activity-mediated synapse removal and ECM degradation (Menassa and Gomez-Nicola, 2018; Reemst et al., 2016; Tong and Vidyadaran, 2016). Hence, pathological activation of microglia during development could cause dysregulation of key neurodevelopmental processes. Further, aberrant activation of these cells during early development could lead to abnormal immune responses throughout development (Carloni et al., 2021; Hollander et al., 2020).

5.1.1.2. Macroglia

Macroglia are comprise both astrocytes and oligodendrocytes (Dietz et al., 2020) which sequentially arise from SVZ progenitors in the developing brain during a process known as 'gliogenesis', which commences at ~GD15 in rats (Gotz and Huttner, 2005; Marin et al., 2010; Tong and Vidyadaran, 2016). Thus, the MIA model used in this study, induced through administration of poly(I:C) on GD15, has the capacity to disturb this process.

I. Astrocytes

Astrocytes are specified first from radial glial cells in the SVZ during gliogenesis (Zheng et al 2022). The switch from neurogenesis to gliogenesis (i.e., the gliogenic switch) is primarily driven by the IL-6 family of cytokines and various bone morphogenetic proteins (BMPs), which promote intracellular signalling cascades which induce gliogenesis at ~GD15 in rats (Miller and Gauthier et al., 2007; Naik et al., 2017; Sarkar et al., 2019). Hence, immature astrocytes are present in the developing brain prenatally from GD16/GD18 in mice/rats, respectively (Bayraktar et al., 2015; Miller and Gauthier, 2007). Immature astrocytes proliferate during the early postnatal period, peaking at PD6/10 in mice/rats, to form mature astrocytes which account for ~35% non-neuronal cells in the adult brain (Verkhratsky et al., 2017; Zheng et al 2022). Astrocytes are critical during normal brain development, functioning in BBB formation, with barrier permeability regulated by astrocytic end-processes; axon outgrowth and synapse formation through secretion/presentation of key molecules including cytokines (e.g., TNFα/TGFβ), proteoglycans (e.g., glypicans) and morphogens (e.g., Wingless); and ECM formation through secretion of matrix components (Abbink et al., 2019; Allen and Eroglu, 2017; Reemst et al., 2016). Astrocytic processes also form primarily at synapses in the adult brain and modulate synaptic signalling via neurotransmitter secretion and uptake (Allen and Eroglu, 2017). Therefore, any perturbations in the development and function of these cells could have critical impacts on the developing brain. Further, as with microglia, astrocytes can also take on an activated state under stress or inflammatory conditions, called reactive astrogliosis, during which they secrete inflammatory mediators (Abbink et al., 2019; Pekny and Pekna, 2014; Sofroniew, 2014). Astrogliosis can be protective, aiding in the normal immune response, however excess astrogliosis can cause tissue damage, excitotoxicity and neuronal degeneration (Pekny and Pekna, 2014; Sofroniew, 2014).

II. Oligodendrocyte progenitor cells (OPCs) and oligodendrocytes

OPCs are also specified from the same population of SVZ progenitors which differentiate to form astrocytes. OPC specification is driven by various signalling pathways, including sonic hedgehog and fibroblast growth factor (FGF) signalling (Bergles and Richardson, 2016; Baydyuk et al., 2020). There are three waves of OPC generation during mammalian neurodevelopment. OPCs initially originate in the SVZ at ~GD12/GD15 in mice/rats (van Tilborg et al., 2018) with two later waves of OPC generation occurring in a progressively dorsal pattern within the ventral telencephalon at approximately GD15/GD18 and PD0/PD1 in mice/rats, respectively (Bergles and Richardson, 2016; van Tilborg et al., 2018). Pro-inflammatory cytokines, including IL-6, TNFα and IL-1β (upregulated in the foetal brain in response to MIA; Chapter 2, Figure 2.15), influence OPC proliferation and survival (Favrais et al., 2011; Taylor et al., 2010). Of note, OPC pools remain present in the mammalian cortex throughout life at a low-level comprising ~2-5% of non-neuronal cells in the brain (Dawson et al., 2003). This adult pool of OPCs has multiple roles, including modulation of synaptic signalling and replenishment of oligodendrocyte cell populations (Levine et al., 2001). That said, the majority of OPCs differentiate into mature oligodendrocytes, the critical myelin-forming cell in the brain (van Tilborg et al., 2018) accounting for up to 50% of non-neuronal cells in the adult brain (Valério-Gomes et al., 2018; Verkhratsky et al., 2017). This differentiation process occurs from birth into young adulthood, through differentiation first into pre-myelinating oligodendrocytes and then mature oligodendrocytes through expression of specific proteins (Figure 5.1; Kuhn et al., 2019). Oligodendrocyte differentiation is regulated by extracellular signals, including integrin-ECM contacts, neuronal activity and inflammatory signalling (Baydyuk et al., 2020; Lourenço and Grãos, 2016). Mature oligodendrocytes function to myelinate axons and support ECM structures (Carulli et al., 2006; Hamashima et al., 2020). The formation of these structures is critical for normal neuronal signal propagation along the axon, synapse formation, plasticity and synaptic receptor density (Saab and Nave, 2017; Xin and Chan, 2020). ECMs and myelin sheaths also protect neurons from inflammatory damage (Saab and Nave, 2017).

Myelin is a critical structural component of the CNS, formed from the wrapping of oligodendrocyte processes around axons (Stadelmann et al., 2019). The membranes and cytoplasm of these processes subsequently compact, followed by the enrichment of lipids and critical myelin proteins within the compacted layers (Stadelmann et al., 2019). These proteins include myelin basic protein (MBP), myelin associated glycoprotein (MAG), myelin oligodendrocyte glycoprotein (MOG), 2′,3′-Cyclic nucleotide 3′-phosphodiesterase (CNP) and proteolipid protein (PLP; Akiyama et al., 2002; Stadelmann et al., 2019). Myelination is a tightly regulated process, beginning in the early postnatal period in rodents and continuing into adolescence, peaking at ~PD20-21 in rats (Sarkar et al., 2019). For example, expression of MBP, accounting for ~1/3 of myelin composition, consists of various isoforms that are developmentally regulated through alternate splicing, with exon 2-containing isoforms involved in active myelination and hence expressed predominantly during early development, while exon

2-spliced isoforms are the primary MBP isoforms in mature myelin structures (Martinsen and Kursula, 2022; Siu et al., 2015). The temporal expression and splicing of myelin genes are regulated by various oligodendrocyte transcription factors, including OLIG1/2, SOX10, MYRF and QKI (Figure 5.1; Emery and Lu, 2015; Wu et al., 2002). Myelin structures are susceptible to inflammation and degradation, leading to demyelination of axons. Remyelination can be achieved in later development through the differentiation of adult OPCs into mature myelinating oligodendrocytes (Skaper, 2019).

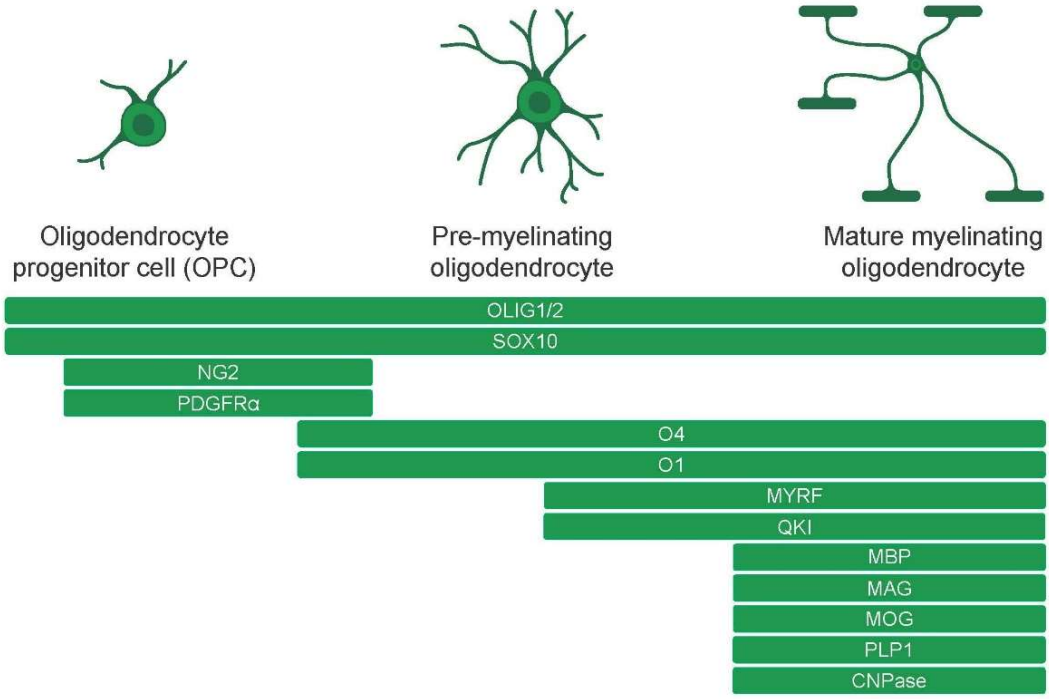

Figure 5.1. Oligodendrocyte differentiation
Oligodendrocyte lineage markers (OLIG) 1/2 and transcription factor SOX10 are expressed throughout the lineage. OPCs (PDGFRα+, NG2+) differentiate first into pre-myelinating oligodendrocytes (O4+, O1+) during which activation of transcription factors MYRF and QKI enable expression of myelin genes, promoting differentiation of mature myelinating oligodendrocytes (O4+, O1+, MBP+, MAG+, MOG+, CNAPse+, PLP1+).

5.1.2. Epigenetics in glial cell development

Epigenetic mechanisms play important roles in the development and function of both microglia and macroglia. For microglia, their ability to learn and adapt to immune responses has been suggested to be epigenetically regulated (Carloni et al., 2021). Indeed, microglial loss of MECP2, a critical DNAm-binding protein, induces dysregulated neuroinflammatory responses, with an altered transcriptome, favouring an exacerbated pro-inflammatory response (Cronk et al., 2015; Jin et al., 2015; Zhao et al., 2017). Further, microglial immune “priming” or memory has been hypothesised to be epigenetically programmed, though this work to date has primarily been investigated in relation to histone modifications (Martins-Ferreira et al., 2021). Moreover,

epigenetic mechanisms are important in the specification, differentiation and proliferation of different macroglia cell types from the SVZ NPC pool, with DNAm and demethylation required for the gliogenic switch. It has been shown that inhibition of *Dnmt1* in NPCs promotes astrogenesis (Fan et al., 2005) through hypomethylation of astrocyte-specific genes (e.g., *Gfap*) leading to upregulation of astrocyte-specific gene expression, thereby inducing astrocyte differentiation (Hatada et al., 2008; Takizawa et al., 2001). Likewise, inhibition of *Dnmt1* in OPCs has been shown to inhibit oligodendrocyte differentiation and maturation (Egawa et al., 2019) through disturbed expression of key myelin transcripts and perturbation of critical splicing events (Moyon et al., 2016). Moreover, in mature macroglia, DNAm changes have been implicated in astrocyte function and are thought to play a role in upregulation of genes promoting astrogliosis via STAT3-signalling (Neal and Richardson, 2018). In adult oligodendrocyte lineage cells, disturbances to DNA demethylation through activation of TET enzymes and DNMT inhibition, leads to reduced adult OPC differentiation and inhibited remyelination following injury (Arthur-Farraj and Moyon, 2021). Conversely, DNA hypermethylation in oligodendrocytes leads to dysregulation of various oligodendrocyte-specific transcription factors, causing aberrant myelin gene expression and abnormal myelination (Chen et al., 2021b). Of note, as with microglia, epigenetic memory has also been postulated in oligodendrocyte lineage cells which may affect their differentiation and mature function and increase susceptibility to myelin dysmorphology (Li et al., 2022).

5.1.3. Glial dysfunction in schizophrenia and MIA

Glial cell dysfunction is now a well-recognised pathologic feature in schizophrenia. As outlined in Chapter 2, neuroinflammatory disturbances are frequently identified in schizophrenia. In line with this, post-mortem schizophrenia brains have revealed increased active microglial density in critical brain regions (Bernstein et al., 2015; Frick et al., 2013), with such changes hypothesised to drive neuroinflammatory disturbances in schizophrenia (Laskaris et al., 2016). Functional changes to macroglia have been less well evaluated, but as with microglia, reactive astrocytes have also been identified in the brains of schizophrenia patients and are thought to further contribute to observed neuroinflammatory disturbances (Müller and Schwarz, 2010). Oligodendrocytes, by contrast, have been more frequently studied through their roles in myelination. Reduced white matter connectivity and integrity has been suggested to be an early-stage pathological marker of schizophrenia (Kubicki et al., 2003), with reduced expression of myelin proteins and consequent hypomyelination identified frequently in the brains of schizophrenia patients (Francisco et al., 2022; Vikhreva et al., 2016), with reduced white matter integrity specifically associated with cognitive deficits (Holleran et al., 2020; Zong et al., 2021). Further, differential DNAm of immune genes in peripheral blood samples has been linked to presentation of white matter deficits, indicating a plausible link between inflammation, epigenetics and oligodendrocyte pathology (Zong et al., 2021). Taken together, these studies support the role of dysfunctional glia in schizophrenia pathology.

Given the importance of cytokines in the role of glial cell development, these cells have also gained interest in the MIA field. Indeed, studies have shown increased microglial activation, reactive astrocytes and white matter abnormalities in the brains of MIA-offspring (Crum et al., 2017; Fernández de Cossío et al., 2021; Lee et al., 2021; Namvarpour et al., 2022; Ozaki et al., 2020; Page et al., 2021; Xia et al., 2020). Corresponding changes in expression of glial cell-enriched genes have also been explored in MIA models, with particular focus on glial cell markers *Iba1* and *Gfap*, enriched from microglia and astrocytes, respectively (Woods et al., 2021). However, the expression of these genes provide limited functional information without concomitant evaluation of cell density changes. Further, few studies have evaluated glial cell changes across the developmental timeline or evaluated epigenetic changes which may modulate MIA-induced glial cell dysregulation.

5.1.4. Chapter aims

Chapter 4 demonstrated hundreds of differentially methylated genes in the PFC of adult females experiencing MIA-induced cognitive deficits. These changes were enriched at genes expressed from glial cells. As outlined above, epigenetic regulation plays a fundamental role in glial cell development and function. It is therefore plausible that the observed gene-specific DNAm changes in MIA-exposed offspring may represent changes to glial cell development, leading to altered function. This is further supported by the evidence that cytokine signalling can alter the differentiation and proliferation of glia cells, postulating a mechanistic link between MIA, foetal brain cytokine imbalances and abnormal glial cell development. It was hypothesised in this Chapter that MIA and resulting foetal neuroinflammation would perturb the temporal development of macroglia and microglia, driven by differential methylation and consequent expression of glial-specific genes, thus, underscoring malfunction of these cells. To explore this hypothesis, glial gene targets were selected from the RRBS dataset (Chapter 4, Appendix 7) which are normally expressed only from one glial cell type (Appendix 9) and have demonstrated a previous association with schizophrenia (see Table 5.1 for summary of selected candidates evaluated in this Chapter). How these genes are dysregulated both transcriptionally and epigenetically by MIA has yet to be analysed, particularly across development. Hence, the overarching aim of this Chapter was to evaluate how the DNAm and expression of these gene candidates are developmentally impacted by MIA and whether there is any evidence of concordant glial cell maldevelopment by:

i) Evaluating the effect of MIA on individual glial cell densities/morphologies as a measure of cellular maldevelopment.
ii) Evaluating MIA-induced changes to glial-cell-specific gene regulation across development by measurement of DNAm profiles of selected candidate gene regulatory elements and how these correlate with changes in gene/protein expression.

Table 5.1. Summary of selected glial cell-enriched candidate gene functions

Summary of selected candidate gene functions, alongside their associations with neurological diseases and changes previously identified in MIA models. RRBS finding indicates the gene regions and directionality of methylation changes identified. *Indicates the region used for downstream analysis.
§Note: this gene did not pass acceptance criteria for pyrosequencing but as it is closely related to *Mbp* that did satisfy this requirement, it was analysed for gene expression

Candidate gene	RRBS finding	Glial cell enrichment	Function(s)	Implication for role pathogenesis of neurological disease	Previous change in a MIA model	References
Sgk1 (Serum/ glucocorticoid regulated kinase 1)	↓Promoter* ↓Exon 10	Microglia	Upregulated in the brain in response to cortisol/corticosteroid signalling via glucocorticoid receptors to mediate downstream effects of this pathway.	Dysregulation of the SGK1-GSKβ pathway identified in schizophrenia patients. SGK1 is upregulated in major depressive disorder and reduced in post-traumatic stress disorder.	Differentially methylated in the PFC of adult mice.	Anacker et al., 2013; Dattilo et al., 2020; Licznerski et al., 2015; Richetto et al., 2017b; Stertz et al., 2021.
Irs1 (Insulin receptor substrate 1)	↑Exon 1* ↑Intron 1	Microglia	Activated downstream of insulin receptor, functions in downstream insulin signalling and modulation of inflammation.	*IRS1* promoter is differentially methylated in schizophrenia patient brains. Altered IRS1 phosphorylation identified in Alzheimer's and cognitive decline.	Differentially methylated in the PFC of adult mice.	Chen et al., 2015; Li et al., 2020b; Richetto et al., 2017b; Tanokashira et al., 2019; Wu et al., 2020.
Tgfbr2 (TGFβ receptor 2)	↓Intron 1* ↑Introns 3, 7	Microglia	Constitutive receptor for TGFβ, roles in anti-inflammatory signalling and microglial activation.	*TFGBR2* mRNA elevated in peripheral blood samples from schizophrenia patients. Dysregulated TGFβ in plasma of schizophrenia patients.	Differentially methylated in the PFC of adult mice.	Bierie and Moses, 2010; Numata et al., 2008; Pan et al., 2022; Richetto et al., 2017b; Zhang et al., 2019a.
Gpc4 (Glypican 4)	↓Promoter* ↓Intron 1	Astrocytes	Cell surface heparan sulphate proteoglycan, roles in synapse formation and regulating synaptic receptor density.	*GPC4* mRNA upregulated in Alzheimer's disease. Mutations in several glypicans identified in schizophrenia patients.	Differentially methylated in the PFC of adult mice.	Allen et al., 2012; Farhy-Tselnicker et al., 2017; Kamimura and Maeda, 2021; Ma et al., 2021; Richetto et al., 2017b.
Nfasc (Neurofascin)	↑Exons 21, 22 ↓Introns 1*, 4, 6, 7, 8 ↑Intron 22	Oligodendrocytes	Cell adhesion molecule, roles in perinodal ECM formation, axon outgrowth, synapse formation, myelination and neuron-glial interactions.	Genetic variants in the *NFASC* gene associated with schizophrenia. Elevated CSF NFASC in Alzheimer's patients.	Differentially methylated in the PFC of adult mice.	Chang et al., 2014; Duits et al., 2018; Fawcett et al., 2019; Richetto et al., 2017b; Roussos and Haroutunian, 2014; Wu et al., 2020.
Mbp (Myelin basic protein)	↓Exon 2* ↓Introns 1, 3	Oligodendrocytes	Major protein component in the myelin sheath, expressed form mature oligodendrocyte cells.	*MBP* gene variants and differential methylation identified in schizophrenia patients. MBP expression abnormalities and demyelination found in multiple sclerosis.	Differentially methylated in the PFC of adult mice. Differentially expressed in various MIA models.	Ayalew et al., 2012; Boggs, 2006; Martinsen and Kursula, 2022; Woods et al., 2021; Wu et al., 2020.

Candidate gene	RRBS finding	Glial cell enrichment	Function(s)	Implication for role pathogenesis of neurological disease	Previous change in a MIA model	References
§*Mag* (Myelin associated glycoprotein)	↓Exon 1 ↓Intron 11	Oligodendrocytes	Major component in the myelin sheath, expressed form mature oligodendrocyte cells.	Genetic variants in the *MAG* gene associated with schizophrenia.	Differentially expressed in various MIA animal models.	Ayalew et al., 2012; Boggs, 2006; Martinsen and Kursula, 2022; Woods et al., 2021; Wu et al., 2020.

5.2. MATERIALS AND METHODS

Note: the following methods were performed on samples collected from PR1 (GD21 FC) and PN2 (PD1 FC, PD21-100 PFC).

5.2.1. Quantification of glial cell density

5.2.1.1. Selection of glial cell markers

Owing to the over-representation of glial-enriched genes in the RRBS dataset (Chapter 4, Figure 4.22B), IHC and IF were used to quantify individual glial cell densities in the adolescent and adult PFC to evaluate if there were any morphological or developmental changes to these cell lines as a result of MIA. Glia can be broadly divided into microglia and macroglia (consisting of astrocytes, oligodendrocytes and OPCs). Various cell-specific glial markers exist, however, there is a lack of consensus in the literature regarding the optimal marker, with results varying in a regional, developmental and species-specific manner (Dawson et al., 2003; Jurga et al., 2020; Kuhn et al., 2019; Lin et al., 2017; Souza et al., 2013; Valério-Gomes et al., 2018; Waller et al., 2016; Zhang et al., 2019b), creating a challenge when selecting the best marker for each cell group. With this in mind, individual glial cell-specific markers were selected based on guidance from previous experimentation in-house (Murray et al., 2019), general literature consensus and antibody availability (Table 5.2). Following marker selection, antibodies were validated for optimal stain use. For all IHC/IF optimisations, see Appendix 14.

Table 5.2. Selection of glial cell-specific markers

Glial cell type	Selected marker	Reason for selections	References
Oligodendrocyte	OLIG2	✓OLIG2 is generally accepted to be representative of the entire oligodendrocyte lineage. ✗ OLIG2 will detect both immature and mature oligodendrocyte cells.	Kuhn et al., 2019; Valério-Gomes et al., 2018.
OPC	NG2	✓ Accepted marker for OPCs. ✗ NG2+ cells may also denote progenitors capable of differentiating into astrocytes.	Dawson et al., 2003; Kuhn et al., 2019.
Astrocyte	GFAP	✓Across species GFAP is recognised as being exclusively expressed by astrocytes. Other common astrocyte markers e.g., S100B, another astrocyte marker, is also expressed by OPCs. ✗ GFAP does not stain all cortical astrocyte cells.	Souza et al., 2013; Waller et al., 2016; Zhang et al., 2019b.
Microglia	IBA1	✓IBA1 is a well-recognised cross-species microglia marker on which we have successfully published before. ✗ IBA1 is also expressed by macrophages.	Jurga et al., 2020; Lin et al., 2017; Murray et al., 2019.

5.2.1.2. Immunofluorescence (IF)

Oligodendrocytes (OLIG2+ cells) and astrocytes (GFAP+ cells) differentiate from the same cellular progenitor pool, specified in rats on ~GD15 (the time of MIA induction in the model). Given that these processes are in part regulated by the IL-6 family of cytokines, it was hypothesised the ratio of these cellular groups may be disturbed. Accordingly, the aim was to quantify these two cell types from the same sample through a co-staining protocol. As co-staining is more amenable to IF than IHC, IF was selected to quantify these cell types.

Sectioned tissue samples (30µM) stored in cryoprotectant (see Chapter 2, Section 2.2.2) were drawn up using a Pasteur pipette and transferred to a labelled net-well, which was then placed in a cell culture plate well (12-well plate, Corning, Ewloe, UK) containing 2mL 1XPBS (Oxoid, Basingstoke, UK). The net-well containing the sample was then transferred through successive incubations of buffers, allowing infiltration of the buffer into the net-well, with containment of tissue sections within the net-well. This provided a useful technique to enable multiple incubations without risk of damaging tissue sections through excessive handling. First, the samples were washed 3x5min in 2mL 1XPBS to remove cryoprotectant. For antigen retrieval, the sample net-wells were transferred to a glass trough (74mmx105mmx85mm) containing 50mL antigen retrieval buffer (Table 5.3). The trough was then transferred to a water bath (SLS Lab Pro, Galveston, USA) heated to 80°C and incubated as per buffer-specific conditions (Table 5.3). The sample net-wells were returned to 12-well culture plates and washed 3x5min in 2mL 1XPBS. The samples then underwent protein blocking for 1h at room temperature in 1.5mL 5% serum protein block. 5% serum protein block was also used to dilute the primary and secondary antibodies and was prepared (10mL) as follows: 4µL Triton-X (Sigma-Aldrich, Gillingham, UK), 500µL normal goat serum (Vector Labs, London, UK), 9.496mL 1XPBS. Following protein block the sample was washed for 2x5min in 2mL 1XPBS prior to primary antibody incubation.

Table 5.3. Antigen retrieval buffers and conditions

Buffer	Buffer preparation	Incubation time	Antibody
Sodium Citrate	1.47g sodium citrate (Sigma-Aldrich) 350µL Tween 20 (Sigma-Aldrich) 500mL dH_2O pH6.0 (adjusted by HCl)	30min	anti-IBA1 anti-OLIG2/anti-GFAP
Tris-EDTA	1.21g Trizma Base (Sigma-Aldrich) 0.37g EDTA (Sigma-Aldrich) 0.5mL Tween 20 (Sigma-Aldrich) 1000mL dH_2O pH9.0 (adjusted by HCl)	10min	anti-NG2

As the IF was a co-stain protocol, the primary antibody solution contained two primary antibodies diluted together in 1.5mL 5% serum protein block and hence optimisation experiments (see Appendix 14, Section 1) were used to show that there was no cross-reactivity between these two primary antibodies (raised in different hosts, Table 5.4) that would influence staining patterns. Accordingly, samples were placed in 1.5mL primary antibody solution containing the optimal dilution of both primary antibodies (Table 5.4) and incubated for 48h at 4°C.

Table 5.4. Immunofluorescence primary antibody dilutions for glial cell markers

Antibody	Details	Dilution factor and titre
Anti-GFAP	Chicken polyclonal Abcam, ab4674 (Lot GR3368950; 19.4mg/mL)	1:3,000 (6.5µg/mL)
Anti-OLIG2	Rabbit monoclonal [EPR2673] Abcam, ab109186 (Lot GR3300367; 131µg/mL)	1:1,000 (0.131µg/mL)

Following primary antibody incubations, samples were washed 2x5min in 2mL 1XPBS and then transferred to 1.5mL secondary antibody solutions and incubated for 2h at room temperature in the dark. Secondary fluorescent antibodies (cross-reactive to the two primary antibody host species) were both diluted 1:1,000 (2µg/mL) in 5% serum protein block. Secondary fluorescent antibodies used were the goat anti-chicken IgY H&L Alexa Fluor® 488 (ab150169; 2mg/mL; Abcam, Cambridge, UK) for GFAP and goat anti-rabbit IgG H&L Alexa Fluor® 594 (ab150080; 2mg/mL; Abam, Cambridge, UK) for OLIG2. Following secondary antibody incubations, samples were then washed with 3x5min 2mL 1XPBS and then transferred from the net-wells to a petri dish containing dH_2O using a Pasteur pipette.

The sections were then carefully mounted using a paintbrush and Pasteur pipette onto Menzel Gläser SuperFrost® Plus adhesion slides (ThermoFisher, Oxford, UK) and left to dry at room temperature for 2h in the dark. Mounted tissue sections were then covered with Aqueous Fluoroshield Mounting Medium with DAPI (Abcam, Cambridge, UK), rapidly cover-slipped and left to dry for 1h at room temperature. Slides were then imaged within 48h at the Bioimaging Core Facility (University of Manchester, UK) using a 3D-Histech Pannoramic-250 microscope slide-scanner with DAPI (350/440 Ex/Em), FITC (Alexa Fluor® 488; 490/525 Ex/Em) and TRITC (Alexa Fluor® 594; 555/607 Ex/Em) filter sets. Images were acquired using a 5X, 10X, 20X and 40X 0.80 Plan Apochromat objectives (Zeiss) and uploaded into CaseVeiwer (v2.4.0, 3D-Histech, Budapest, Hungary) for analysis.

5.2.1.3. Immunohistochemistry (IHC)

IHC was selected to assess microglia (IBA1+ cells) using our in-house pre-optimised methodology (Murray et al., 2019). For NG2+ OPCs, while IF was desired to allow better comparison with the OLIG2+ cell staining, optimisation experiments (Appendix 14, Section 2) showed that IHC resulted in lower background signal than IF and hence NG2+ OPCs were quantified by IHC. As with IF, sectioned tissue samples (30µM) stored in cryoprotectant (see Chapter 2, Section 2.2.2) were drawn up using a Pasteur pipette and transferred to a labelled net-well which was then placed in a cell culture plate well (12-well plate, Corning, Ewloe, UK) containing 2mL 1XPBS (Oxoid, Basingstoke, UK). The samples were then washed 3x5min in 2mL 1XPBS. For antigen retrieval, the sample net-wells were transferred to a glass trough (74mmx105mmx85mm) containing 50mL antigen retrieval buffer (Table 5.3) and transferred to a water bath (SLS Lab Pro, Galveston, USA) heated to 80°C and incubated as per buffer-specific conditions (Table 5.3). The sample net-wells were then returned to 12-well culture plates and

washed 3x5min in 2mL 1XPBS. Samples then underwent two successive blocking incubations: a peroxidase block and a protein block. Endogenous peroxidase activity was blocked by incubation with 1.5mL 1.5% hydrogen peroxide block solution (150µL methanol (Fisher, Loughborough, UK), 1.5µL Triton-X (Sigma-Aldrich, Gillingham, UK), 22.5µL hydrogen peroxide (Sigma-Aldrich, Gillingham, UK), 1317µL 1XPBS) for 30min at room temperature on an orbital shaker, followed by 2x5min 2mL 1XPBS washes. The samples were then incubated in 1.5mL 5% serum protein block for 1h at room temperature. 5% serum protein block was prepared as follows (10mL): 4µL Triton-X (Sigma-Aldrich, Gillingham, UK), 500µL normal horse serum (Vector Labs, London, UK), 9.469mL 1XPBS. Following protein block, 2x5min 2mL 1XPBS washes were performed. Primary antibody dilutions were prepared in 1.5mL 5% serum protein block and incubated under antibody-specific conditions (Table 5.5).

Table 5.5. IHC primary antibody conditions for glial cell markers

Marker	Antibody	Dilution	Incubation
IBA1	goat polyclonal, Abcam, ab5076 (Lot: GR3374909; 0.5mg/mL)	1:2,000 (0.25µg/mL)	24h 4°C
NG2	rabbit polyclonal, Chemicon, AB5320 (1mg/mL)	1:500 (2µg/mL)	48h 4°C

After primary antibody incubations, the samples were washed 2x5min in 2mL 1XPBS and transferred to 1.5mL secondary antibody solutions and incubated for 2h at room temperature. Secondary biotinylated antibodies (cross-reactive to the primary antibody host species) were diluted 1:200 (7.5µg/mL) in 5% serum protein block. Biotinylated secondary antibodies included the horse anti-goat IgG antibody (H+L), biotinylated (BA-9500-1.5; 1.5mg/mL; Vector Labs, London, UK) for IBA1 and the horse anti-rabbit IgG antibody (H+L), biotinylated (BA-1100-1.5; 1.5mg/mL; Vector Labs, London, UK) for NG2. For detection of secondary antibody binding, the VECTASTAIN® ABC-HRP Peroxidase (Vector Labs, London, UK) and DAB (3,3'-diaminobenzidine) Substrate Peroxidase (HRP), with Nickel (Vector Labs, London, UK) kits were used. These solutions were prepared prior to use as per manufacturer's directions: for ABC, to 5mL 1XPBS, 1 drop reagent A (Avidin) and 1 drop reagent B (Biotinylated peroxidase) were added and the solution incubated for 30min prior to use; for DAB, to 5mL dH_2O, 2 drops of buffer stock solution, hydrogen peroxide and nickel solution and 4 drops DAB substrate were added. Following completion of secondary antibody incubation, samples were washed with 2x5min 2mL 1XPBS before incubation for 45min in the dark in 1.5mL ABC solution at room temperature. The samples were then washed 3x5min with 2mL 1XPBS and placed in 1.5mL DAB solution for 15 min, during which the samples began a colour change to purple-grey. The samples were then rapidly transferred to 2mL dH_2O to stop the colour change reaction. Free floating sections were then transferred from the net-well to a petri dish containing 1XPBS using a Pasteur pipette. The sections were carefully mounted using a paintbrush and Pasteur pipette onto Menzel Gläser SuperFrost® Plus adhesion slides (ThermoFisher, Oxford, UK) and left to dry at room temperature for 2h.

Once dry, the slides were dehydrated by successive incubations for 5min in 70%, 90% and then 100% (v/v) ethanol solutions. These solutions were prepared from 100% ethanol (Fisher, Loughborough, UK) diluted in dH_2O. Finally, the slides were incubated in Histo-Clear (National Diagnostics, Charlotte, USA) for 5min. DPX mounting medium (Sigma-Aldrich, Gillingham, UK) was used to fix coverslips (VWR, Lutterworth, UK) over the tissue sections.

Cover-slipped slides were left to set for 1 week and then imaged at the Bioimaging Core Facility (University of Manchester, UK) using a 3D-Histech Pannoramic-250 microscope slide-scanner with brightfield filter sets. Images were acquired using 5X, 10X, 20X and 40X 0.80 Plan Apochromat objectives (Zeiss) and uploaded into CaseVeiwer (v2.4.0, 3D-Histech, Budapest, Hungary) for analysis.

5.2.1.4. Negative controls

For both IHC and IF, negative controls were performed using: i) omission of primary antibodies; ii) replacement of primary antibody with corresponding concentration (µg/mL) of species-specific IgG (Table 5.6). No staining was observed in negative controls (see Appendix 14, Supplementary Figures S14.2&5&6), validating that the observed staining for each methodology was specific to primary antibody binding.

Table 5.6. IHC/IF negative controls (glial cell markers)

Primary antibody	Corresponding control
Anti-IBA1, goat polyclonal	Goat IgG Control Antibody (Vector Labs, I-5000-5)
Anti-NG2, rabbit polyclonal	Rabbit IgG, Control Antibody (Vector Labs, I-1000-5)
Anti-OLIG2, rabbit monoclonal	
Anti-GFAP, chicken polyclonal	Normal Chicken IgY Antibody, (Chemicon, AC146)

5.2.1.5. IHC and IF analysis

CaseVeiwer (v2.4.0, 3D-Histech, Budapest, Hungary) was used to analyse the tissue sections, with slide identifiers randomly generated to blind counters to sample identity.

I. Calculating cell density

First, each hemispheric PFC region on a slide was annotated using the Rat Brain Stereotaxic Co-ordinates as a guide (6^{th} Edition, Paxinos and Watson, 2007; Figure 2.2). A minimum of five PFC sections, corresponding to 10 split hemispheric sections per sample, were annotated on each slide. Three additional $1mm^2$ 'training' annotations were also drawn on the slides. The cells within these three training regions and one randomly selected PFC annotation, were manually counted, by two independent experimenters, using the built-in manual annotation tool within the software. These manual counts were used to train and test the efficiency of the automated scoring software.

Automated cell counting was performed within each defined PFC annotation using the CaseViewer software add-on, HistoQuant Wizard (3D-Histech, Budapest, Hungary). The

HistoQuant algorithm was “trained” to recognise the stain for each cell type, by manually identifying the stain within the three training annotations. Within the algorithm general settings: ‘fill gaps’ was set to full capacity and size exclusion settings for each cell type was set as per Table 5.7. Subsequently, the trained algorithm was employed to count the number of cells present in the training annotations and was required to be within ±5% of the manual count for each of the trained regions before proceeding. When this stage was passed, the average % accuracy of the algorithm at this stage was compared between groups, to ensure no over- or underscoring bias, with no significant differences identified.

Table 5.7. HistoQuant algorithm size exclusions

Stain	Lower size exclusion	Upper size exclusion
IBA1+	50	500
NG2+	50	500
GFAP+	20	500
OLIG2+	5	200

Size represents an arbitrary unit within the algorithm to distinguish background counting.

Successfully trained algorithms were then used to automatically count cells in all PFC annotations within the slide on which they had been trained. These automated cell counts were subsequently compared to the manually counted PFC annotation and were found to be within the range of -5.3% to +7.4% of the manual count, providing confidence in the robustness of the algorithm training. Following this final check, cell density per mm^2 of each PFC annotation was calculated and averaged across all PFC sections on a slide, to give an average cell density/PFC mm^2 for each sample.

II. Scoring microglia cell morphology

Given that IBA1+ microglia possess multiple morphologically disparate activation states, each with different functions, a quantification of the ratio of these various activation states within the PFC was undertaken. For this analysis, automated cell counting was not possible due to the morphological subtlety of the differences between IBA1+ microglia cell morphologies and the variability in DAB background staining, which together prevented the algorithm from accurately distinguishing microglial activation states with the granularity required. Instead, each automatically counted microglial cell from six randomly selected PFC annotations per slide were manually scored for their activation state. Based on previous publications assessing the morphology of rat IBA1+ cells (Fernández-Arjona et al., 2017, 2019; Kongsui et al., 2014; Morrison et al., 2017; Wyatt-Johnson et al., 2017), the automatically counted IBA1+ microglia were manually ‘binned’ into four morphological states: ramified/resting, rod-like, ameboid/intermediate and hypercomplex/hyper-ramified determined by distinct cellular structures (Figure 5.2). Each morphological state was then calculated as a percentage of total IBA1+ cells/PFC section, averaged across the six selected sections.

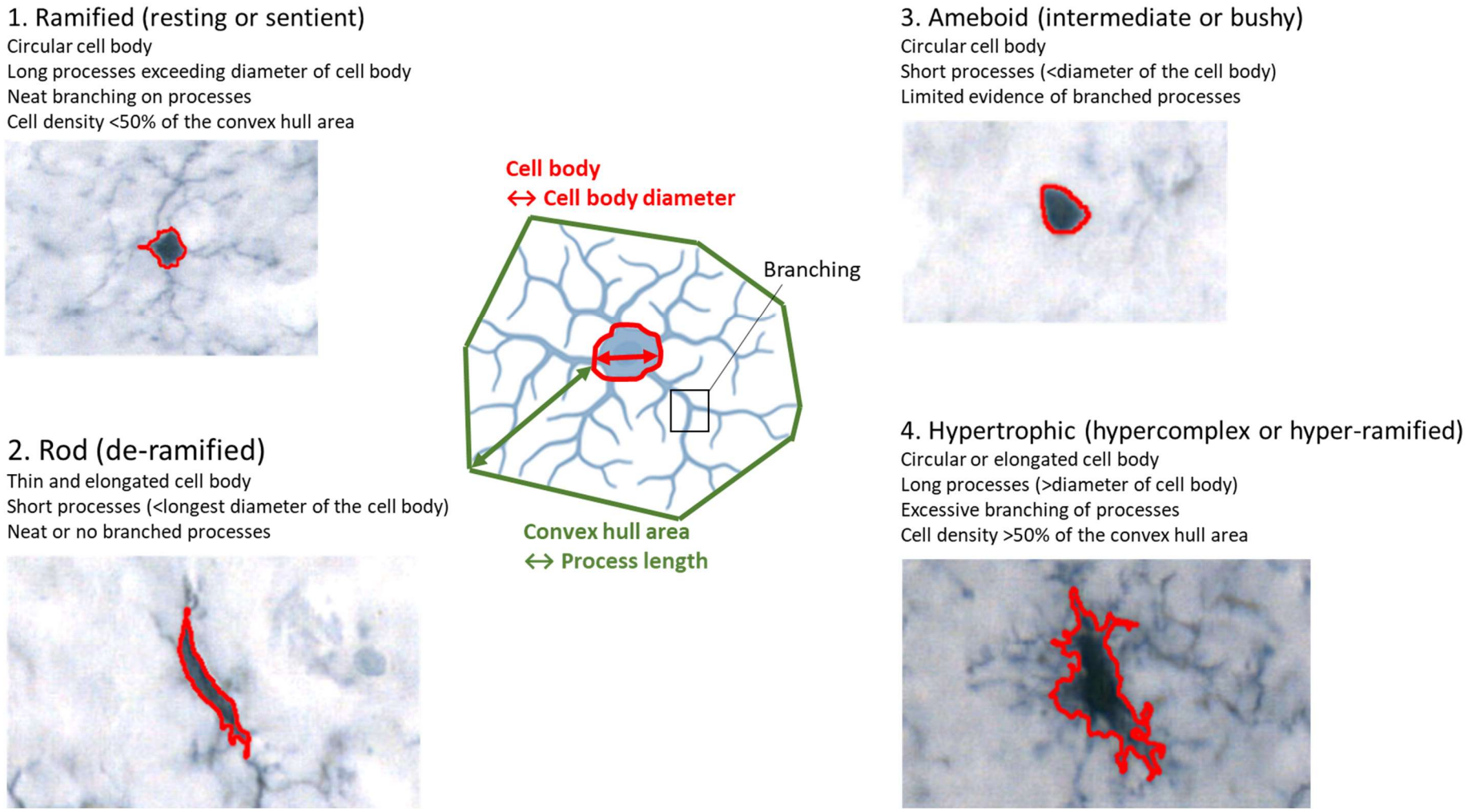

Figure 5.2. Morphological characterisation of microglia activation states
Depiction of the morphological scoring of IBA1+ microglia in the rat PFC. Using previous morphometric guidelines (Fernández-Arjona et al., 2017, 2019; Kongsui et al., 2014; Morrison et al., 2017; Wyatt-Johnson et al., 2017), the cell body, process length and branching and convex hull area were used to classify and therefore 'bin' the cells into four distinct morphological groups as shown.

5.2.2. Nucleic acid extraction

The nucleic acid extraction method employed in PN1 needed to be optimised for PN2 to support the sequencing methods. While the nucleic acid extraction methodology used for PR1/PN1 (Qiagen RNeasy and DNeasy kits; Chapter 3, Section 3.2.1.1) worked successfully on prenatal samples (Appendix 2, Supplementary Figure S2.1), these kits produced variable results for gDNA/RNA yields and quality from postnatal tissue (Appendix 2. Supplementary Figure S2.2). Hence, alternative methods were considered: i) a TRIzol™ Reagent (Invitrogen, Loughborough, UK) based method, ii) a non-membrane-based column extraction method (GenElute™, Merck, Gillingham, UK), iii) a membrane-based column extraction, with similar technology to Qiagen method, which negated the need of splitting the original lysate (InnuPREP DNA/RNA mini kit, Analytik Jena, Jena, Germany). These individual methodologies are outlined in Appendix 10. For all techniques trialled, RNA/DNA quantity was measured using ThermoFisher NanoDrop® and QuantiFluor® ONE dsDNA System (Promega, Southampton, UK), respectively, as described previously (Chapter 4, Section 4.2.1). While quality was assessed using agarose gel electrophoresis (Chapter 3, Section 3.2.1.2).

Accordingly, it was found that the innuPREP DNA/RNA mini kit (Analytik Jena, Jena, Germany) produced RNA and gDNA of optimal yield and quality for downstream analysis, when compared to other trialled methods (Appendix 10) or previously used Qiagen method (Appendix 2). Hence, this kit was used for all future nucleic acid extractions, performed as per kit instructions. Briefly, stored tissue samples in RNAlater were thawed on ice and excess RNAlater solution removed by aspiration. 500µL Lysis Solution RL was added to the frozen tissue sample and the sample homogenised with pestle until tissue was no longer visible. The sample was incubated for a further 10min at room temperature to allow complete sample lysis. The lysed sample was then transferred to Spin Filter D and centrifuged at 10,000xg for 2min. At this stage the gDNA binds to the membrane and the filtrate contains the RNA. 400µL 70% ethanol was then added to the RNA-containing filtrate and the solution added to Spin Column R and centrifuged at 10,000xg for 2min to bind the RNA. The spin columns containing DNA (D) and RNA (R) were then processed in parallel: 500µL wash solution HS was added and centrifuged at 10,000xg for 1min, followed by addition of 700µL wash solution LS, centrifuged at 10,000xg for 1min. In both cases the filtrate was discarded. The columns were then dried by centrifugation at 10,000xg for 2min. To the Spin Filter D 80µL Elution buffer was added and to Spin Filter R 50µL RNase-free water. The tubes were incubated for 1min at room temperature before centrifuging for 1min at 6,000xg to elute the samples.

5.2.3. Bisulphite-pyrosequencing

5.2.3.1. Assay design

Pyromark assay design software (v2.0.2., Qiagen, Manchester, UK) was used to design pyrosequencing assays for DNA regions of interest, as identified by the RRBS (Chapter 4,

Section 4.3.4) focusing on the final 54 interconnected genes (Chapter 4, Figure 4.22A; Appendix 9). Briefly, for each gene, the ≤100bp region of DNA sequence containing ≥2 DMCs was extracted from the UCSC genome browser (Rat assembly Rn5.0; Lee et al., 2022) including the 300bp sequences upstream and downstream. For each individual gene, this therefore created an input sequence up to 700bp in length. If the DMCs of interest were ≥100bp apart the candidate gene was excluded, as limiting technical factors reduce the pyrosequencing system's accuracy during longer sequencing reads (Mashayekhi and Ronaghi, 2007). The input sequences were uploaded into the assay design software as 'region of interest'. Pre-defined methodological criteria was used to exclude non-viable candidates: when a sequence was 'too CpG dense' such that the software was not able to design a specific assay, the candidate gene was discarded; occasionally (due to sequence composition/length) the DMCs of interest were not measurable in a single pyrosequencing assay therefore, due to sample constraints, these candidate sequences were deemed as 'non assayable' for the purpose of this study; candidate genes which returned poor pyrosequencing assay scores (<60%) were discarded as being unlikely to perform efficiently. Of the final candidate genes which passed the assay design stage, a final consideration was made to minimise the number of candidate genes for downstream analysis. Here, the directional changes in methylation (as identified by the RRBS), at all DMCs within the assayed sequence, were assessed. Genes were excluded for having bi-directional (increases and decreases) methylation changes in the same region, making functional interpretation challenging. Ten genes withstood the acceptance criteria (Appendix 9), six of which will be analysed here. Table 5.8 shows the top scoring assay for each gene (inclusive of forward and reverse PCR primers (one biotinylated) and sequencing primers). Primers were obtained lyophilised from Invitrogen (Loughborough, UK) and reconstituted to 100µM using Tris-EDTA buffer pH8.0 (Invitrogen, Loughborough, UK) and stored at -20°C.

5.2.3.2. Bisulphite conversion

For bisulphite conversion of DNA samples, the EZ DNA Methylation-Gold Kit (Zymo Research, Irvine, USA) was used. Briefly, gDNA samples were diluted to 100ng/20µL in nuclease-free water (Ambion, Waltham, USA). M-Wash buffer and CT conversion reagents were prepared as per kit specifications: by adding 96mL 100% ethanol (Fisher, Loughborough, UK) to the M-Wash buffer concentrate; and 900µL nuclease-free water (Ambion, Waltham, USA), 300µL M-Dilution buffer and 50µL M-Dissolving buffer to the CT reagent salt. The CT reagent salt was then left to dissolve for 10min at room temperature with regular vortexing. 130µL prepared CT conversion reagent was added to each 20µL DNA sample, followed by incubation in a ^{3}Prime thermal cycler (Techne, London, UK) at 98°C for 10min followed by a 64°C incubation for 2.5h. Following the incubation, 600µL M-Binding buffer was added to a Zymo-Spin IC column, followed by the reaction mixture from the thermal cycler. The column was then mixed by inversion. The Zymo-Spin IC column was centrifuged at 10,500xg for 30s and the flow-through discarded. 100µL M-Wash buffer was added to the column, centrifuged at 10,500xg for 30s and the flow-through discarded. 200µL M-Desulphonation buffer was added to the column and incubated at room

temperature for 18min after which it was centrifuged at 10,500xg for 30s and the flow-through discarded. Two further washes were performed, both using 200µL M-Wash Buffer with centrifugation at 10,500xg for 30s. The column was then transferred into a sterile RNAse/DNAse-free 1.5mL Eppendorf. 11µL M-Elution buffer was added to the column and centrifuged at 16,000xg for 30s to elute the bisulphite-converted DNA (bis-DNA). This process was performed twice for each sample in parallel and the two eluted volumes combined and stored at -80°C. A pooled bis-DNA sample (1µL pooled from each prepared sample) was created to use as a positive control to assess intra- and inter-plate variability during pyrosequencing.

5.2.3.3. Bisulphite PCR (bis-PCR)

Forward and reverse primers (Table 5.8) for bis-PCR were diluted 1:10 in Tris-EDTA buffer pH8.0 (Invitrogen, Loughborough, UK) to create 10µM stocks. Equal volumes of these 10µM solutions were combined to create a stock forward and reverse primer mix, with each primer present at a 5µM concentration. bis-PCR reactions used the Pyromark PCR kit (Qiagen, Manchester, UK). As per kit instructions, bis-PCR reactions were prepared as follows to create a final volume of 25µL: 12.5µL 2XPyromark PCR Master Mix, 2.5µL 10XCoralLoad Concentrate, 7µL nuclease-free water, 1µL 5µM forward/reverse primer mix and 2µL bis-DNA sample. For negative controls 2µL of nuclease-free water was added in place of sample and for positive controls 2µL pooled control sample was added. Prepared bis-PCR reactions were loaded onto a ^{3}Prime thermal cycler (Techne, London, UK) and incubated as follows: 15min 95°C (1 cycle); 30s 94°C, 30s 56°C, 30s 72°C (45 cycles); 10min 72°C. Following bis-PCR 5µL of product from each sample was assessed by agarose gel electrophoresis to confirm a single amplicon of predicted size (Table 5.8). Gels were prepared at 2% (w/v) agarose (Bioline, London, UK) in 1XTAE and a 1:10,000 dilution of GelRed (VWR, Lutterworth, UK). 1XTAE solution was prepared from a 1:50 dilution of 50XTAE stock (Cleaver Scientific, Rugby, UK). A 25bp HyperLadder™ (Bioline, London, UK) was loaded to assess bis-PCR amplicon size. Gel electrophoresis was performed in 1XTAE at 100V for 2.5h. Gels were visualised on a GelDoc XR (Bio-rad, Watford, UK) on automatic exposure. A representative bis-PCR gel for each gene can be found in Appendix 4, Section 3, Supplementary Figures S4.10-S4.15.

5.2.3.4. Pyrosequencing

Pyrosequencing was performed using the Pyromark Q24 Advance reagents, with enzyme and substrate salts reconstituted in 700µL nuclease-free water (Ambion, Waltham, USA). The Pyromark Q24 Advanced software and machine (Qiagen, Manchester, UK) were used for all pyrosequencing assays. The candidate gene assays were created with default settings using the ‘sequence to analyse’ generated by the assay design software (Section 5.2.3.1; Table 5.8).

Table 5.8. Pyrosequencing assay design

Gene	Genomic region (strand)	UCSC Rn5.0 genome reference	Sequence to analyse (total number of CpG sites)	bis-PCR forward primer (5'-3')	bis-PCR reverse primer (5'-3')	PCR product size (bp)	(Pyro)sequencing primer (5'-3')
Mbp	Exon 2 (+/-)	Chr18: 78480225-78480237	TTYGTAGTYGTTTYGGG TTGTGTTATATGTATAA GGTAA **(3)**	GGTAGGTATTTTGGTTAAAGTAGAGT	CCTATCCTAATCTATATAACCCTCTCA*	186	AGTAGGAGTTTTTTGTTTTTTTATG (+)
Nfasc	Intron 1 (-)	Chr13: 54573476-54,573,680	TYGTTAGTTAYGAAAGT TAGTGAATTYGGGGAG TAGTAAAATTTTAAAGT GA **(3)**	TTGGTAGTTTTTAGTTTAGAGGTATAGT	CTTCCTTAACTTCTCTCTCAATATTT*	286	GATTATGATAGGTTTAGGTTTT (+)
Gpc4	Promoter (+)	ChrX: 139513312-139513332	ATAGYGGATTYGGGGG TGGGGGGTGGGGGAY GGGATTTGG AATTTATAGTTGGG TTG **(3)**	ATAGTTTATTTTAGTGGGTTAGGGTTGTA	CTCTCAACCCAACTATAAATTCCA*	210	GTTATTGGTATTGTTTTGATTTAA (+)
Sgk1	Promoter (+)	Chr1: 25661285-25661295.	ATCCYTCTCCAATCCTA ACCATTCCYAACACYAA AAAAAAAC **(3)**	ATAGAAAGGGAAGGATTTGGATGT*	AAAAAAACCAATCTCAACAACTTAAT	129	ATTAAATAATAAAATTAACAAACC (-)
Tgfbr2	Intron 1 (-)	Chr8: 123670209-123670231	TTTTTGYGATGGGATTT GGAGGGTAATTYGGGT TAGGTGT TTTTATTGAA T **(2)**	AGTTTTTAGGAAGGAGTTTTAGTTT	TCTCTAACCTCACTATTTCCTAACCTACT*	228	AGGAGTTTTAGTTTTTGTATTA (+)
Irs1	Exon 1 (-)	Chr9: 87831272-87831355	TTGTGGYGTTTTATATT TTTATTGTTATTATYGTT GTTTTTTTTTGTAGTTTT TGTTTTAAAAGATATTG TGTTGTTAGTTYGYGTA GGYGTYGAGAAGGTTT **(6)**	TTGAGGGTGTTGTTTAATATTTTTGAT	CCAAAATAAACCTAAATCCCAACCATAA*	344	ATATATTTTTAAAGGATGTAGAG (+)

Key: Y-CpG sites identified by RRBS as increased in methylation. Y-CpG sites identified by RRBS as decreased in methylation. Y-additional CpG sites present within the sequence to analyse. *Biotinylated primer. +Positive strand. -Negative strand

In a 24-well PCR plate, 70µL bead solution (prepared by adding 26.4µL Streptavidin Sepharose High Performance beads (Sigma-Aldrich, Gillingham, UK) to a solution of 765.6µL dH_2O and 1056µL Binding Buffer) was added to each well. 10µL bis-PCR product was then added to each well, including 22 individual samples, 1 negative control (nuclease-free water only) and 1 positive control (Section 5.2.3.2). The plate was then shaken at 14,000rpm, at room temperature for 10min (MixMate PCR96; Eppendorf, Hamburg, Germany) to bind biotinylated PCR products to the streptavidin beads. During this incubation, the sequencing primer mix was prepared, consisting of 648µL Annealing Buffer and 2µL 100µM sequencing primer. Following the incubation, the vacuum pump on the Pyromark Q24 vacuum station was used to draw up the bead-bound sample from the PCR plate. These vacuum-bound samples were then processed through 70% ethanol (5s), denaturing solution (5s) and wash buffer (15s). All vacuum station buffers were prepared as per manufacturer's instructions (Table 5.9).

Table 5.9. Pyromark vacuum station buffer preparation

Buffer	Preparation
70% ethanol	700mL molecular grade ethanol (Fisher, UK) and 300mL dH_2O.
Denaturing solution	0.2M NaOH (Fisher, UK) in 1L dH_2O.
Wash buffer	10mM Trizma base (Sigma, UK) in 1L dH_2O. Adjusted to pH7.8 with acetic acid (glacial).

The vacuum was then turned off and the beads mixed on a Q24 pyrosequencing plate containing 25µL/well of prepared sequencing primer mix. The Q24 sequencing plate was incubated at 85°C for 2min (Dri-Block DB-2D; Techne, London, UK) before being loaded onto the machine. The machine cartridge was then prepared as per the software instructions, with 140µL of enzyme and substrate solution used for each gene assay, while nucleotide volumes were assay-specific (see Appendix 11, Section 1). The cartridge was then placed into the machine and the sequencing program commenced. The data was retrieved as %methylation at each CpG site in the sequence to analyse. The mean %methylation of the CpG sites within the sequence to analyse was also calculated to give 'average CpG methylation' across the sequence. All negative samples retuned no interpretable data while positive control samples showed clear passable peaks (see Appendix 11, Section 2). To assess expected sample variability the average CpG methylation of each assay positive control was compared across plates (Table 5.10). %CV was <1.7 for all assays, with methylation ranging <1.7% between the positive control repeats. These criteria therefore form the standard variability of the assays. Between-group differences in methylation percentage would hence be required to exceed this to be considered not just an artefact of assay variability.

Table 5.10. Pyrosequencing intra-assay positive control assessment

Assay	PC1	PC2	PC3	PC4	PC AV	%CV	PC RANGE
Mbp	95.67	95.33	94.67	94.33	95.25	1.08	1.34
Sgk1	60.75	61.00	60.50	61.00	60.81	0.39	0.50
Nfasc	49.33	49.67	51.00	50.00	50.00	1.44	1.67
Gpc4	35.33	35.67	35.67	35.67	35.58	0.47	0.33
Tgfbr2	28.50	28.00	29.00	29.00	28.63	1.67	1.00
Irs1	39.33	39.83	40.67	40.33	40.04	1.46	1.00

Results indicate mean %methylation of the CpG sites within each assay across four plates. Abbreviations: PC, positive control. AV, Average.

5.2.4. mRNA expression analysis

All reverse transcription and qPCR reactions were performed as previously described (Chapter 3, Section 3.2.2). Again, the Gene Globe software (Qiagen, Manchester, UK) was used, with the rat genome (*Rattus norvegicus*) searched for suitable primers for each candidate gene of interest. In this Chapter, this included genes identified in the RRBS analysis that were involved in glial cell development (Chapter 4; Appendix 9: *Mbp, Mag, Nfasc, Gpc4, Sgk1, Irs1, Tgfbr2*) alongside transcription factors closely involved in the transcriptional regulation of oligodendrocyte maturation (*Olig2, Myrf, Qki*). See Table 5.11 for a full list of QuantiTect primer assays used. As found previously, a 1:50 cDNA dilution was optimal for all candidate genes following a dilution trial, consistently producing Ct values 15-30 across development (Chapter 3, Section 3.2.2.2).

As previously described, stability of expression for six common reference genes: *Gapdh, Ubc, Ywhaz, B2m, Actb, Mdh1* (GeNorm primer panel, Z-HK-SY-RA-600; PrimerDesign Ltd., Chandler's Ford, UK) were analysed for PR1/PN2 samples using GeNorm (Vandesompele et al., 2002; Chapter 3, Section 3.2.2.3). Based on this analysis, it was determined that three reference genes (*Gapdh, Ubc* and *B2m*) were optimal for expression normalisation in developing cortex samples from PR1/PN2 (Appendix 3, Supplementary Figure S3.3). Notably *Gapdh* and *Ubc*, were also the most stable reference genes in PR1/PN1 suggesting robust stability of these reference genes between cohorts, while *Actb* remained the least stable reference gene. The geometric mean of the three selected reference genes was used to normalise candidate gene expression values.

Table 5.11. QuantiTect primer assays (Chapter 5)

Gene	QuantiTect primer assay (Cat no.)	Amplicon size (bp)	Exons spanned
Mbp	Rn_Mbp_1_SG (QT00199255)	117	1/2/3
Mag	Rn_Mag_1_SG (QT00199255)	118	7/8
Olig2	Rn_Olig2_1_SG (QT00386505)	92	-
Myrf	Rn_Myrf_2_SG (QT02374379)	102	4/5
Qki	Rn_Qk_2_SG (QT01683465)	161	2/3
Nfasc	Rn_Nfasc_1_SG (QT00174538)	96	5/6/7
Sgk1	Rn_Sgk1_3_SG (QT02349774)	114	9/10
Gpc4	Rn_Gpc4_2_SG (QT01586655)	117	6/7
Tgfbr2	Rn_Tgfbr2_1_SG (QT00182315)	81	3/4
Irs1	Rn_Irs1_1_SG (QT00374801)	111	-

Finally, agarose gel electrophoresis was performed to assess correct amplicon size, as described previously (Chapter 3, Section 3.2.2.4). A single clear band of predicted size (Table 5.11) was taken to indicate successful qPCR efficiency and the generation of a single, gene-specific amplicon. A representative qPCR gel for each gene is shown in Appendix 4, Section 3, Supplementary Figures S4.6-S4.15.

5.2.5. Preparation of cytosolic and membrane protein lysates

Cytosolic and membrane protein fractions were prepared from whole tissue lysates (Chapter 2, Section 2.2.3). For separation into cytosolic and membrane fractions, whole tissue lysate samples were centrifuged for 15min (800xg, 4°C) to pellet cellular debris and large organelles. The supernatant was transferred to a fresh Eppendorf tube and centrifuged for a further 20min (12,000xg, 4°C) to pellet cell membranes. The final supernatant, containing the cytosolic protein fraction, was removed into a fresh aliquot, while the pellet (containing the membrane fraction) was reconstituted in 25µL 1XPBS (Oxoid, Basingstoke, UK). Prepared protein fractions were stored at -80°C for later use. Protein lysate concentrations were quantified using a Bradford assay (Chapter 2, Section 2.2.3.1) where membrane and cytosolic fractions were diluted 1:100 before quantification.

5.2.6. ProteinSimple Western (WES)

WES kit reagents (ProteinSimple, San Jose, USA) were prepared as per manufacturer's guidelines: 40µL dH_2O was added to powdered DTT to produce a 400mM solution; 20µL 10XSample buffer and 20µL prepared 400mM DTT were added to the powdered fluorescent master mix to make a 5XFluorescent master mix solution; 20µL dH_2O used to reconstitute lyophilised biotinylated ladder; 200µL Luminol-S and 200µL Peroxide were mixed to create a Luminol-Peroxide solution. All protein lysate samples were diluted in 0.1XSample dilution buffer (prepared from 10XSample buffer diluted 1:100 in dH_2O) while antibodies were diluted in antibody diluent (refer to antibody-specific protocols for sample and antibody dilution factors). 4µL diluted samples were mixed with 1µL 5XFluorescent master mix and then denatured by heating in a water bath (SLS Lab Pro, Galveston, USA) at 95°C for 5min (cytosolic fractions) and 40°C for 30min (membrane fractions) as recommended by ProteinSimple and then stored on ice. The reconstituted biotinylated ladder, prepared samples, reagents, diluted primary antibodies and provided secondary antibodies were then loaded onto a standard WES plate as directed by the kit guidelines (see Appendix 12, Supplementary Figure S12.1). The plate was then spun briefly and loaded onto the WES instrument, after the addition of the wash buffer, along with the WES capillary. The standard WES protocol used the 12-230kDa 25 capillary cartridge (SMW003/4). All antibodies for selected candidate proteins of interest were tested for their suitability on the ProteinSimple WES platform as this platform allows for increased throughput and lower sample protein demand compared to a standard Western blot. For suitability on WES an antibody had to demonstrate a clear immunoreactive band at the expected molecular weight using the standard WES protocol, with minimal background/off target effects. For this Chapter, the only antibody which was shown to be compatible with WES was the anti-SGK1 antibody (rabbit polyclonal; 28454-1-AP, 900µg/mL; Proteintech, Manchester, UK), producing a band of anticipated molecular weight (55-58kDa) with limited off-target effects (Supplementary Figure S12.2). A representative WES blot image can be seen in Figure 5.3. For validation experiments see Appendix 12, Section 2.

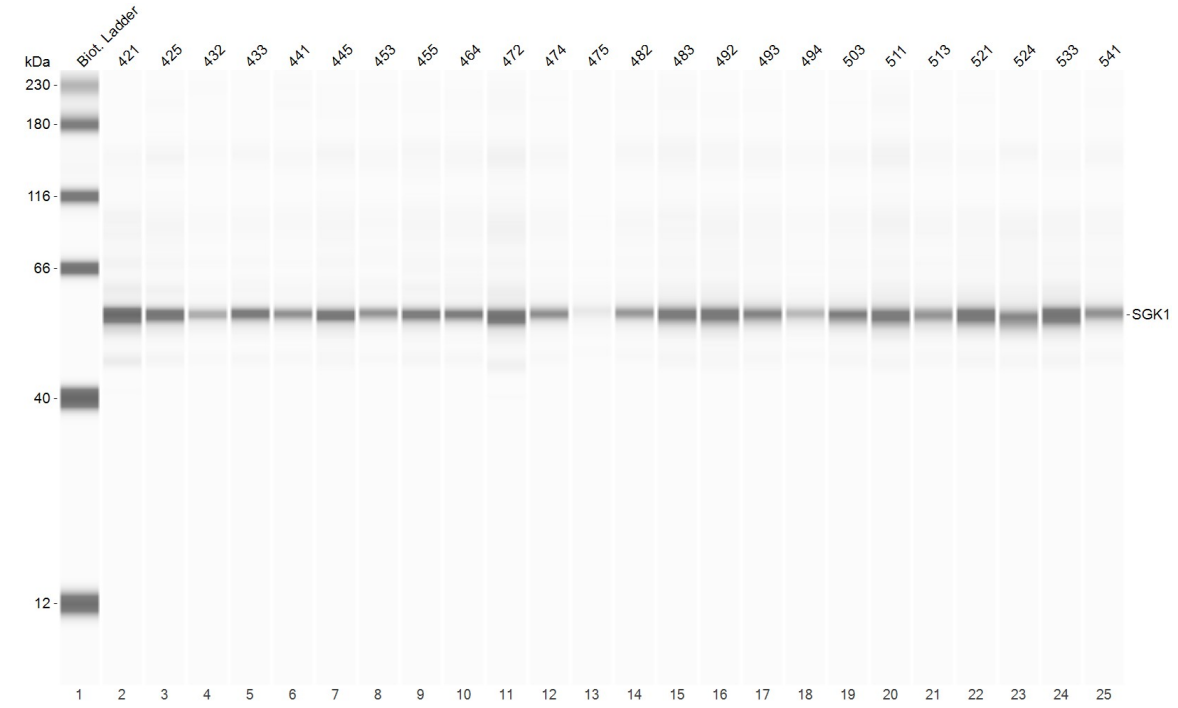

Figure 5.3. Representative WES blot image for SGK1
Figure shows the raw WES chemiluminescence image obtained by the WES machine for the anti-SGK1 antibody. The biotinylated ladder is shown in lane 1. Samples are in lanes 2-25 with sample ID indicated across the top. The anti-SGK1 band detected is at ~55-58kDa and is present in all lanes with varying intensity.

5.2.6.1. Antibody optimisations: determining the dynamic range

The WES dynamic range is defined as the experimental conditions under which the output signal increases in a linear fashion with protein concentration but where the antibody concentration is near saturation (Nelson et al., 2017). The dynamic range is required to enable reproducible, accurate signal quantification and was determined for each WES antibody (Appendix 12, Section 3). To achieve this, three protein concentrations at each developmental age were trialled in the selected cellular fraction along with four antibody concentrations. Graphs were plotted at each developmental age for: i) all protein concentrations for each individual antibody dilution using area under the curve (AUC); ii) all antibody concentrations at each individual protein concentration using peak height (chemiluminescence). Protein concentration graphs were assessed to identify the protein concentration within the linear phase of the curve. Antibody concentration graphs were assessed for the concentration where near signal saturation (curve plateau) was achieved. For the anti-SGK1 antibody used in this Chapter, the optimal experimental WES conditions are shown in Table 5.12.

Table 5.12. anti-SGK1 antibody optimal conditions

Timepoint/Tissue	Antibody dilution and titre	Protein concentration
GD21 FC	1:50 (18µg/mL)	1.4µg/µL
PD1 FC		1.4µg/µL
PD21 PFC		1.2µg/µL
PD35 PFC		1.0µg/µL
PD100 PFC		0.6µg/µL

5.2.6.2. Normalisation of target protein expression to total protein

To normalise target protein expression signal, ProteinSimple (San Jose, USA) total protein detection modules were used (DM-TP01). These modules attach biotin to all proteins in the sample. Subsequent incubation with streptavidin-HRP followed by Luminol-Peroxide generates a chemiluminescent signal for total captured protein. AUC of the total protein signal can then be used to normalise candidate protein AUC values. These assays were hence performed on all samples, at the same concentration at which they were optimised for the target antibody of interest (e.g., Table 5.12 for SGK1) and denatured under the same conditions. For these assays, preparation of the WES plate was as described previously (Appendix 12, Supplementary Figure S12.1), but instead of primary antibody the total protein labelling reagent was used and in place of HRP-conjugated secondary antibody, total protein streptavidin-HRP was used.

5.2.6.3. WES analysis

All WES experiments were analysed using the Compass for Simple Western software (v6.1.0, ProteinSimple, San Jose, USA). A WES output included a representative blot image (Figure 5.3) and an electropherogram quantifying chemiluminescence signal (Figure 5.4).

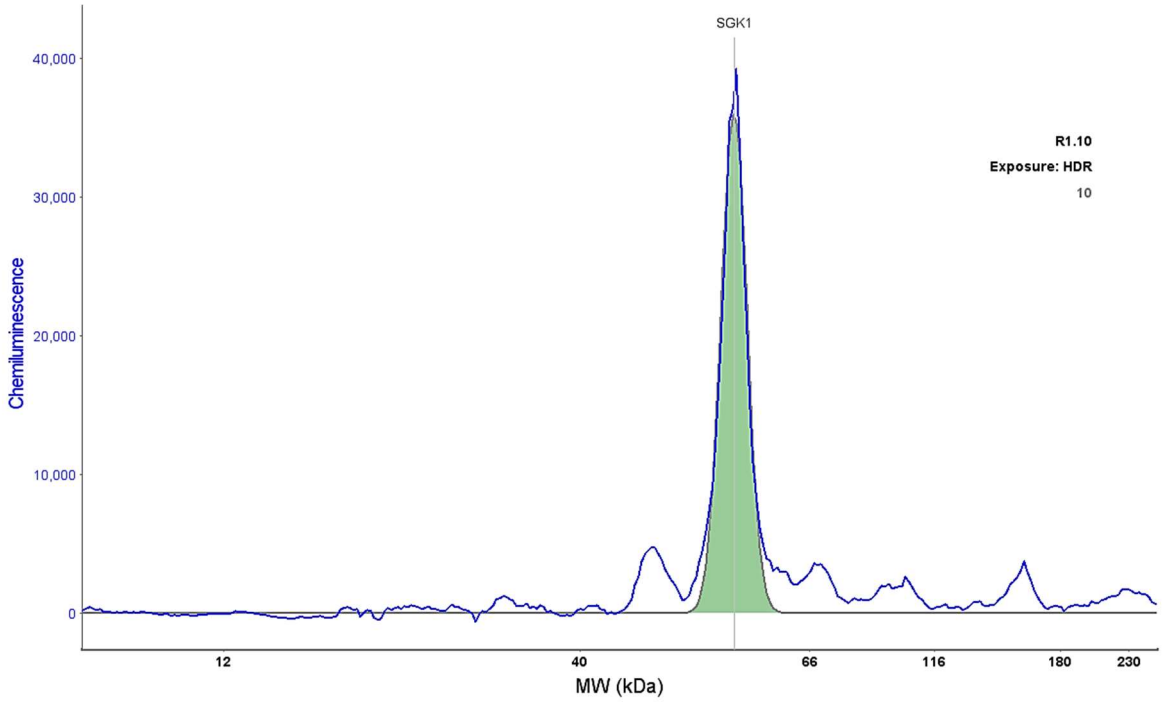

Figure 5.4. Representative WES electropherogram for SGK1
Figure shows a representative electropherogram of a sample on the WES machine. The primary SGK1 peak is indicated in green at 55-58kDa.

Default settings for the electropherogram analysis were used; with exposure set to high dynamic range (HDR) and automatic baseline fit. The peak of interest was identified manually and any other peaks excluded. For each sample, the AUC for the identified target protein peak was used as the target signal. This target protein AUC value was divided by the total protein AUC

(performed on the same sample at the same concentration), to give a normalised target protein expression value for statistical analysis.

5.2.7. Western blotting

All other selected target antibodies which were deemed incompatible with WES, were assayed using a standard Western blot. For this Chapter, this included the anti-MBP (rabbit polyclonal, 10458-1-AP, 500µg/mL; Proteintech, Manchester, UK) and anti-GPC4 (rabbit polyclonal, 13048-1-AP, 650µg/mL; Proteintech, Manchester, UK). Western blots were performed as described in Chapter 3, Section 3.2.3.2, unless otherwise indicated.

5.2.7.1. Western antibody validations

Each antibody was validated for its target specificity by protein size (as determined by the molecular weight ladder) and cell fraction enrichment, with developmental expression pattern used as further validation where applicable. In addition, negative control blots, which excluded the primary antibody from the assay, were used to show the specificity of the immunoreactive product against the background. See Appendix 13 for individual Western antibody validations.

Through these validation experiments, the anti-MBP antibody demonstrated immunoreactive bands at isoform sizes of approximately 14kDa, 17kDa, 18.5kDa and 21.5kDa (Supplementary Figure S13.1; Akiyama et al., 2002; Kruger et al., 1999), while the anti-GPC4 band was observed at the predicted molecular weight of ~62kDa (Supplementary Figure S13.3; Hagihara et al., 2000; Xiong et al., 2016) as anticipated in the rat brain. Further, in line with i) their functions as membrane-bound proteins, both were enriched in the cell membrane fraction (Supplementary Figures S13.1&3; Akiyama et al., 2002; Hagihara et al., 2000); ii) with neurodevelopment in the rat, MBP was also almost non-detectable, with the exception of a faint 21.5kDa isoform, in early development (GD21/PD1) prior to the onset of myelination at PD10, while postnatal MBP expression increased significantly between PD1 and PD100 (Supplementary Figure S13.2; Akiyama et al., 2002; Downes and Mullins, 2014). These validations demonstrated the specificity of the selected antibodies for the target proteins of interest. Further, negative control blots showed these bands were specific to the primary antibodies (Supplementary Figure S13.10B).

5.2.7.2. Antibody optimisations: determining the linear range

Following validation, antibodies were optimised to identify the experimental conditions under which the linear range of the assay was achieved (Pillai-Kastoori et al., 2020), a methodological state comparable to the dynamic range of a WES assay. This, as with WES optimisations, was achieved through trials of multiple antibody dilutions and protein concentrations. For individual Western antibody optimisations, see Appendix 13, Section 2. These experiments showed similar optimal experimental conditions for GPC4 and MBP (Table 5.13). Given that MBP and GPC4 were present in the same fraction (Supplementary Figures S13.1&3), with similar optimal

experimental conditions, but very different molecular weights, 14-22kDa and 60-65kDa, respectively, it was decided they could be quantified from the same sample on a single Western blot using successive primary antibody incubations.

Table 5.13. MBP and GPC4 optimal conditions

Antibody	GD21 and PD1 FC	PD21 PFC	PD35 and 100 PFC
MBP (rabbit polyclonal, Proteintech, 10458-1-AP)	100µg protein/well 1:5,000 (0.1µg/mL) antibody dilution	50µg protein 1:5,000 (0.1µg/mL) antibody dilution	25 or 50µg protein 1:5,000 (0.1µg/mL) antibody dilution
GPC4 (rabbit polyclonal, Proteintech, 13048-1-AP)	100µg protein/well 1:1,000 (0.65µg/mL) antibody dilution	50µg protein 1:1,000 (0.65µg/mL) antibody dilution	25µg protein 1:1,000 (0.65µg/mL) antibody dilution

To achieve this, it was first determined in what order to perform the primary antibody probes. Optimisation experiments showed that the anti-GPC4 antibody was most efficient following an overnight 4°C incubation, while the anti-MBP antibody performed equally well using an overnight 4°C incubation or 3h room temperature incubation (Appendix 13, Supplementary Figure S13.9). Therefore, it was decided that the standard Western blotting protocol would be followed (Chapter 3, Section 3.2.3.2), with the anti-GPC4 antibody used as the first primary antibody probe (1:1,000 dilution (0.65µg/mL); overnight, 4°C). Subsequently, following equilibration of the blot to room temperature on day 2, the blot was washed (4x5min standard washes) and a second primary antibody probe performed for 3h at room temperature using the anti-MBP antibody (1:5,000 dilution (0.1µg/mL)). This second primary antibody probe was followed by 4x5min standard washes prior to the incubation of the blot with the reference antibody (anti-GAPDH). A representative Western blot is shown in Figure 5.5.

5.2.7.3. Selecting a reference antibody for normalisation

Given the large sample demand in some Western optimisations (see Appendix 13, Section 2), it was determined that a reference antibody, which could be assayed on the same blot as the target protein, would be most optimal to normalise target protein expression for Western blots. However, this demanded the use of a stably expressed protein within each cellular fraction. Given the findings from the mRNA reference gene stability panel (Appendix 3), the stability of the proteins encoded by the least (*Actb*, encoding β-actin/ACTB) and most (*Gapdh*, encoding GAPDH) stable reference gene was evaluated in both cytosolic and membrane cellular fractions. For this, cytosolic or membrane fraction samples, inclusive of all sexes, developmental ages and groups were randomly selected for a stability assessment. 20µg protein was loaded/well and the standard Western blotting protocol was followed (Chapter 3, Section 3.2.3.2), until drying of the PVDF membrane. After this, the blots were placed in 1XPBS and stored overnight at 4°C. The following day they were equilibrated to room temperature for 1h and then processed through two successive reference antibody probes, both for 2h at room temperature as per the standard protocol, with standard washes between the addition of each

reference antibody. The first incubation was a 1:2,000 (1µg/mL) dilution of the anti-ACTB antibody (mouse monoclonal, A2228, 2mg/mL; Merck, Gillingham, UK), the second a 1:2,000 (0.5µg/mL) dilution of the anti-GAPDH antibody (mouse monoclonal, 60004-1-Ig, 1mg/mL; Proteintech, Manchester, UK). This stability assessment (see Appendix 13, Section 3, Supplementary Figures S13.13&14) demonstrated that GAPDH was the most stable protein across both cellular fractions in all experimental conditions and hence the anti-GAPDH antibody was selected as the reference antibody for all further Western blotting experiments.

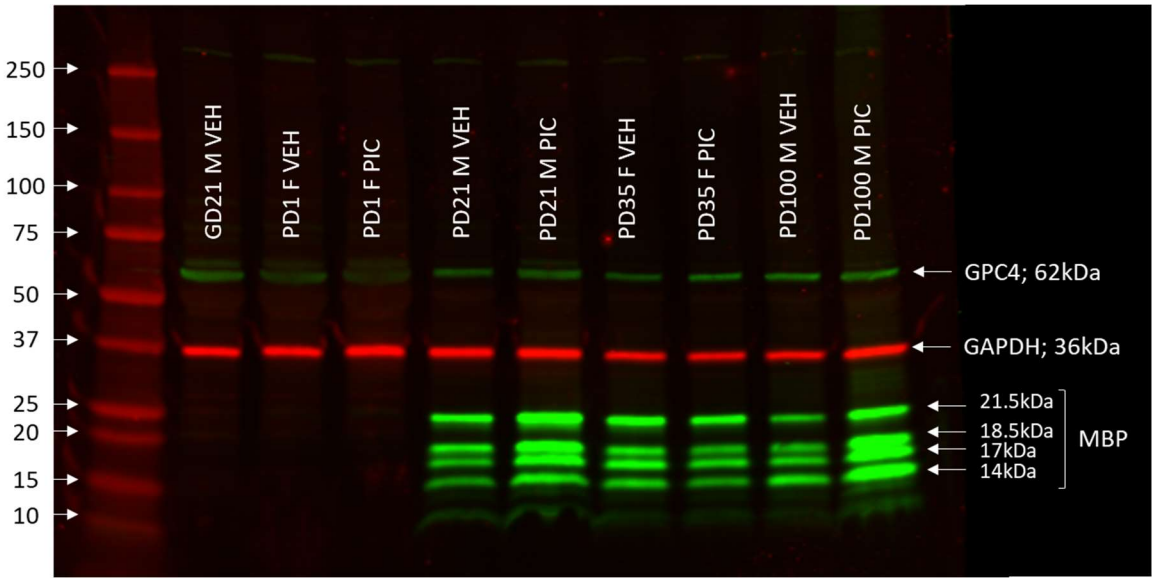

Figure 5.5. Representative GPC4/MBP Western blot
Membrane lysate was loaded at pre-optimised µg/well (Table 5.13). Western blot was run as per standard conditions (Chapter 3, Section 3.2.3.2) but primary antibody incubations were performed sequentially: first an overnight incubation at 4°C using 1:1,000 (0.65µg/mL) anti-GPC4, then on day 2, a second primary antibody incubation was performed for 3h at room temperature using 1:5,000 (0.1µg/mL) anti-MBP. Finally, a 1:2,000 (0.5µg/mL) anti-GAPDH antibody incubation was performed as reference. Molecular weight (kDa) ladder is indicated on the left. Abbreviations: GD, gestational day; PD, postnatal day; M, male; F, female; PIC, poly(I:C); VEH, vehicle

5.2.7.4. Western blot analysis

Western blot analysis was performed using ImageStudio Lite (v5.2, Li-Cor, Cambridge, UK) using default software settings with a median background adjustment. For analysis, a rectangle was drawn around each target protein and reference protein band. The same size rectangle was used for each target/reference band across every blot to maintain inter-blot consistency in background and signal quantification. The obtained signal for each target protein band was divided by the signal for the reference protein (GAPDH) band in the same lane to give a normalised target protein expression value for statistical analysis.

5.2.8. Statistics

Foetal/offspring molecular outputs (including the following dependent variables in this Chapter: cell density, %DNAm, relative gene expression, relative protein expression), were analysed as described in Chapter 2, Section 2.2.5 and Chapter 3, Section 3.2.6, in SPSS v28.0 (IBM). Briefly, within-group outliers were excluded using SPSS extreme outlier function. Between-group and

post-hoc sex comparisons were analysed by GLMM including Dam as a random factor and the following four predictors: fixed factors (sex, group) and covariates (maternal IL-6 and TNFα), with p-values≤0.05 considered statistically significant and 0.05<p≤0.08 highlighted as trending towards significance. Where the effects of all four predictors were insignificant, the phrase 'there were no significant effects of any predictors' will be used. Post-hoc Pearson's (r) or Spearman's (rho) correlations were used to evaluate directionality of relationship between numerical dependant variables and covariates. Note that for each pyrosequencing assay, the methylation of each CpG site and the average CpG methylation was analysed. This approach was chosen as, while methylation across a genomic regulatory region (including CGIs, promoters, exon 1 and intron 1; Anastasiadi et al., 2018; Brenet et al., 2011; Deaton and Bird, 2011; Moore et al., 2013) is generally considered to drive gene expression, the RRBS analysis identified significant differences in only a subset of CpG sites within the selected regulatory sequences (Table 5.8). Likewise, age- and disease-associated DNAm changes, including those identified in schizophrenia, are often CpG site-specific (Chen et al., 2021a; Grodstein et al., 2021; Jin et al., 2023; Pries et al., 2017; Steg et al., 2021). Hence, analysis of both average and individual CpG site methylation changes across a genomic region could distinguish if individual CpG sites are particularly susceptible to MIA-induced and/or developmental alterations in methylation.

Graphs were generated using GraphPad Prism (v9.0), with n-numbers for dam per group (N) and foetuses/pups per sex per group (n) indicated in figure legends. Data represented as mean ±SEM, where individual points represent individual animals. Note: group*sex interactions are not indicated on graphs, instead post-hoc analyses by sex are outlined on graphs where significant.

5.3. RESULTS

Note: as the aims of this Chapter were to evaluate specific glial cell developmental changes, results are presented by glial cell type.

5.3.1. Glial cell densities in the PFC: an overview

Perfused PFC tissue samples were collected at PD35 and PD100 only (Chapter 2, Section 2.2.2). A summary of the staining densities for each cell type can be found in Table 5.14. OLIG2+ oligodendrocytes had the greatest cell density, followed closely by GFAP+ astrocytes, IBA1+ microglia and finally NG2+ OPCs had the lowest density, in agreement with others (Dawson et al., 2003; Verkhratsky et al., 2017). There were no obvious changes in overall cell densities between PD35 and PD100 determined by overlaps between density values (mean ±SEM), but for individual microglia activation states there was a reduction in IBA1+ amoeboid cells between PD35 to PD100 (-48.72%) and an increase in rod (+48.36%) and hypertrophic (+314.58%) microglial cells.

Table 5.14. Summary of glial cell density/PFCmm^2 (mean ±SEM)

Cell type	PD35	PD100
IBA1+ Microglia	157±4	149±4
%Ramified	88.46±0.94	88.15±0.79
%Rod	2.44±0.23	3.62±0.40
%Ameboid	8.21±0.77	4.21±0.23
%Hypertrophic	0.96±0.17	3.98±0.60
GFAP+ Astrocytes	340±14	336±18
OLIG2+ Oligodendrocytes	397±10	392±16
NG2+ OPCs	105±4	103±3

5.3.2. Dysregulation of microglia in the developing cortex

5.3.2.1. IBA1+ microglia density changes

A representative IBA1+ stain is shown in Figure 5.6C. There were no significant effects of any predictors on IBA1+ cell density in the PD35 and PD100 PFC (Figure 5.6A). However, IBA1+ microglia have distinct morphologies analogous to their activation state (Fernández-Arjona et al., 2017, 2019; Kongsui et al., 2014; Morrison et al., 2017; Wyatt-Johnson et al., 2017). Accordingly, the morphologies of the various activation states (ramified, rod, ameboid, hypertrophic; Figure 5.2) were scored. Results from this analysis (Figure 5.6B) showed a significant reduction in ramified IBA1+ microglia in poly(I:C)-offspring relative to vehicle-offspring at both ages, with a main effect of group at PD35 (GLMM: $F_{1,18}$=4.61, p=0.046) and a main effect of both group (GLMM: $F_{1,17}$=11.45, p=0.004) and a trend to a main effect of maternal TNFα (GLMM: $F_{1,17}$=3.63, p=0.074) at PD100. This appears due to an increase in ameboid IBA1+ microglia in poly(I:C)-offspring relative to vehicle at PD35 (main effect of group, GLMM:

$F_{1,18}$=7.67, p=0.013) and an increase in hypertrophic IBA1+ microglia in poly(I:C)-offspring relative to vehicle at PD100 (main effect of group, GLMM: $F_{1,18}$=13.15, p=0.002). There were no significant differences in the density of rod cells at either timepoint.

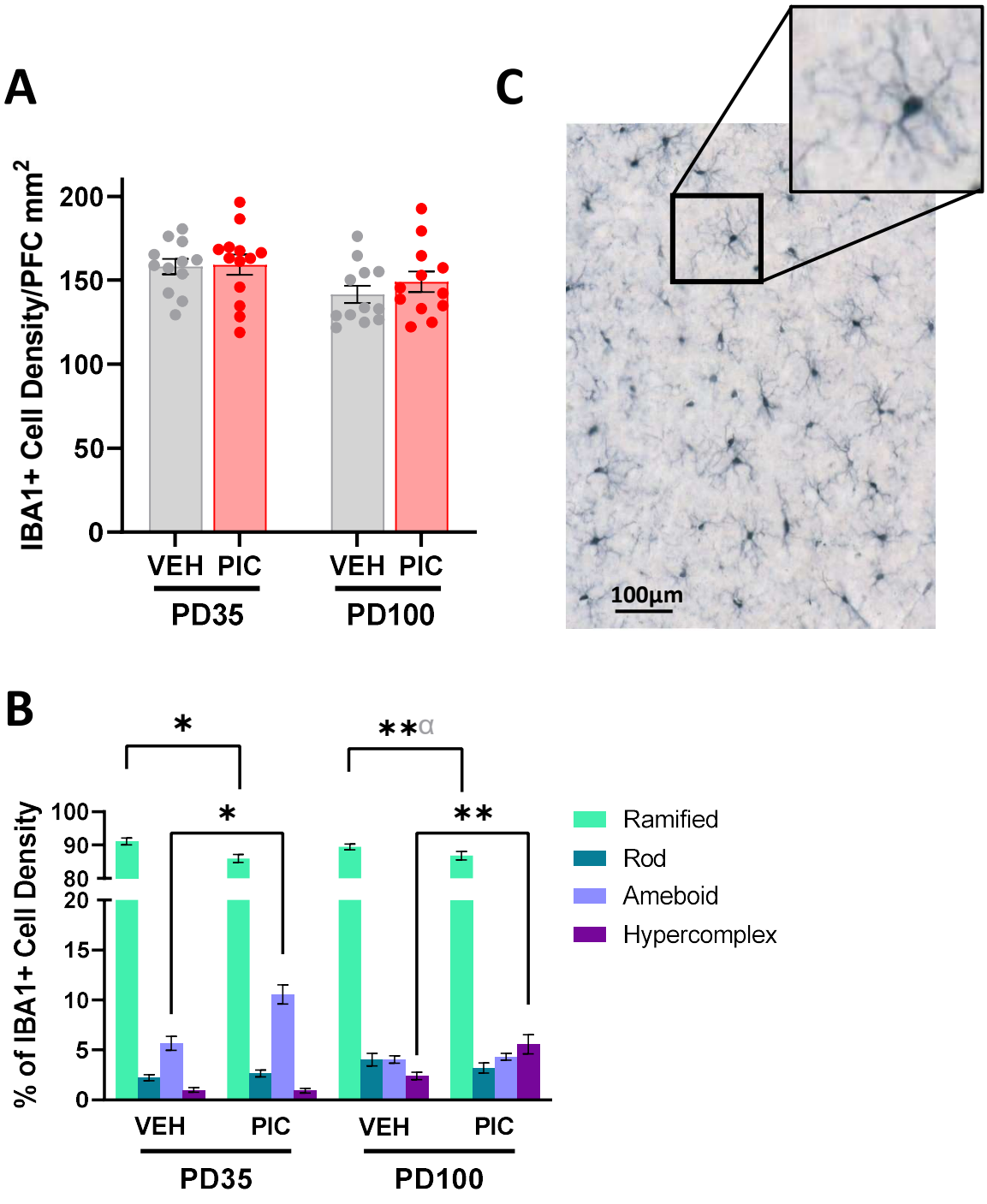

Figure 5.6. IBA1+ Microglia cell density

A. IBA1+ microglia cell density**. B.** Quantification of IBA1+ microglia activation states by morphology. Bars represent mean ±SEM (N=6, n=6-7), dots represent individual animals. **C.** Representative IBA1+ stain, 10X magnification, inset shows magnification of a typical ramified microglia. Π-shaped black bars show GLMM results. Black symbols show significant main effects of: group, *p<0.05, **p<0.01; Grey symbols show trending main effects (0.05<p<0.08) in the GLMM: maternal TNFα, α. Abbreviations: PIC, poly(I:C); VEH, vehicle; PD, postnatal day.

5.3.2.2. Differential methylation of microglia-enriched genes

I. *Sgk1*

SGK1 is the serum/glucocorticoid response kinase, upregulated in response to glucocorticoid signalling and has been previously associated with schizophrenia. The RRBS identified reduced methylation in the *Sgk1* gene promoter (Table 5.8; Appendix 9). This promoter region, containing four CpG sites was analysed by pyrosequencing across the developmental timeline (GD21-PD100).

GD21 FC

There was no significant effect of any predictors on average CpG methylation or on methylation of any individual CpG sites, with the exception of CpG2 where there was a significant main effect of sex (GLMM: $F_{1,11.38}$=6.71, p=0.025), with females having higher methylation at CpG2 than males (Figure 5.7C).

PD1 FC

For average CpG methylation there was a group*sex interaction (GLMM: $F_{2,11}$=9.12, p=0.005). Post-hoc analysis showed a main effect of maternal TNFα in females (GLMM: $F_{1,7}$=14.67, p=0.006), corresponding to a negative correlation between maternal plasma TNFα and female average *Sgk1* promoter methylation (r=-0.823, p=0.006) and a main effect of group in males (GLMM: $F_{1,5}$=8.34, p=0.034), with increased *Sgk1* promoter methylation in the poly(I:C)-males relative to vehicle-males (Figure 5.7A). This pattern was observed similarly across CpG1 and CpG2 but not CpG3 and CpG4 (Table 5.15; Figure 5.7B-D).

Table 5.15. *Sgk1* promoter methylation PD1 statistics

CpG site	Minimal GLMM	Post-hoc females	Post-hoc males
CpG1	Group*sex: $F_{2,6.94}$=6.53, p=0.025	MatTNFα: $F_{1,7}$=17.17, p=0.004 r=-0.843, p=0.004	Group: $F_{1,4}$=18.02, p=0.013 MatTNFα: $F_{1,4}$=10.86, p=0.030 Increase in poly(I:C)-males relative to vehicle
CpG2	Group*sex: $F_{3,12.53}$=4.44, p=0.024	MatTNFα: $F_{1,7}$=12.71, p=0.009 r=-0.803, p=0.009	Group: $F_{1,8}$=6.04, p=0.039; Increase in poly(I:C)-males relative to vehicle
CpG3	Group*sex: $F_{3,17}$=3.01, p=0.059	NSP	Group: $F_{1,8}$=8.45, p=0.02; Increase in poly(I:C)-males relative to vehicle
CpG4	Group*sex: $F_{3,17}$=2.98, p=0.061	NSP	Group: $F_{1,8}$=6.61, p=0.033; Increase in poly(I:C)-males relative to vehicle

Abbreviations: MatTNFα, 3h maternal TNFα plasma concentration; NSP, no significant effects of any predictors.

PD21 PFC

For average CpG methylation there was a significant main effect of sex (GLMM: $F_{1,3.93}$=12.02, p=0.026) with increased *Sgk1* promoter methylation in females relative to males (Figure 5.7A), with no significant effects of any predictors on methylation at the individual CpG sites (Figure 5.7B-D).

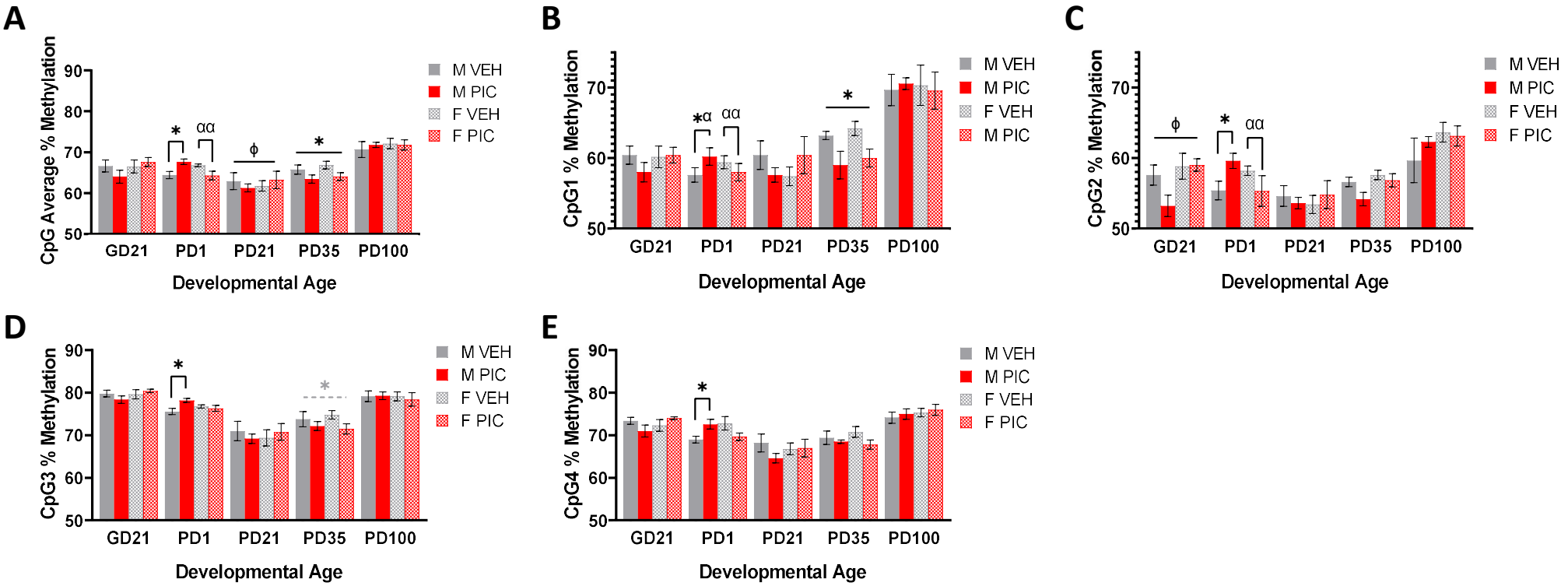

Figure 5.7. *Sgk1* promoter methylation
A. Average % methylation. **B.** CpG1 % methylation. **C.** CpG2 % methylation. **D.** CpG3 % methylation. **E.** CpG4 % methylation. Bars represent mean ±SEM (N=5-7, n=5-7). Black significance bars represent significant results of the GLMM, — shaped significance bars represent results across the whole developmental stage, Π shaped bars represent post-hoc GLMM within a single sex. Black symbols show significant main effects of: group, *p<0.05; maternal TNFα, αp<0.05, ααp<0.01; sex, ϕp<0.05. Grey dashed bars and symbols represent trending results of the GLMM (0.05<p<0.08). Abbreviations: GD, gestational day; PD, postnatal day; M, male; F, female; PIC, poly(I:C); VEH, vehicle.

PD35 PFC

For average CpG methylation there was a significant main effect of group (GLMM: $F_{1,17}$=5.55, p=0.031) with reduced *Sgk1* promoter methylation in poly(I:C)-offspring relative to vehicle (Figure 5.7A). For the individual CpG sites, there were no significant effects of any predictors on CpG2 and CpG4 methylation, however there was a main effect of group for CpG1 (GLMM: $F_{1,10.32}$=7.29, p=0.022) and a trending main effect of group for CpG3 (GLMM: $F_{1,20}$=4.10, p=0.056), both with reduced methylation in poly(I:C)-offspring relative to vehicle-offspring (Figure 5.7B-D).

PD100 PFC

There were no significant effects of any predictors on average CpG methylation or methylation at the individual CpG sites (Figure 5.7).

II. *Tgfbr2*

TGFBR2 (transforming growth factor beta receptor 2) is a tyrosine receptor kinase, which forms a dimer with TGFBR1 to bind TGFβ, an anti-inflammatory cytokine. The RRBS identified a significant reduction in methylation in the *Tgfbr2* gene intron 1 (Table 5.8; Appendix 9). This region, containing two CpG sites was analysed by pyrosequencing across the developmental timeline (GD21-PD100).

GD21 FC

For the average CpG methylation there was a significant group*sex interaction (GLMM: $F_{3,13.17}$=7.04, p=0.005). Post-hoc analysis showed a significant main effect of group in both females (GLMM: $F_{1,8}$=5.98, p=0.040), with reduced methylation in poly(I:C)-females relative to vehicle-females (Figure 5.8A) and males (GLMM: $F_{1,8}$=15.02, p=0.005), with increased methylation in poly(I:C)-males relative to vehicle-males (Figure 5.8A). This pattern was observed across both CpG sites when considered individually (Table 5.16; Figure 5.8B&C).

Table 5.16. *Tgbr2* intron 1 methylation GD21 statistics

CpG site	Minimal GLMM	Post-hoc females	Post-hoc males
CpG1	Group*sex: $F_{3,12.82}$=2.92, p=0.074	Group: $F_{1,8}$=4.94, p=0.057 Reduced in poly(I:C)-females relative to vehicle-females	NSP
CpG2	Group*sex: $F_{3,13.28}$=7.62, p=0.003	Group: $F_{1,7}$=4.46, p=0.073 Reduced in poly(I:C)-females relative to vehicle-females	Group: $F_{1,9}$=17.8, p=0.002 Increase in poly(I:C)-males relative to vehicle-males

Abbreviations: NSP, no significant effects of any predictors

PD1 FC

For the average CpG methylation there was a significant main effect of sex (GLMM: $F_{1,7.22}$=10.96, p=0.012) with increased methylation in females relative to males (Figure 5.8A), this was true for both CpG sites when considered individually: CpG1 (GLMM: $F_{1,8.1}$=6.52, p=0.034; Figure 5.8B) and CpG2 (GLMM: $F_{1,6.78}$=9.45, p=0.019; Figure 5.8C).

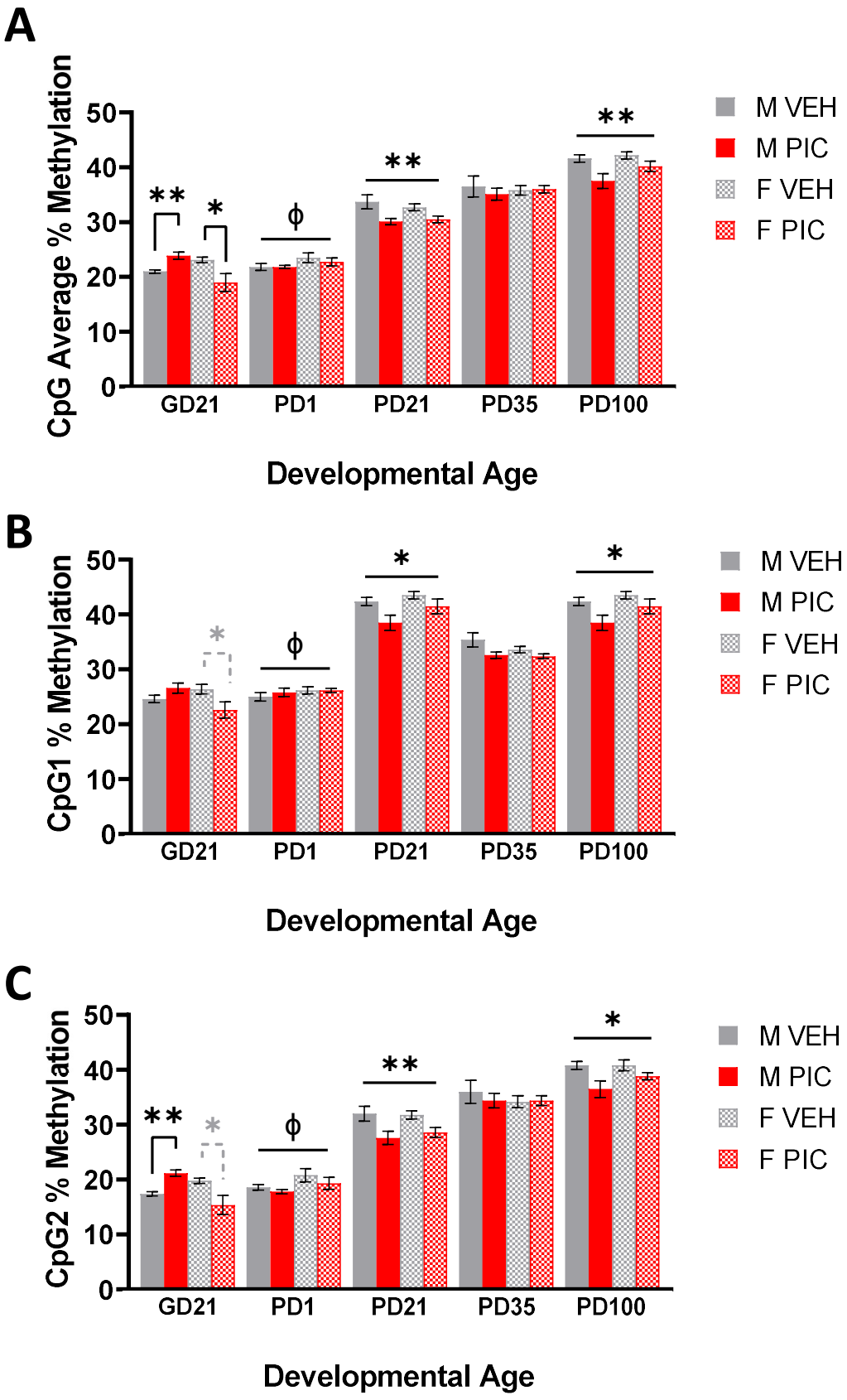

Figure 5.8. *Tgfbr2* intron 1 methylation
A. Average % methylation. **B.** CpG1 % methylation. **C.** CpG2 % methylation. Bars represent mean ±SEM (N=5-6, n=5-6). Black significance bars show significant results of the GLMM, — shaped significance bars represent results across the whole developmental stage, Π-shaped bars show post-hoc GLMM within a single sex. Black symbols show significant main effects of: group, *p<0.05, **p≤0.01; sex, ϕp<0.05. Grey dashed bars and grey symbols represent trending results of the GLMM (0.05<p<0.08). Abbreviations: GD, gestational day; PD, postnatal day; M, male; F, female; PIC, poly(I:C); VEH, vehicle.

PD21 PFC

For the average CpG methylation there was a significant main effect of group (GLMM: $F_{1,15}$=12.69, p=0.003) with reduced methylation in poly(I:C)-offspring relative to vehicle-offspring (Figure 5.8A), observed also for both individual CpG sites: CpG1 (GLMM: $F_{1,18}$=6.10, p=0.024; Figure 5.8B) and CpG2 (GLMM: $F_{1,18}$=13.86, p=0.002; Figure 5.8C).

PD35 PFC

There were no significant effects of any predictors on average CpG methylation or methylation of the individual CpG sites (Figure 5.8).

PD100 PFC

For the average CpG methylation there was a significant main effect of group (GLMM: $F_{1,17}$=8.40, p=0.010) with reduced methylation in poly(I:C)-offspring relative to vehicle (Figure 5.8A), observed also for both individual CpG sites: CpG1 (GLMM: $F_{1,17}$=6.35, p=0.022; Figure 5.8B) and CpG2 (GLMM: $F_{1,17}$=7.21, p=0.016; Figure 5.8C).

III. *Irs1*

IRS1 (insulin receptor substrate 1) is the response substrate downstream of insulin signalling. Reduced IRS1 has been associated with cognitive decline and inflammation. The RRBS identified a significant increase in methylation in the *Irs1* exon 1 (Table 5.8; Appendix 9). This region, containing six CpG sites was analysed by pyrosequencing across the developmental timeline (GD21-PD100).

GD21 and PD1 FC

There were no significant effects of any predictors on average CpG methylation or methylation of the individual CpG sites (Figure 5.9).

PD21 PFC

For the average CpG methylation there was a trend to a main effect of group (GLMM: $F_{1,18}$=3.56, p=0.075) with reduced methylation in poly(I:C)-offspring relative to vehicle-offspring (Figure 5.9A). However, there were different effects of predictors on individual CpG site methylation. There were no significant effects of any predictors on methylation at CpG1 or CpG3 (Figure 5.9B&D). At CpG2 there was a main effect of group (GLMM: $F_{1,15}$=10.12, p=0.006) with reduced methylation in poly(I:C)-offspring relative to vehicle-offspring (Figure 5.9C). At CpG4, CpG5 and CpG6 there were significant group*sex interactions, with post-hoc analyses showing a consistent significant main effect of group only in male offspring (Table 5.17; Figure 5.9E-G).

Table 5.17. *Irs1* exon 1 methylation PD21 statistics

CpG site	Minimal GLMM	Post-hoc females	Post-hoc males
CpG4	Group*sex: $F_{3,16}$=6.18, p=0.005	NSP	Group: $F_{1,6}$=21.35, p=0.004; Decrease in poly(I:C)-males relative to vehicle-males
CpG5	Group*sex: $F_{3,13}$=8.11, p=0.003	NSP	Group: $F_{1,6}$=17.52, p=0.006; Decrease in poly(I:C)-males relative to vehicle-males
CpG6	Group*sex: $F_{3,13}$=4.01, p=0.032	NSP	Group: $F_{1,6}$=14.40, p=0.009; Decrease in poly(I:C)-males relative to vehicle-males

Abbreviations: NSP, no significant effects of any predictors

PD35 PFC

There were no significant effects of any predictors on average CpG methylation (Figure 5.9A). However, there were significant effects of different predictors on individual CpG site methylation. For CpG3 there was a significant main effect of maternal TNFα (GLMM: $F_{1,15}$=10.43, p=0.006; Figure 5.9D), corresponding to a significant positive correlation between maternal TNFα concentration and methylation at CpG3 (r=0.640, p=0.006). For CpG6 there was a significant group*sex interaction (GLMM: $F_{3,12.82}$=3.62, p=0.043) and post-hoc analysis showed a main effect of group in the females (GLMM: $F_{1,6}$=10.08, p=0.019), with increased methylation at CpG6 in poly(I:C)-females relative to vehicle-females (Figure 5.9G). There were no significant effects of any predictors on methylation at CpG1, CpG2, CpG4 or CpG5 (Figure 5.9B-C&E-F).

PD100 PFC

For the average CpG methylation there was a significant main effect of group (GLMM: $F_{1,20}$=6.45, p=0.020) with increased methylation in poly(I:C)-offspring relative to vehicle-offspring and a main effect of sex (GLMM: $F_{1,20}$=12.91, p=0.002), with reduced methylation in females relative to males (Figure 5.9A). However, there were differences in the significant effects of the predictors on individual CpG site methylation (Table 5.18; Figure 5.9B-G).

Table 5.18. *Irs1* exon 1 methylation PD100 statistics

CpG site	Minimal GLMM
CpG1	Sex: $F_{1,8.39}$=6.61, p=0.032, Reduced in females relative to males
CpG2	Sex: $F_{1,16}$=7.25, p=0.016, Reduced in females relative to males Group: $F_{1,16}$=3.96, p=0.064, Increased in poly(I:C)-offspring relative to vehicle-offspring
CpG3	Sex: $F_{1,16}$=12.56, p=0.003, Reduced in females relative to males Group: $F_{1,16}$=9.79, p=0.006, Increased in poly(I:C)-offspring relative to vehicle-offspring
CpG4	Sex: $F_{1,20}$=18.96, p<0.001, Reduced in females relative to males Group: $F_{1,20}$=5.19, p=0.034, Increased in poly(I:C)-offspring relative to vehicle-offspring
CpG5	Sex: $F_{1,16}$=14.64, p=0.001, Reduced in females relative to males Group: $F_{1,16}$=16.37, p<0.001, Increased in poly(I:C)-offspring relative to vehicle-offspring
CpG6	Sex: $F_{1,16}$=19.12, p<0.001, Reduced in females relative to males Group: $F_{1,16}$=6.95, p=0.018, Increased in poly(I:C)-offspring relative to vehicle-offspring

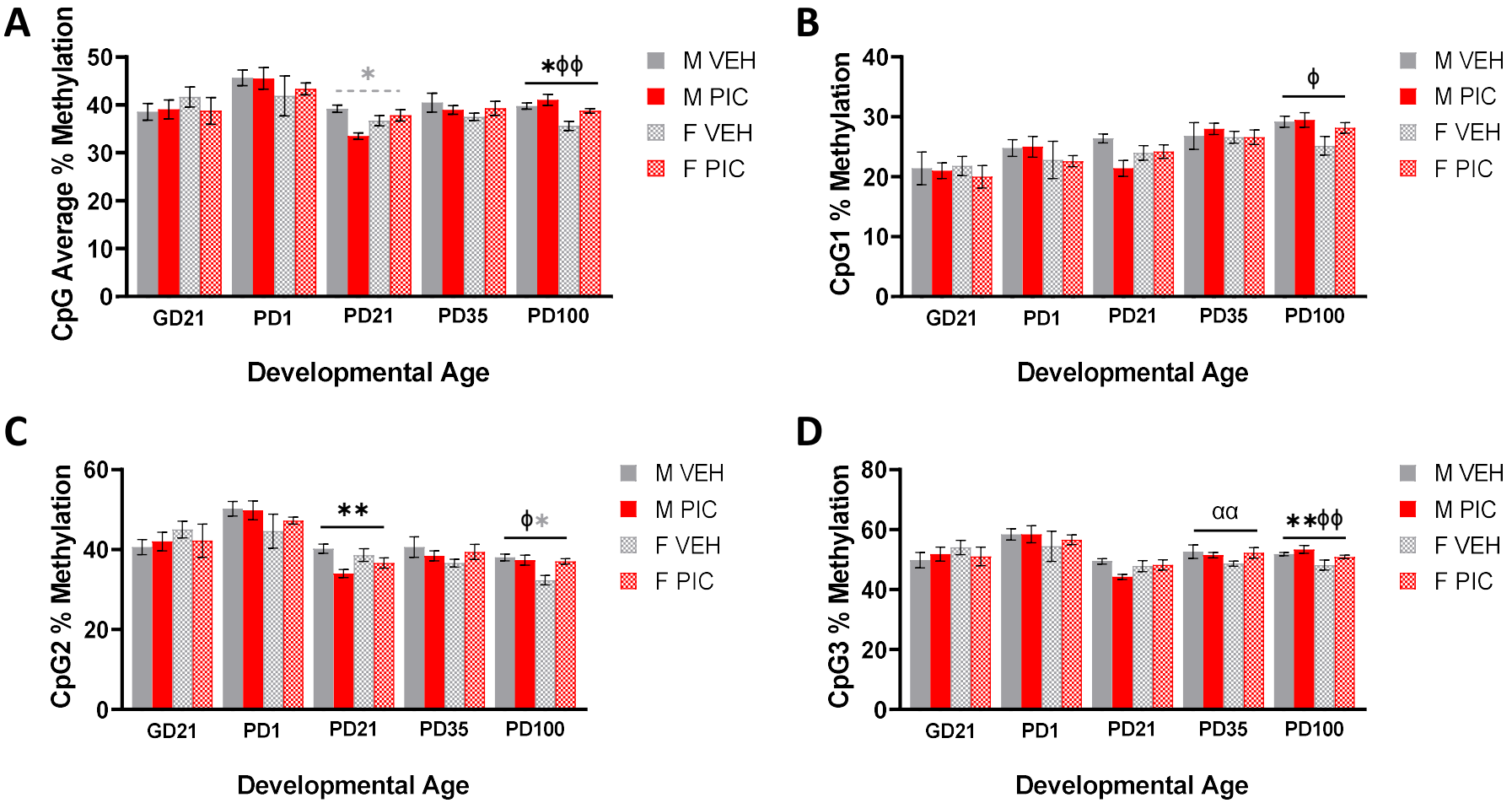

Figure 5.9, Page 1/2

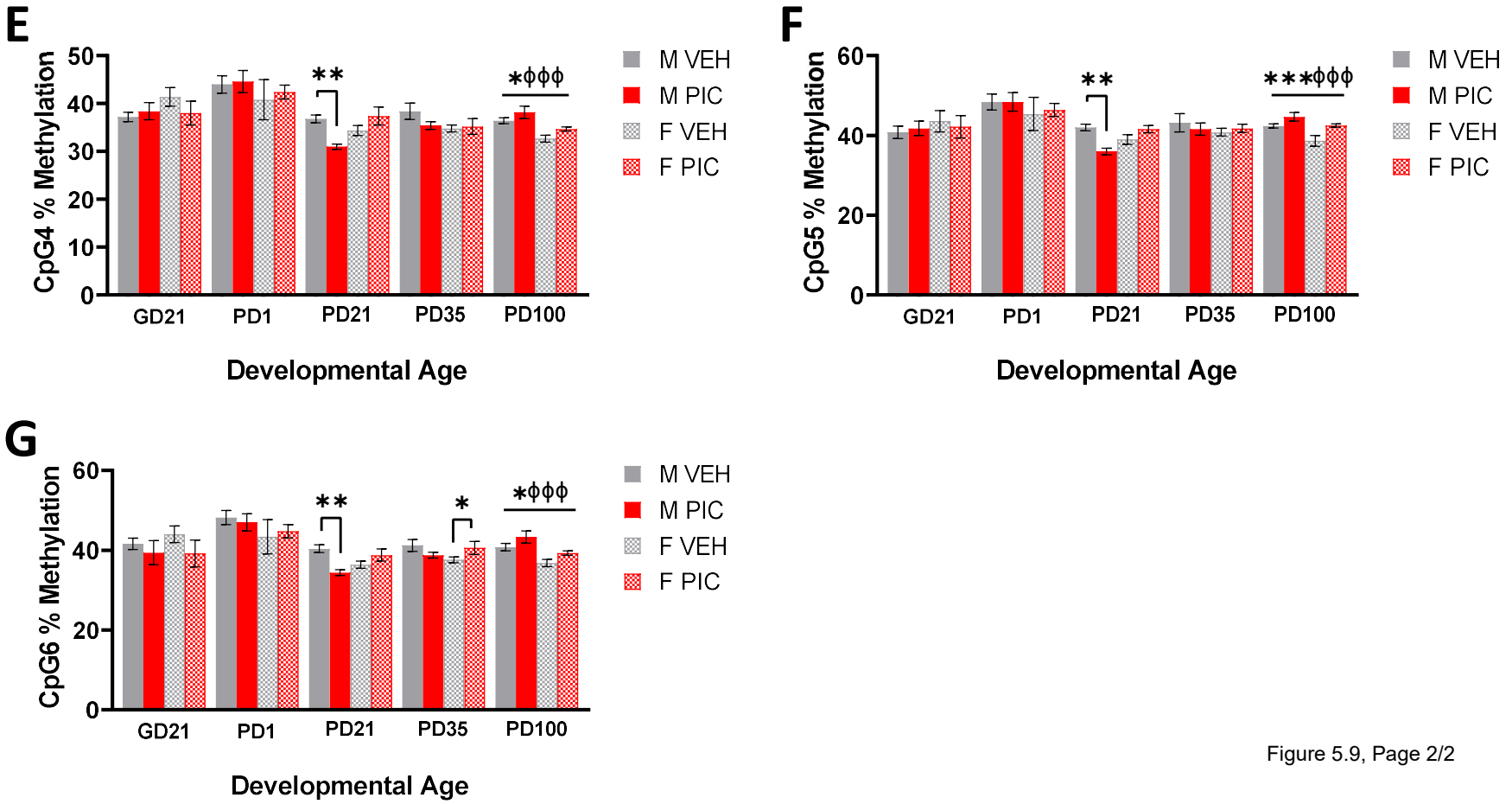

Figure 5.9, Page 2/2

Figure 5.9. *Irs1* exon 1 methylation

A. Average % methylation. **B.** CpG1 % methylation. **C.** CpG2 % methylation. **D.** CpG3 % methylation. **E.** CpG4 % methylation. **F.** CpG5 % methylation. **G.** CpG6 % methylation. Bars represent mean ±SEM (N=5-6, n=5-6). Black significance bars show significant results of the GLMM. — shaped significance bars represent results across the whole developmental stage, Π-shaped bars represent post-hoc GLMM within a single sex. Black symbols show significant main effects of: group, *p<0.05, **p<0.01; ***p<0.001; maternal TNFα, ααp<0.01; sex, ϕp<0.05, ϕϕp<0.01, ϕϕϕp≤0.001. Grey dashed bars and/or grey symbols represent trending results of the GLMM (0.05<p<0.08). Abbreviations: GD, gestational day; PD, postnatal day; M, male; F, female; PIC, poly(I:C); VEH, vehicle.

5.3.2.3. Differential mRNA expression of microglia-enriched genes

I. *Sgk1*

GD21 FC

There was a significant group*sex interaction (GLMM: $F_{3,15}$=5.64, p=0.009). Post-hoc analysis showed a significant main effect of group in the males (GLMM: $F_{1,7.89}$=12.49, p=0.008), with an increase in *Sgk1* mRNA expression in poly(I:C)-males relative to vehicle-males (Figure 5.10A).

PD1 FC

There was a trending group*sex interaction (GLMM: $F_{3,6.11}$=4.68, p=0.051). Post-hoc analysis showed a trending effect of group in the females (GLMM: $F_{1,10}$=4.22, p=0.067), with increased *Sgk1* mRNA expression in poly(I:C)-females relative to vehicle-females (Figure 5.10A).

PD21 and PD35 PFC

There was a main effect of group for both PD21 (GLMM: $F_{1,12.60}$=17.70, p=0.001) and PD35 (GLMM: $F_{1,14.81}$=4.72, p=0.046) with increased *Sgk1* mRNA expression in poly(I:C)-offspring relative to vehicle (Figure 5.10A).

PD100 PFC

There was a significant main effect of maternal TNFα (GLMM: $F_{1,24}$=46.30, p<0.001; Figure 5.10A) corresponding to a positive correlation between maternal TNFα and *Sgk1* mRNA expression (rho=0.497, p=0.010).

II. *Tgfbr2*

GD21 FC

There were no significant effects of any predictors on *Tgfbr2* expression (Figure 5.10B).

PD1 FC

There was a trend to a main effect of sex (GLMM: $F_{1,8.63}$=4.31, p=0.069), with increased *Tgfbr2* mRNA expression in females relative to males (Figure 5.10B).

PD21 PFC

There was a trend to a main effect of sex (GLMM: $F_{1,10.98}$=4.78, p=0.051), with increased *Tgfbr2* mRNA expression in females relative to males and a trend to a main effect of group (GLMM: $F_{1,10.08}$=4.43, p=0.061) with increased *Tgfbr2* mRNA expression in poly(I:C)-offspring relative to vehicle-offspring (Figure 5.10B).

PD35 PFC

There were no significant effects of any predictors on PD35 *Tgfbr2* expression (Figure 5.10B).

PD100 PFC

There was a significant main effect of group (GLMM: $F_{1,22}$=17.85, p<0.001), with increased *Tgfbr2* mRNA expression in poly(I:C)-offspring relative to vehicle (Figure 5.10B).

III. *Irs1*

GD21 FC

There was a significant main effect of group (GLMM: $F_{1,19}$=4.48, p=0.048), with increased *Irs1* mRNA expression in poly(I:C)-foetuses relative to vehicle-foetuses (Figure 5.10C).

PD1 FC

There was a trend to a main effect of group (GLMM: $F_{1,21}$=3.91, p=0.061), with decreased *Irs1* mRNA expression in poly(I:C)-offspring relative to vehicle-offspring (Figure 5.10C).

PD21 and PD35 PFC

There were no significant effects of any predictors on PD21 or PD35 *Irs1* expression (Figure 5.10C).

PD100 PFC

There was a significant main effect of group (GLMM: $F_{1,26}$=12.94, p=0.001), with decreased *Irs1* mRNA expression in poly(I:C)-offspring relative to vehicle-offspring and a main effect of sex (GLMM: $F_{1,26}$=7.50, p=0.011), with reduced *Irs1* mRNA expression in females relative to males (Figure 5.10C).

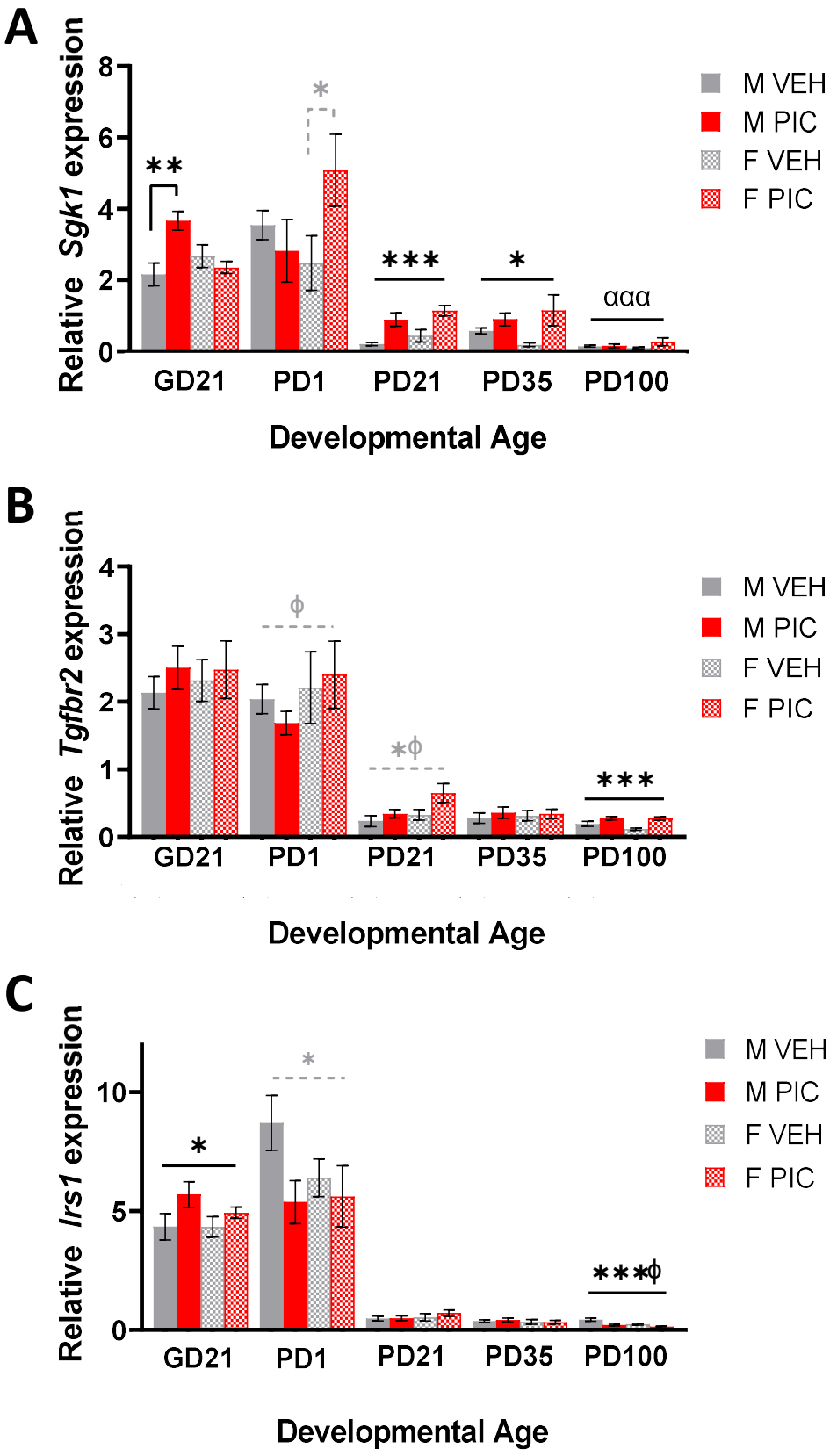

Figure 5.10. Microglia-enriched gene expression
Relative mRNA expression, (normalised to the geometric mean of three reference genes as described in methods). **A**. *Sgk1* (N=5-8, n=5-10) **B.** *Tgfbr2* (N=5-8, n=5-8). **C.** *Irs1* (N=5-8, n=5-8). Bars represent mean ±SEM. Black significance bars represent significant GLMM results, — shaped significance bars show results across whole developmental age, Π shaped bars show post-hoc GLMM within a single sex. Black symbols show significant main effects of: group, *p<0.05, **p<0.01, ***p≤0.001; maternal TNFα, αααp<0.001; sex, ϕp<0.05. Grey dashed bars and symbols represent trending results of the GLMM (0.05<p<0.08). Abbreviations: GD, gestational day; PD, postnatal day; M, male; F, female; PIC, poly(I:C); VEH, vehicle.

5.3.2.4. Differential protein expression of SGK1

SGK1 was selected for protein quantification as it demonstrated the most significant MIA-induced changes in mRNA expression of the microglial genes (Figure 5.10)

GD21 FC

There was a significant main effect of group (GLMM: $F_{1,8.29}$=5.62, p=0.044; Figure 5.11), with increased SGK1 protein expression in poly(I:C)-foetuses relative to vehicle-foetuses.

PD1 FC

There was a significant group*sex interaction (GLMM: $F_{3,11}$=4.85, p=0.022). Post-hoc analysis showed a significant main effect of group in the females (GLMM: $F_{1,7}$=5.11, p=0.050) with increased SGK1 protein expression in poly(I:C)-females relative to vehicle-females (Figure 5.11), mirroring the trend seen for *Sgk1* mRNA expression (Figure 5.10A).

PD21 and PD35 PFC

There were main effects of group for both PD21 (GLMM: $F_{1,21}$=7.21, p=0.014) and PD35 (GLMM: $F_{1,11.57}$=4.70, p=0.052), with increased SGK1 protein expression in poly(I:C)-offspring relative to vehicle-offspring (Figure 5.11), again with the same direction of change seen for *Sgk1* mRNA expression (Figure 5.10A).

PD100 PFC

There was a trending group*sex interaction (GLMM: $F_{3,11.64}$=3.48, p=0.051). Post-hoc analysis showed a significant main effect of maternal TNFα in the males (GLMM: $F_{1,6.98}$=6.57, p=0.037; Figure 5.11) corresponding to a negative correlation between maternal TNFα and SGK1 protein expression (r=-0.694, p=0.026).

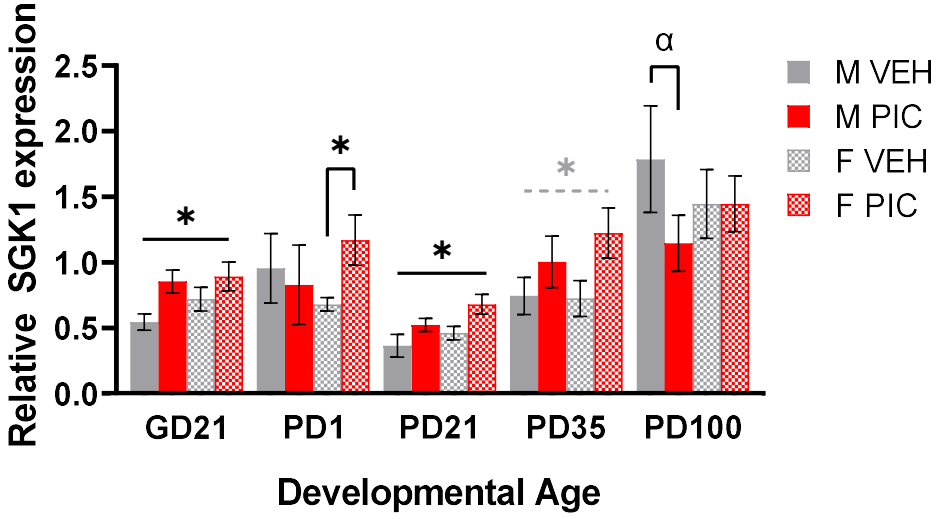

Figure 5.11. SGK1 protein expression
Relative SGK1 protein expression normalised to total protein. Bars represent mean ±SEM (N=5-7, n=5-7). Black significance bars represent significant GLMM results, — shaped significance bars show results across a given developmental age, Π-shaped bars show post-hoc GLMM within a single sex. Black symbols show significant main effects of: group, *p≤0.05; maternal TNFα, αp<0.05. Grey dashed bars and symbols represent trending results of the GLMM (0.05<p<0.08). Abbreviations: GD, gestational day; PD, postnatal day; M, male; F, female; PIC, poly(I:C); VEH, vehicle.

5.3.3. Dysregulation of astrocytes in the developing cortex

5.3.3.1. GFAP+ astrocyte density changes

There was a significant main effect of group at PD35 (GLMM: $F_{1,9.58}$=5.16, p=0.048; Figure 5.12) with a reduced number of GFAP+ astrocytes in poly(I:C)-offspring relative to vehicle-offspring. Likewise, at PD100 there was a significant main effect of maternal IL-6 (GLMM: $F_{1,18}$=4.42, p=0.050; Figure 5.12), corresponding to a negative correlation between maternal IL-6 and GFAP+ astrocyte density (r=-0.444, p=0.050). A representative GFAP+ stain is shown in Figure 5.12B.

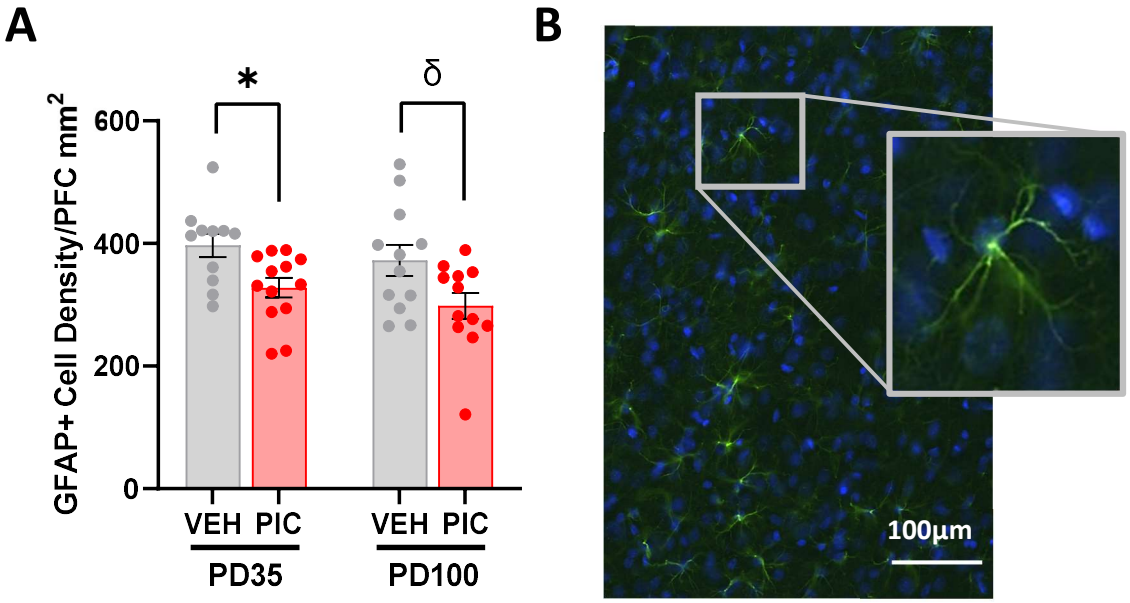

Figure 5.12. GFAP+ Astrocyte density
A. GFAP+ astrocyte density, bars represent mean ±SEM, dots show individual animals, (N=5-6, n=5-6). **B.** Representative GFAP+ stain, 10X magnification with inset depicting magnified astrocyte (DAPI, blue; GFAP, green). Π-shaped black bars show GLMM results within a single age. Symbols show significant main effect of group, *p<0.05; maternal IL-6, δp≤0.05. Abbreviations: PIC, poly(I:C); VEH, vehicle; PD, postnatal day.

5.3.3.2. Differential methylation of astrocyte-enriched gene, *Gpc4*

GPC4 is a cell surface heparin sulphate proteoglycan, primarily expressed in astrocytes in the CNS. It has been associated with the development and regulation of glutamatergic synapses. The RRBS identified a reduction in methylation of the *Gpc4* promoter (Table 5.8; Appendix 9). The promoter region, containing three CpG sites was evaluated by pyrosequencing across the developmental timeline (GD21-PD100).

GD21 FC

For the average CpG methylation there was a significant main effect of sex (GLMM: $F_{1,13.58}$=102.43, p<0.001), with increased *Gpc4* promoter methylation in females relative to males (Figure 5.13A). This main effect of sex was consistent even when CpG sites were considered individually: CpG1 (GLMM: $F_{1,13.74}$=96.66, p<0.001; Figure 5.13B); CpG2 (GLMM: $F_{1,13.0}$=91.42, p<0.001; Figure 5.13C); CpG3 (GLMM: $F_{1,18}$=107.31, p<0.001; Figure 5.13D).

PD1 FC

For the average CpG methylation there was a significant main effect of sex (GLMM: $F_{1,6.39}$=179.62, p<0.001), with increased *Gpc4* promoter methylation in females relative to males, group (GLMM: $F_{1,15.14}$=19.16, p<0.001) and a group*sex interaction (GLMM: $F_{1,7.54}$=42.17, p<0.001). Post-hoc analysis revealed a significant main effect of group in males (GLMM: $F_{1,6}$=34.46, p=0.001), with decreased methylation in poly(I:C)-males relative to vehicle-males (Figure 5.13A). By comparison, the analysis of each individual CpG site (Table 5.19; Figure 5.13B-D), resulted in a reduction in methylation of the three CpG sites in poly(I:C)-males relative to vehicle-males and an association between CpG site methylation and maternal cytokine concentrations in the female offspring.

Table 5.19. *Gpc4* promoter methylation PD1 statistics

CpG site	Minimal GLMM	Post-hoc females	Post-hoc males
CpG1	Group*sex: $F_{1,10.82}$=24.13, p<0.001 Sex: $F_{1,8.03}$=85.44, p<0.001	MatTNFα: $F_{1,3}$=23.81, p=0.016 No correlation observed	Group: $F_{1,9}$=23.81, p<0.001 Decrease in poly(I:C)-males relative to vehicle-males
CpG2	Group*sex: $F_{1,6.49}$=51.59, p<0.001 Sex: $F_{1,6.29}$=204.59, p<0.001	MatIL6: $F_{1,3}$=14.45, p=0.032 r=0.910, p=0.032	Group: $F_{1,9}$=23.98, p<0.001 Decrease in poly(I:C)-males relative to vehicle-males
CpG3	Group*sex: $F_{1,6.96}$=49.59, p<0.001 Sex: $F_{1,5.8}$=232.64, p<0.001	MatIL6: $F_{1,3}$ =14.02, p=0.033 r=0.908, p=0.033	Group: $F_{1,9}$=34.02, p<0.001 Decrease in poly(I:C)-males relative to vehicle-males

Abbreviations: MatTNFα/MatIL6, 3h maternal TNFα/IL-6 plasma concentration

PD21 PFC

For the average CpG methylation there was a significant main effect of sex (GLMM: $F_{1,18}$=53.61, p<0.001), with increased *Gpc4* promoter methylation in females relative to males and a trend to a group*sex interaction (GLMM: $F_{2,18}$=2.95, p=0.078). Post-hoc analysis revealed a main effect of group in the females (GLMM: $F_{1,9}$=5.93, p=0.038) with increased methylation in poly(I:C)-females relative to vehicle-females and a significant main effect of both maternal IL-6 (GLMM: $F_{1,6}$=8.15, p=0.029) and TNFα (GLMM: $F_{1,6}$=7.21, p=0.036) in the males, with decreased methylation in poly(I:C)-males relative to vehicle-males (Figure 5.13A). Results for the individual CpG sites (Table 5.20; Figure 5.13B-D), showed a reduction in methylation of the CpG1 and CpG2 in poly(I:C)-males relative to vehicle-males, but an increase in poly(I:C)-females relative to vehicle-females

Table 5.20. *Gpc4* promoter methylation PD21 statistics

CpG site	Minimal GLMM	Post-hoc females	Post-hoc males
CpG1	Group*sex: $F_{2,18}$=3.93, p=0.056 Sex: $F_{1,18}$=38.47, p<0.001	Group: $F_{1,9}$=8.24, p=0.018 Increase in poly(I:C)-females relative to vehicle-females	MatIL6: $F_{1,6}$=9.17, p=0.023 MatTNFα: $F_{1,6}$=8.06, p=0.030 Decrease in poly(I:C)-males relative to vehicle-males
CpG2	Group*sex: $F_{2,10.89}$=3.95, p=0.051 Sex: $F_{1,10.64}$=63.02, p<0.001	Group: $F_{1,9}$=7.42, p=0.023 Increase in poly(I:C)-females relative to vehicle-females	MatIL6: $F_{1,6}$=8.92, p=0.024 MatTNFα: $F_{1,6}$=8.46, p=0.027 Decrease in poly(I:C)-males relative to vehicle-males
CpG3	Sex: $F_{1,20}$=58.2, p<0.001	NSP	NSP

Abbreviations: MatTNFα/MatIL6, 3h maternal TNFα/IL-6 plasma concentration; NSP, no significant effects of any predictors

PD35 PFC

For the average CpG methylation there was a significant main effect of sex (GLMM: $F_{1,16}$=154.89, p<0.001), with increased *Gpc4* promoter methylation in females relative to males and a group*sex interaction (GLMM: $F_{2,16}$=5.02, p=0.02). Post-hoc analysis revealed a trend to a main effect of group in the males (GLMM: $F_{1,8}$=4.42, p=0.069), with decreased methylation in poly(I:C)-males relative to vehicle-males (Figure 5.13A). However, the results for each individual CpG site were sex-specific (Table 5.21; Figure 5.13B-D).

Table 5.21. *Gpc4* promoter methylation PD35 statistics

CpG site	Minimal GLMM	Post-hoc females	Post-hoc males
CpG1	Group*sex: $F_{2,20}$=4.39, p=0.026 Sex: $F_{1, 20}$=161.32, p<0.001	Group: $F_{1, 9}$=9.09, p=0.015 Increase in poly(I:C)-females relative to vehicle-females	NSP
CpG2	Group*sex: $F_{1,20}$=6.37, p=0.020 Sex: $F_{1, 20}$=218.41, p<0.001	NSP	Group: $F_{1, 7.99}$=4.48, p=0.067 Decrease in poly(I:C)-males relative to vehicle-males
CpG3	Group*sex: $F_{1,20}$=, 7.18, p=0.014 Sex: $F_{1, 20}$=222.34, p<0.001	NSP	Group: $F_{1, 7.99}$=4.90, p=0.058 Decrease in poly(I:C)-males relative to vehicle-males

Abbreviations: NSP, no significant effects of any predictors

PD100 PFC

For the average CpG methylation (Figure 5.13A) there was a significant main effect of sex (GLMM: $F_{1,18}$=46.93, p<0.001), with increased *Gpc4* promoter methylation in females relative to males and a trend to a main effect of maternal TNFα (GLMM: $F_{1,18}$=4.18, p=0.056), corresponding to a negative correlation between maternal TNFα and *Gpc4* promoter methylation (rho=-0.311, p=0.071). However, results for individual CpG sites were sex-specific (Table 5.22; Figure 5.13B-D).

Table 5.22. *Gpc4* promoter methylation PD100 statistics

CpG site	Minimal GLMM	Post-hoc females	Post-hoc males
CpG1	Sex: $F_{1,25}$=68.65, p<0.001	NSP	NSP
CpG2	Sex: $F_{1,24}$=59.76, p<0.001	NSP	MatTNFα: $F_{1,9}$=6.45, p=0.032 Decrease in poly(I:C)-males relative to vehicle-males
CpG3	Sex: $F_{1,25}$=59.15, p<0.001	Group: $F_{1,10}$=5.65, p=0.039 Decrease in poly(I:C)-females relative to vehicle-females	NSP

Abbreviations: MatTNFα, 3h maternal TNFα plasma concentration; NSP, no significant effects of any predictors

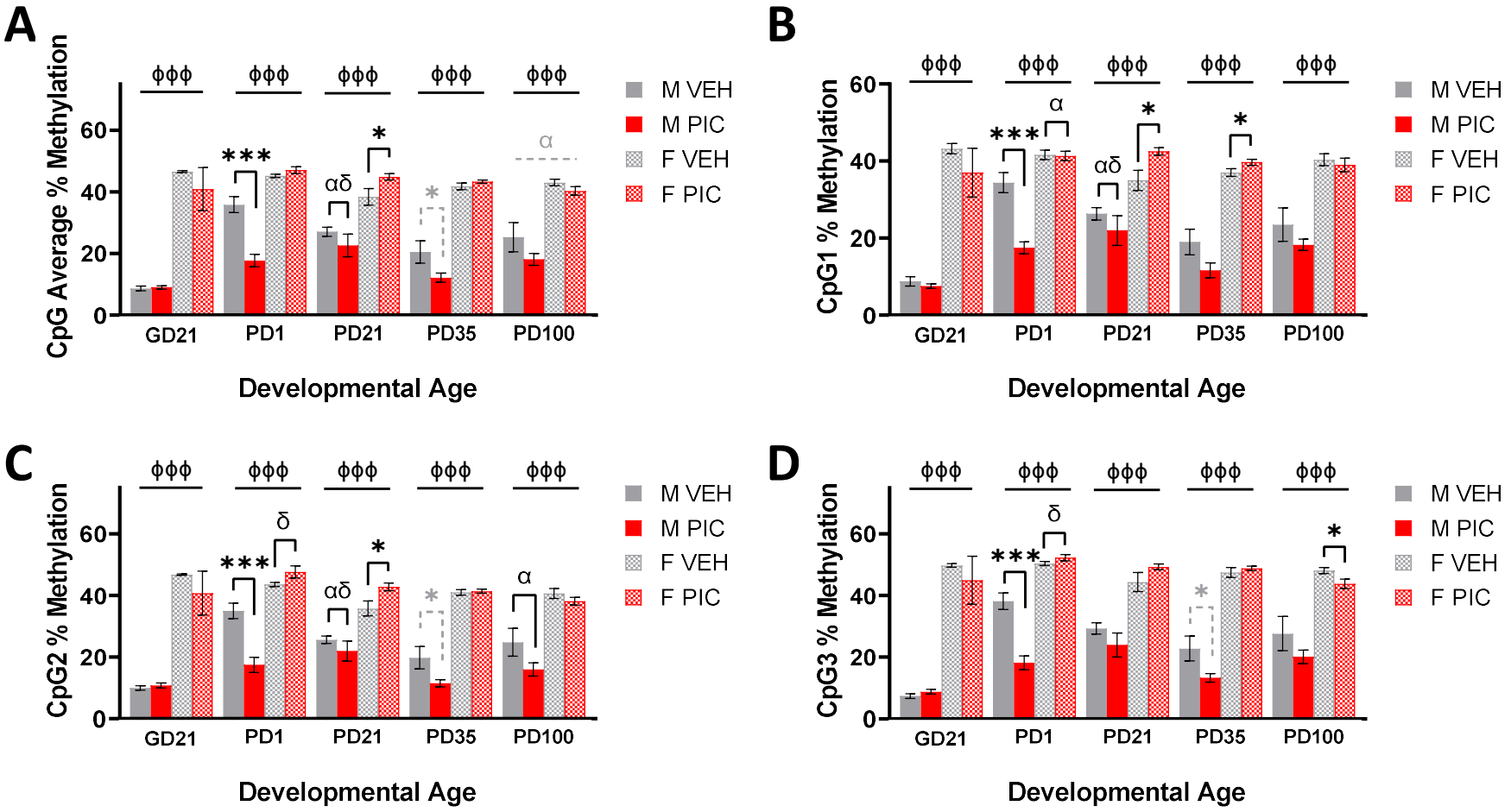

Figure 5.13. *Gpc4* promoter methylation
A. Average percentage methylation. **B.** CpG1 % methylation. **C.** CpG2 % methylation. **D.** CpG3 % methylation. Bars represent mean ±SEM (N=5-7, n=5-7). Black significance bars show significant results of the GLMM. — shaped significance bars represent results across the whole developmental stage, Π-shaped bars represent post-hoc GLMM within a single sex. Symbols show significant main effects of: group, *p<0.05, ***p≤0.001; maternal TNFα, αp<0.05; maternal IL-6, δp<0.05; sex, ϕϕϕp<0.001. Grey dashed bars and symbols represent trending results of the GLMM (0.05<p<0.08). Abbreviations: GD, gestational day; PD, postnatal day; M, male; F, female; PIC, poly(I:C); VEH, vehicle.

5.3.3.3. Differential mRNA/protein expression of astrocyte-enriched, *Gpc4*

GD21 FC

For mRNA, there was a significant group*sex interaction (GLMM: $F_{3,11.69}$=5.06, p=0.018). Post-hoc analysis showed a significant main effect of group in females (GLMM: $F_{1,7}$=10.57, p=0.014), with reduced *Gpc4* mRNA expression in poly(I:C)-females relative to vehicle-females (Figure 5.14A).

There were no significant effects of any predictors on GPC4 protein expression (Figure 5.14B).

PD1 FC

For mRNA, there was a significant main effect of sex (GLMM: $F_{1,4.15}$=12.63, p=0.022), with increased *Gpc4* mRNA expression in females relative to males. Post-hoc analysis showed a significant main effect of group in the males (GLMM: $F_{1,10}$=7.04, p=0.024), with reduced *Gpc4* mRNA expression in poly(I:C)-males relative to vehicle-males (Figure 5.14A).

For protein, there was a significant main effect of sex (GLMM: $F_{1,5.71}$=11.32, p=0.016), with increased GPC4 expression in females relative to males and a significant group*sex interaction (GLMM: $F_{2,9.53}$=6.15, p=0.019). Post-hoc analysis showed a significant main effect of group in the males (GLMM: $F_{1,9}$=5.47, p=0.044) with increased GPC4 protein expression in poly(I:C)-males relative to vehicle-males (Figure 5.14B).

PD21 PFC

For mRNA, there was a significant main effect of sex (GLMM: $F_{1,10.10}$=11.51, p=0.007), with increased *Gpc4* mRNA expression in females relative to males and a group*sex interaction (GLMM: $F_{1,10.10}$=22.54, p<0.001). Post-hoc analysis showed a significant main effect of group in the females (GLMM: $F_{1,10.75}$=17.46, p=0.002), with increased *Gpc4* mRNA expression in poly(I:C)-females relative to vehicle-females (Figure 5.14A).

For protein there was a trend to a main effect of group (GLMM: $F_{1,23}$=4.30, p=0.067) with decreased GPC4 protein expression in poly(I:C)-offspring relative to vehicle (Figure 5.14B).

PD35 PFC

For mRNA, there were no significant effects of any predictors on *Gpc4* mRNA expression (Figure 5.14A).

For protein there was a trend to a main effect of group (GLMM: $F_{1,22}$=4.00, p=0.068), with decreased GPC4 protein expression in poly(I:C)-offspring relative to vehicle (Figure 5.14B).

PD100 PFC

For mRNA, there was a significant group*sex interaction (GLMM: $F_{3,28}$=4.40, p=0.012). Post-hoc analysis showed a significant main effect of group in the males (GLMM: $F_{1,11.47}$=7.03, p=0.022), with reduced *Gpc4* mRNA expression in poly(I:C)-males relative to vehicle-males (Figure 5.14A) and a significant main effect of group in the females (GLMM: $F_{1,16}$=6.17,

p=0.024), with increased *Gpc4* mRNA expression in poly(I:C)-females relative to vehicle-females (Figure 5.14A).

For protein, there was a significant group*sex interaction (GLMM: $F_{3,22}$=4.05, p=0.020). Post-hoc analysis showed a significant main effect of group in both females (GLMM: $F_{1,12}$=5.26, p=0.041; with increased GPC4 expression in poly(I:C)-females relative to vehicle-females; Figure 5.14B) and males (GLMM: $F_{1,10}$=5.70, p=0.038; with decreased GPC4 expression in poly(I:C)-males relative to vehicle-males; Figure 5.14B).

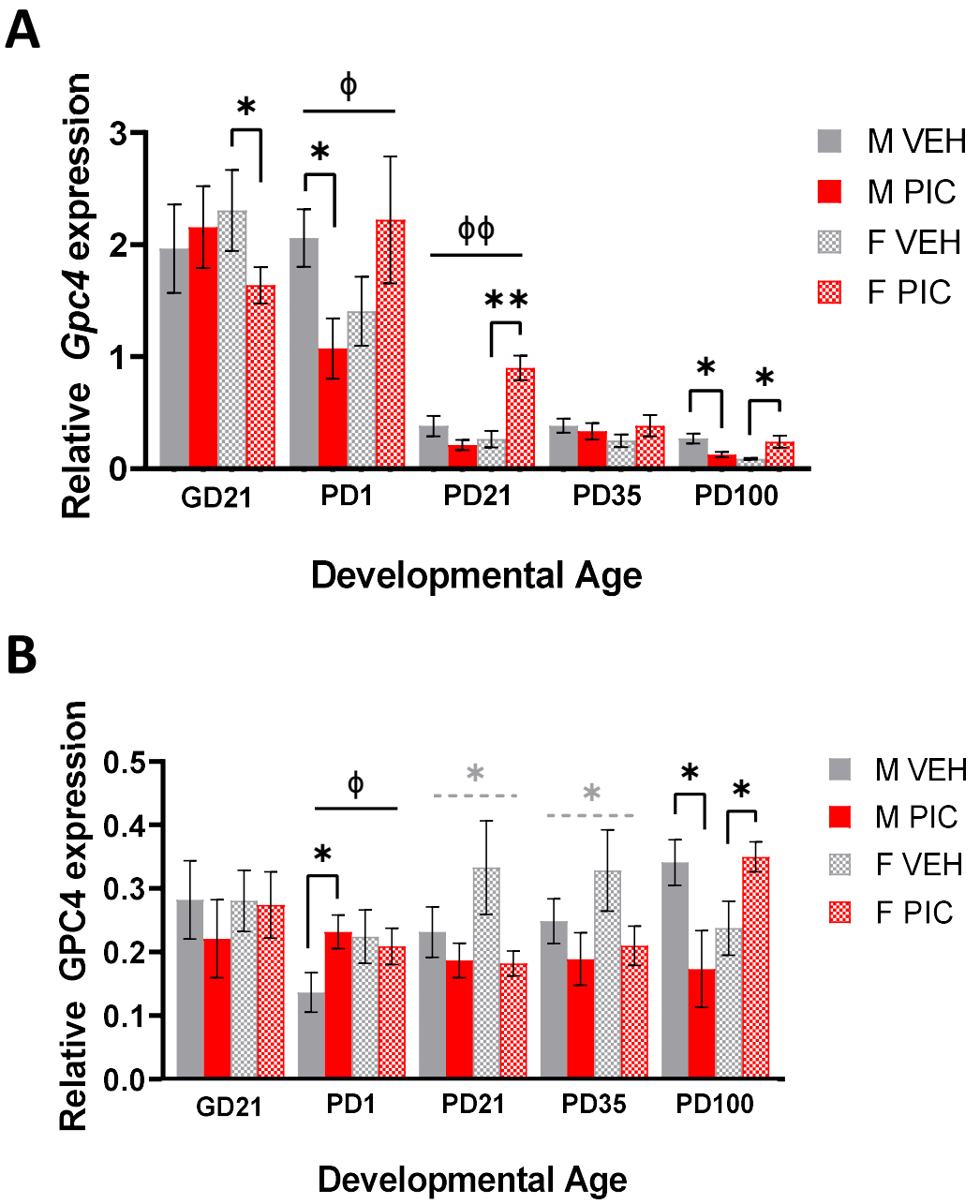

Figure 5.14. Astrocyte-enriched *Gpc4* gene and protein expression
A. Relative mRNA expression (normalised to the geometric mean of three reference genes as detailed in methods), bars show mean ±SEM (N=5-9, n=5-10). **B.** Relative protein expression (normalised to the GAPDH reference protein), bars represent mean ±SEM (N=5-7, n=5-7). Black significance bars represent significant GLMM results, — shaped significance bars show results across whole developmental age, Π shaped bars show post-hoc GLMM within a single sex. Black symbols show significant main effects of: group, *p<0.05, **p<0.01; sex, ϕp<0.05, ϕϕp<0.01. Grey dashed bars and symbols represent trending results of the GLMM (0.05<p<0.08). Abbreviations: GD, gestational day; PD, postnatal day; M, male; F, female; PIC, poly(I:C); VEH, vehicle.

5.3.4. Dysregulation of oligodendrocytes in the developing cortex

5.3.4.1. OLIG2+ oligodendrocytes and NG2+ OPC density changes

There was a significant main effect of group at PD35 (GLMM: $F_{1,8.85}$=7.02, p=0.027) with increased OLIG2+ oligodendrocyte density in the poly(I:C)-offspring relative to vehicle (Figure 5.15A). Conversely, while there was also a main effect of group for NG2+ OPCs (GLMM: $F_{1,10.98}$=8.97, p=0.012) this represented reduced NG2+ OPC density in poly(I:C)-offspring relative to vehicle (Figure 5.15B).

At PD100, for OLIG2+ oligodendrocytes, there was a significant main effect of group (GLMM: $F_{1,18}$=10.47, p=0.005), with, again, increased OLIG2+ oligodendrocytes in the poly(I:C)-offspring relative to vehicle-offspring (Figure 5.15A). For NG2+ OPCs there was a main effect of maternal IL-6 (GLMM: $F_{1,18}$=4.53, p=0.047; Figure 5.15B), corresponding to a negative correlation between maternal plasma IL-6 and NG2+ OPCs (r=-0.448, p=0.047). These results would indicate an overall reduction in immature oligodendrocytes and a concurrent increase in mature oligodendrocytes.

Accordingly, the ratio of NG2+ OPCs:OLIG2+ oligodendrocytes was calculated within each sample. This showed a significant main effect of group at both PD35 (GLMM: $F_{1,10.84}$=15.78, p=0.002) and PD100 (GLMM: $F_{1,22}$=14.01, p=0.01), with a reduction in the NG2+:OLIG2+ cell ratio, indicative of a greater density of mature oligodendrocytes and concurrent reduction in OPC density, in poly(I:C)-offspring relative to vehicle (Figure 5.15C).

Representative OLIG2+ and NG2+ stains are shown in Figure 5.15D-E.

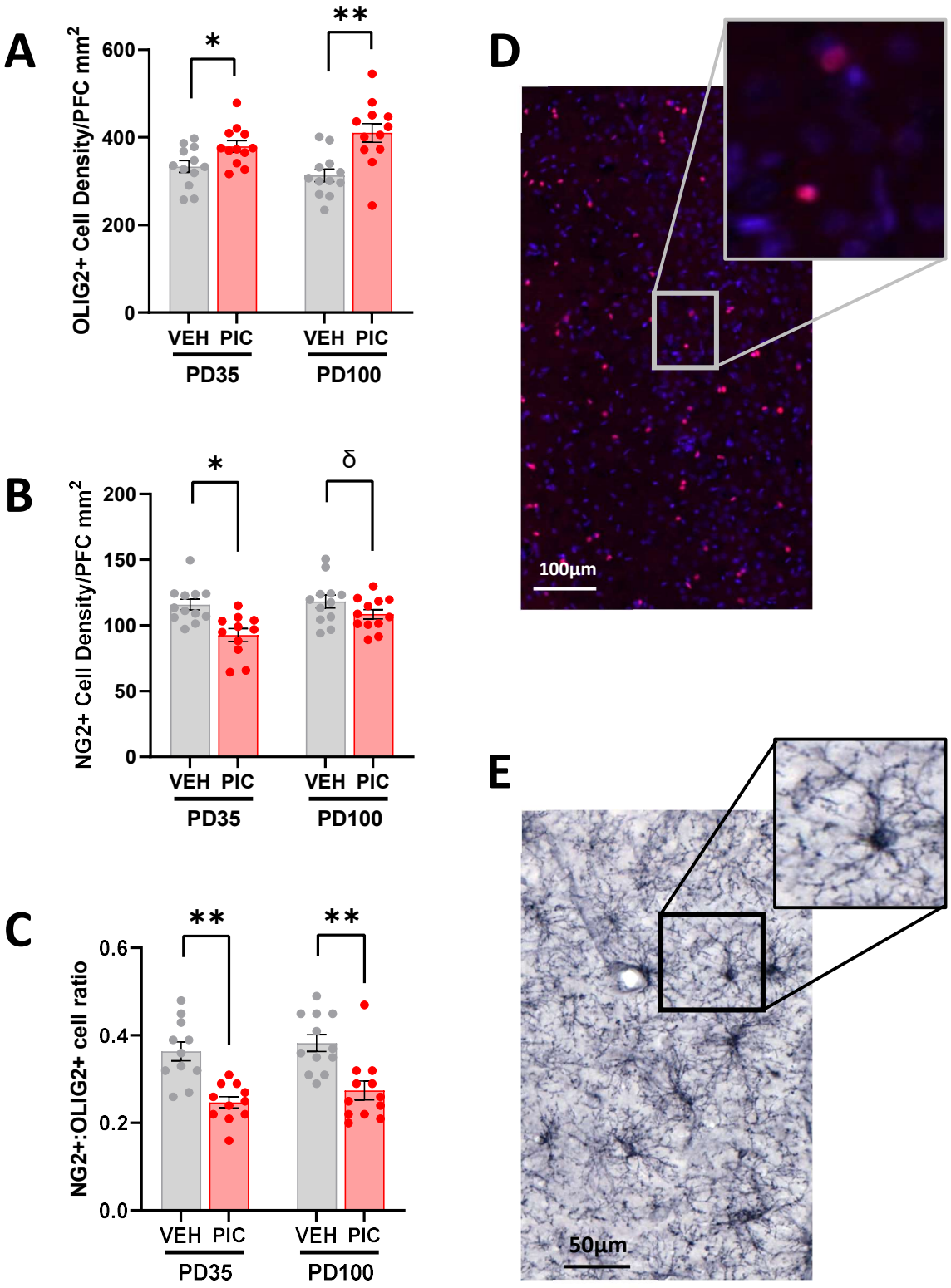

Figure 5.15. OLIG2+ oligodendrocyte and NG2+ OPC density
A. OLIG2+ oligodendrocyte cell density. **B.** NG2+ OPC cell density. **C.** NG2+:OLIG2+ cell ratio. Bars represent mean ±SEM, dots represent individual animals (N=5-6, n=5-6). Π-shaped black bars show GLMM results within a single age; Black symbols show significant main effect of: group, *p<0.05, **p≤0.01; maternal IL-6, δp<0.05. Abbreviations: PIC, poly(I:C); VEH, vehicle; PD, postnatal day. **D.** Representative OLIG2+ stain is indicated, 20X magnification, inset shows magnification of OLIG2+ nuclei (DAPI, blue; OLIG2, pink). **E.** Representative NG2+ stain is indicated, 10X magnification, inset shows magnified adult OPC with typical branched processes.

5.3.4.2. Differential methylation of oligodendrocyte-enriched genes

I. *Nfasc*

NFASC (Neurofascin) is an adhesion molecule located at the perinodal region, involved in intracellular and extracellular matrix contacts. The RRBS identified a reduction in methylation in intron 1 of the *Nfasc* gene (Table 5.8; Appendix 9). This region, containing three CpG sites was analysed by pyrosequencing across the developmental timeline (GD21-PD100).

GD21 FC

There was no significant effects of any predictors on average CpG methylation or methylation of any of the individual CpG sites (Figure 5.16A-C), with the exception of CpG3 where there was a trend to a main effect of sex (GLMM: $F_{1,9.56}$=4.45, p=0.062), with females having reduced methylation at CpG3 than males (Figure 5.16D).

PD1 FC

For average CpG methylation there was a significant main effect of group (GLMM: $F_{1,8.95}$=9.77, p=0.012) with reduced methylation in poly(I:C)-offspring relative to vehicle-offspring and a trend to a main effect of sex (GLMM: $F_{1,3.06}$=6.67, p=0.080), with females having reduced methylation relative to males (Figure 5.16A). When the CpG sites were considered individually, there were no significant effects of any predictors on methylation at CpG2 or CpG3, while CpG1 showed a main effect of group (GLMM: $F_{1,12.69}$=8.39, p=0.013), with reduced methylation in poly(I:C)-offspring relative to vehicle-offspring (Figure 5.16C-D).

PD21 PFC

For average CpG methylation there was a significant group*sex interaction (GLMM: $F_{3,14}$=5.48, p=0.011). Post-hoc analysis showed a significant main effect of maternal IL-6 (GLMM: $F_{1,6}$=6.05, p=0.049) and a trend to a main effect of group (GLMM: $F_{1,6}$=5.33, p=0.060) in females, with increased methylation in poly(I:C)-females relative to vehicle-females (Figure 5.16A). Similar results were also noted when the CpG sites were considered individually (Table 5.23; Figure 5.16B-D).

Table 5.23. *Nfasc* intron 1 methylation PD21 statistics

CpG site	Minimal GLMM	Post-hoc females	Post-hoc males
CpG1	Group*sex: $F_{3,14}$=5.81, p=0.009	Group: $F_{1,8}$=12.74, p=0.007; Increase in poly(I:C)-females relative to vehicle-females	NSP
CpG2	Group*sex: $F_{3,17}$=3.06, p=0.056	Group: $F_{1,8}$=12.70, p=0.009; Increase in poly(I:C)-females relative to vehicle-females	NSP
CpG3	Group*sex: $F_{3,14}$=4.37, p=0.056	Group: $F_{1,8}$=5.51, p=0.047; Increase in poly(I:C)-females relative to vehicle-females	NSP

Abbreviations: NSP, no significant effects of any predictors

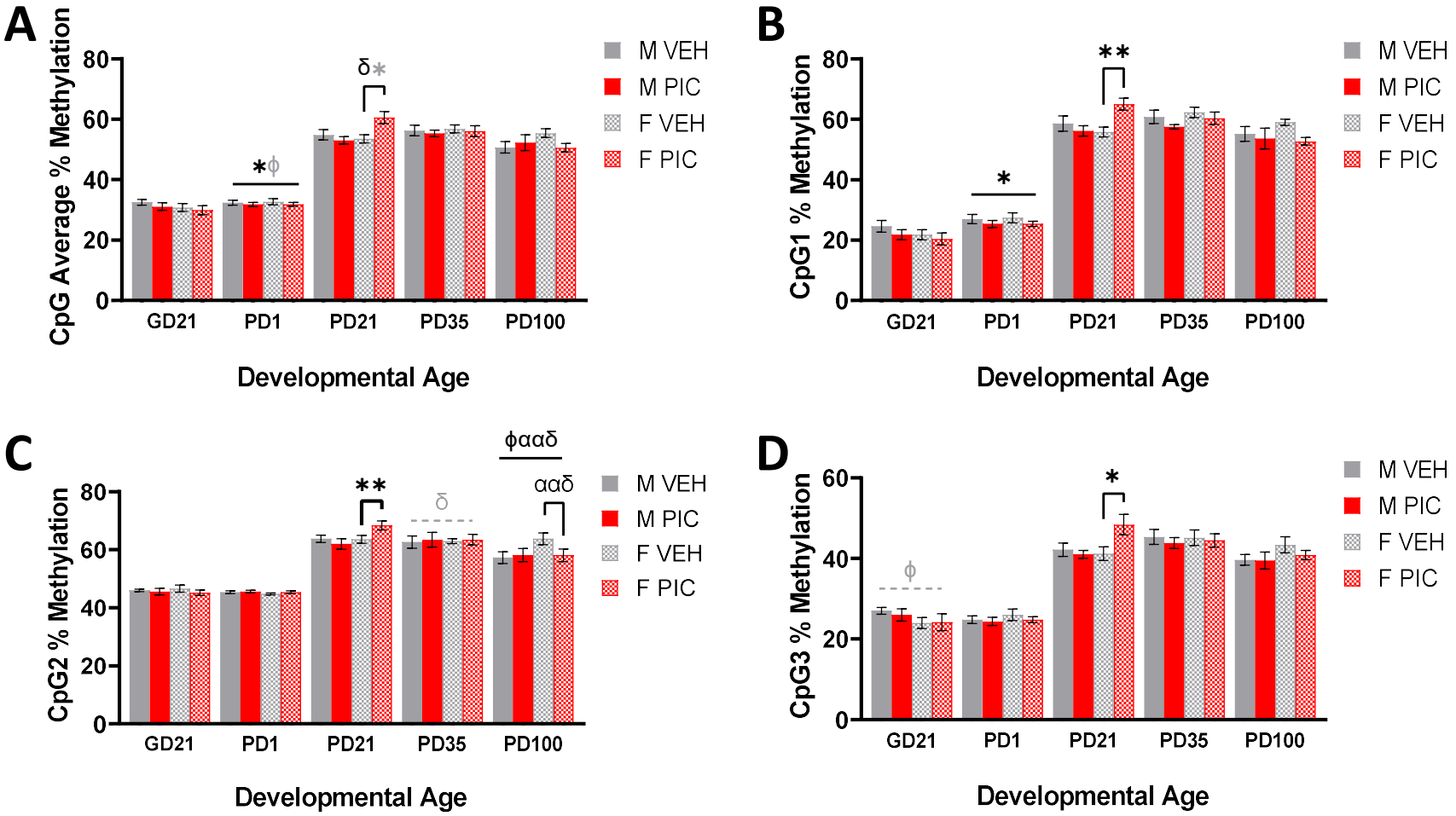

Figure 5.16. *Nfasc* intron 1 methylation

A. Average percentage methylation. **B.** CpG1 % methylation. **C.** CpG2 % methylation. **D.** CpG3 % methylation. Bars represent mean ±SEM (N=5-7, n=5-7). Black significance bars show significant results of the GLMM. — shaped significance bars represent results across the whole developmental age, Π-shaped bars represent post-hoc GLMM within a single sex. Black symbols show significant main effects of: sex, ϕp<0.05; group, *p<0.05, **p<0.01; maternal TNFα, ααp<0.01; maternal IL-6, δp<0.05. Grey dashed bars and/or symbols represent trending (0.05<p≤0.08) results of the GLMM. Abbreviations: GD, gestational day; PD, postnatal day; M, male; F, female; PIC, poly(I:C); VEH, vehicle.

PD35 PFC

There was no significant effects of any predictors on average CpG methylation or methylation of any of the individual CpG sites, with the exception of CpG2 where there was a trend to a main effect of maternal IL-6 (GLMM: $F_{1,14.87}$=3.75, p=0.072; Figure 5.16C), corresponding to a trending negative correlation between maternal IL-6 and CpG2 methylation (r=-0.403, p=0.070).

PD100 PFC

There was no significant effects of any predictors on average CpG methylation or methylation of any of the individual CpG sites, with the exception of CpG2 (Figure 5.16C) where there was a main effect of sex (GLMM: $F_{1,9.56}$=7.03, p=0.025), with females having increased methylation relative to males, alongside a main effect of maternal IL-6 (GLMM: $F_{1,15.41}$=4.79, p=0.044) and maternal TNFα (GLMM: $F_{1,15.66}$=9.14, p=0.008). Post-hoc analysis by sex showed a main effect of maternal IL-6 (GLMM: $F_{1,7}$=8.37, p=0.023) and maternal TNFα (GLMM: $F_{1,7}$=14.90, p=0.006) in the females. That said, no post-hoc correlations between maternal cytokines and CpG2 methylation were significant.

II. *Mbp*

MBP (Myelin basic protein) is the major myelin protein of the CNS. Four major isoforms exist (21.5kDa, 18.5kDa, 17kDa and 14kDa) developmentally regulated by splicing of exon 2 (Akiyama et al., 2002; Kruger et al., 1999). The RRBS identified a reduction in methylation of exon 2 in the *Mbp* gene (Table 5.8; Appendix 9). This region, containing three CpG sites was analysed by pyrosequencing across the developmental timeline (GD21-PD100).

GD21 FC

There was no significant effect of any predictors on average CpG methylation or methylation of the individual CpG sites (Figure 5.17).

PD1 FC

For average CpG methylation there was a significant main effect of group (GLMM: $F_{1,11.33}$=76.17, p=0.030), with increased methylation in poly(I:C)-offspring relative to vehicle-offspring (Figure 5.17A). However, there were no significant effects of any predictors on methylation of the individual CpG sites, with the exception of CpG2, where there was a trend to a main effect of group (GLMM: $F_{1,13.67}$=4.15, p=0.062), with increased methylation at CpG2 in poly(I:C)-offspring relative to vehicle-offspring (Figure 5.17C).

PD21 PFC

For the average CpG methylation, there was a significant main effect of group (GLMM: $F_{1,18}$=12.29, p=0.003), with decreased methylation in poly(I:C)-offspring relative to vehicle-offspring (Figure 5.17A). This main effect of group remained when the CpG sites were considered individually: CpG1 (GLMM: $F_{1,18}$=11.99, p=0.003; Figure 5.17B); CpG2 (GLMM: $F_{1,18}$=11.92, p=0.003; Figure 5.17C); CpG3 (GLMM: $F_{1,18}$=12.42, p=0.002; Figure 5.17D).

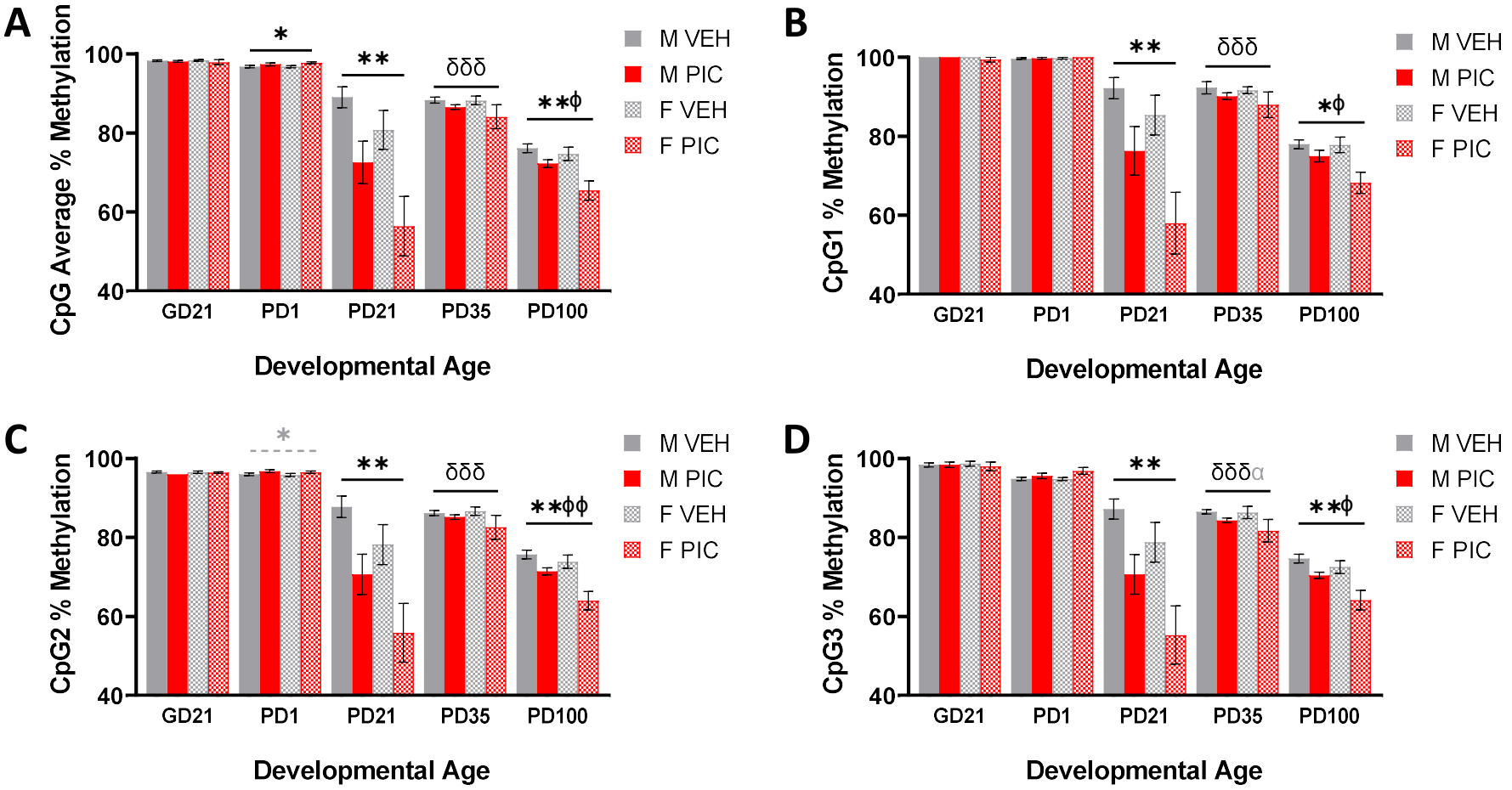

Figure 5.17. *Mbp* exon 2 methylation
A. Average percentage methylation. **B.** CpG1 % methylation. **C.** CpG2 % methylation. **D.** CpG3 % methylation. Bars represent mean ±SEM (N=5-7, n=5-8). Black significance bars show significant results of the GLMM. — shaped significance bars represent results across the whole developmental age, Π-shaped bars represent post-hoc GLMM within a single sex. Black symbols show significant main effects of group, *p<0.05, **p<0.01; maternal IL-6, δδδp<0.001; sex, ϕp<0.05, ϕϕp<0.01. Grey dashed bars and/or symbols represent trending (0.05<p<0.08) results of the GLMM: group *; maternal TNFα α. Abbreviations: GD, gestational day; PD, postnatal day; M, male; F, female; PIC, poly(I:C); VEH, vehicle.

PD35 PFC

There was a significant main effect of maternal IL-6 on average CpG methylation (GLMM: $F_{1,10.12}$=35.79, p<0.001; Figure 5.17A), corresponding to a negative correlation between maternal plasma IL-6 and *Mbp* exon 2 methylation (r=-0.825, p<0.001). This main effect of maternal IL-6 was identified when the CpG sites were considered individually (Figure 5.17B-D): CpG1 (GLMM: $F_{1,11.88}$=24.52, p<0.001; r=-0.753, p<0.001); CpG2 (GLMM: $F_{1,10.49}$=28.27, p<0.001; r=-0.5818, p<0.001); CpG3 (GLMM: $F_{1,19}$=17.14, p<0.001; r=-0.679, p<0.001). Of note, for CpG3 there was also a trend to a main effect of maternal TNFα, corresponding to a negative correlation between maternal TNFα and CpG3 methylation (GLMM: $F_{1,19}$=3.63, p=0.072; r=-0.598; p=0.003).

PD100 PFC

For average CpG methylation, there was a main effect of both sex (GLMM: $F_{1,16.72}$ =7.91, p=0.012), with females having reduced methylation relative to males and group (GLMM: $F_{1,16.97}$=11.64, p=0.003) with reduced methylation in poly(I:C)-offspring relative to vehicle-offspring (Figure 5.17A). These main effects of both sex and group were observed likewise when each CpG site was considered individually (Table 5.24; Figure 5.17B-D).

Table 5.24. *Mbp* exon 2 methylation PD100 statistics

CpG site	Minimal GLMM
CpG1	Sex: $F_{1,14.12}$=5.04, p=0.041; Reduced methylation in females relative to males Group: $F_{1,14.54}$=6.92, p=0.019; Decreased methylation in poly(I:C)-offspring relative to vehicle-offspring
CpG2	Sex: $F_{1,15.16}$=9.67, p=0.007; Reduced methylation in females relative to males Group: $F_{1,14.86}$=12.64, p=0.003; Decreased methylation in poly(I:C)-offspring relative to vehicle-offspring
CpG3	Sex: $F_{1,17.85}$=7.60, p=0.013; Reduced methylation in females relative to males Group: $F_{1,16.82}$=11.36, p=0.004; Decreased methylation in poly(I:C)-offspring relative to vehicle-offspring

5.3.4.3. Differential mRNA expression of oligodendrocyte genes

I. *Nfasc*

GD21 FC

There were no significant effects of any predictors on *Nfasc* expression (Figure 5.18A).

PD1 FC

There was a significant main effect of group (GLMM: $F_{1,20}$=5.03, p=0.036) with reduced *Nfasc* mRNA expression in poly(I:C)-offspring relative to vehicle-offspring (Figure 5.18A).

PD21 and PD35 PFC

There was a significant main effect of group for both PD21 (GLMM: $F_{1,23}$=13.44, p=0.001) and PD35 (GLMM: $F_{1,21}$=5.94, p=0.024) with increased *Nfasc* mRNA expression in poly(I:C)-offspring relative to vehicle-offspring (Figure 5.18A).

PD100 PFC

There was a significant main effect of sex (GLMM: $F_{1,24}$=7.33, p=0.012) with increased *Nfasc* expression in males relative to females and a group*sex interaction (GLMM: $F_{2,24}$=5.98,

p=0.008). Post-hoc analysis showed a significant main effect of group in the males (GLMM: $F_{1,11}$=5.70, p=0.036), with reduced *Nfasc* mRNA expression in poly(I:C)-males relative to vehicle-males (Figure 5.18A) and a significant main effect of group in the females (GLMM: $F_{1,13}$=4.63, p=0.050), with increased *Nfasc* mRNA expression in poly(I:C)-females relative to vehicle-females (Figure 5.18A).

II. *Mbp*

GD21 FC

There was a significant main effect of group (GLMM: $F_{1,18}$=82.28, p<0.001) with reduced *Mbp* mRNA expression in poly(I:C)-foetuses relative to vehicle-foetuses (Figure 5.18B)

PD1 FC

There were no significant effects of any predictors on *Mbp* expression (Figure 5.18B).

PD21 PFC

There was a significant main effect of group (GLMM: $F_{1,21}$=4.52, p=0.042), with increased *Mbp* mRNA expression in poly(I:C)-offspring relative to vehicle-offspring (Figure 5.18B).

PD35 and PD100 PFC

There were no significant effects of any predictors on *Mbp* expression (Figure 5.18B).

III. *Mag*

Mag (Myelin associated glycoprotein) is another abundant myelin protein in the CNS. *Mag* was also identified in the RRBS but, given the greater significance of *Mbp* and sample constraints, it was not analysed by pyrosequencing (See Appendix 9), however its relative mRNA expression was analysed alongside *Mbp*.

GD21 FC

There was a significant main effect of group (GLMM: $F_{1,18}$=4.62, p=0.046), with increased *Mag* mRNA expression in poly(I:C)-foetuses relative to vehicle-foetuses (Figure 5.18C).

PD1 FC

There was a significant main effect of group (GLMM: $F_{1,10.27}$=5.92, p=0.035), with reduced *Mag* mRNA expression in poly(I:C)-offspring relative to vehicle-offspring (Figure 5.18C).

PD21 PFC

There were no significant effects of any predictors on *Mag* expression *(*Figure 5.18C).

PD35 PFC

There was a significant main effect of group (GLMM: $F_{1,10.7}$=9.73, p=0.01) with increased *Mag* mRNA expression in poly(I:C)-offspring relative to vehicle-offspring (Figure 5.18C).

PD100 PFC

There were no significant effects of any predictors on *Mag* expression (Figure 5.18C).

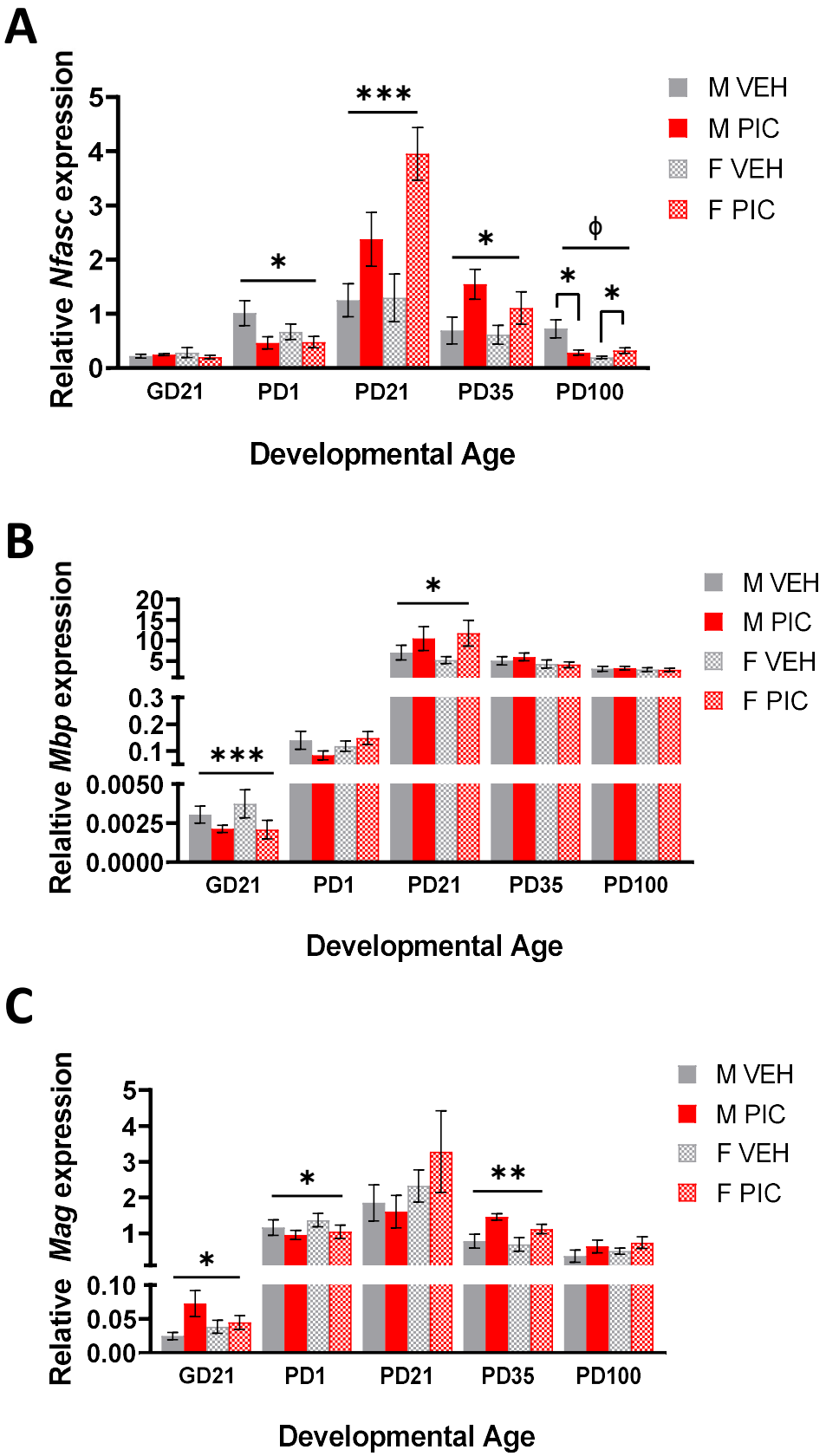

Figure 5.18. Oligodendrocyte-enriched gene expression
Relative mRNA expression (normalised to the geometric mean of three reference genes as detailed in methods) **A**. *Nfasc* (N=5-7, n=5-8). **B.** *Mbp* (N=5-8, n=5-10) **C**. *Mag* (N=5-6, n=5-6). Bars represent mean ±SEM. Black significance bars represent significant GLMM results, — shaped significance bars show results across whole developmental age, Π-shaped bars show post-hoc GLMM within a single sex. Black symbols show significant main effects of group, *p≤0.05, **p≤0.01, ***p≤0.001; sex, ϕp<0.05. Abbreviations: GD, gestational day; PD, postnatal day; M, male; F, female; PIC, poly(I:C); VEH, vehicle.

5.3.4.4. Differential expression of oligodendrocyte transcription factors

Given the significant differences in expression of oligodendrocyte genes, transcription factors (*Olig2, Myrf, Qki*) important in oligodendrocyte development (Figure 5.1) were investigated.

I. *Olig2*

OLIG2 (Oligodendrocyte transcription factor 2) is a lineage-specific transcription factor for oligodendrocyte cells and is therefore a key transcription factor for the expression of oligodendrocyte genes (Emery and Lu, 2015). There were no significant effects of any predictors on *Olig2* expression in the GD21 or PD1 FC or PD21 PFC. In the PD35 PFC there was a trend to a main effect of group (GLMM: $F_{1,10.43}$=3.51, p=0.079), with increased *Olig2* mRNA expression in poly(I:C)-offspring relative to vehicle-offspring (Figure 5.19A). In the PD100 PFC there was a main effect of sex (GLMM: $F_{1,15}$=11.30, p=0.004) with increased *Olig2* mRNA expression in females relative to males and a main effect of maternal TNFα (GLMM: $F_{1,15}$=25.60, p<0.001; Figure 5.19A), corresponding to a positive correlation between maternal TNFα and *Olig2* mRNA expression (rho=0.528, p=0.024).

II. *Myrf*

MYRF (Myelin regulatory factor) is the transcription factor which promotes the expression of myelin proteins during oligodendrocyte maturation (Emery and Lu, 2015). In the GD21 FC there was a trend to a main effect of group (GLMM: $F_{1,16}$=4.32, p=0.054), with increased *Myrf* mRNA expression in poly(I:C)-foetuses relative to vehicle (Figure 5.19B), while in the PD1 FC there was a main effect of sex (GLMM: $F_{1,14.09}$=4.98, p=0.042), with reduced *Myrf* mRNA expression in females relative to males. In the PD21 PFC there was a main effect of group (GLMM: $F_{1,11.35}$=12.05, p=0.005) with increased *Myrf* mRNA expression in poly(I:C)-offspring relative to vehicle (Figure 5.19B). Similarly, in the PD35 PFC there was a main effect of maternal IL-6 (GLMM: $F_{1,8.04}$=8.85, p=0.018; Figure 5.19B), corresponding to a positive correlation between maternal IL-6 and PD35 *Myrf* mRNA expression (r=0.617, p=0.004). In the PD100 PFC there was a main effect of sex (GLMM: $F_{1,16.04}$=18.93, p<0.001), with reduced *Myrf* mRNA expression in females relative to males and a trending main effect of group (GLMM: $F_{1,11.65}$=3.63, p=0.080), with reduced *Myrf* mRNA expression in poly(I:C)-offspring relative to vehicle (Figure 5.19B).

III. *Qki*

QKI (Quaking) is a transcription factor enriched in oligodendrocytes which has been shown to regulate the splicing of myelin gene isoforms during oligodendrocyte development (Wu et al., 2002). There were no significant effects of any predictors on *Qki* expression in the GD21 or PD1 FC or PD35 PFC. In the PD21 PFC there was a significant group*sex interaction (GLMM: $F_{3,20}$=3.57, p=0.032). Post-hoc analysis showed a main effect of group in the females (GLMM: $F_{1,12}$=30.10, p<0.001) with increased *Qki* mRNA expression in poly(I:C)-females relative to vehicle-females (Figure 5.19C). In the PD100 PFC, there was a main effect of sex (GLMM:

$F_{1,22}$=5.64, p=0.027), with reduced *Qki* mRNA expression in females relative to males and a trend to a main effect of group (GLMM: $F_{1,22}$=3.34, p=0.080), with increased *Qki* mRNA expression in poly(I:C)-offspring relative to vehicle-offspring (Figure 5.19C).

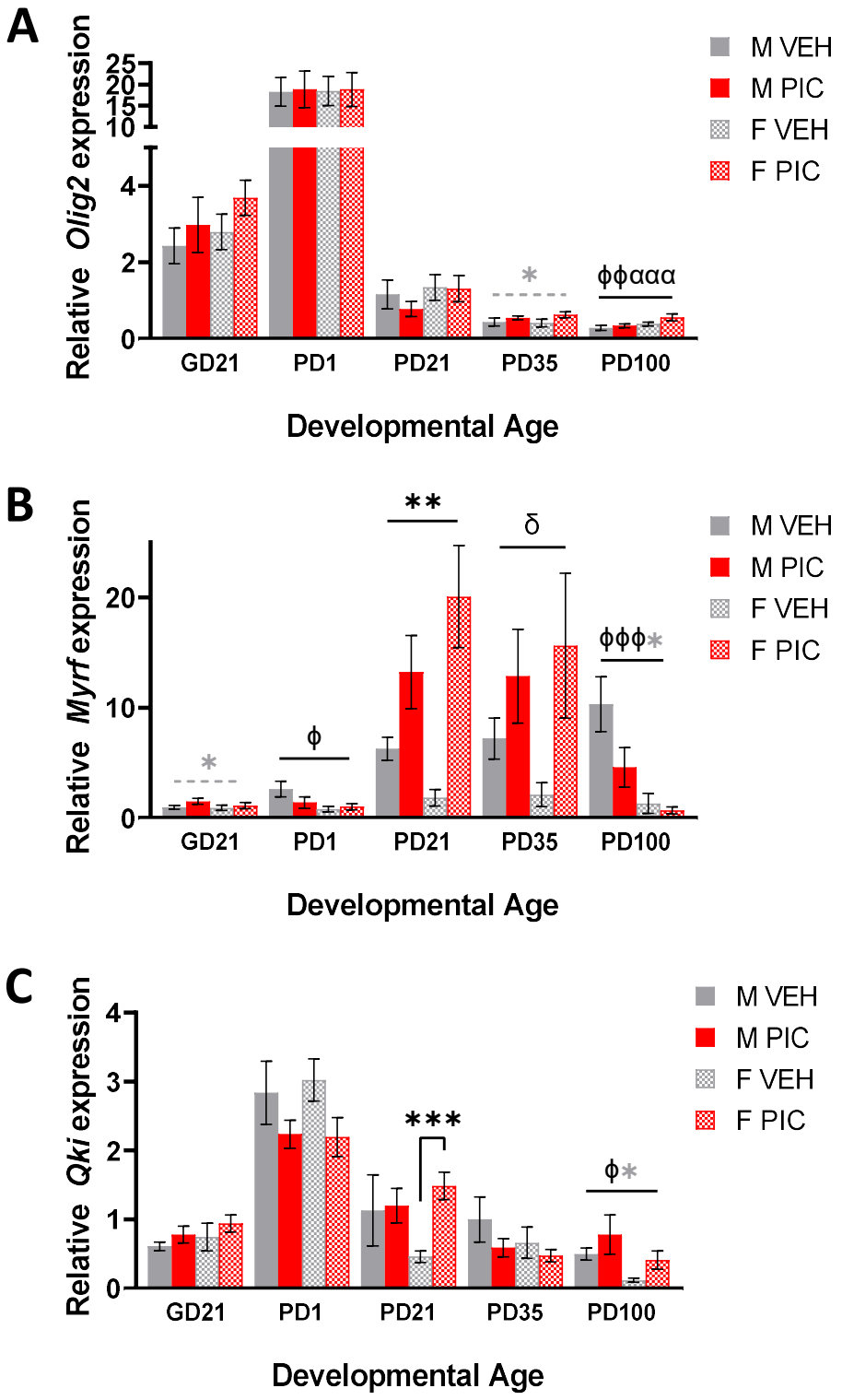

Figure 5.19. Oligodendrocyte transcription factor gene expression
Relative mRNA expression (normalised to the geometric mean of three reference genes as detailed in methods) **A**. *Olig2* (N=5-6, n=5-6). **B.** *Myrf* (N=5-7, n=5-7). **C.** *Qki* (N=5-7, n=5-7). Bars represent mean ±SEM. Black significance bars represent significant GLMM results, — shaped significance bars show results across whole developmental age, Π-shaped bars show post-hoc GLMM within a single sex. Black symbols show significant main effects of: group, **p<0.01, ***p<0.001; sex, ϕp<0.05, ϕϕp<0.01, ϕϕϕp<0.001; maternal IL-6, δp<0.05; maternal TNFα, ααα<0.001. Grey dashed bars and/or symbols (0.05<p≤0.08) represent trending results of the GLMM. Abbreviations: GD, gestational day; PD, postnatal day; M, male; F, female; PIC, poly(I:C); VEH, vehicle.

5.3.4.5. Differential protein expression of MBP

While there were few significant changes in expression of *Mbp* mRNA expression, this accounts for all splice variants. Thus, protein expression which can delineate between MBP isoform expression is important for understanding the differences in developmental myelin expression changes. Accordingly, total MBP protein expression was evaluated alongside the expression of each of the individual MBP isoforms (21.5kDa, 18.5kDa, 17kDa, 14kDa). Developmentally, an increase in total MBP expression was observed from pre-myelination (GD21-PD1) to post-myelination (PD21-100). Further, the expression of exon 2-containing isoforms (21.5kDa/17kDa) was highest during early active myelination (PD21), while exon 2-spliced isoforms (18.5kDa/14kDa) were highest at PD35-PD100 when active myelination has ended (Table 5.25). This is in line with the literature and supports the validity of the isoforms identified by the antibody.

Table 5.25. MBP isoform expression summary

MBP expression	GD21 FC	PD1 FC	PD21 PFC	PD35 PFC	PD100 PFC
Total MBP	0.007±0.001	0.011±0.002	2.026±0.202	1.604±0.200	1.708±0.201
Exon 2 containing isoforms	0.007±0.001	0.011±0.002	1.235±0.134	0.774±0.106	0.561±0.056
Exon 2 spliced isoforms	ND	ND	0.805±0.110	0.902±0.125	1.165±0.168

Data shown as mean ±SEM. ND, not detectable.

GD21 FC

The only detectable MBP isoform was the 21.5kDa and for this there were no significant effects of any predictors (Figure 5.20A&B).

PD1 FC

The only detectable MBP isoform was the 21.5kDa and for this there was a trend to a main effect of group (GLMM: $F_{1,17}$=3.93, p=0.064), with reduced 21.5kDa expression in poly(I:C)-offspring relative to vehicle-offspring (Figure 5.20A&B).

PD21 PFC

All MBP isoforms were detected at PD21. For total MBP expression there was a trend to a main effect of group (GLMM: $F_{1,22}$=4.02, p=0.057), with reduced MBP expression in poly(I:C)-offspring relative to vehicle-offspring (Figure 5.20A).

When the individual isoforms were analysed, there were no significant effects of any predictors on 18.5kDa isoform expression (Figure 5.20C). However, for the 21.5kDa and 17kDa isoforms there was a significant main effect of group (21.5kDa GLMM: $F_{1,21}$=6.20, p=0.021; 17kDa GLMM: $F_{1,21}$=5.39, p=0.030) with reduced 21.5kDa and 17kDa MBP isoform expression in poly(I:C)-offspring relative to vehicle-offspring (Figure 5.20B&D). For the 14kDa isoform there was a trend to a main effect of sex (GLMM: $F_{1,20}$=3.29, p=0.075), with post-hoc analysis showing a main effect of both group (GLMM: $F_{1,8}$=9.09, p=0.017) and maternal IL-6 (GLMM: $F_{1,8}$=5.46,

p=0.048) in males, corresponding to increased 14kDa isoform expression in poly(I:C)-males relative to vehicle-males (Figure 5.20E). Overall, there was a significant reduction in expression of exon 2-containing MBP isoforms in poly(I:C)-offspring relative to vehicle-offspring (main effect of group, GLMM: $F_{1,21}$=6.29, p=0.020), but no significant difference in expression of exon 2-spliced isoforms (Figure 5.20F&G).

PD35 PFC

All MBP isoforms were detected at PD35. For total MBP expression there was a trend to a main effect of sex (GLMM: $F_{1,11.96}$=3.92, p=0.071), with increased MBP expression in females relative to males (Figure 5.20A).

When the individual isoforms were analysed, there were no significant effects of any predictors on 21.5kDa isoform expression (Figure 5.20B). However, for the 18.5kDa and 14kDa isoforms there was a main effect of group (18.5kDa GLMM: $F_{1,10.83}$=4.99, p=0.048; 14kDa GLMM: $F_{1,10.72}$=5.39, p=0.041) with increased 18.5kDa and 14kDa MBP isoform expression in poly(I:C)-offspring relative to vehicle-offspring (Figure 5.20C&E). For the 17kDa isoform there was a trend to a main effect of sex (GLMM: $F_{1,18}$=3.61, p=0.074) and a group*sex interaction (GLMM: $F_{2,18}$=2.82, p=0.080). Post-hoc analysis revealed a main effect of group in females (GLMM: $F_{1,6.67}$=8.14, p=0.026) corresponding to reduced 17kDa MBP isoform expression in poly(I:C)-females relative to vehicle-females (Figure 5.20D). Overall, there was a significant increase in expression of exon 2-spliced MBP isoforms in poly(I:C)-offspring relative to vehicle-offspring (main effect of group, GLMM: $F_{1,7.84}$=6.62, p=0.034), but no significant difference in expression of exon 2-containing isoforms (Figure 5.20F&G). Of note, when expression of exon 2-spliced isoform was analysed, alongside the main effect of group, there was a main effect of sex (GLMM: $F_{1,9.85}$=5.77, p=0.038), with overall increased expression of exon 2-spliced isoforms in females relative to males.

PD100 PFC

All MBP isoforms were detected at PD100. For total MBP expression there was a significant main effect of group (GLMM: $F_{1,9.74}$=8.69, p=0.015), with reduced MBP expression in poly(I:C)-offspring relative to vehicle-offspring (Figure 5.20A).

When the individual isoforms were analysed, there were no significant effects of any predictors on 21.5kDa and 17kDa isoform expression (Figure 5.20B&D). However, for the 18.5kDa and 14kDa isoforms there was a main effect of group (18.5kDa GLMM: $F_{1,12.89}$=3.74, p=0.075; 14kDa GLMM: $F_{1,10.77}$=6.75, p=0.025) with reduced 18.5kDa and 14kDa MBP isoform expression in poly(I:C)-offspring relative to vehicle-offspring (Figure 5.20C&E). However, there was a significant reduction in expression of both exon 2-spliced (main effect of group, GLMM: $F_{1,19}$=7.68, p=0.012) and exon 2-containing MBP isoforms (main effect of group, GLMM: $F_{1,9.83}$=9.76, p=0.011; main effect of IL-6, GLMM: $F_{1,14.13}$=4.41, p=0.054) in poly(I:C)-offspring relative to vehicle-offspring (Figure 5.20F&G).

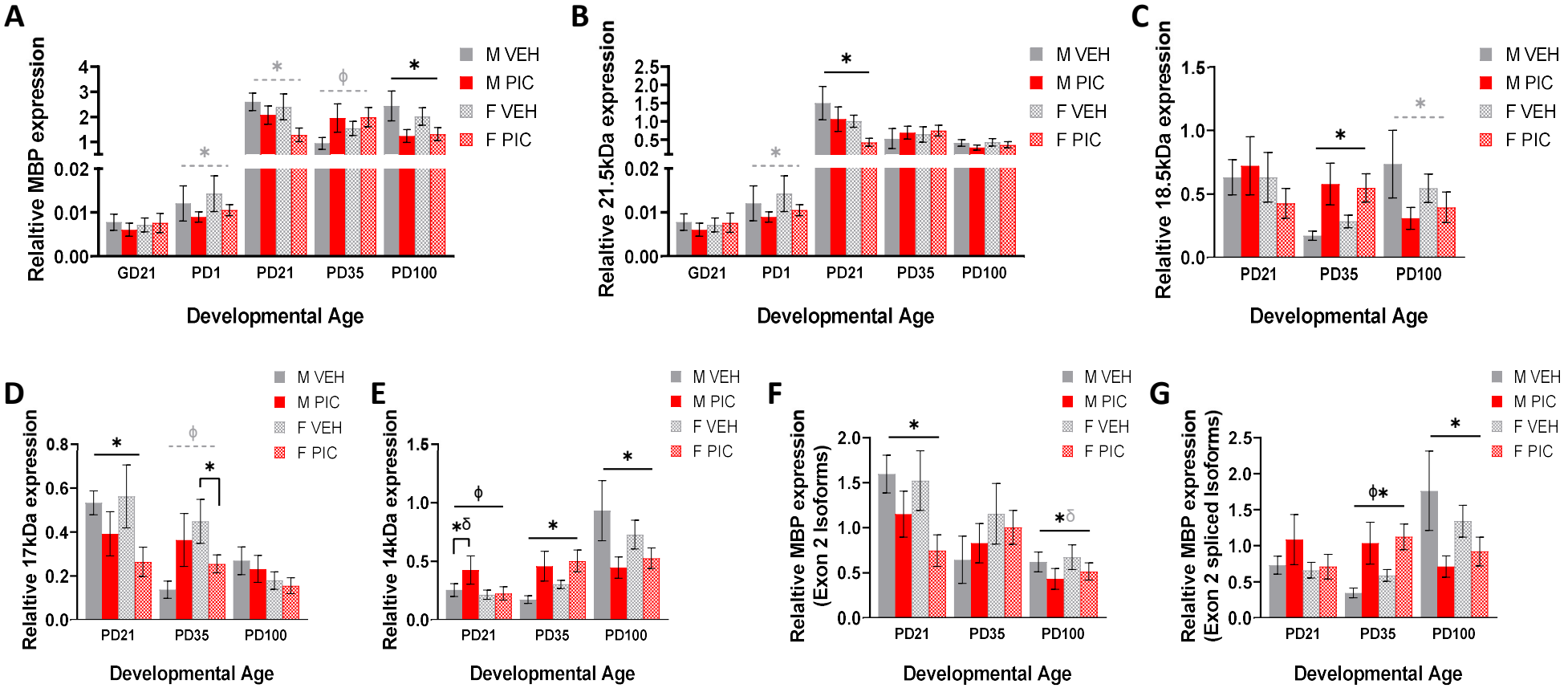

Figure 5.20. MBP protein expression
Relative protein expression (normalised to the GAPDH reference protein as described in methods) **A.** Total MBP expression. **B.** 21.5kDa isoform. **C.** 18.5kDa isoform. **D.** 17kDa isoform. **E.** 14kDa isoform. **F.** Exon 2-containing isoforms. **G.** Exon 2-spliced isoforms. Bars represent mean ±SEM (N=5-7, n=5-7). Black significance bars represent significant GLMM results, — shaped significance bars show results across whole developmental age, Π-shaped bars show post-hoc GLMM within a single sex. Black symbols show significant main effects of: group, *p<0.05; maternal IL-6, δp<0.05; sex, ϕp<0.05. Grey dashed bars and/or symbols represent trending (0.05<p≤0.08) results of the GLMM. Abbreviations: GD, gestational day; PD, postnatal day; M, male; F, female; PIC, poly(I:C); VEH, vehicle.

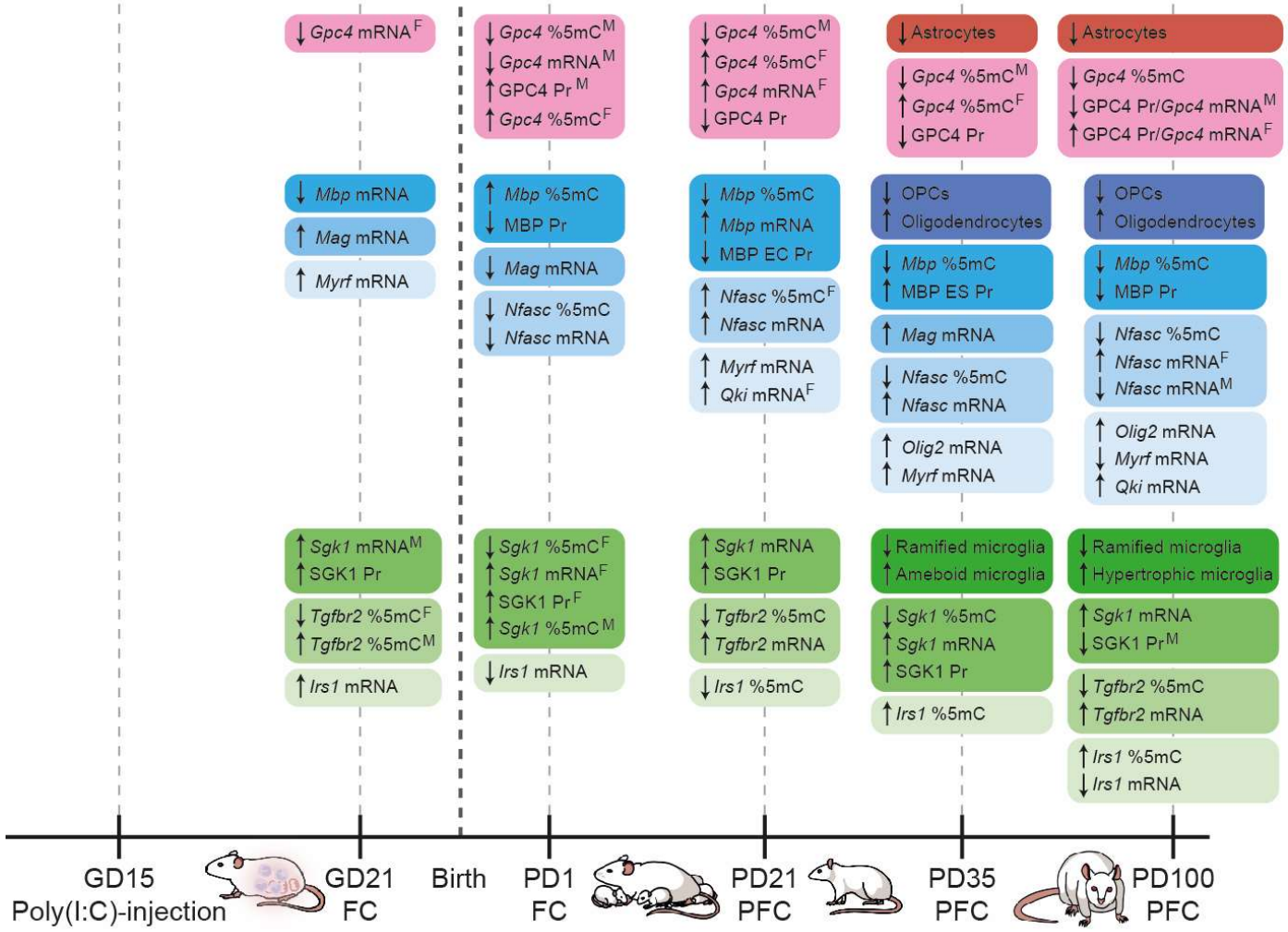

Figure 5.21. Summary of significant findings from Chapter 5

Summary of the MIA-induced molecular changes in the developing cortex. Timeline (bottom) indicates the developmental age and tissue analysed: frontal cortex (FC) or prefrontal cortex (PFC). Red/pink: astrocyte changes; Blue: oligodendrocyte changes; Green: microglial changes. Abbreviations: ↓Decrease; ↑Increase; F, female-specific result; M, male-specific result; Pr, protein; %5mC, methylation; EC, exon 2 containing isoforms; ES, exon 2 spliced isoforms.

5.4. DISCUSSION

A key hypothesis of this Chapter was that MIA and subsequent foetal neuroinflammation, would alter macroglia and microglial cell development, resulting from MIA-induced epigenetic dysregulation of glial-specific genes. The aims of this Chapter were therefore to evaluate developmental changes to glial cells including, glial cell densities/morphologies and changes in DNAm and expression of glial cell-specific candidate genes. The results of this Chapter achieved these aims and support this hypothesis, showing key changes to glial cell development and altered temporal expression of glial cell genes in the developing cortex of MIA-exposed offspring. Critically, findings from cell density/morphology analysis and gene/protein expression support altered immune profiles of microglia and accelerated macroglia development. A summary of the findings in this Chapter can be found in Figure 5.21 and will be discussed in-depth below.

5.4.1. MIA increases microglial activation

Under homeostatic conditions, microglia exist in a resting/ramified state, however, as the critical CNS immune cells, microglia are responsible for responding to injury or infection, where they transition to an activated state, including ameboid “phagocytic” morphology and hypertrophic “hyper-ramified” states (Fernández-Arjona et al., 2017). MIA did not affect total PFC IBA1+ microglial density at PD35 or PD100 (Figure 5.6A), however MIA did induce a reduction in ramified IBA1+ microglia in both PD35 and PD100, with a concurrent increase in active forms of microglia (Figure 5.6B). This was underpinned by increases in ameboid IBA1+ microglia in the PD35 PFC and hypertrophic IBA1+ microglia in the PD100 PFC. It should be noted that IBA1 is also expressed by tissue macrophages and, while these typically only infiltrate the brain under injury, it cannot be discounted that some of the IBA1+ cells were macrophages. However, given that macrophage morphology does not resemble the observed ramified/hypertrophic/rod microglia, any IBA1+ macrophages present in the tissue samples would be more akin to the morphology shape of the ameboid cells (Jurga et al., 2020; Toku et al., 1999) and hence is unlikely to significantly influence the results. The observed developmental differences in MIA-driven changes in active forms of microglia at PD35 and PD100 is likely due to disturbances in the typical microglia phenotypes observed at these ages. Microglia typically demonstrate a phagocytic (ameboid) morphology during early brain development to enable removal, pruning and modulation of developing synapses, while in the adult brain, there is a propensity towards hypertrophic microglia, associated with aging and neuroinflammation (Blagburn-Blanco et al., 2022; Schwarz et al., 2012; Shahidehpour et al., 2021; Xu et al., 2022). The results observed in this study support this notion, with an age-related reduction in IBA1+ amoeboid microglia and increases in rod and hypertrophic cells between PD35 to PD100, irrespective of group (Figure 5.6; Table 5.14). The MIA-driven increase in ameboid microglia in adolescence (PD35) postulates excessive or imbalanced synaptic pruning capacity which may reduce synaptic connections/plasticity and disturb EI signalling balance (Geloso and D’Ambrosi, 2021).

Excessive microglia synapse engulfment has been demonstrated in *in vitro* cell cultures derived from schizophrenia patients (Sellgren et al., 2019). Conversely, the increased hypertrophic cell density observed in adulthood (PD100) could suggest a culmination of a chronic neuroinflammatory profile and/or advanced aging in MIA-offspring, either of which could provoke neuronal damage (Muzio et al., 2021; Shahidehpour et al., 2021). Of note, both ameboid and hypertrophic microglia secrete pro-inflammatory modulators, including cytokines IL-6 and TNFα (Geloso and D'Ambrosi, 2021; Muzio et al., 2021). Hence, the increased density of active microglia at PD35-PD100 may underscore the increased IL-6 protein expression in the PFC (Chapter 2, Figure 2.16D&E). Taken together, these results indicate MIA-induced dysregulation of microglia activity in the developing PFC.

A number of studies have evaluated microglia in MIA models, reviewed recently by Carloni et al. (2021). Generally, these have shown increased microglia reactivity and pro-inflammatory functionality. Accordingly, minocycline treatment, which partially inhibits microglia reactivity, has been demonstrated to ameliorate schizophrenia-like behaviours in MIA-offspring (Xia et al., 2020), supporting a mechanistic link between MIA, dysfunctional microglia and behavioural deficits. When considering how MIA impacts microglia development, microglia are responsive to cytokines (Frank et al., 2007; Perry, 2007) and hence it could be postulated that the observed foetal neuroinflammatory disturbance following MIA (Chapter 2, Figure 2.15&Figure 2.16A) induces chronic microglia dysregulation. Indeed, a recent study demonstrated that MIA alters postnatal microglia function, dampening their response to future immune challenge (Hayes et al., 2022). This finding would suggest adaptive programming in MIA-exposed microglia which prenatally determines later immune function. In line with this postulate, the RRBS results obtained from the PFC of MIA-exposed adult females demonstrated significant dysregulation of immune-related and microglia-enriched genes (Chapter 4). It could be suggested that MIA induces epigenetic perturbations in the regulation of microglia. To examine this possibility, expression and epigenetic regulation of selected microglia candidate genes, *Sgk1*, *Tgfbr2* and *Irs1* were investigated.

5.4.1.1. *Sgk1* and the stress response

Sgk1 is a kinase activated downstream of glucocorticoid signalling (Table 5.1) and its expression is disturbed in various neurological disorders (Dattilo et al., 2020; Licznerski et al., 2015; Stertz et al., 2021). Glucocorticoids (cortisol/corticosteroid) are released into the blood as part of the physiological stress response, regulated by the HPA axis (Figure 1.2). Glucocorticoids bind the ubiquitous GR, leading to activation of downstream signalling (via SGK1) and the expression of stress response genes (Smith and Vale, 2006). Elevated systemic glucocorticoids have been identified in schizophrenia patients alongside differential methylation and expression of the GR gene, *Nr3c1* (Bradley and Dinan, 2010; Liu et al., 2020a, 2020b; Sinclair et al., 2011). Further, inflammation and glucocorticoids have a complex relationship: while glucocorticoids can exert anti-inflammatory effects, chronic inflammation induces glucocorticoid resistance, leading to exacerbated inflammatory responses (Straub and Cutolo, 2016). Microglia express GRs and

are the most glucocorticoid-responsive cells in the CNS, with chronic stress proposed to activate microglia and potentiate neuroinflammation (Diaz-Jimenez et al., 2021; Frank et al., 2007).

A significant reduction in *Sgk1* promoter methylation was found in the PFC of adult females exposed to MIA. To evaluate when these changes present, methylation of this promoter was evaluated across development (GD21-PD100). This showed increased methylation in the GD21 male FC and reduced methylation in the PD1 female FC, with both sexes having reduced methylation in the PD35 PFC (Figure 5.7). However, this reduction was not observed at PD100. Whether this reduction in *Sgk1* promoter methylation would have occurred again at PD175, as observed in the RRBS, is unclear. Overall, these results suggest some developmental plasticity in the methylation of this promoter. As promoter methylation often regulates gene transcription (Moore et al., 2013), *Sgk1* mRNA expression was evaluated and found, by contrast, to be rather consistent across development, with increased *Sgk1* mRNA expression observed in MIA-offspring across the developmental window (Figure 5.10A). Despite a lack of significant *Sgk1* between-group methylation changes at GD21, PD21 or PD100, there was a consistent negative correlation between promoter methylation and *Sgk1* mRNA expression across development (Table 5.26). Further, except for PD100, MIA-driven *Sgk1* mRNA expression corresponds to MIA-driven changes in SGK1 protein expression across development (Figure 5.11). It must be acknowledged that active SGK1 is phosphorylated and hence it cannot be confirmed whether the observed increase in protein expression here corresponds directly to increased SGK1 activity, as this would require evaluation of phospho-forms of the protein. Nonetheless, taken together, the data suggests chronic increases in *Sgk1*/SGK1 expression, which is epigenetically regulated in response to MIA. Increased SGK1 expression could result from i) hyperactive glucocorticoid signalling and/or ii) a compensatory effect of reduced GR expression/glucocorticoid resistance (Dattilo et al., 2020). Increased SGK1 expression could have consequences for various brain developmental processes. Indeed, hyperactivation of SGK1 has been suggested to promote anti-neurogenic activity through negative regulation of neurotrophic factors (e.g., BDNF) and exacerbated inflammatory response (Dattilo et al., 2020).

Table 5.26. Correlations between *Sgk1* promoter methylation and mRNA expression

Developmental age	Correlation coefficient
GD21	CpG1: r=-0.383, p=0.077; CpG2: r=-0.435, p=0.049
PD1	CpG4: rho=-0.553, p=0.009
PD21	CpG4: r=-0.254, p=0.08
PD35	Average promoter methylation: r=-0.238, p=0.08
PD100	CpG4: r=-0.306, p=0.079

5.4.1.2. *Tgfbr2* and *Irs1* in anti-inflammatory signalling

Tgfbr2 is the constitutive receptor for the cytokine, TGFβ, while *Irs1*, encodes the insulin receptor substrate, activated downstream of insulin signalling. Both these genes are associated with neurological disease development (Numata et al., 2008; Tanokashira et al., 2019), upregulation of anti-inflammatory signalling pathways (Bierie and Moses, 2010; Chen et al., 2015) and are enriched for expression in microglia. The RRBS showed a reduced intron 1

methylation for *Tgfbr2* and increased exon 1 methylation for *Irs1*. Methylation and expression of both genes was hence investigated across development.

For *Tgfbr2,* the results demonstrated sex-specific MIA-induced intron 1 methylation at GD21, with increased methylation in males and reduction in females. However, at PD21 and PD100 there was a sustained reduction in methylation in MIA-exposed males and females (Figure 5.8). This could indicate prenatal differential methylation adaptation to MIA between sexes, which converges postnatally. As with promoter methylation, intron 1 methylation negatively correlates with gene expression (Anastasiadi et al., 2018). Accordingly, *Tgfbr2* mRNA expression was shown to be increased from PD21 to PD100, demonstrating a negative correlation between mRNA expression and intron 1 methylation across development (Table 5.27), suggesting a developmental relationship between *Tgfbr2* methylation and expression.

Table 5.27. Correlations between *Tgfbr2* intron 1 methylation and gene expression

Developmental age	Correlation coefficient
GD21	Average intron 1 methylation: r=-0.790 p<0.001
PD1	Non-significant
PD21	Average intron 1 methylation: rho=-0.569, p=0.009
PD35	CpG2: r=-0.468, p = 0.037
PD100	Average intron 1 methylation: r=-0.437, p=0.037

Increased expression of *Tgfbr2* mRNA is perhaps contradictory to the pro-inflammatory state of microglia, given that TGFβ is an anti-inflammatory cytokine. However, this finding has been observed in the systemic circulation of schizophrenia patients (Numata et al., 2008). Hence, it could be postulated that upregulation of *Tgfbr2* mRNA may be an attempt to compensate for reduced TGFβ secretion. Indeed, elevated IL-6 has been shown to reduce TGFβ secretion (Luckett-Chastain and Gallucci, 2009). Further, TGFβ has been shown to be secreted primarily from OPCs, bind to and activate TGFBR2 on microglia, promoting an anti-inflammatory phenotype and preventing chronic microglial activation (Zhang et al., 2019a). Therefore, the elevated IL-6 (Chapter 2, Figure 2.16) and reduced OPC density (Figure 5.16B) observed in these animals would be expected to potentiate reduced TGFβ availability, reducing TGFβ-TGFBR2 binding and promoting microglia activation. Indeed, TGFBR2 deficient microglia favour the hypertrophic morphologies observed here in adult animals (Zöller et al., 2018).

For *Irs1*, the most consistent change in exon 1 methylation in MIA offspring was an increase, observed at CpG3 and CpG5 at PD35 and across CpG2-6 at PD100 (Figure 5.9), consistent with findings from the RRBS. Conversely, there was a MIA-driven increase in *Irs1* mRNA expression at GD21 and a reduction at PD1, suggesting early changes in expression of this gene are not driven by exon 1 methylation. However, there was a significant MIA-induced reduction in *Irs1* mRNA expression at PD100, in line with increased exon 1 methylation (Brenet et al., 2011). This suggests that MIA-induced dysregulation of *Irs1* presents primarily in adulthood. This may be explained by the relationship of *Irs1* and aging. *Irs1* expression in the brain reduces with age (Sánchez-Sarasúa et al., 2021) and early reductions are associated with neurodegeneration (Tanokashira et al., 2019), implying the observed reduction in *Irs1*

expression at PD100 may be evidence of advanced aging. Further, as *Irs1* is an anti-inflammatory mediator, the observed reduction in *Irs1* expression at PD100 would be coincident with the increased hypertrophic microglial phenotype and IL-6 elevations. Inflammatory cytokines reduce IRS1 expression (de Luca and Olefsky, 2008) and inflammation has recently been suggested as a critical mechanism linking insulin resistance and schizophrenia (Perry et al., 2021).

Overall, the results indicate a MIA-induced pro-inflammatory microglia phenotype, supported by both morphology and dysregulation of microglial-enriched genes.

5.4.2. MIA disturbs development of macroglia cells

Macroglia comprises both astrocytes and oligodendrocytes which sequentially arise from SVZ progenitors during gliogenesis (Dietz et al., 2020). Results from IHC/IF indicate key disturbances to macroglia cell ratios in MIA-offspring in both PD35 and PD100 PFC (Figure 5.12; Figure 5.15), with reduced GFAP+ astrocyte cells and overall increases in OLIG2+ oligodendrocyte cells, concurrent to a reduction in NG2+ OPCs. It could be hypothesised that prenatal inflammation, notably the observed IL-6 elevation from GD16-21 (Chapter 2, Figure 2.15&Figure 2.16A) leads to abnormal proliferation and differentiation of glial progenitors in the SVZ of the foetal brain. IL-6 family cytokines are critical in promoting the gliogenic switch (Miller and Gauthier et al., 2007), providing a plausible mechanistic link between foetal neuroinflammation and the observed changes in macroglia densities. Differentiation of macroglia cells is also epigenetically regulated through the induction of glial-specific gene expression (Chen et al., 2021b; Hatada et al., 2008; Takizawa et al., 2001). Hence, it could be that foetal IL-6 induces epigenetic dysregulation of glial progenitors, leading to long-term dysregulation of macroglia development, driven through changes in glial-specific gene expression. This is supported by the over-representation of macroglia-enriched genes in the RRBS dataset (Chapter 4; Appendix 9).

5.4.2.1. MIA induces astrocyte dysregulation in sex-specific patterns

Astrocytes are critical throughout neurodevelopment and ongoing modulation of synaptic signalling (Abbink et al., 2019; Allen and Eroglu, 2017; Reemst et al., 2016). Astrocytes also respond functionally to pro-inflammatory signals, including signals from activated microglia, such as those observed at PD35 and PD100, transitioning to a reactive and proliferative state (Abbink et al., 2019; Pekny and Pekna, 2014; Sofroniew, 2014). Hence, it is unexpected that the GFAP+ astrocyte density was reduced in MIA-offspring PFC (Figure 5.12). That said, as no morphometric analyses of these cells was performed, it cannot be discounted that the GFAP+ cells did not possess a reactive phenotype. Indeed, while astrocytic density in MIA models has produced mixed results (Anderson et al., 2022; de Souza et al., 2015; Ding et al., 2019; Paylor et al., 2016; Xia et al., 2020), likely attributable to methodological heterogeneity and brain region analysed, more recent studies have shown altered astrocyte morphology and functionality in the

brains of MIA-offspring (Hayes et al., 2022; Saavedra et al., 2021). Further, given that GFAP+ astrocytes do not account for the entire astrocyte population in the PFC (Souza et al., 2013; Waller et al., 2016; Zhang et al., 2019b), it is possible that, while GFAP+ astrocyte density is reduced, other astrocyte populations are increased. It may also be that reduced GFAP+ astrocyte densities reflect disturbed astrocyte development. The observed elevation in pro-inflammatory IL-6 in the foetal brain (Chapter 2, Figure 2.15&Figure 2.16A) coincides with the start of astrogenesis (Sarkar et al., 2019). Studies evaluating astrocyte development following IL-6 challenge have produced mixed results, including increased (Levison et al., 2000; Nakanishi et al., 2007) and decreased (Kumari et al., 2020; Velloso et al., 2022) astrocyte cell densities. These inter-study discrepancies might relate to different timings of cytokine/immune exposure (Anderson et al., 2022) and brain region analysed. Nonetheless they implicate that reduced astrocyte density observed in this study could result from: i) dysregulated astrocyte differentiation, such as postulated in schizophrenia patients (Liu et al., 2019); ii) disturbed astrocyte migration (Wei et al., 2011); iii) increased loss of astrocytes due to cell death or phagocytosis (Kumari et al., 2020). Indeed, activated microglia have been shown to preferentially phagocytose immature astrocytes in the developing brain (VanRyzin et al., 2019) and thus it could be postulated that foetal neuroinflammation promotes both increased gliogenesis and activated microglia, which in turn preferentially degrade immature astrocytes over oligodendrocytes. Irrespective of cause, the observed reduction in GFAP+ astrocytes may cause reduced synapse formation, glutamate uptake and hence disturbed synaptic signalling/connectivity in the developing brain (Abbink et al., 2019).

The only astrocytic candidate gene withstanding the selection criteria (Appendix 9) was GPC4, which functions particularly in glutamatergic synapse development (Allen et al., 2012; Farhy-Tselnicker et al., 2017; Kamimura and Maeda, 2021; Ma et al., 2021). Loss of GPC4 has been associated with moderate behavioural deficits, including hyperactivity and social deficits (Dowling and Allen, 2018), while increased GPC4 is associated with epilepsy and seizures (Xiong et al., 2016). RRBS analysis showed reduced promoter methylation for *Gpc4* in adult MIA-females. Through development there was a highly significant effect of sex on *Gpc4* promoter methylation, with consistently increased promoter methylation in females relative to males (Figure 5.13). This undoubtedly relates to *Gpc4* being coded on the X-chromosome. Due to females possessing two X-chromosomes and the resulting female X-chromosome inactivation process, approximately 95% of X-chromosome-encoded genes are more highly methylated in females relative to males (Wang et al., 2021c). In line with the overall sex-difference in *Gpc4* promoter methylation, there were also sex-differences in MIA-induced epigenetic dysregulation of *Gpc4*. There was a reduction in *Gpc4* promoter methylation across development in poly(I:C)-males and an increase in poly(I:C)-females from PD1-PD21, transitioning to reduced *Gpc4* promoter methylation at PD100 in both sexes (Figure 5.13). However, despite the assumption that promoter methylation downregulates gene expression (Moore et al., 2013), MIA-induced changes in promoter methylation did not robustly mirror changes in *Gpc4* mRNA expression. MIA-exposed males showed overall reductions in *Gpc4*

mRNA expression across postnatal development (PD1-100) while MIA-exposed females showed an initial reduction in *Gpc4* mRNA expression prenatally followed by an increase postnatally, though these were not significant at each developmental age (Figure 5.14). These findings present an unexpected relationship between promoter methylation and gene expression, with positive correlations observed between individual CpG methylation and *Gpc4* mRNA expression from GD21-PD21, before establishing the typical negative correlations at PD35-PD100 (Table 5.28).

Table 5.28. Correlations between *Gpc4* promoter methylation and gene expression

Developmental age	Correlation coefficient
GD21	Females: CpG3: rho=0.404, p=0.079; Males: CpG1: rho=0.753, p=0.012; CpG3: rho=0.673, p=0.033
PD1	CpG1: r=0.387, p=0.075; CpG3: r=0.373, p=0.08
PD21	Average promoter methylation: r=0.459, p=0.032
PD35	CpG2: rho=-0.370, p=0.075
PD100	CpG3: r=-0.340, p=0.080

The initial negative relationship may result from altered hydroxymethylation in the *Gpc4* promoter in early development. As previously outlined, bisulphite conversion methods cannot distinguish between DNAm and DNAhm (Booth et al., 2013). However, opposed to DNAm, DNAhm promotes active transcription of genes (Chen et al., 2014) and hence would be expected to positively correlate with gene expression. DNAhm is usually enriched at developmental genes which become highly expressed in adolescence and adulthood (Lister et al., 2013; Shi et al., 2017; Wen et al., 2014), as would be expected for *Gpc4*. Notably the switch from positive to negative correlations occurs towards to end of synaptogenesis (Sarkar et al., 2019) during which synaptic plasticity reduces.

GPC4 protein expression results showed reduced expression in MIA-exposed offspring from both sexes across development, though this transitions to increased GPC4 protein expression in MIA-exposed adult (PD100) females, mirroring the pattern of changes in *Gcp4* mRNA expression. Overall, this would suggest a temporal lag between changes to *Gpc4* DNAm/mRNA expression which is later established in the protein expression. One limit to this study is that the membrane fraction was used for quantification of GPC4 protein expression. Hence, it cannot be discounted that there is no difference in the amount of GPC4 secreted from astrocytes as a result of MIA (Farhy-Tselnicker et al., 2017). Nonetheless, the results support sex-specific and temporal MIA-induced dysregulation of *Gpc4*. This could have critical consequences for formation of glutamatergic synapses and establishment of cortical circuitry. The overall reduction in GPC4 expression, notably in males, would be expected to reduce glutamatergic synapse formation and imbalance synaptic receptor clusters (Allen et al., 2012; Farhy-Tselnicker et al., 2017). While elevations in GPC4 observed in adult females may potentiate a neurodegenerative phenotype, similar to those observed in Alzheimer's disease (Ma et al., 2021).

5.4.2.2. MIA accelerated oligodendrocyte lineage development

It was observed that there was an overall increase in OLIG2+ oligodendrocyte cells, alongside a reduction in NG2+ OPCs in MIA-offspring PD35 and PD100 PFC (Figure 5.15), implying increased numbers of pre-myelinating/mature oligodendrocytes (Figure 5.1). Incorrect oligodendrocyte development has been identified in other models of MIA and early-life inflammation, including both reductions and increases in the numbers of oligodendrocyte lineage cells, with this discordance most likely attributable to timing of immune insult and brain region analysed (Anderson et al., 2022; Canales et al., 2021; Makinodan et al., 2008; Mouihate et al., 2017; Page et al., 2021; Velloso et al., 2022). The MIA model used here causes foetal neuroinflammation during OPC specification in the SVZ (~GD15 in rats; Sarkar et al., 2019) and initial oligodendrogenesis. As mentioned earlier, IL-6 promotes gliogenesis and the differentiation of OPCs into mature oligodendrocytes (Favrais et al., 2011; Taylor et al., 2010; Valerio et al., 2002), providing a possible mechanistic relationship between elevated foetal IL-6 (Chapter 2, Figure 2.15&Figure 2.16A) and increased number of oligodendrocytes observed. However, one limitation here is the inability to distinguish pre-myelinating from mature-myelinating OLIG2+ cells, which precludes determination of whether the observed OLIG2+ cells are under-developed. However, the reduction in the OPC pool as early as adolescence suggests a premature differentiation of oligodendrocytes resulting in an overly mature phenotype, such as has been noted in recent studies using early-life/chronic stress paradigms (Poggi et al., 2022; Teissier et al., 2020).

To lend further support to this hypothesis, the mRNA expression of developmental oligodendrocyte-specific transcription factors, *Olig2, Myrf* and *Qki* (Figure 5.1) were measured. Of note, dysregulation of *Myrf* and *Qki* have been demonstrated in the PFC of schizophrenia patients (Lauriat et al., 2008; Lin et al., 2021). *Olig2,* a transcription factor expressed from all oligodendrocyte lineage cells, showed MIA-induced increases in mRNA expression only at PD35-PD100 (Figure 5.19A), corresponding to observed OLIG2+ cell density increases (Figure 5.15A). This could suggest that the observed differences in oligodendrocyte development primarily occur during the peak of OPC differentiation at ~PD14-PD30 in rodents (Nishiyama et al., 2021). However, the transcription factors involved in oligodendrocyte maturation (*Myrf, Qki*) showed more extensive developmental disturbances. There was a MIA-induced increase in *Myrf* mRNA expression from PD21-35, becoming reduced expression at PD100. These results are consistent with findings previously reported in MIA models (Namvarpour et al., 2022; Page et al., 2021). This would also be concordant with the cell ratio findings, indicating accelerated maturation of the lineage and advanced myelination during juvenile and adolescent periods, followed by reduced capacity to remyelinate in adulthood. Likewise, *Qki* showed MIA-induced increases in mRNA expression at PD21 and PD100. Given the role of *Qki* in myelin gene splicing (Wu et al., 2002) these results would indicate ongoing splice dysregulation in the oligodendrocyte lineage cells in MIA-offspring. Taken together, the results support critical developmental disturbances in the oligodendrocyte cell lineage, indicative of premature

maturation. Altered oligodendrocyte development could have impacts on the normal functions of oligodendrocytes in the developing brain. Indeed, disturbances in the ratio of immature:mature oligodendrocytes could impact on myelin and ECM formation. Formation of myelin and ECM structures marks the closure of the critical period of plasticity in juvenile/adolescent PFC development (Larsen and Luna, 2018). During this critical period, the PFC has enhanced plasticity, essential for normal cognitive development and hence disturbed neurobiological function within this period (e.g., altered myelin/ECM formation), could result in neuropathology, including schizophrenia (Guirado et al., 2020; Morishita et al., 2015). In support of disturbed oligodendrocyte development, several oligodendrocyte-enriched genes withstood the selection criteria from the RRBS analysis (Appendix 9). Three were investigated here, *Nfasc, Mbp* and *Mag* (the latter analysed for gene expression only).

I. *Nfasc* and ECM malformation

Nfasc is involved in perinodal ECM formation, important in normal signal conduction in the developing brain (Chang et al., 2014; Fawcett et al., 2019). The RRBS showed reduced methylation at intron 1 of the *Nfasc* gene. When measured across development, *Nfasc* demonstrated developmental switches, matching the directionality of methylation differences between MIA- and vehicle-offspring. This could imply a degree of developmental plasticity in the regulation of this gene, underpinned by DNAm, which is disturbed in MIA-offspring. While MIA-driven changes in methylation were often CpG-specific, there were MIA-induced decreases in methylation from GD21-PD1, reversing to increases from PD21-35 and reduced again at PD100 (Figure 5.16). As with intron 1 methylation, the expression of *Nfasc* mRNA was also developmentally dysregulated with similar directionality in MIA-exposed offspring, including: reduction at PD1, increased at PD21-35 and sex-specific changes at PD100 (Figure 5.16A). These findings correspond to a lack of correlation between intron 1 methylation and *Nfasc* mRNA expression in early development (GD21-PD1), a positive correlation at PD21, becoming a negative correlation from PD35-PD100 (Table 5.29). This might suggest that the MIA-induced changes in *Nfasc* mRNA expression in early development, perhaps driven by transcription factor binding/other epigenetic mechanisms, lead to established DNAm-mediated dysregulation of *Nfasc* in adolescent and adult offspring.

Table 5.29. Correlations between intron 1 methylation and *Nfasc* mRNA expression

Developmental age	Correlation coefficient
GD21	No significant correlations
PD1	No significant correlations
PD21	CpG3: rho=0.471, p=0.042
PD35	CpG1: rho=-0.369, p=0.071
PD100	Average intron 1 methylation: r=-0.473, p=0.019

Of note, the technique for evaluating mRNA expression used here cannot distinguish the various splice variants which exist for this gene. Given that different splice variants of this gene function differentially in ECM formation (Chang et al., 2014; Fawcett et al., 2019), the interpretations here should be considered with this in mind. Nevertheless, the disturbed expression of *Nfasc*,

particularly the elevation in expression observed from PD21-35 would indicate premature formation of the ECM. Given that PD21-35 corresponds to the critical period for the PFC (Guirado et al., 2020; Larsen and Luna, 2018; Morishita et al., 2015), advanced ECM formation could promote early closure of this period and thereby contribute to reduced cognitive flexibility in MIA-offspring.

II. *Mbp, Mag* and myelin malformation

Mbp and *Mag* are both critical components of the myelin sheath, expressed exclusively from oligodendrocytes (Kuhn et al., 2019) and differential methylation and expression of both these genes has been identified in the PFC of schizophrenia patients (Lin et al., 2021). Both these myelin genes withstood the selection criteria (Appendix 9), however, given the similarity in function and sample constraints, it was determined that while both genes would be evaluated for mRNA expression, only *Mbp* DNAm would be analysed. When analysed in MIA models previously, the results for mRNA/protein expression of both genes have shown inconsistent results (Valdés-Tovar et al., 2022; Woods et al., 2021), likely attributable to model heterogeneity. Nonetheless, the results have generally shown age-specific increases and decreases.

Mbp has four primary isoforms created from alternate splicing of exon 2 (Akiyama et al., 2002; Kruger et al., 1999). Developmental changes in expression of individual MBP isoforms has previously been demonstrated following MIA (Farrelly et al., 2015; Fatemi et al., 2009a), though how these relate to epigenetic dysfunction have yet to be explored. The RRBS identified a reduction in *Mbp* exon 2 methylation. When evaluated across development, there was almost 100% methylation of this region prenatally (GD21), before reducing steadily across postnatal development. This is likely because myelination only commences postnatally (Sarkar et al., 2019) and hence the *Mbp* gene is expected to be epigenetically silenced prior to this (Reik, 2007). Accordingly, MIA-driven changes in *Mbp* methylation were only observed postnatally, beginning at PD1 with a MIA-induced increase in exon 2 methylation, followed by MIA-induced reductions from PD21-100 (Figure 5.17). However, few MIA-driven changes in *Mbp* mRNA expression were identified, with the only significant differences including reduced *Mbp* mRNA in MIA-exposed foetuses at GD21 and increases in MIA-offspring at PD21 (Figure 5.19B). Of note, for *Mag*, a MIA-induced increase in mRNA expression was observed at GD21, followed by a reduction at PD1 and increase at PD35 (Figure 5.19C). Taken together, while these findings indicate early developmental dysregulation of myelin gene mRNA expression, there appear little MIA-driven changes, particularly in *Mbp* expression, during the PFC critical period, with no changes in expression of either observed at the occurrence of the cognitive deficit (PD100), despite significant changes in DNAm. Evaluation of the association between exonic methylation and splicing has found increased methylation in retained exons and reduced methylation in spiced exons (Li et al., 2018b; Shayevitch et al., 2018). This phenomenon could postulate that the observed changes in exon 2 methylation would influence expression of *Mbp* splice variants. However, mRNA expression analysis used here is unable to distinguish between such splice

variants and hence MBP isoform expression was measured instead by protein (Figure 5.20), to explore the relationship between exon 2 methylation and dysregulated *Mbp* isoform expression.

As outlined above, myelination begins in the early postnatal period, peaking at ~PD20-21 in rats (Sarkar et al., 2019), with exon 2-containing isoforms more prevalent during active myelination in early development, while exon 2-spliced isoforms are prevalent in mature myelin (Akiyama et al., 2002; Kruger et al., 1999). Accordingly, MBP protein expression increased significantly between PD1 and PD21, where there was peak expression of exon 2-containing MBP isoforms. Expression of exon 2-containing isoforms steadily reduced from PD21-100, while exon 2-spliced isoforms increased. When considering the effect of MIA, there was only a statistically significant difference in total MBP protein expression at PD100, with reduced expression in MIA-offspring (Figure 5.20A), corroborating findings in previous MIA models and in schizophrenia (Francisco et al., 2022; Vikhreva et al., 2016; Woods et al., 2021). However, there was MIA-driven reductions in expression of exon 2-containing isoforms (21.5kDa/17kDa) at PD21 and increases in exon 2-spliced isoforms (18.5kDa/14kDa) at PD35 (Figure 5.20). These results imply a premature switch from active myelination to mature myelination during the critical period in the PFC (PD21-35) which could result in malformed myelin structures. However, at PD100 there was a MIA-induced reduction in all MBP isoforms. Given there was no change in mRNA expression, it could be hypothesised that this MIA-induced reduction in MBP protein is due to increased myelin degradation or demyelination, alongside inefficient remyelination. Such a hypothesis would align with the observed neuroinflammation and microglia activation, which could promote myelin degradation (Briones and Woods, 2014) and the reduced OPC:mature oligodendrocyte ratio, indicating premature oligodendrocyte maturation and reduced plasticity.

Critically, the changes in MBP isoform expression from PD21-100 appears determined by exon 2 methylation, with positive correlations between average exon 2 methylation and exon 2 retention (rho=0.215, p=0.080) and a negative correlation between average exon 2 methylation and exon 2 splicing (rho=-0.227, p=0.071). Likewise, the onset of isoform expression changes at PD21 correspond with MIA-induced changes in expression of transcription factors *Myrf* and *Qki*, which regulate myelin gene expression and splicing (Emery and Lu, 2015; Wu et al., 2002), suggesting a link between oligodendrocyte maturation, perhaps driven by changes in DNAm, converging in altered myelin gene expression.

5.5. SUMMARY

The results of this Chapter show key changes to glial cell development in the PFC of MIA-exposed offspring. These changes appear to be, in part, due to dysregulation of glial cell-enriched gene expression. Microglia (IBA1+) were predominantly found in active morphological phenotypes in adolescence and adulthood, which would promote a pro-inflammatory state, aligning with the observed increase in IL-6 (Chapter 2). The developmental activation of microglia also includes upregulation of gene and protein expression of *Sgk1*/SGK1 and *Tgfbr2*, alongside downregulation of anti-inflammatory *Irs1*. The observed changes support the notion of a chronically altered neuroinflammatory state in the developing brain caused by MIA. Alongside these changes in microglia, macroglia cell ratios were disturbed in MIA-offspring. Unlike microglia, macroglia arise from SVZ NPCs during gliogenesis, a process regulated by the IL-6 family cytokines. Here, it was demonstrated that GFAP+ astrocyte density was reduced, alongside dysregulation of astrocyte-specific GPC4 mRNA and protein expression. These changes could be due to increased astrocytic cell death and/or increased astrocytic phagocytosis by microglia. Meanwhile, there was an increased number of OLIG2+ oligodendrocytes and concurrent reduction in NG2+ OPCs. This indicates a premature differentiation of OPCs into mature oligodendrocytes, supported by MIA-induced developmental dysregulation in expression of key oligodendrocyte-specific genes, including, myelin transcription factors (*Myrf*, *Qki*), ECM (*Nfasc*) and myelin (*Mag*, *Mbp*) genes. Notably, DNAm appears the key regulator of changes in macroglia-gene expression, implying a link between MIA, foetal neuroinflammation, epigenetic dysregulation, leading to changes in glial cell development and function. Together, these findings postulate accelerated maturation of these cells in the MIA-offspring brain, consistent with recent findings in mouse models (Canales et al., 2021). Critically, microglia and macroglia support synapse formation, plasticity and neuronal signalling (Reemst et al., 2016; Saab and Nave, 2017; Xin and Chan, 2020). Hence, the observed developmental glial cell changes could have critical impacts on PFC circuitry and the observed cognitive deficit in adulthood. Indeed, the majority of MIA-induced changes to glial cell function (measured through transcriptomic/proteomic changes) occur during the critical period (PD21-35) of plasticity, associated with higher cognitive development governed by the PFC (Guirado et al., 2020; Larsen and Luna, 2018; Morishita et al., 2015). The closure of this period is marked by establishment of the EI balance and formation of ECM and myelin structures. All these processes could be disrupted by changes to glial cell function. Further, altered synaptic function and signalling following developmental disturbances within the critical period could undoubtedly contribute to the observed PFC-mediated cognitive deficit in MIA-exposed offspring (Chapter 2, Figure 2.18). To understand how the observed glial cell changes contribute to the cognitive phenotype, the postulated link between MIA-induced glial maldevelopment and perturbed synaptic function will form the main focus of the final Chapter.

CHAPTER 6. MIA-induced changes to the formation and structure of the neuronal ECM and synapses

6.1. INTRODUCTION

Chapter 5 highlighted key changes to macroglia and microglia in the developing cortex in response to MIA. Glia are involved in various neurodevelopmental functions, including: modulation of neuroinflammation, synaptic development and plasticity and support of normal neuronal signalling (Allen and Eroglu, 2017; Saab and Nave, 2017; Xin and Chan, 2020). Hence, MIA-induced changes to glia would be expected to have consequences for neuronal development and ongoing neuronal signalling. Some of the key findings from Chapter 5 suggest accelerated maturation of oligodendrocytes, with concordant developmental alterations in myelin and perinodal ECM formation, through dysregulation of *Mbp, Mag* and *Nfasc*. Furthermore, the observed developmental activation of microglia alongside elevations in IL-6 (Chapter 2, Figure 2.16), SGK1 (Chapter 5, Figure 5.7&Figure 5.10A) and reduction in IRS-1 (Chapter 5, Figure 5.9&Figure 5.10C), postulate a microglial inflammatory state which would precipitate disturbed synaptic pruning and ECM/myelin remodelling (Jang et al., 2020). Accordingly, it is hypothesised that the observed MIA-induced changes in glial cells (Chapter 5) would provoke structural changes to myelin and the neural ECM, which could in turn, or concomitantly, alter synapse formation and plasticity to perturb neuronal signalling and result in cognitive deficits.

6.1.1. The brain extracellular space

There are two critical extracellular structures surrounding neurons in the brain: myelin sheaths and the ECM. Myelin is the major constituent of the CNS 'white matter', suggested to comprise ~40% of the brain (Hildebrand et al., 1993). Myelin forms through the ensheathment of axons by oligodendrocyte processes, condensing into compact myelin structures which support signal propagation, neuron metabolism and regulate synaptic plasticity (Bonetto et al., 2021; Stadelmann et al., 2019; see Chapter 5, Section 5.1.1.2. for more detail). By comparison, the neural ECM accounts for ~20% of the brain weight (Nicholson and Syková, 1998) and forms as a lattice-like structure around neuron cell bodies, axons and synapses, composed from various secreted proteins and structural components (see Section 6.1.1.1).

6.1.1.1. Structure of the neural ECM

The neural ECM is a complex structure of interconnected components, including: hyaluronan, proteoglycans and tenascins (Figure 6.1; Fawcett et al., 2019; Jang et al., 2020). Hyaluronan (or hyaluronic acid) is a polymer which forms the main structural backbone of the neural ECM. Bound to this backbone are chondroitin sulphate proteoglycans (CSPGs): Aggrecan, Brevican, Neurocan and Versican. These CSPG-hyaluronan bindings are stabilised by hyaluronan and proteoglycan link proteins (HAPLNs), while Tenascin (Tnsc) glycoproteins (Tnsc-C and Tnsc-R) link the CSPGs together to complete the lattice-like structure (Figure 6.1; Bosiacki et al., 2019; Dzyubenko et al., 2016; Fawcett et al., 2019; Jang et al., 2020). There are, broadly speaking, three ECM structures surrounding neurons: the perineuronal nets (PNNs), the perinodal

(axonal) ECM and the perisynaptic ECM (Dankovich and Rizzoli, 2022; Fawcett et al., 2019; Jang et al., 2020; Tewari et al., 2022).

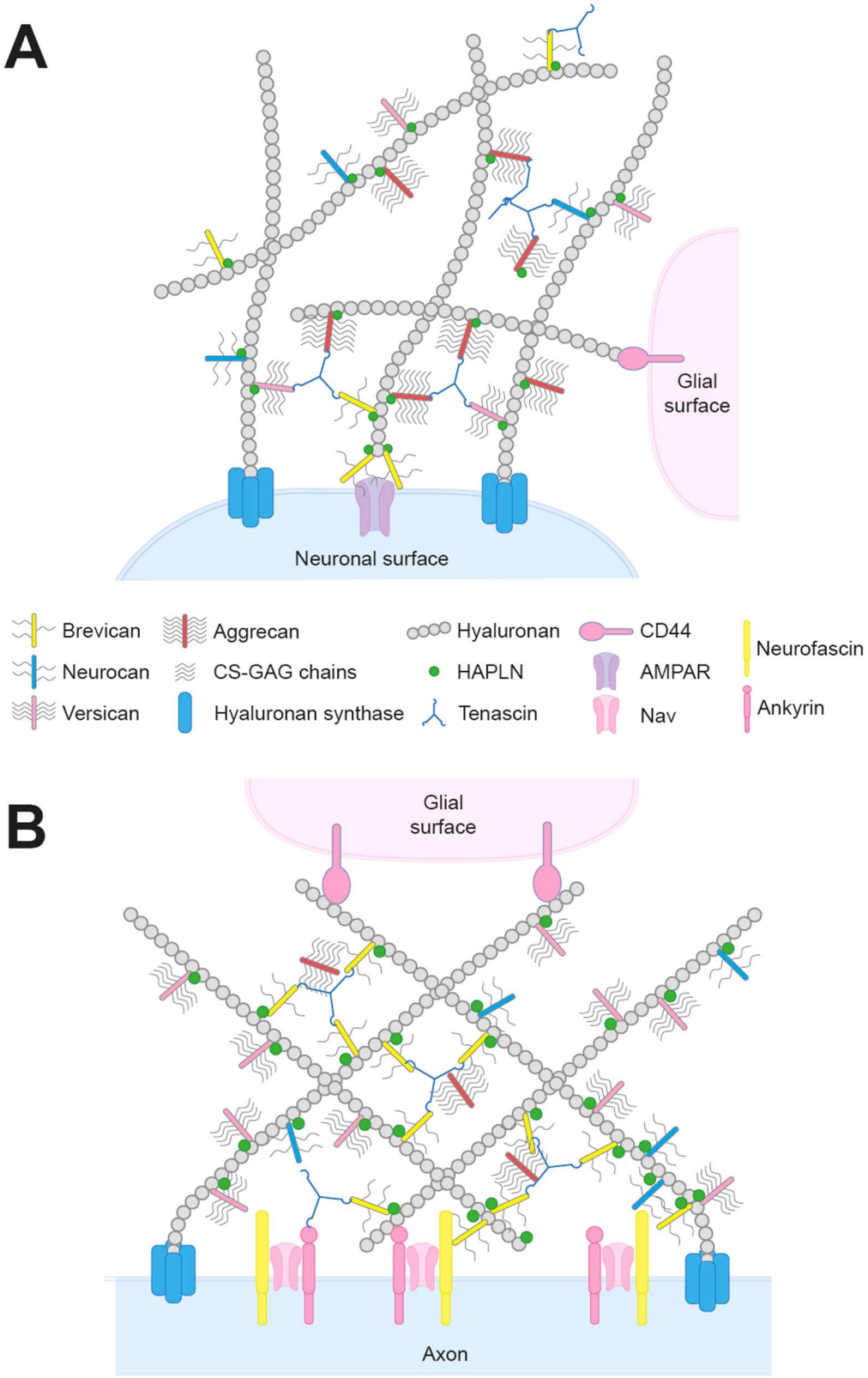

Figure 6.1. Overview of neural ECM structures
A. PNN/perisynaptic ECM. **B.** Perinodal ECM. Schematic of the components involved in neural ECM structures. A central key outlines the individual components and cell surface molecules. Abbreviations: AMPAR, AMPA receptor; Nav, Na^{2+} channels. Figures adapted from Fawcett et al. (2019)

The perinodal and perisynaptic ECMs form at the nodes of Ranvier along the neuronal axon and at synapses, respectively, while PNNs are tightly associated with the neuronal cell bodies (Fawcett et al., 2019; Jang et al., 2020; Tewari et al., 2022). While they are all structurally similar, there are some variations in the ratio of individual components: while Neurocan and Aggrecan are the most enriched CSPGs in the PNN, Versican and Brevican are more enriched in the perinodal and perisynaptic ECMs (Fawcett et al., 2019; Jang et al., 2020). Cell adhesion and cell surface molecules are important in both the formation and stability of the neural ECM. Several cell adhesion molecules interact with the neural ECM to anchor and stabilise the ECM, including astrocytic CD44, which binds hyaluronan and neuronal N-CAM, which binds CSPGs (Dzwonek and Wilczynski, 2015; Grumet et al., 1993). Meanwhile, Neurofascins and Ankyrins both play roles in ECM formation. Neurofascin is critical for the assembly of the perinodal and perisynaptic ECMs (but not PNNs), through recruitment of Brevican and Versican (Hedstrom et al., 2007; Susuki et al., 2013), while Ankyrin G permits perinodal ECM formation through assembly of proteins (including Na^{2+} channels and Neurofascin) at the nodes of Ranvier and Ankyrin R is indispensable for normal PNN formation (Hedstrom et al., 2008; Stevens et al., 2021; Yang et al., 2017).

6.1.2. Role of glia in neural ECM formation and maintenance

6.1.2.1. Macroglia

Compared to myelin sheath components, which are produced exclusively from oligodendrocytes (Akiyama et al., 2002; Stadelmann et al., 2019), the components of the neural ECM have more diverse origins. Critically, while a few components are produced directly from the neurons they form around, several components are produced in high quantities, sometimes exclusively, from macroglia cells (Table 6.1).

Table 6.1. Cell origins of neural ECM components

ECM component	Neuron	Astrocyte	Oligodendrocyte	OPC
Aggrecan	++	+		
Brevican	*	+++		
Neurocan	+++			
Versican	*	*	+++	++
Hyalronan	++	++		
Tenascin-R	++	*	++	++
Tenascin-C	*	+++		
HAPLNS	++			

+++Robust evidence of high mRNA/protein expression of this ECM component from this cell type under physiological conditions. ++ Robust evidence of moderate mRNA/protein expression of this ECM component from this cell type under physiological conditions. + Evidence of moderate mRNA/protein expression of this ECM component from this cell type under physiological conditions *in vitro* only. *Limited evidence of mRNA/protein expression of this ECM component from this cell type under restricted experimental conditions. Table amalgamated from Dzyubenko et al., (2016) and Bosiacki et al., (2019).

Hence, macroglia dysfunction, explored throughout Chapter 5, could result in disturbed expression of these components, supported by the observed differential expression of *Nfasc*

(Figure 5.18A) and thereby perturb the normal development and structure of the neuronal ECM. In addition, Chapter 5 provided evidence of developmentally disturbed myelin protein expression and oligodendrocyte/OPC ratios. Studies indicate a complex and co-dependent relationship between the development of myelin and the neural ECM (Colognato and Tzvetanova, 2011). Indeed, early developmental ECM structures appear critical for normal oligodendrocyte differentiation and maturation (Su et al., 2021). Likewise, ECM signalling, via β-integrins, is important for the initiation of the remyelination processes within the mature brain, with overexpression of ECM components from macroglia shown to inhibit OPC differentiation and remyelination (Colognato and Tzvetanova, 2011; Su et al., 2021). However, during neurodevelopment, the final perinodal ECM structure only forms after axon myelination at PD20-22 in mice (~PD22-24 in rats; Oohashi et al., 2002), while the diameter of axon myelination influences the composition of the assembling perinodal ECM (Bekku et al., 2009).

Given this interlinking relationship between myelin and the neural ECM, it could be suggested that the observed dysregulation of myelin proteins, alongside altered oligodendrocyte cell ratios (Chapter 5), could both arise from, or contribute to, neural ECM alterations.

6.1.2.2. Microglia and inflammation

While microglia do not typically produce any of the neural ECM components, they can regulate ECM remodelling. Neural ECM remodelling is important during normal neurodevelopment for maintaining synaptic plasticity (Reinhard et al., 2015; see Section 6.1.4). Microglia have been shown to phagocytose ECM components, notably around the perisynaptic ECM, to enable synaptic connections to form (Crapser et al., 2021). Likewise, microglia can secrete matrix metalloproteinases (MMPs), including the MMP-2 and MMP-9, which can enzymatically remodel the neural ECM (Crapser et al., 2021; Gray et al., 2008). Microglia in turn can be activated by ECM damage (Rolls et al., 2008), which is important for damage repair after CNS injury (Crapser et al., 2021; Rolls et al., 2008). However, these normal processes can become disturbed in disease conditions (Reinhard et al., 2015). Indeed, active microglia can secrete excess MMPs which can cause axon and ECM damage and demyelination as observed in multiple sclerosis (Könnecke and Bechmann, 2013; Newman et al., 2001) and excess spontaneous neuronal signalling, a common feature of epilepsy (Konopka et al., 2013). Excess MMP activation also promotes neuroinflammation, with MMP-driven degradation of CSPGs and hyaluronan causing activation of astrocytes and microglia (Jang et al., 2020; Könnecke and Bechmann, 2013; Rolls et al., 2008) and elevations in pro-inflammatory cytokines (Jang et al., 2020; Wang et al., 2006). That said, the neural ECM can also be protective against inflammation. Indeed, activated astrocytes can secrete excess CSPGs to remodel the neural ECM and prevent spread of damage (Pekny and Pekna, 2014), while PNNs protect neurons they surround from damage induced by inflammation (Cabungcal et al., 2013; Reichelt et al., 2019). Taken together, these studies support a possible relationship between the observed microglia activation (Chapter 5) and neural ECM dysregulation.

6.1.3. Parvalbumin interneurons (PVIs) and PNNs

While perinodal and perisynaptic ECMs are present across all neuronal types, PNNs primarily surround cell bodies of PVIs in the PFC (Fawcett et al., 2019; Tewari et al., 2022). The PFC is responsible for the complex integration of multiple inputs to inform cognitive function, known as executive function (Ferguson and Gao, 2018), consistently impaired in MIA-exposed adult offspring (Figure 2.18; Potter et al., 2023). PVIs are fast-spiking GABAergic inhibitory interneurons, comprising ~50% of the total PFC interneuron population, enriched in cortical layers II-VI (Kawaguchi and Kubota, 1997; Llorca and Deogracias, 2022; Nahar et al., 2021). PVIs are characterised by expression of the calcium-binding protein parvalbumin (PV) and can be subdivided into chandelier cells (make contacts with pyramidal cell axons) and basket cells (form contacts with dendrites of various neurons; Caillard et al., 2000; Nahar et al., 2021). PVIs produce inhibitory GABA signals, critical for establishment of the correct EI balance during cortical development, hypothesised to be critical for PFC executive function (Ferguson and Gao, 2018). PVIs are also considered important for their role in the synchronisation of ongoing PFC gamma-oscillations (Nahar et al., 2021). Gamma oscillations refer to network oscillations in the gamma range (20-80Hz), synchrony of which is important for cognitive development (Kriener et al., 2022; Mably and Colgin, 2012). These frequencies accelerate across the rodent juvenile period (PD10-28), increasing from low frequency (~20Hz) to high frequency (~50-60Hz) oscillations, coinciding with increasing PV expression (Bitzenhofer et al., 2020). Of note, reduced frequency gamma-oscillations, hypothesised to result from disturbed PVI function, have been identified in schizophrenia (Chung et al., 2022; Kaar et al., 2019; Nahar et al., 2021).

During neurodevelopment, PVIs are generated from the medial ganglionic eminence at ~GD16-17 in rats, before migrating to the cortical layers (Hu et al., 2017; Llorca and Deogracias, 2022). Hence PVI development could be disturbed by the observed foetal neuroinflammation in this period (Chapter 2, Figure 2.15). These prenatally specified PVIs become readily detectable in the rat PFC at ~PD18-PD20 (Ouellet and Villers-Sidani, 2014; Qu et al., 2016). Concordantly, gene and protein expression of PNN components and PNN density increases across the juvenile and adolescent period in the rat, before becoming relatively stable in adulthood (Deepa et al., 2006; Gao et al., 2018; Jakovljević et al., 2021; Mafi et al., 2020; Ueno et al., 2018; Wen et al., 2018). PNN formation is thought to be critical for normal PVI function as studies have shown that PNN depletion using the enzyme, chondroitinase ABC (Ch-ABC), reduces PVI inhibitory output, resulting in altered EI balance and inhibited PVI maturation (Bucher et al., 2021; Wingert and Sorg, 2021).

6.1.4. The role of the ECM in synaptic plasticity and cognition

6.1.4.1. The critical period of the PFC

Critical periods are phases during brain development where there are pronounced levels of plasticity, where the brain is particularly vulnerable to perturbations in the developing synaptic

circuitry (Larsen and Luna, 2018). The PFC critical period occurs during juvenile-adolescent development (~PD14-35 in rats; Caballero et al., 2016; Schalbetter et al., 2022). This critical period is essential for normal synaptic structural and functional plasticity and thereby formation of the neural circuitry underscoring PFC-mediated higher cognitive functions (Guirado et al., 2020; Larsen and Luna, 2018). Various developmental processes occur during this time, including, synapse formation, synaptic pruning by microglia, dopamine innervation of the cortical layers, PVI maturation and positioning and establishment of the EI balance (Caballero et al., 2016; Hensch, 2005; Morishita et al., 2015; Schalbetter et al., 2022). Notably, the closure of this period is marked by formation of myelin sheaths and the ECM (Larsen and Luna, 2018), which restrict synapse formation (i.e., synaptic structural plasticity; Dzyubenko et al., 2016). Disturbances to these processes can therefore predispose individuals to cognitive deficits (Morishita et al., 2015; Schalbetter et al., 2022).

6.1.4.2. Role of myelin and the neural ECM in structural synaptic plasticity

I. Myelin

Myelin sheaths form throughout the critical period (Downes and Mullins, 2014; Larsen and Luna, 2018; McGee et al., 2005). Glycoproteins, MAG and MOG, expressed exclusively from myelinating oligodendrocytes (Figure 5.1), both inhibit synaptic plasticity (McKerracher et al., 1994; Schafer et al., 1996; Wang et al., 2002). While the effect of MAG is time-dependent, with promotion of dendrite outgrowth during early development before becoming a potent inhibitor of dendritic outgrowths after PD8 in rats (Giger et al., 2008), MOG exclusively inhibits neurite outgrowth, with its expression at the nodes of Ranvier preventing abnormal axon formation (Huang et al., 2005). These inhibitory functions are thought to be driven through neuronal NOGO receptors, which bind myelin proteins (e.g., MAG/MOG/MBP) and promote intracellular signal cascades which inhibit dendritic outgrowth (McGee et al., 2005).

II. ECM

Neural ECMs mature at the closure of the PFC critical period (Larsen and Luna, 2018). The neural ECM is suggested to act as a physical barrier, preventing formation of new neuron-neuron contacts (Bosiacki et al., 2019; Wilson et al., 2020) as well as inhibiting synaptic growth through binding to integrins and semaphorins (Dzyubenko et al., 2016). *In vitro* studies demonstrate that excess neural ECM accelerates the maturation of neuronal activity and networks (Lam et al., 2019). In line with this, PNN formation restricts PVI plasticity. PNN formation is activity-dependent, with PNN formation increasing on active neurons to maintain high PVI firing rate (Favuzzi et al., 2017; McRae et al., 2007). The formation of PNNs is thought to consolidate mature PVI dynamics in the PFC (Bucher et al., 2021). Accordingly, digestion of PNNs and ECMs using Ch-ABC, or inhibition of individual ECM components, produces

molecular phenotypes consistent to those seen in the PFC critical period (Bosiacki et al., 2019; Carulli et al., 2010; Morishita et al., 2015).

6.1.4.3. Role of ECM signalling in functional synaptic plasticity

Beyond the developmental role of the neural ECM in structural plasticity during the critical period, the ECM and its signalling pathways are also important in modulating ongoing LTP. LTP is a form of activity-induced functional synaptic plasticity and has long been considered critical for learning and memory (Bliss and Lomo, 1973; Bliss, 1979; Collingridge and Bliss, 1987). In its simplest form, LTP is an alteration in synaptic efficacy through the strengthening of associations between active neuronal synapses, which is thought to underpin the storage of information in the brain during the processes of learning and memory (Bliss and Lomo, 1973; Bliss, 1979; Collingridge and Bliss, 1987; Lynch, 2004). LTP is thought to rely primarily on glutamatergic signalling, with a pivotal role for NMDA receptors (Collingridge and Bliss, 1987; Zhao et al., 2005). However, more recent work has also implicated a role for post-synaptic glutamatergic α-amino-3-hydroxy-5-methyl-4-isoxazolepropionic acid (AMPA) receptors (Chater and Goda, 2014; Choquet and Opazo, 2022). It has been suggested that the neural ECM regulates functional synaptic plasticity primarily through the modulation of glutamatergic receptors of the AMPA and NMDA subtypes, thereby influencing LTP and cognition (Frischknecht and Gundelfinger, 2012).

I. Lateral diffusion of synaptic AMPA receptors

Correct receptor density and turnover at synapses is important for normal synaptic transmission and strength (Choquet and Opazo, 2022; Maynard and Triller, 2019). Receptor diffusion is a key mechanism by which synaptic receptor density is regulated, with receptors alternating between ‘mobile’ and ‘trapped’ states (Meier et al., 2001; Thomas et al., 2005). Further, correct AMPA receptor diffusion is important for recycling of desensitised receptors during neuronal signal propagation, essential for LTP (Choquet and Opazo, 2022; Penn et al., 2017). The perisynaptic ECM acts as a physical barrier to receptor lateral diffusion, with hyaluronan matrices demonstrated to restrict AMPA receptor 1 (GLuA1) diffusion and reduce receptor turnover (Frischknecht et al., 2009), while Brevican directly interacts with GLuA1 to aid in its clustering (or trapping) within the synapse (Favuzzi et al., 2017).

II. β-integrins and NMDA/AMPA receptor regulation

Integrins form heterodimeric transmembrane receptors composed of α and β subunits. Integrins are expressed on both neurons and glia and act as neural ECM receptors (Wu and Reddy, 2012). β1-containing integrins, in particular, have been shown to be indispensable for LTP through their role in regulating NMDA receptor diffusion and mobility within the synaptic membrane, via contacts with various ECM components (Bernard-Trifilo et al., 2005; Michaluk et al., 2009; Nagy et al., 2006; Schweitzer et al., 2017). Moreover, β1-integrins, in co-operation with Reelin signalling, are also important for the normal developmental NMDA receptor switch

from NR2B to NR2A expression (Groc et al., 2007). By comparison, both β1- and β3-containing integrins have both been associated with AMPA receptor regulation. Notably, β3-containing integrins appear critical in activity-dependent phagocytosis of AMPA receptor 2 (GLuA2; Cingolani et al., 2008), while β1-containing integrins are important for normal GLuA1-mediated signalling (Chan et al., 2006).

III. Reelin signalling and NMDA receptor regulation

Reelin is a large extracellular matrix glycoprotein with important roles throughout neurodevelopment, mediated through binding to the dimeric receptors, very low density lipoprotein receptor (VLDLR) and apolipoprotein E receptor 2 (ApoER2; Lee and D'Arcangelo, 2016; Yasui et al., 2010). During prenatal and early postnatal development, Reelin-receptor binding primarily regulates neuronal migration. For this, Reelin, secreted from Cajal-Retzuis cells (Lee and D'Arcangelo, 2016; Trotter et al., 2013), binds its receptors and induces phosphorylation of the cytosolic adaptor protein, Disabled 1 (DAB1; Figure 6.2A; Chen et al., 2004; Howell et al., 1999; Trotter et al., 2013). Phosphorylation of DAB1 activates various downstream signalling pathways which regulate cortical neuron migration (Figure 6.2A; Chen et al., 2004; Lee and D'Arcangelo, 2016).

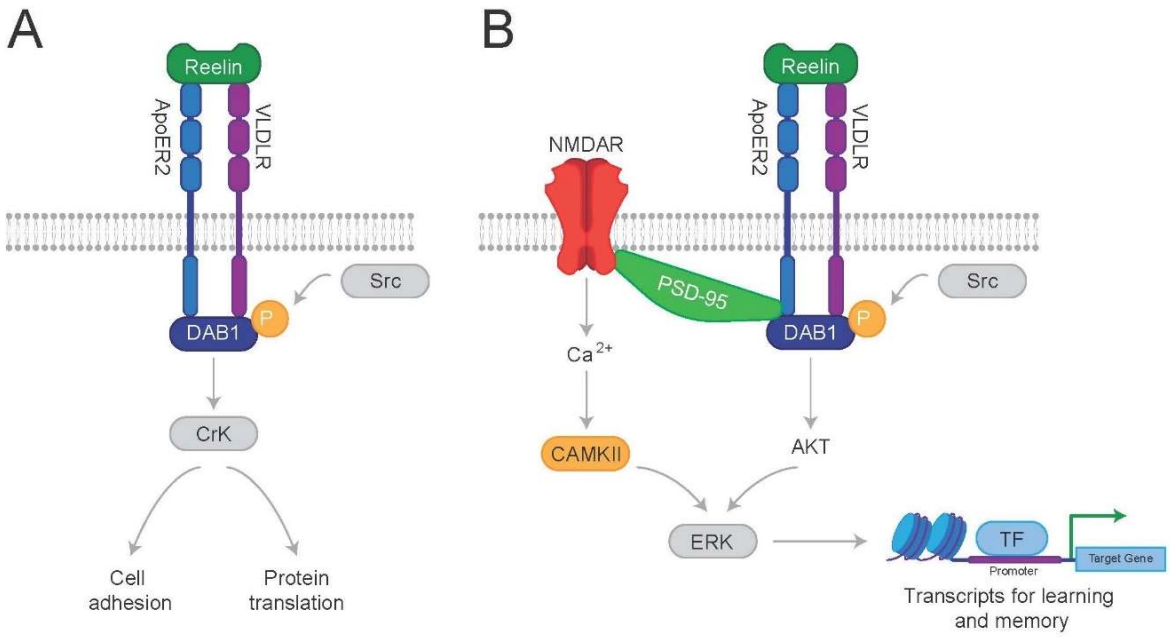

Figure 6.2. Reelin signalling
A. Overview of prenatal and early developmental Reelin signalling. Reelin binds receptors VDLR and ApoER2, leading to phosphorylation of DAB1 adaptor protein by Src family kinases. Phosphorylated DAB1 activates the CRK family of proteins, which, in turn, promote signalling cascades which i) modulate cell adhesion proteins to aid in neuronal migration and lamination or ii) promote protein translation required for dendrite development. **B.** Overview of postnatal Reelin signalling. Reelin binds receptors VDLR and ApoER2, leading to i) activation of PSD95, which, in turn, activates NMDA receptors (NMDAR), causing calcium influx and activation of CAMKII, ii) non-canonical DAB1 signalling and downstream AKT activation, both converge in ERK-driven transcription of genes required for learning and memory. Figure adapted from Woods et al. (2023).

In later postnatal development, Reelin secretion is restricted to GABAergic interneurons, where Reelin signalling becomes associated with LTP (Lee and D'Arcangelo, 2016). Here, Reelin-receptor binding promotes PSD95-mediated functional regulation of NMDA receptors (Figure

6.2B; Beffert et al., 2005; Chen et al., 2005; Ventruti et al., 2011). Moreover, Reelin signalling also regulates the NMDA receptor composition within the synapse through regulating NR2B mobility (Campo et al., 2005; Groc et al., 2007; Sinagra et al., 2005).

6.1.5. The role of the neural ECM in schizophrenia

GWAS have identified schizophrenia risk variants in genes encoding MMPs and CSPGs (Wu et al., 2020), while analysis of schizophrenia post-mortem brains have demonstrated altered expression (both increases and decreases) of CSPGs and other ECM components (Pantazopoulos et al., 2010, 2021) and reduced PNN density in various brain regions, including the PFC (Enwright et al., 2016; Mauney et al., 2013; Pantazopoulos et al., 2010). Such changes have been hypothesised to contribute to PVI dysfunction and predispose individuals to pathophysiology (Steullet et al., 2017). That said, changes in PV expression and PVI density have been less consistent (Fawcett et al., 2019). β-integrins and their signalling pathways are also becoming frequently implicated in the pathogenesis of schizophrenia, through their roles in neurodevelopment (Carneiro, 2010; He et al., 2022). However, one of the most robust findings is a reduction in ECM glycoprotein, Reelin (Berretta, 2012; Guidotti et al., 2000). Likewise, the *RELN* gene, which encodes the Reelin protein, is one of the most robust and extensively studied epigenetic targets in schizophrenia, with *RELN* DNA hypermethylation, coinciding with up to 50% downregulation of Reelin expression in the cortex and hippocampus of schizophrenia patients (Guidotti et al., 2016; Kho et al., 2022; Nabil Fikri et al., 2017; Pries et al., 2017). Taken together these studies show accumulating evidence for the role of ECM dysfunction in schizophrenia, which could have crucial impacts on cognition and LTP.

6.1.6. Chapter aims

Chapter 5 highlighted key changes to both macroglia and microglia in the developing PFC in response to MIA including notable developmental dysregulation of several genes (*Mbp*, *Mag, Nfasc*) enriched from oligodendrocytes and the cell adhesion molecule *Gpc4*, enriched from astrocytes. These genes possess important roles in cortical extracellular structure and synapse formation (Allen et al., 2012; Chang et al., 2014; Fawcett et al., 2019; Saab and Nave, 2017). Critically, the observed MIA-induced temporal changes in glial cells (Chapter 5) show these genes are expressed prematurely in the developing cortex of MIA-offspring, driven by altered DNAm. The advanced expression of these genes would be expected to promote malformation of myelin and the neural ECM and infer premature closure to the PFC critical period, which would limit synaptic plasticity and perturb cognitive development. Notably, evaluation of the remaining RRBS candidate genes that withstood the acceptance criteria for downstream analysis (refer to Appendix 9), identified all as involved in cell adhesion and ECM-related signalling pathways (see Table 6.2 for summary of selected candidates evaluated in this Chapter). This finding further supports the idea that MIA may induce ECM alterations. It was therefore hypothesised that MIA-induced changes to glia and myelin development (Chapter 5),

occur alongside altered neural ECM formation and that these changes wither in turn, or concomitantly, alter synapse formation and plasticity, and thus underscore the observed cognitive deficit (Chapter 2). This Chapter aims to explore this hypothesis by:

i) Evaluating changes to PNN component expression and density to provide supportive evidence for altered neural ECM formation.
ii) Analyse MIA-induced developmental dysregulation of ECM adhesion and Reelin signalling genes by measurement of DNAm profiles of selected candidate gene regulatory elements and how these correlate with changes in gene/protein expression.
iii) Establish whether MIA-induced changes to the neural ECM formation and Reelin signalling coincide with changes in the expression of key synaptic proteins involved in LTP.

Table 6.2. Summary of selected neuronal-cell enriched candidate gene functions

Table summarises the functions of the selected candidate genes used in this study, alongside their associations with neurological diseases and changes previously identified in MIA models. RRBS finding indicates the gene regions and direction of methylation changes identified. *Indicates the region focused on for downstream analysis.
§Note: this gene did not pass stringency for pyrosequencing but as it is closely related to two that did (*Dab1* and *Camk2b*) it was analysed for gene expression but not DNAm

Candidate gene	RRBS Finding	Cell enrichment	Function(s)	Implication for role pathogenesis of neurological disease	Previous change in a MIA model	References
Ank3 (Ankyrin G)	↑ Intron 1* ↓ Introns 6, 9, 10	Neurons/ Oligodendrocytes	Cell surface ankyrin linking membrane proteins to underlying cytoskeleton. ANK3/ANKG is enriched at nodes of Ranvier with roles in neuronal signalling, myelination and perinodal ECM formation.	Genetic variants in *ANK3* gene associated with BPD, ASD and schizophrenia.	Differentially methylated in the PFC of adult mice exposed to MIA.	Chang et al., 2014; Leussis et al., 2012; Richetto et al., 2017b; Roussos and Haroutunian, 2014; Wu et al., 2020; Yoon et al., 2022.
Nrxn2 (Neurexin 2)	↓ Exons 1* ↑ Exon 21 ↓ Introns 1, 15	Neurons (Inhibitory/ Excitatory)	Neuronal cell surface adhesion molecule, binding neuroligins on adjacent synapses. Important in regulating synaptogenesis, synapse assembly and EI balance.	Genetic and epigenetic variants in *NRXN2* gene associated with schizophrenia and ASD.	Differentially methylated in the PFC of adult mice exposed to MIA.	Born et al., 2015; Harkin et al., 2017; Lin et al., 2023; Richetto et al., 2017b; Wu et al., 2020.
Dab1 (Disabled-1)	↓ Promoter* ↓ Introns 3, 7	Neurons (Excitatory)	Adaptor protein phosphorylated downstream of Reelin receptor binding. Involved in neuronal migration, dendrite outgrowth and synaptic plasticity.	Genetic variants in *DAB1* gene associated with schizophrenia. Differentially expressed in schizophrenia.	Differentially methylated in the PFC of adult mice exposed to MIA.	Chen et al., 2004, 2005; Lee and D'Arcangelo, 2016; Richetto et al., 2017b; Trotter et al., 2013; Wu et al., 2020.
Camk2b (Ca^{2+}/ Calmodulin dependent kinase IIβ)	↓ Exons 16*, 18 ↓ Introns 1, 3, 5, 15, 16, 17, 18	Neurons (Excitatory)	*Camk2b* forms the second highest expressed subunit of the holoenzyme, CAMKII kinase, associated with neuronal migration, synapse formation LTP and synaptic plasticity.	Genetic variants in *CAMK2B* gene associated with schizophrenia and intellectual disability.	Differentially methylated in the PFC of adult mice exposed to MIA.	Nicole and Pacary, 2020; Proietti Onori and van Woerden, 2021; Richetto et al., 2017b; Wu et al., 2020.
§*Reln* (Reelin)	↓ Exon 28 ↑ Introns 1, 2, 10	Neurons (Inhibitory)	Extracellular glycoprotein, secreted from Cajal-Retzuis cells in early development, regulating neuronal migration, becoming enriched in GABAergic interneurons postnatally, regulating synaptic plasticity and LTP.	Genetic and epigenetic variants in *RELN* gene associated with BPD, ASD and schizophrenia.	Differentially methylated in the PFC of adult mice exposed to MIA. Differentially expressed in offspring from MIA models.	Chen et al., 2005; Lee and D'Arcangelo, 2016; Richetto et al., 2017b; Woods et al., 2021; Wu et al., 2020.

6.2. MATERIALS AND METHODS

Note: the following methods were performed on samples collected from cohorts PR1 (GD21 FC) and PN2 (PD1 FC, PD21-100 PFC).

6.2.1. IHC

Chapter 5 suggested a dysregulation of macroglia cell development, resulting in aberrant expression of key macroglia genes in juveniles through to adulthood in MIA-exposed offspring. Results showed dysregulated expression of astrocyte-enriched adhesion molecule, *Gpc4*, alongside oligodendrocyte-enriched extracellular molecules involved in ECM formation (*Nfasc*) and myelin formation (*Mag, Mbp*). Evaluation of MBP protein expression showed developmental dysregulation of myelin maturity. To evaluate if there were changes to other extracellular structures, IHC was used to assess PVIs (PV+ cells) and their critical ECM, the PNN (WFA+ staining), utilising an in-house, pre-optimised methodology (verbal communication, Jennifer Fletcher). WFA (*Wisteria Floribunda Agglutin*), is a lectin which has been demonstrated in several studies to bind to *N*-acetylgalactosamines, found attached to CSPGs within PNNs (Härtig et al., 2022; Fawcett et al., 2019). Biotin-conjugated WFA is therefore the most widely used method for analysis of PNNs to date (Härtig et al., 2022).

IHC for PV+ cells and WFA+ PNNs was performed as described previously, unless otherwise indicated (Chapter 5, Section 5.2.1.3), using sodium citrate antigen retrieval (Chapter 5, Table 5.3) and 5% horse serum protein block to dilute the primary and secondary antibodies. Primary antibodies were incubated under antibody-specific conditions (Table 6.3).

Table 6.3. IHC primary antibody conditions for PV+ and PNN+ staining

Marker	Antibody/Lectin	Dilution and titre	Incubation
PV	Mouse monoclonal anti-PV (Swant 235; Swant, 1mg/mL)	1:5,000 (0.2µg/mL)	24h 4°C
PNN	Wisteria Floribunda Lectin (WFA, WFL), Biotinylated (B-1355-2, Vector Labs, 2mg/mL)	1:1,000 (2µg/mL)	12h 4°C

After primary antibody incubations, the sections stained for PV+ cells were washed and transferred to their secondary antibody solution, containing horse anti-rabbit IgG antibody (H+L), biotinylated (BA-1100-1.5; 1.5mg/mL; Vector Labs, London, UK) diluted and incubated as previously outlined in Chapter 5. However, as the WFA primary antibody is already biotinylated, no secondary antibody incubation was required and hence these sections were progressed straight to ABC-DAB detection.

Prior to detection methods, all sections were washed. Detection of biotin (on secondary antibody for PV+ or on the WFA+) was performed as described in Chapter 5, Section 5.2.1.3. The only difference was for the WFA+ stain, where preparation of DAB was amended to exclude the nickel solution. The nickel solution causes the colour formed by the reaction to be purple-grey (see Supplementary Figures S14.5-7). Exclusion of the nickel causes the colour reaction to be

red-brown. PV is present throughout the cell body cytosol of PVIs (Permyakov and Uversky, 2022) and hence the stain morphology appears as the outline of the cell. As the PNN forms around the cell body and proximal dendrites of PVIs (Shen, 2018), the pattern of staining is very similar between these two stains. Therefore, by selecting a different DAB coloured reaction product for the two stains, they are more clearly delineated.

The samples were incubated in their respective DAB reagents for 10min and then rapidly transferred to 2mL dH_2O to stop the colour change reaction. The sections were carefully mounted onto Menzel Gläser SuperFrost® Plus adhesion slides (Thermo Fisher, Oxford, UK), cover-slipped and imaged as described in Chapter 5, Section 5.2.1.3.

6.2.1.1. Negative controls

For both PV+ and WFA+ staining, a negative control was performed using omission of primary antibodies/lectin. For PV+, a second negative control was performed using replacement of the anti-PV primary antibody with corresponding concentration (µg/mL) of species-specific IgG (mouse IgG control antibody, I-2000-1; Vector Labs, London, UK). No staining was observed in negative controls (see Appendix 14, Supplementary Figures S14.7&S14.8), validating that the observed staining for each methodology was specific to target binding.

6.2.1.2. IHC analysis

CaseVeiwer (v2.4.0, 3D-Histech, Budapest, Hungary) was used to analyse the tissue sections, with slide identifiers randomly generated to blind individuals undertaking cell counting to sample identity. As described in Chapter 5, Section 5.2.1.5, each hemispheric PFC region on a slide was annotated using the Rat Brain Stereotaxic Co-ordinates as a guide (6^{th} Edition, Paxinos and Watson, 2007; Figure 2.2).

A minimum of five PFC sections, corresponding to 10 split hemispheric sections per sample, were annotated on each slide. However, as PV+ cells are enriched in cortical layers II-VI (Nahar et al., 2021), there was a large signal gradient across the cortical tissue sections. This precluded automated scoring due to inconsistencies in background DAB colouring. Instead, the PV+ cells and WFA+ PNN within these annotations, were manually counted, by two independent experimenters, using the built-in manual annotation tool within the software. Following this, PV and PNN density per mm^2 of each PFC annotation was calculated and averaged across all PFC sections on a slide, to give an average density/PFC mm^2 for each sample.

6.2.2. Nucleic acid extraction and quantification

Nucleic acid extraction was performed using the innuPREP DNA/RNA mini kit (Analytik Jena, Jena, Germany) as described in Chapter 5, Section 5.2.2. Extracted RNA and gDNA quantity were assessed using ThermoFisher NanoDrop® and QuantiFluor® ONE dsDNA System (Promega, Southampton, UK) respectively, as described previously (Chapter 4, Section 4.2.1). Sample quality was assessed using agarose gel electrophoresis (Chapter 3, Section 3.2.1.2).

6.2.3. mRNA expression analysis

All reverse transcription and qPCR reactions were performed as previously described (Chapter 3, Section 3.2.2) with the Gene Globe software (*Rattus norvegicus*; Qiagen, Manchester, UK) searched for primers targeting each of the candidate genes of interest. In this Chapter, this included genes, identified by the RRBS analysis, involved in neuronal signalling (Chapter 4; Appendix 9: *Dab1, Ank3, Camk2b, Nrxn2, Reln*) alongside additional candidate genes (*Acan, Bcan, Vcan, Ncan*). A full list of QuantiTect primer assays used can be found in Table 6.4. As found previously a 1:50 cDNA dilution was optimal for all candidate genes following a dilution trial, consistently producing Ct values15-30 across development (Chapter 3, Section 3.2.2.2). As samples used in this study were the same as those in Chapter 5, the geometric mean of the same three stable reference genes (*Gapdh, Ubc* and *B2m*; Appendix 3. Supplementary Figure S3.3) was used to normalise candidate gene expression values.

Finally, agarose gel electrophoresis was performed to confirm predicted amplicon size, as described previously (Chapter 3, Section 3.2.2.4). A single clear band of predicted size (Table 6.4) was taken as an indicator of effective qPCR amplification. A representative qPCR gel for each gene can be found in Appendix 4, Section 4.

Table 6.4. QuantiTect primer assays (Chapter 6)

Gene	QuantiTect primer assay (Cat no.)	Amplicon Size (bp)	Exons spanned
Ank3	Rn_Ank3_2_SG (QT01606899)	92	4/5
Nrxn2	Rn_RGD:620211_1_SG (QT00178507)	92	11/12
Camk2b	Rn_Camk2b_1_SG (QT00183407)	88	2/3/4
Dab1	Rn_Dab1_1_SG (QT00188517)	119	11/12
Reln	Rn_Reln_1_SG (QT00195699)	118	13/14
Vcan	Rn_Vcan_1_SG (QT01598814)	146	10/11/12
Bcan	Rn_Bcan_1_SG (QT00176638)	144	6/7
Acan	Rn_Acan_1_SG (QT00189518)	90	2/3
Ncan	Rn_Ncan_1_SG (QT00177240)	89	11/12

6.2.4. Bisulphite pyrosequencing

6.2.4.1. Assay design

As outlined in Chapter 5, Section 5.2.3.1, the Pyromark assay design software (v2.0.2., Qiagen, Manchester, UK) was used to design pyrosequencing assays for DNA regions of interest, as identified by the RRBS analysis. Ten genes withstood the acceptance criteria for pyrosequencing (Appendix 9), four of which will be analysed here. The top scoring pyrosequencing assay for each of these four genes (inclusive of forward and reverse PCR primers (one biotinylated) and sequencing primers) can be found in Table 6.5, all ordered from Invitrogen (Loughborough, UK) and prepared as described in Section 5.2.3.1.

6.2.4.2. Bisulphite conversion and bis-PCR

All bisulphite conversions and bisPCR were performed as described in Chapter 5, Section 5.2.3.2-5.2.3.3 using forward and reverse primers specific to the genes in this Chapter (Table 6.5). Following bis-PCR, 5µL product from each sample was assessed by agarose gel electrophoresis to confirm a single amplicon of predicted size (Table 6.5). For a representative bis-PCR gel for each gene see Appendix 4, Section 4, Supplementary Figures S4.18-S4.21.

6.2.4.3. Pyrosequencing

Pyrosequencing was performed using the Pyromark Q24 Advance reagents and software (Qiagen, Manchester, UK), as described in Chapter 5, Section 5.2.3.4, with the data retrieved as %methylation at each CpG site in the sequence to analyse. The mean of the CpG sites within the sequence was also calculated to give average CpG methylation. All negative samples returned no interpretable data while positive control samples showed clear passable peaks (see Appendix 11, Section 2). %CV was <1.6% for all assays, with methylation ranging <1.5% between the positive control repeats (Table 6.6). These criteria therefore form the standard variability of the assays. Between-group differences in methylation percentage would hence be required to exceed this to be considered not just an artefact of assay variability.

Table 6.5. Pyrosequencing assay design

Gene	Genomic region (strand)	UCSC Rn5.0 genome reference	Sequence to analyse (total number of CpG sites)	bis-PCR forward primer (5'-3')	bis-PCR reverse primer (5'-3')	PCR product size (bp)	(Pyro)sequencing primer (5'-3')
Ank3	Intron 1 (-)	Chr20: 22393877-22393921	TTTTTGGTAYGGAG TAGTTGGGTTTTTAT AATGTGTTGATGGA GTAGTTTTTTYGGG GATTGTATATTGATT TAAGATGG **(2)**	GGAAAAGTGTTTTTGGTTTAGGGAAGAT	AAAAAAAATCCAAACACACCAATTTAT*	234	ATGGAATTTGTGGTGAA (+)
Nrxn2	Exon 1 (-)	Chr1: 228790348-228790384	YGGYGAGGTGGGT TGYGATTGTAGTTA TATTGGTTTYGGYG GTAAGTTTTGTAGT GAAGGTGAGTT **(5)**	GTTGTTGGGTAGTTAGGGTT	CCCCTCCCAACACAAACCAATAAATC*	231	GTTTTTGTATAGTGTTAGTTTT (+)
Camk2b	Intron 16/18/21 (-) (Internal CpG island)	Chr14: 86896016-86896037	CYAAACCYTCAACA ACYACYACTTTAAA ACCTATACYTAA ATCTCCC **(5)**	TTTTTGGGGGGTAAATTTAAGTG*	ACCTAATAATCATCCCTATTTTCTCC	197	ACCACAAAACAACTCAT (-)
Dab1	Promoter (+)	Chr5: 127881334-127881382	TATGTGYGGTTYGG GGTGTTTTTTTTGAA GGGAGGAGTTTTTT TTTTGGAGAGGATT TTYGATGAGTTTGG TTAAGGTT **(3)**	TGAAATGTTTTTGTTGGTGTATGT	AACCCCCAACCTTAACCAAACTC*	209	TGTAGTATTTAGATAGAGTGAATGA (+)

Key: Y - CpG sites identified via the RRBS as increased in methylation. Y-CpG sites identified via the RRBS as decreased in methylation. Y - additional CpG sites present within the sequence to analyse. *Biotinylated primer. +Positive strand . -Negative strand

Table 6.6. Pyrosequencing intra-assay control assessment

Assay	PC1	PC2	PC3	PC4	PC AV	%CV	RANGE
Ank3	80.00	79.50	78.50	79.80	79.45	0.84	1.50
Nrxn2	19.00	19.60	19.00	19.40	19.25	1.56	0.60
Camk2b	73.00	72.00	72.20	72.50	72.43	0.60	1.00
Dab1	68.67	68.67	68.00	69.33	68.67	0.79	1.33

All results indicate average % methylation of the CpG sites within each assay. Abbreviations: PC, positive control. AV, Average.

6.2.5. Preparation of cytosolic and membrane protein lysates

Cytosolic and membrane protein lysate fractions were prepared from whole tissue lysates as described in Chapter 5, Section 5.2.5. and protein concentrations quantified using a Bradford assay (Chapter 2, Section 2.2.3.1) where membrane and cytosolic fractions were diluted 1:100 before quantification.

6.2.6. WES assay protocol and optimisation

For all WES assays the standard WES protocol was performed as described in Chapter 5, Section 5.2.6, with the ProteinSimple total protein detection modules used for normalisation of target protein expression signal. All WES experiments were analysed using the Compass for Simple Western software (v6.1.0, ProteinSimple, San Jose, USA) as described in Chapter 5, Section 5.2.6.3. For this Chapter, several antibodies were compatible with WES, including the anti-PSD95 (mouse monoclonal, ab2723; Abcam, Cambridge, UK; 1mg/mL), anti-NR2A (rabbit polyclonal, PPS012; R&D systems, Abingdon, UK; 0.2mg/mL) anti-NR2B (rabbit polyclonal, PPS013; R&D systems, Abingdon, UK; 0.2mg/mL), anti-GRIA1 (GLuA1; mouse monoclonal, 67642-1-Ig; Proteintech, Manchester, UK; 1.1mg/mL) and anti-PV (rabbit monoclonal; LS-B14122; LSBio, Seattle, USA; 1mg/mL). Note that validations of these antibodies, including cell fraction enrichment, had already been shown on WES (b-neuro, verbal communication), with receptor proteins, GLuA1, NR2A and NR2B enriched in the membrane fraction and PV and PSD95 enriched in the cytosol, as expected. The dynamic range (Nelson et al., 2017; Chapter 5, Section 5.2.6.1) was optimised for each antibody used on the WES platform (see Appendix 13, Section 3). For each WES antibody used in this Chapter, the optimal experimental conditions are shown in Table 6.7. A representative WES blot and electropherogram for each target can be seen in Figure 6.3-Figure 6.7.

Table 6.7. Summary of optimal conditions for WES antibodies (Chapter 6)

Timepoint/ Tissue		PD21 PFC		PD35 PFC		PD100 PFC	
Condition		Antibody dilution and titre	Protein concentration and fraction applied	Antibody dilution and titre	Protein concentration and fraction applied	Antibody dilution and titre	Protein concentration and fraction applied
Antibody target	PSD95	1:50 (20µg/mL)	0.8µg/µL Cytosolic	1:50 (20µg/mL)	0.4µg/µL Cytosolic	1:50 (20µg/mL)	0.4µg/µL Cytosolic
	PV	1:50 (20µg/mL)	0.8µg/µL Cytosolic	1:50 (20µg/mL)	0.8µg/µL Cytosolic	1:50 (20µg/mL)	0.4µg/µL Cytosolic
	NR2A	1:100 (2µg/mL)	0.035µg/µL Membrane	1:100 (2µg/mL)	0.01µg/µL Membrane	1:100 (2µg/mL)	0.035µg/µL Membrane
	NR2B	1:100 (2µg/mL)	0.01µg/µL Membrane	1:100 (2µg/mL)	0.075µg/µL Membrane	1:100 (2µg/mL)	0.075µg/µL Membrane
	GLuA1	1:200 (5.5µg/mL)	0.0025µg/µL Membrane	1:500 (2.2µg/mL)	0.00125µg/µL Membrane	1:500 (2.2µg/mL)	0.005µg/µL Membrane

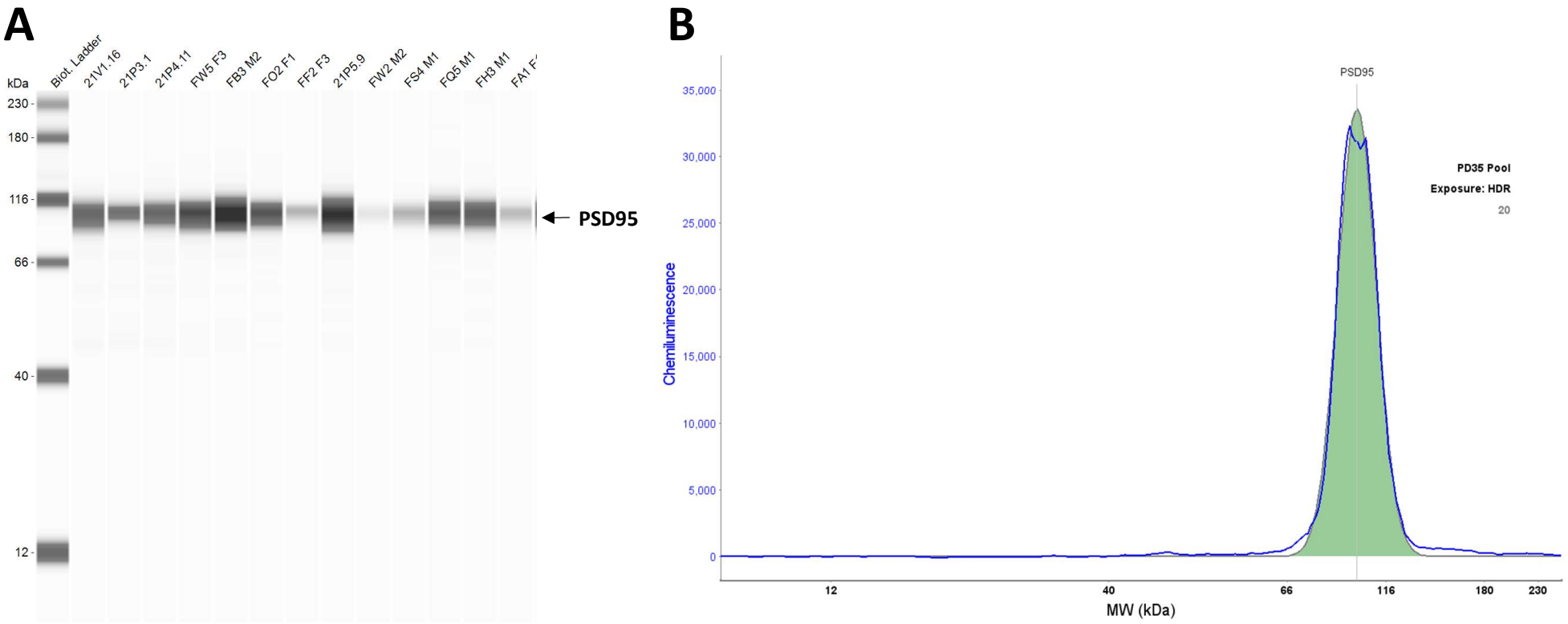

Figure 6.3. Representative WES blot and electropherogram for PSD95
A. Representative WES blot for PSD95 showing chemiluminescent band at ~95-100kDa. Molecular weight ladder (kDa) is indicated on the left, with sample identifiers across the top. **B.** Representative WES electropherogram for PSD95 showing chemiluminescent peak at ~95-100kDa.

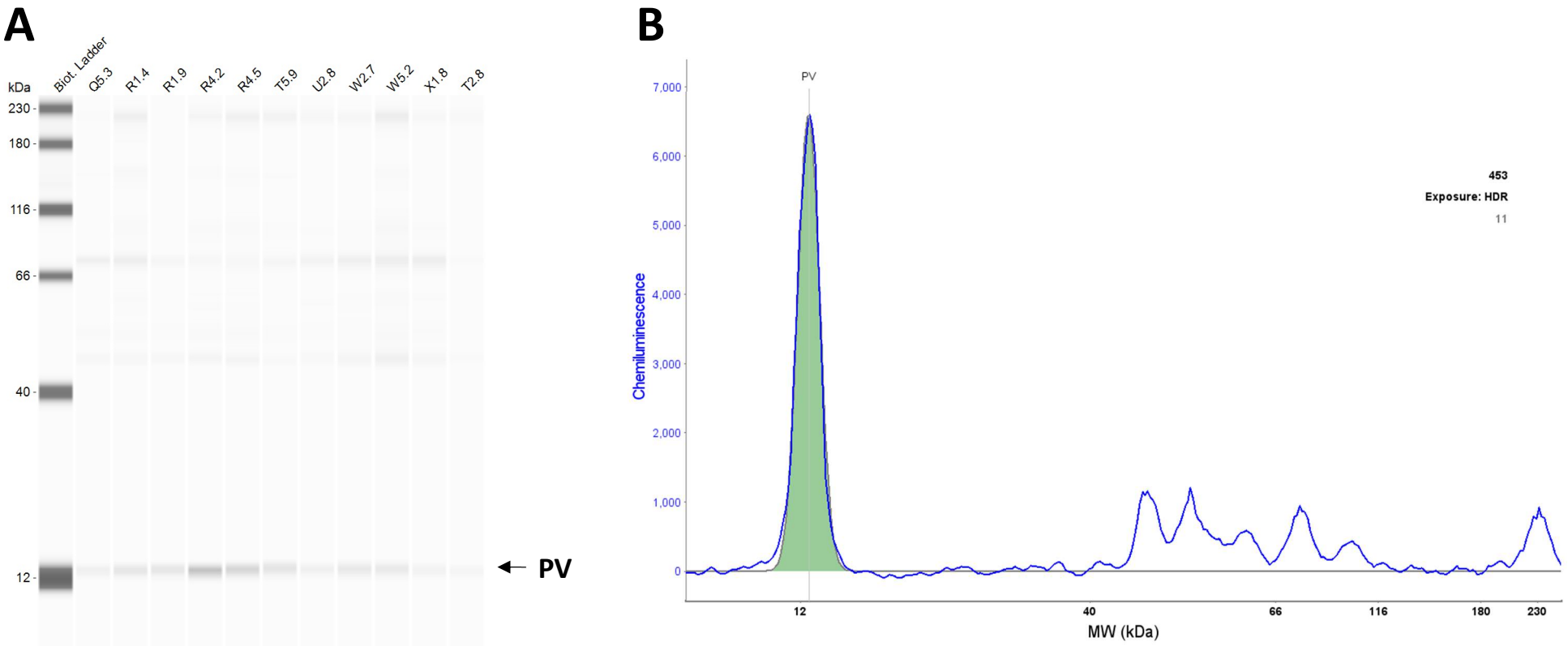

Figure 6.4. Representative WES blot and electropherogram for PV
A. Representative WES blot for PV showing primary chemiluminescent band at ~12kDa. Molecular weight ladder (kDa) is indicated on the left, with sample identifiers across the top. **B.** Representative WES electropherogram for PV showing primary chemiluminescent peak at ~12kDa.

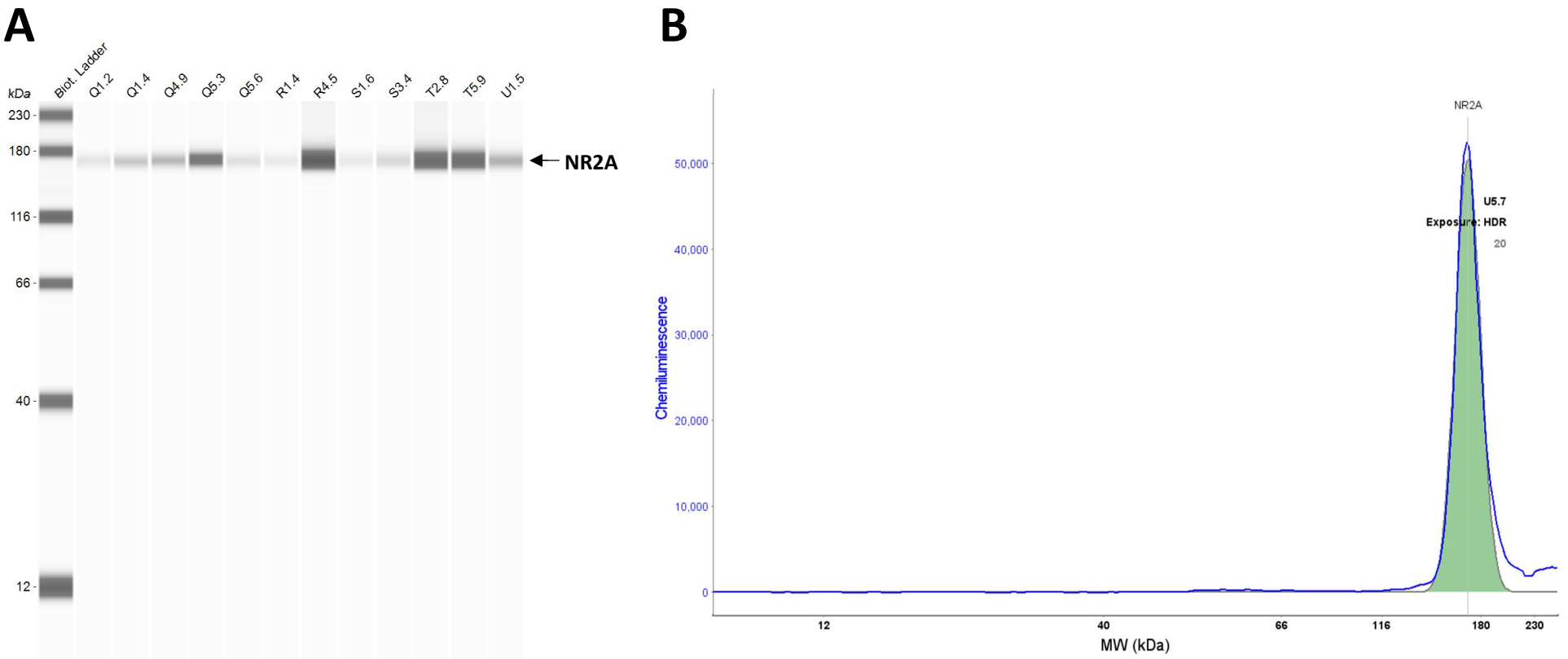

Figure 6.5. Representative WES blot and electropherogram for NR2A
A. Representative WES blot for NR2A showing single chemiluminescent band at ~170kDa. Molecular weight ladder (kDa) is indicated on the left, with sample identifiers across the top.
B. Representative WES electropherogram for NR2A showing single chemiluminescent peak at ~170kDa.

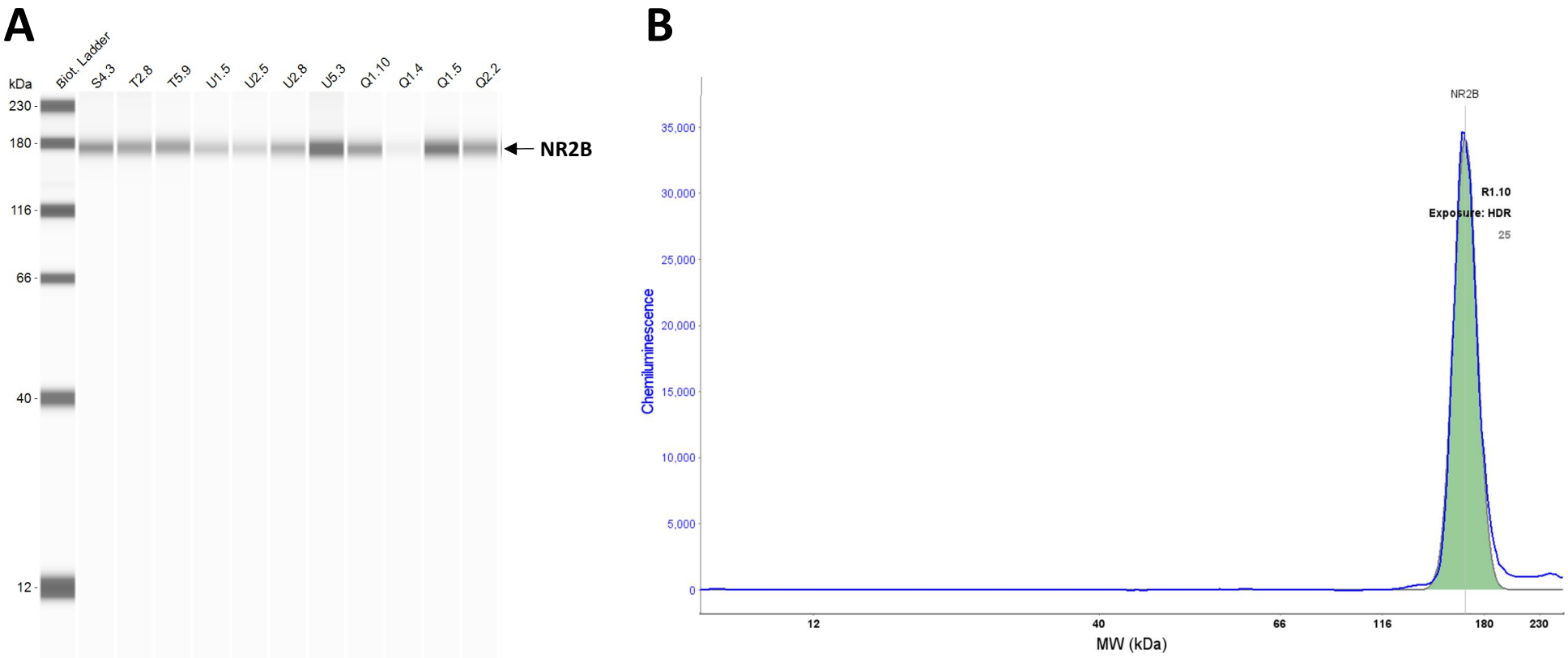

Figure 6.6. Representative WES blot and electropherogram for NR2B
A. Representative WES blot for NR2B showing single chemiluminescent band at ~170kDa. Molecular weight ladder (kDa) is indicated on the left, with sample identifiers across the top.
B. Representative WES electropherogram for NR2B showing single chemiluminescent peak at ~170kDa.

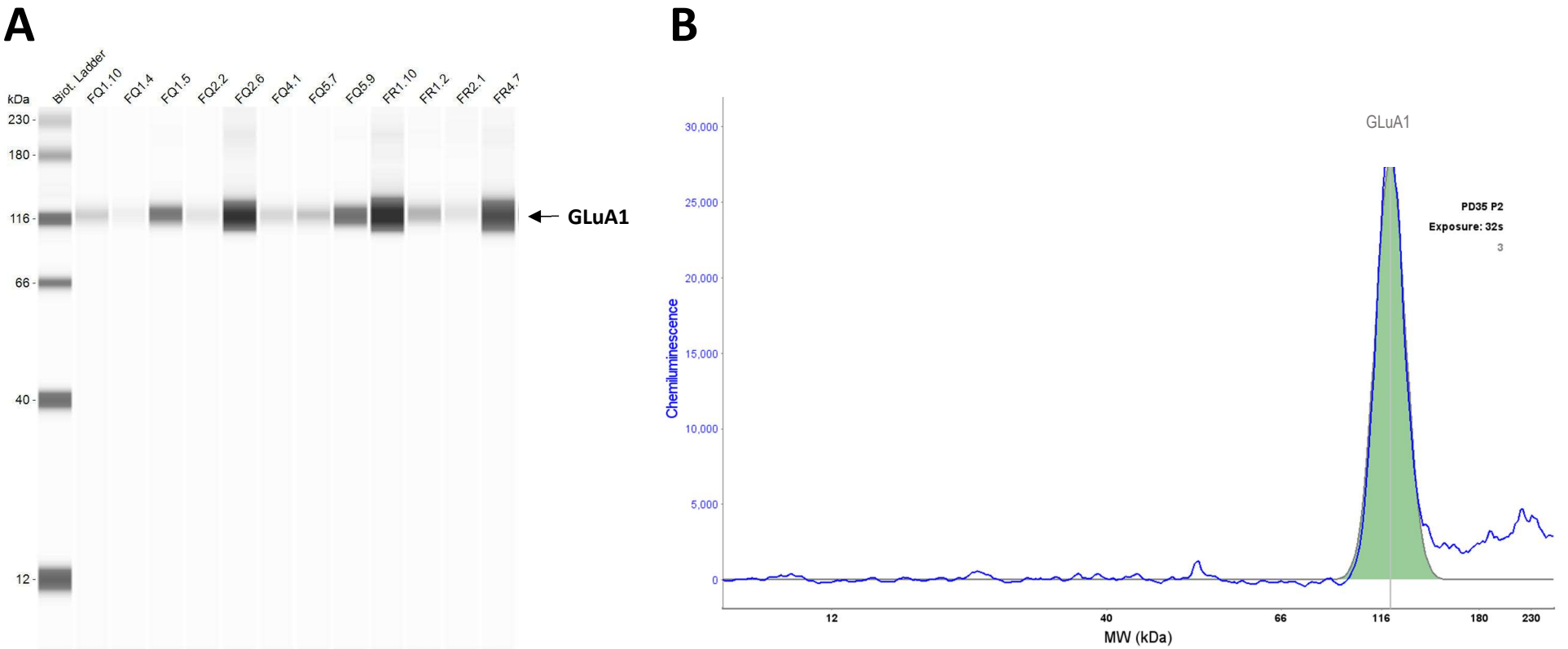

Figure 6.7. Representative WES blot and electropherogram for GLuA1
A. Representative WES blot for GLuA1 showing single chemiluminescent band at ~110-20kDa. Molecular weight ladder (kDa) is indicated on the left, with sample identifiers across the top. **B.** Representative WES electropherogram for GLuA1 showing single chemiluminescent peak at ~110-120kDa.

6.2.7. Western blotting

All selected target antibodies which were incompatible with WES were assayed using a standard Western blot. For this Chapter, this included the anti-DAB1 (rabbit monoclonal [EP2248Y], ab68461, 0.205mg/mL; Abcam, Cambridge, UK). Western blots were performed as described in Chapter 3, Section 3.2.3.2, unless otherwise indicated.

6.2.7.1. Western antibody validations

The DAB1 antibody was validated (Appendix 13, Section 1) for its target specificity by protein size and cell fraction enrichment (Supplementary Figure S13.4), with the expected developmental expression pattern (Supplementary Figure S13.5) used as further validation. In addition, negative control blots, which excluded the primary antibody from the assay, were used to show the specificity of primary antibody binding from background signal. Through these validation experiments (Appendix 13), the anti-DAB1 antibody demonstrated a clear enrichment of immunoreactive signal in the cytosolic fraction, expected as DAB1 is primarily cytosolic (Trotter et al., 2013). This anti-DAB1 signal was found to migrate at a molecular weight of ~80kDa (Figure 6.8; Supplementary Figure S13.4&S13.5) in agreement with the literature which has described the primary rat brain DAB1 isoform of 80kDa (Alvarez-Dolado et al., 1999; Bock et al., 2003; Fatemi et al., 2009b; Kang et al., 2020; Kolaka et al., 2019; Sato et al., 2007). In addition, as expected, DAB1 was found to be more highly expressed in foetal and early development compared to adulthood (Lee and D'Arcangelo et al., 2016), acting as a further validation of the antibody specificity (Supplementary Figure S13.5). Further, negative control blots showed these bands were specific to the anti-DAB1 primary antibody (Supplementary Figure S13.12B).

Of note, given that active DAB1 is phosphorylated (pDAB1), the ratio of DAB1:pDAB1 can give an index of Reelin signalling activity. Attempts to quantify pDAB1 expression by Western blotting were also undertaken. Three anti-pDAB1 rabbit polyclonal antibodies from different suppliers (Table 6.8) were trialled on cytosolic lysate samples (PD1-100) ranging from 50-200µg/well using the standard Western blotting protocol (Chapter 3, Section 3.2.3.2). However, no immunoreactive band of the correct size could be identified across any of the samples or conditions used (Appendix 13, Section 1). Hence, it was determined that quantification of pDAB1 would not be feasible in available samples.

Table 6.8. Summary of pDAB1 antibodies

Antibody details	pDAB1 target	Antibody conditions trialled
3327; Cell Signalling Technology, Danvers, USA	pTyrosine 220	**Dilutions:** 1:200 (5µg/mL); 1:500 (2µg/mL), 1:1000 (1µg/mL) **Incubations:** Overnight (4°C and room temperature) and 3h (room temperature)
STJ196282; St John's Laboratory, London, UK		
ab78200; Abcam, Cambridge, UK	pTyrosine 232	

Note: these phosphorylated tyrosine (pTyrosine) residues were selected for being phosphorylated downstream of Reelin signalling (Keshvara et al., 2001).

Following validation, antibodies were optimised to identify the experimental conditions under which the linear range of the assay was achieved (Pillai-Kastoori et al., 2020; Chapter 5, Section 5.2.7.2), For complete DAB1 Western antibody optimisations, see Appendix 13, Section 2. Optimal experimental conditions for the anti-DAB1 antibody are shown in Table 6.9.

Table 6.9. anti-DAB1 antibody optimal conditions

Antibody	GD21 and PD1 FC	PD21-100 PFC
anti-DAB1 (rabbit monoclonal [EP2248Y], ab68461; Abcam)	50µg protein/well 1:1,000 (0.205µg/mL) antibody dilution	75µg protein 1:1,000 (0.205µg/mL) antibody dilution

Note: All anti-DAB1 primary antibody incubations were performed overnight at 4°C

Once the optimal conditions were established (Table 6.9) the anti-DAB1 Western blotting protocol was performed on all samples, using the standard Western blotting protocol (Chapter 3, Section 3.2.3.2), with anti-GAPDH as a reference antibody, previously determined to show stability of expression (Chapter 5, Section 5.2.7.3). A representative Western blot for DAB1 can be found in Figure 6.8.

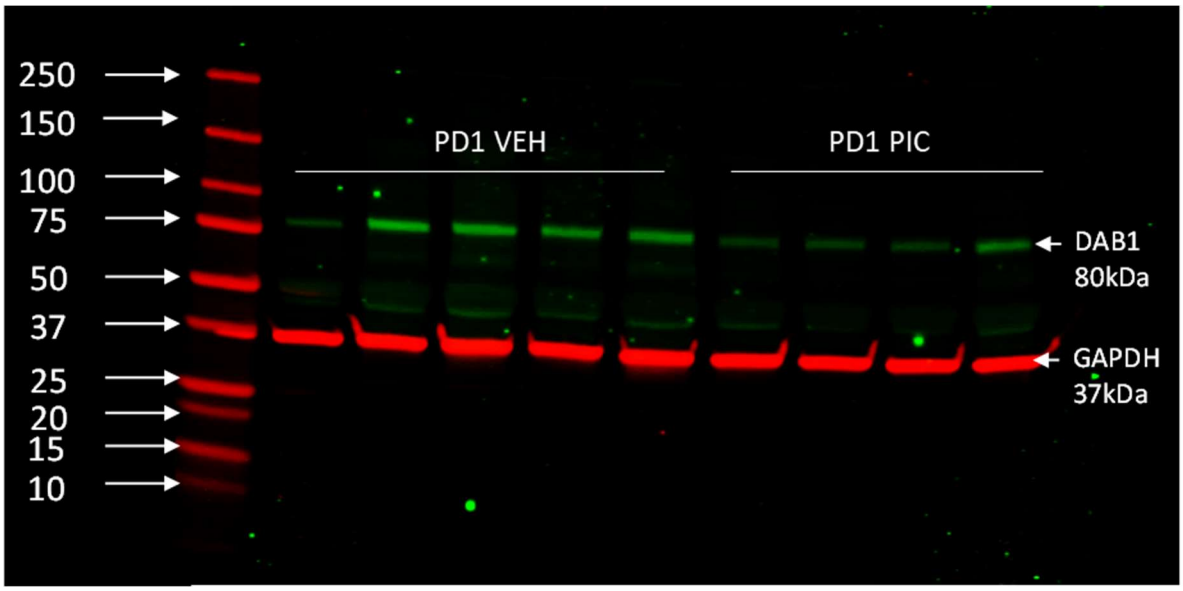

Figure 6.8. Representative DAB1 Western blot
Western blot was run according to optimal conditions (Table 6.9). Molecular weight ladder (kDa) is indicated on the left. Two bands are shown, one indicating DAB1 (~80kDa) in green, the second indicating the reference antibody, GAPDH (~37kDa) in red. Abbreviations: PD, postnatal day; VEH, Vehicle; PIC, poly(I:C).

6.2.7.2. Western blot analysis

Western blot analysis was performed using ImageStudio Lite (v5.2, Li-Cor, Cambridge, UK) as described in Chapter 5, Section 5.2.7.4, with the obtained signal for the DAB1 target protein band divided by the signal for the GAPDH reference protein band in the same lane to give a normalised target protein expression value for statistical analysis.

6.2.8. Statistics

Foetal/offspring molecular outputs (including the following dependent variables in this Chapter: PNN density, PV+ cell density, %DNAm, relative gene expression, relative protein expression) were analysed as described in Chapter 2, Section 2.2.5 and Chapter 3, Section 3.2.6, in SPSS v28.0 (IBM). Briefly, within-group outliers were excluded using SPSS extreme outlier function. Between-group and post-hoc sex comparisons were analysed by GLMM including dam as a random factor and the following predictors: fixed factors (sex, group) and covariates (maternal IL-6 and TNFα), with p-values≤0.05 considered statistically significant and $0.05<p\leq0.08$ highlighted as trending towards significance. Where the effects of all four predictors were insignificant, the phrase 'there were no significant effects of any predictors' will be used. Post-hoc Pearson's (r) or Spearman's (rho) correlations were used to evaluate directionality of relationship between numerical dependent variables and covariates. For each pyrosequencing assay, the methylation of each CpG site the average methylation across the CpG sites within the sequence were analysed, as described in Chapter 5, Section 5.2.8.

Graphs were generated using GraphPad Prism (v9.0), with n-numbers for dam per group (N) and foetuses/pups per sex per group (n) indicated in figure legends. Data represented as mean ±SEM, where individual points represent individual animals. Note: group*sex interactions are not indicated on graphs, instead post-hoc analyses by sex are shown on graphs where significant.

6.3. RESULTS

6.3.1. Changes to PVIs and PNNs during postnatal cortical development

6.3.1.1. mRNA expression of PNN components

Given the observed glial cell changes observed in Chapter 5, it was postulated that alongside myelin malformation, the neural ECM would be altered, including the perinodal/perisynaptic ECM, evidenced by altered regulation of *Nfasc* (Chapter 5, Figure 5.16&Figure 5.18A) and PNNs. For the latter, critical CSPGs of the PNN were assessed, including: Aggrecan (*Acan),* Brevican *(Bcan),* Neurocan *(Ncan),* Versican *(Vcan)*. These were examined in the adolescent (PD35) and adult (PD100) PFC to correspond with sample developmental timepoints available for IHC quantification of PNN density.

I. *Acan*

In the PD35 PFC there was a significant main effect of maternal TNFα (GLMM: $F_{1,10.32}$=17.18, p=0.002; Figure 6.9A) corresponding to a positive correlation between maternal TNFα and *Acan* mRNA expression in the PD35 PFC (r=0.751, p<0.001). In the PD100 PFC there was a significant main effect of group (GLMM: $F_{1,22}$=5.20, p=0.033; Figure 6.9A) with increased *Acan* mRNA expression in the PD100 PFC of poly(I:C)-offspring relative to vehicle-offspring.

II. *Bcan*

In the PD35 PFC there was a trend to a main effect of maternal TNFα (GLMM: $F_{1,9.56}$=4.37, p=0.064; Figure 6.9B) corresponding to a positive correlation between maternal TNFα and *Bcan* mRNA expression (r=0.521, p=0.027). In the PD100 PFC there were no significant effects of any predictors on *Bcan* expression.

III. *Ncan*

In the PD35 PFC there was a significant main effect of maternal TNFα (GLMM: $F_{1,10.24}$=14.63, p=0.003; Figure 6.9C) corresponding to a positive correlation between maternal TNFα and *Ncan* mRNA expression (r=0.721, p<0.001). In the PD100 PFC there was a trend to a main effect of sex (GLMM: $F_{1,18}$=3.70, p=0.070; Figure 6.9C) with increased *Ncan* mRNA expression in females relative to males.

IV. *Vcan*

In the PD35 PFC there was a significant main effect of maternal TNFα (GLMM: $F_{1,9.65}$=10.96, p=0.008; Figure 6.9D) corresponding to a positive correlation between maternal TNFα and *Vcan* mRNA expression (r=0.694, p=0.001). In the PD100 PFC there was a significant main effect of

group (GLMM: $F_{1,10.37}$=8.49, p=0.015; Figure 6.9D) with increased *Vcan* mRNA expression in poly(I:C)-offspring relative to vehicle-offspring.

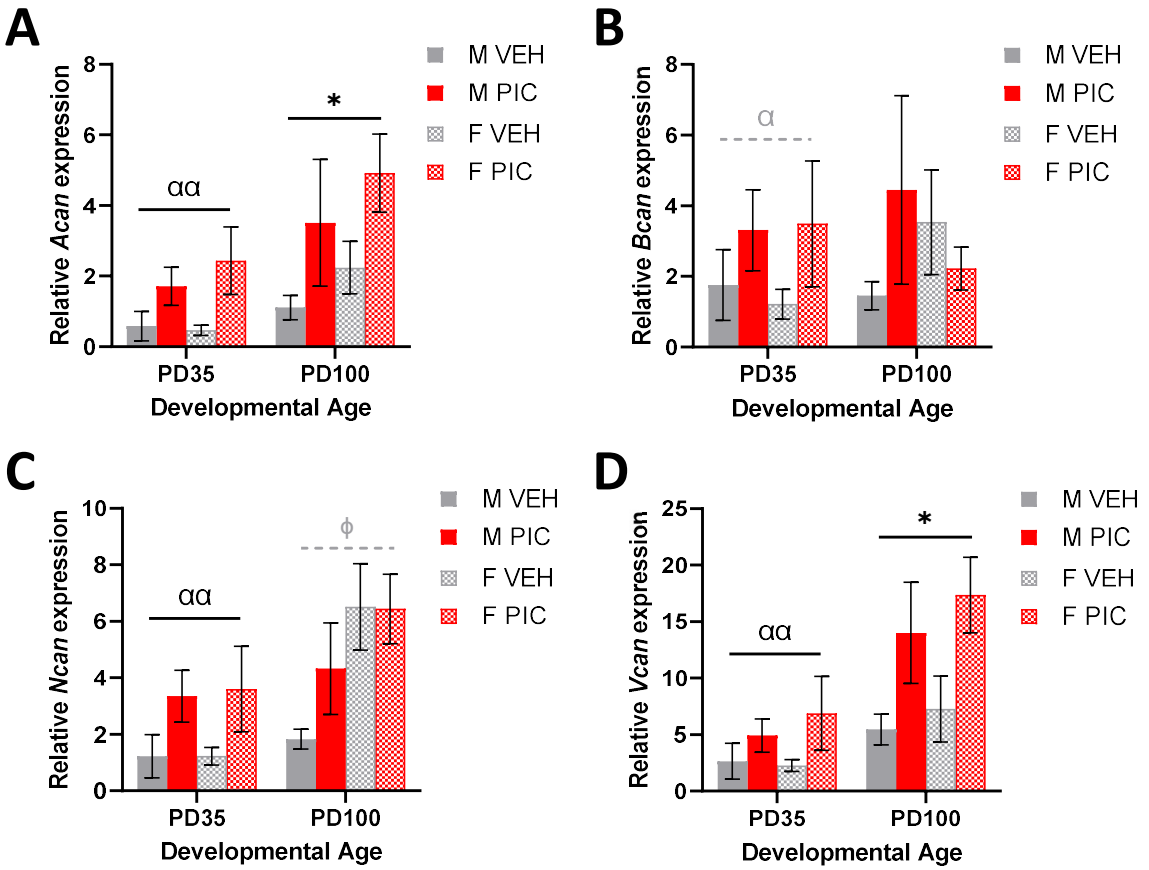

Figure 6.9. mRNA expression of PNN components
Relative mRNA expression (normalised to the geometric mean of 3 reference genes). **A.** *Acan*. **B.** *Bcan*. **C.** *Ncan*. **D.** *Vcan*. Bars represent mean ±SEM (N=5-7, n=5-7). Black significance bars represent significant GLMM results. Black symbols show significant main effects of: group, *p<0.05; maternal TNFα, αα$p<0.01. Grey dashed bars and symbols represent trending (0.05<p<0.08) GLMM results: sex, ϕ; maternal TNFα, α. Abbreviations: PD, postnatal day; M, male; F, female; PIC, poly(I:C); VEH, vehicle.

6.3.1.2. PNN and PV+ cell density changes

For PNN density, in the PD35 PFC, there was a significant main effect of group (GLMM: $F_{1,9.91}$=5.99, p=0.035; Figure 6.10A) with a significant increase in PNN density in poly(I:C)-offspring relative to vehicle-offspring. Likewise, in the PD100 PFC there was also a significant main effect of group, with increased PNN density in poly(I:C)-offspring relative to vehicle-offspring (GLMM: $F_{1,15}$=7.22, p=0.017; Figure 6.10A) alongside main effects of both maternal IL-6 (GLMM: $F_{1,15}$=8.28, p=0.012) and maternal TNFα (GLMM: $F_{1,15}$=10.73, p=0.005). Post-hoc correlation analysis showed these latter effects corresponded to positive correlations between maternal cytokine concentrations and increased PNN density (IL6: rho=0.408, p=0.080; TNFα: rho=0.643, p=0.003), indicating a positive relationship between MIA and PNN formation. However, there were no significant effects of any predictors on PFC PV+ cell density at either PD35 or PD100 (Figure 6.10B). Representative PNN (WFA+) and PV+ stains can be found in Figure 6.10C&D.

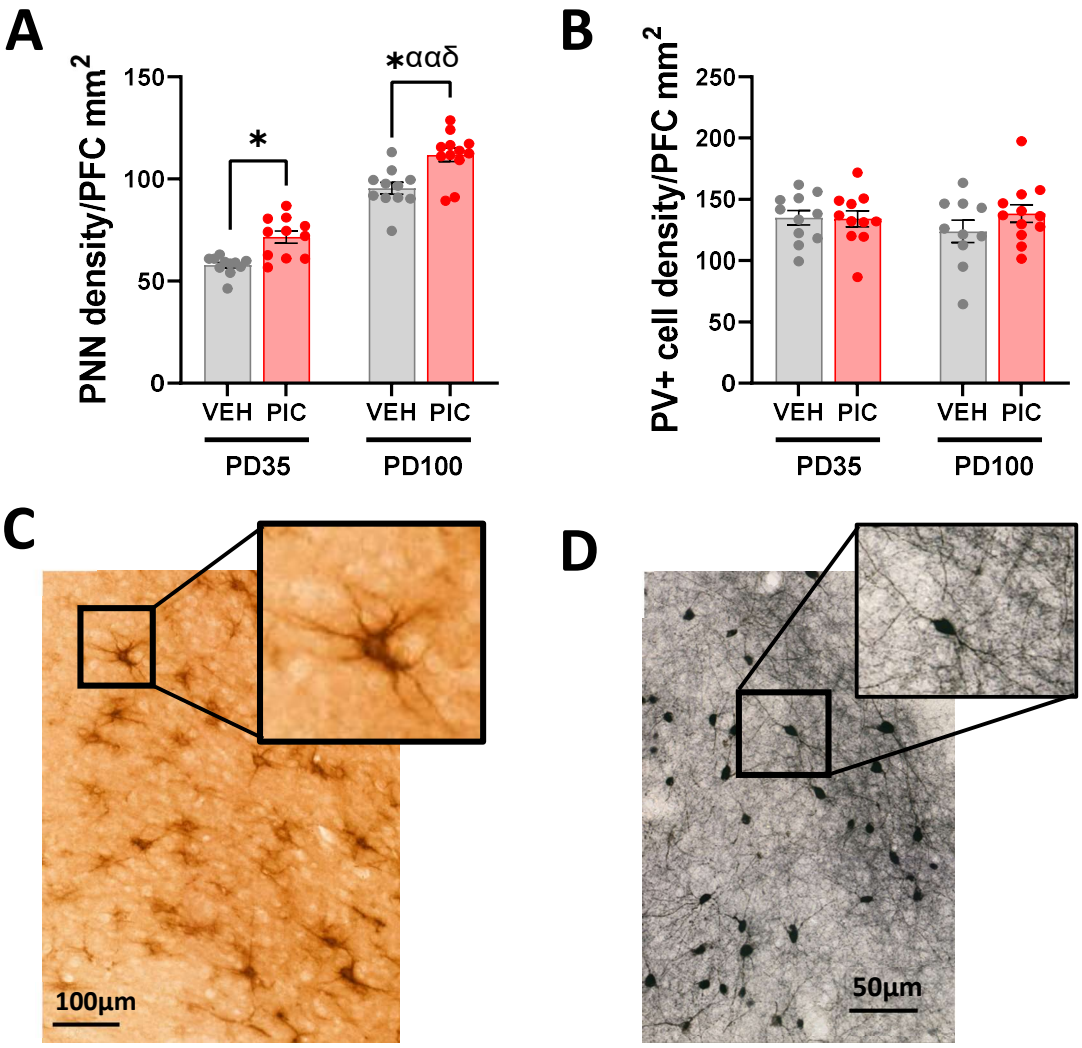

Figure 6.10. PNN and PV+ cell density changes
A. WFA+ PNN density. **B.** PV+ interneuron density. Bars represent mean ±SEM (N=5-6, n=5-6). Dots represent individual animals. Π-shaped black bars show GLMM results within a developmental age; Symbols show significant main effects of: group, *p<0.05; maternal IL-6, δp<0.05, maternal TNFα, ααp<0.01. Abbreviations: PIC, poly(I:C); VEH, vehicle; PD, postnatal day. **C.** Representative WFA+ stain indicated, 10X magnification, inset shows magnified WFA+ PNN. **D.** Representative PV+ stain indicated, 20X magnification, inset shows magnified PV+ cell.

6.3.1.3. PV protein expression changes

While there were no changes in PV+ cell density, the pronounced increase in PNN density could indicate PVI dysfunction. Sufficient PV protein expression is critical for effective PVI function. It was accordingly hypothesised that while PVI density was unchanged in MIA-offspring, identified PV+ cells could contain altered PV protein expression, which could result in dysregulated GABAergic output. Hence total PV protein expression was evaluated. PVIs appear in the cortex from ~PD8 (Hu et al., 2017; Llorca and Deogracias, 2022), therefore, while IHC samples were only available at PD35-100, PV protein expression was measured in the PD21-100 PFC.

There were no significant effects of any predictors on PV protein expression at PD21 or PD35, but there was a significant main effect of group at PD100 (GLMM: $F_{1,12.59}$=5.76, p=0.033), with reduced PV expression in poly(I:C)-offspring relative to vehicle-offspring (Figure 6.11).

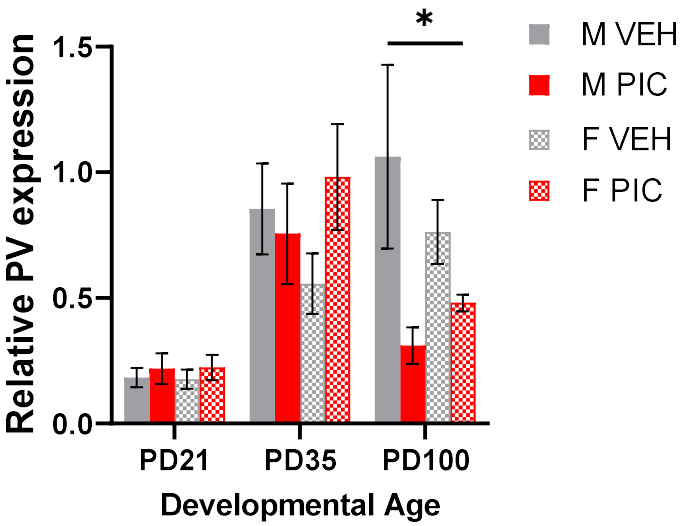

Figure 6.11. PV protein expression
Relative PV protein expression (normalised to total protein). Bars represent mean ±SEM (N=5-7, n=5-7). Black significance bars represent significant GLMM results within a developmental age. Black symbols show significant main effects of: group, *p<0.05. Abbreviations: PD, postnatal day; M, male; F, Female; VEH, vehicle; PIC, poly(I:C).

6.3.2. Dysregulation of cell adhesion molecules in the developing cortex

6.3.2.1. DNAm changes

I. *Ank3*

ANK3 (Ankyrin G) is an adhesion molecule located at the nodes of Ranvier, involved in intracellular-extracellular matrix contacts. The RRBS analysis identified a significant increase in methylation in intron 1 of the *Ank3* gene (Table 6.5; Appendix 9). This region, containing two CpG sites, was therefore analysed by pyrosequencing across the developmental timeline (GD21-PD100).

GD21 FC

For average CpG methylation there was a significant main effect of sex (GLMM: $F_{1,6.07}$=8.47, p=0.027), with reduced *Ank3* intron 1 methylation in females relative to males (Figure 6.12A). This main effect of sex was also found when the CpG sites were considered individually: CpG1 (GLMM: $F_{1,5.73}$=6.54, p=0.045; Figure 6.12B) and CpG2 (GLMM: $F_{1,6.33}$=8.66, p=0.024; Figure 6.12C).

PD1 FC

There were no significant effects of any predictors on average CpG methylation or CpG2 methylation, but there was a trend to a main effect of group for CpG1 methylation (GLMM: $F_{1,15.49}$=3.56, p=0.078; Figure 6.12B), with reduced methylation at CpG1 in poly(I:C)-offspring relative to vehicle-offspring.

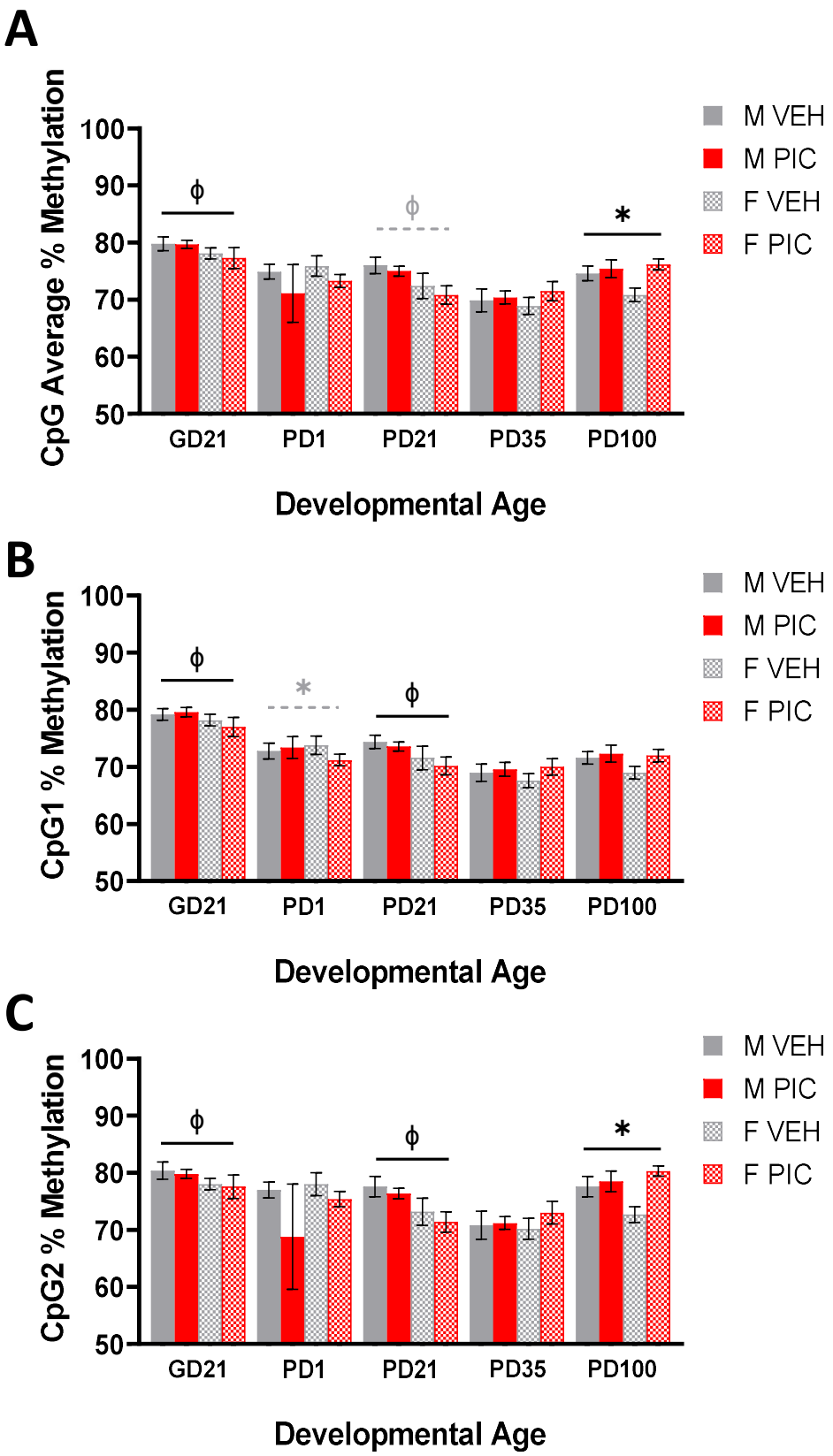

Figure 6.12. *Ank3* intron 1 methylation
A. Average % methylation. **B.** CpG1 % methylation. **C.** CpG2 % methylation. Bars represent mean ±SEM (N=5-6, n=5-6). Black significance bars represent significant results of the GLMM. Black symbols show significant main effects of: group, *p<0.05; sex, ϕp<0.05. Grey dashed bars and symbols represent trending (0.05<p<0.08) results of the GLMM. Abbreviations: GD, gestational day; PD, postnatal day; M, male; F, female; VEH, vehicle; PIC, poly(I:C).

PD21 PFC

For average CpG methylation there was a trend to a main effect of sex (GLMM: $F_{1,15}$=3.56, p=0.079), with reduced *Ank3* intron 1 methylation in females relative to males (Figure 6.12A). This main effect of sex was significant for CpG1 (GLMM: $F_{1,18}$=4.78, p=0.042; Figure 6.12B) and CpG2 (GLMM: $F_{1,18}$=7.42, p=0.014; Figure 6.12C) when analysed individually.

PD35 PFC

There were no significant effects of any predictors on average CpG methylation or methylation of the individual CpG sites (Figure 6.12).

PD100 PFC

For average CpG methylation there was a significant main effect of group (GLMM: $F_{1,17}$=7.72, p=0.013), with increased *Ank3* intron 1 methylation in poly(I:C)-offspring relative to vehicle-offspring (Figure 6.12A). This main effect of group was also significant for CpG2 (GLMM: $F_{1,21}$=7.61, p=0.012; Figure 6.12C), but there were no significant effects of any predictors on CpG1 methylation (Figure 6.12B).

II. *Nrxn2*

Nrxn2 (Neurexin 2) is an adhesion molecule involved in regulation of synapse formation and stability during normal neurodevelopment (Born et al., 2015; Harkin et al., 2017; Lin et al., 2023). The RRBS analysis identified a significant reduction in methylation in exon 1 of the *Nrxn2* gene (Table 6.5; Appendix 9). This region, containing five CpG sites was therefore analysed by pyrosequencing across development (GD21-PD100).

GD21 FC

For average CpG methylation there was a significant main effect of sex (GLMM: $F_{1,15}$=6.96, p=0.019), with reduced *Nrxn2* exon 1 methylation in females relative to males (Figure 6.13A). This main effect of sex was also found when the CpG sites were considered individually (Table 6.10). Of note for CpG1 and CpG5 there were also significant group*sex interactions. Post-hoc analysis revealed a main effect of group in females only at both CpG1 and CpG5 (Table 6.10), with reduced methylation at CpG1 and CpG5 in poly(I:C)-females relative to vehicle-females (Figure 6.13B&F).

Table 6.10. *Nrxn2* exon 1 methylation GD21 statistics

CpG site	Minimal GLMM	Post-hoc females	Post-hoc males
CpG1	Sex: $F_{1,8.99}$=40.39, p<0.001 Group*sex: $F_{2,8.79}$=3.70, p=0.068	Group: $F_{1,6.0}$=16.58, p=0.005 Decrease in poly(I:C)-females relative to vehicle-females	NSP
CpG2	Sex: $F_{1,15}$=3.76, p=0.072	NSP	NSP
CpG3	Sex: $F_{1,18}$=5.56, p=0.030	NSP	NSP
CpG4	Sex: $F_{1,18}$=6.97, p=0.017	NSP	NSP
CpG5	Sex: $F_{1,13}$=4.57, p=0.052 Group*sex: $F_{2,13}$=4.79, p=0.028	Group: $F_{1,8}$=9.85, p=0.014 Decrease in poly(I:C)-females relative to vehicle-females	NSP

Abbreviations: NSP, no significant effects of any predictors

PD1 FC

There were no significant effects of any predictors on average CpG methylation or methylation of any of the individual CpG sites (Figure 6.13).

PD21 PFC

There were no significant effects of any predictors on average CpG methylation or methylation of CpG1, CpG3 or CpG5. However, for CpG2 there was a main effect of sex (GLMM: $F_{1,20}$=4.56, p=0.045), with reduced CpG2 methylation in females relative to males (Figure 6.13C). Likewise, there was a trend to a main effect of sex for CpG4 (GLMM: $F_{1,20}$=3.71, p=0.069; Figure 6.13E) again with females having reduced CpG4 methylation relative to males.

PD35 PFC

For average CpG methylation there was a trend to a main effect of maternal IL-6 (GLMM: $F_{1,18}$=3.50, p=0.078; Figure 6.13A), corresponding to a trending negative correlation between maternal IL-6 and *Nrxn2* exon 1 methylation (r=-0.403, p=0.078). This appears primarily driven by CpG4 where there was also a trend to a main effect of maternal IL-6 (GLMM: $F_{1,18}$=3.71, p=0.070; Figure 6.13E) corresponding to a trending negative correlation between maternal IL-6 and CpG4 methylation (r=-0.414, p=0.070). For CpG1 there was a main effect of sex, (GLMM: $F_{1,18}$=4.75, p=0.043; Figure 6.13B) with reduced CpG1 methylation in females relative to males. There were no significant effects of any predictors on methylation of CpG2, CpG3 or CpG5.

PD100 PFC

For average CpG methylation there was a trend to a main effect of maternal TNFα (GLMM: $F_{1,13.67}$=4.08, p=0.064; Figure 6.13A), corresponding to a trending negative correlation between maternal TNFα and *Nrxn2* exon 1 methylation (r=-0.397 p=0.079). This relationship between maternal cytokine concentrations and *Nrxn2* exon 1 methylation appears driven by CpG2 and CpG3. For CpG2 there was a trend to main effect of maternal IL-6 (GLMM: $F_{1,12.63}$=4.28, p=0.060; Figure 6.13C) corresponding to a negative correlation between maternal IL-6 and CpG2 methylation (r=-0.4.35, p=0.049). For CpG3, there was a main effect of maternal TNFα (GLMM: $F_{1,15.0}$=4.55, p=0.050; Figure 6.13D), corresponding to a negative correlation between maternal TNFα and CpG3 methylation (r=-0.432, p=0.050). There were no significant effects of any predictors on methylation of CpG1, CpG4 or CpG5.

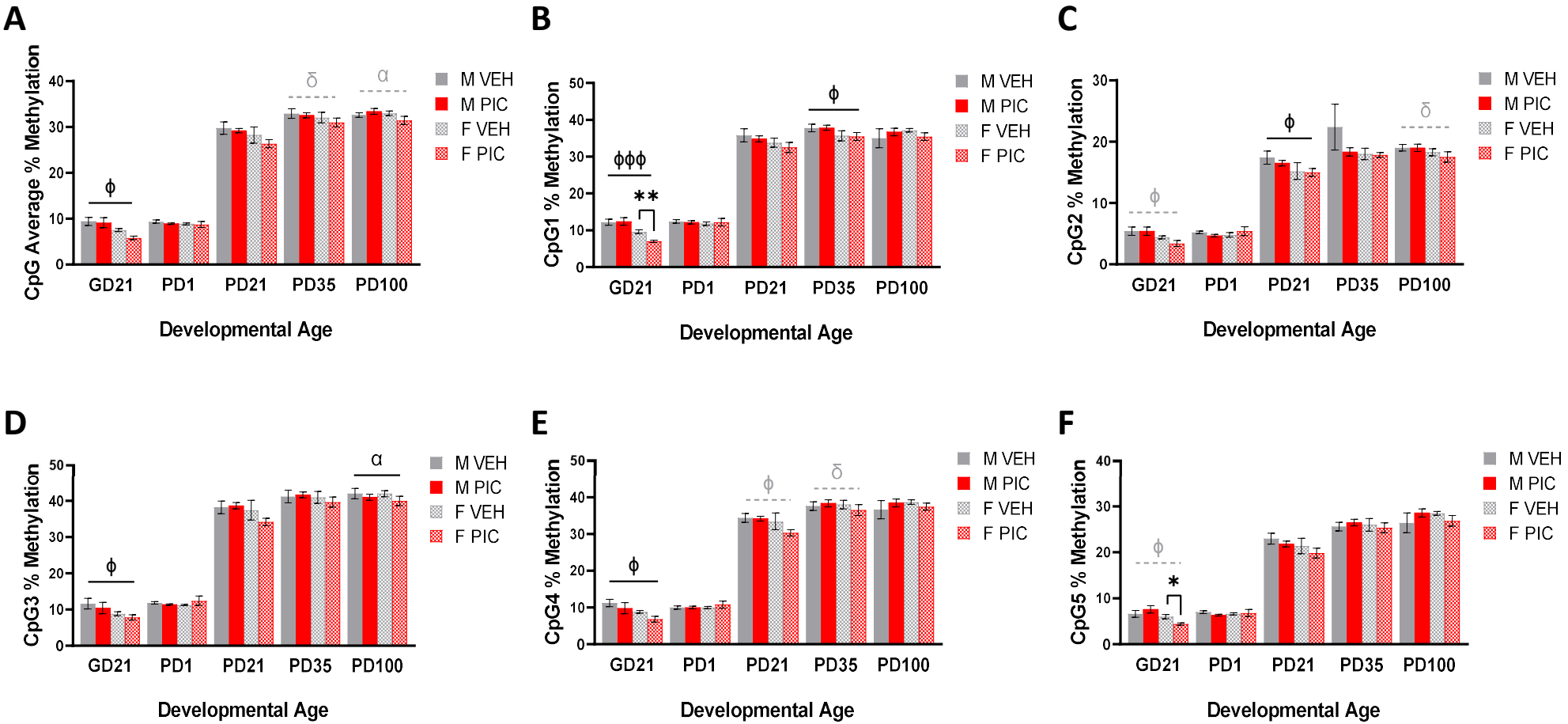

Figure 6.13. *Nrxn2* exon 1 methylation

A. Average % methylation. **B.** CpG1 % methylation. **C.** CpG2 % methylation. **D.** CpG3 % methylation. **E.** CpG4 % methylation. **C.** CpG5 % methylation Bars represent mean ±SEM (N=5-7, n=5-7). Black significance bars represent significant results of the GLMM, — shaped significance bars represent results across a developmental age, Π-shaped bars represent post-hoc GLMM within a single sex. Black symbols show significant main effects of: group, *p<0.05, **p<0.01; sex, ϕp<0.05, ϕϕϕp<0.001; maternal TNFα, αp<0.05. Grey dashed bars and symbols represent trending (0.05<p<0.08) results of the GLMM: sex, ϕ; maternal TNFα, α; maternal IL-6, δ. A Abbreviations: GD, gestational day; PD, postnatal day; M, male; F, female; VEH, vehicle; PIC, poly(I:C).

6.3.2.2. Changes to gene mRNA expression

I. *Ank3*

GD21 FC

There was a trend to a main effect of maternal IL-6 (GLMM: $F_{1,16}$=4.31, p=0.054; Figure 6.14A), corresponding to a positive correlation between maternal plasma IL-6 and *Ank3* mRNA expression (rho=0.573, p=0.013).

PD1 FC

There was a significant main effect of group (GLMM: $F_{1, 12.52}$=4.68, p=0.050) with reduced *Ank3* mRNA expression in poly(I:C)-offspring relative to vehicle-offspring (Figure 6.14A).

PD21 PFC

There were no significant effects of any predictors on *Ank3* mRNA expression (Figure 6.14A).

PD35 PFC

There was a trend to a main effect of group (GLMM: $F_{1,12.9}$=4.15, p=0.063) with reduced *Ank3* mRNA expression in poly(I:C)-offspring relative to vehicle-offspring (Figure 6.14A).

PD100 PFC

There was a trend to a main effect of group (GLMM: $F_{1,13.47}$=3.86, p=0.070) with reduced *Ank3* expression in poly(I:C)-offspring relative to vehicle-offspring and a main effect of sex (GLMM: $F_{1,14.22}$=14.22, p=0.002) with reduced *Ank3* mRNA expression in females relative to males (Figure 6.14A).

II. *Nrxn2*

In contrast to *Ank3*, there were far fewer changes in mRNA expression observed for *Nrxn2*, with no significant effects of any predictors on *Nrxn2* expression in the GD21 FC, PD21 PFC or PD35 PFC.

PD1 FC

There was a trend to a main effect of group (GLMM: $F_{1,19.17}$=3.90, p=0.063), with reduced *Nrxn2* mRNA expression in poly(I:C)-offspring relative to vehicle-offspring (Figure 6.14B).

PD100 PFC

There was a main effect of sex (GLMM: $F_{1,23}$=6.52, p=0.018) with reduced *Nrxn2* mRNA expression in females relative to males (Figure 6.14B).

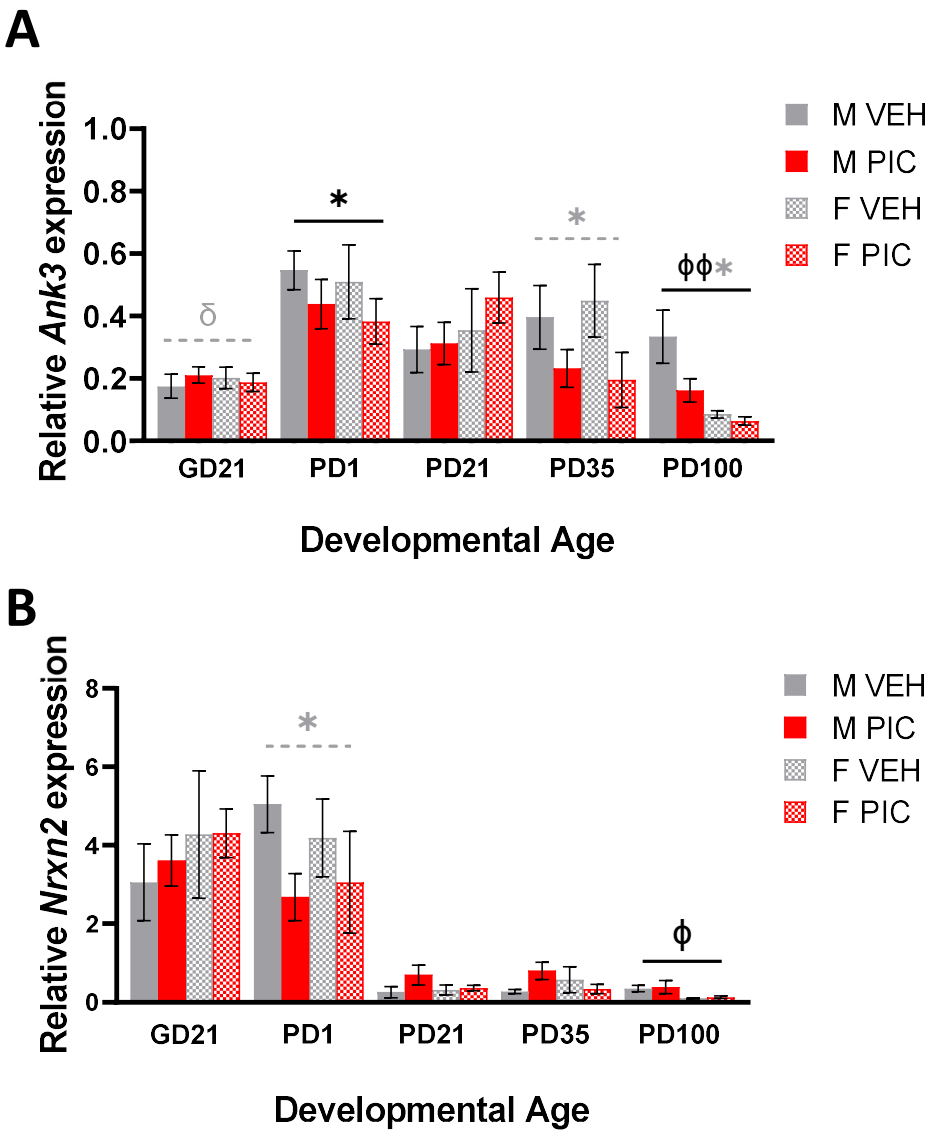

Figure 6.14. mRNA expression of cell adhesion molecules
Relative mRNA expression (normalised to the geometric mean of three reference genes as described in methods). **A.** *Ank3* (N=5-8, n=5-8). **B.** *Nrxn2* (N=5-8, n=5-9). Bars represent mean ±SEM. Black significance bars represent significant GLMM results across a developmental age. Black symbols show significant main effects of: group, *p≤0.05; sex, ϕp<0.05, ϕϕp<0.01. Grey dashed bars and/or symbols represent trending (0.05<p<0.08) GLMM results: group, *; maternal IL-6, δ. Abbreviations: GD, gestational day; PD, postnatal day; M, male; F, female; VEH, vehicle; PIC, poly(I:C).

6.3.3. Alterations to the Reelin signalling pathway in the developing cortex

Several Reelin signalling genes were enriched in the final 54 genes from the RRBS (Chapter 4, Figure 4.22A; Appendix 9). Reelin signalling has been shown to be dysregulated in several neurodevelopmental disorders, including schizophrenia (Guidotti et al., 2016; Kho et al., 2022; Nabil Fikri et al., 2017; Pries et al., 2017). Further, Reelin signalling is critical for a range of prenatal and postnatal neurodevelopmental processes (Lee and D'Arcangelo, 2016). Three genes involved in the Reelin signalling pathway will be analysed here: *Dab1*, *Camk2b* and *Reln* itself (the latter for gene expression only).

6.3.3.1. DNAm changes

I. *Dab1*

DAB1 (Disabled 1) is an adapter molecule which becomes phosphorylated following Reelin-receptor coupling, to activate the downstream outcomes of the Reelin signalling pathway (Trotter et al., 2013). The RRBS analysis identified a significant decrease in methylation of the *Dab1* promoter (Table 6.5; Appendix 9). This region, containing three CpG sites was therefore analysed by pyrosequencing across the developmental timeline (GD21-PD100).

GD21 FC

There were no significant effects of any predictors on average CpG methylation or methylation of CpG1 or CpG3 (Figure 6.15). However, for CpG2 there was a trend to a group*sex interaction (GLMM: $F_{3,8.35}$=3.41, p=0.071). Post-hoc analysis by sex showed a trend to a main effect of group in females (GLMM: $F_{1,8.0}$=4.81, p=0.060), with reduced CpG2 methylation in poly(I:C)-females relative to vehicle-females (Figure 6.15C).

PD1 FC

For average CpG methylation, there was a main effect of maternal TNFα (GLMM: $F_{1,10.15}$=7.93, p=0.018; Figure 6.15A), corresponding to a negative correlation between maternal TNFα and average *Dab1* promoter methylation (r=-0.586, p=0.011). This main effect of maternal TNFα was also observed when each CpG was analysed individually (Table 6.11; Figure 6.15B-D).

Table 6.11. *Dab1* promoter methylation PD1 statistics

CpG site	Minimal GLMM	Post-hoc correlation
CpG1	Maternal TNFα: $F_{1,11.21}$=4.79, p=0.050	r=-0.516, p=0.028
CpG2	Maternal TNFα: $F_{1,10.03}$=5.77, p=0.037	r=-0.536, p=0.022
CpG3	Maternal TNFα: $F_{1,10.85}$=7.50, p=0.020	r=-0.586, p=0.011

PD21 PFC

There were no significant effects of any predictors on average CpG methylation or methylation of CpG1. However, for CpG2 and CpG3 there was a trend to a main effect of maternal TNFα (CpG2: GLMM: $F_{1,11.36}$=3.83, p=0.075; CpG3: GLMM: $F_{1,9.70}$=3.93, p=0.077; Figure 6.15C&D), corresponding to negative correlations between maternal TNFα and both CpG2 methylation (r=-0.425, p=0.062) and CpG3 methylation (r=-0.468, p=0.037).

PD35 PFC

There were no significant effects of any predictors on average CpG methylation or methylation of CpG1. However, for CpG2 and CpG3 there was a trend to a main effect of group (CpG2: GLMM: $F_{1,10.26}$=4.09, p=0.070; CpG3: GLMM: $F_{1,24}$=3.43, p=0.076; Figure 6.15C&D), with reduced CpG2 and CpG3 methylation in poly(I:C)-offspring relative to vehicle-offspring.

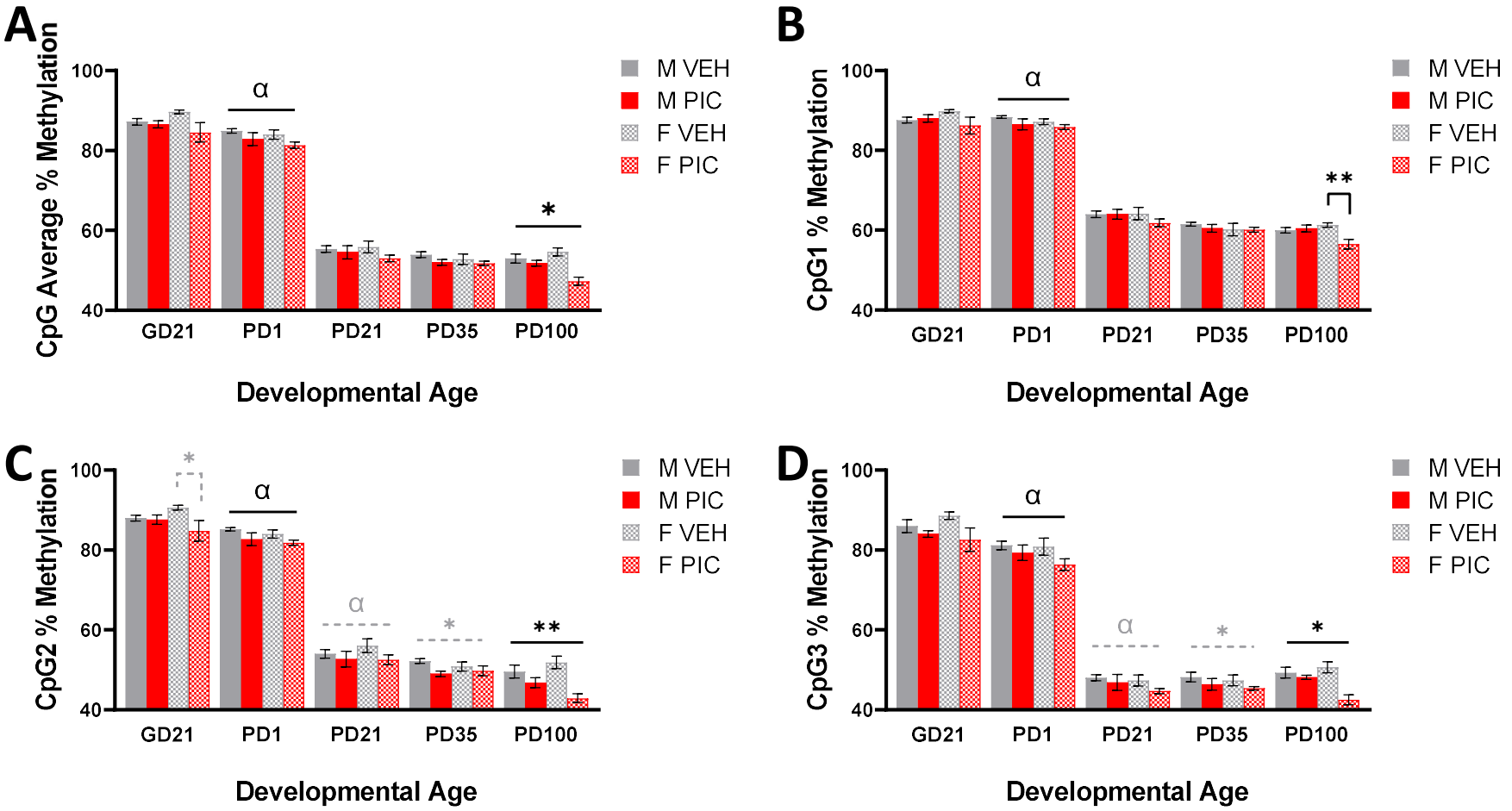

Figure 6.15. *Dab1* promoter methylation
A. Average % methylation. **B.** CpG1 % methylation. **C.** CpG2 % methylation. **D.** CpG3 % methylation. Bars represent mean ±SEM (N=5-8, n=5-9). Black significance bars represent significant results of the GLMM, — shaped significance bars represent results across a developmental age, Π-shaped bars represent post-hoc GLMM within a single sex. Black symbols show significant main effects of: group, *p<0.05; **p≤0.01; maternal TNFα, αp≤0.05. Grey dashed bars and symbols represent trending (0.05<p<0.08) GLMM results. Abbreviations: GD, gestational day; PD, postnatal day; M, male; F, female; VEH, vehicle; PIC, poly(I:C)

PD100 PFC

For average CpG methylation, there was a main effect of group (GLMM: $F_{1,13.46}$=7.87, p=0.014; Figure 6.15A), corresponding to reduced methylation in poly(I:C)-offspring relative to vehicle-offspring. This main effect of group was also observed for CpG2 (GLMM: $F_{1,15.01}$=8.57, p=0.010; Figure 6.15C) and CpG3 (GLMM: $F_{1,13.33}$=7.76, p=0.015; Figure 6.15D) when analysed individually. For CpG1 there was a group*sex interaction (GLMM: $F_{3,15.47}$=6.12, p=0.006). Post-hoc analysis showed a main effect of group in the females (GLMM: $F_{1,12}$=10.53, p=0.007; Figure 6.15B), with reduced CpG1 methylation in poly(I:C)-females relative to vehicle-females.

II. *Camk2b*

CAMKIIβ (Calmodulin kinase IIβ) is a protein kinase which becomes phosphorylated downstream of NMDA receptor signalling. In postnatal development this occurs downstream of the Reelin signalling pathway (Figure 6.2B). The RRBS analysis identified a significant decrease in methylation in the CGI of the *Camk2b* gene (Table 6.5; Appendix 9). This region, containing five CpG sites was therefore analysed by pyrosequencing across the developmental timeline (GD21-PD100).

GD21 FC

For average CpG methylation there was a main effect of sex (GLMM: $F_{1,8.24}$=6.17, p=0.037) with increased methylation in females relative to males (Figure 6.16A), alongside a main effect of maternal IL-6 (GLMM: $F_{1,7.61}$=11.43, p=0.010; Figure 6.16A), corresponding to a positive correlation between maternal IL-6 and average CpG methylation (r=0.669, p=0.003). However, there were differences in the effects of predictors on individual CpG methylation (Table 6.12; Figure 6.16B-F), though the general effect was an increase in methylation in poly(I:C)-foetuses relative to vehicle-foetuses.

Table 6.12. *Camk2b* CGI methylation GD21 statistics

CpG site	Minimal GLMM
CpG1	Sex: $F_{1,14}$=8.37, p=0.012; Increase methylation in females relative to males Group: $F_{1,14}$=6.29, p=0.025; Increase methylation in poly(I:C)-foetuses relative to vehicle
CpG2	Maternal IL-6: $F_{1,15}$=10.61, p=0.005; Corresponding to a positive correlation between maternal IL-6 and CpG2 methylation (r=0.644, p=0.005)
CpG3	Sex: $F_{1,14}$=14.99, p=0.002; Increase methylation in females relative to males Group: $F_{1,14}$=17.14, p=0.01; Increase methylation in poly(I:C)-foetuses relative to vehicle
CpG4	Maternal IL-6: $F_{1,7.95}$=8.43, p=0.020; Corresponding to a positive correlation between maternal IL-6 and CpG2 methylation (r=0.637, p=0.006)
CpG5	NSP

Abbreviations: NSP, no significant effects of any predictors

PD1 FC

There were no significant effects of any predictors on average CpG methylation or methylation of CpG1, CpG2, CpG3 or CpG4 (Figure 6.16). For CpG5 there was a trend to a group*sex interaction (GLMM: $F_{4,11}$=3.10, p=0.071). Post-hoc analysis showed a main effect of group in

the females (GLMM: $F_{1,8.0}$=9.13, p=0.017) with increased CpG5 methylation in poly(I:C)-females relative to vehicle-females (Figure 6.16F).

PD21 PFC

There were no significant effects of any predictors on average CpG methylation or methylation of any individual CpG sites (Figure 6.16).

PD35 PFC

There were no significant effects of any predictors on average CpG methylation, or methylation of CpG1, CpG2, CpG3 or CpG4 (Figure 6.16). For CpG5 there was a trend to a main effect of group (GLMM: $F_{1,17}$=3.77, p=0.069), with increased CpG5 methylation in poly(I:C)-offspring relative to vehicle-offspring (Figure 6.16F).

PD100 PFC

For average CpG methylation there was a group*sex interaction (GLMM: $F_{3,15.22}$=5.52, p=0.009). Post-hoc analysis showed a main effect of group in both males (GLMM: $F_{1,8.17}$=7.76, p=0.023; with increased methylation in poly(I:C)-males relative to vehicle-males; Figure 6.16A) and females (GLMM: $F_{1,8.0}$=6.76, p=0.032; with decreased methylation in poly(I:C)-females relative to vehicle-females; Figure 6.16A). This pattern was observed when each of the CpG sites were analysed individually (Table 6.13; Figure 6.16B-F).

Table 6.13. *Camk2b* CGI methylation PD100 statistics

CpG site	Minimal GLMM	Post-hoc females	Post-hoc males
CpG1	Group*sex: $F_{3,17}$=3.70, p=0.033	Group: $F_{1,8.0}$=7.02, p=0.029 Decrease in poly(I:C)-females relative to vehicle	Group: $F_{1,7.64}$=5.27, p=0.050 Increase in poly(I:C)-males relative to vehicle
CpG2	Group*sex: $F_{3,15.43}$=3.27, p=0.050	Group: $F_{1,8.0}$=3.89, p=0.080 Decrease in poly(I:C)-females relative to vehicle	Group: $F_{1,8.04}$=5.87, p=0.042 Increase in poly(I:C)-males relative to vehicle
CpG3	Group*sex: $F_{3,13.99}$=6.35, p=0.006	Group: $F_{1,8.0}$=4.47, p=0.067 Decrease in poly(I:C)-females relative to vehicle	Group: $F_{1,8.01}$=7.38, p=0.026 Increase in poly(I:C)-males relative to vehicle
CpG4	Group*sex: $F_{3,15.31}$=7.02, p=0.003	Group: $F_{1,8.0}$=6.83, p=0.031 Decrease in poly(I:C)-females relative to vehicle	Group: $F_{1,8.29}$=10.50, p=0.011 Increase in poly(I:C)-males relative to vehicle
CpG5	Group*sex: $F_{3,13.94}$=6.06, p=0.007	Group: $F_{1,8.0}$=8.00, p=0.022 Decrease in poly(I:C)-females relative to vehicle	Group: $F_{1,7.01}$=7.16, p=0.032 Increase in poly(I:C)-males relative to vehicle

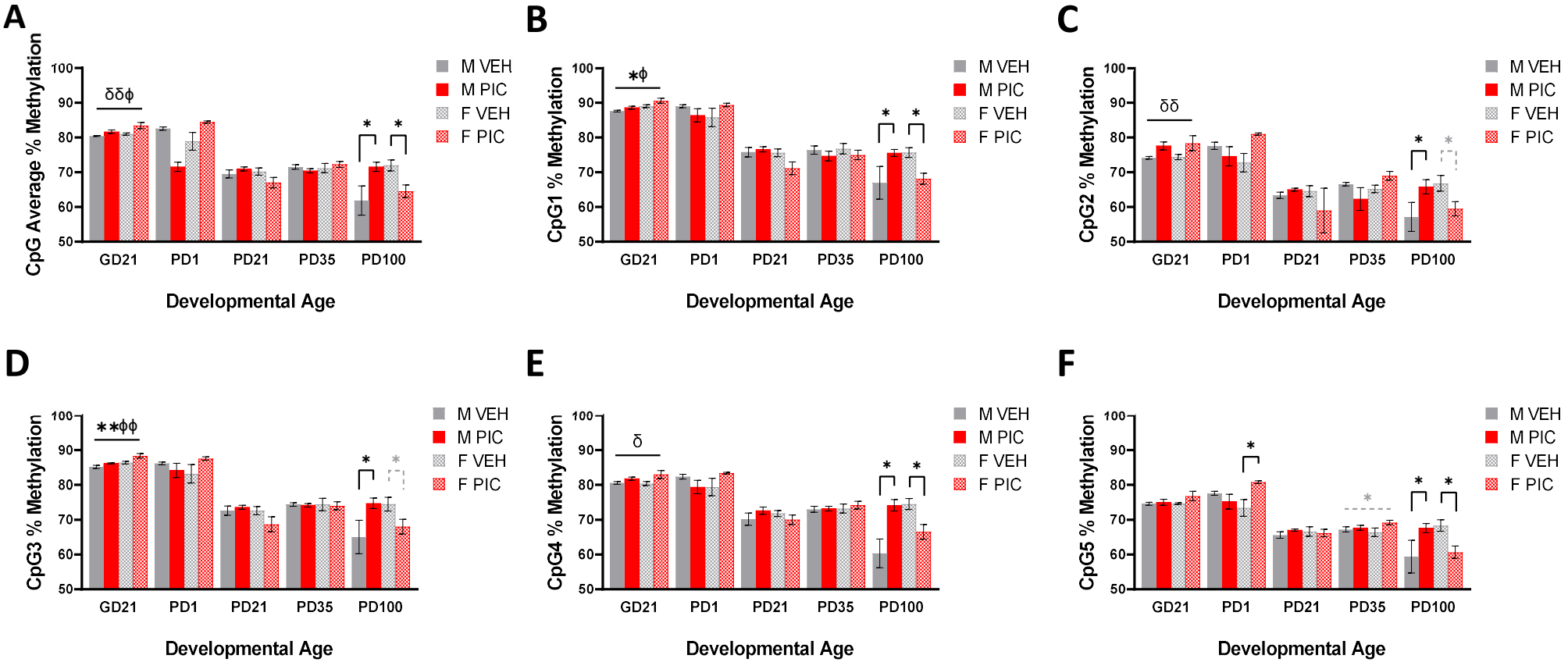

Figure 6.16. *Camk2b* CGI methylation
A. Average % methylation. **B.** CpG1 % methylation. **C.** CpG2 % methylation. **D.** CpG3 % methylation. **E.** CpG4 % methylation. **F.** CpG5 % methylation. Bars represent mean ±SEM (N=5-7, n=5-7). Black significance bars represent significant results of the GLMM, — shaped significance bars represent results across the whole timepoint, Π-shaped bars represent post-hoc GLMM within a single sex. Black symbols show significant main effects of: group, *p≤0.05; **p<0.01; maternal IL-6,δ p<0.05, δδp≤0.01; sex, ϕp<0.05, ϕϕp<0.01. Grey dashed bars and symbols represent trending (0.05<p≤0.08) results of the GLMM. Abbreviations: GD, gestational day; PD, postnatal day; M, male; F, female; VEH, vehicle; PIC, poly(I:C).

6.3.3.2. mRNA and protein expression changes

I. *Reln*

While *Reln* did not withstand the selection criteria for pyrosequencing, it was analysed for mRNA expression owing to its connection with both *Dab1* and *Camk2b*. However, there were limited changes in *Reln* expression with no significant effects of any predictors on *Reln* expression in the PD1 FC, PD21 or PD35 PFC.

GD21 FC

There was a trend to a main effect of sex (GLMM: $F_{1,14}$=4.04, p=0.064; Figure 6.17A), with increased *Reln* mRNA expression in females relative to males, alongside a group*sex interaction (GLMM: $F_{2,14}$=4.30, p=0.035). Post-hoc analysis showed a trend to a main effect of group in the females (GLMM: $F_{1,7.0}$=4.53, p=0.071) with reduced *Reln* expression in poly(I:C)-females relative to vehicle-females (Figure 6.17A).

PD100 PFC

There was a main effect of sex (GLMM: $F_{1,14.04}$=8.68, p=0.011; Figure 6.17A), with increased *Reln* mRNA expression in males relative to females, alongside a main effect of group (GLMM: $F_{1,15.83}$=4.95, p=0.043; Figure 6.17A), with reduced *Reln* mRNA expression in poly(I:C)-offspring relative to vehicle-offspring.

II. *Dab1*/DAB1

Both *Dab1* mRNA and DAB1 protein expression was measured across cortex development. There was a positive correlation between the two during early developmental ages (GD21-PD21; rho=0.689, p<0.001). However, in during later developmental ages (PD35-100) there was a negative correlation between the two (rho=-0.301, p=0.021). The latter could be attributable to changes in DAB1 protein degradation (Lee and D'Arcangelo, 2016).

GD21 FC

For mRNA, there was a main effect of group (GLMM: $F_{1,16}$=4.83, p=0.043), with increased *Dab1* mRNA expression in poly(I:C)-foetuses relative to vehicle (Figure 6.17B).

There were no significant effects of any predictors on DAB1 protein expression (Figure 6.17C).

PD1 FC

There was a main effect of group (GLMM: $F_{1,13.52}$=7.26, p=0.018), with reduced *Dab1* mRNA expression in poly(I:C)-offspring relative to vehicle-offspring (Figure 6.17B).

For DAB1 protein expression, there was a main effect of group (GLMM: GLMM: $F_{1,20.81}$=12.09, p=0.002; Figure 6.17C), with reduced DAB1 protein expression in poly(I:C)-offspring relative to vehicle-offspring.

PD21 PFC

For mRNA, there was a main effect of group (GLMM: $F_{1,25}$=4.55, p=0.043), with increased *Dab1* mRNA expression in poly(I:C)-offspring relative to vehicle-offspring (Figure 6.17B).

For DAB1 protein expression, there was a main effect of maternal TNFα (GLMM: $F_{1,22}$=4.79, p=0.040; Figure 6.17C), corresponding to a positive correlation between maternal TNFα and DAB1 protein expression (rho=0.423, p=0.040), alongside a trend to a main effect of maternal IL-6 (GLMM: $F_{1,22}$=3.40, p=0.079; Figure 6.17C) though the latter did not correspond to a significant post-hoc correlation.

PD35 PFC

There were no significant effects of any predictors on *Dab1* mRNA or DAB1 protein expression (Figure 6.17B&C).

PD100 PFC

For mRNA, there was a main effect of sex (GLMM: $F_{1,28}$=9.77, p=0.004), with increased *Dab1* mRNA expression in males relative to females (Figure 6.17B) and a group*sex interaction (GLMM: $F_{2,28}$=4.80, p=0.016). Post-hoc analysis showed a main effect of group in the females (GLMM: $F_{1,13.62}$=6.67, p=0.022) with increased *Dab1* mRNA expression in poly(I:C)-females relative to vehicle-females (Figure 6.17B).

For DAB1 protein expression, there was a main effect of maternal IL-6 (GLMM: $F_{1,23}$=5.53, p=0.028; Figure 6.17C), corresponding to a positive correlation between maternal IL-6 and DAB1 protein expression (rho=0.440, p=0.028), alongside a trend to a main effect of maternal TNFα (GLMM: $F_{1,23}$=3.24, p=0.080; Figure 6.17C) though the latter did not correspond to a significant post-hoc correlation.

III. *Camk2b*

There were no significant effects of any predictors on *Camk2b* expression in the GD21 or PD1 FC or PD35 PFC.

PD21 PFC

There was a main effect of group (GLMM: $F_{1,24}$=6.89, p=0.015; Figure 6.17D), with increased *Camk2b* mRNA expression in the poly(I:C)-offspring relative to vehicle-offspring.

PD100 PFC

There was a trend to a group*sex interaction (GLMM: $F_{3,26}$=2.78, p=0.064). Post-hoc analysis showed that, in the females, there was a significant main effect of both maternal IL-6 (GLMM: $F_{1,11.39}$=5.74, p=0.035; Figure 6.17D) and maternal TNFα (GLMM: $F_{1,11.38}$=20.14, p<0.001; Figure 6.17D), corresponding to positive correlations between maternal cytokines and *Camk2b* mRNA expression (maternal IL-6: rho=0.760, p=0.001; maternal TNFα: rho=0.760, p=0.001). By comparison, in the males, there was a trend to a main effect of group (GLMM: $F_{1,11.0}$=4.26, p=0.063; Figure 6.17D) with reduced *Camk2b* mRNA expression in poly(I:C)-males relative to vehicle-males.

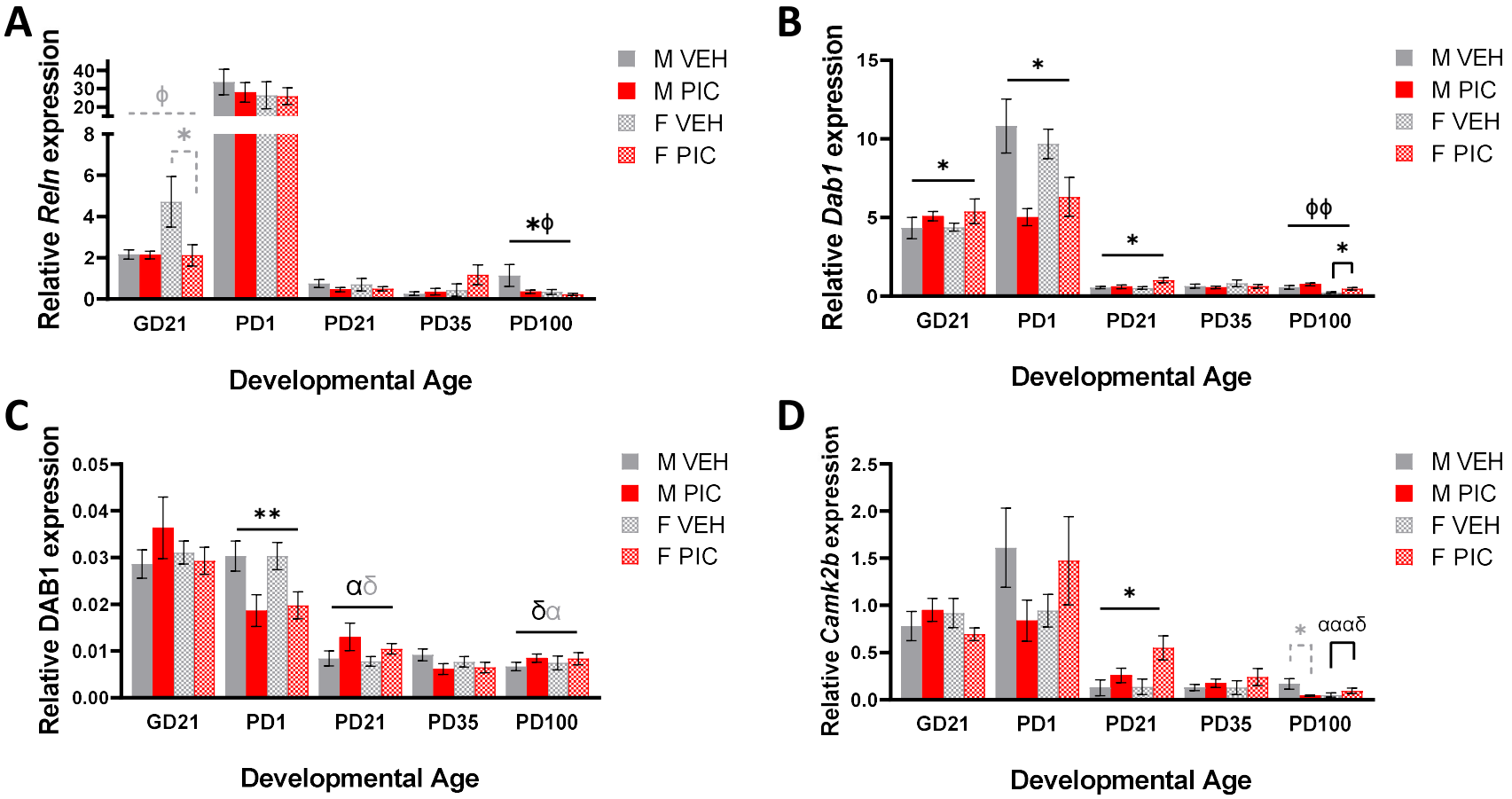

Figure 6.17. Altered expression of Reelin signalling genes

Relative mRNA expression was normalised to the geometric mean of three reference genes; Relative protein expression was normalised to the GAPDH reference protein; both described in methods. **A.** *Reln* mRNA expression (N=5-8, n=5-8). **B.** *Dab1* mRNA expression (N=5-8, n=5-9). **C.** DAB1 protein expression (N=6-8, n=6-9). **D.** *Camk2b* mRNA expression (N=5-8, n=5-9). Bars represent mean ±SEM. Black significance bars represent significant results of the GLMM, — shaped significance bars represent results across a developmental age, Π shaped bars represent post-hoc GLMM within a single sex. Black symbols show significant main effects of: group, *p<0.05, **p<0.01; sex, ϕϕp<0.01; maternal IL-6, δp<0.05; maternal TNFα, αp<0.05, αααp<0.001. Grey dashed bars and symbols represent trending (0.05<p<0.08) results of the GLMM. Abbreviations: GD, gestational day; PD, postnatal day; M, male; F, female; VEH, vehicle; PIC, poly(I:C).

6.3.4. Expression of synaptic proteins in the developing cortex

Given the evidenced MIA-induced dysregulation of the neural ECM, it would be expected that this would result in altered synaptic receptor clustering, due to altered receptor diffusion and positioning in response to ECM density. Likewise, Reelin signalling, also shown to be dysregulated, is known to modulate synaptic receptors, via post-synaptic density protein 95 (PSD95), a critical mediator of postsynaptic receptor clustering and function. Hence, changes in glutamatergic receptor and PSD95 protein expression was measured. Note, as ECM structures, such as myelin and PNNs, only form postnatally and the Reelin pathway only mediates this pathway in later development, only PD21-100 PFC samples were analysed here.

I. PSD95

There were no significant effects of any predictors on PSD95 expression at PD21. However, at PD35 there was a trend to a main effect of group (GLMM: $F_{1,11.85}$=4.31, p=0.060; Figure 6.18) with reduced PSD95 protein expression in poly(I:C)-offspring relative to vehicle-offspring. Likewise, at PD100 there was a main effect of group (GLMM: $F_{1,26}$=28.65, p<0.001; Figure 6.18), with reduced PSD95 protein expression in poly(I:C)-offspring relative to vehicle-offspring

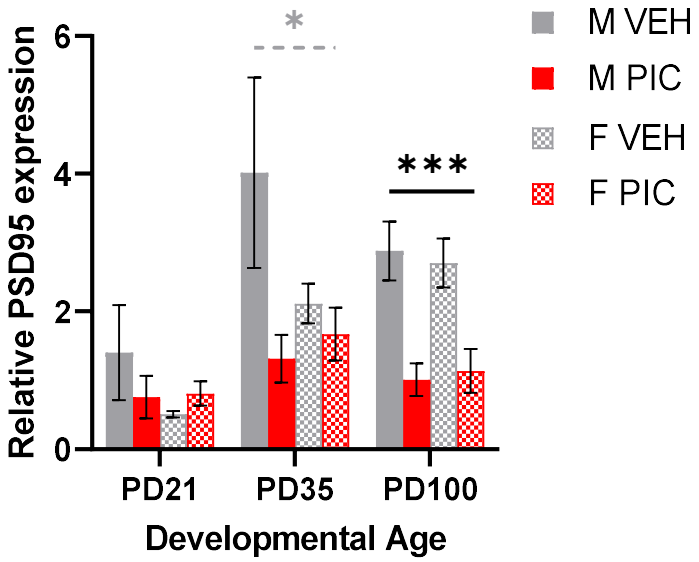

Figure 6.18. PSD95 protein expression
Relative protein expression (normalised to total protein). Bars represent mean ±SEM (N=5-8, n=5-8). Black significance bars represent significant GLMM results across a developmental age. Black symbols show significant main effects of: group, ***p<0.001. Grey dashed bars and symbols represent trending (0.05<p<0.08) GLMM results. Abbreviations: PD, postnatal day; M, male; F, female; VEH, vehicle; PIC, poly(I:C).

II. AMPA receptor 1: GLuA1

The GLuA1 receptor was selected for being a key modulator of NMDA receptor ratios and is affected by ECM density. It also associates with the astrocytic protein GPC4 to modulate glutamatergic synapse formation (Allen et al., 2012), of which there were significant changes in expression observed in Chapter 5 (Figure 5.14).

In the PD21 PFC there was a main effect of both group (GLMM: $F_{1,11.0}$=5.64, p=0.037; Figure 6.19), with reduced GLuA1 in poly(I:C)-offspring relative to vehicle-offspring and sex (GLMM: $F_{1,2.04}$=30.66, p=0.030; Figure 6.19), with reduced GLuA1 protein expression in males relative to females. Likewise, in the PD35 PFC there remained a trend to a main effect of group (GLMM: $F_{1,22}$=4.05, p=0.057; Figure 6.19), with reduced GLuA1 protein expression in poly(I:C)-offspring relative to vehicle-offspring. There were no significant effects of any predictors in the PD100 PFC.

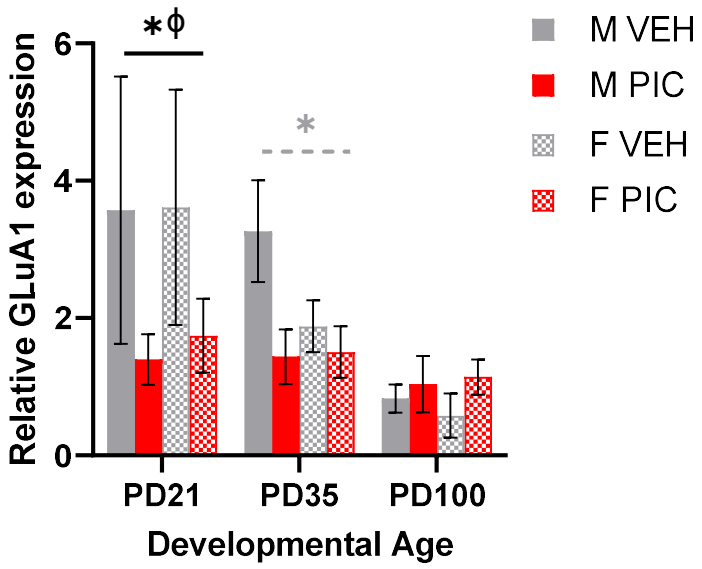

Figure 6.19. GLuA1 protein expression
Relative protein expression (normalised to total protein). Bars represent mean ±SEM (N=5-7, n=5-7). Black significance bars represent significant GLMM results across a developmental age. Black symbols show significant main effects of: group, *p<0.05; sex, ϕp<0.05. Grey dashed bars and symbols represent trending (0.05<p<0.08) GLMM results. Abbreviations: PD, postnatal day; M, male; F, female; VEH, vehicle; PIC, poly(I:C).

III. NMDA receptors: NR2A and NR2B

The NMDA receptors NR2A and NR2B have been frequently associated with LTP and cognition. They are also influenced by: ECM and myelin, which perturbs their positioning, AMPA receptor signalling and PSD95/CAMKII, which are influenced by GPC4 (Chapter 5) and Reelin signalling, respectively.

NR2A

There were no significant effects of any predictors on NR2A expression at PD21 or PD35. At PD100 there was a trend to a main effect of sex (GLMM: $F_{1,15}$=3.93, p=0.066; Figure 6.20A), with reduced NR2A protein expression in females relative to males. Post-hoc analysis showed a main effect of group in the females (GLMM: $F_{1,10.0}$=5.78, p=0.037; Figure 6.20A), with reduced NR2A protein expression in poly(I:C)-females relative to vehicle-females.

NR2B

At PD21 there was a significant main effect of sex (GLMM: $F_{1,5.20}$=10.86, p=0.020; Figure 6.20B), with reduced NR2B protein expression in females relative to males. At PD35 there was

a significant main effect of group (GLMM: $F_{1,14.27}$=5.53, p=0.034; Figure 6.20B) with reduced NR2B protein expression in poly(I:C)-offspring relative to vehicle-offspring. By contrast, at PD100 there was also a trend to a main effect of group (GLMM: $F_{1,9.45}$=3.99, p=0.075; Figure 6.20B) with increased NR2B protein expression in poly(I:C)-offspring relative to vehicle-offspring.

NR2A:2B ratio

There were no significant effects of any predictions on the NR2A:2B ratio at PD21 or PD35. At PD100 there was a trend to a main effect of sex (GLMM: $F_{1,14}$=6.13, p=0.027; Figure 6.20C), with reduced NR2A:2B ratios in females relative to males, alongside a main effect of group (GLMM: $F_{1,14}$=15.82, p=0.01; Figure 6.20C), with a reduced NR2A:2B ratio in poly(I:C)-offspring relative to vehicle-offspring.

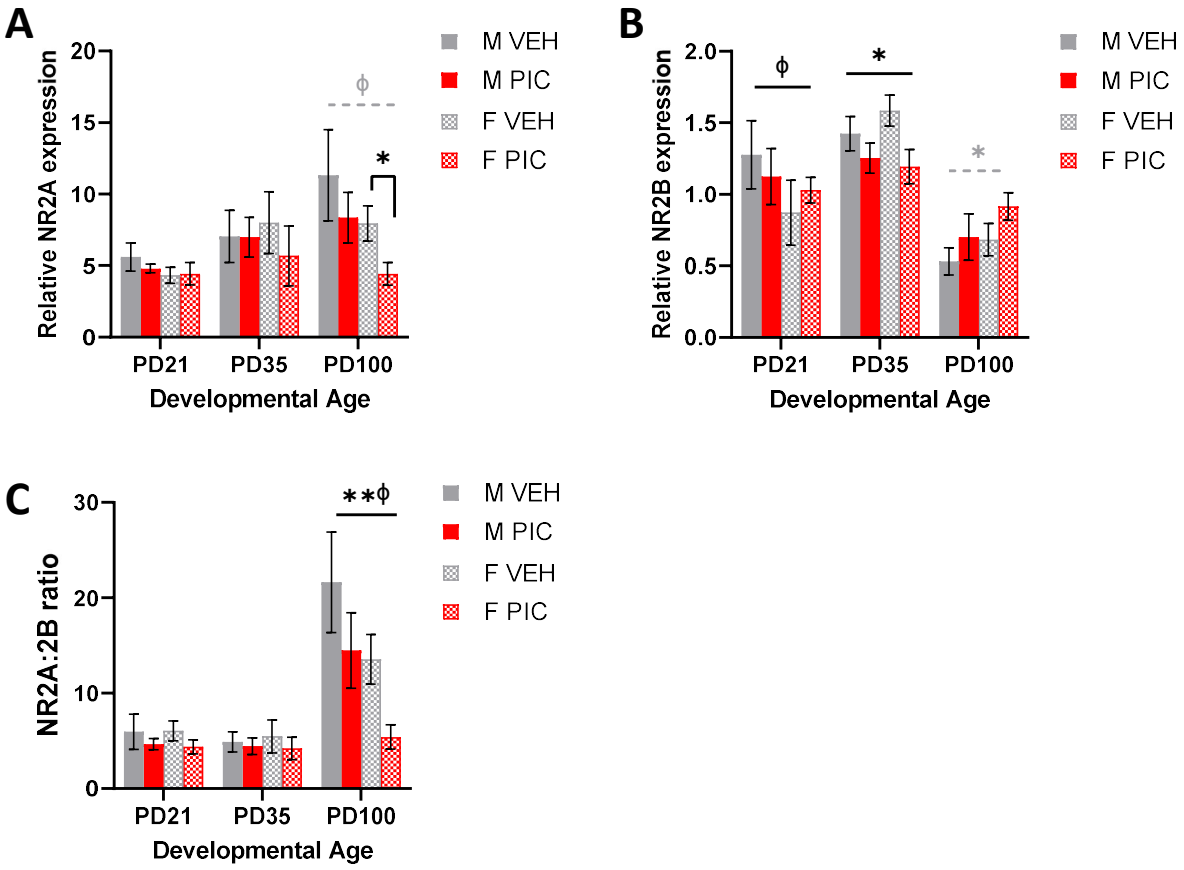

Figure 6.20. NMDA receptor protein expression
Relative protein expression (normalised to total protein). **A.** NR2A. **B.** NR2B. **C.** NR2A:2B ratio. Bars represent mean ±SEM (N=5-7, n=5-7). Black significance bars represent significant GLMM results. — shaped significance bars represent results across a developmental age, Π-shaped bars represent post-hoc GLMM within a single sex. Black symbols show significant main effects of: group, *p<0.05, **p≤0.01; sex, ϕp<0.05. Grey dashed bars and symbols represent trending (0.05<p<0.08) GLMM results. Abbreviations: PD, postnatal day; M, male; F, female; VEH, vehicle; PIC, poly(I:C).

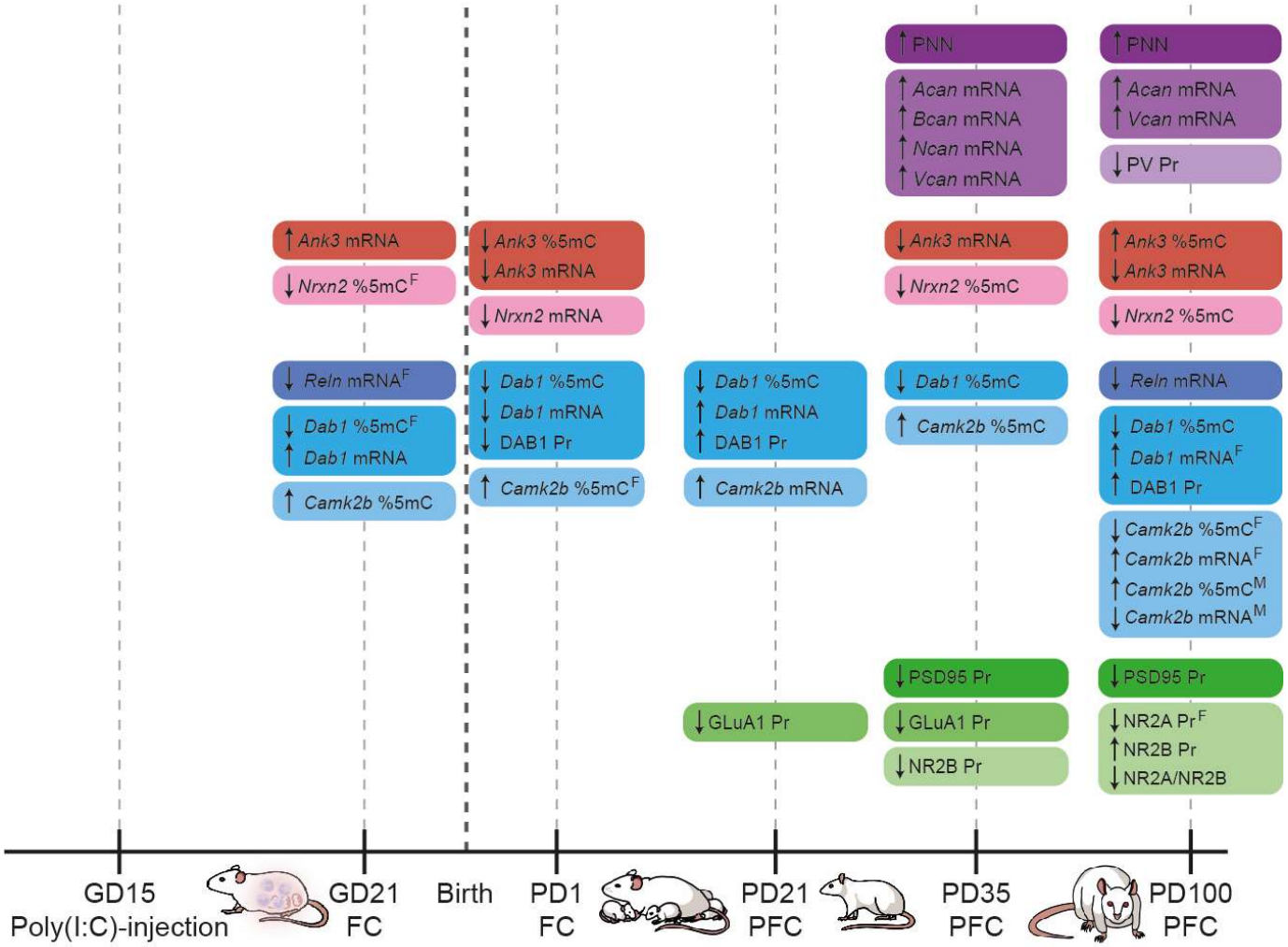

Figure 6.21. Summary of significant findings from Chapter 6

Summary of the MIA-induced molecular changes in the developing cortex. Timeline (bottom) indicates the developmental age and tissue analysed: frontal cortex (FC) or prefrontal cortex (PFC). Purple: PNN/PVI changes; Red/pink: adhesion molecule changes; Blue: Reelin signalling changes; Green: synaptic protein changes. Abbreviations: ↓Decrease; ↑Increase; F, female-specific result; M, male-specific result; Pr, protein; %5mC, methylation

6.4. DISCUSSION

A key hypothesis of this Chapter was that MIA-induced changes to glia and myelin development (Chapter 5) would be synonymous with altered neural ECM formation and in turn, or concomitantly, alter synapse formation and plasticity. The aims of this chapter were therefore to evaluate changes to PNN component expression and density to provide supportive evidence for altered neural ECMs and to measure the developmental DNAm profiles and concordant changes in mRNA/protein expression of the four remaining RRBS-identified candidate genes, involved in ECM adhesion and Reelin signalling. Finally, this chapter critically aimed to explore possible functional outcomes of MIA-induced changes to the neural ECM formation and Reelin signalling, through analysis of the expression of key synaptic proteins involved in LTP which could underscore the observed adult cognitive deficit (Chapter 2). The results reported support the hypothesis of this Chapter through evidenced increases in CSPG expression and PNN density from PD35, consistent with the results observed for oligodendrocyte development and myelin formation in Chapter 5. Further, this study has demonstrated reduced Reelin signalling and expression of essential synaptic proteins throughout the critical period and into adulthood. These findings would be expected to result in reduced LTP and hence have consequences for normal cognitive development. A summary of the results from this Chapter can be seen in Figure 6.21 and will be discussed in-depth below.

6.4.1. MIA induced PNN malformation, with indication of PVI signalling deficits

Data from Chapter 5 postulated disturbed extracellular structures in the brain. To evaluate this further, the neural ECM was assessed here through PNN staining with WFA. There was a marked increase in PNN density at both PD35 and PD100, with no change in PVI density (Figure 6.10). The latter is perhaps not unsurprising, given previous studies in MIA models which have suggested a greater impact on density of somatostatin (SST)+ interneurons than PVIs (Vasistha et al., 2019; Woods et al., 2021). Of note, as the staining technique used individually applied markers for PVIs and PNNs (PV+ and WFA+, respectively) and did not perform co-stain analysis, it was not possible to determine if the increased PNN density is due to an increase in the number of PVIs coated in PNNs, or whether the PNNs have assembled on neurons other than PVIs. That said, PNNs are nearly exclusively located on PVIs in the PFC (Fawcett et al., 2019), which allows a degree of confidence in the interpretation of the data. Accordingly, the increased PNN density as early as PD35, suggests accelerated maturation of the PNNs and PVIs. Similar accelerated maturation (i.e., evidence of late-stage/mature biological markers in earlier development) was identified for the oligodendrocyte lineage and expression of myelin constituents in Chapter 5. These findings are supported by recent work in a mouse model of MIA which demonstrated advanced maturation of GABAergic interneuron and macroglia populations in the foetal brain following MIA, evidenced through early expression of late-stage

lineage markers (Canales et al., 2021). Taken together, the findings in this study would postulate early closure of the critical period in the PFC following MIA and hence reduced synaptic plasticity (Lam et al., 2019; Wilson et al., 2020). Determination of CSPG expression showed increases in *Acan, Bcan, Ncan* and *Vcan* at PD35, indicating the observed increase in PNN density could be derived from MIA-induced upregulation of ECM components. However, only *Acan* and *Vcan* remained elevated at PD100. Notably, *Vcan* is expressed almost exclusively from oligodendrocytes (Table 6.1) and hence the observed elevation in *Vcan* expression at both PD35 and PD100 would correspond to the observed increases in oligodendrocyte cell density at these developmental stages (Chapter 5, Figure 5.15A). *Ncan*, by contrast, is expressed from the PVIs around which the PNN forms (Table 6.1), indicating a coincident and robust change in the ECM transcriptome of both oligodendrocytes and PVIs as a result of MIA. These changes in CSPG expression could dysregulate the ratio of components within the assembling ECM, which would have functional consequences. Indeed, Brevican has been shown to interact with and regulate GLuA1 function and clustering (Favuzzi et al., 2017), while hyaluronan regulates both AMPA and NMDA receptors (Frischknecht et al., 2009; Schweitzer et al., 2017). Hence, overrepresentation of Versican and Neurocan at the expense of other components at PD100 may cause disturbed function of the PNN in adulthood. Moreover, overexpression of individual PNN components can inhibit remyelination (Colognato and Tzvetanova, 2011; Su et al., 2021). Myelination is a process with plasticity and its composition and thickness is critical for normal signal velocity and conduction along axons. These features of myelin can be influenced by learning and experience during the critical period (Giger et al., 2008). Hence, myelination has been suggested to play a role in ongoing brain plasticity (Bonetto et al., 2021). Inhibition of these processes by excess CSPG expression could lead to ineffective myelin remodelling and could explain the observed reduction in MBP expression in adulthood (PD100) following MIA, postulated to result from inefficient remyelination in Chapter 5.

Five previous studies have investigated PNN changes following MIA and it should be noted the findings of these studies contrast with the data reported here, with the primary findings of MIA-induced reductions or no changes in PNN density (Casquero-Veiga et al., 2023; Mao et al., 2022; Nakamura et al., 2021; Paylor et al., 2016; Wegrzyn et al., 2021). There could be several explanations for this. First, the studies which found decreases were primarily located in the hippocampus (Mao et al., 2022; Wegrzyn et al., 2021) and amygdala (Casquero-Veiga et al., 2023), neither of which were measured here. Hence, there could be regional differences in PNN density disturbances in the brain following MIA. Indeed, in agreement with this, Paylor et al. (2016) and Casquero-Veiga et al. (2023), investigated several brain regions and identified both developmental and regional differences in PNN density changes following MIA. Notably, while Paylor et al. (2016) demonstrated reduced PNN density in the PFC, Casquero-Veiga et al. (2023) found no differences. Second, model heterogeneity may also contribute to differences in results. Paylor et al. (2016) and Casquero-Veiga et al. (2023) share analogous methodology to that used here, inducing MIA on GD15 in rats. However, Paylor et al. (2016) used the high molecular weight form of poly(I:C), while Casquero-Veiga et al. (2023) used sigma-supplied

poly(I:C), both of which are known to induce a more severe and variable sickness response than LMW poly(I:C) from InvivoGen, as used here (Kowash et al., 2019; Mueller et al., 2019) and therefore, could produce more phenotypically disparate molecular responses in MIA-offspring. Indeed, a recent review of rodent models of ELS paradigms revealed both increases and decreases in PNN densities that were dependent on the severity and duration of the environmental stress (Spijker et al., 2020). Taken together, it could hence be postulated that methodological differences may contribute to disparate results on PFC PNN density between this and other studies. Further, Paylor et al. (2016) demonstrate temporal reductions and recoveries in the PNN density during late postnatal development, implying these extracellular structures are developmentally adaptable in response to MIA. Likewise, a recent study within an ELS paradigm demonstrated that PNN and perisynaptic density first decreased in response to stress, followed by a later-life increase (Koskinen et al., 2021). With this in mind, it could be postulated that evaluation of the PNN density at earlier (e.g., PD21) or later (e.g., >PD100) developmental stages could illuminate whether developmental shifts occur in PNN density in response to MIA. This concept is supported by data from Chapter 5, that demonstrated increased myelin protein expression during the critical period followed by a notable reduction in adult offspring. Hence, the same adaptive capacity may exist for the PNNs, but with a slightly lagging developmental timeframe. That said, these avenues of investigation remain to be explored.

While reduced PNNs are often observed in post-mortem schizophrenia studies, it is interesting to note that the converse is true in major depression and chronic pain studies, where increased PNN densities have been identified (Carceller et al., 2022; Mascio et al., 2022). Given that both schizophrenia and major depression present with deficits in PFC cognitive flexibility (Maramis et al., 2021; Murphy et al., 2012; Zhu et al., 2021), it suggests that both reduced and increased PNN density can promote similar cognitive deficits. This is likely due to the role of PNNs in PVI function. PVIs are thought to be critical modulators of cognitive functions underscored by the PFC (Murray et al., 2015). Hence, it was hypothesised that while there were no changes in PVI density, their function may be altered as a result of the observed PNN alterations. To explore this, total PV protein expression was evaluated from PD21-PD100 (after PV expression is detected in the rat PFC; Bitzenhofer et al., 2020). No studies in MIA models to date have measured PV protein expression and all studies using mRNA expression have reported no significant changes (Woods et al., 2021). Here, in contrast, no change in PV protein expression was identified during the critical period (PD21-35), during which the PNN is maturing, however, in adulthood (PD100), there was a significant reduction in PV protein expression (Figure 6.11). PV is a calcium-binding protein important for regulating calcium dynamics following signal input into PVIs (Caballero et al., 2014; Caillard et al., 2000). Typically, PV protein expression increases during cortical maturation (Bitzenhofer et al., 2020; Caballero et al., 2014), as observed in the vehicle animals in this study (Figure 6.11). Conversely, poly(I:C)-offspring showed the expected increased PV expression PD21-PD35, followed by a marked developmental reduction in PV expression between PD35-PD100. Notably, this is the time-

period over which we have observed the appearance of cognitive deficits in MIA-offspring (Chapter 2; Potter et al., 2023). Reduced PV protein expression would be expected to cause signalling irregularities within the PVIs which could predispose individuals to cognitive deficits (Caillard et al., 2000). Indeed, reduced PV expression in the PFC has been shown to reduce PVI inhibitory output, leading to EI imbalances (Caballero et al., 2014, 2020), thought to be a defining feature of PFC-mediated cognitive deficits (Ferguson and Gao, 2018) and frequently identified in schizophrenia (Liu et al., 2021). It could therefore be hypothesised that malformed PNNs, possibly as a result of glial cell dysfunction during the critical period, promotes dysfunctional PVIs by early adulthood, which contribute to the development of cognitive deficits in MIA-offspring. Indeed, the identified changes to myelin (Chapter 5) and the neural ECM would be expected, whether in turn or concomitantly, to alter synapse formation and plasticity throughout the critical period and into adulthood. This hypothesis is further supported by determination of the remaining four RRBS candidate genes (that withstood the acceptance criteria (Appendix 9)), as all four are involved in cell adhesion and ECM-related signalling pathways (Table 6.2), consistent with the postulate that MIA induces ECM changes, of relevance for cognitive deficits.

6.4.2. MIA leads to subtle changes in cell adhesion molecules, *Ank3* and *Nrxn2*

Ank3 is involved in perinodal ECM structure formation, important in normal signal conduction in the developing brain (Chang et al., 2014; Fawcett et al., 2019). The RRBS showed increased methylation at intron 1 of the *Ank3* gene. When evaluated across development, this gene demonstrated developmental switches in the directionality of methylation differences between MIA and vehicle-offspring. This could imply a degree of developmental plasticity in the regulation of this gene which is critically disturbed in MIA-offspring, with MIA-induced reductions in intron 1 methylation from GD21-PD21 and an increase at PD100 (Figure 6.12). *Ank3* mRNA expression, by contrast, was generally reduced in MIA-offspring across postnatal development (Figure 6.14A). Increased *Ank3* gene methylation has been shown to be one of the most robust DNAm changes in prenatal and ELS paradigms across rats, NHP and human studies, associated with reduced *Ank3* mRNA expression (Luoni et al., 2016). However, in this study there were no significant correlations between intron 1 methylation and *Ank3* mRNA expression. This could indicate that the MIA-induced changes in *Ank3* expression are driven by alternative mechanisms, such as histone modifications, perhaps working in combination with observed DNAm changes. ANKG (encoded by *Ank3*), is essential for the formation of the nodes of Ranvier, including *Nfasc* recruitment (Hedstrom et al., 2008). Hence, the reduction in *Ank3* expression observed across development could lead to a destabilisation of the nodes of Ranvier, promoting dysregulated perinodal ECM formation. Indeed, reduced *Ank3* expression, as observed here, has been suggested to cause dysregulated neuronal signalling, EI

imbalances and thereby contribute to the development of neuropathology (Smith et al., 2014; Yoon et al., 2022).

Nrxn2 is a member of the neurexin family of proteins, (NRXN1-3), all of which are expressed in the brain (Harkin et al., 2017). Presynaptic NRXNs modulate synapse formation through trans-synaptic binding to postsynaptic neuroligins (Born et al., 2015). The RRBS showed a decrease in the methylation at exon 1 of the *Nrxn2* gene. When measured across development, this gene showed limited methylation differences between MIA and vehicle-offspring, with a reduced methylation in GD21 poly(I:C)-females and a TNFα-driven reduction in methylation in PD100 offspring (Figure 6.13). However, there were even fewer changes in mRNA expression, with a MIA-induced reduction at PD1 only (Figure 6.14B). That said, there was a significant negative correlation between exon 1 methylation and *Nrxn2* mRNA expression across development (rho=-0.717, $p<0.001$), indicating a relationship between DNAm and expression. This implies that MIA-driven changes in methylation of *Nrxn2* gene are influencing changes in expression, though these alone do not appear to achieve statistical significance. Of note, *Nrxn2* encodes two isoforms: NRXN2α and NRXN2β, with KO studies indicating a greater functional role for NRXN2α in synapse formation (Born et al., 2015). However, given that the method of gene expression analysis used could not discriminate the different isoform transcripts, it is impossible to discern whether these are differentially affected by the changes in methylation. Determination of the separate *Nrxn2* isoforms would be an avenue for future research.

Taken together, these data support subtle MIA-driven changes in cell adhesion molecules within the Ankyrin and Neurexin families. Notably, robust MIA-associated changes to the DNAm of these genes appears primarily in late postnatal development (PD35-PD100), far later than observed for glial genes. Hence, it is unlikely that these changes arise from the immediate effect of foetal neuroinflammation. Instead, it could be postulated that these changes result from ongoing adaptive events and signalling pathways in the developing brain following MIA.

6.4.3. MIA dysregulates the Reelin signalling pathway across development

One of the major functionally-enriched group of genes in the final 54 interconnected RRBS candidate genes (Appendix 9) was those involved in Reelin signalling, which included: *Reln, Dab1, Dab2ip, Grin2a* and *Camk2b*. Of these, two withstood the final selection criteria for pyrosequencing: *Dab1* and *Camk2b*. However, the expression of *Reln* was also determined. Reelin is an extracellular matrix glycoprotein, which binds to its receptors to induce phosphorylation of the cytosolic adaptor protein, *Dab1*/DAB1 (Figure 6.2; Chen et al., 2004; Howell et al., 1999; Trotter et al., 2013). During prenatal and early postnatal development, Reelin signalling regulates neuronal migration (Figure 6.2A; Lee and D'Arcangelo, 2016; Trotter et al., 2013). In later postnatal development, Reelin secretion is restricted to GABAergic interneurons in the cortex and hippocampus, where Reelin signalling becomes associated with LTP (Lee and D'Arcangelo, 2016). Here, Reelin signalling promotes PSD95-mediated functional regulation of

NMDA receptors (Figure 6.2B; Beffert et al., 2005; Chen et al., 2005; Ventruti et al., 2011) and regulates NMDA receptor composition within the synapse to maintain the normal developmental NR2A:NR2B ratios (Campo et al., 2005; Groc et al., 2007; Sinagra et al., 2005). Reelin-mediated NMDA receptor activation leads to CAMKII activation (Figure 6.2B). CAMKII is a holoenzyme formed from various subunits, primarily CAMKIIα (encoded by *Camk2a*) and CAMKIIβ (encoded by *Camk2b*; Nicole and Pacary, 2020). Results in this study showed a MIA-induced reduction in *Reln* mRNA expression in the prenatal FC (supported by findings from Kowash, 2019) and in the adult PFC (Figure 6.17A). Reduced Reelin expression has frequently been identified in the PFC of schizophrenia patients (Guidotti et al., 2000). However, very little work has explored the Reelin pathway in MIA models, although the main agreement was for reduced Reelin expression following MIA (Woods et al., 2021). Of note, a recent study on postnatal viral infection demonstrated reduced Reelin signalling along the DAB1-PSD95-NMDA axis comparable to the results observed here (Vinay et al., 2022). These studies begin to identify a role for abnormal Reelin signalling following MIA (Woods et al., 2023). Critically, reduced *Reln* expression would be expected to alter its downstream pathway components, however these have been less well analysed in MIA models, with only our study to date considering epigenetic changes in this pathway (Woods et al., 2021, 2023). Here, both *Dab1* and *Camk2b* were analysed for changes to gene methylation and expression.

The *Dab1* promoter methylation was generally decreased across postnatal development (Figure 6.15). By comparison, *Dab1* gene/protein expression fluctuated across postnatal development in response to MIA (Figure 6.17B-C), with a reduction in both mRNA and protein expression at PD1, becoming an increase in *Dab1* mRNA expression at PD21 and PD100, with positive correlations between maternal cytokine concentrations and DAB1 protein expression at these developmental stages. Of note, there was a direct correlation between *Dab1* mRNA and protein expression across development as expected ($rho=0.610$, $p<0.001$). The acute reduction in *Dab1*/DAB1 expression at PD1 could have critical functional implications, as this timing involves a key period of neurogenesis and neuronal migration, regulated by Reelin signalling. Indeed, it has been demonstrated that transient early-life (PD1-7) reduction in DAB1 protein results in subtle structural abnormalities within distinct cortical layers and hippocampal regions, consistent with altered neuronal migration, alongside adult behavioural deficits relevant for schizophrenia (Teixeira et al., 2014). By comparison, the postnatal MIA-induced elevations in *Dab1* gene/DAB1 protein expression from PD21-PD100 could be a result of reduced Reelin-receptor signalling in this period. The increased neuronal ECM density in this period could act to restrict Reelin availability, as has been demonstrated in extracellular plaques in Alzheimer's disease (Pujadas et al., 2014), or dysregulate Reelin proteolytic cleavage by extracellular enzymes (e.g., MMPs; Lussier et al., 2016). In *Reeler* mice, which possess LOF mutations in the *Reln* gene, there is increased DAB1 protein expression (Howell et al., 1999). This is due to accumulation of inactive adaptor protein in the absence of active Reelin signalling, as DAB1 activity and degradation are both regulated by Reelin-induced DAB1 phosphorylation (pDAB1; Lee and D'Arcangelo, 2016). Hence, reduced Reelin signalling/availability would be anticipated to result

in increased DAB1 protein, as observed, but reduced pDAB1 (Howell et al., 1999). With this in mind, measurement of pDAB1 expression was attempted. However, despite testing various anti-pDAB1 antibodies (Table 6.8) no immunoreactive band of the correct molecular size could be identified across any of the samples or conditions used (Appendix 13, Supplementary Figure S13.6). This limits the interpretation of whether the postnatal increase in DAB1 protein expression translates to a functional increase or decrease in Reelin signalling. Nonetheless, the ongoing dysregulation of this pathway is evident from the findings presented.

The relationship between *Dab1* mRNA expression and promoter methylation also fluctuated across development (Table 6.14), with an initial unexpected positive correlation between promoter methylation and mRNA expression, followed by the typical negative correlation in later development. As outlined in Chapter 5, bisulphite-pyrosequencing prevents the delineation of DNAm from DNAhm (Booth et al., 2013). This could infer that the quantified promoter methylation at PD1 is actually representative of promoter hydroxymethylation, known to drive increased mRNA transcription (Chen et al., 2014). Taken together, this correlative data therefore suggests a regulatory role for *Dab1* promoter modifications in *Dab1* gene and protein expression. Further, given that the dysregulation of DAB1 appears to arise subsequent to reduced prenatal Reelin signalling (Figure 6.17A; Kowash, 2019), it could be hypothesised that MIA-induced prenatal changes to Reelin expression precipitate persistent dysregulation of DAB1 in the postnatal period, leading to ongoing defective Reelin signalling.

Table 6.14. *Dab1* mRNA expression correlations with *Dab1* promoter methylation

CpG site	CpG1	CpG2	CpG3	CpG Average
GD21	No Correlation	No Correlation	No Correlation	No Correlation
PD1	rho=0.453, p=0.03	rho=0.523, p=0.01	No Correlation	rho=0.605, p=0.004
PD21	rho=-0.564, p=0.005	rho=-0.387, p=0.068	rho=-0.462, p=0.026	rho=-0.449, p=0.036
PD35	No Correlation	No Correlation	rho=-0.364, p=0.008	rho=-0.619, p<0.001
PD100	rho -0.811, p=0.047	No Correlation	No Correlation	rho=-0.402, p=0.038

Despite the inability to measure the DAB1:pDAB1 ratio, *Camk2b*, a further downstream marker of the postnatal Reelin pathway (Figure 6.2B), was investigated. *Camk2b* encodes the β-subunit of the CAMKII holoenzyme which acts downstream of the Reelin signalling pathway during its roles in LTP (Figure 6.2B). The CAMKIIβ-subunit forms the second most prevalent subunit in the brain and is expressed both prenatally and postnatally, unlike the most common CAMKIIα-subunit which is exclusively expressed postnatally (Nicole and Pacary, 2020). As well as functioning downstream of Reelin-mediated NMDA activation, CAMKII can also feedback to modulate NMDA receptor signalling and increase AMPA receptor insertion into the synaptic membrane (Onori and van Woerden, 2021). Here, *Camk2b* CGI methylation was increased in the GD21 FC of poly(I:C)-foetuses, followed by sex-specific changes in the PD100 PFC, with an increase in poly(I:C)-males relative to vehicle-males and a reduction in poly(I:C)-females relative to vehicle-females (Figure 6.16). When *Camk2b* mRNA expression was measured there was also sex-specific effects in adulthood, with reduced *Camk2b* expression in poly(I:C)-males

relative to vehicle-males and an increase in *Camk2b* expression in poly(I:C)-females relative to vehicle-females (Figure 6.17D). CAMKII subunits have been shown to work in an overlapping fashion in genetic KO models (Kool et al., 2019) and this could imply that the differences observed in *Camk2b* expression in response to MIA may be in opposition to those observed for the primary *Camk2a* subunit. Nonetheless, it is noteworthy that the observed sex-specific dysregulation of *Camk2b* in adult MIA-offspring has been implicated previously, with CAMKII shown to have sex-specific roles and responses during LTP (Jain et al., 2019; Rafa-Zabłocka et al., 2019; Yin et al., 2021). Indeed, one of these recent studies showed that different chronic environmental stressors produced sex-specific changes in hippocampal CAMKII expression, consistent with the findings for *Camk2b* here (Yin et al., 2021; Figure 6.17D). This suggests that MIA and other environmental stressors can induce sex-specific adaptive functions of CAMKII. This is supported by consideration of the relationship between *Camk2b* CGI methylation and mRNA expression, which showed no significant correlations, except for PD100, where there was a negative correlation between *Camk2b* mRNA expression and CGI methylation (rho=-0.469, p=0.019). This suggests that not only is the expression of CAMKII altered in a sex-specific pattern in response to MIA, but the transcriptional regulation is also. Further, the occurrence of changes in *Camk2b* gene expression primarily in later postnatal development (PD21-PD100), align with the functional switch of Reelin signalling towards LTP in the postnatal period (Figure 6.2), supporting the hypothesis of ongoing deficits in Reelin signalling (Woods et al., 2023).

Taken together, these data postulate ongoing MIA-induced dysregulation of components of the Reelin signalling pathway, primarily across postnatal development, showing in general, a reduction in Reelin signalling. This finding is analogous to the observation that reduced Reelin signalling has been one of the most robust molecular findings in schizophrenia patients, suggested to contribute to the observed cognitive deficits (Berretta, 2012; Guidotti et al., 2000). This hypothesis has been supported by *in vivo* rodent studies. Mice harbouring heterozygous mutations in the *Reln* gene (heterozygous *Reeler* mice) exhibit multiple cognitive behavioural abnormalities similar to those seen in schizophrenia, including executive function and reversal learning deficits (Brigman et al., 2006; Krueger et al., 2006; Larson et al., 2003). Further, mice with mutations in the signal transduction machinery, including receptors, ApoER2 and VLDLR (Trommsdorff et al., 1999; Weeber et al., 2002) and DAB1 (Howell et al., 2000; Trotter et al., 2013), possess phenotypic deficits comparable to those observed in *Reeler* mice, including deficits in LTP and cognition. Collectively, this suggests that developmental Reelin signalling abnormalities can promote the development of the observed cognitive deficits seen in this model and observed in schizophrenia. That said, it is noteworthy that the changes to the downstream molecule CAMKII, present only in adulthood, at the time of the appearance of cognitive deficits. This could imply that there is a developmental window in this pathway which could be modulated to therapeutic advantage. In support of this, a recent study showed that injection of recombinant Reelin into the adolescent hippocampus of MIA-affected offspring prevented the development of behavioural deficits (Ibi et al., 2020).

6.4.4. MIA-induced neurodevelopmental changes converge in synaptic protein disturbances in adulthood

The results outlined in this Chapter, appear to converge on a molecular phenotype in the PFC which would be anticipated to impact on synaptic development and function throughout the critical period, with a key role for deficits in LTP. To explore this framework, expression of synaptic glutamatergic receptors involved in the process of LTP were measured, including: GLuA1 (AMPA receptor 1), NR2A and NR2B (Chater and Goda, 2014; Choquet and Opazo, 2022; Collingridge and Bliss, 1987; Zhao et al., 2005). PSD95 protein expression was also determined as this protein is downstream of the Reelin signalling pathway (Figure 6.2; Woods et al., 2023) and is also known to regulate the function of NMDA and AMPA receptors (Béïque et al., 2006). All synaptic proteins showed the expected developmental patterns of expression, with postnatal increases (PD21-100) in expression of PSD95 (Han et al., 2010; Zheng et al., 2012) and NR2A (Wenzel et al., 1997), alongside decreases in GLuA1 across the PD21-PD100 timeframe (Arai et al., 1997; Insel et al., 1990) and, less pronounced, decreases in NR2B expression (Wenzel et al., 1997). MIA in turn induced marked changes in expression of all these proteins, in developmentally-specific patterns (Figure 6.18-Figure 6.20).

PSD95 showed a trend to a reduction in poly(I:C)-offspring in the PD35 PFC, becoming a significant reduction in the PD100 PFC (Figure 6.18), the latter of which was found for PSD95 mRNA expression in our recent publication investigating the Reelin pathway (Woods et al., 2023). PSD95 is enriched in the post-synaptic glutamatergic synapses (Coley and Gao, 2018), where it acts as a scaffold protein and directly interacts with NMDA receptors NR2A and NR2B via its PDZ domain (Kornau et al., 1995; Niethammer and Sheng, 1996) and with AMPA receptors (including GLuA1) via the AMPA receptor auxiliary subunit, Stargazin (Bats et al., 2007; Chen et al., 2000). PSD95 can also be activated following Reelin signalling in later postnatal development, through interaction with the Reelin receptor ApoER, to modulate NMDA receptor densities (Beffert et al., 2005; Chen et al., 2005; Ventruti et al., 2011). The observed reduction in PSD95 (PD35-PD100; Figure 6.18) in this study corresponds to findings in schizophrenia patients (Catts et al., 2015; Funk et al., 2017) and previous findings in MIA models (Woods et al., 2021, 2023), with PSD95 KO animals demonstrating PFC-associated cognitive phenotypes comparable to those observed in MIA-offspring (Coley and Gao, 2019). Reduced PSD95 expression from PD35-100 would be consistent with the reduced Reelin signalling observed across the postnatal period (Section 6.4.3), with reduced PSD95 expression identified following both genetic inhibition of the Reelin signalling pathway (Ampuero et al., 2017; Ventruti et al., 2011) and following infection-induced reductions in Reelin signalling (Vinay et al., 2022; Woods et al., 2023). MIA-induced reductions in PSD95 expression, would be expected to have consequences for synapse formation, stability and regulation of receptor subunits and ongoing LTP (Coley and Gao, 2018). Indeed, PSD95 is important in the normal developmental regulation of NMDA receptors within the synapse, with reduced PSD95 shown to increase synaptic NR2B subunits (Béïque et al., 2006; Bustos et al., 2014; Coley and Gao, 2019), which could in turn

lead to excess excitability and neuronal damage (Coley and Gao, 2018; Monaco et al., 2015). Further, PSD95 is known to also regulate AMPA receptors, with PSD95 loss associated with reduced GLuA1 expression and AMPA current (Béïque et al., 2006; Coley and Gao, 2019). Through its roles in glutamatergic synaptic development, PSD95 is also suggested to function in EI balance, with PSD95 overexpression driving increased EI (Levinson et al., 2005) and inhibition the opposite (Prange et al., 2004). Taken together, these studies support the idea that the observed MIA-induced reductions in PSD95 contribute to the development of the cognitive phenotype in adulthood.

Several of the findings in this study, including the changes in ECM density, PV expression, Reelin signalling and PSD95 expression would be expected to disturb synaptic glutamatergic receptor ratios which could have consequences for LTP and cognition. The AMPA receptor, GLuA1, showed reduced expression in poly(I:C)-offspring in both the PD21 and PD35 PFC, encompassing the critical period for the PFC, but with no differences in adulthood (Figure 6.19). This AMPA receptor was selected for its association with LTP (Chater and Goda, 2014; Choquet and Opazo, 2022), but also as it is known to be regulated by the neural ECM (Favuzzi et al., 2017; Frischknecht et al., 2009) and signals in conjunction with astrocytic GPC4 to modulate glutamatergic synapse formation (Allen et al., 2012). Reduced hippocampal GLuA1 mRNA and protein expression have also been identified in schizophrenia patients, though results in the PFC have been less consistent (Iasevoli et al., 2014; Kilonzo et al., 2022). The early reductions in GLuA1 could result from several molecular pathways. First, the reduction in GLuA1 coincides with reduced GPC4 expression in this period (Chapter 5, Figure 5.14). Studies have indicated that astrocytic GPC4 is important in recruitment of GLuA1 to the synaptic membrane (Allen et al., 2012), providing a further link between altered glial function and synaptic dysfunction. Second, GABAergic interneuron dysfunction, as postulated in Section 6.4.1, has been suggested to reduce the AMPA receptor concentration in the postsynaptic membrane (Howard et al., 2014). Third, changes in neural ECM composition, notably loss of Brevican, is also associated with altered AMPA receptor concentration in the synaptic membrane (Favuzzi et al., 2017). Nonetheless, reduced GLuA1, as a result of any of these processes, could indicate a propensity for reduced glutamatergic synapse formation and function and deficient LTP during this critical period, as LTP would be dependent on increased AMPA receptor recruitment to the synaptic membrane (Park, 2018; Selemon, 2013). However, scrutiny of developmental GLuA1 expression (PD21-100) suggests that in MIA-offspring, GLuA1 expression reaches its adult level by PD21, from which it never recovers (Figure 6.19). Hence, this could indicate an early maturation of the glutamatergic synapses, analogous to the early maturation of the PNNs (Section 6.4.1). In any case, taken together, the MIA-induced reduction in membrane GLuA1 from PD21-35 would indicate reduced synaptic plasticity, which could precipitate the development of PFC-associated cognitive deficits (Kilonzo et al., 2022).

By comparison, two NMDA receptors, NR2A and NR2B, were measured as both are known to be associated with LTP (Collingridge and Bliss, 1987; Zhao et al., 2005) and dictate the

functional properties of the heterotetrametric NMDA receptors (Paoletti et al., 2013). Previous studies in MIA models have shown developmental- and tissue-specific changes in NMDA receptor expression patterns (Woods et al., 2021). Similarly, the findings here showed reduced NR2A expression in poly(I:C)-offspring at PD100 (Figure 6.20A) and reduced NR2B expression at PD35 which became a trending increase at PD100 (Figure 6.20B). Hence, these results show a MIA-induced developmental dysregulation of synaptic NMDA receptor expression in the postnatal PFC, which could have several detrimental consequences for NMDA receptor function. Indeed, NR2A and NR2B subunit expression is tightly regulated during normal development, important for normal PFC development and function (Yashiro and Philpot, 2008). The reduction in NR2B in poly(I:C)-offspring may be an acceleration of the normal NR2B reduction and hence an early maturation of the synapses, in line with elevated PNN density in this time-period (Monaco et al., 2015; Yashiro and Philpot, 2008). The reduction in NR2B receptor subunit in adolescence would also be indicative of reduced synaptic plasticity during this period. Indeed, PFC NR2B subunit expression remains higher than in any other brain region owing to its critical function in cognitive development and flexibility (Monaco et al., 2015). Reduced plasticity in adolescence has been suggested to predispose individuals to deficits in working memory in adulthood (Selemon, 2013), providing a plausible link between the observed reductions in molecular markers of plasticity from PD21-35 and the ASST deficit in adult MIA-offspring. Notably, this adolescent NMDA phenotype shifts considerably in the adult PFC, with a trend to increased NR2B expression and reduced NR2A expression (significant in females only). Of note, this pattern of NMDA receptor subunit expression has been demonstrated as a result of infection-induced Reelin downregulation (Vinay et al., 2022). Indeed, the increase in synaptic NR2B from PD35-100 would align with both reduced Reelin signalling and reduced PSD95 expression, observed in this study, with both shown to regulate the normal developmental reduction in NR2B subunit accumulation in the synapse (Coley and Gao, 2019; Groc et al., 2007). This increase in synaptic NR2B may be an attempt to compensate for the reduced GLuA1 and NR2B expression during the critical period to correct the deficits in adolescent synaptic plasticity. However, elevated NR2B has been associated with glutamatergic excitotoxicity and cell death (Cohen et al., 2015; Monaco et al., 2015). On the other hand, NMDA receptor hypofunction (such as could be postulated by the observed reduction in expression of NR2B in adolescence and NR2A in adulthood) has been long thought to be an important predisposing feature of schizophrenia (Cohen et al., 2015; Nakazawa and Sapkota, 2020; Olney and Faber, 1995). Animal models using NMDA receptor antagonists (e.g., PCP/MK-801), have been shown to promote a breadth of behavioural phenotypes relevant to schizophrenia, including cognitive deficits (Cadinu et al., 2018; Javitt and Zukin, 1991; Koek et al., 1988; Neill et al., 2010), with NMDA receptor hypofunction thought to lead to GABAergic disinhibition, attributed to reduced NMDA-activation of PVIs, thereby promoting dysfunctional connectivity in the PFC (Nakazawa and Sapkota, 2020). Indeed, NR2A inhibition has been shown to reduce PV and GAD67 expression (Kinney et al., 2006), reduce PVI function (Wang et al., 2021a) and induce alterations in gamma oscillations (Kocsis, 2012), all indicated in schizophrenia. Of note,

MIA-induced changes in NR2A expression align with the presentation of reduced PV expression in adulthood (Figure 6.11) lending support to this notion. Finally, the normal developmental change in the NR2A:NR2B ratio is considered critical for ongoing cognitive function. When this was calculated, the NR2A:NR2B ratio was found to be increased from PD21 to PD100 (Figure 6.20C), as would be expected (Yashiro and Philpot, 2008). However, the poly(I:C)-offspring demonstrated a reduced NR2A:NR2B ratio in the PD100 PFC (Figure 6.20C). This would imply a developmental dysregulation of the NR2A:NR2B ratio, converging in an immature synaptic phenotype and EI imbalance in adulthood (Monaco et al., 2015). Of note, the appearance of these deficits between adolescence and adulthood, may provide the opportunity for therapeutic intervention. In line with this, a recent genetic study showed rescue of developmental NMDA receptor hypofunction in adulthood could ameliorate cognitive deficits (Mielnik et al., 2021).

6.5. SUMMARY

It was postulated that the observed changes in glial cells (Chapter 5) would promote structural changes to myelin and the neural ECM and, whether in turn, or concomitantly, alter synapse formation and plasticity, leading to cognitive deficits. This hypothesis was supported by the designation of the remaining four candidate genes, *Ank3, Nrxn2, Dab1 and Camk2b*, to pathways involved in cell adhesion and ECM-related signalling. The aims of this Chapter were therefore to explore changes in ECM and synaptic development in MIA-offspring. The results reported have shown accelerated maturation of the neural ECM, evidenced through increased CSPG expression and PNN density by PD35 (Figure 6.10) and consistent with the results observed for oligodendrocyte development and myelin formation observed in Chapter 5. These findings are in agreement with recent studies that have indicated premature aging in the developing brain following MIA (Canales et al., 2021). The premature formation of myelin and the neural ECM would be expected to precipitate reduced synaptic plasticity and early closure to the critical period of PFC development (Larsen and Luna, 2018). In support of this, the results demonstrated reduced Reelin signalling, PSD95, GLuA1 and NR2B expression during this period (PD21-PD35; Figure 6.17-Figure 6.20). These findings would predict reduced LTP and hence consequences for normal cognitive development in the PFC (Monaco et al., 2015; Ventruti et al., 2011). Particularly, the prolonged NMDA receptor hypofunction (suggested by reduced NR2B expression in adolescence and NR2A expression in adulthood) would be expected to induce GABAergic disinhibition and the reduced PV expression observed here (Kinney et al., 2006). This would be representative of findings in schizophrenia (Cohen et al., 2015; Nakazawa and Sapkota, 2020; Olney and Faber, 1995) and other animal models (Abdul-Monim et al., 2007; Cadinu et al., 2018; Javitt and Zukin, 1991; Koek et al., 1988; Reynolds and Neill, 2016) and could underscore the executive function deficit in MIA-exposed animals. Notably, there was a marked switch in the molecular phenotype between PD35 and PD100, coincident with the emergence of PFC-associated cognitive deficits. These included a reduction in PV expression (Figure 6.11) and a decrease in the NR2A:NR2B ratio, reflected by a decrease in NR2A expression and increased NR2B expression (Figure 6.20). The occurrence of this switch around the time of the emergence of the behavioural phenotype suggests that interventions in these pathways may be of therapeutic benefit. Indeed, correction of Reelin signalling and NMDA receptor hypofunction in late adolescence has been shown to improve cognitive outcomes (Ibi et al., 2020; Mielnik et al., 2021), adding weight to the concept that greater mechanistic insights can lead to the identification of targeted molecular loci with the potential for therapeutic advantage.

CHAPTER 7. DISCUSSION

7.1. General discussion

Schizophrenia is a neuropsychiatric disorder, comprising positive, negative and cognitive symptoms which severely impact quality of life (Figure 1.1; Castillejos et al., 2018; Charlson et al., 2018). Since the 1950s, the mainstay of schizophrenia therapy has relied on antipsychotics, which primarily ameliorate positive symptoms, with little impact on negative and cognitive symptom domains (Naber and Lambert, 2012; Spark et al., 2022). However, antipsychotics face several challenges, including patient non-compliance, severe side-effects and lack of efficacy (Ibrahim and Tamminga, 2011; Muench and Hamer, 2010; Semahegn et al., 2020). Hence, there is critical need for novel therapeutic strategies. This is hindered by the complex and multifactorial nature of schizophrenia, comprising both genetic and environmental risk factors. Critically, schizophrenia is hypothesised to arise following disturbed neurodevelopment. Epidemiology studies have demonstrated that maternal infection, notably maternal viral infection, which induces MIA, associates with a significant proportion of schizophrenia cases (Brown and Derkits, 2010; Weinberger, 1987).

To study this paradigm and elucidate the mechanistic pathways that underpin this disorder, research effort has focused on the development of preclinical animal models of MIA (Meyer and Feldon, 2010). We have previously characterised a model for MIA, administering the viral mimetic, poly(I:C), on GD15 in pregnant Wistar rat dams (Kowash et al., 2019; Murray et al., 2019). The principal aim of my thesis was to investigate the molecular mechanisms that contribute to impaired neurodevelopment as a consequence of MIA, with particular focus on epigenetic programming and to delineate the pathways that then predispose offspring to behavioural deficits later in life.

This thesis has validated that GD15 exposure to poly(I:C) induces acute MIA, shown by marked elevations in maternal plasma cytokines IL-6 and TNFα at 3h post-treatment (Figure 2.6), alongside significant weight loss in the 24h period post-MIA (Figure 2.8), likely due to reduced foetal weight at GD16 (Figure 2.10). However, MIA had a limited effect on litter size, in line with previous studies (Figure 2.9; Arsenault et al., 2014; Kowash et al., 2019). Of note, while offspring exposed to MIA *in utero* had reduced bodyweight during early postnatal development (Figure 2.13), this phenotype did not persist in the post-weaning period, indicating that this altered growth phenotype was normalised by puberty and, importantly, prior to any behavioural phenotyping in adolescence (PD35). Further, there was very little impact of MIA on overall brain weight across any of the postnatal developmental stages assessed (Figure 2.14), although it is worth commenting that we have reported here and previously, a significantly increased foetal brain:bodyweight ratio at GD21 following MIA (Figure 2.10; Kowash et al., 2022). Together, the weight data show that adolescent and adult MIA-offspring appear, for the most part, largely identical to their vehicle counterparts. From this it was hypothesised that any mechanisms which contribute to MIA-induced behavioural phenotypes are likely underscored by changes at the molecular level. This hypothesis formed the basis of the research conducted for this thesis. In

this final discussion, the key mechanistic findings linking MIA to the observed cognitive phenotype will be examined, along with limitations of the study and future directions. A summary of the key findings from this thesis can be found in Figure 7.1.

7.1.1. Key findings: developing a mechanistic hypothesis

MIA promotes increased methylation capacity and abnormal epigenetic patterning in the developing cortex

We have previously demonstrated that MIA induces altered amino acid transport capacity of the placenta from GD15-21 (Kowash et al., 2022). Notably, a placental transport decrease of leucine at 24h post-MIA (GD16), was followed by an increase at GD21. This study has added to these findings by evaluating expression of both system L (also examined in the placenta in Kowash et al., 2022) and system A amino acid transport changes in the developing cortex. Importantly, both these amino acid transport systems transport methionine as a substrate (Tsitsiou et al., 2009), critical for the formation of the methyl donor SAM and hence methylation capacity (Ducker and Rabinowitz, 2017; Mentch and Locasale, 2016). A major finding was that both these amino acid transport systems were developmentally dysregulated in response to MIA (Figure 3.7). Hence, it was hypothesised that the observed changes in expression of the genes encoding these amino acid transporters would cause associative perturbations in 1C metabolism. Evidence to support this hypothesis was obtained, with an increase in the SAM/SAH ratio prenatally (GD21) and subsequent dysregulation in adulthood (PD175; Figure 3.8). The SAM/SAH ratio is considered an index of cellular methylation capacity (Caudill et al., 2001) and therefore it is proposed that the observed changes in SAM/SAH ratio are likely to reflect an alteration of cellular methylation pathways in response to MIA. Notably, there was a corresponding increase in DNMT expression and activity in the prenatal cortex, alongside ongoing dysregulation into adulthood (Figure 4.8&4.9), converging in changes in global DNAm patterns (Figure 4.12). Of particular note, changes were most significant in the prenatal cortex.

From these findings, it is postulated that MIA induced changes to placental and brain amino acid transport, supporting altered brain methylation demand, leading to altered epigenetic patterning in the developing brain. These changes are likely to be adaptive prenatally, to enable immediate cellular responses to MIA-induced signalling pathways. However, prenatal epigenetic programming as a result of MIA is likely to have consequences on brain developmental trajectory and, as a result, postnatal function. This concept aligns with the DOHaD hypothesis, which postulates that an adverse early-life environment programs developing organs and predisposes the individual for later life disease (Bianco-Miotto et al., 2017; Gillman, 2005). Critically, epigenetic mechanisms are thought to mediate this link (Szyf et al., 2007). In support of this postulate, ELS models have shown that deficient MCB alters methylation of the *Nr3c1* gene in the hippocampus of offspring, leading to altered GR expression and stress responsivity (Szyf et al., 2007; Weaver et al., 2004).

To investigate DNAm changes within the MIA paradigm, differentially methylated genes were profiled in the PFC of animals experiencing cognitive deficits, in an effort to identify how MIA-induced changes in epigenetic patterning of the developing cortex affect behavioural functional outcomes. The analysis showed that differential methylation occurred in genes associated with processes important in normal brain development and function (Figure 4.18-4.21), supporting the concept that dysregulated epigenetic mechanisms participate as a mediator of altered neurodevelopmental trajectory following MIA. These genes were also significantly enriched for schizophrenia risk-factor genes (Table 4.8), further supporting a role for MIA-induced epigenetic dysregulation in precipitating the observed behavioural phenotype. Moreover, given that DNAm plays a crucial role in cellular development, through developmental regulation of cell-specific transcriptomes, it was of particular interest that the differentially methylated genes showed enrichment for glia-expressed genes (Figure 4.22B). This could imply that glial cells are particularly sensitive to MIA-induced epigenetic dysregulation. In this context, gliogenesis is known to occur over the late gestational period in rats (GD16-22) into the early postnatal period (Figure 1.3; Miller and Gauthier et al., 2007; Naik et al., 2017; Sarkar et al., 2019). As glial cells are developing over late gestation, it could leave these cells particularly vulnerable to MIA-induced epigenetic dysfunction. In line with this, the notable increase in DNAm in the GD21-PD21 FC aligns with the peak period of gliogenesis. It can thus be suggested that the changes observed in methylation pathways may conceivably reflect altered glial cell development, driven by dysregulated epigenetic patterning in the SVZ progenitors. Indeed, these cell fate decisions are driven by waves of DNAm changes and hence expediated cell development following MIA, could increase DNAm demand, as observed. However, what drives this change in epigenetic patterning and what the long-lasting consequences are for glia function remain poorly defined. Hence, this aspect was investigated further.

MIA-induced foetal neuroinflammation leads to epigenetic repatterning and premature glial development

This study showed that MIA induces acute changes in the foetal brain neuroinflammatory profile, with an increase in pro-inflammatory cytokines 24h post-MIA induction (Figure 2.15), with evidence that this could be sustained throughout the last week of gestation (Figure 2.16A). Such elevations in pro-inflammatory cytokines could conceivably drive the observed increased DNMT activity, as both IL-6 and IL-1β have been shown to upregulate DNAm pathways (Li et al., 2012; Seutter et al., 2020). Inflammation-induced upregulation in DNMT expression and activity would be expected to increase methylation demand in the prenatal brain between GD16 (time of cytokine elevation) and GD21 (observed increase in methylation), due to the function of DNMTs in cellular differentiation processes in the foetal brain and hence the increased SAM/SAH ratio may reflect this increased demand. It is also possible that the notable increase in IL-6 could have critical impacts on cell development in the foetal brain. GD15-16 comprises a period of multiple neurodevelopmental processes, including waves of neurogenesis, the production of GABAergic interneurons and the specification of glial cell progenitors (Figure 1.3; Sarkar et al.,

2019). The IL-6 family of neuropoietic cytokines are critical regulators of the gliogenic switch and subsequent glial cell differentiation/maturation (Miller and Gauthier et al., 2007; Naik et al., 2017; Taylor et al., 2010), commencing around GD16 in rats (Figure 1.3; Sarkar et al., 2019). These processes are regulated in part by changes in DNAm in progenitor cells, with increased methylation (silencing) of neuronal genes and reduced methylation (activation) of glial genes to promote glial cell specification (Amberg et al., 2019; Egawa et al., 2019; Hatada et al., 2008). Hence, it could be postulated that the elevation in IL-6 and concurrent induction of DNMTs across late foetal development, disrupts the normal epigenetic programming of these developmental events, with particular impact on macroglia cell development. Indeed, this was evidenced by determination of the expression of genes critical in the development and mature function of these cells. In general, results showed an early upregulation of expression (mRNA/protein) of genes involved in synapse (e.g., *Gpc4*), myelin (e.g., *Myrf, Mag, Mbp*) and ECM (e,g, *Nfasc, Ank3, Bcan, Vcan*) formation, across early postnatal brain development (PD1-PD35) indicative of accelerated maturation of these cells. Further, these changes in expression appear driven, at least in part, by alterations in DNAm, implying adaptive epigenetic programming of these genes has occurred in response to MIA. Further, results showed disturbed macroglia ratios, particularly, a reduction in GFAP+ astrocytes (Figure 5.12) and a coincident increase in OLIG2+ oligodendrocytes (Figure 5.15A). Astrocytes and oligodendrocytes develop from the same NPC pool in a sequential pattern, regulated in part by the IL-6 family of neuropoietic cytokines (Miller and Gauthier et al., 2007; Naik et al., 2017; Taylor et al., 2010). Hence, the data suggests that MIA-induced foetal IL-6 elevations may induce accelerated gliogenesis and, particularly, oligodendrocyte differentiation. In line with this, results demonstrated a reduction in NG2+ OPCs relative to total OLIG2+ oligodendrocytes (Figure 5.15), suggesting MIA has promoted the formation of mature oligodendrocytes at the cost of the progenitor pool.

Of note, changes in macroglia developmental ratios might be exacerbated by altered microglia. As outlined, microglia are the critical immune cells in the CNS and are likely responsible for the observed increase in pro-inflammatory cytokines in the foetal brain. However, microglia also have critical roles in neurodevelopment (Menassa and Gomez-Nicola, 2018; Mosser et al., 2017; Reemst et al., 2016). Given that microglia colonise the foetal brain prior to the time of the immune insult in this model (Menassa and Gomez-Nicola, 2018; Tong and Vidyadaran, 2016), it is unlikely that their development or colonisation would be critically altered. Consistent with this, there were no differences in IBA1+ cell densities in the cortex of MIA-exposed offspring. That said, measurement of microglia-enriched genes (*Sgk1, Irs1, Tgfbr2*) showed developmental changes in expression of these genes (Figure 5.10) supporting a MIA-induced change in ongoing microglia function, favouring a pro-inflammatory phenotype. Active microglia, especially in the prenatal period, have been shown to phagocytose early astrocytes (VanRyzin et al., 2019) and hence might explain the deficit in astrocytes relative to oligodendrocytes.

Overall, these results suggest that MIA-induced foetal neuroinflammation permitted accelerated macroglia development, a phenotype supported by recent RNA-sequencing in a MIA model (Canales et al., 2021) and cell tracking in ELS models (Poggi et al., 2022; Teissier et al., 2020), likely driven in part by epigenetic mechanisms. The altered programming of these cells may lead to postnatal malfunction of these cells, likely with consequences for PFC-mediated cognition.

Accelerated macroglia development following MIA reduces synaptic plasticity during the critical period

The PFC is essential in higher cognitive development, integrating past experience with current goals to select appropriate behavioural programs, in a process called executive function (Ferguson and Gao, 2018; Orellana and Slachevsky, 2013). Due to its complex function, the PFC develops over a highly protracted developmental period. Importantly, during juvenile and adolescent development there are essential waves of synaptic plasticity, including structural and functional remodelling, forming the correct neural networks critical for normal cognitive processes (Guirado et al., 2020; Larsen and Luna, 2018). Meanwhile, the formation of extracellular structures, including myelin and the neural ECM, mark the closure of the critical period of the PFC (~PD14-35 in rats; Larsen and Luna, 2018). It was hypothesised that the accelerated maturation of macroglia and altered microglia function could lead to the perturbation of this key developmental period and predispose offspring to cognitive deficits. Macroglia and microglia play critical roles in supporting the formation and maintenance of myelin and the neural ECM and hence early maturation of these cells could conceivably cause premature formation of these structures and early closure of the critical period. Indeed, results from this study provided support for this hypothesis. Notably, MIA induced an early reduction in expression of early exon 2-containing MBP (early developmental isoforms) at PD21 followed increased expression of exon 2-spliced MBP (late developmental isoforms) at PD35 (Figure 5.20). Together this expression pattern would indicate advanced maturation of the myelin structure, with a premature switch to the expression of late-developmental myelin. Likewise, expression of multiple neural ECM components (*Nfasc, Acan, Vcan, Ncan, Bcan*) showed an upregulation in expression in MIA-offspring across the critical period (PD21-35), suggesting premature or excessive formation of the neural ECM. This was corroborated by an increased WFA+ density at PD35 (Figure 6.10A), supporting increased PNN formation during this time. Together, these results suggest accelerated PFC maturation, which would be expected to precipitate a loss of synaptic plasticity during the critical period.

In agreement with this, the results across Chapters 5 and 6 provided preliminary evidence for dysregulated synapse formation and removal. Indeed, at PD35 there was an increase in ameboid forms of microglia in MIA-offspring (Figure 5.6B). Ameboid microglia are involved in normal phagocytosis and remodelling of synapses and hence the increased density of this form of microglia could promote excessive or imbalanced synaptic pruning which may result in reduced synaptic connections and plasticity (Geloso and D'Ambrosi, 2021). Likewise, there was a reduction in astrocytic GPC4 expression in MIA-offspring (Figure 5.14). GPC4 has been shown

to be important in normal glutamatergic synapse formation, through communication with GLuA1 receptors (Allen et al., 2012). Accordingly, there was reduced GLuA1 expression in MIA offspring throughout the critical period (Figure 6.19). This receptor plays several roles in glutamatergic synapse formation, including the aforementioned role in communicating with astrocytic GPC4 and hence this observed reduction in GLuA1, coincident with reduced GPC4, would be anticipated to exacerbate abnormal synapse formation and plasticity during this period. Notably, the expression of the GLuA1 receptor appeared to reach adult levels very early in development in MIA-offspring (Figure 6.19), also indicating an early developmental PFC maturation. Further to this finding, analysis of the NMDA receptors, implicated in altered cognitive phenotypes, showed a reduction in NR2B expression in MIA-offspring in this period (Figure 6.20B). NR2B is downregulated as part of the normal developmental glutamatergic switch from NR2B to NR2A (Béïque et al., 2006). However, the reduction in the expression of this receptor subunit in MIA-offspring at PD35 could further support early developmental maturation. Critically, NR2B has been linked to altered cognitive function (Monaco et al., 2015) and, further, reduced expression of this receptor would be reflective of NMDA receptor hypofunction, a key pathological finding in schizophrenia (Cadinu et al., 2018).

Overall, these findings suggest MIA-induced cell-specific epigenetic programming promotes accelerated maturation of the PFC, with reduced synaptic plasticity during the critical period (PD14-35). However, it must be noted that the molecular changes present at a stage (PD21-35) where there is no evidence of behavioural deficits (Chapter 2). Such altered developmental processes may contribute to altered adult PFC function, which could promote development of cognitive dysfunction. Hence the next aim was to investigate how these molecular changes converge in a PFC cognitive deficit.

MIA-induced changes in neurodevelopmental trajectory results in an abnormal molecular and behavioural phenotype in adulthood

Behavioural phenotyping demonstrated a deficit in the ASST, resulting in an increased ID/ED shift, representative of an executive function deficit, a phenotype critically underscored by the PFC (Orellana and Slachevsky, 2013), presented only in adult offspring (Figure 2.18). This would imply that the aforementioned MIA-induced developmental abnormalities observed in the early postnatal PFC (PD1-35) predispose offspring to an impaired adult cognitive phenotype. Hence, it was next important to consider how the accelerated maturation of the PFC would impact the function of the adult PFC. Interestingly, there were critical molecular differences in the adult PFC, compared to the adolescent PFC. First, between PD35 and PD100 there was a MIA-associated reduction in Reelin signalling, including increased DAB1 expression and sex-specific changes in *Camk2b* expression (Figure 6.17). Reelin and its signalling pathway have long been of interest in schizophrenia (Guidotti et al., 2000, 2016), likely owing to the function of Reelin in cognition in later postnatal development, notably through modulation of NMDA receptor function, mediated via PSD95 (Figure 6.2B; Beffert et al., 2005). Further, normal postnatal Reelin signalling is important in the normal glutamatergic NMDA receptor switch (Groc

et al., 2007). Hence, the observed downregulation of Reelin signalling in adult MIA-offspring could lead to disturbed NMDA receptor function in adulthood. In line with this, a MIA-associated reduction in PSD95 was also observed (Figure 6.18). This could be due to reduced Reelin signalling or, given that PSD95 is located within synapses, particularly glutamatergic synapses, it could reflect an overall reduction in glutamatergic synapses in adulthood, perhaps due to loss of synapse formation and excessive pruning as hypothesised in the previous section. In either case, the reduced Reelin signalling and concomitant reduction in PSD95, would be hypothesised to impact NMDA receptors.

NMDA receptors showed a marked change in expression between PD35 and PD100 in MIA-offspring. There was a switch toward a more immature phenotype reminiscent of that expected in juveniles, with reduced NR2A expression and increased NR2B expression, resulting in a robust reduction in the NR2A:NR2B ratio (Figure 6.20), consistent with reduced Reelin and PSD95 (Campo et al., 2005; Groc et al., 2007; Singara et al., 2005). These NMDA receptor changes are likely to impact critical PFC-mediated cognitive functions owing to their roles in LTP (Collingridge and Bliss, 1987; Zhao et al., 2005). MIA-induced changes in these glutamatergic-associated proteins, also coincide with reduced PV expression, indicative of GABAergic disinhibition (Caballero et al., 2014, 2020). Taken together, these findings accord with an EI imbalance in the adult PFC, with the reduced NR2A:NR2B ratio precipitating excess glutamatergic signalling in adults (Monaco et al., 2015). In support of excess glutamatergic signalling, there was a change in microglia phenotype from PD35 to PD100, with an increased pro-inflammatory hypertrophic phenotype (Figure 5.6B), concomitant to elevated brain IL-6 (Figure 2.16). This suggests a transition to a pro-inflammatory state in the cortex between adolescence and adulthood. If so, it would be expected that there would be evidence of structural damage. Accordingly, there was reduced MBP protein expression at PD100 (Figure 5.20) with no change in MBP mRNA expression (Figure 5.18B), which could indicate MBP protein degradation. However, while there was no evidence for neural ECM damage at PD100, this possibility cannot be discounted from occurring as the pathology progresses, in alignment with previous studies denoting reduced PFC PNNs in MIA models and schizophrenia (Bucher et al., 2021; Paylor et al., 2016). Further, the reduced OPC pool due to the early maturation of the oligodendrocyte cell lineage (Figure 5.15) could also indicate a particular susceptibility of myelin to inflammatory-induced damage, as the lack of OPCs would diminish the efficiency of remyelination in the PFC (Briones and Woods, 2014). Nonetheless, taken together, these findings provide evidence that support specific developmental inflammation-mediated influences on the adult brain.

Overall, these findings postulate a molecular shift between PD35 and PD100, reminiscent of an immature neuro-phenotype, perhaps to overcome the advanced maturation during the critical period (PD21-35). This shift converges in glutamatergic receptor and PV protein expression changes, microglial activation and demyelination, hypothesised to underscore the appearance of cognitive deficits in this period.

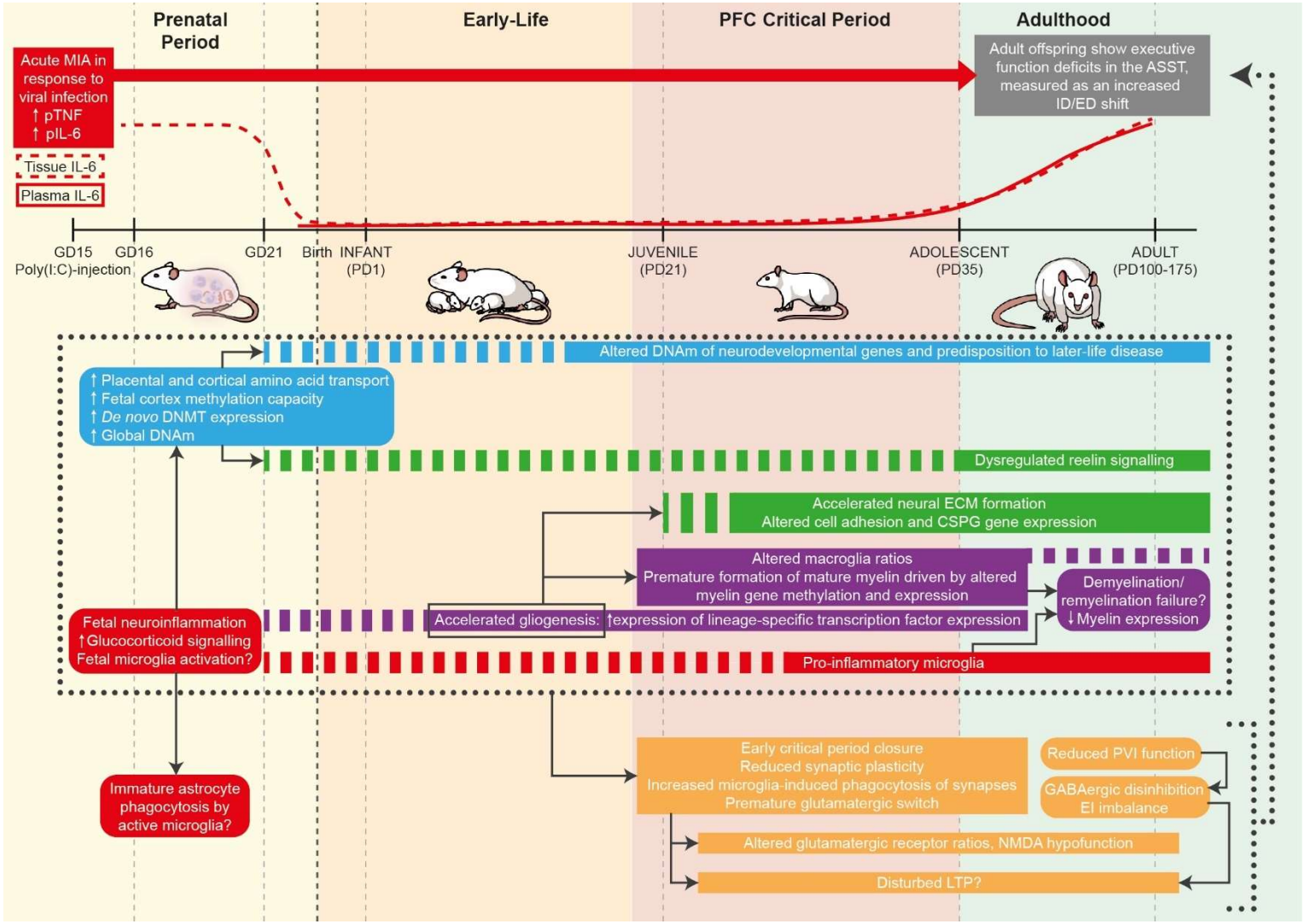

Figure 7.1. Summary of the key mechanistic hypothesis underscoring MIA-induced cognitive deficits

Summary of the key molecular hypothesis of the thesis: MIA induces ongoing epigenetic, inflammatory and macroglia deficits, resulting in abnormal neuro-developmental events during the developmentally critical period of the PFC (shown as a dotted box) which together perturb neuronal signalling into adulthood, underscoring the development of the PFC-mediated cognitive deficit (dotted line linking molecular changes to phenotype). The developmental timeline is depicted, delineated into key developmental periods (prenatal, early-life, critical period, adulthood). Longitudinal MIA-induced changes are indicated above and below the timeline. Above: dam changes (MIA) and offspring outputs including tissue (dotted red line) and plasma IL-6 (solid red line) changes depicted along the timeline and behavioural deficits in adulthood. Below: various neuro-molecular outputs at the key developmental stages at which they occur. Extrapolated dotted lines indicate evidence for an ongoing process, solid boxes indicate the key stage of a process. **Colour coding:** red: inflammatory changes; purple: macroglia changes; green: ECM changes; orange: neuronal signalling changes; grey: behavioural measures.

.

7.1.2. Conclusions and clinical relevance

In the model of MIA studied here, induced foetal neuroinflammatory dysregulation promoted perturbed neurodevelopment with impacts on different cell types, with macroglia cell development particularly affected, likely driven by altered epigenetic patterning. These adaptive epigenetic patterns, as evidenced by altered DNAm, seemed to persist postnatally, resulting in altered functional profiles (measured via transcriptomic/proteomic changes) of these cells across neurodevelopment. Dysfunctional glia are likely to precipitate loss of synaptic plasticity and early closure of the PFC critical period. These neurodevelopmental changes during the critical period precede neurodevelopmental regression, EI imbalance and inflammation in adulthood, manifesting in a PFC-mediated cognitive deficit, relevant for schizophrenia (Figure 7.1). Notably, the molecular phenotype characterised here in the adult PFC of MIA-offspring demonstrates key similarities to findings from studies in schizophrenia patients, including, PVI dysfunction (Liu et al., 2021; Wang et al., 2021a), glutamatergic imbalance (Cohen et al., 2015; Nakazawa and Sapkota, 2020), pro-inflammatory phenotype and active microglia (Bernstein et al., 2015; Frick et al., 2013) and loss of myelin protein expression (Francisco et al., 2022; Vikhreva et al., 2016). In line with this, the differentially methylated genes in adult MIA-offspring were shown to be significantly enriched for schizophrenia-risk genes (Table 4.8). Together, these findings would support the preclinical relevance of this model for a schizophrenia phenotype. That said, it should be acknowledged that some of the molecular results conflict with the common findings from schizophrenia studies, such as the increased oligodendrocyte and PNN density (Bucher et al., 2021).

Schizophrenia is a highly heterogenous disorder and is often used as an ‘umbrella term’ for schizophrenia, schizoaffective disorder and psychosis (American Psychiatric Association, 2022). This could in part explain the lack of efficacy in clinical therapeutics, including anti-psychotics (Naber and Lambert, 2012; Spark et al., 2022) and anti-inflammatories (Çakici et al., 2019; Cho et al., 2019; Jeppensen et al., 2020), due to a lack of appreciation for patient subtypes and stratification during trial recruitment. Indeed, work by Clementz et al. (2022) has postulated three patient biotypes, comprising different genetic and environmental risk factors and resulting phenotypes (Clementz et al., 2022). In line with this, MIA is suspected to be a risk factor for ~30% of schizophrenia patients (Akbarian, 2014) and most likely acts as a primer for schizophrenia development which synergises with other genetic and environmental risk factors to promote disease development (Choudhury and Lennox, 2021). It could therefore be postulated that the preclinical MIA model phenotypes demonstrated here represent a narrow subtype of schizophrenia patients, notably those with high basal inflammatory state and cognitive phenotypes (Woods et al., 2021).

Critically, the results presented here support a window for intervention prior to the onset of altered behaviours, between adolescence and adulthood, where molecular changes are present (Figure 7.1). This work also provides preliminary evidence for potential systemic biomarkers

(e.g., IL-6) which track the pathogenesis progression of the disorder that could be indicative of potential timings for interventions. Indeed, such investigations are now taking place in a clinical setting for schizophrenia. The Psychosis Immune Mechanism Stratified Medicine Study (PIMS), is seeking to stratify patients into high inflammatory groups, based on genetic variants and peripheral biomarkers in the IL-6 pathway and subsequently provide targeted intervention by way of the IL-6 inhibitor Tocilizumab (UK Research and Innovation, 2023). Such studies might offer an analogous framework for which the MIA model characterised here could be used as a suitable model for preclinical drug testing for subsets of patients with high inflammatory profiles or risk. Moreover, the molecular findings described here could also be used to preclinically investigate additional pathways for intervention in these patient subtypes, including microglial activation inhibitors, glutamatergic and GABAergic modulators (see Section 7.3.3). Overall, the research undertaken in this thesis supports a robust MIA model, resulting in altered molecular and behavioural phenotypes, that highlight its promise as a preclinical model with direct relevance for schizophrenia. Such models may also be inherently important in the coming years following the recent SARS-CoV-2 pandemic, with emerging evidence already suggesting exposed children have increased risk of neurodevelopmental impairment (Shook et al., 2022; Shuffrey et al., 2022) and hence our understanding of the mechanisms which link MIA and altered neurodevelopment are becoming ever more critical.

7.2. Limitations

There are a few limitations in this study that may influence the interpretation of the results and which should be considered alongside the conclusions outlined above.

I. Epigenetic analysis

The examination of epigenetic changes following MIA-induction formed an important aspect of this study, performed in line with the growing recognition of the role that epigenetics plays in mediating the long-term consequences of early-life adversity on development (Bianco-Miotto et al., 2017; Woods et al., 2021). Techniques for epigenetic analysis possess unique limitations and the methods employed here, primarily bisulphite-based sequencing, while a gold standard in the field (Beck et al., 2022; Kyrdyukov and Bullock, 2016), has one important limitation: it cannot distinguish DNAhm from DNAm. In many tissues, this would pose little issue as DNAhm is typically present in the genome at low quantities. However, in the brain, DNAhm is estimated to account for 40% of CpG modifications (Cheng et al., 2015). DNAm and DNAhm have opposing functions in upregulating and downregulation gene expression, respectively (Quina et al., 2006; Shi et al., 2017). Therefore, the inability to distinguish these epigenetic marks using bisulphite-methodology limits complete interpretation of how the observed changes in DNA modifications impact gene/protein expression. For example, there were occasional datasets where the observed DNA modification was positively correlated with gene expression (e.g.,

Table 6.14), in contradiction to the role of DNAm in inhibiting gene expression (Anastasiadi et al., 2018; Brenet et al., 2011; Saxonov et al., 2006; Tazi and Bird, 1990). It cannot be discounted that DNAhm accounted for the observed changed modification, which would be expected to positively correlate with gene expression (Hon et al., 2014; Shi et al., 2017). However, this does pose interesting pathways for future research. Indeed, DNAhm has been demonstrated to be particularly altered in GABAergic interneurons in schizophrenia, suggesting this epigenetic mechanism could critically associate with this neuropsychiatric disorder (Kozlenkov et al., 2018).

II. Cell specificity

Another limitation is the heterogenous cellular nature of the brain and the lack of granularity of events at the level of specific cell-types. We, like many others in the MIA field, have, to date, focused our research on whole brain regions (Woods et al., 2021), which comprise a heterogenous sample of glia and neurons. However, individual cell types have distinct epigenomic and transcriptomic profiles (Keil et al., 2018; Kozlenkov et al., 2018; Roadmap Epigenomics Consortium et al., 2015). In this study, the DNAm and gene expression results have been stratified by individual cell-types by primarily selecting genes with known single cell-type enrichment (Appendix 9) in an effort to minimise this confound. That said, it is impossible to confirm that the observed changes are definitively derived from a single cell-type, particularly true for the synaptic proteins. This creates a limitation when attempting to interpret the functional consequences of the data. For example, when considering the NMDA receptors (Figure 6.20), delineation of which individual cell-types experience MIA-induced changes in the expression of these receptors would be more informative than that of whole tissue. Hypofunction of these receptors on PVIs is known to reduce GABAergic inhibition due to lack of glutamatergic innervation, which, in turn, can lead to increased glutamatergic signalling due to lack of inhibitory input (Nakazawa and Sapkota, 2020). By contrast, changes in expression of NMDA receptors within the post-synaptic membrane on glutamatergic pyramidal neurons are closely associated with alterations in LTP (Monaco et al., 2015). As the analyses in this study were performed on whole tissue, without using immunohistochemical co-localisation or single-cell isolation, it is not possible to determine if one, or both, of these functional consequences are occurring. Further, the conclusions in this study are based on gene/protein expression changes which limits the functional interpretation of the findings. Again, this is particularly important for receptors, where function cannot necessarily be interpreted by expression alone. Indeed, synaptic receptors can transition between active/inactive conformations and can be shuttled between the synapse and extra-synaptic space (Meier et al., 2001; Thomas et al., 2005; Vyklicky et al., 2021). While the results provide preliminary evidence for changes in glutamatergic conductance in the PFC following MIA, these conclusions would need to be confirmed with a form of functional analysis.

III. Biomarkers

A final limitation is the restrictive nature of the biomarker analysis performed in this study. Biomarkers are used clinically as predictive markers of disease progression and prognosis.

While biomarkers are well identified in oncology, biomarkers for complex neurological disorders have been harder to identify (Henry and Hayes, 2012; Lleó, 2021). Nonetheless, research is progressing to identify early-stage biomarkers for schizophrenia, to guide clinical intervention strategies and stratify clinically high-risk individuals. In this study, IL-6 was measured as a systemic inflammatory biomarker, selected for its association with ELS and adverse outcomes, including cognitive deficits and psychosis (Khandaker et al., 2014; King et al., 2021; Perry et al., 2021). Further, the IL-6 pathway is currently being investigated in a clinical setting for schizophrenia, together with genetic variants and peripheral biomarkers that associate with this pathway, to stratify patients into high inflammatory profiles and assess how these patients respond to the IL-6 inhibitor Tocilizumab (UK Research and Innovation, 2023). However, while IL-6 was justifiably selected to align with current clinical research, in this study, IL-6 concentration was measured in plasma collected from post-mortem trunk blood. Given the method of culling used (Chapter 2), there is the possibility that the observed systemic IL-6 concentration is differentially affected in MIA-offspring compared to vehicle-offspring following CO_2 exposure (Wang et al., 2010). Second, by collecting plasma only after culling, it was not possible to examine how IL-6 concentration changes temporally within MIA-exposed offspring, which could be more informative and analogous to the clinical setting. With these limitations in mind, future analysis using live blood sampling at discrete developmental stages would be needed to delineate how IL-6 (and other potential biomarkers) change over the course of disorder progression. Further, given the ongoing debate of the most appropriate biomarkers for schizophrenia (Borovcanin et al., 2017; Maes et al., 2020; Miller and Goldsmith, 2020; Zhou et al., 2021), evaluation of a wider profile of peripheral biomarkers would increase the predictability of phenotype progression.

7.3. Future directions

7.3.1. Overcoming the key limitations

I. Alternate epigenetic mechanisms

Beyond DNAm and DNAhm, analysis of histone modifications and ncRNAs would provide further detail of how MIA causes epigenetic programming in the developing brain. Indeed, all three mechanisms have been shown to be important in the developing brain (Christopher et al., 2017; Jakovcevski and Akbarian, 2012) and have been previously evidenced in MIA models (Woods et al., 2021). Further, epigenetic mechanisms are known to interact (Cedar and Bergman, 2009; Holz-Schietinger and Reich, 2012; Peschansky and Wahlestedt, 2014) and hence by evaluating them in parallel, this would enable a more in-depth mechanistic understanding of the role of these processes in predisposing offspring to neurodevelopmental abnormalities following MIA. Moreover, these mechanisms have temporally different functions

during development. For example, in general, histone modifications have been suggested to occur prior to changes in DNAm during epigenetic reprogramming events (Monk et al., 1987; Santos et al., 2005). Hence, future work evaluating these mechanisms would aid in identification of whether changes to epigenetic mechanisms occur with the same temporality across the developmental timeline and whether such changes are consistent across mechanisms at the same loci in response to MIA. This could aid in identification of the developmental sequence of robust programming events which predispose offspring to pathology following MIA.

II. Single-cell evaluation

Future work should aim to evaluate single-cell changes following MIA. This study provides preliminary evidence for alterations in several cell-types following MIA, including both neurons and glia. For evaluation of select cell changes, an immunofluorescence-based co-staining protocol could be used. For example, the PVI IHC methodology (Chapter 6) could be adapted to co-stain for NMDA receptors on the surface of PVIs in order to measure NR2A and NR2B densities on PVIs specifically, circumventing the limitation specific to the findings for these receptors outlined above. However, to evaluate multiple single-cell epigenetic and transcriptomic changes following MIA, a single cell isolation protocol would be required. This would enable isolation of nucleic acids and protein from homogenous cell populations which could be used to fine-tune the mechanistic hypothesis.

III. Brain region

This study has used a single brain region, the PFC. While this brain region was selected for its critical role in the observed increased ID/ED shift (Orellana and Slachevsky, 2013), the hippocampus-PFC connectivity is critical in normal cognitive functions across a broad range of cognitive tasks and dysconnectivity between these two regions has been implicated in schizophrenia (Sigurdsson and Duvarci, 2016). Hence it would be useful to examine if there is a disconnect and/or differences between these two regions following MIA, which could be further contributing to MIA-induced behavioural deficits.

7.3.2. Identifying the timeframe of the proposed molecular shift

A key strength of this study was the longitudinal stages of brain development analysed, spanning both prenatal and postnatal timepoints. However, within this there was one critical developmental ‘gap’ between PD35-PD100. While we have identified no behavioural phenotypes in PD35 MIA-offspring, our more recent work has shown the emergence of cognitive deficits from PD50 (Lorusso et al., 2022; Woods et al., 2023). This creates a key question: does the proposed molecular shift (See Section 7.1.1) occur prior to the emergence of cognitive deficits (e.g., between PD35-PD50), or after the onset of cognitive phenotypes. The lack of intermediary timepoints evaluated in this study prevents the resolution of this question but does provide future research possibilities. Intermediate developmental timepoints could be used to identify the temporality between molecular changes and cognitive deficits and therefore aid in

identification of which molecular changes are predisposing, causal or consequent to the neuropathology of MIA. Further, it could narrow the window for therapeutic intervention.

7.3.3. *In vivo* functional validation

In order to support clinical research, a functional validation of the outlined mechanisms (Section 7.1.1) would be important to establish their contributory role in the resulting phenotype.

Several previous models have used therapeutic intervention (e.g., antipsychotics), which have been shown to ameliorate MIA-induced molecular and behavioural deficits (Borrell et al., 2002; Meyer et al., 2010; Piontkewitz et al., 2009; Zuckerman and Weiner, 2003; Zuckerman et al., 2003), supporting the postulate that MIA-induced neuropathology is adaptable and exhibits a degree of plasticity, offering therapeutic opportunity. Likewise previous studies in MIA and ELS models have shown that some behavioural changes could be overcome with anti-inflammatory modulators, such as minocycline, a microglia activation inhibitor (Giovanoli et al., 2016; Han et al., 2019). This would support an anti-inflammatory approach to overcome MIA-induced deficits in this study. As previously outlined, recent work in schizophrenia clinical trials is exploring the use of IL-6 receptor antibody, Tocilizumab (UK Research and Innovation, 2023), applying similar reasoning. Of note, Tocilizumab administration has been shown to ameliorate cognitive deficits in Alzheimer's and autoimmune dysfunction in rats (Elcioğlu et al., 2016; Poutoglidou et al., 2016). This would be an interesting approach given the evidence for increased systemic and brain IL-6 elevations in adolescent and adult offspring (Figure 2.16). A future intervention study using administration of a similar anti-inflammatory drug in i) adolescence; ii) adulthood, could help uncover if and how inflammation and elevated IL-6 contributes to the development of the cognitive deficits. Moreover, with the goal to identify novel pathways for therapeutic intervention, functional validation of the involvement of the hypothesised mechanisms (Section 7.1.1) would be crucial. Several approaches could be taken, each targeting different aspects of the proposed pathology. First, a recent study demonstrated that injection of recombinant Reelin into the hippocampus could ameliorate MIA-induced behavioural deficits in mice (Ibi et al., 2020). Given the evidence of a PFC Reelin signalling deficit in this model, a similar validation approach could be applied to our model in the future. Second, studies beyond the MIA field have used *in vivo* degradation of the neural ECM using ch-ABC (Bosiacki et al., 2019; Carulli et al., 2010; Morishita et al., 2015) to evaluate its function in cognition. Given the debate in the literature around how PNNs influence behaviours (Carceller et al., 2022; Mascio et al., 2022), it would be interesting to apply this approach in the adolescent/adult MIA-offspring to assess whether the increased PNN density (Figure 6.10A) contributes to, or protects against, the development of the cognitive deficits. Finally, much of the behavioural deficits are hypothesised to arise due to changes in NMDA receptor expression in adolescence and adulthood (Section 7.1.1). However, this study did not provide evidence for a functional alteration to these receptors. Future work exploring this could be achieved through neural electrophysiology to measure synaptic currents from PFC

slices, used to evaluate the functional properties of AMPA and NMDA receptors (Pons-Bennaceur and Lozovaya, 2017).

7.3.4. Identification of mechanisms of susceptibility/resilience

A key future consideration to implement into the analyses would be a clustering paradigm. We and others, have shown that the effect of MIA on offspring behavioural and molecular phenotypes is variable and can in fact be delineated by 'susceptible' and 'resilient' offspring (Mueller et al., 2021; Lorusso et al., 2022). These studies effectively stratify MIA-exposed offspring into two clusters: those that display limited behavioural abnormalities (resilient) and those that display apparent behavioural phenotypes (susceptible). Critically, using these clusters, predictive associations could be identified with respect to molecular changes. Indeed, Mueller et al. (2021) have shown that resilient MIA-offspring show molecular patterns comparable to the control group, while susceptible MIA-offspring are distinguished from both (Mueller et al., 2021). Further, they demonstrated that this translated to differences in systemic inflammatory biomarkers (Mueller et al., 2021). With this work in mind, one possible future approach would be to attribute the same clustering analyses to the data here. Stratifying MIA-offspring in such a way has particular clinical relevance as it can identify which molecular phenotypes and biomarkers underscore particular behavioural domains. Hence, this approach could be critically important in improving identification of novel therapeutic pathways for distinct symptom subtypes.

7.4. Summary

To summarise, this thesis has established that maternal exposure to the viral mimetic poly(I:C) results in a robust MIA and cognitive deficits in adult offspring. The major aim of this thesis was to examine the developmental molecular mechanisms which link exposure to MIA *in utero* to adult cognitive deficits. This work has shown that MIA evokes various molecular changes in the cortex across the longitudinal developmental timeline. The findings from this study implicate an intriguing molecular hypothesis, whereby MIA induces foetal neuroinflammatory dysregulation, perturbing cellular, particularly glial cell, development, likely driven by altered epigenetic patterning, including schizophrenia risk genes. These adaptive epigenetic patterns seem to persist postnatally, resulting in altered glial cell function across neurodevelopment. Dysfunctional glia, in turn, precipitate loss of synaptic plasticity and early closure of the PFC critical period. Critically, these neurodevelopmental changes during the critical period precede EI imbalance and inflammation in adulthood, manifesting in a PFC-mediated cognitive deficit. The results support a window for intervention between adolescence and adulthood, prior to the onset of cognitive behaviours and provides preliminary evidence for potential peripheral biomarkers to track the disease progression, aligning with similar clinical aims. Overall, the research collated as part of this thesis establish a robust MIA model, resulting in molecular and behavioural phenotypes that affords promise as a preclinical model with direct relevance for schizophrenia. Such a model is incredibly important in our understanding of the links between maternal infection, MIA and NDD outcomes, especially in light of the recent SARS-CoV-2 pandemic which, as with other prenatal viral infections, is hypothesised to increase risk of offspring NDDs.

APPENDICES

Appendix 1. Poly(I:C) integrity

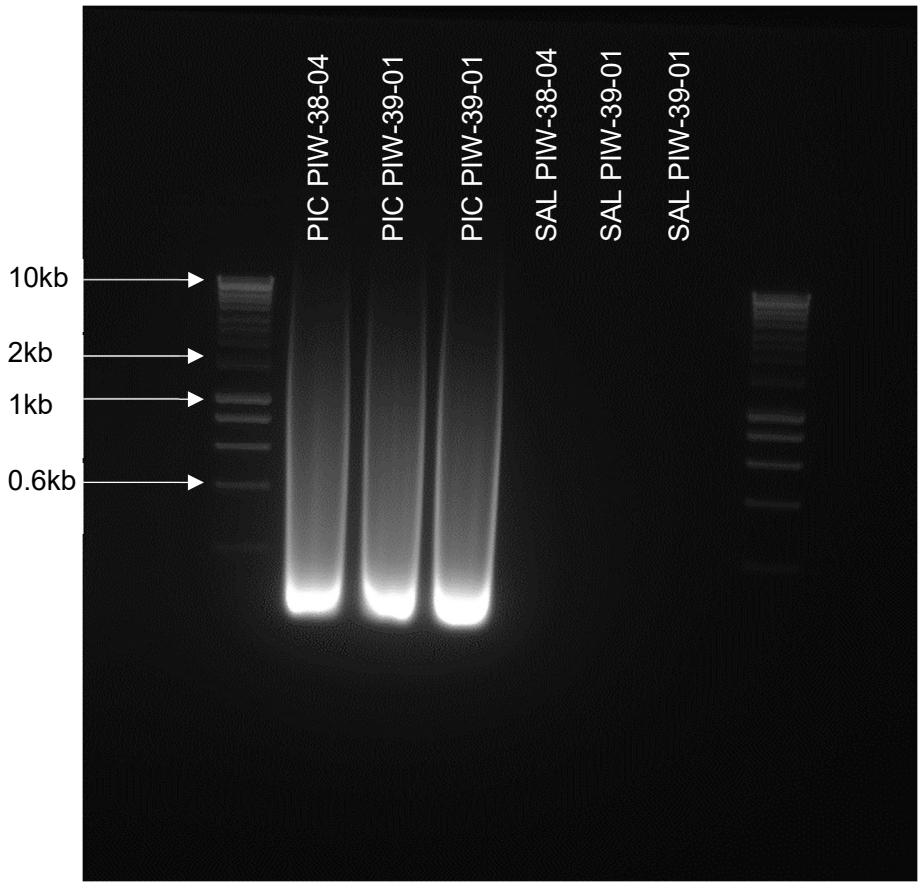

Supplementary Figure S1.1. Representative poly(I:C) quality gel
2%agarose/1XTAE with 1:10,000 Gel Red stain (VWR, Lutterworth, UK). 10µL Poly(I:C) samples (10mg/mL) or saline control were mixed with 3µL DNA loading dye (Bioline, London, UK) and loaded at 10µL per well. 5µL 10kb Hyperladder (Bioline, London, UK) loaded in the flanking wells. Electrophoresis performed in 1XTAE buffer at 120V for approximately 45min. Gel imaged by Syngene GeneSnap software (Cambridge, UK) and UV fluorescence with a default exposure time. Poly(I:C) Lot numbers are indicated above lane, matched to saline diluent. Abbreviations: PIC, poly(I:C); SAL, saline.

Appendix 2. Qiagen DNA/RNA gels

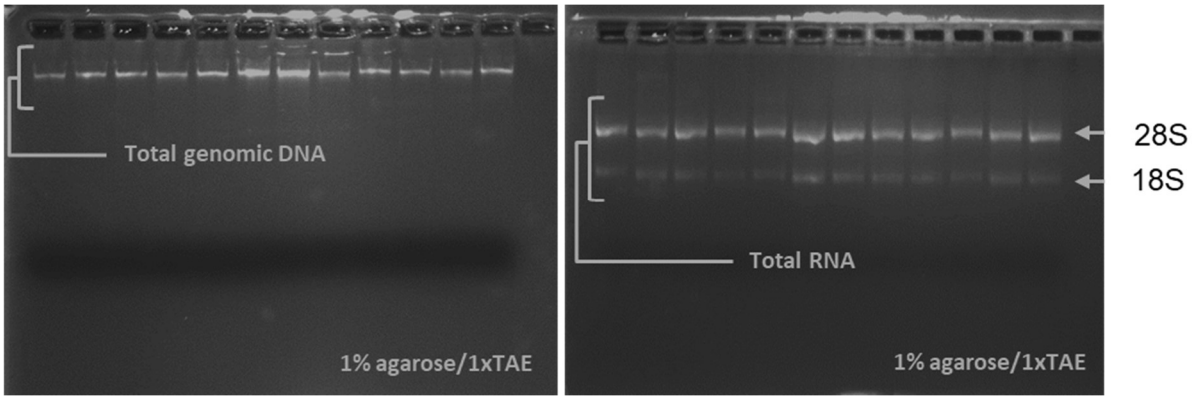

Supplementary Figure S2.1. Representative DNA and RNA quality gel (PR1/PN1 Cohort)
1%agarose/1XTAE with 1:10,000 Gel Red stain (VWR, Lutterworth, UK). RNA samples loaded at 800ng/well and gDNA samples loaded at 50ng/well. Electrophoresis performed in 1XTAE buffer at 120V for approximately 45min. Gel imaged by Syngene GeneSnap software (Cambridge, UK) and UV fluorescence with a default exposure time. Each lane represents an individual sample.

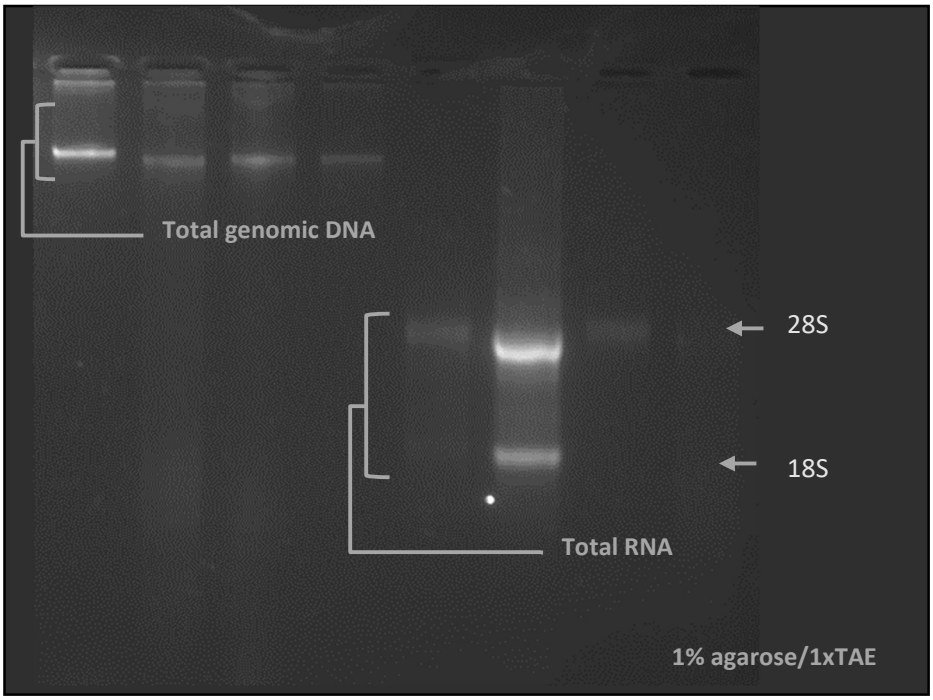

Supplementary Figure S2.2. Representative DNA and RNA quality gel (PN2 - QIAGEN)
1%agarose/1XTAE with 1:10,000 Gel Red stain (VWR, Lutterworth, UK). RNA samples loaded at 800ng/well and gDNA samples loaded at 50ng/well. Electrophoresis performed in 1XTAE buffer at 120V for approximately 45min. Gel imaged by Bio-rad Gel Doc XR+ (Watford, UK) under UV fluorescence with a default exposure time. Each lane represents an individual sample. Note variability in RNA and gDNA quality generated with this extraction kit.

Appendix 3. GeNorm analysis

The geNorm M indicates the average expression stability value of remaining reference genes at each step during stepwise exclusion of the least stable reference gene and a value of ≤0.5 is generally considered stable. Accordingly, the lowest geNorm M value indicates the most stable reference genes across development. The geNorm V value indicates the pairwise variation between two sequential normalization factors containing an increasing number of genes. A large variation means that the added gene has a significant effect and should preferably be included for calculation of a reliable normalization factor, with values ≤0.15 used as cut-off value under which addition of extra reference genes provides no benefit.

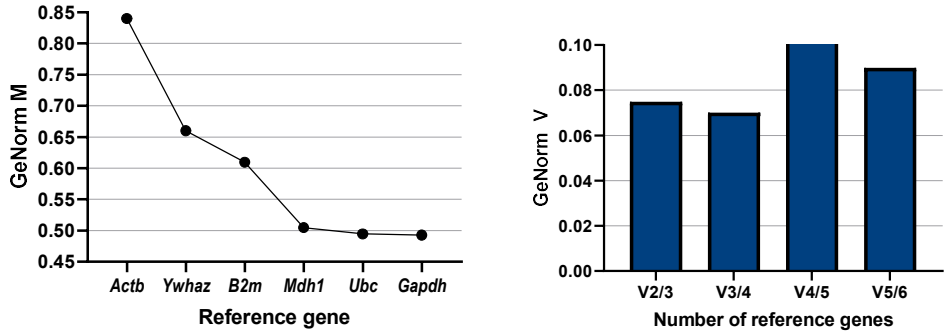

Supplementary Figure S3.1. GeNorm analysis (PR and PN1 Cohorts).
Demonstrates that 3 reference genes should be used in normalisation analysis based on the lowest GeNorm V value. The three most stable reference genes are *Mdh1, Ubc* and *Gapdh* with Genorm M values ≤0.5.

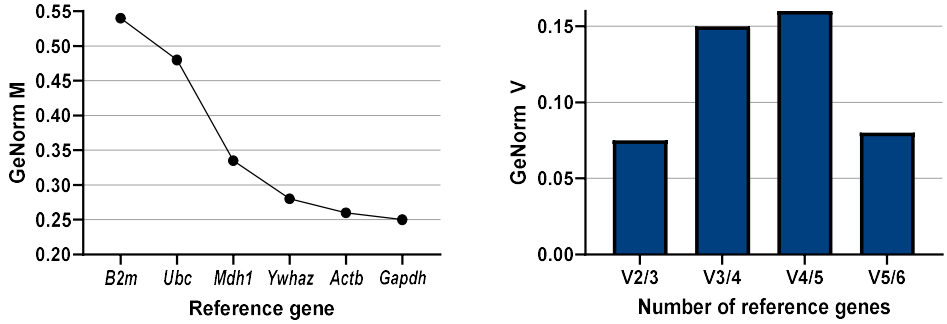

Supplementary Figure S3.2. GeNorm analysis (Placenta)
Demonstrates that 2 reference genes should be used in normalisation analysis based on the lowest sequential GeNorm V value. The two most stable reference genes are *Actb* and *Gapdh* with Genorm M values <0.5.

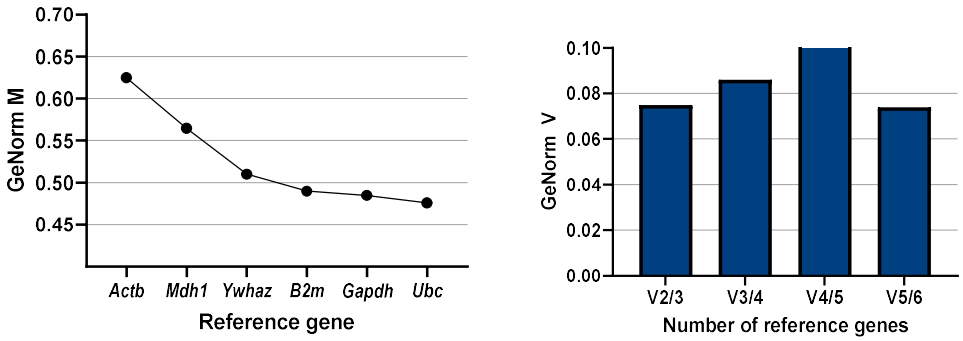

Supplementary Figure S3.3. GeNorm analysis (PR1 and PN2 Cohorts)
Demonstrates that 3 reference genes should be used in normalisation analysis based on the lowest sequential GeNorm V value. The three most stable reference genes are *B2m, Ubc* and *Gapdh* with Genorm M values <0.5.

Appendix 4. Representative PCR gels

All agarose gels were prepared with 2% agarose (w/v; Bioline, London, UK) in 1XTAE (Cleaver Scientific, Rugby, UK) with a 1:10,000 dilution of GelRed stain (VWR, Lutterworth, UK). Electrophoresis was performed at 100V for 2.5h. Ladder (base pair; bp) is annotated on each figure on the left. Sample group is given above lane. Negative (NEG) is qPCR assay water blank. Abbreviations: M, male; F, female; VEH, vehicle control; PIC, poly(I:C).

1. Chapter 3

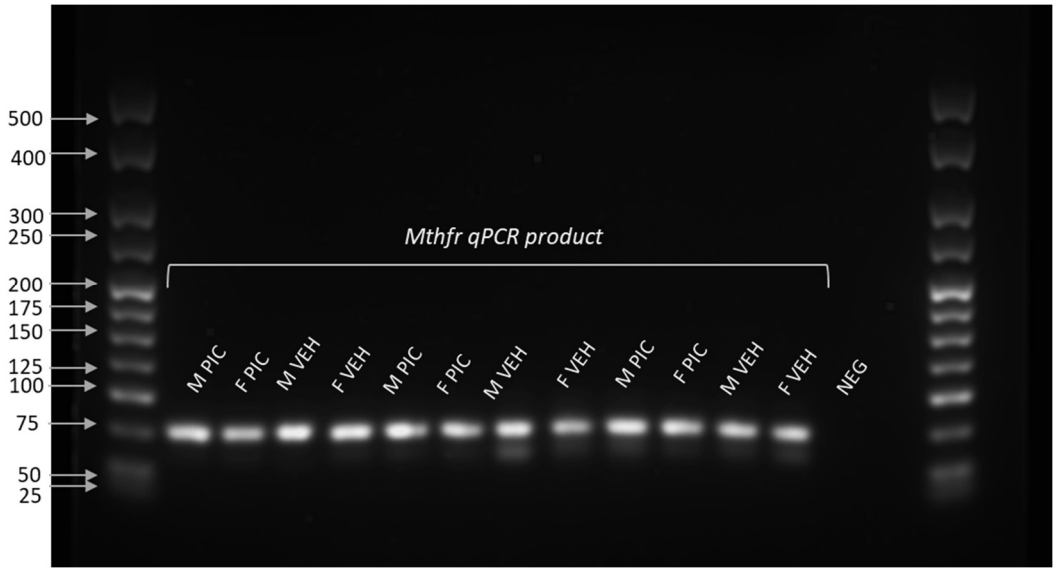

Supplementary Figure S4.1. Representative PCR gel for *Mthfr* (68bp)

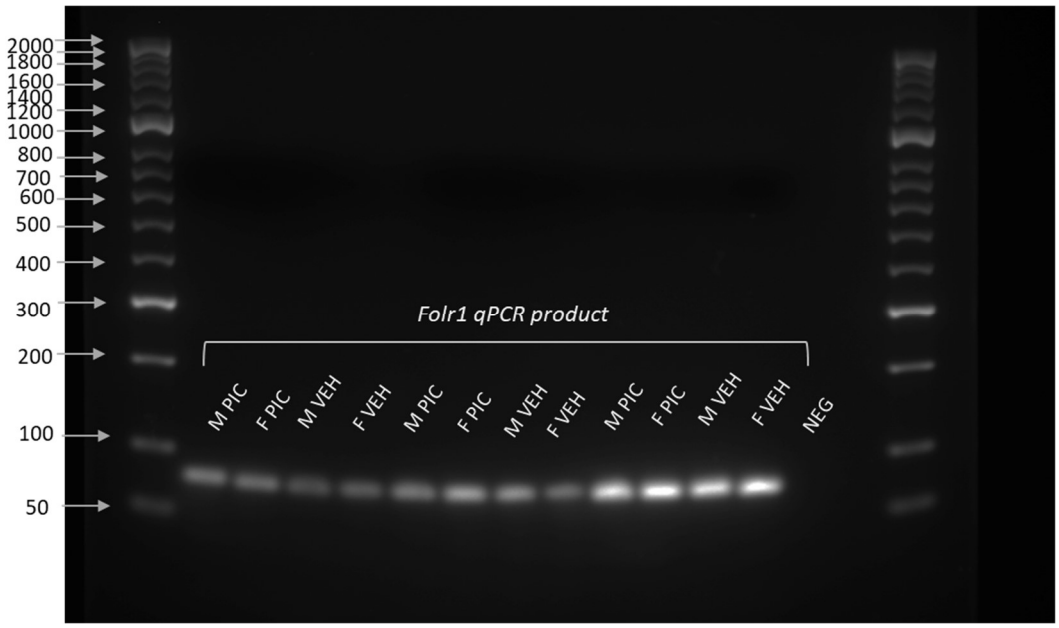

Supplementary Figure S4.2. Representative PCR gel for *Folr1* (70bp)

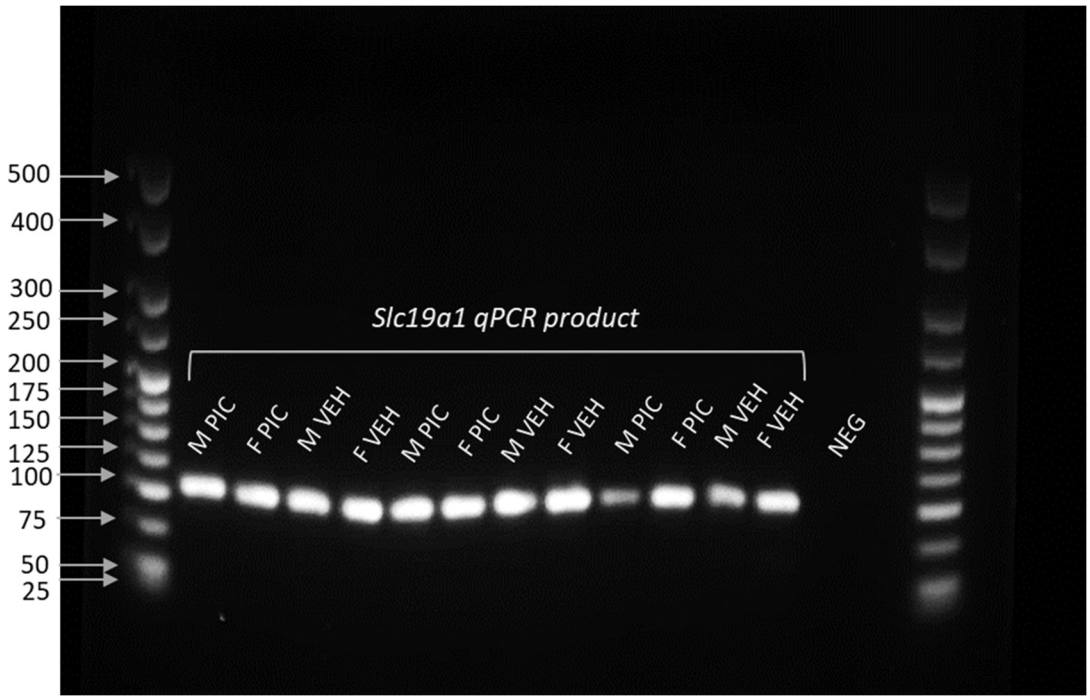

Supplementary Figure S4.3. Representative PCR gel for *Slc19a1* (95bp)

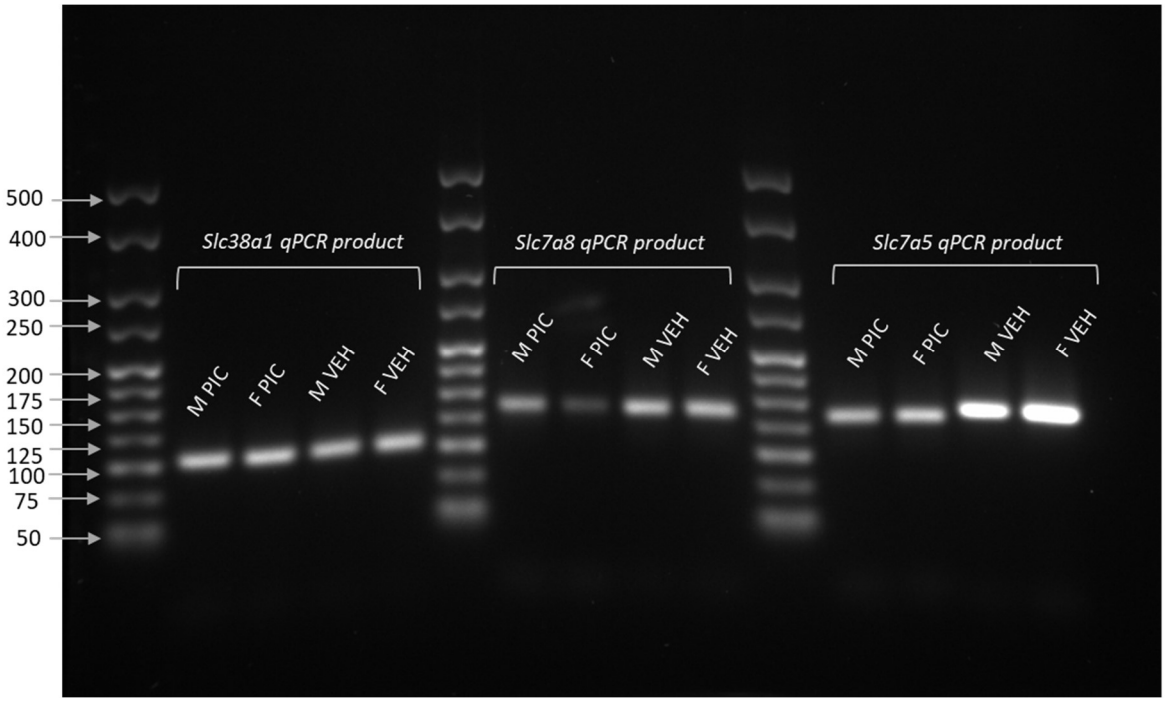

Supplementary Figure S4.4. Representative PCR gel for *Slc38a1* (97bp), *Slc7a8* (131bp) and *Slc7a5* (124bp)

2. Chapter 4

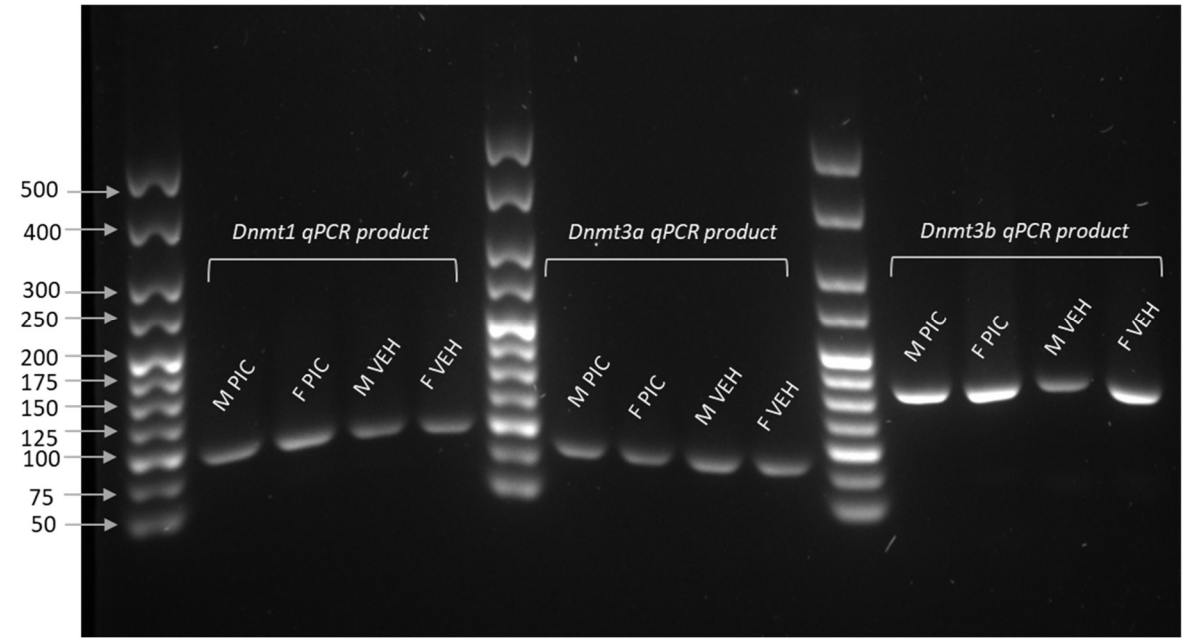

Supplementary Figure S4.5. Representative PCR gel for *Dnmt1* (81bp), *Dnmt3a* (61bp) *and Dnmt3b* (144bp)

3. Chapter 5

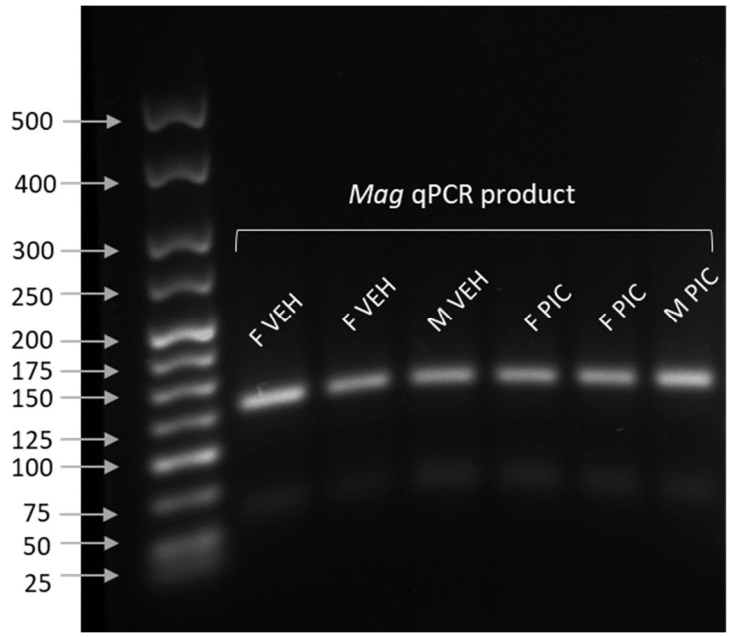

Supplementary Figure S4.6. Representative PCR gel for *Mag* (118bp)

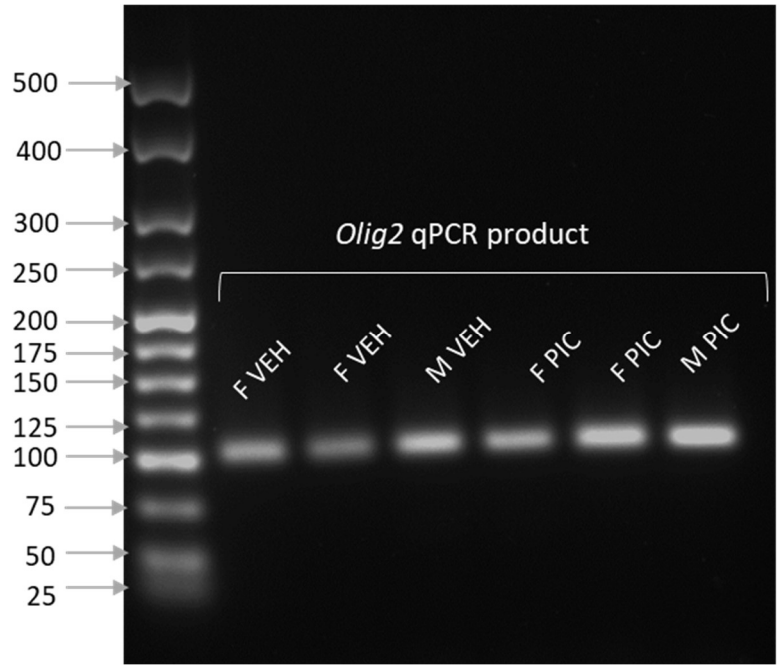

Supplementary Figure S4.7. Representative PCR gel for *Olig2* (92bp)

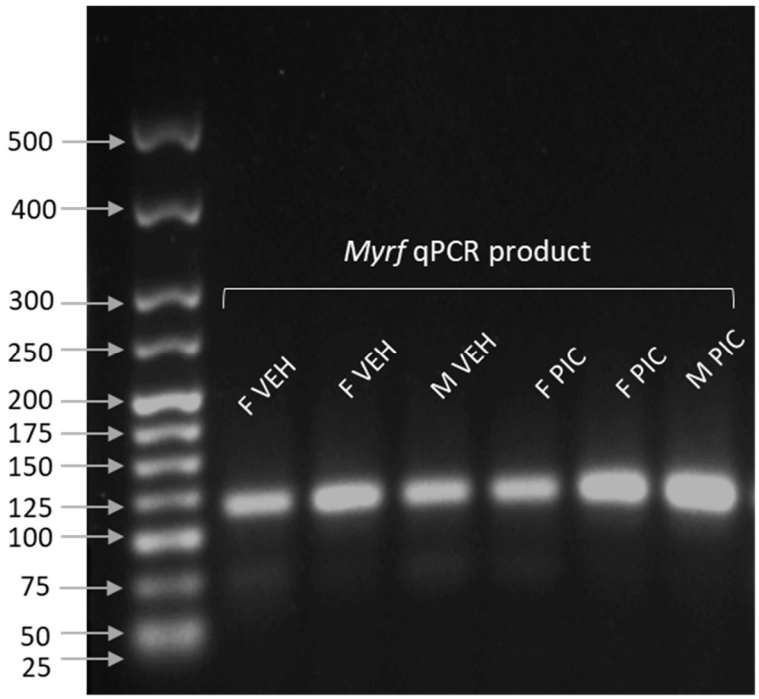

Supplementary Figure S4.8. Representative PCR gel for *Myrf* (102bp)

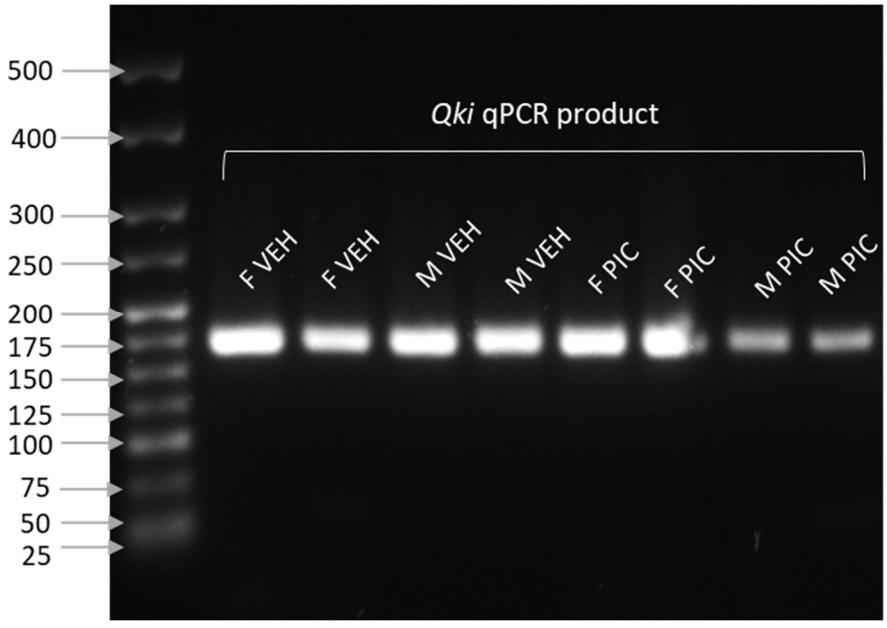

Supplementary Figure S4.9. Representative PCR gel for *Qki* (161bp)

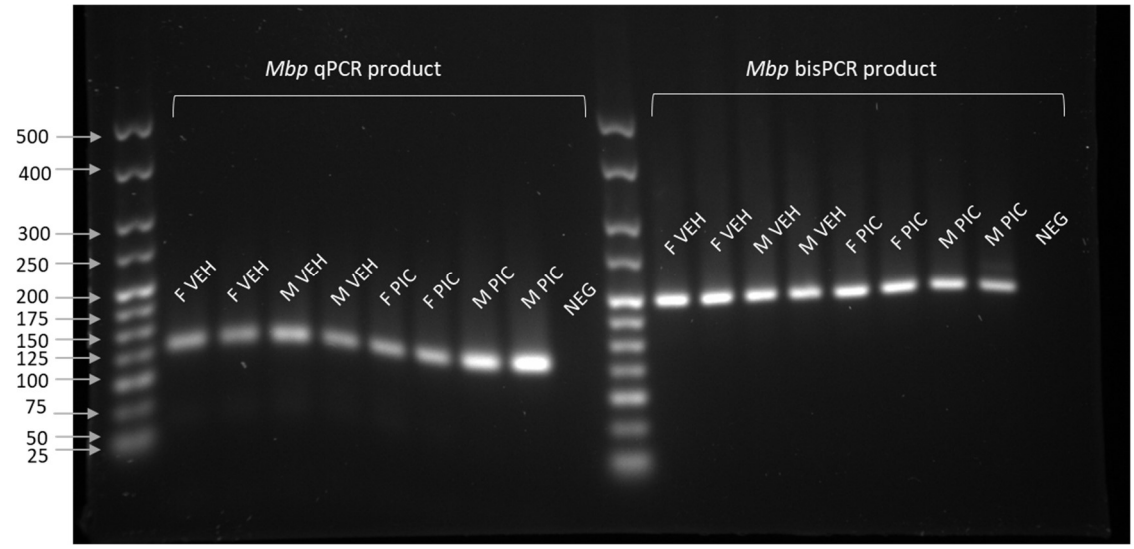

Supplementary Figure S4.10. Representative PCR gel for *Mbp*

Left: qPCR product (117bp); Right: bisPCR product (186bp). NEG, negative control.

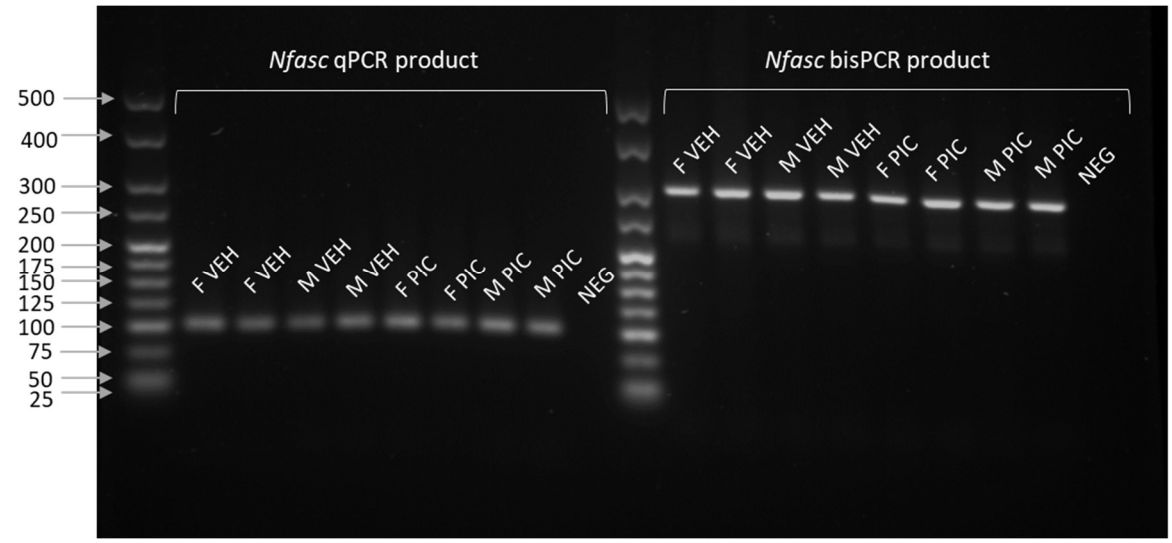

Supplementary Figure S4.11. Representative PCR gel for *Nfasc*

Left: qPCR product (96bp); Right: bisPCR product (286bp). NEG, negative control.

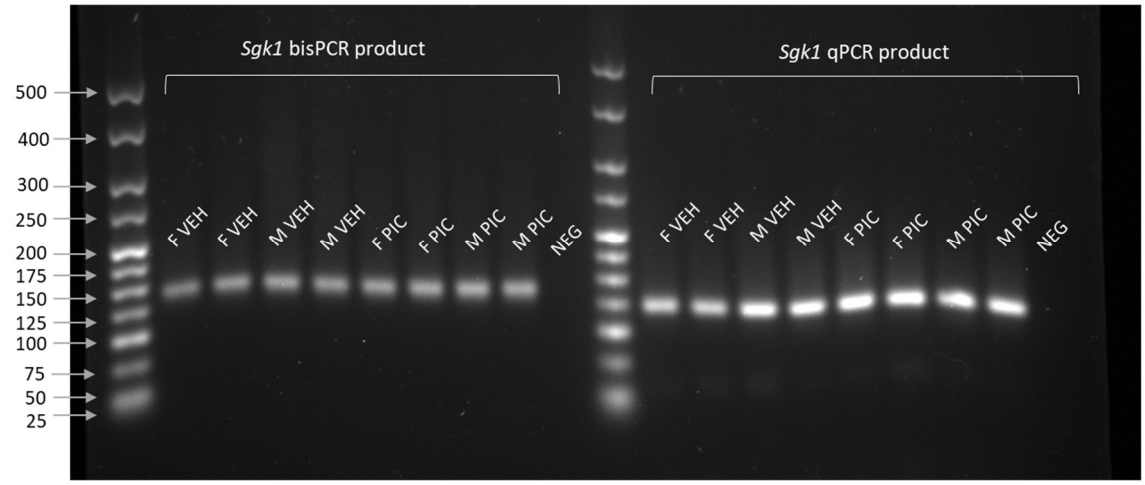

Supplementary Figure S4.12. Representative PCR gel for *Sgk1*

Left: bisPCR product (129bp); Right: qPCR product (114bp). NEG, negative control.

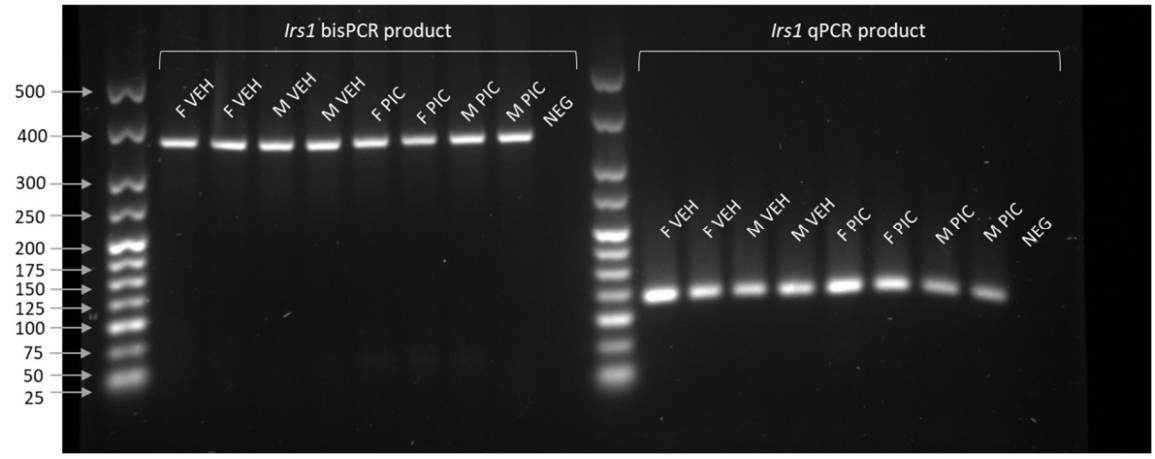

Supplementary Figure S4.13. Representative PCR gel for *Irs1*

Left: bisPCR product (344bp); Right: qPCR product (111bp). NEG, negative control.

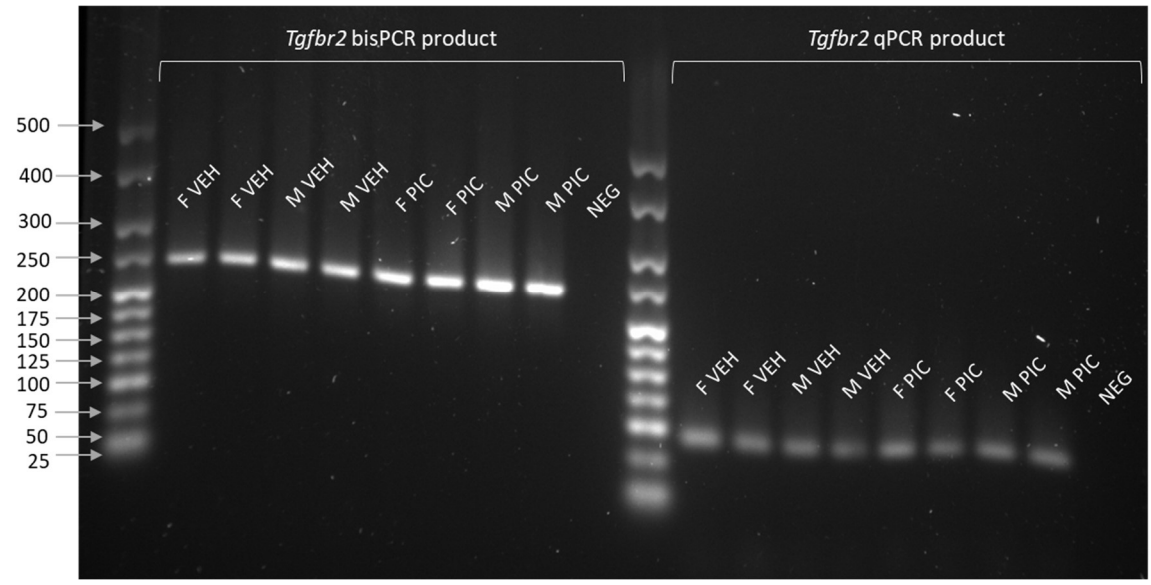

Supplementary Figure S4.14. Representative PCR gel for *Tgfbr2*

Left: bisPCR product (228bp); Right: qPCR product (81bp). NEG, negative control.

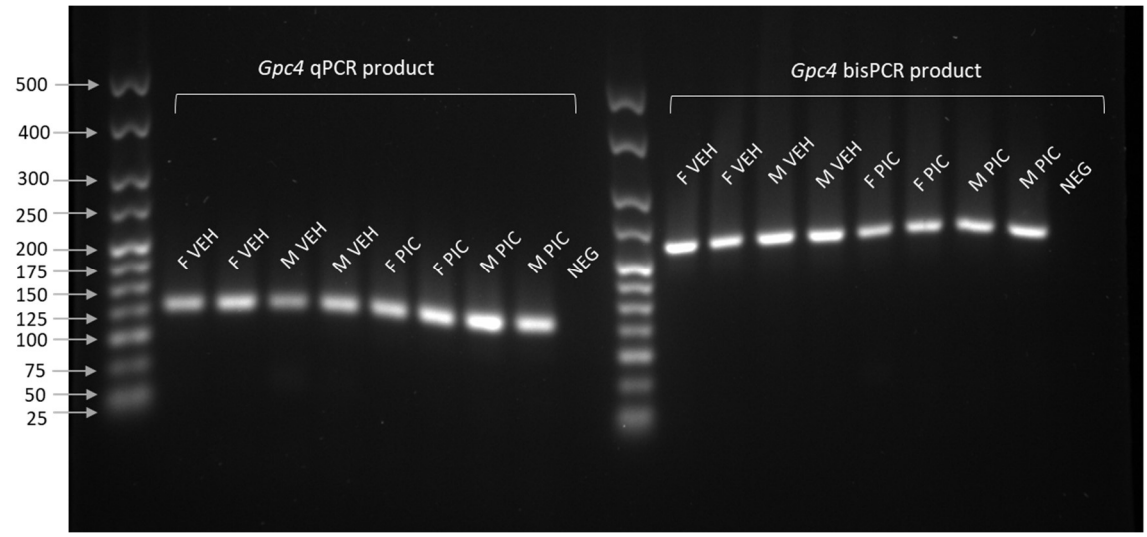

Supplementary Figure S4.15. Representative PCR gel for *Gpc4*

Left: qPCR product (117bp); Right: bisPCR product (210bp). NEG, negative control.

4. Chapter 6

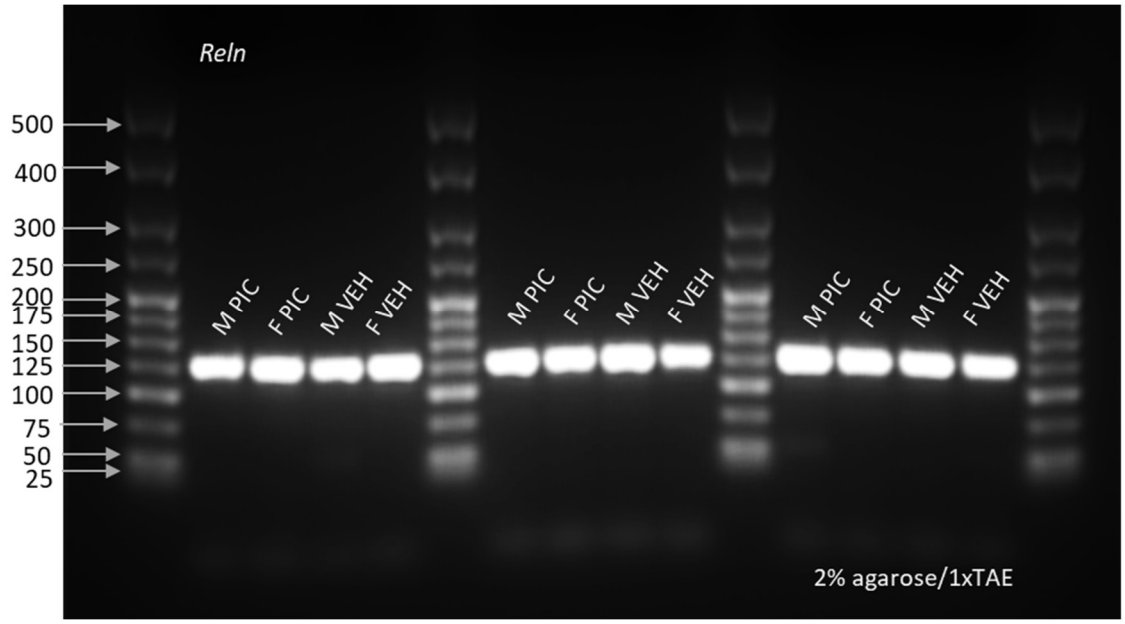

Supplementary Figure S4.16. Representative PCR gel for *Reln* (118bp)

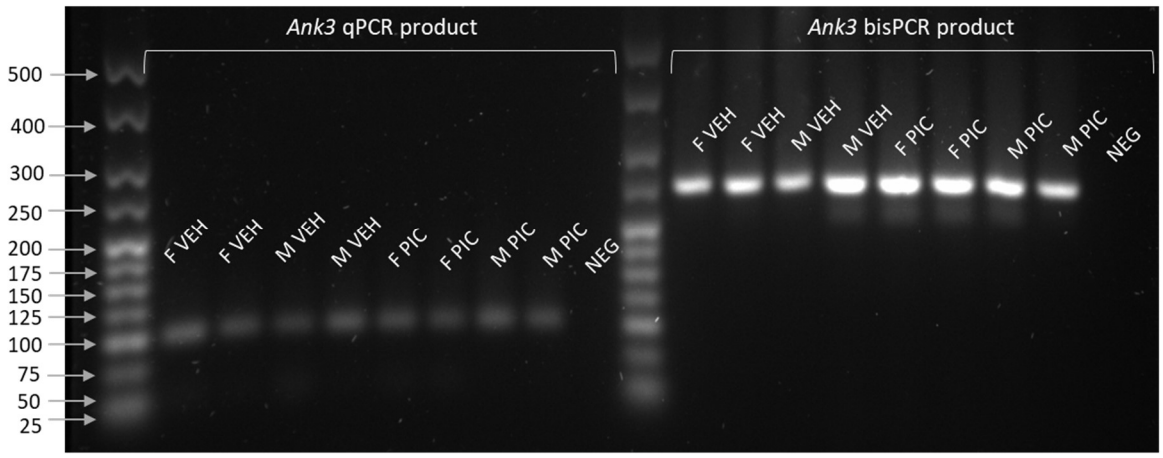

Supplementary Figure S4.18. Representative PCR gel for *Ank3*

Left: qPCR product (92bp); Right: bisPCR product (234bp). NEG, negative control.

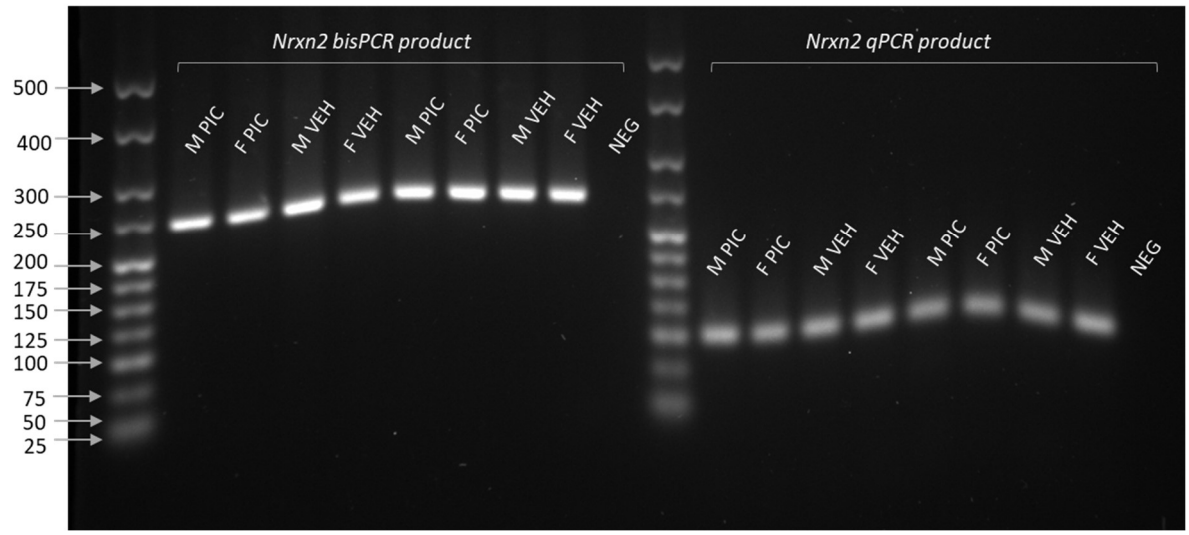

Supplementary Figure S4.19. Representative PCR gel for *Nrxn2*

Left: bisPCR product (231bp); Right: qPCR product (92bp). NEG, negative control.

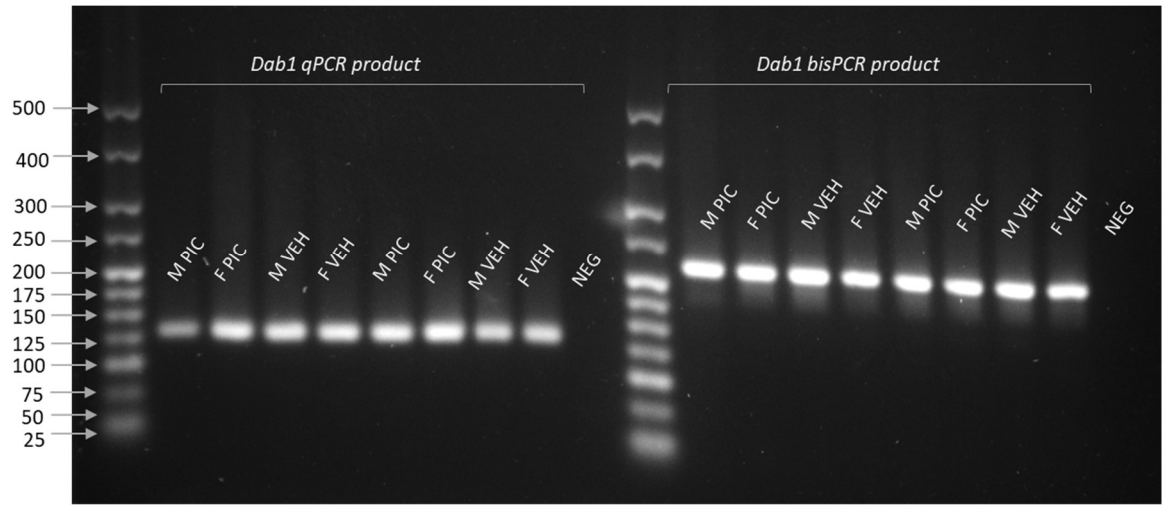

Supplementary Figure S4.20. Representative PCR gel for *Dab1*

Left: qPCR product (119bp); Right: bisPCR product (209bp). NEG, negative control.

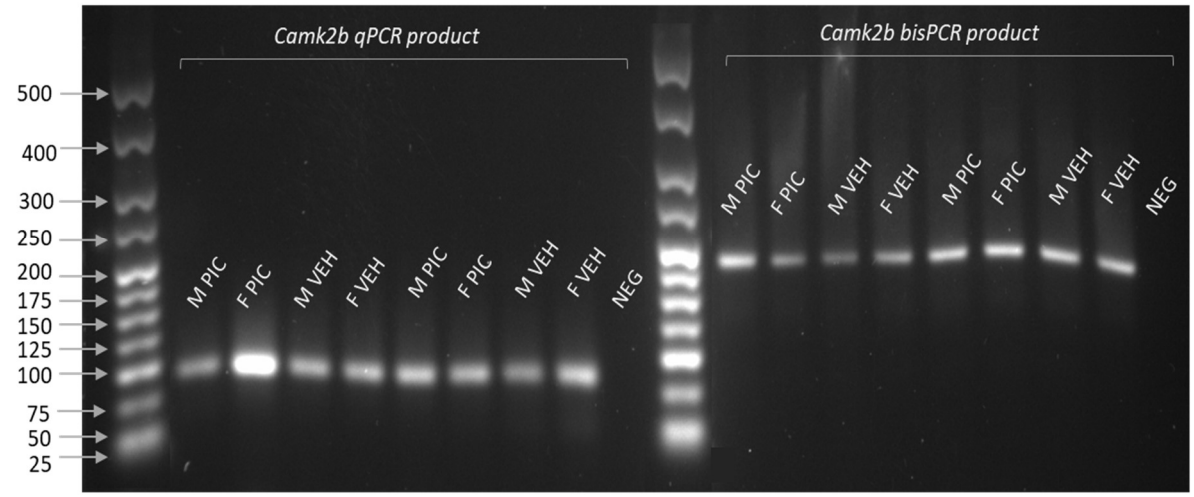

Supplementary Figure S4.21. Representative PCR gel for *Camk2b*

Left: qPCR product (88bp); Right: bisPCR product (197bp). NEG, negative control.

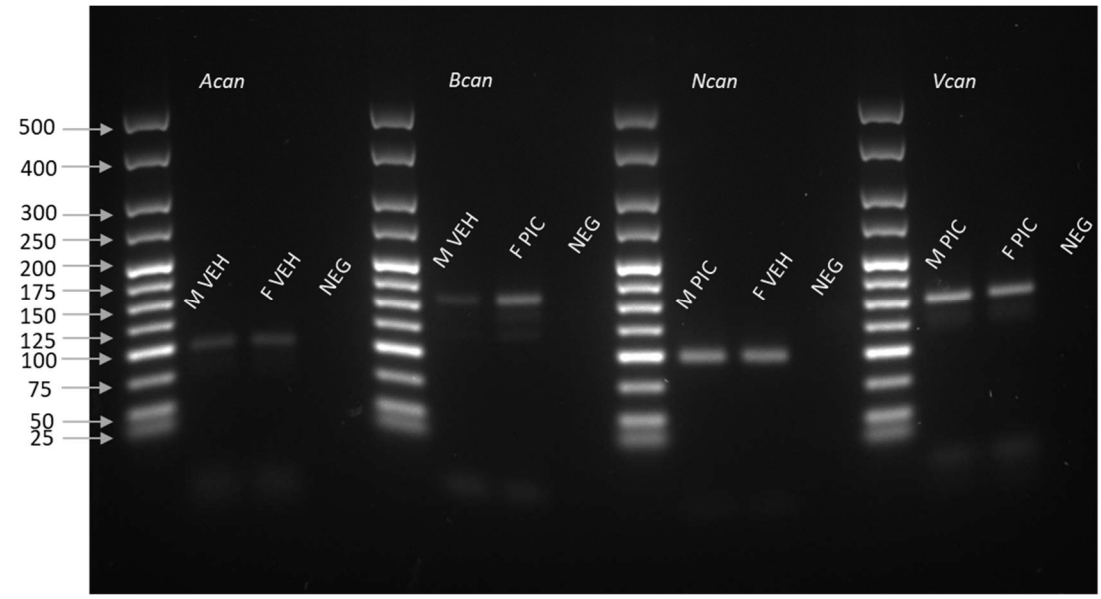

Supplementary Figure S4.22. Representative PCR gel for PNN component genes

From left to right: *Acan* qPCR product (90bp); *Bcan* qPCR product (144bp); *Ncan* qPCR product (89bp); *Vcan* qPCR product (146bp). NEG, negative control.

Appendix 5. DNMT Western optimisation

Supplementary Table S5.1. Summary of the anti-DNMT antibodies trailed

Antibody	Supplier details	Dilution and titre	Predicted molecular weight (kDa)	Figure reference
Mouse monoclonal anti-DNMT1 Antibody	sc-271729; Santa Cruz Biotechnology	1:1000 (0.2µg/mL)	~150-180	1
Mouse monoclonal anti-DNMT1 Antibody	60B1220.1; Novus Biologicals	1:500 (2µg/mL)	~150-180	2
Mouse monoclonal anti DNMT3a Antibody	sc-365769; Santa Cruz Biotechnology	1:100 (2µg/mL)	~100-125	3
Rabbit polyclonal anti DNMT3a Antibody*	GTX129126; GeneTex	1:500 (2µg/mL)	~100-125	4
Rabbit polyclonal anti DNMT3a Antibody	GTX129125; GeneTex	1:500 (2µg/mL)	~100-125	5
Rabbit polyclonal anti DNMT3b Antibody	GTX129127; GeneTex	1:500 (2µg/mL)	~90	6
Mouse monoclonal anti DNMT3b Antibody	sc-81252; Santa Cruz Biotechnology	1:200 (0.5µg/mL)	~90	7
Mouse monoclonal anti DNMT3b Antibody	sc-376043; Santa Cruz Biotechnology	1:100 (2µg/mL)	~90	8

*Antibody selected for validation

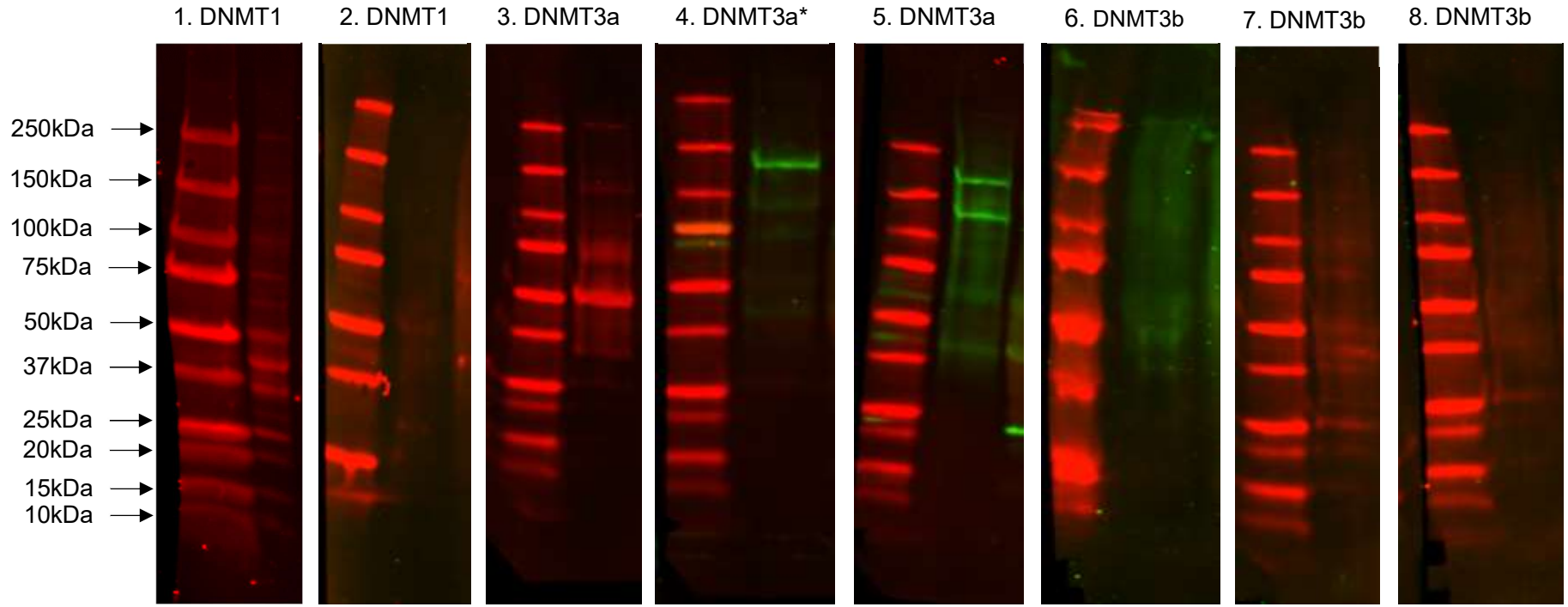

*This antibody produced a single band at the predicted molecular weight and was selected for downstream validations

Supplementary Figure S5.1. DNMT antibody optimisation
Western blots of the initial trials for each of the antibodies listed (Table S5.1) under standard conditions outlined in Chapter 3, Section 3.2.3.2, using the primary antibody dilutions in Table S5.1 and 50µg whole tissue lysate protein per lane. The only antibody that showed a single band of anticipated size, with no non-specific binding (lane 4) was the GeneTex rabbit polyclonal anti-Dnmt3a antibody (GTX126129) and this was therefore used for nuclear fraction validation.

Appendix 6. RRBS methods performed by Diagenode

1. Library preparation protocol

RRBS library preparation was performed by Diagenode, using the following methodology.

Each DNA sample, 100ng in 26µL nuclease-free water, was used to start library preparation. The gDNA was digested with the restriction enzyme MspI: 3µL enzyme buffer was mixed with 1µL MspI restriction enzyme and 4µL enzyme solution added to each sample to create a 30µL reaction volume, incubated at 37°C for 12h. End Preparation Reaction Mix was prepared by mixing 1µL each of the End Preparation Enzyme, spike-in controls (methylated and non-methylated) and dNTP mix. 4µL reaction mix was added to each sample and incubated in three consecutive 20min incubations on a thermal cycler at 30°C, 37°C and 75°C respectively. 5µL adaptors (selecting a different adaptor for each sample) was added to each sample, followed by 41µL Ligation Solution (prepared from 40µL Ligation Buffer + 1µL Ligase enzyme), to bring the final reaction volume to 80µL. The reaction mix was incubated on a thermal cycler for 20 min at 25°C and then 10min at 65°C, allowing for adaptor ligation.

Size selection was performed by adding 60µL AMPure XP Beads incubated for 15min at room temperature to allow adaptor-ligated fragments to bind the beads. The sample tubes were then placed in contact with a magnet for 5min to isolate the bead-bound sample, following which the supernatant was removed. Samples were washed twice with 100µL 80% ethanol and allowed to air dry for 5min at room temperature. Sample tubes were removed from the magnet and 25µL Resuspension Buffer was added and incubated for 5min to elute samples from the beads. The samples were then placed back on the magnet to capture the beads and the supernatant (containing the eluted adaptor-ligated sample) was removed into a clean tube and stored at -20°C for later use.

To quantify the concentrations of adaptor-ligated samples and thereby determine appropriate sample pooling ratios, 3µL each sample was mixed with 6µL nuclease-free water to create a sample dilution. The Quantification Mix was prepared for each sample from 5µL 2XMaster mix, 0.5µL primer mix and 1.5µL nuclease-free water. 7µL Quantification Mix was added to 3µL diluted sample in a qPCR tube. The tube was then loaded onto a thermal cycler and incubated shown in Table S6.1.

Table S6.1: PCR conditions for quantification of adaptor-ligated samples

Cycle step	Temperature (°C)	Time (min:seconds)	Cycles
Initial denaturation	98	3:00	1
Denaturation	95	0:15	
Annealing	60	0:30	25
Extension	72	0:30	

The adaptor-ligated samples were then pooled according to the mean of their Ct values using the RRBS automated pooling aid (https://www.diagenode.com/en/documents/rrbs-pooling-aid; Table S6.2). The prepared pool was then made up to 120µL volume with nuclease-free water.

Table S6.2: Adaptor-ligated sample pooling

Sample name	Adaptor I.D.	Ct mean	Volume sample in pool (µL)
FB4	32	5.215	17.00
FA4	28	4.67	11.65
FA1	17	4.63	11.33
FB3	31	4.55	10.72
FB2	30	4.49	10.28
FB1	29	4.425	9.83
FA3	26	4.345	9.30
FA2	24	4.04	7.53

The pool was processed through bead-based clean-up. 240µL AMPure XP Beads were added and incubated for 15min to allow binding of sample to beads. The sample tubes were then held to a magnet for 5min to isolate the bead-bound sample. The bead-bound samples were washed twice with 500µL 80% ethanol and then air dried for 10min. 36µL resuspension buffer was added and the samples were incubated off the magnet for 5min to allow elution of samples from the beads. The sample tubes were then placed back against the magnet to capture the beads and the supernatant-containing sample transferred to fresh tubes.

Bisulphite conversion was performed on the purified library pools. To begin with, 790µL BS Solubilization Buffer and 300µL BS Dilution Buffer were added to a tube containing BS Conversion Reagent and mixed at room temperature for 10min. 160µL of BS Reaction Buffer was then added and the whole solution mixed for a further 1min at room temperature. 117µL prepared solution was added to 33µL purified sample pool and incubated on a thermal cycler as indicated in Table S6.3.

Table S6.3: Library pool bisulphite conversion PCR incubation

Cycle step	Temperature (°C)	Time (min)	Cycles
Denaturation	95	01:00	20
Conversion	60	10:00	

600µL BS Binding Buffer was added to a BS spin column along with the bisulphite-converted pool. The columns were then centrifuged at full speed (10,000xg) for 30s. 100µL BS wash buffer was then added to the column and centrifuged at 10,000xg for 30s. 200µL desulphonation buffer was added, incubated at room temperature for 30min and then centrifuged at 10,000xg for 30s. Twice, 200µL BS wash buffer was added to the column and centrifuged at 10,000xg for 30s. The column was placed into a clean Eppendorf and 22µL Elution Buffer added, incubated for 2min at room temperature before centrifuging at 10,000xg for 30s to elute sample.

The bisulphite-converted pools were analysed by qPCR to establish an optimal amplification cycle for the Enrichment PCR prior to sequencing. For this purpose, a Reaction Mix was

prepared from 5µL 2XMaster mix, 0.5µL primers and 3.5µL water. 9µL prepared Reaction Mix was added to the well of a qPCR plate with 1µL bisulphite-converted library pool and incubated on a thermal cycler as per Table S6.4. The optimal amplification cycle for the enrichment PCR prior to sequencing is typically obtained as the 'Ct from the qPCR'– 1. The obtained Ct value for this library pool was 14 and hence the number of amplification cycles used for the Enrichment PCR was calculated as 13.

Table S6.4. qPCR protocol for determining optimal number of amplification cycles for a library pool

Cycle step	Temperature (°C)	Time (min:seconds)	Cycles
Initial denaturation	98	3:00	1
Denaturation	95	0:15	30
Annealing	60	0:30	
Extension	72	0:30	

Enrichment PCR was performed first by preparing the Amplification Mix, from 25µL 2XMethylTaq Plus Master mix, 2.5µL primer mix and 3.5µL water. This 31µL Amplification mix was added to 19µL bisulphite-converted library pool and incubated on a thermal cycler as described in Table S6.5.

Table S6.5. Optimal enrichment PCR protocol for the prepared library pool

Cycle step	Temperature (°C)	Time (min:seconds)	Cycles
Initial denaturation	95	5:00	1
Denaturation	98	0:20	13
Annealing	60	0:15	
Extension	72	0:45	
Final Extension	72	7:00	1

The amplified pool was then processed through bead-based sample clean-up. 50µL AMPure XP Beads were added to the amplified pools and incubated for 15min to bind sample to beads. The sample tubes were held against magnet for 5min to isolate bead-bound sample, followed by two washes with 100µL 80% ethanol and air drying for 10min. 15µL resuspension buffer was added and incubated off the magnet for 5min to elute sample from beads. The tubes were then held against magnet to capture the beads and the sample-containing supernatant (the final amplified library pool) was transferred to new tube.

The final prepared amplified library pool concentration was measured using the Qubit® dsDNA HS Assay Kit (Thermo Fisher Scientific, Waltham, USA) and the fragment profile checked by analysing 1µL of pool using the DNF-474 NGS fragment kit and Fragment Analyzer (Agilent; Supplementary Figure S6.1). The RRBS library pool was then sequenced in paired-end mode on an Illumina NovaSeq 3000/4000 (Illumina, San Diego, USA), generating 50 base reads (SE50).

Pool ID	Final pool concentration (ng/μL)	Size (bp)	Molar concentration (nM)
002_0218_P1	1.78	333	8.22

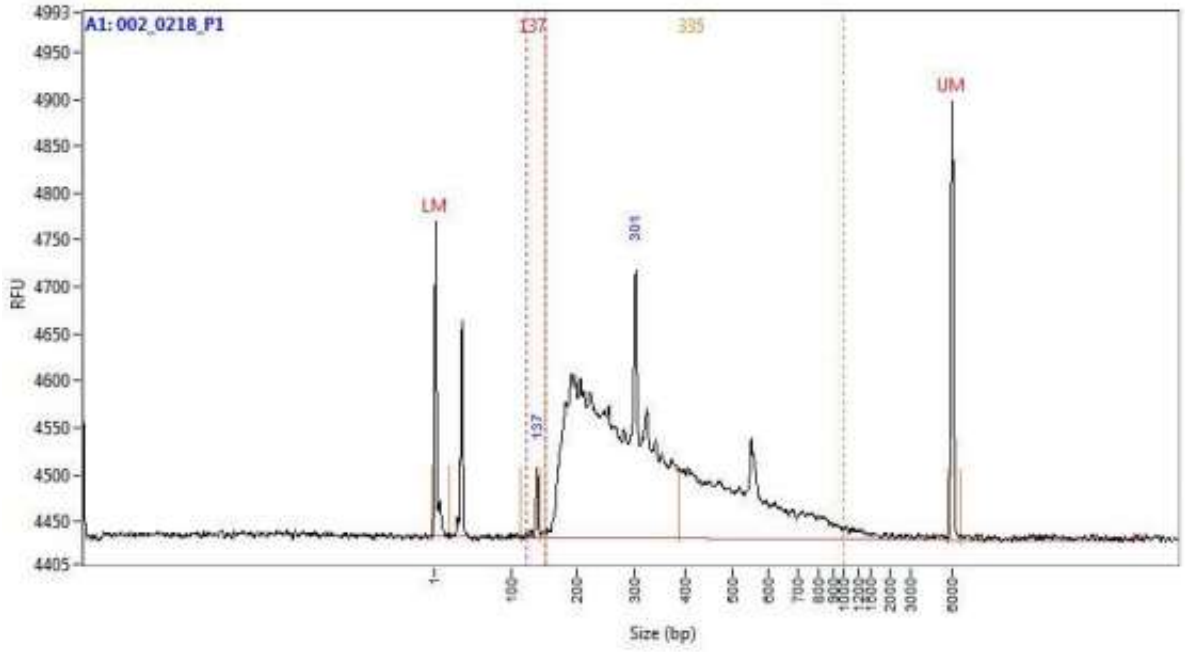

Supplementary Figure S6.1: Electropherogram of RRBS library pool
Top: table of results for pool concentration. Bottom: electropherogram showing various fragments from 100-1000bp for sequencing, with an average fragment size of 333bp.

2. Bioinformatics performed by Diagenode

Quality control of sequencing reads was performed using FastQC v0.11.8 (Andrews, 2010) and adapter removal was performed using Trim Galore! v0.4.1. (Krueger, 2012). Sequence reads were aligned to the rat reference genome Rn5.0 using Bismark v0.20.0 (Krueger and Andrews, 2011). Mapping efficiency was calculated by the number of uniquely mapped sequence reads divided by the total number of reads, with a mapping efficiency 55-70% expected due to sequence redundancy following bisulphite conversion.

The cytosine2coverage and bismark_methylation_extractor modules of Bismark were used to infer methylation state of all uniquely mapped cytosines. The reported cytosines were subsequently filtered to isolate only CpGs captured in all eight samples. The spike-in control sequences (methylated and non-methylated) were used to assess the bisulphite conversion rates to validate the efficiency of the bisulphite treatment, with ≤2% and ≥98% conversion rates considered acceptable, respectively (i.e., percentage of bases converted on the methylated spike-in control should theoretically be 0% while for the non-methylated control it should theoretically be 100%).

Methylkit v1.7.0 (Akalin et al., 2012) an R/Bioconductor package, was used for differential methylation analysis between the two sample groups. The dataset was filtered to discard low coverage CpGs (with coverage <10X in all samples as these reads are less accurate) and for notably high coverage CpGs (CpGs with coverage > 99.9th percentile were discarded as they are likely indicative of a PCR bias to these sequences). Following CpG filtering, a pairwise comparison was performed for ‘Poly(I:C)’ versus ‘Vehicle’ to identify differentially methylated individual CpGs (DMCs) and differentially methylated regions (DMRs), the latter comprising a sequence stretch of 1000bp. Logistic regression was used to compare methylation percentages between groups at each given DMC/DMR. After p-values were computed, the sliding window model (SLIM) was used to correct p-values to q-values, accounting for multiple comparison tests. Statistically significant DMCs and DMRs were identified with a pre-determined q-value cut-off ≤0.01 and a methylation difference ≥25%.

All DMCs and DMRs were annotated to genomic location with the R/Bioconductor package annotatr (Cavalcante and Sartor, 2017), with the refGene and CpG island annotations from UCSC Rat reference genome Rn5.0 (Lee et al., 2022). The annotation comprised two categories: (i) distance to a CpG island including: overlapping a known CpG island; within the 2000bp flanking region of a CpG island (CpG shore); within 2000bp of the CpG shore (CpG shelves) or outside these regions (open sea) and (ii) genic annotation (intergenic, exonic, intronic or promoter).

Using the genic location, DMCs and DMRs were mapped to genes in which promoter or gene body they were located. Gene ontology was performed to determine the enriched biological

processes, molecular functions and cellular components of the genes associated with DMCs using the R/Bioconductor topGO package (Alexa and Rahnenführer, 2022). Reactome Pathway enrichment analysis was also carried out with the R/Bioconductor package ReactomePA (Yu and He, 2016) which uses KEGG (Kyoto Encyclopedia of Genes and Genomes) terms for the analysis. Enrichment analyses was performed using hypergeometric model with FDR used to correct p-values.

Appendix 7. RRBS dataset

This is an online supplement available from: RRBS dataset - Google Sheets

(https://docs.google.com/spreadsheets/d/1hTZtFrqfn_0j9sOS76MDNZz3vefHfc8TL8_BjDOHxZc/edit#gid=0)

Supplementary Table S7.1: Compiled RRBS dataset. This Table represents the compiled data for every DMC and DMR mapped to a genic (exon/intron) or promoter region. The Table headings are as follows:

A: Chromosome – the chromosome containing the DMC/DMR

B: Start – The start position within that chromosome of the differential methylation

C: End - The end position within that chromosome of the differential methylation

D: Width – the length/width (bp) of the differential methylation, 1000=DMR; 1=DMC.

E: Pvalue – significance of the differential methylation

F: Qvalue – pvalue adjusted for multiple testing (q<0.01 was the threshold of this study)

G: meth.diff – the % difference in methylation (poly(I:C) relative to vehicle control; >25% was the cut-off for this study)

H: annot.start – the position within the chromosome where the genomic annotation starts

I: annot.end – the position within the chromosome where the genomic annotation ends

J: annot.width – the length/width (bp) of the annotation window

K. annot.strand – the stand (+ sense; - anti-sense) of DNA on which the annotation was performed

L: annot_ID – the genic or promoter I.D. (Rat Genome Rn5.0) to which the DMC/DMR was annotated

M: annot.tx_ID – the NCBI transcript I.D. to which the genomic annotation was mapped

N: annot.gene_ID - the corresponding NCBI gene I.D. to which the genomic annotation was mapped

O: annot.symbol – the corresponding official gene symbol for the NCBI transcript/gene I.D.

P: DMR_COUNT – total number of DMRs within the dataset mapped to that NCBI transcript/gene

Q: DMC_COUNT – total number of DMCs within the dataset mapped to that NCBI transcript/gene

R: SZ_GENE – presence of the mapped gene within the SZ_GENE dataset (1=present /0=absent)

S: SZ_EXP – presence of the mapped gene within the SZ_EXP dataset (1=present /0=absent)

T: SZ_ME – presence of the mapped gene within the SZ_ME dataset (1=present /0=absent)

U: SZ_EXOME – presence of the mapped gene within the SZ_EXOME dataset (1=present /0=absent)

V: SYSTEMATIC REVIEW – presence of the mapped gene within my systematic review (Woods et al., 2021) as having differential expression in a MIA model (1=present / 0=absent)

W: MIA_DMC – presence of the mapped gene within the MIA_DMC dataset (1=present / 0=absent)

X: MIA_DMR – presence of the mapped gene within the MIA_DMR dataset (1=present / 0=absent)

Appendix 8. RRBS Gene Ontology and KEGG analysis

This is an online supplement available from: RRBS GO and KEGG pathways - Google Sheets

(https://docs.google.com/spreadsheets/d/1WDh5IhnEPqiR93LV7W4dwEgMRqgGYbZrQLVumItFUUU/edit#gid=1689640407)

This appendix is formed of four Tables:

Supplementary Table S8.1: GeneOntology Biological Processes (GO_BP)

Supplementary Table S8.2: GeneOntology Molecular Function (GO_MF)

Supplementary Table S8.3: GeneOntology Cell component (GO_CC)

Supplementary Table S8.4: KEGG pathway enrichment (KEGG)

Gene ontology and KEGG pathway analysis was performed using R/Bioconductor. P-values were corrected as part of the FDR correction. Count represents the number of genes from the dataset enriched in a process.

Appendix 9. Analysis of the 54 interconnected differentially methylated genes

Supplementary Table S9.1: Summary table outlining the properties of the 54 interconnected gene nodes from the STRING network analysis

Gene	Overlaps with other datasets	Number of DMCs	DMC genomic location	Cell-type enrichment (brainRNAseq.org)	Tissue enrichment (Protein Atlas)	STRING GO	Pyrosequencing assay design (assay score)*
Agt	SZ _EXP MIA_DMR	3	Exonic Intronic	Astrocyte	Enriched in: liver Expressed in brain: Y	Neurodevelopment Neurogenesis/Gliogenesis	Y (79%)**
Ank3	**SZ_GENE MIA_DMC MIA_DMR**	**21**	**Exonic Intronic**	**Oligodendrocyte/ Neuron**	**Enriched in: low specificity Expressed in brain: Y**	**Neurodevelopment Neurogenesis/Gliogenesis Cell adhesion**	**Y (65%)**
Ar	SZ_GENE SZ_EXOME MIA_DMC MIA_DMR	4	Exonic Intronic	Neuron	Enriched in: liver Expressed in brain: Y	-	-
Bcl11b	SZ_GENE MIA_DMR	26	Exonic Intronic	Neuron	Enriched in: brain, lymphoid, skin Expressed in brain: Y	Neurodevelopment Neurogenesis/Gliogenesis	Y (67%)**
Camk2b	**SZ_GENE SZ_EXOME MIA_DMR**	**30**	**Exonic Intronic**	**Neuron**	**Enriched in: brain, skeletal muscle Expressed in brain: Y**	**Neurodevelopment Neurogenesis/Gliogenesis Inflammation/stress Glutamatergic signalling**	**Y (82%)**
Celf4	SZ _ME MIA_DMR	21	Exonic Intronic	Neuron	Enriched in: brain Expressed in brain: Y	-	-
Chrna4	SZ_GENE MIA_DMR	4	Exonic Intronic	Neuron	Enriched in: brain, liver Expressed in brain: Y	-	-
Cit	SZ_EXOME MIA_DMR	8	Exonic Intronic	Neuron	Enriched in: brain Expressed in brain: Y	Neurodevelopment Neurogenesis/Gliogenesis	N (>100bp)

Gene	Overlaps with other datasets	Number of DMCs	DMC genomic location	Cell-type enrichment (brainRNAseq.org)	Tissue enrichment (Protein Atlas)	STRING GO	Pyrosequencing assay design (assay score)*
Col16a1	SZ_EXP MIA_DMR	7	Exonic Intronic	Astrocyte	Enriched in: low specificity Expressed in brain: Y	Cell adhesion	N (>100bp)
Dab1	**SZ_EXP SZ_EXOME MIA_DMR**	**6**	**Promoter Intronic**	**Neuron/Astrocyte**	**Enriched in: brain and intestine Expressed in brain: Y**	**Neurodevelopment Neurogenesis/Gliogenesis Glutamatergic signalling**	**Y (71%)**
Dab2ip	SZ_EXOME MIA_DMR	8	Promoter Intronic	Endothelial	Enriched in: low specificity Expressed in brain: Y	Neurodevelopment Neurogenesis/Gliogenesis	N (Not assayable)
Egr2	SZ_GENE MIA_DMR	*5*	Exonic	Microglia	Enriched in: thyroid gland Expressed in brain: Y	Neurodevelopment Neurogenesis/Gliogenesis Cell adhesion	N (58%)
Fmr1	SZ_EXP SZ_EXOME MIA_DMR	12	Exonic Intronic	Astrocyte	Enriched in: low specificity Expressed in brain: Y	Neurodevelopment Neurogenesis/Gliogenesis Glutamatergic signalling	N (too CpG rich)
Gabbr1	SZ_GENE SZ_EXOME MIA_DMR	5	Exonic Intronic	Astrocyte	Enriched in: low specificity Expressed in brain: Y	-	-
Gli1	SZ_EXOME MIA_DMR	5	Exonic	Astrocyte	Enriched in: cervix Expressed in brain: Y	Neurodevelopment	N (Not assayable)
Gpc4	**SZ_EXOME MIA_DMR**	**3**	**Promoter Intronic**	**Astrocyte**	**Enriched in: low specificity Expressed in brain: Y**	**Cell adhesion Glutamatergic signalling**	**Y (83%)**
Grik1	SZ_EXOME MIA_DMR	6	Intronic	Neuron	Enriched in: brain, adrenal gland, retina Expressed in brain: Y	Inflammation/stress Neurodevelopment Glutamatergic signalling	Y (70%)**

Gene	Overlaps with other datasets	Number of DMCs	DMC genomic location	Cell-type enrichment (brainRNAseq.org)	Tissue enrichment (Protein Atlas)	STRING GO	Pyrosequencing assay design (assay score)*
Grin2a	SZ_GENE SZ_ME SZ_EXOME MIA_DMR SYSTEMATIC REVIEW	8	Intronic	Neuron	Enriched in: brain Expressed in brain: Y	Inflammation/stress Neurodevelopment Glutamatergic signalling Cell adhesion Inflammation/stress	N (Not assayable)§
Grin2c	SZ_GENE MIA_DMR	9	Exonic Intronic	Astrocyte	Enriched in: brain, salivary gland, heart Expressed in brain: Y	Inflammation/stress Neurodevelopment Glutamatergic signalling Cell adhesion	N (59%)
Grin2d	SZ_GENE MIA_DMR	6	Exonic Intronic	Neuron	Enriched in: brain Expressed in brain: Y	Inflammation/stress Neurodevelopment Glutamatergic signalling Cell adhesion	N (59%)
Igsf21	SZ_ME MIA_DMC MIA_DMR	12	Exonic Intronic	OPC	Enriched in: brain Expressed in brain: Y	Neurodevelopment Glutamatergic signalling	Y (66%)**
Irs1	**SZ_ME SZ_EXOME MIA_DMR**	**5**	**Exonic Intronic**	**Neuron**	**Enriched in: low specificity Expressed in brain: Y**	**Inflammation/stress**	**Y (67%)**
Itpr1	SZ_ME SZ_EXOME MIA_DMC MIA_DMR	15	Exonic Intronic	Neuron	Enriched in: low specificity Expressed in brain: Y	-	-
Kcnj6	SZ_EXP SZ_MA MIA_DMC MIA_DMR	6	Exonic Intronic	Neuron	Enriched in: brain, pituitary Expressed in brain: Y	-	-

Gene	Overlaps with other datasets	Number of DMCs	DMC genomic location	Cell-type enrichment (brainRNAseq.org)	Tissue enrichment (Protein Atlas)	STRING GO	Pyrosequencing assay design (assay score)*
Lrp4	SZ_EXOME MIA_DMR	3	Exonic	Astrocyte	Enriched in: brain,skin Expressed in brain: Y	Neurodevelopment Neurogenesis/Gliogenesis	Y (>100bp)
Mag	SZ_GENE SYSTEMATIC REVIEW	4	Exonic Intronic	Oligodendrocyte	Enriched in: brain Expressed in brain: Y	Neurodevelopment Neurogenesis/Gliogenesis Cell adhesion	Y (78%)***§
Maml3	SZ_EXOME MIA_DMC MIA_DMR	6	Exonic Intronic	Microglia	Enriched in: low specificity Expressed in brain: Y	-	-
Mbp	**SZ_EXOME SZ_ME MIA_DMR SYSTEMATIC REVIEW**	**12**	**Exonic Intronic**	**Oligodendrocyte**	**Enriched in: brain Expressed in brain: Y**	**Neurodevelopment Neurogenesis/Gliogenesis Cell adhesion**	**Y (85%)**
Med12	SZ_GENE SZ_ME	4	Promoter	Astrocyte	Enriched in: low specificity Expressed in brain: Y	Neurodevelopment Neurogenesis/Gliogenesis	N (57%)
Mmp9	SZ_GENE MIA_DMR SYSTEMATIC REVIEW	6	Exonic	Microglia	Enriched in: bone marrow, lymphoid Expressed in brain: Y	Cell adhesion	N (Not assayable)
Nfasc	**SZ_EXOME MIA_DMC MIA_DMR**	**32**	**Exonic Intronic**	**Oligodendrocyte**	**Enriched in: brain Expressed in brain: Y**	**Neurodevelopment Neurogenesis/Gliogenesis Cell adhesion**	**Y (76%)**
Nfkb1	MIA_DMR SYSTEMATIC REVIEW	4	Exonic Intronic	Microglia	Enriched in: low specificity Expressed in brain: Y	Inflammation/stress	N (50%)
Nr2e1	SZ_ME MIA_DMC MIA_DMR	3	Intronic	Astrocyte	Enriched in: brain, choroid plexus, retina Expressed in brain: Y	Neurodevelopment Neurogenesis/Gliogenesis Glutamatergic signalling	N (>100bp)

Gene	Overlaps with other datasets	Number of DMCs	DMC genomic location	Cell-type enrichment (brainRNAseq.org)	Tissue enrichment (Protein Atlas)	STRING GO	Pyrosequencing assay design (assay score)*
Nr4a2	SZ_GENE MIA_DMC MIA_DMR SYSTEMATIC REVIEW	7	Exonic Intronic	Microglia	Enriched in: adrenal gland, bone marrow, ovary Expressed in brain: Y	Neurodevelopment Neurogenesis/Gliogenesis	N (>100bp)
Nrxn2	**SZ_ME SZ_EXOME MIA_DMC MIA_DMR**	**17**	**Exonic Intronic**	**Neuron**	**Enriched in: brain Expressed in brain: Y**	**Neurodevelopment Cell adhesion**	**Y (71%)**
Ntrk2	SZ_GENE SZ_ME SZ_EXOME MIA_DMC MIA_DMR	11	Intronic	Astrocyte	Enriched in: brain, parathyroid gland Expressed in brain: Y	Neurodevelopment Neurogenesis/Gliogenesis Glutamatergic signalling	N (5%)
Ptprs	SZ_ME SZ_EXOME MIA_DMR	10	Exonic Intronic	Neuron/Astrocyte	Enriched in: low specificity Expressed in brain: Y	Neurodevelopment Neurogenesis/Gliogenesis Cell adhesion	N (Too many CpGs)
Ptprz1	SZ_GENE MIA_DMR	2	Intronic	Astrocyte	Enriched in: brain, skin Expressed in brain: Y	Neurodevelopment Neurogenesis/Gliogenesis	N (>100bp)
Rasal1	SZ_EXOME MIA_DMR	7	Exonic Intronic	Oligodendrocyte	Enriched in: parathyroid gland, salivary gland Expressed in brain: Y	Neurodevelopment Neurogenesis/Gliogenesis	N (>100bp)
Reln	SZ_MIA SZ_EXOME MIA_DMR SYSTEMATIC REVIEW	*5*	Exonic Intronic	Neuron	Enriched in: brain Expressed in brain: Y	Neurodevelopment Neurogenesis/Gliogenesis Glutamatergic signalling Cell adhesion	N (>100bp)[§]

Gene	Overlaps with other datasets	Number of DMCs	DMC genomic location	Cell-type enrichment (brainRNAseq.org)	Tissue enrichment (Protein Atlas)	STRING GO	Pyrosequencing assay design (assay score)*
Runx2	SZ_ME MIA_DMC MIA_DMR	10	Promoter Intronic	Microglia	Enriched in: salivary gland Expressed in brain: Y	Neurodevelopment Neurogenesis/Gliogenesis	N (53%)
Sgk1	**SZ_GENE MIA_DMC MIA_DMR**	**8**	**Promoter Exonic Intronic**	**Microglia**	**Enriched in: parathyroid gland Expressed in brain: Y**	**Neurodevelopment Neurogenesis/Gliogenesis Inflammation/stress**	**Y (63%)**
Slc17a7	SZ_GENE SYSTEMATIC REVIEW	4	Exonic Intronic	Neuron	Enriched in: brain, retina Expressed in brain: Y	Neurodevelopment Glutamatergic signalling	N (Not assayable)
Smad1	MIA_DMC MIA_DMR SYSTEMATIC REVIEW	5	Intronic	Neuron/Astrocyte	Enriched in: low specificity Expressed in brain: Y	Neurodevelopment	N (>100bp)
Sox10	SZ_GENE SZ_ME SZ_EXOME MIA_DMR	5	Promoter Exonic Intronic	Oligodendrocyte	Enriched in: brain, salivary gland Expressed in brain: Y	Neurodevelopment Neurogenesis/Gliogenesis	Y (78%)**
Srcin1	SZ_ME SZ_EXOME MIA_DMR	*18*	Exonic Intronic	Oligodendrocyte	Enriched in: brain Expressed in brain: Y	Neurodevelopment Neurogenesis/Gliogenesis Cell adhesion	N (>100bp)
Srrm4	SZ_ME SZ_EXOME MIA_DMR	11	Intronic	Neuron	Enriched in: brain, retina Expressed in brain: Y	Neurodevelopment Neurogenesis/Gliogenesis	N (Not assayable)
Syp	SZ_EXOME SYSTEMATIC REVIEW	2	Exonic	Neuron	Enriched in: brain, pituitary, retina Expressed in brain: Y	Glutamatergic signalling	N (>100bp)
Tenm2	SZ_EXOME MIA_DMR	13	Intronic	Neuron	Enriched in: brain, heart Expressed in brain: Y	Neurodevelopment Neurogenesis/Gliogenesis Cell adhesion	N (>100bp)

Gene	Overlaps with other datasets	Number of DMCs	DMC genomic location	Cell-type enrichment (brainRNAseq.org)	Tissue enrichment (Protein Atlas)	STRING GO	Pyrosequencing assay design (assay score)*
Tenm3	SZ_ME SZ_EXP MIA_DMC MIA_DMR	11	Exonic Intronic	Neuron	Enriched in: brain, placenta Expressed in brain: Y	Neurodevelopment Neurogenesis/Gliogenesis Cell adhesion	N (Not assayable)
Tgfbr2	**SZ_EXOME MIA_DMR**	**4**	**Intronic**	**Microglia**	**Enriched in: low specificity Expressed in brain: Y**	**Neurodevelopment Inflammation/stress**	**Y (71%)**
Timp2	SZ_EXP SZ_EXOME	4	Exonic Intronic	Neuron	Enriched in: ovary Expressed in brain: Y	Neurodevelopment Neurogenesis/Gliogenesis Cell adhesion	N (57%)
Tle3	SZ_GENE SZ_EXOME MIA_DMR	3	Exonic Intronic	Microglia	Enriched in: bone marrow Expressed in brain: Y	-	-
Trank1	SZ_ME SZ_GENE	4	Exonic Intronic	Neuron	Enriched in: fallopian tube Expressed in brain: Y	-	-

*Pyrosequencing assay design software limitations: 1) the imported sequence between CpGs must be ≤100bp; 2) too CpG dense regions will not be able to design specific assay (too CpG rich); 3) occasionally (due to sequence/CpG distances) the CpGs of interest will not be assayable in a single pyrosequencing assay, due to sample constraints, these sequences were denoted 'non assayable' for the purpose of this study; 4) to limit optimisation required, any assays soring <60% were deemed unacceptable. **To minimise the number of candidate genes for downstream analysis to 10, the changes in methylation in the genes which passed assay design were assessed. The highlighted genes were excluded for having bi-directional (increases and decreases) methylation changes in the same region, making interpretation of their outcomes challenging, these genes were hence excluded.***This gene was removed as two myelin genes (*Mag* and *Mbp)* were present in the final gene list, however *Mag* had the lower scoring assay and the lesser overlap with previous studies and hence was excluded. §These genes were not analysed for methylation changes, but their expression has been analysed. N and Y denotes 'no' and 'yes' respectively.

The top 10 final selected genes are outlined in bold.

Appendix 10. Optimisation of nucleic acid extraction

1. TRIzol™ extraction (Invitrogen, Loughborough, UK)

The samples stored in RNAlater were thawed on ice and excess RNAlater solution removed by aspiration. Sample was lysed using a pestle and mortar in 400µL TRIzol™ reagent. The sample was then incubated on ice for 15min. 80µL chloroform (Sigma-Aldrich, Gillingham, UK) was added and the mixture vortexed and incubated at room temperature for 15min before centrifugation at 12,000xg at 4°C for 15min. At this stage three phases formed: a lower red phenol phase (protein) a white interphase (DNA) and an upper colourless liquid phase (RNA). The upper phase (RNA) was carefully removed (the remaining 2 phases incubated on ice). To the collected RNA phase, isopropyl alcohol (Fisher, Loughborough, UK) was added in a 1:1 volume ratio. The mix was vortexed and incubated on ice for 15 min followed by centrifugation at 12,000xg at 4°C for 10min. The RNA was precipitated into a pellet and the supernatant was removed. 1mL 75% ethanol was added to the pellet and vortexed before incubating on ice for 15min, followed by a 5min centrifugation at 7,500xg at 4°C. The ethanol was removed and the pellet air dried for 5 min before addition 20µL RNAse-free water to resuspend the RNA. The protein-DNA phases were then vortexed and processed using the DNeasy blood and tissue kit (QIAGEN, Manchester, UK) as described in Chapter 3, Section 3.2.1.1.

This method resulted in high concentration/quality RNA but very poor quality gDNA yield (Supplementary Figure S10.1).

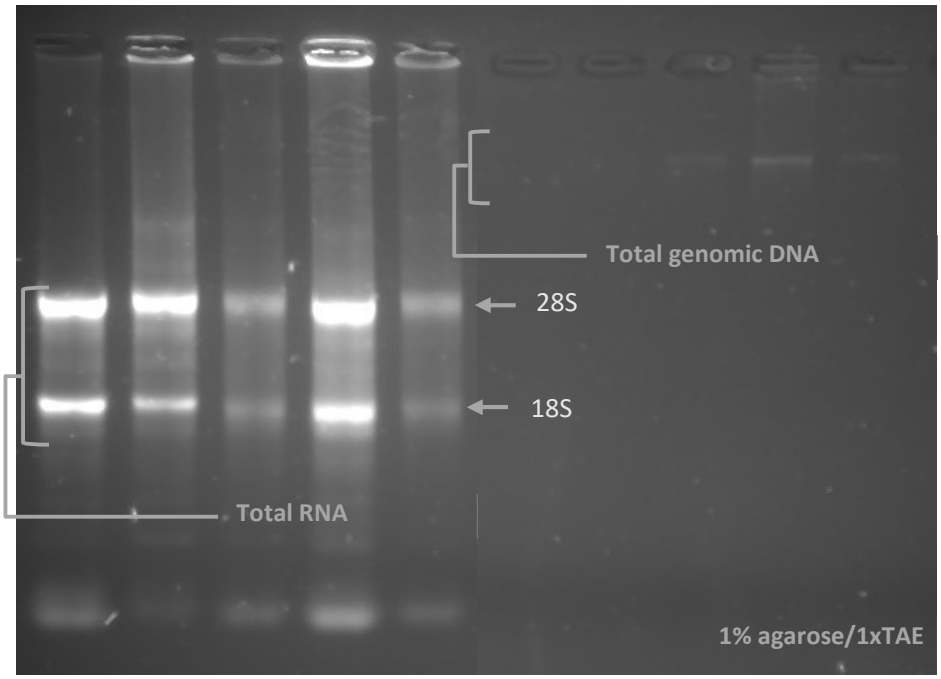

Supplementary Figure S10.1. Representative DNA and RNA quality gel (PN2 - TRIZOL)
1%agarose/1XTAE with 1:10,000 Gel Red stain (VWR, Lutterworth, UK). RNA samples loaded at 800ng/well and gDNA samples loaded at 50ng/well. Electrophoresis performed in 1XTAE buffer at 120V for approximately 45min. Gel imaged by Bio-rad Gel Doc XR+ (Watford, UK) under UV fluorescence with a default exposure time.

2. GenElute-E Single Spin tissue DNA kit (Merck, Gillingham, UK)

Samples stored in RNAlater were thawed on ice and excess RNAlater solution removed by aspiration. The GenElute-E Spin column was vortexed and placed in a reaction tube and left to stand for 20min. Meanwhile, 90µL Tissue Lysis Buffer and 5µL SmartLyse T Protease was added to each tissue sample. The tubes were placed on a thermal shaker (Eppendorf Thermomixer C) and incubated for 30min at 60°C with maximum agitation. The temperature was then increased to 80°C and incubated for a further 10min. 45µL lysed sample was set aside for RNA processing. 0.5µL RNase A was added to the remaining sample volume, intended for gDNA isolation. The samples were vortexed and then incubated for 2min at room temperature. 5µL Clearing Solution T was added and sample vortexed before centrifugation for 2min at maximum speed (16,000xg). The GenElute-E Spin column was then centrifuged for 1min at 1,000xg and placed in a new reaction tube. The sample supernatant was transferred to the spin column and centrifuged for 1min at 1,000xg to elute gDNA. For RNA processing, the set-aside sample was processed using the RNeasy Plus kit (Qiagen, Manchester, UK; Chapter 3, Section 3.2.1.1) beginning with direct addition of the 45µL lysed sample onto the gDNA elimination column.

This method resulted in high concentration gDNA, but with evidence of contamination retained in the wells of the agarose gel, along with very poor/no RNA yield (Supplementary Figure S10.2)

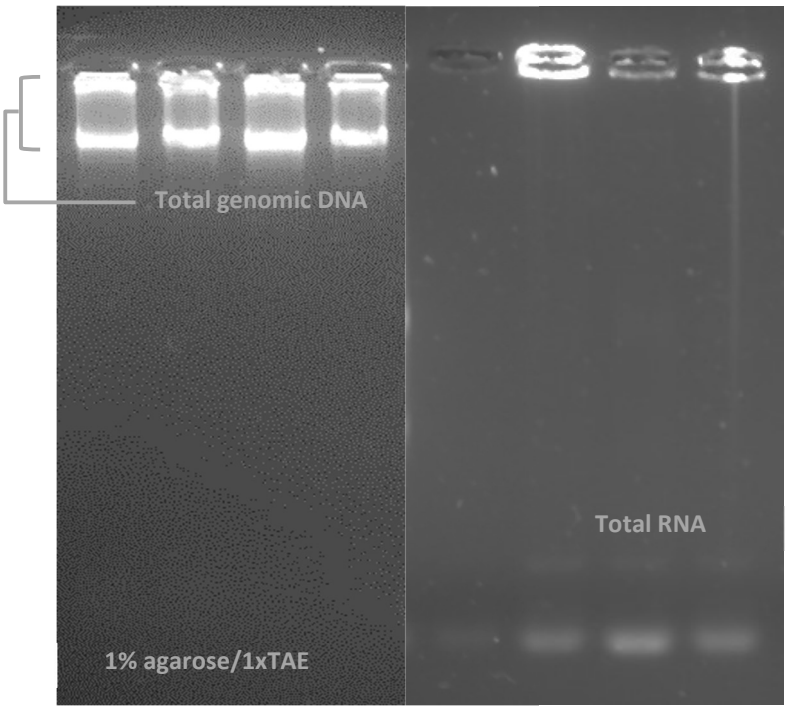

Supplementary Figure S10.2. Representative DNA and RNA quality gel (PN2 - GENELUTE)
1%agarose/1XTAE with 1:10,000 Gel Red stain (VWR, Lutterworth, UK). RNA samples loaded at 100ng/well* and DNA samples loaded at 50ng/well. Electrophoreses performed in 1xTAE buffer at 120V for approximately 45min. Gel imaged by Bio-rad Gel Doc XR+ (Watford, UK) under UV fluorescence with a default exposure time. *As RNA concentration was so low, this was the highest RNA loading achievable for the well volume.

3. innuPREP DNA/RNA mini kit (Analytik Jena, Jena, Germany)

The sample stored in RNAlater was thawed on ice and excess RNAlater solution removed by aspiration. 500µL Lysis solution RL was added to the frozen tissue sample and the sample homogenised with pestle until tissue was no longer visible. The sample was incubated for a further 10min at room temperature to allow complete sample lysis. The lysed sample was transferred to the Spin Filter D (within a receiver tube) and centrifuged at 10,000xg for 2min. At this stage the DNA binds to the membrane and the filtrate contains the RNA. 400µL 70% ethanol was added to the filtrate and the combined solution added to Spin Column R and centrifuged at 10,000xg for 2min to bind the RNA. The spin columns containing DNA (D) and RNA (R) were then proceeded in parallel: with 500µL washing solution HS added and centrifuged at 10,000xg for 1min, followed by addition of 700µL washing solution LS, centrifuged at 10,000xg for 1min. In both cases the filtrate was discarded. The columns were then dried by centrifugation at 10,000xg for 2min. To the Spin Filter D 80µL Elution buffer was added and to Spin Filter R 50µL RNase-free water. The tubes were incubated for 1min at room temperature before centrifugation for 1min at 6,000xg to elute the samples.

This method resulted in high concentration and good integrity quality of both DNA and RNA (Supplementary Figure S10.3)

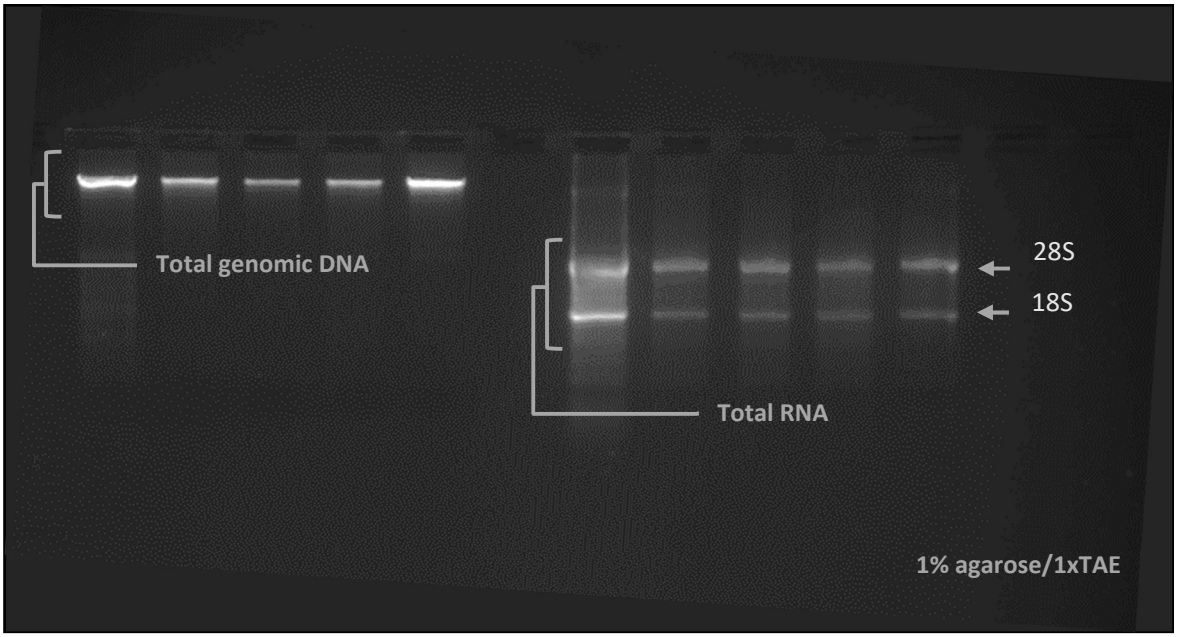

Supplementary Figure S10.3. Representative DNA and RNA quality gel (PN2 cohort - Innuprep)
1%agarose/1XTAE with 1:10,000 Gel Red stain (VWR, Lutterworth, UK). RNA samples loaded at 800ng/well and DNA samples loaded at 50ng/well. Electrophoresis performed in 1XTAE buffer at 120V for approximately 45min. Gel imaged by Bio-rad Gel Doc XR+ (Watford, UK) under UV fluorescence with a default exposure time.

Appendix 11. Pyrosequencing supplementary methods

1. Cartridge preparation

Cartridge preparation was specific to each gene assay. Supplementary Table S11.1. indicates the volumes of each nucleotide added to the cartridge for each pyrosequencing assay utilised.

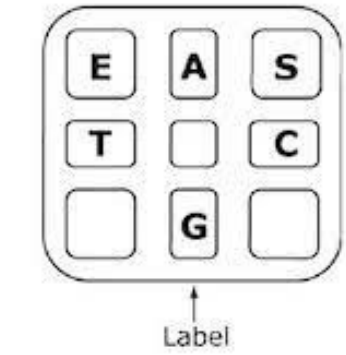

Top view of the cartridge

For all assays:

E: 140µL Enzyme solution

S: 140µL Substrate solution

Nucleotides followed assay-specific loading volumes.

Supplementary Table S11.1. Pyrosequencing assay cartridge preparation

Assay/Gene	A (ATP)	T (TTP)	C (CTP)	G (GTP)	Run time
Mbp	33µL	52µL	47µL	44µL	0h 36min
Sgk1	97µL	44µL	52µL	36µL	0h 53min
Nfasc	60µL	52µL	49µL	55µL	0h 45min
Gpc4	52µL	57µL	49µL	52µL	0h 44min
Irs1	99µL	126µL	113µL	86µL	1h 38min
Tgfbr2	55µL	55µL	52µL	47µL	0h 40min
Ank3	76µL	81µL	70µL	65µL	1h 02min
CamkIIb	107µL	39µL	49µL	52µL	0h 57min
Dab1	76µL	73µL	62µL	65µL	1h 00min
Nrxn2	68µL	68µL	65µL	57µL	0h 58min

2. Representative negative and positive control assays

Mbp

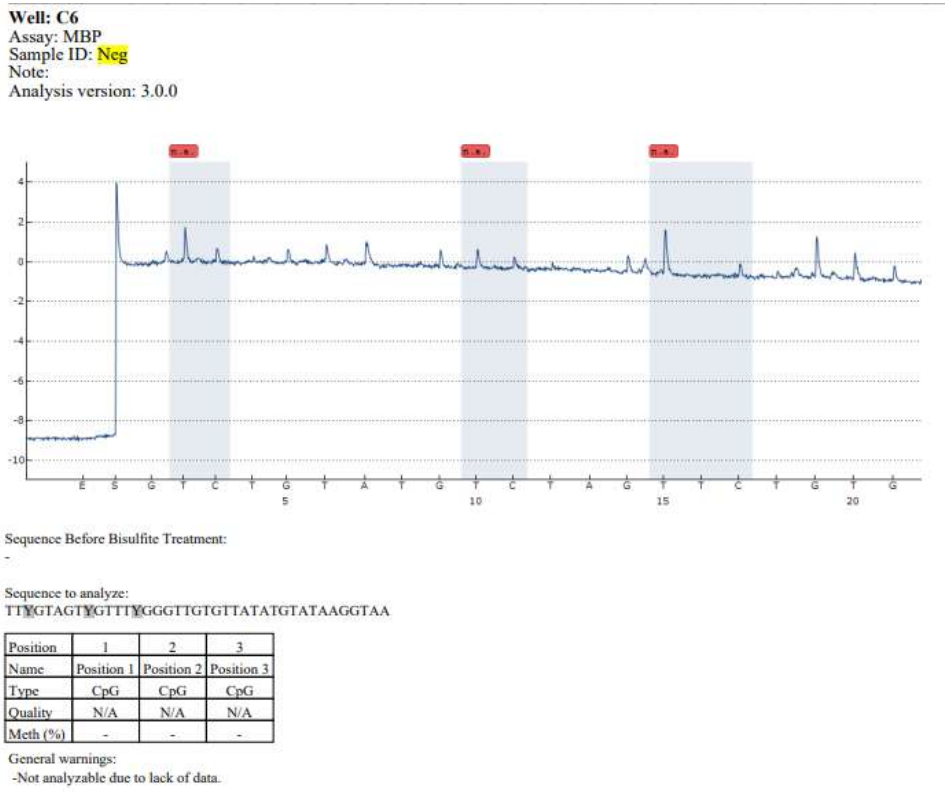

Supplementary Figure S11.1. Representative negative and positive control pyrosequencing reads for *Mbp*
Representative pyrosequencing reads for negative (left) and positive (right) control samples performed on the *Mbp* assay. Negative control shows no obtainable data while the positive shows clear peaks, all of which pass the machines internal quality checks at each CpG position within the sequence.

Sgk1

Well: A1
Assay: SGK1
Sample ID: Neg
Note:
Analysis version: 3.0.0

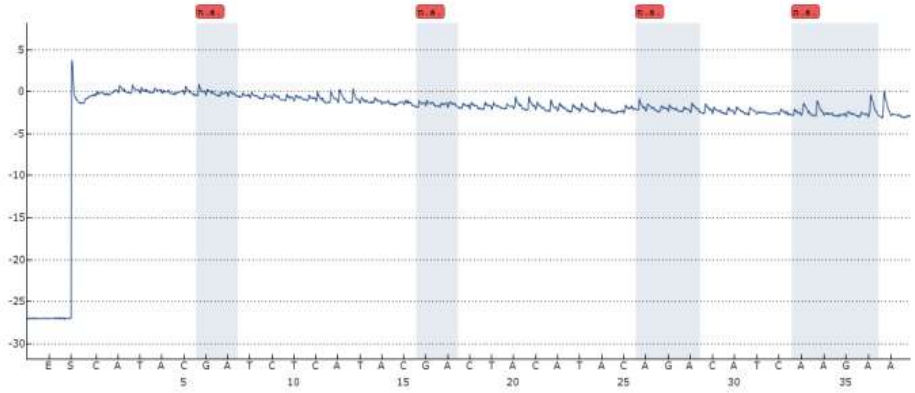

Sequence Before Bisulfite Treatment:
-

Sequence to analyze:
ATCCRTCTCCAATCRCTAACCATTCCRAACACRAAAAAAAAAC

Position	1	2	3	4
Name	Position 1	Position 2	Position 3	Position 4
Type	CpG	CpG	CpG	CpG
Quality	N/A	N/A	N/A	N/A
Meth (%)	-	-	-	-

General warnings:
-Not analyzable due to lack of data.

Warnings:
No additional

Well: A2
Assay: SGK1
Sample ID: Pos
Note:
Analysis version: 3.0.0

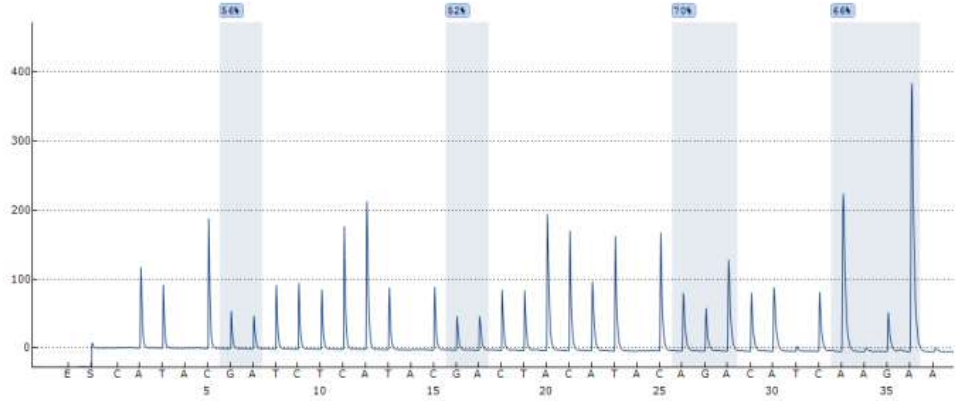

Sequence Before Bisulfite Treatment:
-

Sequence to analyze:
ATCCRTCTCCAATCRCTAACCATTCCRAACACRAAAAAAAAAC

Position	1	2	3	4
Name	Position 1	Position 2	Position 3	Position 4
Type	CpG	CpG	CpG	CpG
Quality	Passed	Passed	Passed	Passed
Meth (%)	56	52	70	66

No warnings.

Supplementary Figure S11.2. Representative negative and positive control pyrosequencing reads for *Sgk1*
Representative pyrosequencing reads for negative (left) and positive (right) control samples performed on the *Sgk1* assay. Negative control shows no obtainable data while the positive shows clear peaks, all of which pass the machines internal quality checks at each CpG position within the sequence.

Nfasc

Well: C7
Assay: nfasc
Sample ID: Neg
Note:
Analysis version: 3.0.0

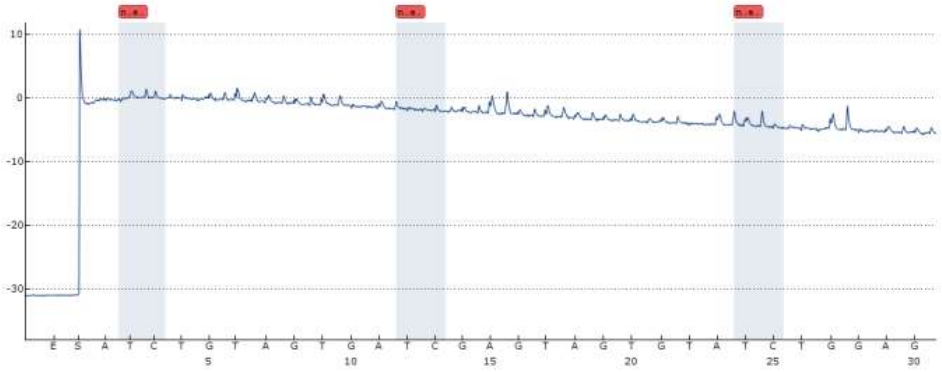

Sequence Before Bisulfite Treatment:
-

Sequence to analyze:
TYGTTAGTTAYGAAAGTTAGTGAATTYGGGGAGTAGTAAAATTTTAAAGTGA

Position	1	2	3
Name	Position 1	Position 2	Position 3
Type	CpG	CpG	CpG
Quality	N/A	N/A	N/A
Meth (%)	-	-	-

General warnings:
-Not analyzable due to lack of data.

Warnings:
No additional

Well: C8
Assay: nfasc
Sample ID: Pos
Note:
Analysis version: 3.0.0

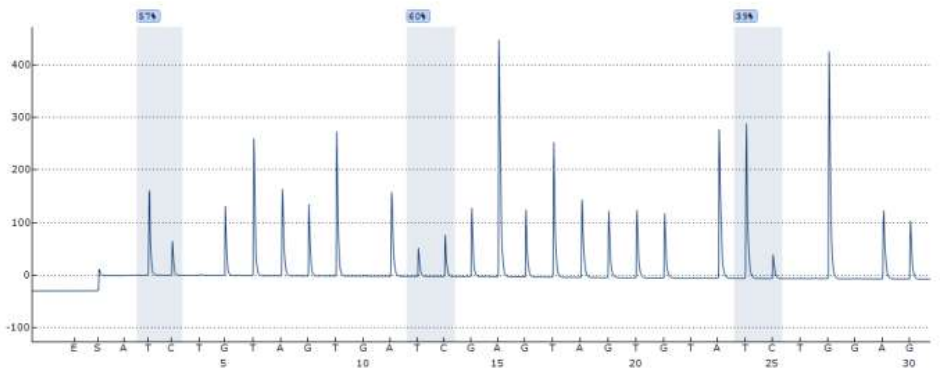

Sequence Before Bisulfite Treatment:
-

Sequence to analyze:
TYGTTAGTTAYGAAAGTTAGTGAATTYGGGGAGTAGTAAAATTTTAAAGTGA

Position	1	2	3
Name	Position 1	Position 2	Position 3
Type	CpG	CpG	CpG
Quality	Passed	Passed	Passed
Meth (%)	57	60	39

No warnings.

Supplementary Figure S11.3. Representative negative and positive control pyrosequencing reads for *Nfasc*
Representative pyrosequencing reads for negative (left) and positive (right) control samples performed on the *Nfasc* assay. Negative control shows no obtainable data while the positive shows clear peaks, all of which pass the machines internal quality checks at each CpG position within the sequence.

Gpc4

Well: C8
Assay: gpc4_2
Sample ID: neg
Note:
Analysis version: 3.0.0

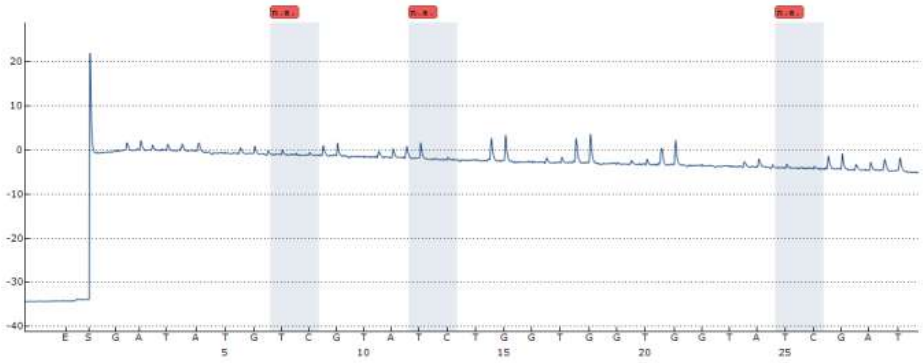

Sequence Before Bisulfite Treatment:
-

Sequence to analyze:
ATAGYGGATTYGGGGGTGGGGGGTGGGGGAYGGGATTTGGAATTTATAGTTGGGTTG

Position	1	2	3
Name	Position 1	Position 2	Position 3
Type	CpG	CpG	CpG
Quality	N/A	N/A	N/A
Meth (%)	-	-	-

General warnings:
-Not analyzable due to lack of data.

Warnings:
No additional

Well: C7
Assay: gpc4_2
Sample ID: pos
Note:
Analysis version: 3.0.0

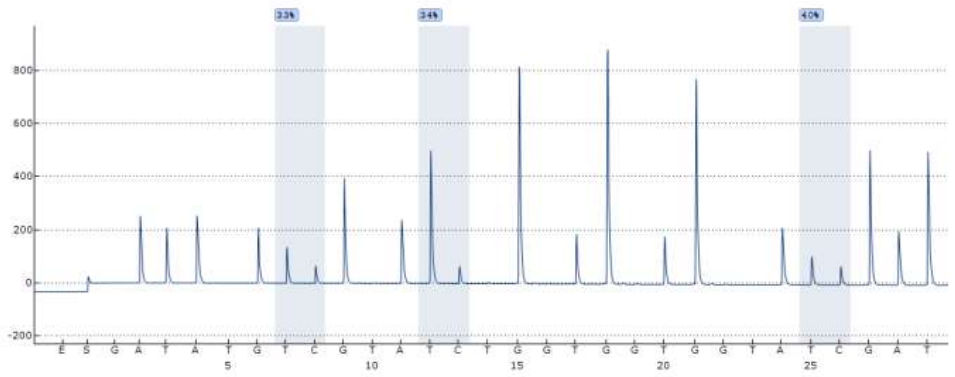

Sequence Before Bisulfite Treatment:
-

Sequence to analyze:
ATAGYGGATTYGGGGGTGGGGGGTGGGGGAYGGGATTTGGAATTTATAGTTGGGTTG

Position	1	2	3
Name	Position 1	Position 2	Position 3
Type	CpG	CpG	CpG
Quality	Passed	Passed	Passed
Meth (%)	33	34	40

No warnings.

Supplementary Figure S11.4. Representative negative and positive control pyrosequencing reads for *Gpc4*
Representative pyrosequencing reads for negative (left) and positive (right) control samples performed on the *Gpc4* assay. Negative control shows no obtainable data while the positive shows clear peaks, all of which pass the machines internal quality checks at each CpG position within the sequence.

Irs1

Well: C8
Assay: irs1_2
Sample ID: neg
Note:
Analysis version: 3.0.0

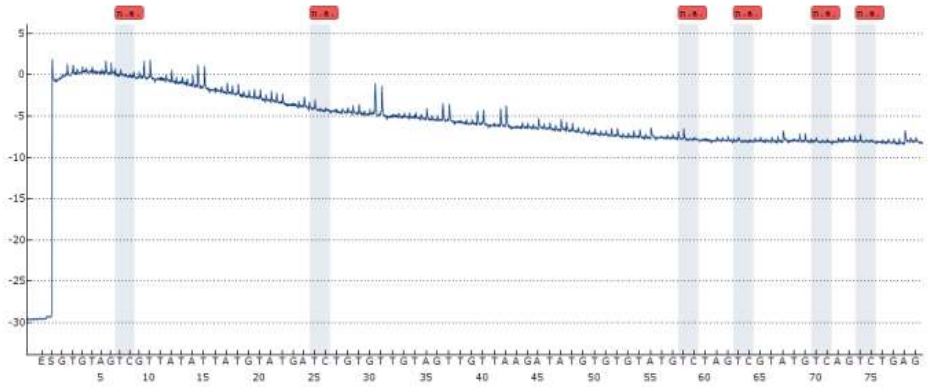

Sequence Before Bisulfite Treatment:
-

Sequence to analyze:
TTGTGGYGTTTTATATTTTTATTGTTATTATYGTTGTTTTTTTTTGTAGTTTTTGTTTTAAAAGATATTGTGTTGTTAGTTYGYGTAGGYGTY
GAGAAGGTTT

Position	1	2	3	4	5	6
Name	Position 1	Position 2	Position 3	Position 4	Position 5	Position 6
Type	CpG	CpG	CpG	CpG	CpG	CpG
Quality	N/A	N/A	N/A	N/A	N/A	N/A
Meth (%)	-	-	-	-	-	-

General warnings:
-Not analyzable due to lack of data.

Warnings:
No additional

Well: C7
Assay: irs1_2
Sample ID: pos
Note:
Analysis version: 3.0.0

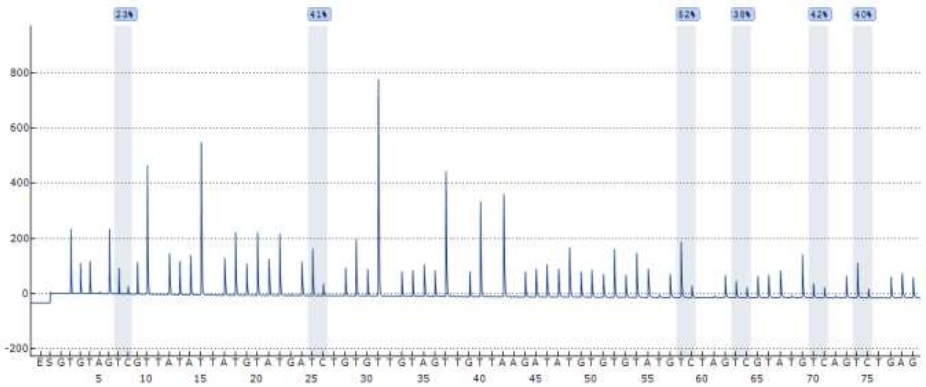

Sequence Before Bisulfite Treatment:
-

Sequence to analyze:
TTGTGGYGTTTTATATTTTTATTGTTATTATYGTTGTTTTTTTTTGTAGTTTTTGTTTTAAAAGATATTGTGTTGTTAGTTYGYGTAGGYGTY
GAGAAGGTTT

Position	1	2	3	4	5	6
Name	Position 1	Position 2	Position 3	Position 4	Position 5	Position 6
Type	CpG	CpG	CpG	CpG	CpG	CpG
Quality	Passed	Passed	Passed	Passed	Passed	Passed
Meth (%)	23	41	52	38	42	40

No warnings.

Supplementary Figure S11.5. Representative negative and positive control pyrosequencing reads for *Irs1*
Representative pyrosequencing reads for negative (left) and positive (right) control samples performed on the *Irs1* assay. Negative control shows no obtainable data while the positive shows clear peaks, all of which pass the machines internal quality checks at each CpG position within the sequence.

Tgfbr2

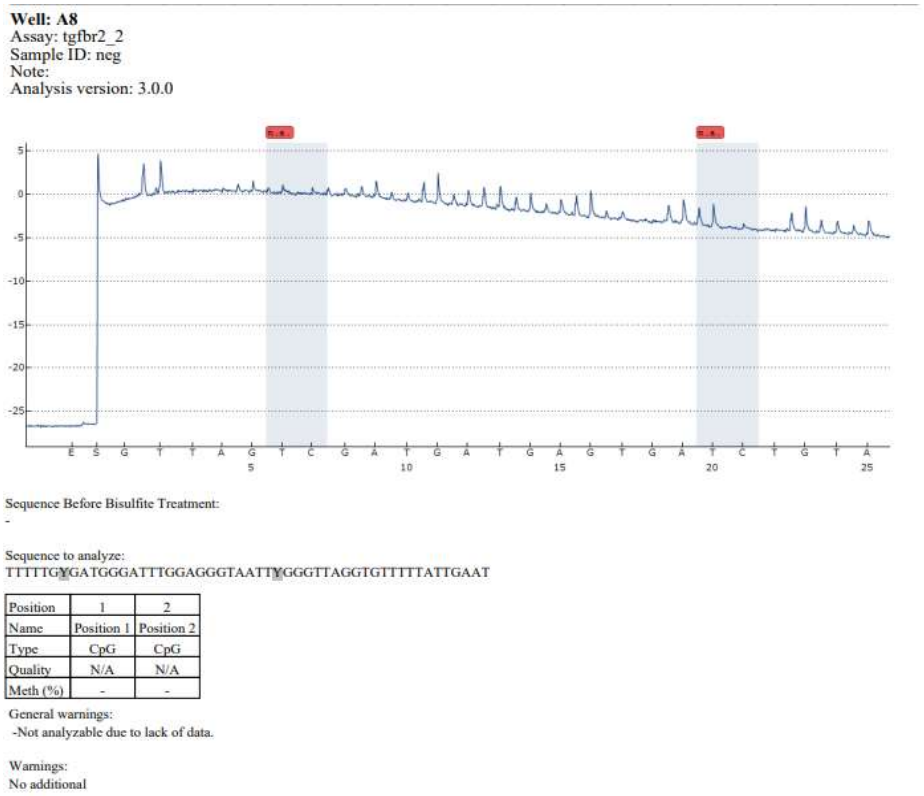

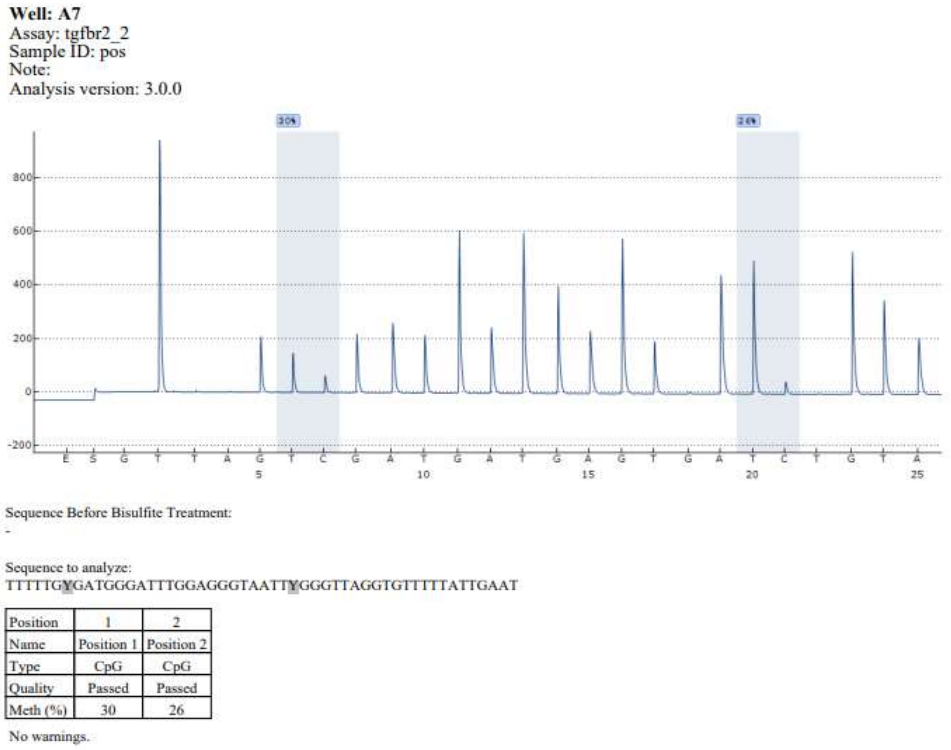

Supplementary Figure S11.6. Representative negative and positive control pyrosequencing reads for *Tgfbr2*
Representative pyrosequencing reads for negative (left) and positive (right) control samples performed on the *Tgfbr2* assay. Negative control shows no obtainable data while the positive shows clear peaks, all of which pass the machines internal quality checks at each CpG position within the sequence.

Ank3

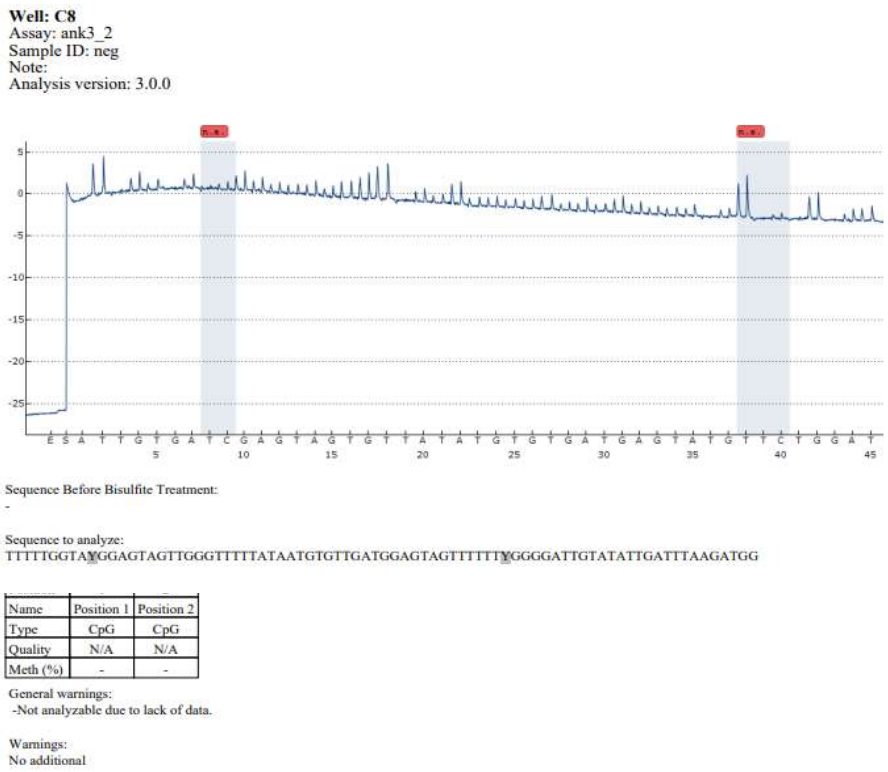

Well: C8
Assay: ank3_2
Sample ID: neg
Note:
Analysis version: 3.0.0

Sequence Before Bisulfite Treatment:
-

Sequence to analyze:
TTTTTGGTAYGGAGTAGTTGGGTTTTTATAATGTGTTGATGGAGTAGTTTTTTYGGGGATTGTATATTGATTTAAGATGG

Name	Position 1	Position 2
Type	CpG	CpG
Quality	N/A	N/A
Meth (%)	-	-

General warnings:
-Not analyzable due to lack of data.

Warnings:
No additional

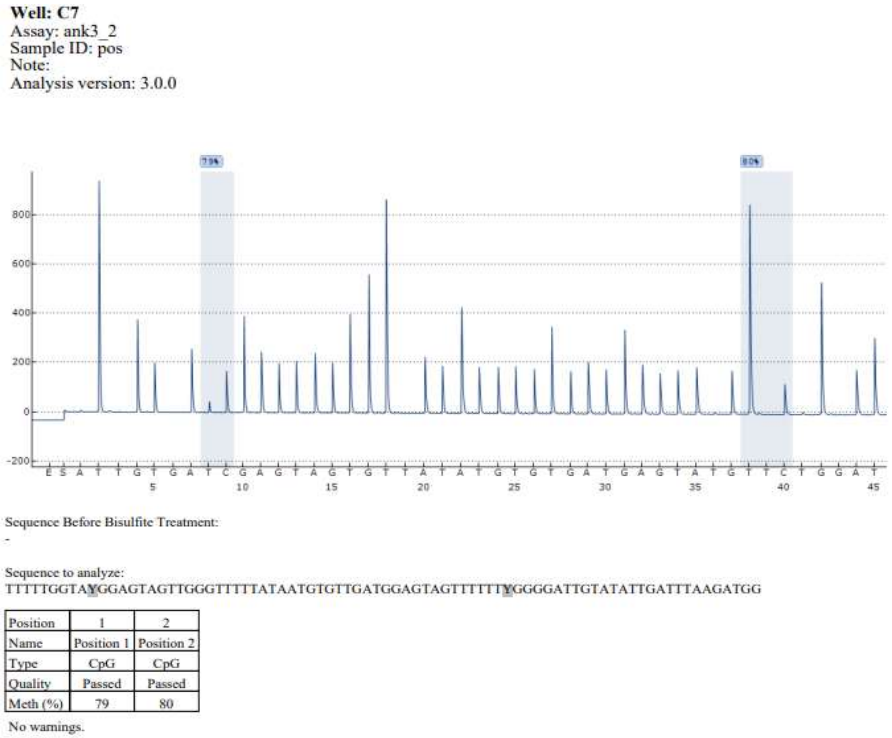

Well: C7
Assay: ank3_2
Sample ID: pos
Note:
Analysis version: 3.0.0

Sequence Before Bisulfite Treatment:
-

Sequence to analyze:
TTTTTGGTAYGGAGTAGTTGGGTTTTTATAATGTGTTGATGGAGTAGTTTTTTYGGGGATTGTATATTGATTTAAGATGG

Position	1	2
Name	Position 1	Position 2
Type	CpG	CpG
Quality	Passed	Passed
Meth (%)	79	80

No warnings.

Supplementary Figure S11.7. Representative negative and positive control pyrosequencing reads for *Ank3*
Representative pyrosequencing reads for negative (left) and positive (right) control samples performed on the *Ank3* assay. Negative control shows no obtainable data while the positive shows clear peaks, all of which pass the machines internal quality checks at each CpG position within the sequence.

Camk2b

Well: C8
Assay: camk2b_2
Sample ID: Neg
Note:
Analysis version: 3.0.0

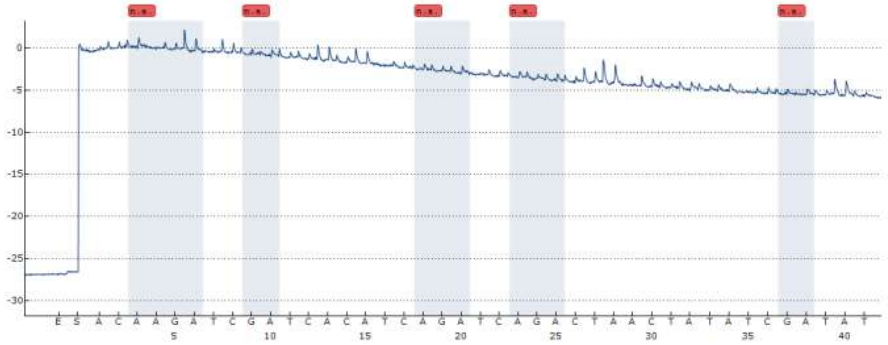

Sequence Before Bisulfite Treatment:
-

Sequence to analyze:
CRAAACCRTCAACAACRACRACTTTAAAACCTATACRTAAATCTCCC

Position	1	2	3	4	5
Name	Position 1	Position 2	Position 3	Position 4	Position 5
Type	CpG	CpG	CpG	CpG	CpG
Quality	N/A	N/A	N/A	N/A	N/A
Meth (%)	-	-	-	-	-

General warnings:
-Not analyzable due to lack of data.

Warnings:
No additional

Well: C7
Assay: camk2b_2
Sample ID: Pos
Note:
Analysis version: 3.0.0

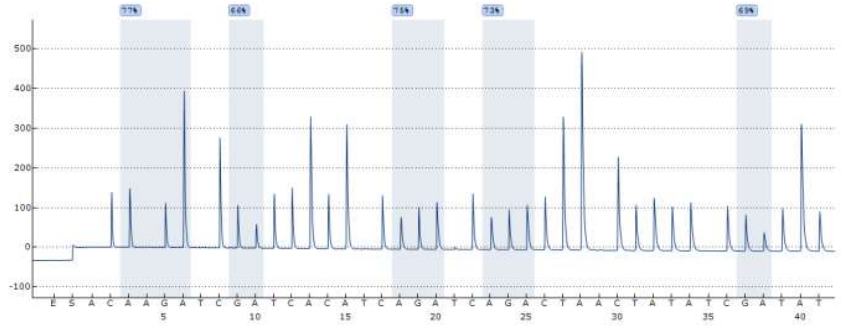

Sequence Before Bisulfite Treatment:
-

Sequence to analyze:
CRAAACCRTCAACAACRACRACTTTAAAACCTATACRTAAATCTCCC

Position	1	2	3	4	5
Name	Position 1	Position 2	Position 3	Position 4	Position 5
Type	CpG	CpG	CpG	CpG	CpG
Quality	Passed	Passed	Passed	Passed	Passed
Meth (%)	77	66	75	73	69

No warnings.

Supplementary Figure S11.8. Representative negative and positive control pyrosequencing reads for *Camk2b*
Representative pyrosequencing reads for negative (left) and positive (right) control samples performed on the *Camk2b* assay. Negative control shows no obtainable data while the positive shows clear peaks, all of which pass the machines internal quality checks at each CpG position within the sequence.

Nrxn2

Well: A8
Assay: nrxn2_2
Sample ID: neg
Note:
Analysis version: 3.0.0

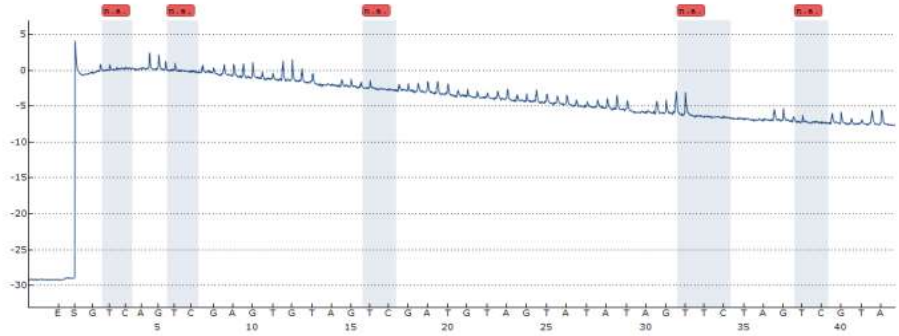

Sequence Before Bisulfite Treatment:
-

Sequence to analyze:
YGGYGAGGTGGGTTGYGATTGTAGTTATATTGGTTTYGGYGGTAAGTTTTGTAGTGAAGGTGAGTT

Position	1	2	3	4	5
Name	Position 1	Position 2	Position 3	Position 4	Position 5
Type	CpG	CpG	CpG	CpG	CpG
Quality	N/A	N/A	N/A	N/A	N/A
Meth (%)	-	-	-	-	-

General warnings:
-Not analyzable due to lack of data.

Warnings:
No additional

Well: A7
Assay: nrxn2_2
Sample ID: pos
Note:
Analysis version: 3.0.0

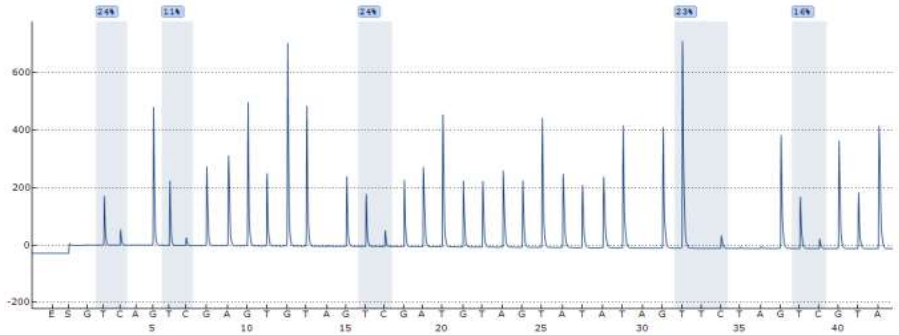

Sequence Before Bisulfite Treatment:
-

Sequence to analyze:
YGGYGAGGTGGGTTGYGATTGTAGTTATATTGGTTTYGGYGGTAAGTTTTGTAGTGAAGGTGAGTT

Position	1	2	3	4	5
Name	Position 1	Position 2	Position 3	Position 4	Position 5
Type	CpG	CpG	CpG	CpG	CpG
Quality	Passed	Passed	Passed	Passed	Passed
Meth (%)	24	11	24	23	16

No warnings.

Supplementary Figure S11.9. Representative negative and positive control pyrosequencing reads for *Nrxn2*
Representative pyrosequencing reads for negative (left) and positive (right) control samples performed on the *Nrxn2* assay. Negative control shows no obtainable data while the positive shows clear peaks, all of which pass the machines internal quality checks at each CpG position within the sequence.

Dab1

Well: A8
Assay: dab1_2
Sample ID: neg
Note:
Analysis version: 3.0.0

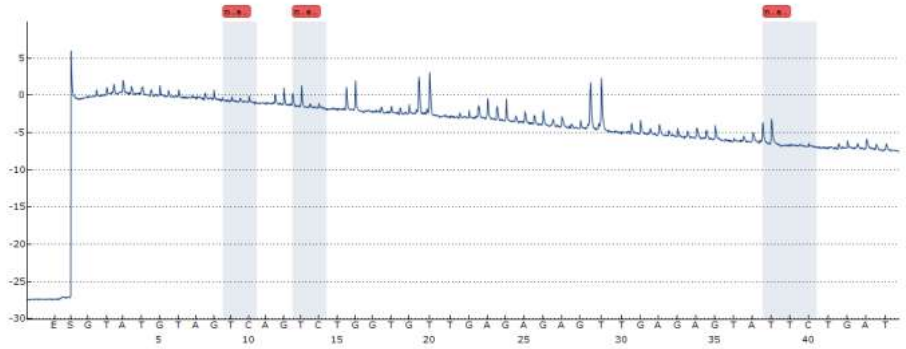

Sequence Before Bisulfite Treatment:
-

Sequence to analyze:
TATGTGYGGTTYGGGGTGTTTTTTTTGAAGGGAGGAGTTTTTTTTTTGGAGAGGATTTTYGATGAGTTTGGTTAAGGTT

Position	1	2	3
Name	Position 1	Position 2	Position 3
Type	CpG	CpG	CpG
Quality	N/A	N/A	N/A
Meth (%)	-	-	-

General warnings:
-Not analyzable due to lack of data.

Warnings:
No additional

Well: A7
Assay: dab1_2
Sample ID: pos
Note:
Analysis version: 3.0.0

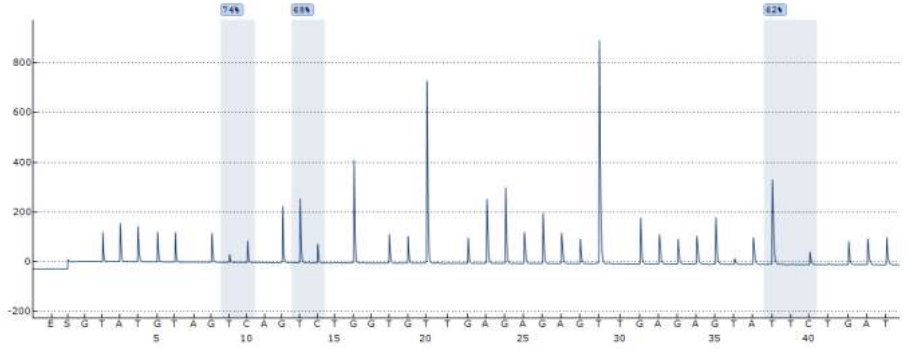

Sequence Before Bisulfite Treatment:
-

Sequence to analyze:
TATGTGYGGTTYGGGGTGTTTTTTTTGAAGGGAGGAGTTTTTTTTTTGGAGAGGATTTTYGATGAGTTTGGTTAAGGTT

Position	1	2	3
Name	Position 1	Position 2	Position 3
Type	CpG	CpG	CpG
Quality	Passed	Passed	Passed
Meth (%)	74	68	62

No warnings.

Supplementary Figure S11.10. Representative negative and positive control pyrosequencing reads for *Dab1*
Representative pyrosequencing reads for negative (left) and positive (right) control samples performed on the *Dab1* assay. Negative control shows no obtainable data while the positive shows clear peaks, all of which pass the machines internal quality checks at each CpG position within the sequence.

Appendix 12: WES supplementary methods

1. WES plate set-up

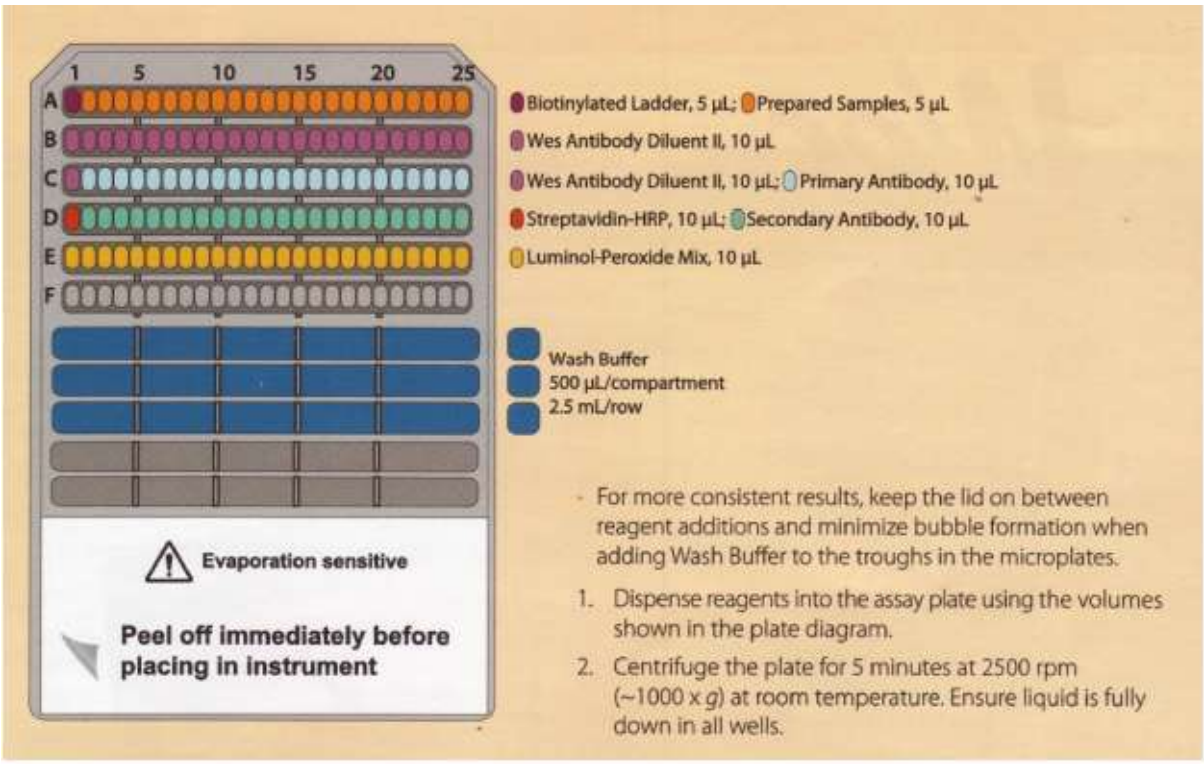

Supplementary Figure S12.1. WES plate set-up
WES plates were prepared as directed. Streptavidin-HRP, antibody diluent, wash buffer and secondary antibodies (anti-rabbit IgG or anti-mouse IgG) were provided in the kit and did not require any additional preparation. For total protein primary antibody is replaced with the total protein labelling reagent and secondary antibody is replaced with total protein streptavidin-HRP.

2. WES antibody validations

Note protocols for the following protein targets (PV, NR2A, NR2B, PSD95, GRIA1) had already been validated previously in-house by the b-neuro laboratory.

i) anti-SGK1 antibody (rabbit polyclonal; Proteintech, 28454-1-AP; 900µg/mL)

The antibody was first validated for its efficiency in detecting SGK1 using the standard Western blot protocol outlined in Chapter 3, Section 3.2.3.2. SGK1 is a primarily cytosolic signalling protein of approximately 55kDa size, depending on post-translational modifications (Lang et al., 2009; Lee et al., 2020). To validate the anti-SGK1 antibody, 20µg of membrane and cytosolic lysates (see Chapter 5, Section 5.2.5) were used to demonstrate an enrichment of the anti-SGK1 immunoreactive band, of predicted size, in the cytosolic fraction (Figure S12.2A). For this validation, a 1:1,000 (0.9µg/mL) primary antibody dilution was used in an overnight incubation at 4°C, as previously described (Chapter 3, Section 3.2.3.2). After the initial validation, the antibody was trialled on the WES to ascertain whether this validation withstood the shift between application platforms. WES validation was performed using the standard WES protocol (see Chapter 5, Section 5.2.6) with a protein concentration of 1µg/µL and an antibody dilution of 1:50 (18µg/mL). This showed an enrichment in the cytosol for the anti-SGK1 immunoreactive band (Figure S12.2B). Of note, a primary band of 55-58kDa and an occasional faint band at 49kDa, were observed. This result has been shown previously when SGK1 was assayed on rat tissue samples using the WES platform (Lee et al., 2020).

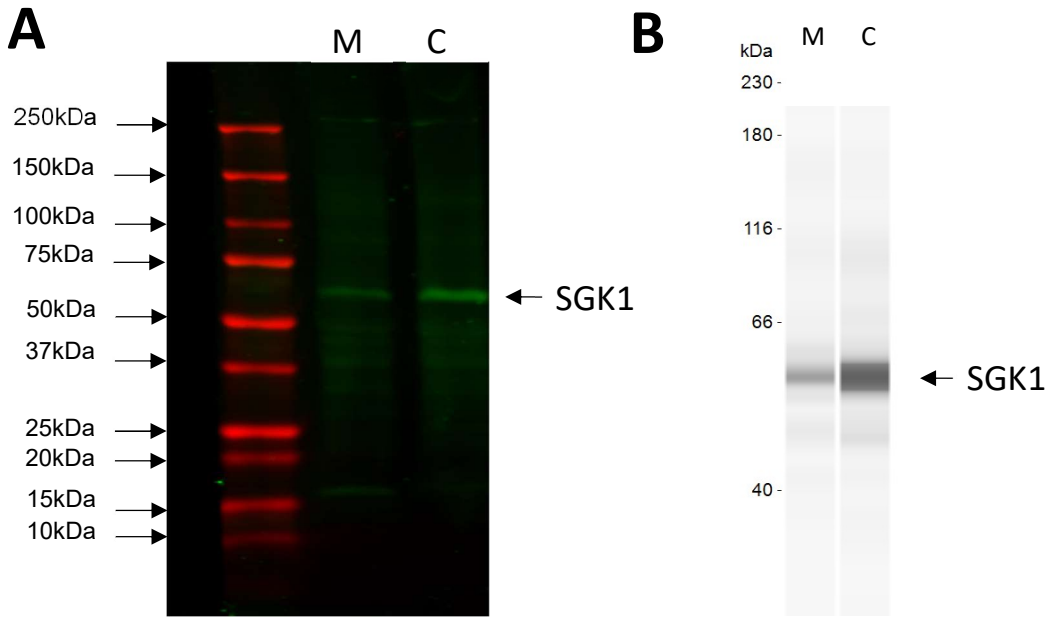

Figure S12.2. Validation of anti-SGK1 antibody
A. Western blot was run as per standard conditions (see Chapter 3, Section 3.2.3.2). 20µg membrane (M) and Cytosolic (C) lysate was loaded per well. 1:1,000 (0.9µg/mL) primary antibody dilution was used. An immunoreactive band of predicted size (55-58kDa), enriched in the cytoplasmic fraction was observed. **B.** WES blot was run as per standard conditions (see Chapter 5, Section 5.2.6) 1µg/µL membrane (M) and Cytosolic (C) lysate was loaded per well. 1:50 (18µg/mL) primary antibody dilution was used. There was a band of predicted size (55-58kDa), clearly enriched in the cytoplasmic fraction.

3. WES antibody optimisations

For all WES antibody optimisations, two graphical plots were created for each timepoint: graph i) protein concentration (AUC) plotted for each antibody dilution; graph ii) antibody dilutions (chemiluminescence) plotted for each protein concentration. For graph (i) the optimal protein concentration was determined by identifying the concentration at which the graph remains linear. For graph (ii) the optimal antibody dilution was determined by identifying the concentration where the graph reaches a plateau. This represents the dynamic range of the assay (Nelson et al., 2017).

i) anti-SGK1 antibody (rabbit polyclonal; Proteintech, 28454-1-AP; 900µg/mL)

Table S12.1 summarises the protein and antibody concentrations used when determining the dynamic range of anti-SGK1 assay. A representative graphical plot for PD21 can be seen in Figure S12.3. Using the graphical plots at each timepoint a 1:50 (18µg/mL) antibody dilution was deemed optimal, with the following protein concentrations GD21 and PD1 FC, 1.4µg/µL; PD21 PFC 1.2µg/µL; PD35 PFC, 1.0µg/µL; PD100 PFC 0.6µg/µL. Samples were therefore performed under these conditions and the AUC taken as the output value for each sample.

Supplementary Table S12.1. Selected concentrations for optimisation of the anti-SGK1 antibody

Sample type	GD21 FC	PD1 FC	PD21 PFC	PD35 PFC	PD100 PFC
Protein concentration (µg/µL)	1.0 1.4 1.8	1.0 1.4 1.8	0.8 1.2 1.6	0.6 1.0 1.4	0.6 1.0 1.4
Antibody dilution	1:20 1:50 1:100 1:200	1:20 1:50 1:100 1:200	1:20 1:50 1:100 1:200	1:20 1:50 1:100 1:200	1:20 1:50 1:100 1:200

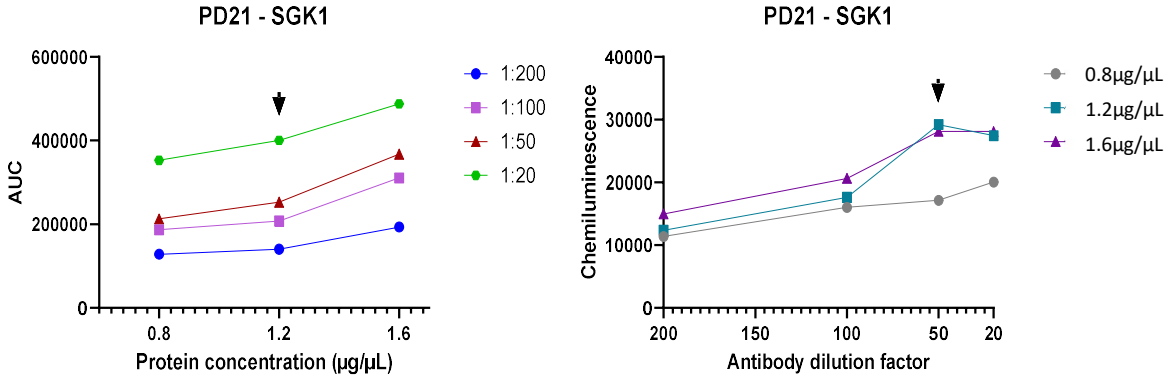

Supplementary Figure S12.3. Representative graphical plots for the anti-SGK1 antibody optimisation
Left: protein concentration with different antibody dilutions; Right: antibody dilution at different protein loadings. Arrow indicates the optimal protein concentration (left) and antibody dilution factor (right) within the sample type.

ii) anti-PSD95 antibody (mouse monoclonal, ab2723; Abcam; 1mg/mL)

Previous in-house pilot studies had validated that the anti-PSD95 antibody produced an immunoreactive band of the correct size (95-100kDa), enriched in the cytoplasm, in line with previous literature (Tojo et al., 1999; Yoo et al., 2019; Zaric et al., 2018), hence the assay was optimised using cytosolic fractions. Table S12.2 summarises the cytosolic protein and corresponding antibody concentrations used when determining the dynamic range of anti-PSD95 assay. A representative graphical plot for PD35 can be seen in Figure S12.3. Using the graphical plots at each developmental age a 1:50 (20µg/mL) antibody dilution was deemed optimal, with the following protein concentrations: PD21 PFC, 0.8µg/µL; PD35 PFC, 0.4µg/µL, PD100 PFC 0.4µg/µL. Samples were therefore performed under these conditions and the AUC taken as the output value for each sample.

Supplementary Table S12.2. Selected concentrations for optimisation of the anti-PSD95 antibody

Sample type	PD21 PFC	PD35 PFC	PD100 PFC
Protein concentration (µg/µL)	0.2 0.4 0.8	0.2 0.4 0.8	0.2 0.4 0.8
Antibody dilution	1:20 1:50 1:100 1:200	1:20 1:50 1:100 1:200	1:20 1:50 1:100 1:200

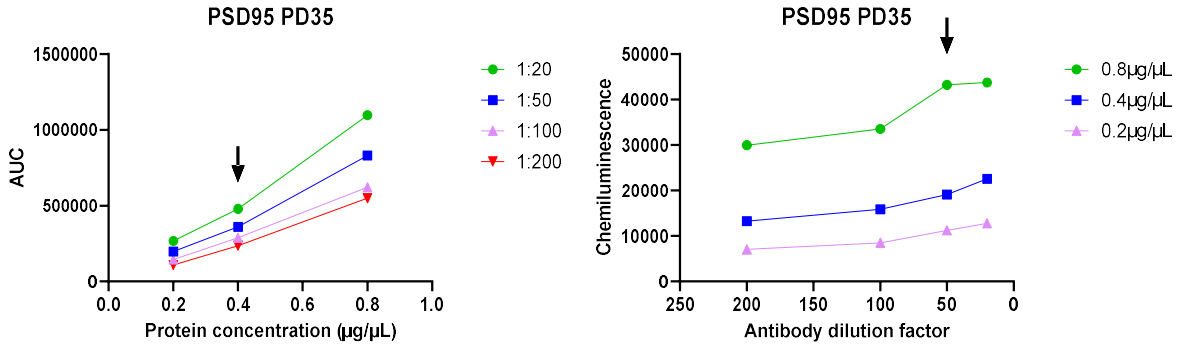

Supplementary Figure S12.3. Representative graphical plots for the anti-PSD95 antibody optimisation
Left: protein concentration with different antibody dilutions; Right: antibody dilution at different protein loadings. Arrow indicates the optimal protein concentration (left) and antibody dilution factor (right) within the sample type.

iii) anti-PV antibody (rabbit monoclonal; LS-B14122, LSBio; 1mg/mL)

Previous in-house pilot studies had validated the anti-PV antibody produced an immunoreactive band of the correct size (10-15kDa), enriched in the cytoplasm as expected (Permyakov and Uversky, 2022), hence the assay was optimised using cytosolic fractions. Table S12.3 summarises the cytosolic protein and antibody concentrations used when determining the dynamic range of anti-PV assay. A representative graphical plot for PD100 can be seen in Figure S12.4. Using the graphical plots at each developmental age a 1:50 (20µg/mL) antibody dilution was deemed optimal, with the following protein concentrations PD21-35 PFC 0.8µg/µL; PD100 PFC 0.4µg/µL. Samples were therefore performed under these conditions and the AUC taken as the output value for each sample.

Supplementary Table S12.3. Selected concentrations for optimisation of the anti-PV antibody

Sample type	PD21 PFC	PD35 PFC	PD100 PFC
Protein concentration (µg/µL)	0.2 0.4 0.8	0.2 0.4 0.8	0.2 0.4 0.8
Antibody dilution	1:20 1:50 1:100 1:200	1:20 1:50 1:100 1:200	1:20 1:50 1:100 1:200

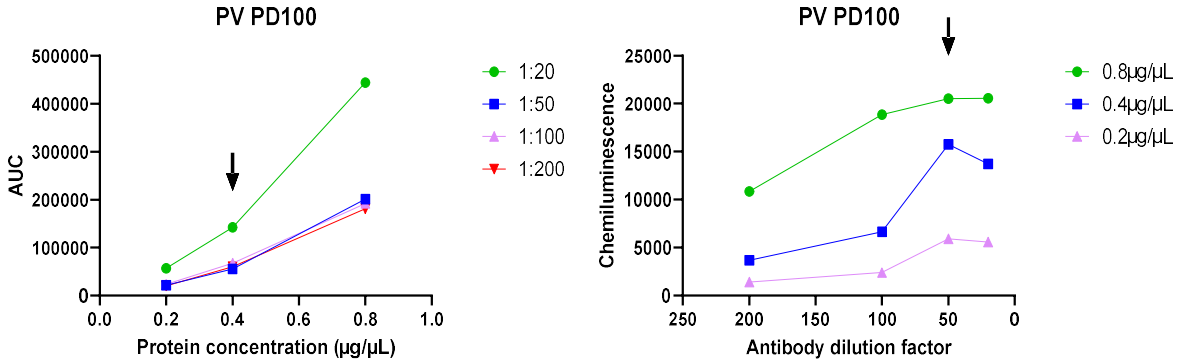

Supplementary Figure S12.4. Representative graphical plots for the anti-PV antibody optimisation
Left: protein concentration with different antibody dilutions; Right: antibody dilution at different protein loadings. Arrow indicates the optimal protein concentration (left) and antibody dilution factor (right) within the sample type.

iv) anti-NR2A (PPS012) and anti-NR2B antibodies (PPS013; rabbit polyclonal, R&D systems; 0.2mg/mL)

Previous in-house pilot studies had validated the anti-NR2A and anti-NR2B antibodies produced immunoreactive bands of approximately 170-175kDa, enriched in the membrane fraction as expected (Anastasio and Johnson, 2008; Di Luca et al., 1999; Zaric et al., 2018). Hence for both these antibodies, the assay was optimised using membrane fractions. Table S12.4 summarises the membrane protein and corresponding antibody concentrations used when determining the dynamic range of both the anti-NR2A and anti-NR2B assays. A representative graphical plot for PD21 can be seen in Figure S12.5. Using the graphical plots at each developmental age a 1:100 (2µg/mL) antibody dilution was deemed optimal for both assays across all timepoints, with the protein concentrations for each antibody were as follows:

- anti-NR2A: PD21 PFC, 0.035µg/µL; PD35 PFC 0.01µg/µL; PD100 PFC 0.035µg/µL
- anti-NR2B: PD21 PFC, 0.01µg/µL; PD35 PFC 0.075µg/µL; PD100 PFC 0.075µg/µL

Samples were therefore performed under these conditions and the AUC taken as the output value for each sample.

Supplementary Table S12.4. Selected concentrations for optimisation of the anti-NR2A antibody

Sample type	PD21 PFC	PD35 PFC	PD100 PFC
Protein concentration (µg/µL)	0.010 0.035 0.075	0.010 0.035 0.075	0.010 0.035 0.075
Antibody dilution	1:20 1:50 1:100 1:200	1:20 1:50 1:100 1:200	1:20 1:50 1:100 1:200

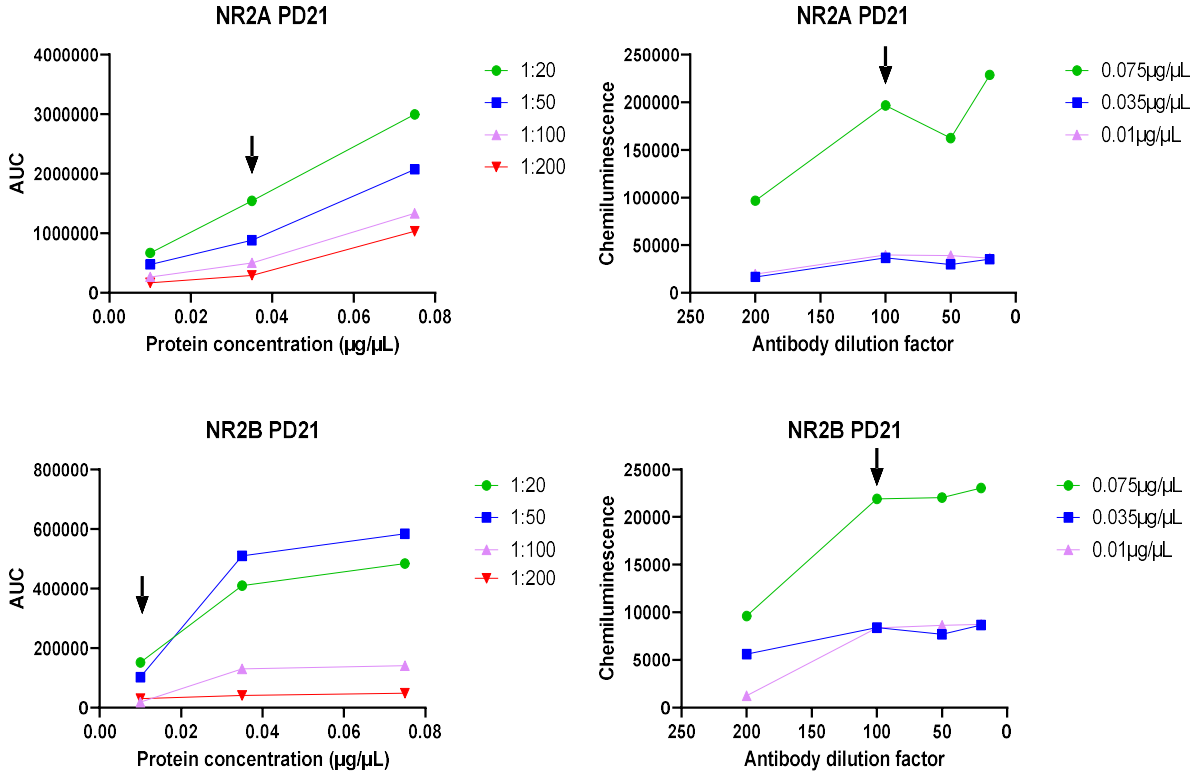

Supplementary Figure S12.5. Representative graphical plots for the anti-NR2A and anti-NR2B antibody optimisation

Left: protein concentration with different antibody dilutions; Right: antibody dilution at different protein loadings. Arrow indicates the optimal protein concentration (left) and antibody dilution factor (right) within the sample type.

v) anti-GRIA1 antibody (GLuA1; mouse monoclonal, 67642-1-Ig; Proteintech; 1.1mg/mL)

Previous in-house pilot studies had validated the anti-GLuA1 antibody produced an immunoreactive band of the anticipated size (100-120kDa), enriched in the membrane fraction as expected (Hradetzky et al., 2012; Kennard et al., 2014), hence the assay was optimised using membrane fractions. Table S12.5 summarises the membrane protein and corresponding antibody concentrations used when determining the dynamic range of anti-GLuA1 assay. A representative graphical plot for PD100 can be seen in Figure S12.6. Using the graphical plots at each timepoint, optimal conditions were determined and are indicated with an asterisk within Table S12.5. Samples were therefore performed under these conditions and the AUC taken as the output value for each sample.

Supplementary Table S12.5. Selected concentrations for optimisation of the anti-GRIA1 antibody

Sample type	PD21 PFC	PD35 PFC	PD100 PFC
Protein concentration (µg/µL)	0.005 0.0025* 0.00125	0.005 0.0025 0.00125*	0.005* 0.0025 0.00125
Antibody dilution	1:200* 1:500 1:1000 1:2000	1:200 1:500* 1:1000 1:2000	1:200 1:500* 1:1000 1:2000

*Indicates the optimal concentration for sample type

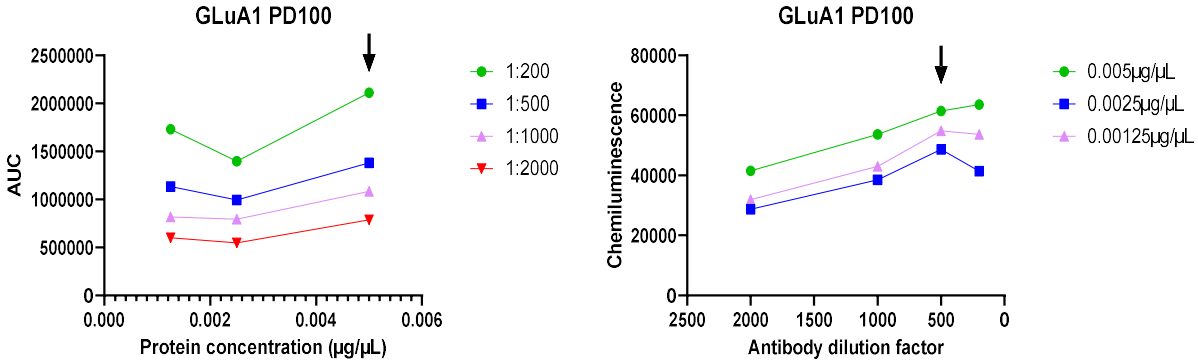

Supplementary Figure S12.6. Representative graphical plots for the anti-GRIA1 antibody optimisation
Left: protein concentration with different antibody dilutions; Right: antibody dilution at different protein loadings. Arrow indicates the optimal protein concentration (left) and antibody dilution factor (right) within the timepoint.

Appendix 13: Western blotting supplementary methods

1. Western blotting antibody validations

i) anti-MBP antibody (rabbit polyclonal, Proteintech, 10458-1-AP; 500µg/mL)

The antibody was first validated for its efficiency in detecting MBP using the standard Western blotting protocol outlined in Chapter 3, Section 3.2.3.2. Rat MBP is a primarily extracellular membrane-bound protein with isoforms of approximately 14-22 kDa size (Akiyama et al., 2002; Kruger et al., 1999). Therefore, to validate the anti-MBP antibody, 20µg of membrane and cytosolic lysates were used to demonstrate an enrichment of the anti-MBP immunoreactive band(s), of predicted size, in the membrane fraction (Figure S13.1). For this validation, a 1:1,000 (0.5µg/mL) primary antibody dilution was used in an overnight incubation at 4°C, as previously described (Chapter 3, Section 3.2.3.2). This showed immunoreactive bands in the membrane fraction corresponding to isoform sizes 14, 17, 18.5 and 21.5kDa.

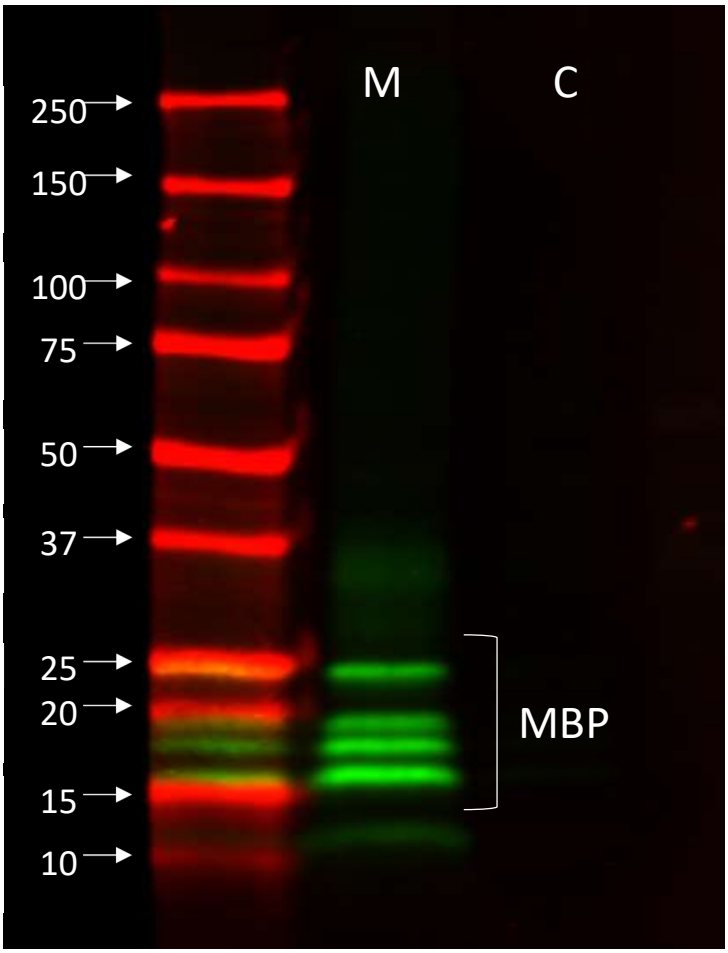

Supplementary figure S13.1. Fractional validation of the anti-MBP antibody
Western blot was run as per standard conditions (Chapter 3, Section 3.2.3.2). 20µg membrane (M) and cytosolic (C) lysate was loaded per well. 1:1,000 (0.5µg/mL) primary antibody dilution was used. Bands of anticipated size were observed, enriched in the membrane fraction. Molecular weight ladder (kDa) is indicated on the left.

After the initial validation, the anti-MBP antibody was trialled using developmental membrane samples as a further validation for the specificity of this antibody for MBP. Myelination peaks in the juvenile period in rats (Akiyama et al., 2002; Downes and Mullins, 2014) and here there was an observed increase in the density of MBP bands across advancing postnatal development (Figure S13.2).

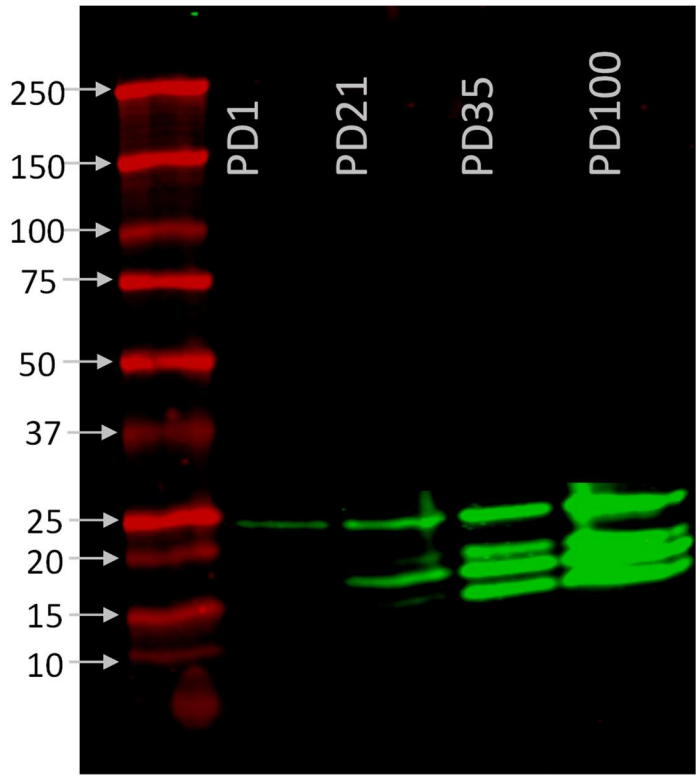

Supplementary figure S13.2. Developmental validation of the anti-MBP antibody
Western blot was run as per standard conditions (Chapter 3, Section 3.2.3.2). 50µg membrane lysate was loaded per well for various postnatal developmental ages: PD1, 21, 35 and 100. 1:1,000 (0.5µg/mL) primary antibody dilution was used. Bands of predicted size were observed, with increasing density across development. Molecular weight ladder (kDa) is indicated on the left.

ii) anti-GPC4 antibody (rabbit polyclonal, Proteintech, 13048-1-AP; 650µg/mL)

The antibody was first validated for its efficiency in detecting GPC4 using the standard Western blotting protocol outlined in Chapter 3, Section 3.2.3.2. Rat GPC4 is a transmembrane protein of approximately 62.5kDa size (Hagihara et al., 2000; Xiong et al., 2016). Therefore, to validate the anti-GPC4 antibody, 20µg of membrane and cytosolic lysates were used to demonstrate an enrichment of the anti-GPC4 immunoreactive band, of predicted size, in the membrane fraction (Figure S13.3). For this validation, a 1:1,000 (0.65µg/mL) primary antibody dilution was used in an overnight incubation at 4°C, as previously described (Chapter 3, Section 3.2.3.2). This demonstrated an enrichment for an immunoreactive band in the membrane fraction corresponding to approximately 62kDa.

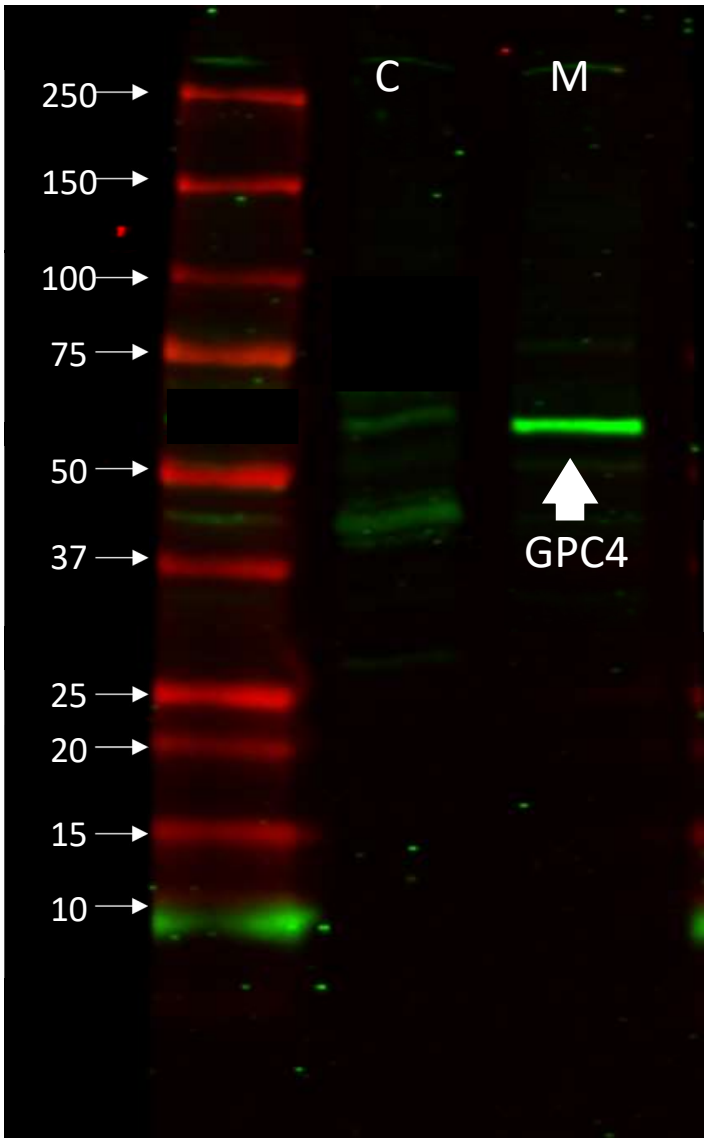

Supplementary Figure S13.3. Fractional validation of the anti-GPC4 antibody
Western blot was run as per standard conditions (Chapter 3, Section 3.2.3.2). 20µg membrane (M) and cytosolic (C) lysate was loaded per well. 1:1,000 (0.65µg/mL) primary antibody dilution was used. A single immunoreactive band of predicted size was observed, enriched in the membrane fraction. Molecular weight ladder (kDa) is indicated on the left.

iii) anti-DAB1 antibody (rabbit monoclonal [EP2248Y], ab68461; Abcam; 0.205mg/mL)

The antibody was first validated for its efficiency in detecting DAB1 using the standard Western blotting protocol outlined in Chapter 3, Section 3.2.3.2. Rat brain DAB1 is a cytosolic protein and of approximately 80kDa size (Alvarez-Dolado et al., 1999; Bock et al., 2003; Fatemi et al., 2009b; Kang et al., 2020; Kolaka et al., 2019; Sato et al., 2007; Trotter et al., 2013). Therefore, to validate the anti-DAB1 antibody, 50µg membrane and cytosolic lysates were used to demonstrate an enrichment of the anti-DAB1 immunoreactive band, of predicted size, in the cytosolic fraction (Figure S13.4). For this validation, a 1:1,000 (0.205µg/mL) primary antibody dilution was used in an overnight incubation at 4°C, as previously described (Chapter 3, Section 3.2.3.2). This demonstrated an enrichment for an immunoreactive band in the cytosolic fraction corresponding to approximately 80kDa.

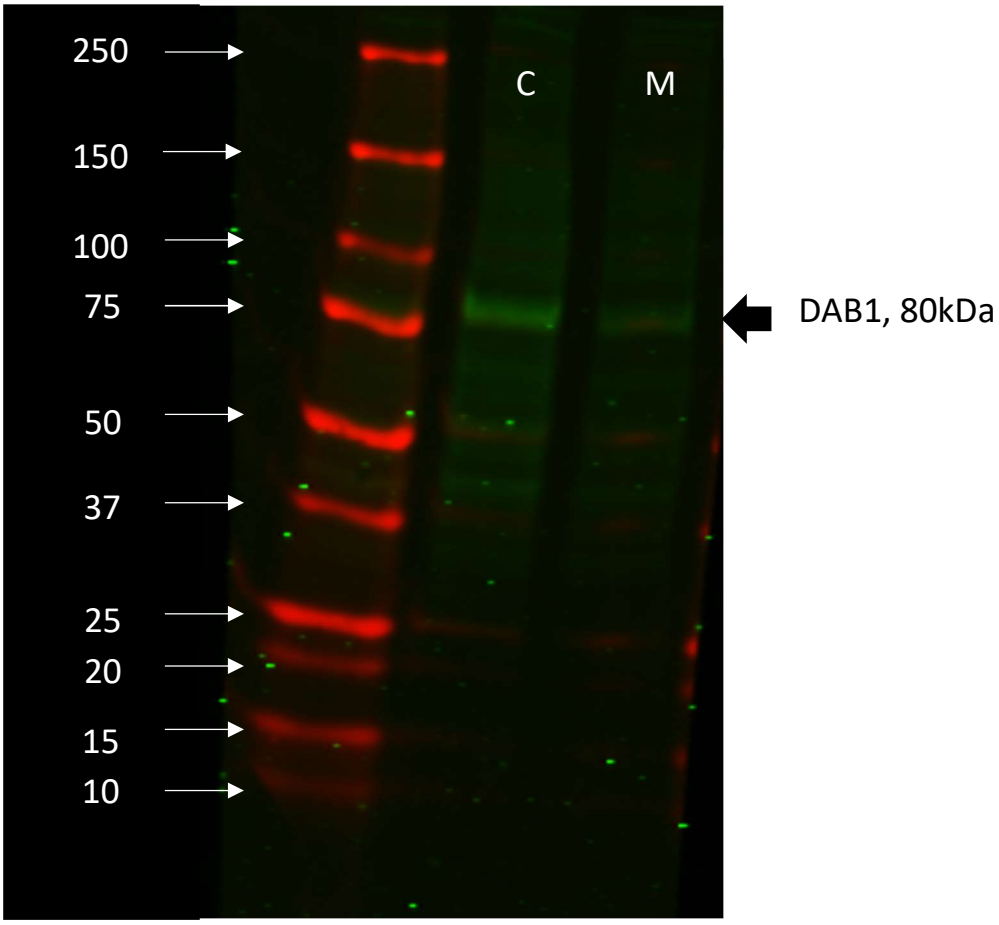

Supplementary Figure S13.4. Fractional validation of the anti-DAB1 antibody
Western blot was run as per standard conditions (Chapter 3, Section 3.2.3.2). 50µg membrane (M) and cytosolic (C) lysate was loaded per well. 1:1,000 (0.205µg/mL) primary antibody dilution was used. A single immunoreactive band of predicted size was observed, enriched in the cytosolic fraction. Molecular weight ladder (kDa) is indicated on the left.

After the initial validation, the anti-DAB1 antibody was trialled using developmental cytosol samples as a further validation for the specificity of this antibody. DAB1 is known to be more highly expressed during early brain development (Lee and D'Archangelo, 2016) and there was an observed decrease in DAB1 band intensity across postnatal development (Figure S13.5).

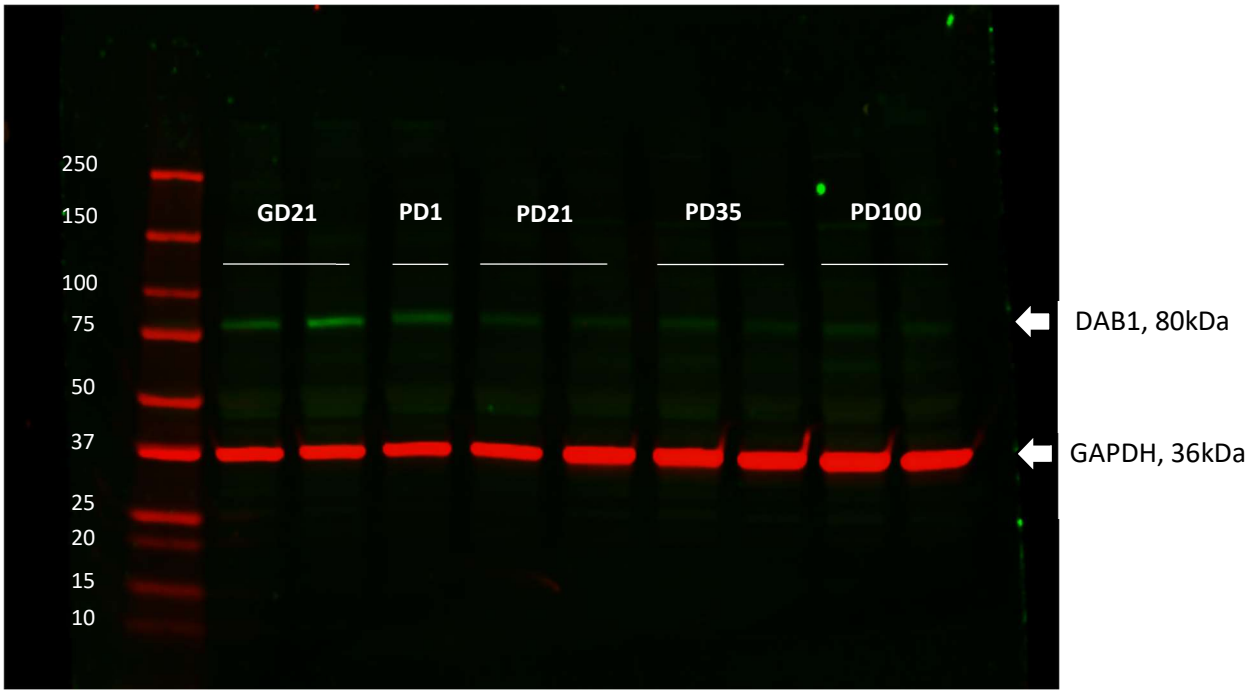

Supplementary Figure S13.5. Developmental validation of the anti-DAB1 antibody
Western blot was run as per standard conditions (Chapter 3, Section 3.2.3.2). 50µg cytosolic lysate was loaded per well, including GD21-PD100. 1:1,000 (0.205µg/mL) primary antibody dilution was used. A single immunoreactive band of predicted size was observed, enriched in early developmental ages of GD21 and PD1. GAPDH reference protein also shown. Molecular weight ladder (kDa) is indicated on the left.

iv) anti-pDAB1 antibody trials

Following quantification of total DAB1, attempts were made to identify an antibody to quantify pDAB1. Three selected phospho-antibodies from three different suppliers were trialled on cytosolic lysate samples (PD1, PD21 and PD100; Supplementary Figure S13.6). No band of the correct size could be identified across any of the samples or conditions used (Supplementary Table S13.1). Therefore, none of these antibodies were deemed suitable for further use.

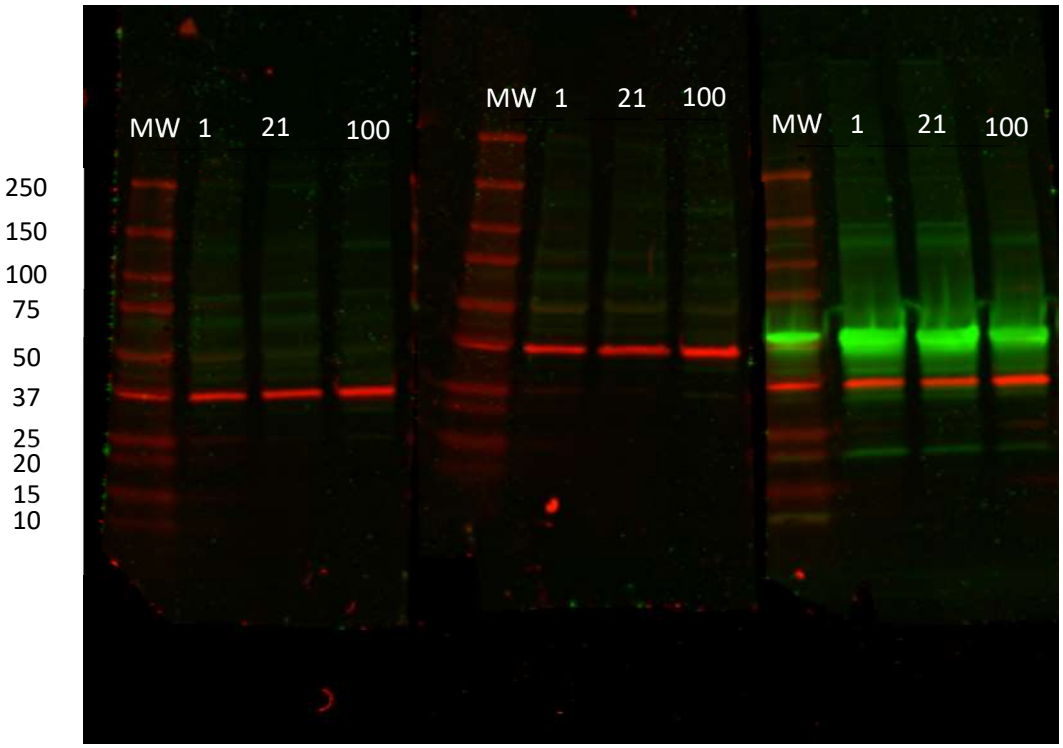

Supplementary Figure S13.6. Representative blots for anti-pDAB1 antibody trials
Western blot was run as per standard conditions (Chapter 3, Section 3.2.3.2). 100µg cytosolic lysate was loaded per well, across different postnatal ages (PD1, PD21 and PD100). 1:500 dilution of each of the three primary antibodies (Chapter 6, Table 6.8) was used. Molecular weight ladder (kDa) is indicated on the left. Antibodies were (left to right): Cell Signalling Technology, 3327S; St John's Laboratory, STJ196282; Abcam, ab78200. Red single immunoreactive band shows GAPDH as reference protein, confirming protein integrity of all samples.

Supplementary Table S13.1. pDAB1 antibody trial methodologies

Methodological stage	Conditions trialled
Primary antibody dilution	1:200 (5µg/mL); 1:500 (2µg/mL), 1:1,000 (1µg/mL)
Primary antibody incubation	Overnight: 4°C and room temperature 3h: room temperature
Sample protein loadings	50, 75, 100, 200µg/well
Blocking buffer	2% and 5%BLOTTO 5%BSA in 1XPBS.

2. Western blotting antibody optimisations

For all antibodies two graphical plots were created for each sample type: i) protein concentration at each antibody dilution; ii) antibody dilutions at each protein concentration. For graph (i) the optimal protein concentration was determined by identifying the concentration at which the graph remains linear. For graph (ii) the antibody dilution was determined by identifying where the graph reaches a plateau. This represents the linear range of the assay. In contrast to WES optimisations the outputs for these conditions was signal intensity.

i) anti-MBP antibody (rabbit polyclonal, Proteintech, 10458-1-AP; 500µg/mL)

Table S13.2 summarises the protein and antibody concentrations used when determining the linear range of the assay. A representative graphical plot for PD35 can be seen in Figure S13.7 Using the graphical plots at each developmental age a 1:5,000 (0.1µg/mL) antibody dilution was deemed optimal, with the following protein inputs/well GD21 and PD1 FC, 100µg/well; PD21 PFC 50µg/well; PD35 and PD100 PFC 25-50µg/well.

Supplementary Table S13.2. Selected concentrations for optimisation of the anti-MBP antibody

Sample type	GD21 FC	PD1 FC	PD21 PFC	PD35 PFC	PD100 PFC
Protein loading (µg/well)	75 100 125	75 100 125	10 25 50 75	10 25 50 75	10 25 50 75
Antibody dilution	1:1000 1:5000 1:10000	1:1000 1:5000 1:10000	1:1000 1:5000 1:10000	1:1000 1:5000 1:10000	1:1000 1:5000 1:10000

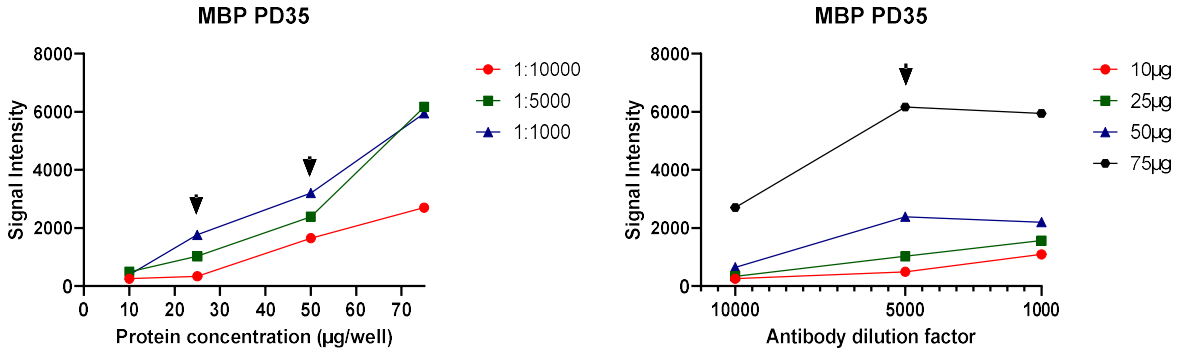

Supplementary Figure S13.7. Representative graphical plots for the anti-MBP antibody optimisation
Left: protein concentration at different antibody dilutions; Right: antibody dilution at different protein loadings. Arrow(s) indicates the optimal antibody protein concentration (linear phase) and antibody dilution (plateau) within the sample type.

ii) anti-GPC4 antibody (rabbit polyclonal, Proteintech, 13048-1-AP; 650µg/mL)

Table S13.3 summarises the protein and antibody concentrations used when determining the linear range of the assay. A representative graphical plot for GD21 can be seen in Figure S13.8. Using the graphical plots at each timepoint a 1:1,000 (0.65µg/mL) antibody dilution was deemed optimal, with the following protein inputs/well GD21 and PD1 FC, 100µg/well; PD21 PFC 50µg/well; PD35 and PD100 PFC 25µg/well.

Supplementary Table S13.3. Selected concentrations for optimisation of the anti-GPC4 antibody

Sample type	GD21 FC	PD1 FC	PD21 PFC	PD35 PFC	PD100 PFC
Protein loading (µg/well)	50 100 150	50 100 150	25 50 75	25 50 75	25 50 75
Antibody dilution	1:500 1:1000 1:2000	1:500 1:1000 1:2000	1:500 1:1000 1:2000	1:500 1:1000 1:2000	1:500 1:1000 1:2000

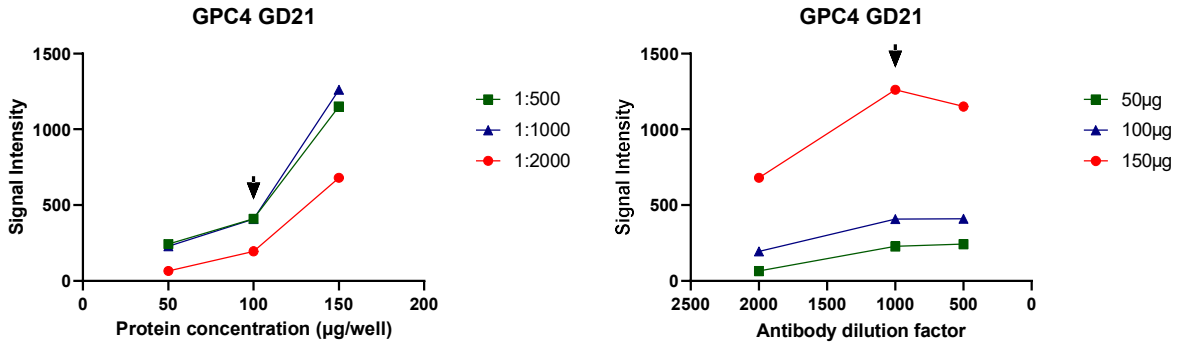

Supplementary Figure S13.8. Representative graphical plots for the anti-GPC4 antibody optimisation
Left: protein concentration at different antibody dilutions; Right: antibody dilution at different protein loading. Arrow indicates the optimal antibody protein concentration (linear phase) and antibody dilution (plateau) within the sample type.

iii) MBP and GPC4 double antibody probe and validation by negative control

Given that MBP and GPC4 were enriched in the same cellular fraction (membrane), with similar optimal protein inputs, but very different molecular weights, 14-22kDa and 60-65kDa, respectively, it was determined they could be quantified from the same sample on a single Western blot using successive primary antibody incubations. To achieve this, it was first determined in what order to perform the primary antibody probes. For this, a standard Western blotting protocol was used (Chapter 3, Section 3.2.3.2) however, for each of the primary antibodies both the standard overnight incubation at 4°C or a 3h room temperature incubation was performed to assess which antibody might be compatible for use as a second primary antibody probe on day 2 of the standard protocol. The results from this optimisation are shown in Supplementary Figure S13.9. They show a clearer band for GPC4 following an overnight incubation at 4°C, but clearer bands for MBP following a 3h room temperature incubation. It was therefore determined that for the analysis of MBP and GPC4, the standard Western blotting protocol would be followed (Chapter 3, Section 3.2.3.2), with the anti-GPC4 antibody used as the first primary antibody probe (overnight, 4°C). However, following equilibration of the blot to room temperature on day 2, the blot was washed (4x5min standard washes) and a second primary antibody probe would be performed for 3h at room temperature using the anti-MBP antibody. This second primary antibody probe would be followed by 4x5min standard washes prior to the incubation of the blot with the reference antibody.

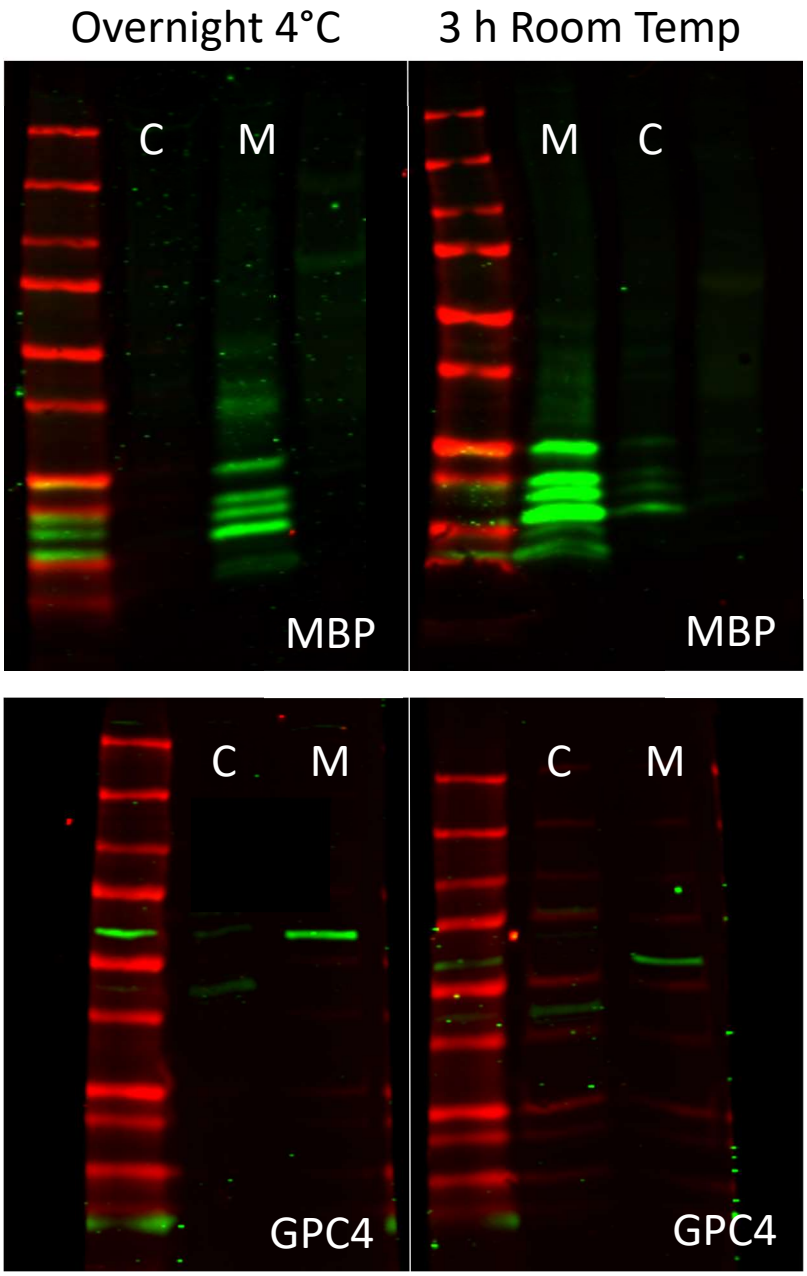

Supplementary Figure S13.9. Optimisation of anti-MBP and anti-GPC4 antibodies for different primary antibody probe conditions
Western blot was run as per standard conditions (Chapter 3, Section 3.2.3.2) but primary antibody incubations were performed either using the standard overnight incubation at 4°C or a 3h room temperature incubation. 50µg PD21 membrane (M) or cytosolic (C) lysate was loaded per well. 1:1,000 (0.65µg/mL) anti-GPC4 or 1:5,000 (0.1µg/mL) anti-MBP primary antibody dilution was used.

Following this trial, a complete protocol was performed using the double antibody probe protocol (Supplementary Figure S13.10A). In addition, to determine the specificity of the observed immunoreactive banding pattern was due to the primary antibodies, a negative control was performed with omission of all primary and reference antibodies (Supplementary Figure S13.10B). This negative blot showed no immunoreactive bands were present, in contrast to the positive control, indicating that the observed immunogenic bands are a result of primary antibody binding.

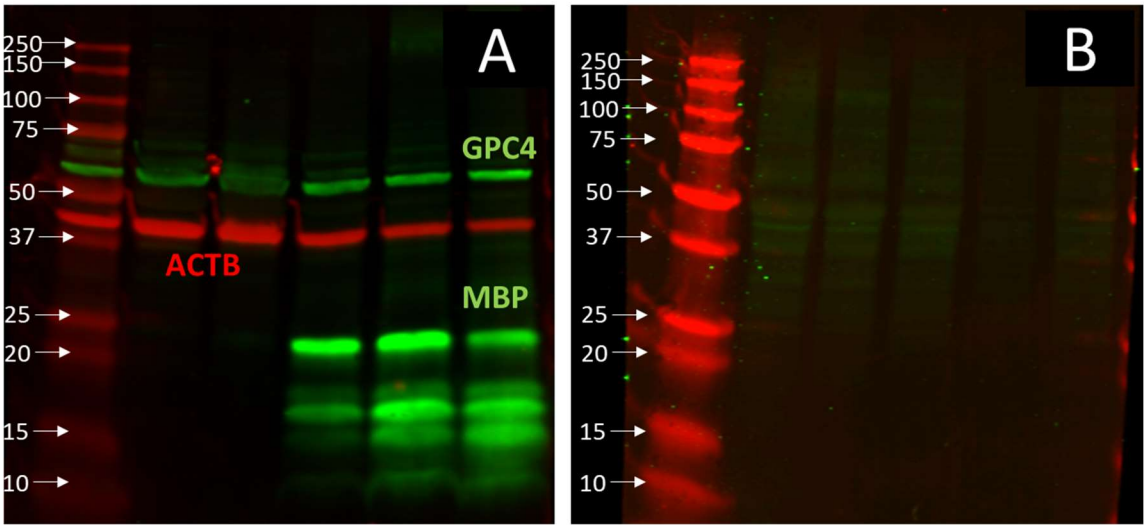

Supplementary Figure S13.10. anti-MBP and anti-GPC4 dual probe and negative control

A. Positive control. membrane lysates were loaded as outlined in the optimisation. Western blot was run as per standard conditions (Chapter 3, Section 3.2.3.2) but primary antibody incubations were performed using first an overnight incubation at 4°C using 1:1,000 (0.65µg/mL) anti-GPC4 and then on day 2 a second primary antibody incubation was performed for 3h at room temperature using 1:5,000 (0.1µg/mL) anti-MBP. A 1:2,000 (1µg/mL) ACTB (β-actin) dilution was used for the reference antibody incubation. Molecular weight ladder (kDa) is indicated on the left.

B. Negative control. Membrane lysates were identical to those used for the positive control. Western blot was run as per standard conditions (Chapter 3, Section 3.2.3.2) but all primary antibodies were omitted. All other conditions were identical, including the addition of the secondary Li-Cor antibodies. Molecular weight ladder (kDa) is indicated on the left.

.

iv) anti-DAB1 antibody (rabbit monoclonal [EP2248Y], ab68461; Abcam; 0.205mg/mL)

Table S13.4 summarises the protein and antibody concentrations used when determining the linear range of the assay. A representative graphical plot for PD100 can be seen in Figure S13.11. Using the graphical plots at each developmental age a 1:1,000 (0.205µg/mL) antibody dilution was deemed optimal, with the following protein inputs/well: GD21-PD1 FC, 50µg/well; PD21-100 PFC 75µg/well.

Supplementary Table S13.4. Selected concentrations for optimisation of the anti-DAB1 antibody

Sample type	GD21 FC	PD1 FC	PD21 PFC	PD35 PFC	PD100 PFC
Protein loading (µg/well)	25 50 75	25 50 75	50 75 100	50 75 100	50 75 100
Antibody dilution	1:500 1:1000 1:2000	1:500 1:1000 1:2000	1:500 1:1000 1:2000	1:500 1:1000 1:2000	1:500 1:1000 1:2000

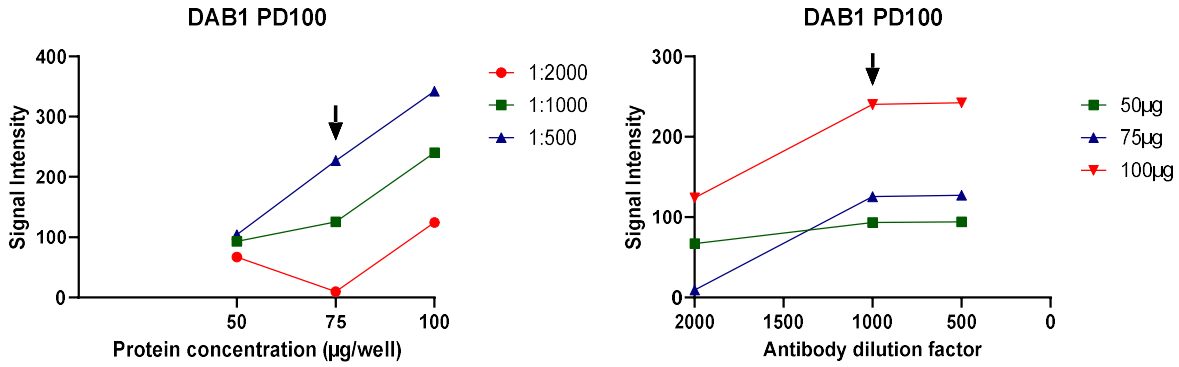

Supplementary Figure S13.11. Representative graphical plots for the anti-DAB1 antibody optimisation
Left: protein concentration at different antibody dilutions; Right: antibody dilutions at different protein loadings. Arrow(s) indicates the optimal antibody protein concentration (linear phase) and antibody dilution (plateau) for this sample type.

Following this optimisation, a complete protocol was performed using the optimised methodology (Supplementary Figure S13.12A). In addition, to determine the specificity of the observed immunoreactive banding pattern was due to the primary antibodies, a negative control was performed with omission of all primary and reference antibodies (Supplementary Figure S13.12B). This generated a negative blot with no immunoreactive bands present, in contrast to the positive control, indicating that the observed immunogenic bands are a result of the primary antibody binding.

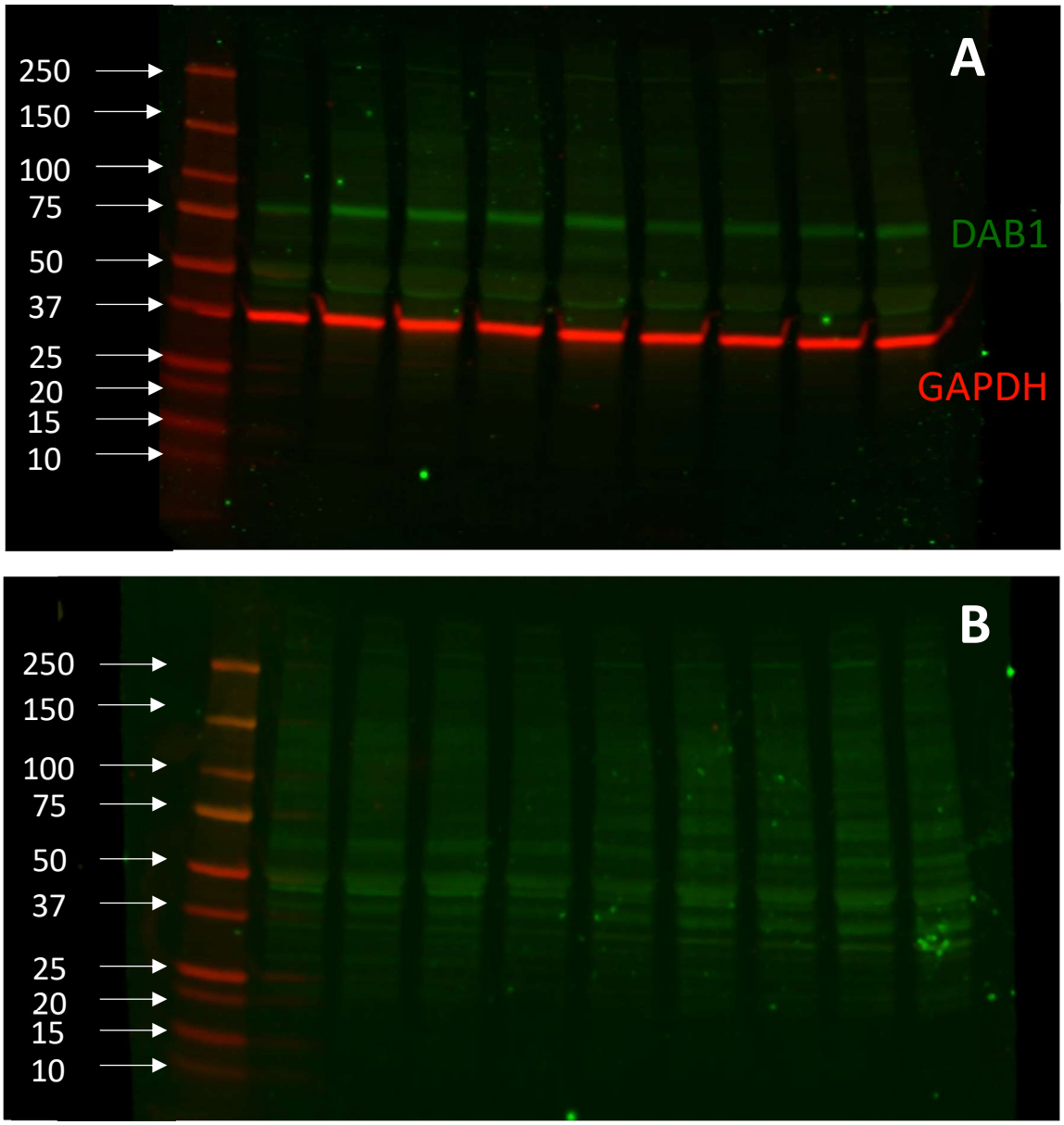

Supplementary Figure S13.12. anti-DAB1 positive and negative control

A. Positive control. Western blot was run as per standard conditions (Chapter 3, Section 3.2.3.2) using the optimised DAB1 conditions outlined above. Molecular weight ladder (kDa) is indicated on the left. GAPDH served as reference protein.

B. Negative control. Identical cytosolic lysates used in the positive control. Western blot was run as per standard conditions (Chapter 3, Section 3.2.3.2) but all primary antibodies were omitted. All other conditions were identical, including the addition of the secondary Li-Cor antibodies. Molecular weight ladder (kDa) is indicated on the left.

3. Western blotting reference protein stability assessments

Normalisation of target protein expression demanded the use of a stably expressed reference protein within each cellular fraction of interest. Given the findings from the mRNA reference gene stability panel (Appendix 3), the stability of the least (*Actb*, encoding β-actin/ACTB) and most (*Gapdh*, encoding GAPDH) stable reference genes were evaluated as proteins in both the cytosolic and membrane cellular fractions. For this, cytosolic or membrane fraction samples, inclusive of all sexes, developmental ages and treatment groups were randomly selected for a stability assessment (n=2/sex/treatment group/timepoint). 20µg protein lysate was loaded per well and the standard Western blotting protocol was followed (Chapter 3, Section 3.2.3.2), until drying of the membrane. After this, the blots were placed in 1XPBS and stored overnight at 4°C. The following day they were equilibrated to room temperature for 1h and then processed through two successive reference antibody probes, both for 2h at room temperature as per the standard protocol, with standard washes between the addition of each reference antibody. The first incubation was a 1:2,000 (1µg/mL) dilution of the anti-ACTB antibody (mouse monoclonal, Merck, Gillingham, UK, A2228; 2mg/mL), the second a 1:2,000 (0.5µg/mL) dilution of the anti-GAPDH antibody (mouse monoclonal, Proteintech, Manchester, UK, 60004-1-Ig; 1mg/mL). The results from these experiments can be seen in Supplementary Figure S13.13.

The optical density of each reference protein was assessed and averaged across each sample type to determine stability (Supplementary Figure S13.14). While ANOVA test statistics showed no significant difference between any of the groups, ACTB showed a greater variance within sample types (Figure 13.14). Hence, GAPDH expression appears the least impacted by age, group or sex across both membrane and cytosolic fractions. This reference antibody was hence selected for use to normalise target protein expression.

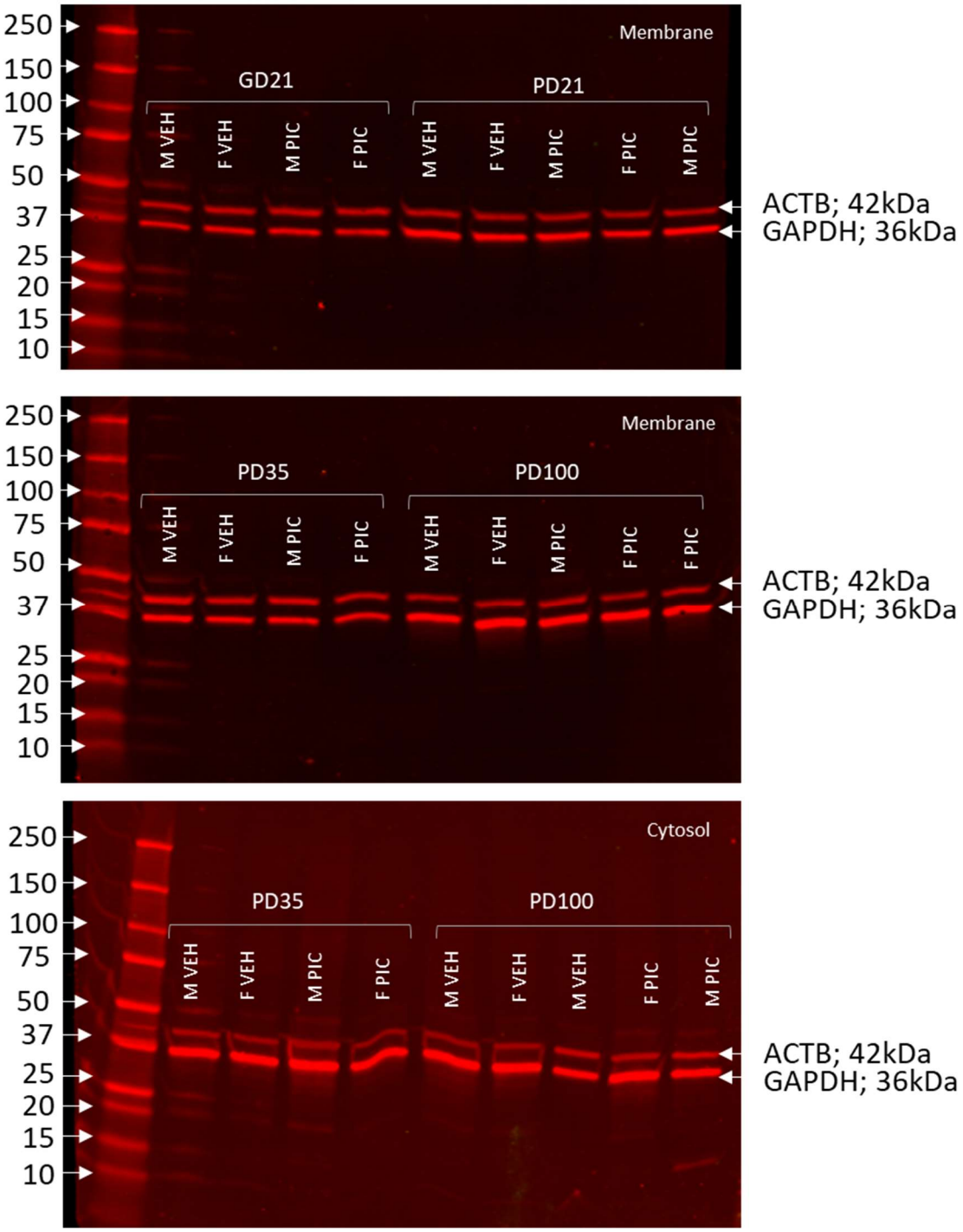

Supplementary Figure S13.13. Representative Western blot images for the assessment of reference protein stability

Western blot was run as per standard conditions (Chapter 3, Section 3.2.3.2) until drying of the membrane. After this, the blots were placed in 1XPBS and stored overnight at 4°C. The following day they were equilibrated to room temperature for 1h and then processed through two successive reference antibody probes, both for 2h at room temperature as per the standard protocol, with standard washes between the addition of each reference antibody. The first incubation was a 1:2,000 (1µg/mL) dilution of the anti-ACTB antibody, the second a 1:2,000 (0.5µg/mL) dilution of the anti-GAPDH antibody. Molecular weight ladder (kDa) is indicated on the left. All samples demonstrated an immunoreactive signal for both reference proteins. Abbreviations: M, Male; F, female; VEH, vehicle; PIC, poly(I:C); PD, postnatal day.

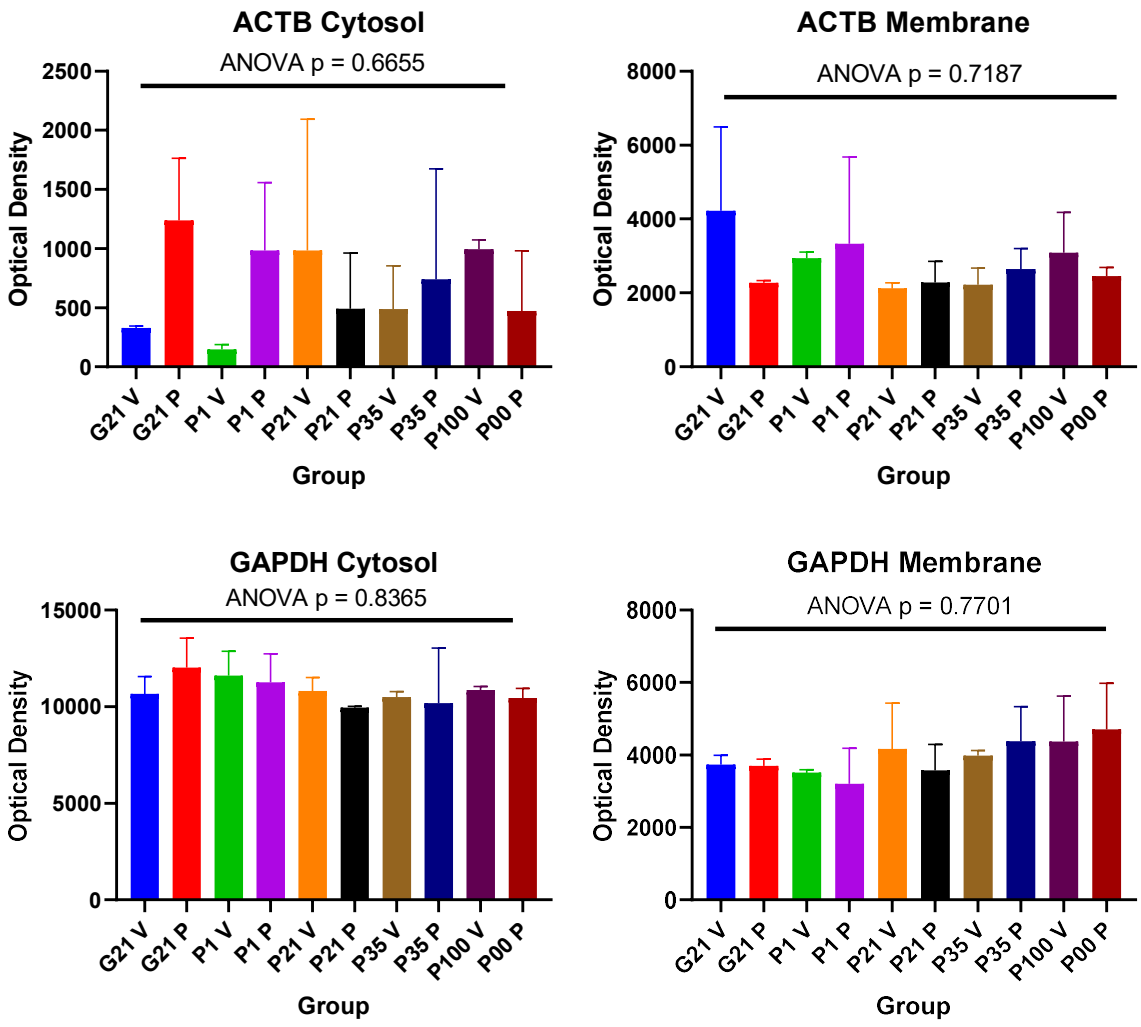

Supplementary Figure S13.14. Analysis of reference protein stability
Immunoreactive signal measured as optical density (mean + SEM) for various cytosolic and membrane samples for ACTB and GAPDH expression. Group is indicated along the x-axis: G21, gestational day; P1-100, postnatal days 1-100; V/P, vehicle/poly(I:C) sample. n=2-3/sex/group/timepoint.

Appendix 14: IF/IHC supplementary methods

Note protocols for: IBA1+ staining (Murray et al., 2019); PV+ and PNN+ staining (Jennifer Fletcher, verbal communication) followed pre-optimised methodology already performed in-house.

1. OLIG2+ and GFAP+ co-stain

Anti-OLIG2 antibody (rabbit monoclonal [EPR2673] Abcam, ab109186; 131µg/mL) and anti-GFAP antibody (chicken polyclonal, Abcam, ab4674; 19.4mg/mL) co-stain (IF)

As a co-stain was desired, primary antibodies were required from two different host-species. The suggested dilutions for the selected antibodies were 1:100 and 1:1,000-1:5,000 for OLIG2 and GFAP, respectively. For the latter (anti-GFAP) the mid-range of 1:3,000 (6.5µg/mL) was selected, for the former (anti-OLIG2), the suggested dilution factor was unworkable given required sample numbers and antibody solution volume required. Alternatively, 1:1,000 (0.131µg/mL) was selected, guided by previous literature using this antibody which suggested greater dilution was still effective. The standard IF protocol was followed (Chapter 5, Section 5.2.1.2), using sodium citrate antigen retrieval as recommended by the manufacturer and a primary antibody incubation at 4°C.

i) Antibody validation by staining pattern

OLIG2 is a transcription factor isolated to the nucleus of oligodendrocytes (Emery and Lu, 2015) while GFAP stains astrocytic processes with a very distinctive pattern (Zhang et al., 2019b). The staining observed for the antibodies incubated individually produced a nuclear only stain by the anti-OLIG2, enriched in the white matter tracts (Figure S14.1A) and demonstrated the distinctive astrocytic stain of GFAP (Figure S14.1B). This validation demonstrated that the antibodies were effective in staining the cells of interest. Next, the two antibodies were tested for their staining pattern when combined during the primary antibody incubation step. This resulted in identical staining patterns to that observed when they had been incubated individually (Figure S14.1C). The co-stain protocol was hence deemed effective as there was no cross-reactivity between the two primary antibodies.

ii) Negative controls

For a final validation of the specificity of the two antibodies, two negative controls were performed: the first excluded the primary antibodies from the solution (Figure S14.2A) and the second included matched species immunoglobulin diluted to the same concentration of the relevant primary antibody (Figure S14.2B). This included: rabbit IgG control antibody (Vector Labs, London, UK, I-1000-5) and normal chicken IgY control antibody (Chemicon, London, UK, AC146). This resulted in no visible staining in either negative control, supporting the specificity of the staining pattern for the primary antibodies.

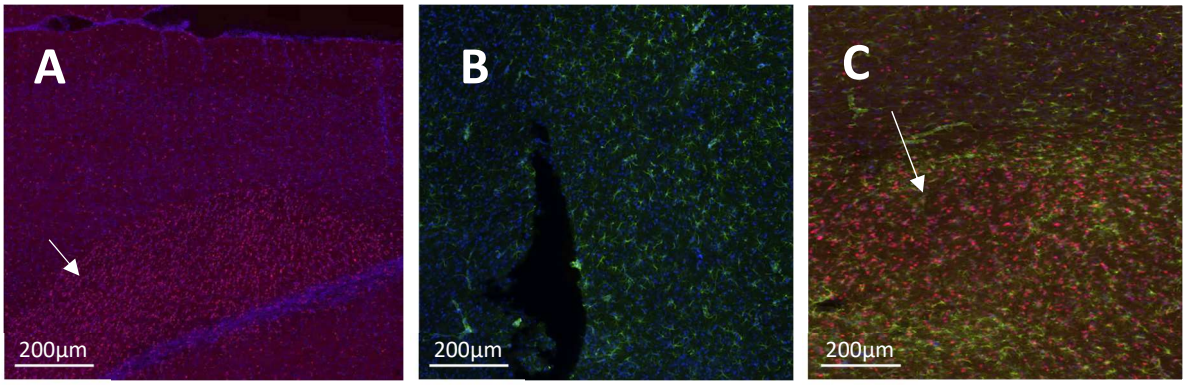

Supplementary Figure S14.1. Validation of IF staining patterns
A. OLIG2+ stain only; **B.** GFAP+ stain only; **C.** OLIG2+ and GFAP+ co-stain. The standard IF protocol was followed (Chapter 5, Section 5.2.1.2), using sodium citrate antigen retrieval as recommended by the manufacturer and an overnight primary antibody incubation at 4°C, with DAPI in the mounting medium. Arrows indicate the increased density of OLIG2+ staining in the white matter tracts.

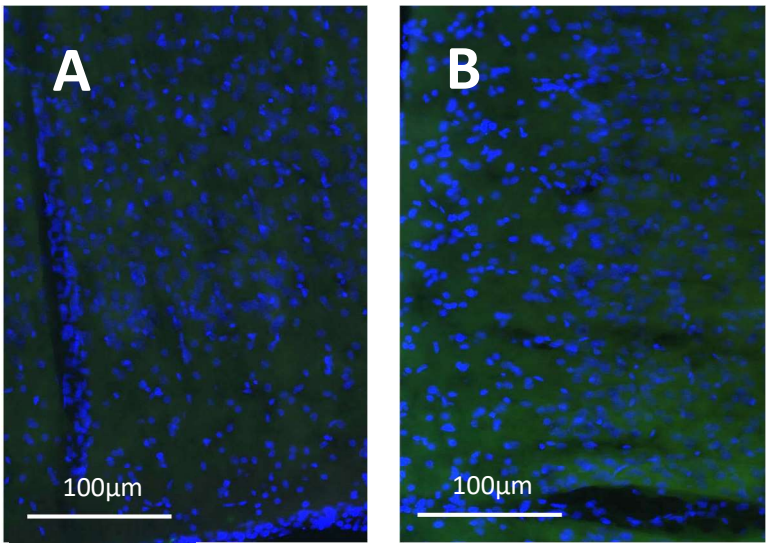

Supplementary Figure S14.2. IF co-stain negative control
A. No primary antibody control (DAPI in the mounting medium); **B.** Primary antibody species-specific IgG control: 0.13µg/mL rabbit IgG and 6.5µg/mL chicken IgY; The standard IF protocol was followed (Chapter 5, Section 5.2.1.2), using sodium citrate antigen retrieval as recommended by the manufacturer and an overnight incubation at 4°C.

iii) Optimisation of incubation conditions

Given that the anti-OLIG2 antibody was required to be diluted to a much lower concentration than recommended, the primary antibody incubation time was extended from the standard 24h to 48h to aid in antibody binding. This improved the clarity of the staining for both OLIG2+ and GFAP+ (Figure S14.3) and hence the primary antibody incubation was extended to 48h for this IF co-stain protocol.

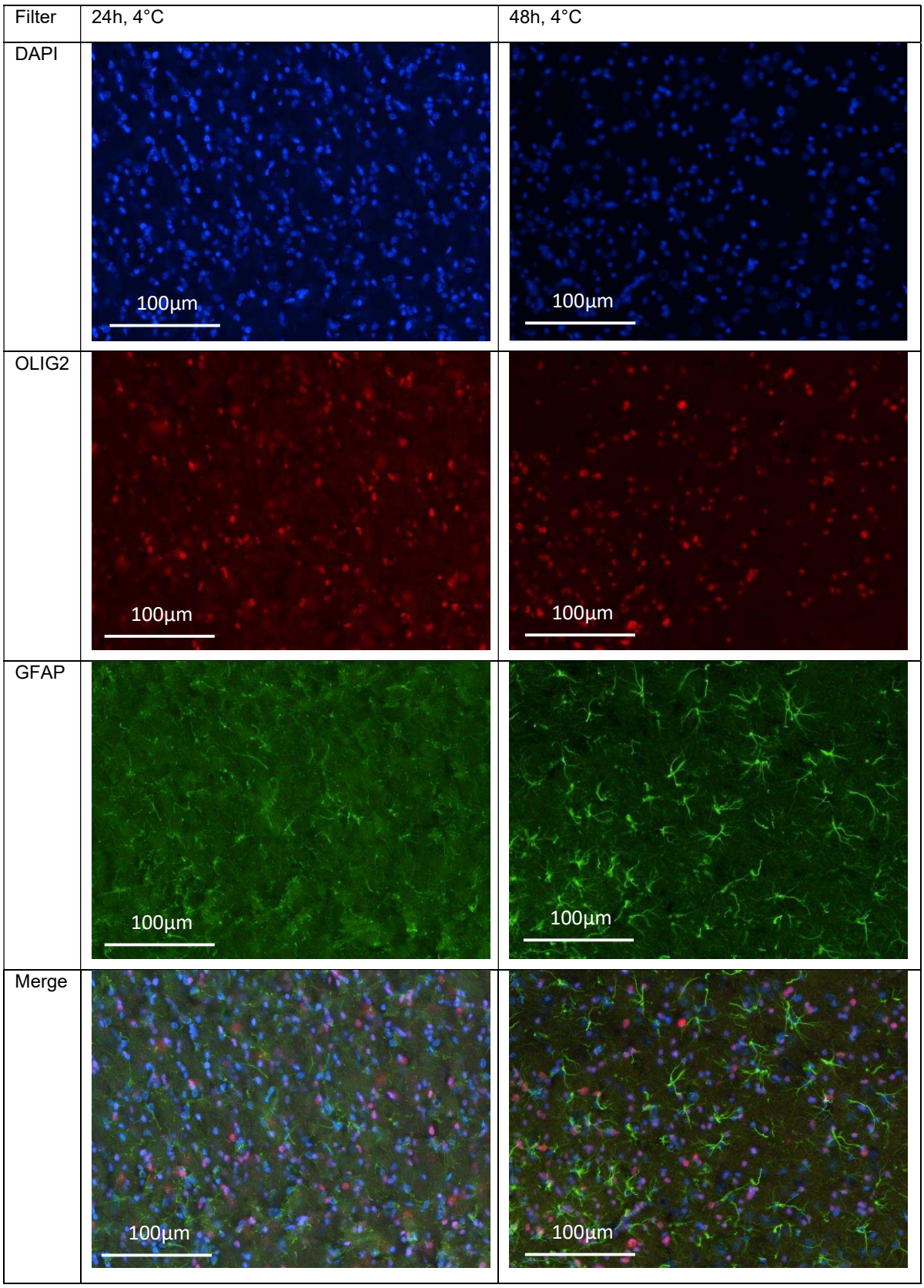

Supplementary Figure S14.3. Optimisation of IF primary antibody incubation
Summary figure of antibody optimisations for primary antibodies used for IF. Images show the staining for a 24h (Left) and 48h (Right) incubation at 4°C. The colours show the following stain: DAPI, blue; OLIG2, pink; GFAP, green.

2. NG2+ stain

Anti-NG2 antibody (rabbit polyclonal, Chemicon, AB5320; 1mg/mL)

While OLIG2 and GFAP were used to quantify oligodendrocytes and astrocytes, respectively, OLIG2 is a marker for the entire oligodendrocyte line, inclusive of OPCs (Valério-Gomes et al., 2018). Hence, it was decided that OPCs, the only retained glial progenitor in the adult CNS, would be quantified by NG2+ staining (Dawson et al., 2003; Kuhn et al., 2019) to obtain a ratio of immature:mature oligodendrocytes.

i) IF

The selected antibody was chosen for being well cited and raised against the rat NG2 protein. It was recommended to be used at a 1:200 (5µg/mL) dilution for IHC. However as this was not feasible for sample numbers, both a 1:500 (2µg/mL) and 1:1,000 (1µg/mL) dilution was tested. IF was initially selected to align with the comparative OLIG2 stain, using the standard protocol (Chapter 5, Section 5.2.1.2) and a 48h primary antibody incubation. As no antigen retrieval method was specifically recommended by the manufacturer both sodium citrate and Tris-EDTA methodology were trialled (Figure S14.4). As with OLIG2, the secondary florescent antibody was goat anti-rabbit IgG H&L Alexa Fluor® 594 (Abcam, ab150080; Lot GR3373513) using the standard 1:1,000 dilution.

The 1:500 primary antibody dilution showed a staining pattern similar to that expected for OPC (Figure S14.4A&B), however the staining pattern was nearly non-detectable at a 1:1,000 primary antibody dilution (Figure S14.4C&D). Antigen retrieval was also found to impact on staining quality. Tris-EDTA antigen retrieval produced notable lower background staining (Figure S14.4B&D) than observed for sodium citrate (Figure S14.4A&C). Nonetheless, this high background signal was still present even with use of Tris-EDTA buffer, making accurate cell counting challenging. Increasing the protein block time and serum concentration did not reduce background (data not shown).

ii) IHC

Given the high background observed with IF, IHC was trialled as an alternative staining method. Using the standard IHC methodology (Chapter 5, Section 5.2.1.3) and optimal methodological factors identified during IF optimisation: a 48h primary antibody incubation, a 1:500 primary antibody dilution and Tris-EDTA buffer antigen retrieval. IHC was found to reduce the background signal and enable identification of individual cell bodies more clearly (Figure S14.5A). As with the IF co-stain, to confirm the specificity of the stain, two negative controls were performed; the first excluded the primary antibody from the solution (Figure S14.5B) and the second included matched species IgG (rabbit IgG control antibody (Vector Labs London, UK, I-1000-5)) diluted to the same concentration (2µg/mL) of the primary antibody (Figure S14.5C). This resulted in no visible staining of the tissue in either case.

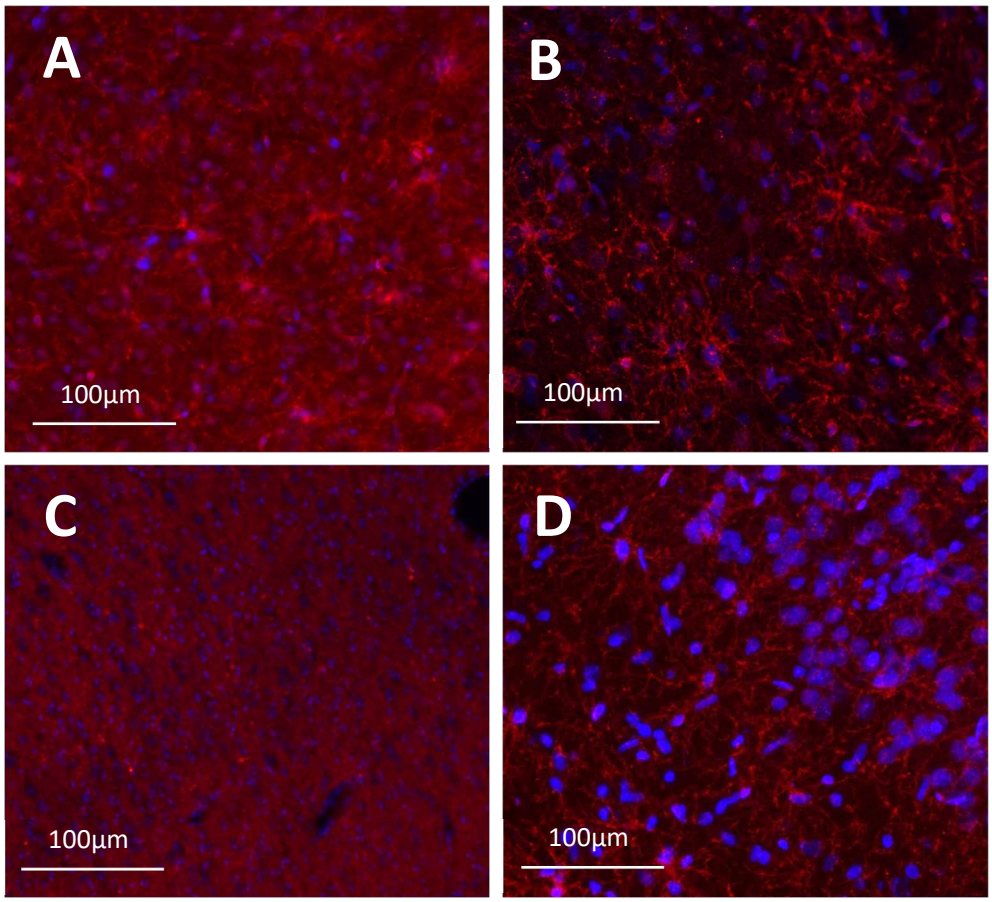

Supplementary Figure S14.4. NG2+ IF optimisation
A. 1:500 primary antibody dilution, sodium citrate buffer antigen retrieval; **B.** 1:500 primary antibody dilution, Tris-EDTA buffer antigen retrieval; **C.** 1:1,000 primary antibody dilution, sodium citrate buffer antigen retrieval; **D.** 1:1,000 primary antibody incubation, Tris-EDTA buffer antigen retrieval.

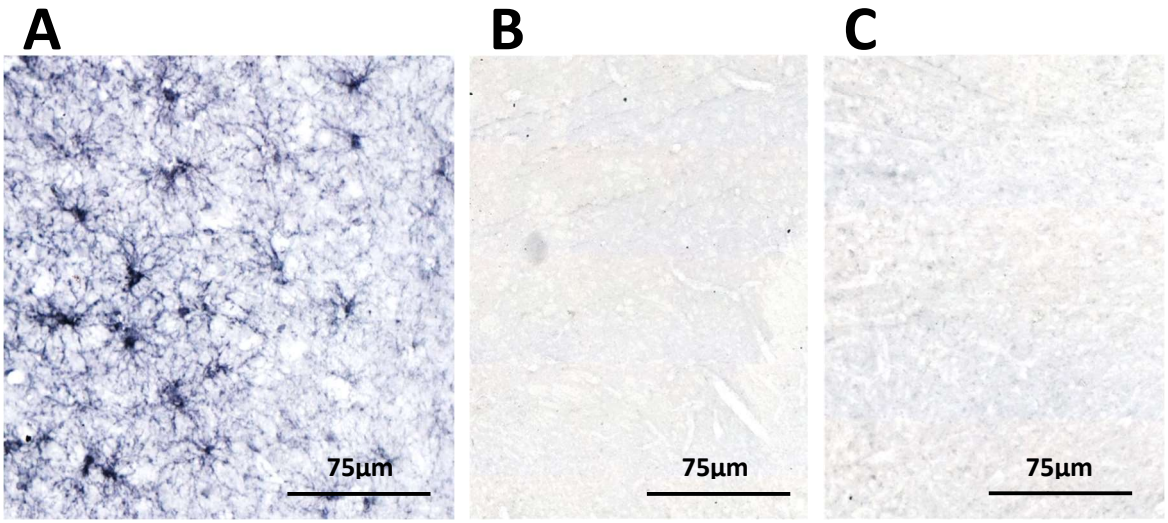

Supplementary Figure S14.5. NG2+ IHC optimisation
Standard IHC protocol was followed with a 48h primary antibody/control incubation, 1:500 (2µg/mL) primary antibody dilution and Tris-EDTA buffer antigen retrieval. **A.** Primary antibody. **B.** No primary antibody control. **C.** Rabbit IgG control (2µg/mL).

3. Positive and negative controls for IBA1+, PV+ and WFA+ stains

i) anti-IBA1 antibody (goat polyclonal, Abcam, ab5076; 0.5mg/mL)

This stain was performed using a protocol pre-optimised in-house previously (Murray et al., 2019; Chapter 5, Section 5.2.1.3), with a 1:2,000 primary antibody dilution (0.25µg/mL) for 24h at 4°C. As per the pre-optimised methodology this resulted in a staining pattern expected for IBA1+ microglial cells (Figure S14.6A). However, to confirm the stain was effective in the tissue samples used in this study, the standard two negative controls were still performed: the first excluded the primary antibody from the solution (Figure S14.6B) and the second included matched species IgG (goat IgG control antibody (Vector Labs, London, UK, I-5000-5)) diluted to the same concentration (0.25µg/mL) as the primary antibody (Figure S14.6C). This resulted in no visible staining of the tissue in either case.

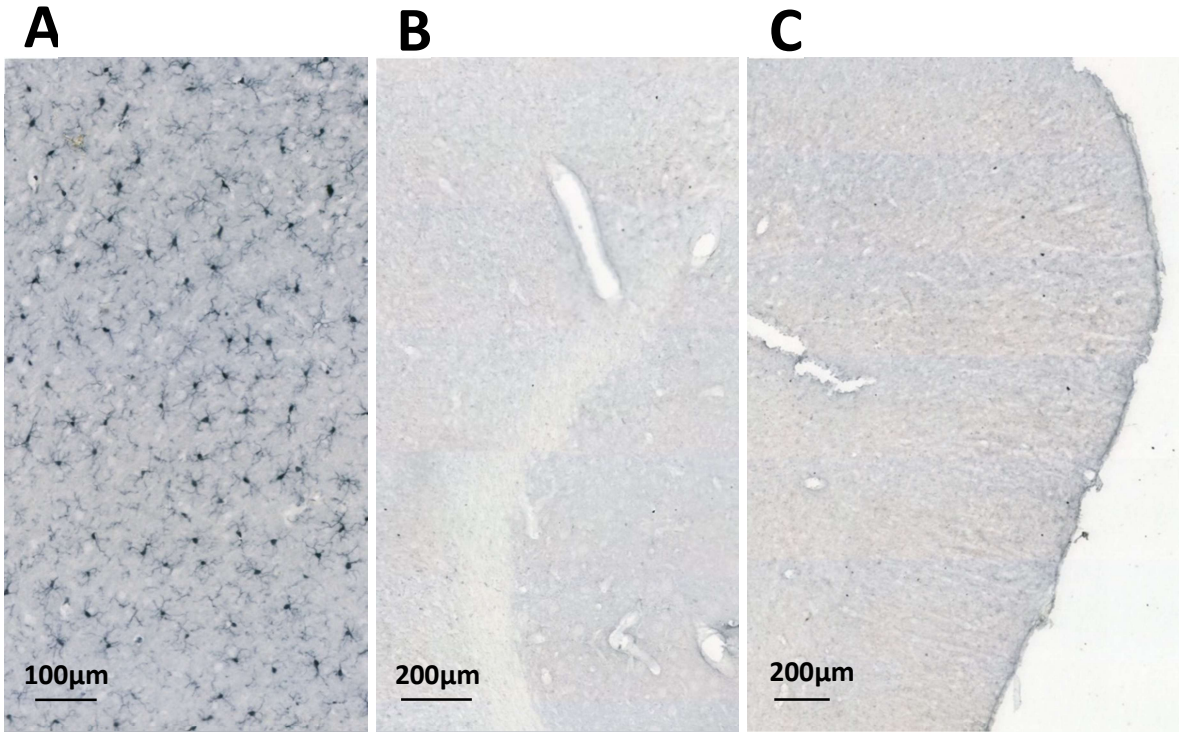

Supplementary Figure S14.6. IBA1+ IHC validation
Standard IHC protocol was followed with a 24 h primary antibody/control incubation, 1:2,000 (0.25µg/mL) primary antibody dilution and sodium citrate buffer antigen retrieval. **A.** Primary antibody. **B.** No primary antibody control. **C.** Rabbit IgG control (0.25µg/mL).

ii) anti-PV antibody (mouse monoclonal, Swant, 235; 1mg/mL)

This stain was performed using a protocol pre-optimised in-house previously (Jennifer Fletcher, verbal communication; Chapter 6, Section 6.2.1), with a 1:5,000 primary antibody dilution (0.2µg/mL) for 24h at 4°C. As per the pre-optimised methodology this resulted in a staining pattern expected for PV+ cells (Figure S14.7A). However, to confirm the stain was effective in the tissue samples used in this study, the standard two negative controls were still performed: the first excluded the primary antibody (Figure S14.7B) and the second included matched species IgG (mouse IgG control antibody, I-2000-1; Vector Labs, London, UK) diluted to the same concentration (0.2µg/mL) as the primary antibody (Figure S14.7C). This resulted in no visible staining of the tissue in either case.

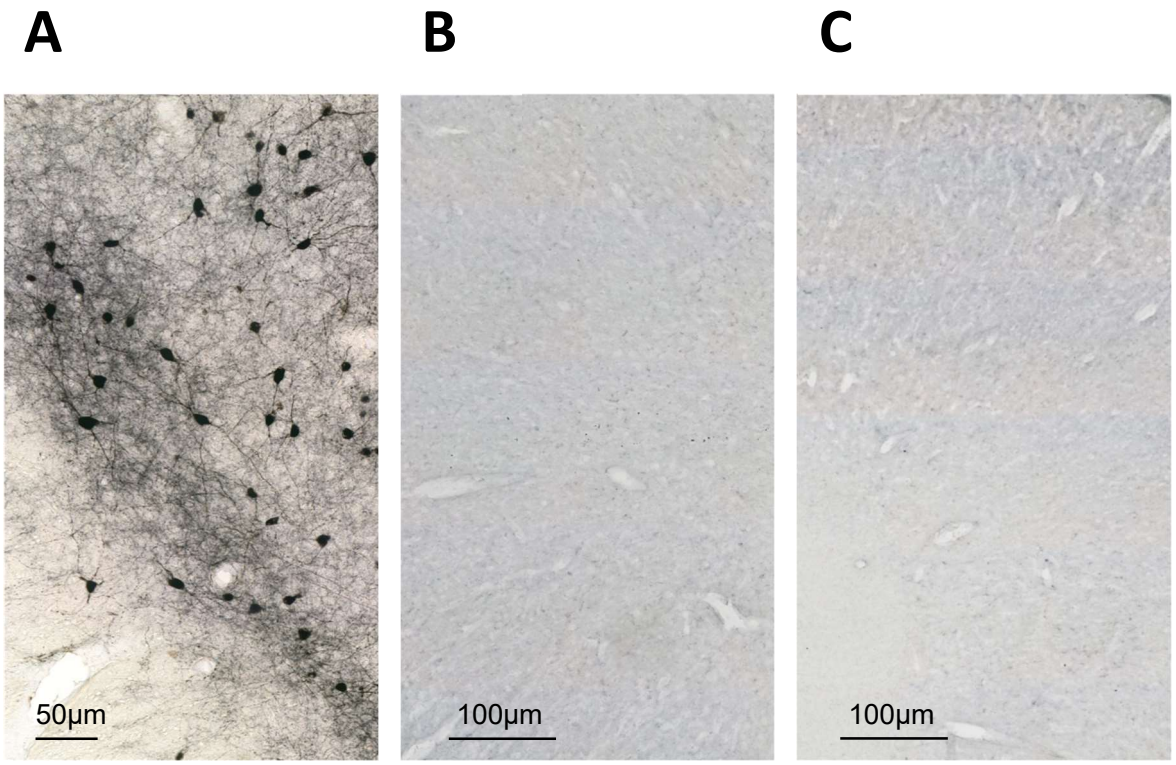

Supplementary Figure S14.7. PV+ IHC validation
Standard IHC protocol was followed with a 24h primary antibody/control incubation, 1:5,000 (0.2µg/mL) primary antibody dilution and sodium citrate buffer antigen retrieval. **A.** Primary antibody. **B.** No primary antibody control. **C.** Mouse IgG control (0.2µg/mL).

iii) WFA (Wisteria Floribunda Lectin (WFA, WFL), Biotinylated (B-1355-2, Vector Labs, 2mg/mL)

This stain was performed using a protocol pre-optimised in-house previously (Jennifer Fletcher, verbal communication; Chapter 6, Section 6.2.1), with a 1:1,000 dilution (2µg/mL) for 12h at 4°C. As per the pre-optimised methodology this resulted in a staining pattern expected for PNN structures (Figure S14.7A). However, to confirm the stain was effective in the tissue samples used in this study, a standard negative control was still performed by excluding the lectin from the solution (Figure S14.7B). This resulted in no visible staining of the tissue.

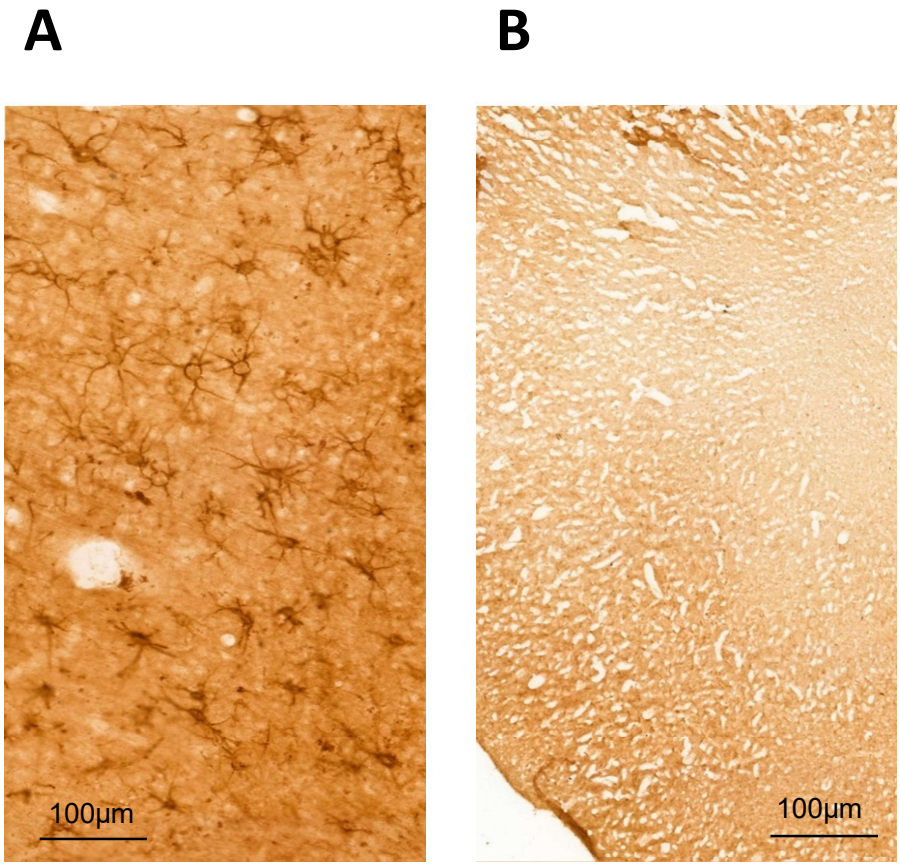

Supplementary Figure S14.8. WFA+ IHC validation
A. Positive lectin incubation. **B**. No lectin negative control. Standard IHC protocol was followed with a 12h primary lectin/control incubation, 1:1,000 (2µg/mL) dilution and sodium citrate buffer antigen retrieval.

REFERENCES

Aapola, U., Kawasaki, K., Scott, H. S., Ollila, J., Vihinen, M., Heino, M., Shintani, A., Kawasaki, K., Minoshima, S., Krohn, K., Antonarakis, S. E., Shimizu, N., Kudoh, J., Peterson, P. (2000). Isolation and initial characterization of a novel zinc finger gene, DNMT3L, on 21q22.3, related to the cytosine-5-methyltransferase 3 gene family. *Genomics, 65*, 293-298.

Abbink, M. R., van Deijk, A. F., Heine, V. M., Verheijen, M. H., Korosi, A. (2019). The involvement of astrocytes in early-life adversity induced programming of the brain. *Glia, 67*, 1637-1653.

Abdolmaleky, H. M., Cheng, K. H., Russo, A., Smith, C. L., Faraone, S. V., Wilcox, M., Shafa, R., Glatt, S. J., Nguyen, G., Ponte, J. F., Thiagalingam, S., Tsuang, M. T. (2005). Hypermethylation of the reelin (RELN) promoter in the brain of schizophrenic patients: a preliminary report. *American Journal of Medical Genetics. Part B, Neuropsychiatric Genetics, 134B,* 60–66.

Abdul-Monim, Z., Neill, J. C., Reynolds, G. P. (2007). Sub-chronic psychotomimetic phencyclidine induces deficits in reversal learning and alterations in parvalbumin-immunoreactive expression in the rat. *Journal of Psychopharmacology, 21,* 198–205.

Adams, W., Kendell, R. E., Hare, E. H., Munkjorgensen, P. (1993). Epidemiologic evidence that maternal influenza contributes to the etiology of schizophrenia - an analysis of scottish, english and danish data. *British Journal of Psychiatry, 163*, 522-534.

Adanty, C., Qian, J., Al-Chalabi, N., Fatemi, A. B., Gerretsen, P., Graff, A., De Luca, V. (2022). Sex differences in schizophrenia: a longitudinal methylome analysis. *Journal of Neurotransmission, 29*,105-114.

Ahmed, S., Roth, R. M., Stanciu, C. N., Brunette, M. F. (2021). The impact of THC and CBD in schizophrenia: a systematic review. *Frontiers in Psychiatry, 12,* 694394.

Aiko, Y., Askew, D. J., Aramaki, S., Myoga, M., Tomonaga, C., Hachisuga, T., Suga, R., Kawamoto, T., Tsuji, M., Shibata, E. (2014). Differential levels of amino acid transporters System L and ASCT2 and the mTOR protein in placenta of preeclampsia and IUGR. *BMC Pregnancy and Childbirth, 14,* 181.

Akalin, A., Kormaksson, M., Li, S., Garrett-Bakelman, F. E., Figueroa, M. E., Melnick, A., Mason, C. E. (2012). methylKit: a comprehensive R package for the analysis of genome-wide DNA methylation profiles. *Genome Biology, 13*, 87.

Akbarian, S. (2014). Epigenetic mechanisms in schizophrenia. *Dialogues in Clinical Neuroscience, 1,* 405-417.

Akbarian, S. (2020). Epigenetic clocks in schizophrenia: promising biomarkers, foggy clockwork. *Biological Psychiatry, 88,* 210-211.

Akbarian, S., Ruehl, M. G., Bliven, E., Luiz, L. A., Peranelli, A. C., Baker, S. P., Roberts, R. C., Burnicy, W. E., Conley, R. C., Jones, E. G., Tamminga, C. A., Guo, Y. (2005). Chromatin alterations associated with down-regulated metabolic gene expression in the prefrontal cortex of subjects with schizophrenia. *Archives of General Psychiatry, 62*, 829-840.

Akira, S., Takeda, K. (2004). Toll-like receptor signalling. *Nature Reviews Immunology, 4*, 499-511.

Akiyama, K., Ichinose, S., Omori, A., Sakurai, Y., Asou, H. (2002). Study of expression of myelin basic proteins (MBPs) in developing rat brain using a novel antibody reacting with four major isoforms of MBP. *Journal of Neuroscience Research, 68*, 19-28.

Alachkar, A., Wang, L., Yoshimura, R., Hamzeh, A. R., Wang, Z., Sanathara, N., Lee, S. M., Xu, X., Abbott, G. W., Civelli, O. (2018). Prenatal one-carbon metabolism dysregulation programs schizophrenia-like deficits. *Molecular Psychiatry, 23*, 282–294.

Aleman, A., Kahn, R. S., Selten, J. P. (2003). Sex differences in the risk of schizophrenia: evidence from meta-analysis. *Archives of General Psychiatry, 60*, 565-571.

Alexa A, Rahnenführer J. (2022). topGO: enrichment analysis for Gene Ontology. R package version 2.48.0. Available at: https://bioconductor.org/packages/release/bioc/html/topGO.html

Alexopoulou, L., Holt, A. C., Medzhitov, R., Flavell, R. A. (2001). Recognition of double-stranded RNA and activation of NF-kappaB by toll-like receptor 3. *Nature, 413*, 732-738.

Allen, N. J., Bennett, M. L., Foo, L. C., Wang, G. X., Chakraborty, C., Smith, S. J., Barres, B. A. (2012). Astrocyte glypicans 4 and 6 promote formation of excitatory synapses via GluA1 AMPA receptors. *Nature, 486,* 410-414

Allen, N. J., Eroglu, C. (2017). Cell biology of astrocyte-synapse interactions. *Neuron, 96*, 697-708.

Allgäuer, L., Cabungcal, J. H., Yzydorczyk, C., Do, K. Q., Dwir, D. (2023). Low protein-induced intrauterine growth restriction as a risk factor for schizophrenia phenotype in a rat model: assessing the role of oxidative stress and neuroinflammation interaction. *Translational Psychiatry, 13*, 30.

Allswede, D. M., Yolken, R. H., Buka, S. L., Cannon, T. D. (2020). Cytokine concentrations throughout pregnancy and risk for psychosis in adult offspring: a longitudinal case-control study. *The Lancet - Psychiatry, 7,* 254-261.

Alvarez-Dolado, M., Ruiz, M., Del Río, J. A., Alcántara, S., Burgaya, F., Sheldon, M., Nakajima, K., Bernal, J., Howell, B. W., Curran, T., Soriano, E., Muñoz, A. (1999). Thyroid hormone regulates reelin and dab1 expression during brain development. *The Journal of Neuroscience, 19*, 6979-6993.

Amberg, N., Laukoter, S., Hippenmeyer, S. (2019). Epigenetic cues modulating the generation of cell-type diversity in the cerebral cortex. *Journal of Neurochemistry, 149*, 12–26.

American Psychiatric Association (2022). Diagnostic and statistical manual of mental disorders (5th Edition, text revision). American Psychiatric Association Publishing. Washington.

Amir, R. E., Van den Veyver, I. B., Wan, M., Tran, C. Q., Francke, U., Zoghbi, H. Y. (1999). Rett syndrome is caused by mutations in X-linked MECP2, encoding methyl-CpG-binding protein 2. *Nature Genetics, 23*, 185-188.

Ampuero, E., Jury, N., Härtel, S., Marzolo, M. P., van Zundert, B. (2017). Interfering of the Reelin/ApoER2/PSD95 signaling axis reactivates dendritogenesis of mature hippocampal neurons. *Journal of Cellular Physiology, 232*, 1187–1199.

Anacker, C., Cattaneo, A., Musaelyan, K., Zunszain, P. A., Horowitz, M., Molteni, R., Luoni, A., Calabrese, F., Tansey, K., Gennarelli, M., Thuret, S., Price, J., Uher, R., Riva, M. A., Pariante, C. M. (2013). Role for the kinase SGK1 in stress, depression and glucocorticoid effects on hippocampal neurogenesis. *Proceedings of the National Academy of Sciences of the United States of America, 110*, 8708-8713.

Anastasiadi, D., Esteve-Codina, A., Piferrer, F. (2018). Consistent inverse correlation between DNA methylation of the first intron and gene expression across tissues and species. *Epigenetics and Chromatin, 11*, 37.

Anastasio, N. C., Johnson, K. M. (2008). Differential regulation of the NMDA receptor by acute and sub-chronic phencyclidine administration in the developing rat. *Journal of Neurochemistry*, *104*,1210-1218.

Anderson, R. C., O'Keeffe, G. W., McDermott, K. W. (2022). Characterisation of the consequences of maternal immune activation on distinct cell populations in the developing rat spinal cord. *Journal of Anatomy, 241*, 938-950.

Andreasen, N. C., Wilcox, M. A., Ho, B. C., Epping, E., Ziebell, S., Zeien, E., Weiss, B., Wassink, T. (2012). Statistical epistasis and progressive brain change in schizophrenia: an approach for examining the relationships between multiple genes. *Molecular Psychiatry, 17*, 1093–1102.

Andrews, S. (2010). FastQC: a quality control tool for high throughput sequence data. Available at: https://www.bioinformatics.babraham.ac.uk/projects/fastqc/.

Anton-Stephens, D. (1954). Preliminary observations on the psychiatric uses of chlorpromazine (largactil). *The Journal of Mental Science, 100*, 543–557.

Antony, A. C. (2007). *In utero* physiology: role of folic acid in nutrient delivery and foetal development. *The American Journal of Clinical Nutrition, 85*, 598-603.

Antunes, C., Sousa, N., Pinto, L., Marques, C. J. (2019). TET enzymes in neurophysiology and brain function. *Neuroscience and Biobehavioral Reviews, 102*, 337-344.

Arai, Y., Mizuguchi, M., Takashima, S. (1997). Developmental changes of glutamate receptors in the rat cerebral cortex and hippocampus. *Anatomy and Embryology, 195*, 65–70.

Aran, D., Toperoff, G., Rosenberg, M., Hellman, A. (2011). Replication timing-related and gene body-specific methylation of active human genes. *Human Molecular Genetics, 20*, 670-680.

Argueta, L. B., Lacko, L. A., Bram, Y., Tada, T., Carrau, L., Rendeiro, A. F., Zhang, T., Uhl, S., Lubor, B. C., Chandar, V., Gil, C., Zhang, W., Dodson, B. J., Bastiaans, J., Prabhu, M., Houghton, S., Redmond, D., Salvatore, C. M., Yang, Y. J., Elemento, O., … Stuhlmann, H. (2022). Inflammatory responses in the placenta upon SARS-CoV-2 infection late in pregnancy. *iScience, 25*, 104223.

Aria, F., Bonini, S. A., Cattaneo, V., Premoli, M., Mastinu, A., Maccarinelli, G., Memo, M. (2020). Brain structural and functional alterations in mice prenatally exposed to LPS are only partially rescued by anti-Inflammatory treatment. *Brain Sciences, 10*, 620.

Arnone, D., McIntosh, A. M., Tan, G. M., Ebmeier, K. P. (2008). Meta-analysis of magnetic resonance imaging studies of the corpus callosum in schizophrenia. *Schizophrenia Research, 101*, 124-132.

Arrode-Brusés, G., Brusés, J. L. (2012). Maternal immune activation by poly I:C induces expression of cytokines IL-1β and IL-13, chemokine MCP-1 and colony stimulating factor VEGF in foetal mouse brain. *Journal of Neuroinflammation, 9*, 83.

Arsenault, D., St-Amour, I., Cisbani, G., Rousseau, L. S., Cicchetti, F. (2014). The different effects of LPS and poly I:C prenatal immune challenges on the behavior, development and inflammatory responses in pregnant mice and their offspring. *Brain, Behavior and Immunity, 38*, 77-90

Arthur-Farraj, P., Moyon, S. (2020). DNA methylation in schwann cells and in oligodendrocytes. *Glia, 68,* 1568-1583.

Ashdown, H., Dumont, Y., Ng, M., Poole, S., Boksa, P., Luheshi, G. N. (2006). The role of cytokines in mediating effects of prenatal infection on the foetus: implications for schizophrenia. *Molecular Psychiatry, 11*, 47-55.

Atladottir, H. O., Thorsen, P., Ostergaard, L., Schendel, D. E., Lemcke, S., Abdallah, M., Parner, E. T. (2010). Maternal infection requiring hospitalization during pregnancy and autism spectrum disorders. *Journal of Autism and Developmental Disorders, 40*, 1423-1430.

August, S. M., Kiwanuka, J. N., McMahon, R. P., Gold, J. M. (2012). The MATRICS Consensus Cognitive Battery (MCCB): clinical and cognitive correlates. *Schizophrenia Research, 134*, 76-82.

Avramopoulos, D. (2018). Recent advances in the genetics of schizophrenia. *Molecular Neuropsychiatry, 4,* 35-51.

Ayalew, M., Le-Niculescu, H., Levey, D. F., Jain, N., Changala, B., Patel, S. D., Winiger, E., Breier, A., Shekhar, A., Amdur, R., Koller, D., Nurnberger, J. I., Corvin, A., Geyer, M., Tsuang, M. T., Salomon, D., Schork, N. J., Fanous, A. H., O'Donovan, M. C., Niculescu, A. B. (2012). Convergent functional genomics of schizophrenia: from comprehensive understanding to genetic risk prediction. *Molecular Psychiatry, 17,* 887-905.

Azevedo, F. A., Carvalho, L. R., Grinberg, L. T., Farfel, J. M., Ferretti, R. E., Leite, R. E., Jacob Filho, W., Lent, R., Herculano-Houzel, S. (2009). Equal numbers of neuronal and nonneuronal cells make the human brain an isometrically scaled-up primate brain. *The Journal of Comparative Neurology, 513*, 532-541.

Bale, T. L. (2016). The placenta and neurodevelopment: sex differences in prenatal vulnerability. *Dialogues in Clinical Neuroscience, 18*, 459-464.

Bale, T. L., Abel, T., Akil, H., Carlezon, W. A. Jr, Moghaddam, B., Nestler, E. J., Ressler, K. J., Thompson, S. M. (2019). The critical importance of basic animal research for neuropsychiatric disorders. *Neuropsychopharmacology, 44*, 1349-1353.

Ban T. A. (2007). Fifty years chlorpromazine: a historical perspective. *Neuropsychiatric Disease and Treatment, 3*, 495–500.

Banks, W. A., Kastin, A. J., Gutierrez, E. G. (1994). Penetration of interleukin-6 across the murine blood-brain barrier. *Neuroscience Letters, 179*, 53-56.

Banks, W. A., Ortiz, L., Plotkin, S. R., Kastin, A. J. (1991). Human interleukin (IL) 1 alpha, murine IL-1 alpha and murine IL-1 beta are transported from blood to brain in the mouse by a shared saturable mechanism. *Journal of Pharmacology and Experimental Therapeutics, 259*, 988-996.

Bannister, A. J., Kouzarides, T. (2011). Regulation of chromatin by histone modifications. *Cell Research, 21,* 381-395.

Barke, T. L., Money, K. M., Du, L., Serezani, A., Gannon, M., Mirnics, K., Aronoff, D. M. (2019). Sex modifies placental gene expression in response to metabolic and inflammatory stress. *Placenta, 78*, 1-9.

Barker, D. J. (1990). The foetal and infant origins of adult disease. *The British Medical Journal, 301.* 1111.

Barker, D. J. (2002). Foetal programming of coronary heart disease. *Trends in Endocrinology and Metabolism, 13*, 364-368.

Barnes A. (2004). Race, schizophrenia and admission to state psychiatric hospitals. *Administration and Policy in Mental Health, 31,* 241–252.

Barski, A., Jothi, R., Cuddapah, S., Cui, K. R., Roh, T. Y., Schones, D. E., Zhao, K. (2009). Chromatin poises miRNA- and protein-coding genes for expression. *Genome Research, 19,* 1742-1751.

Bartel, D. P. (2004). MicroRNAs: genomics, biogenesis, mechanism and function. *Cell, 116*, 281-297.

Bats, C., Groc, L., Choquet, D. (2007). The interaction between Stargazin and PSD-95 regulates AMPA receptor surface trafficking. *Neuron, 53*, 719–734.

Bauman, M. D., Iosif, A. M., Smith, S. E., Bregere, C., Amaral, D. G., Patterson, P. H. (2014). Activation of the maternal immune system during pregnancy alters behavioral development of rhesus monkey offspring. *Biological Psychiatry, 75,* 332–341.

Baydyuk, M., Morrison, V. E., Gross, P. S., Huang, J. K. (2020). Extrinsic factors driving oligodendrocyte lineage cell progression in CNS development and injury. *Neurochemical Research, 45,* 630–642.

Bayer, S. A., Altman, J., Russo, R. J., Zhang, X. (1993). Timetables of neurogenesis in the human brain based on experimentally determined patterns in the rat. *Neurotoxicology, 14*, 83-144.

Bayraktar, O. A., Fuentealba, L. C., Alvarez-Buylla, A., Rowitch, D. H. (2015). Astrocyte development and heterogeneity. *Cold Spring Harbour Perspectives in Biology, 7*, e020362.

Beck, D., Maamar, M. B., Skinner, M. K. (2022). Genome-wide CpG density and DNA methylation analysis method (MeDIP, RRBS and WGBS) comparisons. *Epigenetics, 17*, 518-530.

Beffert, U., Weeber, E. J., Durudas, A., Qiu, S., Masiulis, I., Sweatt, J. D., Li, W.P., Adelmann, G., Frotscher, M., Hammer, R.E., Herz, J. (2005). Modulation of synaptic plasticity and memory by Reelin involves differential splicing of the lipoprotein receptor ApoER2. *Neuron, 47*, 567–579.

Béïque, J. C., Lin, D. T., Kang, M. G., Aizawa, H., Takamiya, K., Huganir, R. L. (2006). Synapse-specific regulation of AMPA receptor function by PSD-95. *Proceedings of the National Academy of Sciences of the United States of America, 103,* 19535–19540.

Bekku, Y., Rauch, U., Ninomiya, Y., Oohashi, T. (2009). Brevican distinctively assembles extracellular components at the large diameter nodes of Ranvier in the CNS. *Journal of Neurochemistry, 108*, 1266-1276.

Berchtold, N. C., Cribbs, D. H., Coleman, P. D., Rogers, J., Head, E., Kim, R., Beach, T., Miller, C., Troncoso, J., Trojanowski, J. Q., Zielke, H. R., Cotman, C. W. (2008). Gene expression changes in the course of normal brain aging are sexually dimorphic. *Proceedings of the National Academy of Sciences of the United States of America, 105*, 15605-15610.

Bergdolt, L., Dunaevsky, A. (2019). Brain changes in a maternal immune activation model of neurodevelopmental brain disorders. *Progress in Neurobiology, 175*, 1-19.

Bergles, D. E., Richardson, W. D. (2016). Oligodendrocyte development and plasticity. *Cold Spring Harbour Perspectives in Biology, 8*, e020453.

Bermick, J., Schaller, M. (2022). Epigenetic regulation of pediatric and neonatal immune responses. *Paediatric Research, 91,* 297-327.

Bernard-Trifilo, J. A., Kramár. E. A., Torp. R., Lin. C. Y., Pineda. E. A., Lynch, G., Gall, C. M. (2005). Integrin signaling cascades are operational in adult hippocampal synapses and modulate NMDA receptor physiology. *Journal of Neurochemistry, 93*, 834–849.

Bernstein, H. G., Steiner, J., Guest, P. C., Dobrowolny, H., Bogerts, B. (2015). Glial cells as key players in schizophrenia pathology: recent insights and concepts of therapy. *Schizophrenia Research, 161*, 4-18.

Berretta S. (2012). Extracellular matrix abnormalities in schizophrenia. *Neuropharmacology, 62*, 1584–1597.

Beveridge, N. J., Cairns, M. J. (2012). MicroRNA dysregulation in schizophrenia. *Neurobiology of Disease, 46*, 263-271.

Bhat, A., Irizar, H., Couch, A. C. M., Raval, P., Duarte, R. R. R., Dutan Polit, L., Hanger, B., Powell, T., Deans, P. J. M., Shum, C., Nagy, R., McAlonan, G., Iyegbe, C. O., Price, J., Bramon, E., Bhattacharyya, S., Vernon, A. C., Srivastava, D. P. (2022). Attenuated transcriptional response to pro-inflammatory cytokines in schizophrenia hiPSC-derived neural progenitor cells. *Brain, Behavior and Immunity, 105*, 82–97.

Bhutani, N., Burns, D. M., Blau, H. M. (2011). DNA demethylation dynamics. *Cell, 146*, 866-872.

Białoń, M., Wąsik, A. (2022). Advantages and limitations of animal schizophrenia models. *International Journal of Molecular Sciences, 23*, 5968.

Bianco-Miotto, T., Craig, J. M., Gasser, Y. P., van Dijk, S. J., Ozanne, S. E. (2017). Epigenetics and DOHaD: from basics to birth and beyond. *Journal of Developmental Origins of Health and Disease, 8,* 513–519.

Bierie, B., Moses, H. L. (2010). Transforming growth factor beta (TGF-beta) and inflammation in cancer. *Cytokine and Growth Factor Reviews, 21*, 49-59.

Bigdeli, T. B., Fanous, A. H., Li, Y., Rajeevan, N., Sayward, F., Genovese, G., Gupta, R., Radhakrishnan, K., Malhotra, A. K., Sun, N., Lu, Q., Hu, Y., Li, B., Chen, Q., Mane, S., Miller, P., Cheung, K. H., Gur, R. E., Greenwood, T. A., Braff, D. L., … Harvey, P. D. (2021). Genome-wide association studies of schizophrenia and bipolar disorder in a diverse cohort of US veterans. *Schizophrenia Bulletin, 47*, 517–529.

Bilbo, S. D., Schwarz, J. M. (2009). Early-life programming of later-life brain and behavior: a critical role for the immune system. *Frontiers in Behavioral Neuroscience, 3*, 14.

Bird, A., Taggart, M., Frommer, M., Miller, O. J., Macleod, D. (1985). A fraction of the mouse genome that is derived from islands of nonmethylated, CpG-rich DNA. *Cell, 40*, 91-99.

Bitzenhofer, J. S. H., PöpplauIleana, J. A., Hanganu-Opatz, I. (2020) Gamma activity accelerates during prefrontal development. *eLife, 9*, e56795.

Blagburn-Blanco, S. V., Chappell, M. S., De Biase, L. M., DeNardo, L. A. (2022). Synapse-specific roles for microglia in development: new horizons in the prefrontal cortex. *Frontiers in Molecular Neuroscience, 15,* 965756.

Bliss, T. V. (1979). Synaptic plasticity in the hippocampus. *Neuroplasticity, 2,* 42-45.

Bliss, T. V., Lomo, T. (1973). Long-lasting potentiation of synaptic transmission in the dentate area of the anaesthetized rabbit following stimulation of the perforant path. *Journal of Physiology, 232*, 331–356.

Blumkin, E., Levav-Rabkin, T., Melamed, O., Galron, D., Golan, H. M. (2011). Gender-specific effect of Mthfr genotype and neonatal vigabatrin interaction on synaptic proteins in mouse cortex. *Neuropsychopharmacology, 36*, 1714-1728.

Bo Mortensen, P., Norgaard-Pedersen, B., Waltoft, B. L., Sorensen, T. L., Hougaard, D., Torrey, E. F., Yolken, R. H. (2007). Toxoplasma gondii as a risk factor for early-onset schizophrenia: analysis of filter paper blood samples obtained at birth. *Biological Psychiatry, 61*, 688-693.

Bobes, J., Arango, C., Garcia-Garcia, M., Rejas, J. (2010). Healthy lifestyle habits and 10-year cardiovascular risk in schizophrenia spectrum disorders: an analysis of the impact of smoking tobacco in the CLAMORS schizophrenia cohort. *Schizophrenia Research, 119*, 101-109.

Bock, H. H., Jossin, Y., Liu, P., Förster, E., May, P., Goffinet, A. M., Herz, J. (2003). Phosphatidylinositol 3-Kinase interacts with the adaptor protein Dab1 in response to Reelin signaling and is required for normal cortical lamination. *Mechanisms of Signal Transduction, 278,* 38772-38779.

Boggs, J. M. (2006). Myelin basic protein: a multifunctional protein. *Cell and Molecular Life Sciences, 63,* 1945-1961.

Boksa, P. (2004). Animal models of obstetric complications in relation to schizophrenia. *Brain Research Reviews, 45,* 1-17.

Boksa, P. (2010). Effects of prenatal infection on brain development and behavior: a review of findings from animal models. *Brain, Behavior and Immunity, 24*, 881-897.

Boktor, J. C., Adame, M. D., Rose, D. R., Schumann, C. M., Murray, K. D., Bauman, M. D., Careaga, M., Mazmanian, S. K., Ashwood, P., Needham, B. D. (2022). Global metabolic profiles in a non-human primate model of maternal immune activation: implications for neurodevelopmental disorders. *Molecular Psychiatry, 7,* 4959-4973.

Bonetto, G., Belin, D., Káradóttir, R. T. (2021). Myelin: A gatekeeper of activity-dependent circuit plasticity? *Science, 374*, eaba6905.

Booth, M. J., Ost, T. W., Beraldi, D., Bell, N. M., Branco, M. R., Reik, W., Balasubramanian, S. (2013). Oxidative bisulfite sequencing of 5-methylcytosine and 5-hydroxymethylcytosine. *Nature Protocols, 8,* 1841-1851.

Bordeleau, M., Fernández de Cossío, L., Chakravarty, M. M, Tremblay, M. È. (2021). From maternal diet to neurodevelopmental disorders: a story of neuroinflammation. *Frontiers in Neuroscience, 14,* 612705.

Born, G., Grayton, H. M., Langhorst, H., Dudanova, I., Rohlmann, A., Woodward, B. W., Collier, D. A., Fernandes, C., Missler, M. (2015). Genetic targeting of NRXN2 in mice unveils role in excitatory cortical synapse function and social behaviors. *Frontiers in Synaptic Neuroscience, 7*, 3.

Borovcanin, M. M, Jovanovic, I., Radosavljevic, G., Pantic, J., Minic Janicijevic, S., Arsenijevic, N., Lukic, M. L. (2017). Interleukin-6 in schizophrenia-is there a therapeutic relevance? *Frontiers in Psychiatry, 8*, 221.

Borrell, J., Vela, J. M., Arevalo-Martin, A., Molina-Holgado, E., Guaza, C. (2002). Prenatal immune challenge disrupts sensorimotor gating in adult rats: implications for the etiopathogenesis of schizophrenia. *Neuropsychopharmacology, 26,* 204-215.

Bosiacki, M., Gąssowska-Dobrowolska, M., Kojder, K., Fabiańska, M., Jeżewski, D., Gutowska, I., Lubkowska, A. (2019). Perineuronal nets and their role in synaptic homeostasis. *International Journal of Molecular Science, 20*, 4108.

Bradley, A. J., Dinan, T. G. (2010). A systematic review of hypothalamic-pituitary-adrenal axis function in schizophrenia: implications for mortality. *Journal of Psychopharmacology, 24*, 91-118.

Brand, B. A., de Boer, J. N., Dazzan, P., Sommer, I. E. (2022). Towards better care for women with schizophrenia-spectrum disorders. *The Lancet - Psychiatry, 9,* 330–336.

Brenet, F., Moh, M., Funk, P., Feierstein, E., Viale, A. J., Socci, N. D., Scandura, J. M. (2011). DNA methylation of the first exon is tightly linked to transcriptional silencing. *PLoS One, 6,* e14524.

Brennecke, J., Stark, A., Russell, R. B., Cohen, S. M. (2005). Principles of microRNA-target recognition. *PLoS Biology, 3*, 404-418.

Brigman, J. L., Padukiewicz, K. E., Sutherland, M. L., Rothblat, L. A. (2006). Executive functions in the heterozygous reeler mouse model of schizophrenia. *Behavioral Neuroscience, 120*, 984-988.

Briones, T. L., Woods, J. (2014). Dysregulation in myelination mediated by persistent neuroinflammation: possible mechanisms in chemotherapy-related cognitive impairment. *Brain, Behavior and Immunity, 35*, 23-32.

Brissos, S., Veguilla, M. R., Taylor, D., Balanzá-Martinez, V. (2014). The role of long-acting injectable antipsychotics in schizophrenia: a critical appraisal. *Therapeutic Advances in Psychopharmacology, 4,* 198–219.

Bronson, S. L., Bale, T. L. (2014). Prenatal stress-induced increases in placental inflammation and offspring hyperactivity are male-specific and ameliorated by maternal anti-inflammatory treatment. *Endocrinology, 155,* 2635-2646.

Bronson, S. L., Bale, T. L. (2016). The placenta as a mediator of stress effects on neurodevelopmental reprogramming. *Neuropsychopharmacology, 41*, 207-218.

Brown, A. S. (2011). The environment and susceptibility to schizophrenia. *Progress in Neurobiology, 93*, 23-58.

Brown, A. S., Begg, M. D., Gravenstein, S., Schaefer, C. A., Wyatt, R. J., Bresnahan, M., Babulas, V., Susser, E. S. (2004). Serologic evidence for prenatal influenza in the etiology of schizophrenia. *Archives of General Psychiatry, 61*, 774-780.

Brown, A. S., Derkits, E. J. (2010). Prenatal infection and schizophrenia: a review of epidemiologic and translational studies. *American Journal of Psychiatry, 167*, 261-280.

Brown, A. S., Susser, E. S. (2008). Prenatal nutritional deficiency and risk of adult schizophrenia. *Schizophrenia Bulletin, 34,* 1054–1063.

Bryant-Greenwood, G. D. (1998). The extracellular matrix of the human foetal membranes: structure and function. *Placenta, 19*, 1-11.

Bucher, E.A., Collins, J.M., King, A.E., Vickers, J.C. Kirkcaldie, M. T. K. (2021). Coherence and cognition in the cortex: the fundamental role of parvalbumin, myelin and the perineuronal net. *Brain Structure and Function, 226*, 2041–2055.

Buckberry, S., Bianco-Miotto, T., Bent, S. J., Dekker, G. A., Roberts, C. T. (2014). Integrative transcriptome meta-analysis reveals widespread sex-biased gene expression at the human foetal-maternal interface. *Molecular Human Reproduction, 20*, 810-819.

Buka, S. L., Cannon, T. D., Torrey, E. F., Yolken, R. H., Perinatal, C. S. G. (2008). Maternal exposure to herpes simplex virus and risk of psychosis among adult offspring. *Biological Psychiatry, 63*, 809-815.

Burghardt, K. J., Khoury, A. S., Msallaty, Z., Yi, Z., Seyoum, B. (2020). Antipsychotic medications and DNA methylation in schizophrenia and bipolar disorder: a systematic review. *Pharmacotherapy, 40*, 331–342.

Bustos, F. J., Varela-Nallar, L., Campos, M., Henriquez, B., Phillips, M., Opazo, C., Aguayo, L. G., Montecino, M., Constantine-Paton, M., Inestrosa, N. C., van Zundert, B. (2014). PSD95 suppresses dendritic arbor development in mature hippocampal neurons by occluding the clustering of NR2B-NMDA receptors. *PLoS One, 9*, e94037.

Butler, M. G., McGuire, A. B., Masoud, H., Manzardo, A. M. (2016). Currently recognized genes for schizophrenia: high-resolution chromosome ideogram representation. *American Journal of Medical Genetics Part B - Neuropsychiatric Genetics, 171*, 181-202.

Caballero, A., Flores-Barrera, E., Cass, D. K., Tseng, K. Y. (2014). Differential regulation of parvalbumin and calretinin interneurons in the prefrontal cortex during adolescence. *Brain Structure and Function, 219*, 395–406.

Caballero, A., Flores-Barrera, E., Thomases, D. R., Tseng, K. Y. (2020). Downregulation of parvalbumin expression in the prefrontal cortex during adolescence causes enduring prefrontal disinhibition in adulthood. *Neuropsychopharmacology, 45,* 1527–1535.

Caballero, A., Granberg, R., Tseng, K. Y. (2016). Mechanisms contributing to prefrontal cortex maturation during adolescence. *Neuroscience and Biobehavioral Reviews, 70*, 4-12.

Cabungcal, J. H., Steullet, P., Morishita, H., Kraftsik, R., Cuenod, M., Hensch, T. K., Do, K. Q. (2013). Perineuronal nets protect fast-spiking interneurons against oxidative stress. *Proceedings of the National Academy of Sciences of the Unites States of America, 110*, 9130-9135.

Cadinu, D., Grayson, B., Podda, G., Harte, M. K., Doostdar, N., Neill, J. C. (2018). NMDA receptor antagonist rodent models for cognition in schizophrenia and identification of novel drug treatments, an update. *Neuropharmacology, 142,* 41–62.

Caillard, O., Moreno, H., Schwaller, B., Llano, I., Celio, M. R., Marty, A. (2000). Role of the calcium-binding protein parvalbumin in short-term synaptic plasticity. *Proceedings of the National Academy of Sciences of the United States of America, 97*, 13372–13377.

Çakici, N., van Beveren, N. J. M., Judge-Hundal, G., Koola, M. M., Sommer, I. E. C. (2019). An update on the efficacy of anti-inflammatory agents for patients with schizophrenia: a meta-analysis. *Psychological Medicine, 49*, 2307-2319.

Caldji, C., Tannenbaum, B., Sharma, S., Francis, D., Plotsky, P. M., Meaney, M. J. (1998). Maternal care during infancy regulates the development of neural systems mediating the expression of fearfulness in the rat. *Proceedings of the National Academy of Sciences of the United States of America, 95*, 5335-5340.

Campo, C. G., Sinagra, M., Verrier, D., Manzoni, O. J., Chavis, P. (2009). Reelin secreted by GABAergic neurons regulates glutamate receptor homeostasis. *PLoS One, 4,* e5505.

Canales, C. P., Estes, M. L., Cichewicz, K., Angara, K., Aboubechara, J. P., Cameron, S., Prendergast, K., Su-Feher, L., Zdilar, I., Kreun, E. J., Connolly, E. C., Seo, J. M., Goon, J. B., Farrelly, K., Stradleigh, T. W., van der List, D., Haapanen, L., Van de Water, J., Vogt, D., McAllister, A. K., Nord, A. S. (2021). Sequential perturbations to mouse corticogenesis following *in utero* maternal immune activation. *eLife, 10,* e60100.

Canetta, S. E., Bao, Y. Y., Co, M. D. T., Ennis, F. A., Cruz, J., Terajima, M., Shen, L., Kellendonk, C., Schaefer, C. A., Brown, A. S. (2014). Serological documentation of maternal influenza exposure and bipolar disorder in adult offspring. *American Journal of Psychiatry, 171,* 557-563.

Cannon, M., Jones, P. B., Murray, R. M. (2002). Obstetric complications and schizophrenia: historical and meta-analytic review. *American Journal of Psychiatry, 159*, 1080-1092.

Căpățînă, O. O., Micluția, I. V., Fadgyas-Stănculete, M. (2021). Current perspectives in treating negative symptoms of schizophrenia: a narrative review. *Experimental and Therapeutic Medicine, 21*, 276.

Carceller, H., Gramuntell, Y., Klimczak, P., Nacher, J. (2022). Perineuronal nets: subtle structures with large implications. *The Neuroscientist*, online ahead of print.

Careaga, M., Taylor, S. L., Chang, C., Chiang, A., Ku, K. M., Berman, R. F., Van de Water, J. A., Bauman, M. D. (2018). Variability in polyIC induced immune response: implications for preclinical maternal immune activation models. *Journal of Neuroimmunology, 323***,** 87-93.

Carloni, E., Ramos, A., Hayes, L. N. (2021). Developmental stressors induce innate immune memory in microglia and contribute to disease risk. *International Journal of Molecular Science, 22*, 13035.

Carlsson, A., Lindqvist, M. (1963). Effect of chlorpromazine or haloperidol on formation of 3methoxytyramine and normetanephrine in mouse brain. *Acta Pharmacologica Toxicologica, 20*, 140-144.

Carneiro A. M. (2010). The emerging role of integrins in neuropsychiatric disorders. *Neuropsychopharmacology, 35,* 338–339.

Carulli, D., Pizzorusso, T., Kwok, J. C., Putignano, E., Poli, A., Forostyak, S. Andrews, M. R., Deepa, S. S., Glant, T. T., Fawcett, J. W. (2010). Animals lacking link protein have attenuated perineuronal nets and persistent plasticity. *Brain, 133,* 2331-2347.

Carulli, D., Rhodes, K. E., Brown, D. J., Bonnert, T. P., Pollack, S. J., Oliver, K., Strata, P., Fawcett, J. W. (2006). Composition of perineuronal nets in the adult rat cerebellum and the cellular origin of their components. *The Journal of Comparative Neurology, 494*, 559-577.

Casquero-Veiga, M., Lamanna-Rama, N., Romero-Miguel, D., Rojas-Marquez, H., Alcaide, J., Beltran, M., Nacher, J., Desco, M., Soto-Montenegro, M. L. (2023). The Poly I:C maternal immune stimulation model shows unique patterns of brain metabolism, morphometry and plasticity in female rats. *Frontiers in Behavioral Neuroscience, 16,* 1022622.

Castillejos, M. C., Martin-Perez, C., Moreno-Kustner, B. (2018). A systematic review and meta-analysis of the incidence of psychotic disorders: the distribution of rates and the influence of gender, urbanicity, immigration and socio-economic level. *Psychological Medicine, 48*, 2101-2115.

Catalanotto, C., Cogoni, C., Zardo, G. (2016). MicroRNA in control of gene expression: an overview of nuclear functions. *International Journal of Molecular Sciences, 17,* 1712.

Catale, C., Bussone, S., Lo Iacono, L., Viscomi, M. T., Palacios, D., Troisi, A., Carola, V. (2020). Exposure to different early-life stress experiences results in differentially altered DNA methylation in the brain and immune system. *Neurobiology of Stress, 13,* 100249.

Catts, V. S., Derminio, D. S., Hahn, C. G., Weickert, C. S. (2015). Postsynaptic density levels of the NMDA receptor NR1 subunit and PSD-95 protein in prefrontal cortex from people with schizophrenia. *Schizophrenia, 1,* 15037.

Caudill, M. A., Wang, J. C., Melnyk, S., Pogribny, I. P., Jernigan, S., Collins, M. D., Santos-Guzman, J., Swendseid, M. E., Cogger, E. A., James, S. J. (2001). Intracellular S-adenosylhomocysteine concentrations predict global DNA hypomethylation in tissues of methyl-deficient cystathionine β-synthase heterozygous mice. *The Journal of Nutrition, 131*, 2811–2818.

Cavalcante, R., Sartor, M. (2017). annotatr: genomic regions in context. *Bioinformatics, 33*, 2381–2383.

Cedar, H., Bergman, Y. (2009). Linking DNA methylation and histone modification: patterns and paradigms. *Nature Reviews Genetics, 10*, 295-304.

Chan, C. S., Weeber, E. J., Zong, L., Fuchs, E., Sweatt, J. D., Davis, R. L. (2006). Beta 1-integrins are required for hippocampal AMPA receptor-dependent synaptic transmission, synaptic plasticity and working memory. *The Journal of Neuroscience, 26*, 223–232.

Chang, K. J., Zollinger, D. R., Susuki, K., Sherman, D. L., Makara, M. A., Brophy, P. J., Cooper, E. C., Bennett, V., Mohler, P. J., Rasband, M. N. (2014). Glial ankyrins facilitate paranodal axoglial junction assembly. *Nature Neuroscience, 17*, 1673-1681.

Charlson, F. J., Ferrari, A. J., Santomauro, D. F., Diminic, S., Stockings, E., Scott, J. G., McGrath, J. J., Whiteford, H. A. (2018). Global epidemiology and burden of schizophrenia: findings from the global burden of disease study 2016. *Schizophrenia Bulletin, 44*, 1195-1203.

Chater, T. E., Goda, Y. (2014). The role of AMPA receptors in postsynaptic mechanisms of synaptic plasticity. *Frontiers in Cellular Neuroscience, 8*, 401.

Chen, K., Ochalski, P. G., Tran, T. S., Sahir, N., Schubert, M., Pramatarova, A., Howell, B. W. (2004) Interaction between Dab1 and CrkII is promoted by Reelin signaling. *Journal of Cell Science, 117*, 4527–4536.

Chen, L., Chen, R., Wang, H., Liang, F. (2015). Mechanisms linking inflammation to insulin resistance. *International Journal of Endocrinology, 2015*, 508409.

Chen, L., Chetkovich, D. M., Petralia, R. S., Sweeney, N. T., Kawasaki, Y., Wenthold, R. J., Bredt, D. S., Nicoll, R. A. (2000). Stargazin regulates synaptic targeting of AMPA receptors by two distinct mechanisms. *Nature, 408,* 936–943.

Chen, Q., Li, D., Jin, W., Shi, Y., Li, Z., Ma, P., Sun, J., Chen, S., Li, P., Lin, P. (2021a). Research progress on the correlation between epigenetics and schizophrenia. *Frontiers in Neuroscience, 15*, 688727.

Chen, X., Huang, N. X., Cheng ,Y. J., Cai, Q. Y., Tian, Y. P., Chen, X. S., Xiao, L. (2021b). DNA Hypermethylation induced by L-methionine leads to oligodendroglial and myelin deficits and schizophrenia-Like behaviors in adolescent mice. *Frontiers in Neuroscience, 15*, 659853.

Chen, Y., Beffert, U., Ertunc, M., Tang, T. S., Kavalali, E. T., Bezprozvanny, I., Herz, J. (2005). Reelin modulates NMDA receptor activity in cortical neurons. *The Journal of Neuroscience, 25*, 8209–8216.

Chen, Y., Damayanti, N. P., Irudayaraj, J., Dunn, K., Zhou, F. C. (2014). Diversity of two forms of DNA methylation in the brain. *Frontiers in Genetics, 5,* e46.

Cheng, Y., Bernstein, A., Chen, D., Jin, P. (2015). 5-hydroxymethylcytosine: a new player in brain disorders? *Experimental Neurology, 268*, 3-9.

Cheslack-Postava, K., Brown, A. S. (2022). Prenatal infection and schizophrenia: a decade of further progress. *Schizophrenia Research, 247*, 7–15.

Chiapponi, C., Piras, F., Piras, F., Caltagirone, C., Spalletta, G. (2016). GABA system in schizophrenia and mood disorders: a mini review on third-generation imaging studies. *Frontiers in Psychiatry, 7*, e61.

Chien, W. T., Leung, S. F., Yeung, F. K., Wong, W. K. (2013). Current approaches to treatments for schizophrenia spectrum disorders, part II: psychosocial interventions and patient-focused perspectives in psychiatric care. *Neuropsychiatric Disease and Treatment, 9*, 1463–1481.

Cho, M., Lee, T. Y., Kwak, Y. B., Yoon, Y. B., Kim, M., Kwon, J. S. (2019). Adjunctive use of anti-inflammatory drugs for schizophrenia: a meta-analytic investigation of randomized controlled trials. *The Australian and New Zealand Journal of Psychiatry, 53,* 742-759.

Choi, G. B., Yim, Y. S., Wong, H., Kim, S., Kim, H., Kim, S. V., Hoeffer, C. A., Littman, D. R., Huh, J. R. (2016). The maternal interleukin-17a pathway in mice promotes autism-like phenotypes in offspring. *Science, 351*, 933–939.

Choquet, D., Opazo, P. (2022). The role of AMPAR lateral diffusion in memory. *Seminars in Cell and Developmental Biology, 125*, 76-83.

Choudhury, Z., Lennox, B. (2021). Maternal immune activation and schizophrenia-evidence for an immune priming disorder. *Frontiers in Psychiatry, 12*, 585742.

Christopher, M. A., Kyle, S. M., Katz, D. J. (2017). Neuroepigenetic mechanisms in disease. *Epigenetics and Chromatin, 10*, e47.

Chung, D. W., Geramita, M. A., Lewis, D. A. (2022). Synaptic variability and cortical gamma oscillation power in schizophrenia. *American Journal of Psychiatry, 179*, 277-287.

Cingolani, L. A., Thalhammer, A., Yu, L. M., Catalano, M., Ramos, T., Colicos, M. A., Goda, Y. (2008). Activity-dependent regulation of synaptic AMPA receptor composition and abundance by beta3 integrins. *Neuron, 58*, 749–762.

Cisternas, C. D., Cortes, L. R., Bruggeman, E. C., Yao, B., Forger, N. G. (2019). Developmental changes and sex differences in DNA methylation and demethylation in hypothalamic regions of the mouse brain. *Epigenetics, 3*, 1-13.

Clancy, B., Darlington, R. B., Finlay, B. L. (2001). Translating developmental time across mammalian species. *Neuroscience, 105*, 7-17.

Clancy, B., Finlay, B. L., Darlington, R. B., Anand, K. J. (2007). Extrapolating brain development from experimental species to humans. *Neurotoxicology, 28*, 931-937.

Cleal, J. K., Lewis, R. M. (2008). The mechanisms and regulation of placental amino acid transport to the human foetus. *Journal of Neuroendocrinology, 20*, 419-426.

Clementz, B. A., Parker, D. A., Trotti, R. L., McDowell, J. E., Keedy, S. K., Keshavan. M. S., Pearlson, G. D., Gershon, E. S., Ivleva, E. I., Huang, L. Y., Hill, S. K., Sweeney, J. A., Thomas, O., Hudgens-Haney, M., Gibbons, R. D., Tamminga, C. A. (2022). Psychosis biotypes: replication and validation from the B-SNIP Consortium. *Schizophrenia Bulletin, 48*, 56-68.

Clementz, B. A., Sweeney, J. A., Hamm, J. P., Ivleva, E. I., Ethridge, L. E., Pearlson, G. D., Keshavan, M. S., Tamminga, C. A. (2016). Identification of distinct psychosis biotypes using brain-based biomarkers. *The American Journal of Psychiatry, 173*, 373–384.

Cohen, S. M., Tsien, R. W., Goff, D. C., Halassa, M. M. (2015). The impact of NMDA receptor hypofunction on GABAergic neurons in the pathophysiology of schizophrenia. *Schizophrenia Research, 167*, 98–107.

Coiro, P., Pollak, D. D. (2019). Sex and gender bias in the experimental neurosciences: the case of the maternal immune activation model. *Translational Psychiatry, 9*, 90.

Coley, A. A., Gao, W. J. (2018). PSD95: a synaptic protein implicated in schizophrenia or autism? *Progress in Neuro-psychopharmacology and Biological Psychiatry, 82,* 187–194.

Coley, A. A., Gao, W. J. (2019). PSD95 deficiency disrupts PFC-associated function and behavior during neurodevelopment. *Scientific Reports, 9*, 9486.

Collingridge, G. L., Bliss, T. V. (1987). NMDA receptors: their role in long-term potentiation. *Trends in Neurosciences, 10*, 288–293

Colognato, H., Tzvetanova, I. D. (2011). Glia unglued: how signals from the extracellular matrix regulate the development of myelinating glia. *Developmental Neurobiology, 71,* 924-955.

Comer, A. L, Carrier, M, Tremblay, M. È., Cruz-Martín, A. (2020). The inflamed brain in schizophrenia: the convergence of genetic and environmental risk factors that lead to uncontrolled neuroinflammation. *Frontiers in Cellular Neuroscience, 14*, 274.

Conen, S., Gregory, C. J., Hinz, R., Smallman, R., Corsi-Zuelli, F., Deakin, B., Talbot, P. S. (2021). Neuroinflammation as measured by positron emission tomography in patients with recent onset and established schizophrenia: implications for immune pathogenesis. *Molecular Psychiatry, 26*, 5398–5406.

Connor, C. M., Dincer, A., Straubhaar, J., Galler, J. R., Houston, I. B., Akbarian, S. (2012). Maternal immune activation alters behavior in adult offspring, with subtle changes in the cortical transcriptome and epigenome. *Schizophrenia Research, 140*, 175-184.

Cooper, R. E., Laxhman, N., Crellin, N., Moncrieff, J., Priebe, S. (2020). Psychosocial interventions for people with schizophrenia or psychosis on minimal or no antipsychotic medication: a systematic review. *Schizophrenia Research, 225,* 15–30.

Correll, C. U., Kim, E., Sliwa, J. K., Hamm, W., Gopal, S., Mathews, M., Venkatasubramanian, R., Saklad, S. R. (2021). Pharmacokinetic characteristics of long-acting injectable antipsychotics for schizophrenia: an overview. *CNS Drugs, 35*, 39–59.

Correll, C. U., Schooler, N. R. (2020). Negative symptoms in schizophrenia: a review and clinical guide for recognition, assessment and treatment. *Neuropsychiatric Disease and Treatment, 16*, 519–534.

Couch, A. C. M., Berger, T., Hanger, B., Matuleviciute, R., Srivastava, D. P., Thuret, S., Vernon, A. C. (2021). Maternal immune activation primes deficiencies in adult hippocampal neurogenesis. *Brain, Behavior and Immunity, 97,* 410–422.

Couch, A. C. M., Solomon, S., Duarte, R. R. R., Marrocu, A., Sun, Y., Sichlinger, L., Matuleviciute, R., Polit, L. D., Hanger, B., Brown, A., Kordasti, S., Srivastava, D. P., Vernon, A. C. (2023). Acute IL-6 exposure triggers canonical IL6Ra signaling in hiPSC microglia, but not neural progenitor cells. *Brain, Behavior and Immunity, 110,* 43–59.

Coyle, P., Tran, N., Fung, J. N. T., Summers, B. L., Rofe, A. M. (2009). Maternal dietary zinc supplementation prevents aberrant behaviour in an object recognition task in mice offspring exposed to LPS in early pregnancy. *Behavioural Brain Research, 197*, 210-218.

Cramer, S., Beveridge, M., Kilberg, M., Novak, D. (2002). Physiological importance of system A-mediated amino acid transport to rat foetal development. *American Journal of Physiology - Cell Physiology, 282*, 153-160.

Crapser, J. D., Arreola, M. A., Tsourmas, K. I., Green, K. N. (2021). Microglia as hackers of the matrix: sculpting synapses and the extracellular space. *Cell and Molecular Immunology, 18*, 2472–2488.

Creighton, S. D., Stefanelli, G., Reda, A., Zovkic, I. B. (2020). Epigenetic mechanisms of learning and memory: implications for aging. *International Journal of Molecular Sciences, 21*, 6918.

Crider, K. S., Yang, T. P., Berry, R. J., Bailey, L. B. (2012). Folate and DNA methylation: a review of molecular mechanisms and the evidence for folate's role. *Advances in Nutrition, 3*, 21-38.

Cronk, J. C., Derecki, N. C., Ji, E., Xu, Y., Lampano, A. E., Smirnov, I., Baker, W., Norris, G. T., Marin, I., Coddington, N., Wolf, Y., Turner, S. D., Aderem, A., Klibanov, A. L., Harris, T. H., Jung, S., Litvak, V., Kipnis, J. (2015). Methyl-CpG Binding Protein 2 regulates microglia and macrophage gene expression in response to inflammatory stimuli. *Immunity, 42*, 679–691.

Crum, W. R., Sawiak, S. J., Chege, W., Cooper, J. D., Williams, S. C. R., Vernon, A. C. (2017). Evolution of structural abnormalities in the rat brain following *in utero* exposure to maternal immune activation: a longitudinal *in vivo* MRI study. *Brain, Behavior and Immunity, 63*, 50-59.

Cunningham, C., Campion, S., Teeling, J., Felton, L., Perry, V. H. (2007). The sickness behaviour and CNS inflammatory mediator profile induced by systemic challenge of mice with synthetic double-stranded RNA (poly I : C). *Brain, Behavior and Immunity, 21*, 490-502.

Curley, A. A., Arion, D., Volk, D. W., Asafu-Adjei, J. K., Sampson, A. R., Fish, K. N., Lewis, D. A. (2011). Cortical deficits of glutamic acid decarboxylase 67 expression in schizophrenia: clinical, protein and cell type-specific features. *American Journal of Psychiatry, 168*, 921-929.

Curtis, D., Vallada, H. P., Nanko, S., Kunugi, H., Powell, J. F., Murray, R. M., McGuffin, P., Owen, M. J., Gill, M., Collier, D. A. (1996). A linkage study of schizophrenia with DNA markers from chromosome 8p21-p22 in 25 multiplex families. *Schizophrenia Research, 22*, 61-68.

da Silva, V. C., Fernandes, L., Haseyama, E. J., Agamme, A. L. D. A., Shinohara, E. M. G., Muniz, M. T. C., D'Almeida, V. (2014). Effect of vitamin B deprivation during pregnancy and lactation on homocysteine metabolism and related metabolites in brain and plasma of mice offspring. *PLoS One, 9*, e92683.

Dabiri, M., Dehghani Firouzabadi, F., Yang, K., Barker, P. B., Lee, R. R., Yousem, D. M. (2022). Neuroimaging in schizophrenia: a review article. *Frontiers in Neuroscience, 16*, 1042814.

Dahlgren, J., Samuelsson, A. M., Jansson, T., Holmang, A. (2006). Interleukin-6 in the maternal circulation reaches the rat foetus in mid-gestation. *Pediatric Research, 60*, 147-151.

Dalgleish, T., Black, M., Johnston, D., Bevan, A. (2020). Transdiagnostic approaches to mental health problems: current status and future directions. *Journal of Consulting and Clinical Psychology, 88*, 179–195.

Daniels, J. K., Spurlock, G., Williams, N. M., Cardno, A. G., Jones, L. A., Murphy, K. C., Asherson, P., Holmans, P., Fenton, I., McGuffin, P., Owen, M. J. (1997). Linkage study of chromosome 6p in sib-pairs with schizophrenia. *American Journal of Medical Genetics, 74*, 319-323.

Dankovich, T. M., Rizzoli, S. O. (2022). The synaptic extracellular matrix: long-lived, stable and still remarkably dynamic. *Frontiers in Synaptic Neuroscience, 14,* 854956.

Dattilo, V., Amato, R., Perrotti, N., Gennarelli, M. (2020). The emerging role of SGK1 (Serum- and Glucocorticoid-Regulated Kinase 1) in major depressive disorder: hypothesis and mechanisms. *Frontiers in Genetics, 11*, 826.

Dauvermann, M. R., Donohoe, G. (2019). Cortisol stress response in psychosis from the high-risk to the chronic stage: a systematic review. *Irish Journal of Psychological Medicine, 36*, 305–315.

Davis, T. H., Cuellar, T. L., Koch, S. M., Barker, A. J., Harfe, B. D., McManus, M. T., Ullian, E. M. (2008). Conditional loss of DICER disrupts cellular and tissue morphogenesis in the cortex and hippocampus. *Journal of Neuroscience, 28*, 4322-4330.

Dawson, M. R., Polito, A., Levine, J. M., Reynolds, R. (2003). NG2-expressing glial progenitor cells: an abundant and widespread population of cycling cells in the adult rat CNS. *Molecular and Cellular Neuroscience, 24*, 476-488.

De Deurwaerdère, P., Di Giovanni, G. (2020). Serotonin in health and disease. *International Journal of Molecular Sciences, 21,* 3500.

de Luca, C., Olefsky, J. M. (2008). Inflammation and insulin resistance. *FEBS Letters, 582*, 97-105.

De Picker, L. J., Victoriano, G. M., Richards, R., Gorvett, A. J., Lyons, S., Buckland, G. R., Tofani, T., Norman, J. L., Chatelet, D. S., Nicoll, J. A. R., Boche, D. (2021). Immune environment of the brain in schizophrenia and during the psychotic episode: a human post-mortem study. *Brain, Behavior and Immunity, 97*, 319–327.

de Sousa Abreu, R., Penalva, L. O., Marcotte, E. M., Vogel, C. (2009). Global signatures of protein and mRNA expression levels. *Molecular Biosystems, 5,* 1512-1526.

de Souza, D. F., Wartchow, K. M., Lunardi PS, Brolese G, Tortorelli, L. S., Batassini, C., Biasibetti, R., Gonçalves, C. A. (2015). Changes in astroglial markers in a maternal immune activation model of schizophrenia in wistar rats are dependent on sex. *Frontiers in Cellular Neuroscience, 9,* 489.

Deaton, A. M., Bird, A. (2011). CpG islands and the regulation of transcription. *Genes and Development, 25*, 1010-1022.

Deepa, S. S., Carulli, D., Galtrey, C., Rhodes, K., Fukuda, J., Mikami, T., Sugahara, K., Fawcett, J. W. (2006). Composition of perineuronal net extracellular matrix in rat brain: a different disaccharide composition for the net-associated proteoglycans. *Journal of Biological Chemistry, 281*, 17789-17800.

DeLisi, L. E., Szulc, K. U., Bertisch, H. C., Majcher, M., Brown, K. (2006). Understanding structural brain changes in schizophrenia. *Dialogues in Clinical Neuroscience, 8*, 71–78.

Dennison, C. A., Legge, S. E., Pardiñas, A. F., Walters, J. T. R. (2020). Genome-wide association studies in schizophrenia: recent advances, challenges and future perspective. *Schizophrenia Research, 217*, 4–12.

Deverman, B. E., Patterson, P. H. (2009). Cytokines and CNS development. *Neuron, 64*, 61-78.

Devlin, A. M., Arning, E., Bottiglieri, T., Faraci, F. M., Rozen, R., Lentz., S. R. (2004). Effect of Mthfr genotype on diet-induced hyperhomocysteinemia and vascular function in mice. *Blood, 103,* 2624–2629.

Di Biase, M. A., Zalesky, A., O'keefe, G., Laskaris, L., Baune, B. T., Weickert, C. S., Olver, J., McGorry, P. D., Amminger, G. P., Nelson, B., Scott, A. M., Hickie, I., Banati, R., Turkheimer, F., Yaqub, M., Everall, I. P., Pantelis, C., Cropley, V. (2017). PET imaging of putative microglial activation in individuals at ultra-high risk for psychosis, recently diagnosed and chronically ill with schizophrenia. *Translational Psychiatry, 7,* e1225.

Di Luca, M., Ruts, L., Gardoni, F., Cattabeni, F., Biessels, G. J., Gispen, W. H. (1999). NMDA receptor subunits are modified transcriptionally and post-translationally in the brain of streptozotocin-diabetic rats. *Diabetologia, 42,* 693-701.

Diaz-Jimenez, D., Kolb, J. P., Cidlowski, J. A. (2021). Glucocorticoids as regulators of macrophage-mediated tissue homeostasis. *Frontiers in Immunology, 12,* 669891.

Dickerson, D. D., Overeem, K. A., Wolff, A. R., Williams, J. M., Abraham, W. C., Bilkey, D. K. (2014). Association of aberrant neural synchrony and altered GAD67 expression following exposure to maternal immune activation, a risk factor for schizophrenia. *Translational Psychiatry, 4,* e418.

Dietz, A. G., Goldman, S. A., Nedergaard, M. (2020). Glial cells in schizophrenia: a unified hypothesis. *The Lancet - Psychiatry, 7*, 272-281.

Dilworth, M. R., Sibley, C. P. (2013). Review: transport across the placenta of mice and women. *Placenta, 34,* 34-39.

Ding, S., Hu, Y., Luo, B., Cai, Y., Hao, K., Yang, Y., Zhang, Y., Wang, X., Ding, M., Zhang, H., Li, W., Lv, L. (2019). Age-related changes in neuroinflammation and prepulse inhibition in offspring of rats treated with Poly I:C in early gestation. *Behavioural and Brain Functions, 15,* 3.

Do, C., Shearer, A., Suzuki, M., Terry, M. B., Gelernter, J., Greally, J. M., Tycko, B. (2017). Genetic-epigenetic interactions in cis: a major focus in the post-GWAS era. *Genome Biology, 18*, 120.

Dong, E., Gavin, D. P., Chen, Y., Davis, J., (2012). Upregulation of TET1 and downregulation of APOBEC3A and APOBEC3C in the parietal cortex of psychotic patients. *Translational Psychiatry, 2*, e159.

Dos Santos, S. E., Medeiros, M., Porfirio, J., Tavares, W., Pessôa, L., Grinberg, L., Leite, R. E. P., Ferretti-Rebustini, R. E. L., Suemoto, C. K., Filho, W. J., Noctor, S. C., Sherwood, C. C., Kaas, J. H., Manger, P. R., Herculano-Houzel, S. (2020). Similar microglial cell densities across brain structures and mammalian species: implications for brain tissue function. *The Journal of Neuroscience, 40*, 4622-4643.

Dowling, C., Allen, N. J. (2018). Mice lacking Glypican 4 display juvenile hyperactivity and adult social interaction deficits. *Brain Plasticity, 4,* 197-209.

Downes, N., Mullins, P. (2014). The development of myelin in the brain of the juvenile rat. *Toxicologic Pathology, 42*, 913-922.

Dube, R. Kar, S. S. (2020). COVID-19 in pregnancy: the foetal perspective – a systematic review. *BMJ Paediatrics, 4*, e000859.

Dubey, H., Sharma, R. K., Krishnan, S., Knickmeyer, R. (2022). SARS-CoV-2 (COVID-19) as a possible risk factor for neurodevelopmental disorders. *Frontiers in Neuroscience, 16*, 1021721.

Ducker, G. S., Rabinowitz, J. D. (2017). One-carbon metabolism in health and disease. *Cell Metabolism, 25,* 27-42.

Dugas, J. C., Cuellar, T. L., Scholze, A., Ason, B., Ibrahim, A., Emery, B., Zamanian, J. L., Foo, L. C., McManus, M. T., Barres, B. A. (2010). Dicer1 and Mir-219 are required for normal oligodendrocyte differentiation and myelination. *Journal of Neurochemistry, 115*, e36.

Duits, F. H., Brinkmalm, G., Teunissen, C. E., Brinkmalm, A., Scheltens, P., Van der Flier, W. M., Zetterberg, H., Blennow, K. (2018). Synaptic proteins in CSF as potential novel biomarkers for prognosis in prodromal Alzheimer's disease. *Alzheimers Research and Therapy, 10*, 5.

Durinck, S., Spellman, P. T., Birney, E., Huber, W. (2009). Mapping identifiers for the integration of genomic datasets with the R/Bioconductor package biomaRt. *Nature protocols, 4,* 1184–1191.

Dutcher, E. G., Pama, E. A. C., Lynall, M. E., Khan, S., Clatworthy, M. R., Robbins, T. W., Bullmore, E. T., Dalley, J. W. (2020). Early-life stress and inflammation: a systematic review of a key experimental approach in rodents. *Brain and Neuroscience Advances, 4,* e2398212820978049.

Dyck, G. J. B., Maayah, Z. H., Eurich, D. T., Dyck, J. R. B. (2022). Understanding the potential benefits of cannabidiol for patients with schizophrenia: a narrative review. *Schizophrenia Bulletin, 3,* sgab053.

Dyer, J. R., Greenwood, C. E. (1988). Evidence for altered methionine methyl-group utilization in the diabetic rat's brain. *Neurochemical Research, 13,* 517-523.

Dziegielewska, K. M., Moller, J. E., Potter, A. M., Ek, J., Lane, M. A., Saunders, N. R. (2000). Acute-phase cytokines IL-1beta and TNF-alpha in brain development. *Cell and Tissue Research, 299*, 335–345.

Dzwonek, J., Wilczynski, G. M. (2015). CD44: molecular interactions, signaling and functions in the nervous system. *Frontiers in Cellular Neuroscience, 9*, 175.

Dzyubenko, E., Gottschling, C., Faissner, A. (2016). Neuron-glia interactions in neural plasticity: contributions of neural extracellular matrix and perineuronal nets. *Neural Plasticity, 2016*, 5214961.

Egawa, N., Shindo, A., Hikawa, R., Kinoshita, H., Liang, A. C., Itoh, K., Lok, J., Maki, T., Takahashi, R., Lo, E. H., Arai, K. (2019). Differential roles of epigenetic regulators in the survival and differentiation of oligodendrocyte precursor cells. *Glia, 67,* 718-728.

Ehrlich, M., Gama-Sosa, M. A., Huang, L. H., Midgett, R. M., Kuo, K. C., McCune, R. A., Gehrke, C. (1982). Amount and distribution of 5-methylcytosine in human DNA from different types of tissues of cells. *Nucleic Acids Research, 10,* 2709-2721.

Eide, M. G., Moster, D., Irgens, L. M., Reichborn-Kjennerud, T., Stoltenberg, C., Skjaerven, R., Susser, E., Abel, K. (2013). Degree of foetal growth restriction associated with schizophrenia risk in a national cohort. *Psychological Medicine, 43*, 2057-2066.

Elcioğlu, H. K., Aslan, E., Ahmad, S., Alan, S., Salva, E., Elcioglu, Ö. H., Kabasakal, L. (2016). Tocilizumab's effect on cognitive deficits induced by intracerebroventricular administration of streptozotocin in Alzheimer's model. *Molecular and Cellular Biochemistry, 420*, 21–28.

Elkis, H., Friedman, L., Wise, A., Meltzer, H. Y. (1995). Meta-analyses of studies of ventricular enlargement and cortical sulcal prominence in mood disorders. Comparisons with controls or patients with schizophrenia. *Archives of General Psychiatry, 52*, 735-746.

Ellenbroek, B., Youn, J. (2016). Rodent models in neuroscience research: is it a rat race? *Disease Models and Mechanisms, 9*, 1079–1087.

Emery, B., Lu, Q. R. (2015). Transcriptional and epigenetic regulation of oligodendrocyte development and myelination in the central nervous system. *Cold Spring Harbour Perspectives in Biology, 7,* a020461.

Enders, A. C., Blankenship, T. N. (1999). Comparative placental structure. *Advanced Drug Delivery Reviews, 38,* 3-15.

Enwright, J. F., Sanapala, S., Foglio, A., Berry, R., Fish, K. N., Lewis, D. A. (2016). Reduced labeling of parvalbumin neurons and perineuronal nets in the dorsolateral prefrontal cortex of subjects with schizophrenia. *Neuropsychopharmacology, 41*, 2206–2214.

Essex, M. J., Boyce, W. T., Hertzman, C., Lam, L. L., Armstrong, J. M., Neumann, S. M., Kobor, M. S. (2013). Epigenetic vestiges of early developmental adversity: childhood stress exposure and DNA methylation in adolescence. *Child Development, 84*, 58–75.

Estes, M. L., McAllister, A. K. (2016). Maternal immune activation: implications for neuropsychiatric disorders. *Science, 353*, 772–777.

Fan, G., Martinowich, K., Chin, M. H., He, F., Fouse, S. D., Hutnick, L., Hattori, D., Ge, W., Shen, Y., Wu, H., ten Hoeve, J., Shuai, K., Sun, Y. E. (2005). DNA methylation controls the timing of astrogliogenesis through regulation of JAK-STAT signaling. *Development, 132,* 3345-3356.

Farhy-Tselnicker, I., van Casteren, A. C. M., Lee, A., Chang, V. T., Aricescu, A. R., Allen, N. J. (2017). Astrocyte-secreted glypican 4 regulates release of neuronal pentraxin 1 from axons to induce functional synapse formation. *Neuron, 96,* 428-445.

Farrelly, L., Föcking, M., Piontkewitz, Y., Dicker, P., English, J., Wynne, K., Cannon, M., Cagney, G., Cotter, D. R. (2015). Maternal immune activation induces changes in myelin and metabolic proteins, some of which can be prevented with risperidone in adolescence. *Developmental Neuroscience, 37*, 43-55.

Fatemi, S. H., Folsom, T. D., Reutiman, T. J., Abu-Odeh, D., Mori, S., Huang, H., Oishi, K. (2009a). Abnormal expression of myelination genes and alterations in white matter fractional anisotropy following prenatal viral influenza infection at E16 in mice. *Schizophrenia Research, 112*, 46-53.

Fatemi, S. H., Folsom, T. D., Rooney, R. J., Mori, S., Kornfield, T. E., Reutiman, T. J., Kneeland, R. E., Liesch, S. B., Hua, K. G., Hsu, J., Patel, D. H. (2012). The viral theory of schizophrenia revisited: abnormal placental gene expression and structural changes with lack of evidence for H1N1 viral presence in placentae of infected mice or brains of exposed offspring. *Neuropharmacology, 62*, 1290-1298.

Fatemi, S. H., Reutiman, T. J., Folsom, T. D. (2009b). Chronic psychotropic drug treatment causes differential expression of Reelin signaling system in frontal cortex of rats. *Schizophrenia Research, 111*, 138-152.

Fatemi, S. H., Reutiman, T. J., Folsom, T. D., Huang, H., Oishi, K., Mori, S., Smee, D. F., Pearce, D. A., Winter, C., Sohr, R., Juckel, G. (2008). Maternal infection leads to abnormal gene regulation and brain atrophy in mouse offspring: implications for genesis of neurodevelopmental disorders. *Schizophrenia Research, 99,* 56-70.

Fatemi, S. H., Sidwell, R., Akhter, P., Sedgewick, J., Thuras, P., Bailey, K., Kist, D. (1998a). Human influenza viral infection *in utero* increases nNOS expression in hippocampi of neonatal mice. *Synapse, 29***,** 84-88.

Fatemi, S. H., Sidwell, R., Kist, D., Akhter, P., Meltzer, H. Y., Bailey, K., Thuras, P., Sedgwick, J. (1998b). Differential expression of synaptosome-associated protein 25 kDa [SNAP-25] in hippocampi of neonatal mice following exposure to human influenza virus *in utero*. *Brain Research, 800***,** 1-9.

Faul, F., Erdfelder, E., Lang, A. G., Buchner, A. (2007). G*Power 3: A flexible statistical power analysis program for the social, behavioral and biomedical sciences. *Behaviour Research Methods, 39*, 175-191.

Favrais G., van de Looij, Y., Fleiss, B., Ramanantsoa, N., Bonnin, P., Stoltenburg-Didinger, G., Lacaud, A., Saliba, E., Dammann, O., Gallego, J., Sizonenko, S., Hagberg, H., Lelièvre, V., Gressens, P. (2011). Systemic inflammation disrupts the developmental program of white matter. *Annals of Neurology, 70*, 550-565.

Favuzzi, E., Marques-Smith, A., Deogracias, R., Winterflood, C. M., Sánchez-Aguilera, A., Mantoan, L., Maeso, P., Fernandes, C., Ewers, H., Rico, B. (2017) Activity-dependent gating of parvalbumin interneuron function by the perineuronal net protein brevican. *Neuron, 95*, 639-655.

Fawal, M. A., Jungas, T., Kischel, A., Audouard, C., Iacovoni, J. S., Davy, A. (2018). Cross talk between one-carbon metabolism, Eph signaling and histone methylation promotes neural stem cell differentiation. *Cell Reports, 23*, 2864-2873.

Fawcett, J. W., Oohashi, T., Pizzorusso, T. (2019). The roles of perineuronal nets and the perinodal extracellular matrix in neuronal function. *Nature Reviews Neuroscience, 20,* 451-465.

Feng, J., Chang, H., Li, E., Fan, G. (2005). Dynamic expression of de novo DNA methyltransferases Dnmt3a and Dnmt3b in the central nervous system. *Journal of Neuroscience Research, 79*, 734-746.

Feng, J., Fouse, S., Fan, G. (2007). Epigenetic regulation of neural gene expression and neuronal function. *Paediatric Research, 61*, 58-63.

Feng, J., Zhou, Y., Campbell, S. L., Le, T., Li, E., Sweatt, J. D., Silva, A. J., Fan, G. (2010). Dnmt1 and Dnmt3a maintain DNA methylation and regulate synaptic function in adult forebrain neurons. *Nature Neuroscience, 13,* 423-430.

Ferguson, B. R., Gao, W. J. (2018). PV interneurons: critical regulators of E/I balance for prefrontal cortex-dependent behavior and psychiatric disorders. *Frontiers in Neural Circuits, 12*, 37.

Fernández-Arjona, M. del M., Grondona, J. M., Fernández-Llebrez, P., López-Ávalos, M. D. (2019). Microglial morphometric parameters correlate with the expression level of IL-1β and allow identifying different activated morphotypes. *Frontiers in Cellular Neuroscience, 13*, 472.

Fernández-Arjona, M. del M., Grondona, J. M., Granados-Durán, P., Fernández-Llebrez, P., López-Ávalos, M. D. (2017). Microglia morphological categorization in a rat model of neuroinflammation by hierarchical cluster and principal components analysis. *Frontiers in Cellular Neuroscience, 11*, 235.

Fernández de Cossío, L., Lacabanne, C., Bordeleau, M., Castino, G., Kyriakakis, P., Tremblay, M. È. (2021). Lipopolysaccharide-induced maternal immune activation modulates microglial CX3CR1 protein expression and morphological phenotype in the hippocampus and dentate gyrus, resulting in cognitive inflexibility during late adolescence. *Brain, Behavior and Immunity, 97*, 440-454.

Ferreira, F. R., de Moura, N. S. B., Hassib, L., Pombo, T. R. (2020). Resveratrol ameliorates the effect of maternal immune activation associated with schizophrenia in adulthood offspring. *Neuroscience Letters, 734*, 135100.

Fitzgerald, E., Sinton, M.C., Wernig-Zorc, S., Morton, N. M., Holmes, M. C., Boardman, J. P., Drake, A. J. (2021). Altered hypothalamic DNA methylation and stress-induced hyperactivity following early life stress. *Epigenetics and Chromatin, 14*, 31.

Fleischhacker, W., Galderisi, S., Laszlovszky, I., Szatmári, B., Barabássy, Á., Acsai, K., Szalai, E., Harsányi, J., Earley, W., Patel, M., Németh, G. (2019). The efficacy of cariprazine in negative symptoms of schizophrenia: Post hoc analyses of PANSS individual items and PANSS-derived factors. *European Psychiatry, 58*, 1–9.

Foley, C., Heron, E. A., Harold, D., Walters, J., Owen, M., O'Donovan, M., Sebat, J., Kelleher, E., Mooney, C., Durand, A., Pinto, C., Cormican, P., Morris, D., Donohoe, G., Gill, M., Gallagher, L., Corvin, A. (2020). Identifying schizophrenia patients who carry pathogenic genetic copy number variants using standard clinical assessment: retrospective cohort study. *The British Journal of Psychiatry, 216*, 275–279.

Fortier, M. E., Joober, R., Luheshi, G. N., Boksa, P. (2004). Maternal exposure to bacterial endotoxin during pregnancy enhances amphetamine-induced locomotion and startle responses in adult rat offspring. *Journal of Psychiatric Research, 38*, 335-345.

Fortier, M. E., Luheshi, G. N., Boksa, P. (2007). Effects of prenatal infection on prepulse inhibition in the rat depend on the nature of the infectious agent and the stage of pregnancy. *Behavioural Brain Research, 181*, 270-277.

Fraga, M. F., Ballestar, E., Paz, M. F., Ropero, S., Setien, F., Ballestart, M. L., Heine-Suner, D., Cigudosa, J. C., Urioste, M., Benitez, J., Boix-Chornet, M., Sanchez-Aguilera, A., Ling, C., Carlsson, E., Poulsen, P., Vaag, A., Stephan, Z., Spector, T. D., Wu, Y. Z., Plass, C., Esteller, M. (2005). Epigenetic differences arise during the lifetime of monozygotic twins. *Proceedings of the National Academy of Sciences of the United States of America, 102*, 10604-10609.

Francisco, R. D., Fernando, V., Norma, E., Madai, M. E., Marcelo, B. (2022). Glial changes in schizophrenia: genetic and epigenetic approach. *Indian Journal of Psychiatry, 64*, 3-12.

Frank, M. G., Baratta, M. V., Sprunger, D. B., Watkins, L. R., Maier, S. F. (2007). Microglia serve as a neuroimmune substrate for stress-induced potentiation of CNS pro-inflammatory cytokine responses. *Brain, Behavior and Immunity, 21,* 47-59.

Frick, L. R., Williams, K., Pittenger, C. (2013). Microglial dysregulation in psychiatric disease. *Clinical and Developmental Immunology, 2013*, e608654.

Frigerio, B., Bizzoni, C., Jansen, G., Leamon, C. P., Peters, G. J., Low, P. S., Matherly, L. H., Figini, M. (2019). Folate receptors and transporters: biological role and diagnostic/therapeutic targets in cancer and other diseases. *Journal of Experimental and Clinical Cancer Research, 38*, 125.

Frischknecht, R., Gundelfinger, E.D. (2012). The brain's extracellular matrix and its Role in synaptic plasticity. In: Kreutz, M., Sala, C. (eds) Synaptic plasticity pp153-171. Advances in experimental medicine and biology, vol970. Springer. Vienna.

Frischknecht, R., Heine, M., Perrais, D, Seidenbecher, C. I., Choquet, D., Gundelfinger, E. D. (2009). Brain extracellular matrix affects AMPA receptor lateral mobility and short-term synaptic plasticity. *Nature Neuroscience, 12,* 897–904.

Fu, K., Bonora, G., Pellegrini, M. (2020). Interactions between core histone marks and DNA methyltransferases predict DNA methylation patterns observed in human cells and tissues. *Epigenetics, 15,* 272–282.

Funk, A. J., Mielnik, C. A., Koene, R., Newburn, E., Ramsey, A. J., Lipska, McCullumsmith, R. E. (2017). Postsynaptic density-95 isoform abnormalities in schizophrenia. *Schizophrenia Bulletin, 43,* 891–899.

Furukawa, S., Kuroda, Y., Sugiyama, A. (2014). A comparison of the histological structure of the placenta in experimental animals. *Journal of Toxicologic Pathology, 27,* 11–18.

Gallego, J. A., Blanco, E. A., Husain-Krautter, S., Madeline Fagen, E., Moreno-Merino, P., Del Ojo-Jimenez, J. A., Ahmed, A., Rothstein, T. L., Lencz, T., Malhotra, A. K. (2018). Cytokines in cerebrospinal fluid of patients with schizophrenia spectrum disorders: new data and an updated meta-analysis. *Schizophrenia Research, 202*, 64-71.

Gamazon, E. R., Stranger, B. E. (2015). The impact of human copy number variation on gene expression. *Briefings in Functional Genomics, 14*, 352–357.

Ganguly, K., Schinder, A. F., Wong, S. T., Poo, M. (2001). GABA itself promotes the developmental switch of neuronal GABAergic responses from excitation to inhibition. *Cell, 105*, 521–532.

Gao, R., Wang, M., Lin, J., Hu, L., Li, Z., Chen, C., Yuan, L. (2018). Spatiotemporal expression patterns of chondroitin sulfate proteoglycan mRNAs in the developing rat brain. *Neuroreport, 29*, 517-523.

Garcez, M. L., Mina, F., Bellettini-Santos, T., Ribeiro, F. M., Ghisi Frassetto, A. Z., Batista-Silva, H., da Luz, A. P., Schiavo, G. L., Medeiros, E. B., Zabot, G. C., Canever, L., Zugno, A. I., Budni, J. (2021). Folic acid supplementation in the gestational phase of female rats improves age-related memory impairment and neuroinflammation in their adult and aged offspring. *The Journals of Gerontology Series A Biological Sciences and Medical Sciences, 76*, 991-995.

Garcia-Flores, V., Romero, R., Xu, Y., Theis, K., Arenas-Hernandez, M., Miller, D., Peyvandipour, A., Galaz, J., Levenson, D., Bhatti, G., Gershater, M., Pusod, E., Kracht, D., Florova, V., Leng, Y., Tao, L., Faucett, M., Para, R., Hsu, C. D., Zhang, G., … Gomez-Lopez, N. (2022) Maternal-foetal immune responses in pregnant women infected with SARS-CoV-2. *Nature Communications, 13*, 320.

Garner, J. P. (2014). The significance of meaning: why do over 90% of behavioral neuroscience results fail to translate to humans and what can we do to fix it? *ILAR Journal, 55*, 438–456.

Gaser, C., Nenadic, I., Buchsbaum, B. R., Hazlett, E. A., Buchsbaum, M. S. (2004). Ventricular enlargement in schizophrenia related to volume reduction of the thalamus, striatum and superior temporal cortex. *American Journal of Psychiatry, 161*, 154-156.

Geloso, M. C., D'Ambrosi, N. (2021). Microglial pruning: relevance for synaptic dysfunction in multiple sclerosis and related experimental models. *Cells, 10,* 686.

Gennarelli, M., Monteleone, P., Minelli, A., Monteleone, A. M., Rossi, A., Rocca, P., Bertolino, A., Aguglia, E., Amore, M., Bellino, S., Bellomo, A., Biondi, M., Bucci, P., Carpiniello, B., Cascino, G., Cuomo, A., Dell'Osso, L., di Giannantonio, M., Giordano, G. M., Marchesi, C., … Italian Network for Research on Psychoses (2022). Genome-wide association study detected novel susceptibility genes for social cognition impairment in people with schizophrenia. *The World Journal of Biological Psychiatry, 23*, 46–54.

George, M., Maheshwari, S., Chandran, S., Manohar, J. S., Sathyanarayana Rao, T. S. (2017). Understanding the schizophrenia prodrome. *Indian Journal of Psychiatry, 59*, 505–509.

Gianfrancesco, O., Bubb, V. J., Quinn, J. P. (2019). Treating the "E" in "G × E": trauma-informed approaches and psychological therapy interventions in psychosis. *Frontiers in Psychiatry, 10*, e9.

Giger, R. J., Venkatesh, K., Chivatakarn, O., Raiker, S. J., Robak, L., Hofer, T., Lee, H., Rader, C. (2008). Mechanisms of CNS myelin inhibition: evidence for distinct and neuronal cell type specific receptor systems. *Restorative Neurology and Neuroscience, 26*, 97-115.

Gillman, M. W. (2005). Developmental origins of health and disease. *New England Journal of Medicine, 353,* 1848-1850.

Gilmore, J. H., Jarskog, L. F., Vadlamudi, S. (2003). Maternal infection regulates BDNF and NGF expression in foetal and neonatal brain and maternal-foetal unit of the rat. *Journal of Neuroimmunology, 138,* 49-55.

Ginhoux, F., Lim, S., Hoeffel, G., Low, D., Huber, T. (2013). Origin and differentiation of microglia. *Frontiers in Cellular Neuroscience, 7,* 45.

Giollabhui, N. M., Breen, E. C., Murphy, S. K., Maxwell, S. D., Cohn, B. A., Krigbaum, N. Y., Cirillo, P. M., Perez, C., Alloy, L. B., Drabick, D. A. G., Ellman, L. M. (2019). Maternal inflammation during pregnancy and offspring psychiatric symptoms in childhood: timing and sex matter. *Journal of Psychiatric Research, 111,* 96-103.

Giovanoli, S., Engler, H., Engler, A., Richetto, J., Feldon, J., Riva, M. A., Schedlowski, M., Meyer, U. (2016). Preventive effects of minocycline in a neurodevelopmental two-hit model with relevance to schizophrenia. *Translational Psychiatry, 6*, e772.

Giovanoli, S., Notter, T., Richetto, J., Labouesse, M. A., Vuillermot, A., Riva, M. A., Meyer, U. (2015). Late prenatal immune activation causes hippocampal deficits in the absence of persistent inflammation across aging. *Journal of Neuroinflammation, 12*, 221.

Giussani, D. A. (2011). The vulnerable developing brain. *Proceedings of the National Academy of Sciences of the United States of America, 108*, 2641-2642.

Glazier, J. D., Cetin, I., Perugino, G., Ronzoni, S., Grey, A. M., Mahendran, D., Marconi, A. M., Pardi, G., Sibley, C. P. (1997). Association between the activity of the system A amino acid transporter in the microvillous plasma membrane of the human placenta and severity of foetal compromise in intrauterine growth restriction. *Pediatric Research, 42*, 514–519.

Glazier, J. D., Jones C. J. P., Sibley C. P. (1990). Preparation of plasma membrane vesicles from the rat placenta at term and measurement of Na+ uptake. *Placenta, 11*, 451-463.

Glazier, J. D., Sibley, C. P., Carter, A. M. (1996). Effect of foetal growth restriction on system A amino acid transporter activity in the maternal facing plasma membrane of rat syncytiotrophoblast. *Peadiatric Research, 40*, 325-329.

Gogos, A., Sbisa, A., Witkamp, D., van den Buuse, M. (2020). Sex differences in the effect of maternal immune activation on cognitive and psychosis-like behaviour in Long Evans rats. *European Journal of Neuroscience, 52*, 2614-2626.

Golan, H. M., Lev, V., Hallak, M., Sorokin, Y., Huleihel, M. (2005). Specific neurodevelopmental damage in mice offspring following maternal inflammation during pregnancy. *Neuropharmacology, 48*, 903-917.

Gomes, F. V., Grace, A. A. (2021). Beyond dopamine receptor antagonism: new targets for schizophrenia treatment and prevention. *International Journal of Molecular Sciences, 22,* 4467.

Gore, A. C., 2013. Fundamental neuroscience (4th Edition). pp799-817. Academic Press. Cambridge, Massachusetts.

Gotz, M., Huttner, W. B. (2005). The cell biology of neurogenesis. *Nature Reviews Molecular Cell Biology, 6,* 777-788.

Grafen, A., Hails, R. (2002). Modern statistics for the life sciences. Oxford University Press. Oxford.

Gray, E., Thomas, T. L., Betmouni, S., Scolding, N., Love, S. (2008). Elevated matrix metalloproteinase-9 and degradation of perineuronal nets in cerebrocortical multiple sclerosis plaques. Journal of *Neuropathology and Experimental Neurology, 67*, 888–899.

Grayson, D. R., Guidotti, A. (2018). DNA methylation in animal models of psychosis. *Progress in Molecular Biology and Translational Science, 157,* 105-132.

Green, M. F., Nuechterlein, K. H., Kern, R. S., Baade, L. E., Fenton, W. S., Gold, J. M., Keefe, R. S., Mesholam-Gately, R., Seidman, L. J., Stover, E., Marder, S. R. (2008). Functional co-primary measures for clinical trials in schizophrenia: results from the MATRICS Psychometric and Standardization Study. *American Journal of Psychiatry, 165*, 221-228.

Greenwood, T. A., Lazzeroni, L. C., Maihofer, A. X., Swerdlow, N. R., Calkins, M. E., Freedman, R., Green, M. F., Light, G. A., Nievergelt, C. M., Nuechterlein, K. H., Radant, A. D., Siever, L. J., Silverman, J. M., Stone, W. S., Sugar, C. A., Tsuang, D. W., Tsuang, M. T., Turetsky, B. I., Gur, R. C., Gur, R. E., … Braff, D. L. (2019). Genome-wide association of endophenotypes for schizophrenia from the Consortium on the Genetics of Schizophrenia (COGS) study. *JAMA Psychiatry, 76*, 1274–1284.

Groc, L., Choquet, D., Stephenson, F. A., Verrier, D., Manzoni, O. J., Chavis, P. (2007). NMDA receptor surface trafficking and synaptic subunit composition are developmentally regulated by the extracellular matrix protein reelin. *Journal of Neuroscience, 27*, 10165–10175.

Grodstein, F., Lemos, B., Yu, L., Klein, H., Iatrou, A., Buchman, A. S., Shireby, G. L., Mill, J., Schneider, J. A., De Jager, P. L., Bennett, D. A. (2021). The association of epigenetic clocks in brain tissue with brain pathologies and common aging phenotypes. *Neurobiology of Disease, 157,* 105428.

Grumet, M., Flaccus, A., Margolis, R. U. (1993). Functional characterization of chondroitin sulfate proteoglycans of brain: interactions with neurons and neural cell adhesion molecules. *Journal of Cell Biology, 120,* 815-824.

Guan, J. S., Haggarty, S. J., Giacometti, E., Dannenberg, J. H., Joseph, N., Gao, J., Nieland, T. J., Zhou, Y., Wang, X., Mazitschek, R., Bradner, J. E., DePinho, R. A., Jaenisch, R., Tsai, L. H. (2009). HDAC2 negatively regulates memory formation and synaptic plasticity. *Nature, 459*, 55-60.

Guarnieri, G., Sarchielli, E., Comeglio, P., Herrera-Puerta, E., Piaceri, I., Nacmias, B., Benelli, M., Kelsey, G., Maggi, M., Gallina, P., Vannelli, G. B., Morelli, A. (2020). Tumor Necrosis Factor α influences phenotypic plasticity and promotes epigenetic changes in human basal forebrain cholinergic neuroblasts. *International Journal of Molecular Science, 21*, 6128.

Gude, N. M., Roberts, C. T., Kalionis, B., King, R. G. (2004). Growth and function of the normal human placenta. *Thrombosis Research, 114*, 397-407.

Guidotti, A., Auta, J., Davis, J. M., Di-Giorgi-Gerevini, V., Dwivedi, Y., Grayson, D. R., Impagnatiello, F., Pandey, G., Pesold, C., Sharma, R., Uzunov, D., Costa, E. (2000). Decrease in reelin and glutamic acid decarboxylase 67 (GAD67) expression in schizophrenia and bipolar disorder: a postmortem brain study. *Archives of General Psychiatry, 57*, 1061–1069.

Guidotti, A., Grayson, D. R., Caruncho, H. J. (2016). Epigenetic RELN dysfunction in schizophrenia and related neuropsychiatric disorders. *Frontiers in Cellular Neuroscience, 10*, 89.

Guidotti, A., Ruzicka, W., Grayson, D. R., Veldic, M., Pinna, G., Davis, J. M., Costa, E. (2007). S-adenosyl methionine and DNA methyltransferase-1 mRNA overexpression in psychosis. *Neuroreport, 18*, 57-60.

Guimond, S., Gu, F., Shannon, H., Kelly, S., Mike, L., Devenyi, G. A., Chakravarty, M. M., Sweeney, J. A., Pearlson, G., Clementz, B. A., Tamminga, C., Keshavan, M. (2021). A diagnosis and biotype comparison across the psychosis spectrum: investigating volume and shape amygdala-hippocampal differences from the B-SNIP Study. *Schizophrenia Bulletin, 47,* 1706–1717.

Guirado, R., Perez-Rando, M., Ferragud, A., Gutierrez-Castellanos, N., Umemori, J., Carceller, H., Nacher, J., Castillo-Gómez, E. (2020). A critical period for prefrontal network configurations underlying psychiatric disorders and addiction. *Frontiers in Behavioral Neuroscience, 14*, 51.

Guma, E., Bordignon, P. D. C., Devenyi, G. A., Gallino, D., Anastassiadis, C., Cvetkovska, V., Barry, A. D., Snook, E., Germann, J., Greenwood, C. M. T., Misic, B., Bagot, R. C., Chakravarty, M. M. (2021). Early or late gestational exposure to maternal immune activation alters neurodevelopmental trajectories in mice: an integrated neuroimaging, behavioral and transcriptional Study. *Biological Psychiatry, 90,* 328–341.

Guo, J. U., Su, Y. J., Shin, J. H., Shin, J. H., Li, H. D., Xie, B., Zhong, C., Hu, S. H., Le, T., Fan, G. P., Zhu, H., Chang, Q., Gao, Y., Ming, G. L., Song, H. J. (2014). Distribution, recognition and regulation of non-CpG methylation in the adult mammalian brain. *Nature Neuroscience, 17,* 215-222.

Guy, J., Hendrich, B., Holmes, M., Martin, J. E., Bird, A. (2001). A mouse Mecp2-null mutation causes neurological symptoms that mimic Rett syndrome. *Nature Genetics, 27,* 322–326.

Hagihara, K., Watanabe, K., Chun, J., Yamaguchi, Y. (2000). Glypican-4 is an FGF2-binding heparan sulfate proteoglycan expressed in neural precursor cells. *Developmental Dynamics, 219*, 353-367.

Hahn, M. A., Qiu, R., Wu, X., Li, A. X., Zhang, H., Wang, J., Jui, J., Jin, S., Jiang, Y., Pfeifer, G. P., Lu, Q. (2013). Dynamics of 5-hydroxymethylcytosine and chromatin marks in mammalian neurogenesis. *Cell Reports, 3,* 291-300.

Hahn, M. A., Szabo, P. E., Pfeifer, G. P. (2014). 5-Hydroxymethylcytosine: a stable or transient DNA modification? *Genomics, 104,* 314-323.

Haijma, S. V., Haren, N. V., Cahn, W., Koolschijn, P. C. M. P., Pol, H. E. H., Kahn, R. S. (2013). Brain volumes in schizophrenia: a meta-analysis in over 18 000 subjects. *Schizophrenia Bulletin, 39,* 1129–1138.

Hales, C. N., Barker, D. J. (1992). Type 2 (non-insulin-dependent) diabetes mellitus: the thrifty phenotype hypothesis. *Diabetologia, 35*, 595-601.

Hales, C. N., Barker, D. J. P. (2001). The thrifty phenotype hypothesis. *British Medical Bulletin, 60*, 5-20.

Hamashima, T., Ishii, Y., Nguyen, L. Q., Okuno, N., Sang, Y., Matsushima, T., Kurashige, Y., Takebayashi, H., Mori, H., Fujimori, T., Yamamoto, S., Sasahara, M. (2020). Oligodendrogenesis and myelin formation in the forebrain require platelet-derived growth factor receptor-alpha. *Neuroscience, 436*, 11-26.

Hameete, B. C., Fernández-Calleja, J. M. S., de Groot, M. W. G. D. M., Oppewal, T. R., Tiemessen, M. M., Hogenkamp, A., de Vries, R. B. M., Groenink, L. (2020). The poly(I:C)-induced maternal immune activation model; a systematic review and meta-analysis of cytokine levels in the offspring. *Brain, Behavior and Immunity - Health, 11*, 100192.

Han, L., Witmer, P. D., Casey, E., Valle, D., Sukumar, S. (2007). DNA methylation regulates microRNA expression. *Cancer Biology and Therapy, 6*, 1284-1288.

Han, S., Nam, J., Li, Y., Kim, S., Cho, S. H., Cho, Y. S., Choi, S. Y., Choi, J., Han, K., Kim, Y., Na, M., Kim, H., Bae, Y. C., Choi, S. Y., Kim, E. (2010). Regulation of dendritic spines, spatial memory and embryonic development by the TANC family of PSD-95-interacting proteins. *The Journal of Neuroscience, 30*, 15102–15112.

Han, Y., Zhang, L., Wang, Q., Zhang, D., Zhao, Q., Zhang, J., Xie, L., Liu, G., You, Z. (2019). Minocycline inhibits microglial activation and alleviates depressive-like behaviors in male adolescent mice subjected to maternal separation. *Psychoneuroendocrinology, 107*, 37-45.

Hånell, A., Marklund, N. (2014). Structured evaluation of rodent behavioral tests used in drug discovery research. *Frontiers in Behavioral Neuroscience, 8,* 252.

Hannon, E., Dempster, E. L., Mansell, G., Burrage, J., Bass, N., Bohlken, M. M., Corvin, A., Curtis, C. J., Dempster, D., Di Forti, M., Dinan, T. G., Donohoe, G., Gaughran, F., Gill, M., Gillespie, A., Gunasinghe, C., Hulshoff, H. E., Hultman, C. M., Johansson, V., Kahn, R. S., Kaprio, J., Kenis, G., Kowalec, K., MacCabe, J., McDonald, C., McQuillin, A., Morris, D. W., Murphy, K. C., Mustard, C. J., Nenadic, I., O'Donovan, M. C., Quattrone, D., Richards, A. L., Rutten, B. P., St Clair, D., Therman, S., Toulopoulou, T., Van Os, J., Waddington, J. L., Wellcome Trust Case Control Consortium 2, CRESTAR consortium, Sullivan, P., Vassos, E., Breen, G., Collier, D. A., Murray, R. M., Schalwyk, L., Mill, J. (2021). DNA methylation meta-analysis reveals cellular alterations in psychosis and markers of treatment-resistant schizophrenia. *eLife, 10,* e58430.

Hanson, K. L., Grant, S. E., Funk, L. H., Schumann, C. M., Bauman, M. D. (2022). Impact of maternal immune activation on nonhuman primate prefrontal cortex development: insights for schizophrenia. *Biological Psychiatry, 92,* 460–469.

Hao, K., Su, X., Luo, B., Cai, Y., Chen, T., Yang, Y., Shao, M., Song, M., Zhang, L., Zhong, Z., Li, W., Lv, L. (2019). Prenatal immune activation induces age-related alterations in rat offspring: effects upon NMDA receptors and behaviors. *Behavioral Brain Research, 370*, 111946.

Hao, L. Y., Hao, X. Q., Li, S. H., Li, X. H. (2010). Prenatal exposure to lipopolysaccharide results in cognitive deficits in age-increasing offspring rats. *Neuroscience, 166,* 763-770.

Harkin, L. F., Lindsay, S. J., Xu, Y., Alzu'bi, A., Ferrara, A., Gullon, E. A., James, O. G., Clowry, G. J. (2017). Neurexins 1-3 each have a distinct pattern of expression in the early developing human cerebral cortex. *Cerebral Cortex, 27*, 216-232.

Harrison, P. J., Law, A. J., Eastwood, S. L. (2003). Glutamate receptors and transporters in the hippocampus in schizophrenia. *Annals of the New York Academy of Sciences, 1003*, 94-101.

Härtig, W., Meinicke, A., Michalski, D., Schob, S., Jäger, C. (2022). Update on perineuronal net staining with Wisteria floribunda Agglutinin (WFA). *Frontiers in Integrative Neuroscience, 16*, 851988.

Harvey, L., Boksa, P. (2012). Prenatal and postnatal animal models of immune activation: relevance to a range of neurodevelopmental disorders. *Developmental Neurobiology, 72*, 1335-1348.

Hashimoto, H., Liu, Y. W., Upadhyay, A. K., Chang, Y. Q., Howerton, S. B., Vertino, P. M., Zhang, X., Cheng, X. D. (2012). Recognition and potential mechanisms for replication and erasure of cytosine hydroxymethylation. *Nucleic Acids Research, 40*, 4841-4849.

Hashimoto, K. (2019). Recent advances in the early intervention in schizophrenia: future direction from preclinical findings. *Current Psychiatry Reports, 21*, 75.

Hatada, I., Namihira, M., Morita, S., Kimura, M., Horii, T., Nakashima, K. (2008). Astrocyte-specific genes are generally demethylated in neural precursor cells prior to astrocytic differentiation. *PLoS One, 3*, e3189.

Hayes, L. N., An, K., Carloni, E., Li, F., Vincent, E., Trippaers, C., Paranjpe, M., Dölen, G., Goff, L. A., Ramos, A., Kano, S. I., Sawa, A. (2022). Prenatal immune stress blunts microglia reactivity, impairing neurocircuitry. *Nature, 610,* 327-334.

He, B., Wang, Y., Li, H., Huang, Y. (2022). The role of integrin beta in schizophrenia: a preliminary exploration. *CNS Spectrums*, 24, 1-10.

He, H., Liu, Q., Li, N., Guo, L., Gao, F., Bai, L., Gao, F., Lyu, J. (2020). Trends in the incidence and DALYs of schizophrenia at the global, regional and national levels: results from the Global Burden of Disease Study 2017. *Epidemiology and Psychiatric Sciences, 29*, e91.

He, P., Chen, G., Guo, C., Wen, X., Song, X., Zheng, X. (2018). Long-term effect of prenatal exposure to malnutrition on risk of schizophrenia in adulthood: evidence from the Chinese famine of 1959-1961. *European Psychiatry, 51*, 42–47.

He, Y. F., Li, B. Z., Li, Z., Liu, P., Wang, Y., Tang, Q. Y., Ding, J. P., Jia, Y. Y., Chen, Z. C., Li, L., Sun, Y., Li, X. X., Dai, Q., Song, C. X., Zhang, K. L., He, C., Xu, G. L. (2011). Tet-mediated formation of 5-carboxylcytosine and its excision by TDG in mammalian DNA. *Science, 333*, 1303-1307.

Hedstrom, K. L., Ogawa, Y., Rasband, M. N. (2008). AnkyrinG is required for maintenance of the axon initial segment and neuronal polarity. *Journal of Cell Biology, 183*, 635-640.

Hedstrom, K. L., Xu, X., Ogawa, Y., Frischknecht, R., Seidenbecher, C. I., Shrager, P., Rasband, M. N. (2007). Neurofascin assembles a specialized extracellular matrix at the axon initial segment. *Journal of Cell Biology, 178*, 875-886.

Henry, N. L., Hayes, D. F. (2012). Cancer biomarkers. *Molecular Oncology, 6*, 140–146.

Hensch, T. (2005). Critical period plasticity in local cortical circuits. *Nature Reviews Neuroscience, 6*, 877–888.

Higgins-Chen, A. T., Boks, M. P., Vinkers, C. H., Kahn, R. S., Levine, M. E. (2020). Schizophrenia and epigenetic aging biomarkers: increased mortality, reduced cancer risk and unique clozapine effects. *Biological Psychiatry, 88*, 224–235.

Hildebrand, C., Remahl, S., Persson, H., Bjartmar, C. (1993). Myelinated nerve fibres in the CNS. *Progress in Neurobiology, 40*, 319-84.

Hilker, R., Helenius, D., Fagerlund, B., Skytthe, A., Christensen, K., Werge, T. M., Nordentoft, M., Glenthoj, B. (2018). Heritability of schizophrenia and schizophrenia spectrum based on the nationwide danish twin register. *Biological Psychiatry, 83*, 492-498.

Hirasawa, G., Takeyama, J., Sasano, H., Fukushima, K., Suzuki, T., Muramatu, Y., Darnel, A. D., Kaneko, C., Hiwatashi, N., Toyota, T., Nagura, H., Krozowski, Z. S. (2000). 11 beta-hydroxysteroid dehydrogenase type II and mineralocorticoid receptor in human placenta. *Journal of Clinical Endocrinology and Metabolism, 85,* 1306-1309.

Ho, N. F., Tng, J. X. J., Wang, M., Chen, G., Subbaraju, V., Shukor, S., Ng, D. S. X., Tan, B. L., Puang, S. J., Kho, S. H., Siew, R. W. E., Sin, G. L., Eu, P. W., Zhou, J., Sng, J. C. G., Sim, K., Medalia, A. (2020). Plasticity of DNA methylation, functional brain connectivity and efficiency in cognitive remediation for schizophrenia. *Journal of Psychiatric Research, 126*, 122-133.

Hollander, J. A., Cory-Slechta, D. A., Jacka, F. N., Szabo, S. T., Guilarte, T. R., Bilbo, S. D., Mattingly, C. J., Moy, S. S., Haroon, E., Hornig, M., Levin, E. D., Pletnikov, M. V., Zehr, J. L., McAllister, K. A., Dzierlenga, A. L., Garton, A. E., Lawler, C. P., Ladd-Acosta, C. (2020). Beyond the looking glass: recent advances in understanding the impact of environmental exposures on neuropsychiatric disease. *Neuropsychopharmacology, 45,* 1086-1096.

Holleran, L., Kelly, S., Alloza, C., Agartz, I. andreassen, O. A., Arango, C., Banaj, N., Calhoun, V., Cannon, D., Carr, V., Corvin, A., Glahn, D. C., Gur, R., Hong, E., Hoschl, C., Howells, F. M., James, A., Janssen, J., Kochunov, P., Lawrie, S. M., … Donohoe, G. (2020). The relationship between white matter microstructure and general cognitive ability in patients with schizophrenia and healthy participants in the ENIGMA consortium. *The American Journal of Psychiatry, 177*, 537–547.

Holliday, R. (1994). Epigenetics: an overview. *Developmental Genetics, 15*, 453-457.

Holz-Schietinger, C., Reich, N. O. (2012). RNA modulation of the human DNA methyltransferase 3A. *Nucleic Acids Research, 40*, 8550-8557.

Hon, G. C., Song, C. X., Du, T., Jin, F., Selvaraj, S., Lee, A. Y., Yen, C., Ye, Z., Mao, S., Wang, B., Kuan, S., Edsall, L. E., Zhao, B. S., Xu, G., He, C., Ren, B. (2014). 5mC oxidation by Tet2 modulates enhancer activity and timing of transcriptome reprogramming during differentiation. *Molecular Cell, 56*, 286–297.

Houtepen, L. C., Vinkers, C. H., Carrillo-Roa, T., Hiemstra, M., van Lier, P. A., Meeus, W., Branje, S., Heim, C. M., Nemeroff, C. B., Mill, J., Schalkwyk, L. C., Creyghton, M. P., Kahn, R. S., Joëls, M., Binder, E. B., Boks, M. P. (2016). Genome-wide DNA methylation levels and altered cortisol stress reactivity following childhood trauma in humans. *Nature Communications, 7*, 10967.

Hovatta, I., Lichtermann, D., Juvonen, H., Suvisaari, J., Terwilliger, J. D., Arajarvi, R., Kokko-Sahin, M. L., Ekelund, J., Lonnqvist, J., Peltonen, L. (1998). Linkage analysis of putative schizophrenia gene candidate regions on chromosomes 3p, 5q, 6p, 8p, 20p and 22q in a population-based sampled Finnish family set. *Molecular Psychiatry, 3*, 452-457.

Howard, M. A., Rubenstein, J. L., Baraban, S. C. (2014). Bidirectional homeostatic plasticity induced by interneuron cell death and transplantation *in vivo*. *Proceedings of the National Academy of Sciences of the United States of America, 111*, 492–497.

Howell, B. W., Herrick, T. M., Cooper, J. A. (1999). Reelin-induced tyrosine phosphorylation of disabled 1 during neuronal positioning. *Genes and Development, 13*, 643-648.

Howell, B. W., Herrick, T. M., Hildebrand, J. D., Zhang, Y., Cooper, J. A. (2000). Dab1 tyrosine phosphorylation sites relay positional signals during mouse brain development. *Current Biology, 10*, 877–885.

Howes O.D., Kapur S. (2009). The dopamine hypothesis of schizophrenia: version III—the final common pathway. *Schizophrenia Bulletin, 35,* 549–562.

Howrigan, D. P., (2017). Contribution of copy number variants to schizophrenia from a genome-wide study of 41,321 subjects. *Nature Genetics, 49,* e651.

Hradetzky, E., Sanderson, T. M., Tsang, T. M., Sherwood, J. L., Fitzjohn, S. M., Lakics, V., Malik, N., Schoeffmann, S., O'Neill, M. J., Cheng, T. M., Harris, L. W., Rahmoune, H., Guest, P. C., Sher, E., Collingridge, G. L., Holmes, E., Tricklebank, M. D., Bahn, S. (2012). The methylazoxymethanol acetate (MAM-E17) rat model: molecular and functional effects in the hippocampus. *Neuropsychopharmacology, 37*, 364-377.

Hsiao, E.Y. Patterson, P.H. (2011). Activation of the maternal immune system induces endocrine changes in the placenta via IL-6. *Brain, Behavior and Immunity, 25*, 604–615.

Hu, J. S., Vogt, D., Sandberg, M., Rubenstein, J. L. (2017). Cortical interneuron development: a tale of time and space. *Development, 144*, 3867-3878.

Huang, J. K., Phillips, G. R., Roth, A. D., Pedraza, L., Shan, W., Belkaid, W., Mi, S., Fex-Svenningsen, A., Florens, L., Yates, J. R. 3rd, Colman, D. R. (2005). Glial membranes at the node of Ranvier prevent neurite outgrowth. *Science, 310,* 1813-1817.

Huang, Y., Zhang, J. L., Yu, X. L., Xu, T. S., Wang, Z. B., Cheng, X. C. (2013). Molecular functions of small regulatory noncoding RNA. *Biochemistry, 78*, 221-230.

Hyde, T. M., Lipska, B. K., Ali, T., Mathew, S. V., Law, A. J., Metitiri, O. E., Straub, R. E., Ye, T. Z., Colantuoni, C., Herman, M. M., Bigelow, L. B., Weinberger, D. R., Kleinman, J. E. (2011). Expression of GABA signaling molecules KCC2, NKCC1 and GAD1 in cortical development and schizophrenia. *Journal of Neuroscience, 31,* 11088-11095.

Iasevoli, F., Tomasetti, C., Buonaguro, E. F., de Bartolomeis, A. (2014). The glutamatergic aspects of schizophrenia molecular pathophysiology: role of the postsynaptic density and implications for treatment. *Current Neuropharmacology, 12*, 219–238.

Ibi, D., Nakasai, G., Koide, N., Sawahata, M., Kohno, T., Takaba, R., Nagai, T., Hattori, M., Nabeshima, T., Yamada, K., Hiramatsu, M. (2020). Reelin supplementation into the hippocampus rescues abnormal behavior in a mouse model of neurodevelopmental disorders. *Frontiers in Cellular Neuroscience, 14*, 285.

Ibrahim, H. M., Tamminga, C. A. (2011). Schizophrenia: treatment targets beyond monoamine systems. *Annual Review of Pharmacology and Toxicology, 51*, 189-209.

Ibrahim, M. L., Klement, J. D., Lu, C., Redd, P. S., Xiao, W., Yang, D., Browning, D. D., Savage, N. M., Buckhaults, P. J., Morse, H C., Liu, K. (2018). Myeloid-derived suppressor cells produce IL-10 to elicit DNMT3b-dependent IRF8 silencing to promote colitis-associated colon tumorigenesis. *Cell Reports, 11*, 3036-3046.

Illingworth, R. S., Gruenewald-Schneider, U., Webb, S., Kerr, A. R., James, K. D., Turner, D. J., Smith, C., Harrison, D. J. Andrews, R., Bird, A. P. (2010). Orphan CpG islands identify numerous conserved promoters in the mammalian genome. *PLoS Genetics, 6*, e1001134.

Inano, K., Suetake, I., Ueda, T., Miyake, Y., Nakamura, M., Okada, M., Tajima, S. (2000). Maintenance-type DNA methyltransferase is highly expressed in post-mitotic neurons and localized in the cytoplasmic compartment. *The Journal of Biochemistry, 128*, 315-321.

Insel, T. R., Miller, L. P., Gelhard, R. E. (1990). The ontogeny of excitatory amino acid receptors in rat forebrain--I. N-methyl-D-aspartate and quisqualate receptors. *Neuroscience, 35*, 31–43.

Institute for Health Metrics and Evaluation (IHME). Findings from the Global Burden of Disease Study (2017). IHME publishing. Seattle, Washington.

Irvine, N., England-Mason, G., Field, C. J., Dewey, D., Aghajafari, F. (2022). Prenatal folate and choline levels and brain and cognitive development in children: a critical narrative review. *Nutrients, 14*, 364.

Ito, S., D'Alessio, A. C., Taranova, O. V., Hong, K., Sowers, L. C., Zhang, Y. (2010). Role of Tet proteins in 5mC to 5hmC conversion, ES-cell self-renewal and inner cell mass specification. *Nature, 466,* 1129-1151.

Ito, S., Shen, L., Dai, Q., Wu, S. C., Collins, L. B., Swenberg, J. A., He, C., Zhang, Y. (2011). Tet proteins can convert 5-methylcytosine to 5-formylcytosine and 5-carboxylcytosine. *Science, 333*, 1300-1303.

Jaaskelainen, E., Juola, P., Hirvonen, N., McGrath, J. J., Saha, S., Isohanni, M., Veijola, J., Miettunen, J. (2013). A systematic review and meta-analysis of recovery in schizophrenia. *Schizophrenia Bulletin, 39*, 1296-1306.

Jaffe, A. E., Gao, Y., Deep-Soboslay, A., Tao, R., Hyde, T. M., Weinberger, D. R., Kleinman, J. E. (2016). Mapping DNA methylation across development, genotype and schizophrenia in the human frontal cortex. *Nature Neuroscience, 19,* 40-47.

Jain, A., Huang, G. Z., Woolley, C. S. (2019). Latent sex differences in molecular signaling that underlies excitatory synaptic potentiation in the hippocampus. *The Journal of Neuroscience, 39*, 1552–1565.

Jain, A., Tuteja, G. (2019). TissueEnrich: tissue-specific gene enrichment analysis. *Bioinformatics, 35*, 1966-1967.

Jakovcevski, M., Akbarian, S. (2012). Epigenetic mechanisms in neurological disease. *Nature Medicine, 18*, 1194-1204.

Jakovljević, A., Tucić, M., Blažiková, M., Korenić, A., Missirlis, Y., Stamenković, V. andjus, P. (2021). Structural and functional modulation of perineuronal nets: in search of important players with highlight on Tenascins. *Cells, 10*, 1345.

Jang, D. G., Sim, H. J., Song, E. K., Kwon, T., Park, T. J. (2020). Extracellular matrixes and neuroinflammation. *BMB Reports, 53*, 491-499.

Janoutova, J., Janackova, P., Sery, O., Zeman, T., Ambroz, P., Kovalova, M., Varechova, K., Hosak, L., Jirik, V., Janout, V. (2016). Epidemiology and risk factors of schizophrenia. *Neuroendocrinology Letters, 37*, 1-8.

Jansson, T., Powell, T. L. (2007). Role of the placenta in foetal programming: underlying mechanisms and potential interventional approaches. *Clinical Science, 113*, 1-13.

Javitt, D. C., Zukin, S. R. (1991). Recent advances in the phencyclidine model of schizophrenia. *American Journal of Psychiatry, 148*, 1301-1308.

Jenuwein, T., Allis, C. D. (2001). Translating the histone code. *Science, 293*, 1074-1080.

Jeppesen, R., Christensen, R. H. B., Pedersen, E. M. J., Nordentoft, M., Hjorthøj, C., Köhler-Forsberg, O., Benros, M. E. (2020). Efficacy and safety of anti-inflammatory agents in treatment of psychotic disorders - a comprehensive systematic review and meta-analysis. *Brain, Behavior and Immunity, 90*, 364-380.

Jeremian, R., Bani-Fatemi, A., Strauss, J. S., Tasmim, S., Dada, O., Graff-Guerrero, A., Gerretsen, P., De Luca, V. (2022a). Investigation of accelerated epigenetic aging in individuals suffering from schizophrenia in the context of lifetime suicide attempt. *Schizophrenia Research, 243*, 222-224.

Jeremian, R., Malinowski, A., Chaudhary, Z., Srivastava, A., Qian, J., Zai, C., Adanty, C., Fischer, C. E., Burhan, A. M., Kennedy, J. L., Borlido, C., Gerretsen, P., Graff, A., Remington, G., Vincent, J. B., Strauss, J. S., De Luca, V. (2022b). Epigenetic age dysregulation in individuals with bipolar disorder and schizophrenia. *Psychiatry Research, 315*, 114689.

Jiang, X., Nardelli, J. (2016). Cellular and molecular introduction to brain development. *Neurobiology of Disease, 92,* 3-17.

Jin, L. W., Horiuchi, M., Wulff, H., Liu, X. B., Cortopassi, G. A., Erickson, J. D., Maezawa, I. (2015). Dysregulation of glutamine transporter SNAT1 in Rett syndrome microglia: a mechanism for mitochondrial dysfunction and neurotoxicity. *The Journal of Neuroscience, 35,* 2516-2529.

Jin, S. G., Wu, X. W., Li, A. X., Pfeifer, G. P. (2011). Genomic mapping of 5-hydroxymethylcytosine in the human brain. *Nucleic Acids Research, 39*, 5015-5024.

Jin, Y., Su, K., Kong, H. E., Ma, W., Wang, Z., Li, Y., Li, R., Allen, E. G., Wu, H., Jin, P. (2023). Cell-type specific DNA methylome signatures reveal epigenetic mechanisms for neuronal diversity and neurodevelopmental disorder. *Human Molecular Genetics*, *32,* 218-30.

Jobe, E. M., Zhao, X. (2017). DNA methylation and adult neurogenesis. *Brain Plasticity, 3*, 5-26.

Johnson, T., Saatci, D., Handunnetthi, L. (2022). Maternal immune activation induces methylation changes in schizophrenia genes. *PLoS one, 17*, e0278155.

Jones, C. A., Watson, D. J., Fone, K. C. (2011). Animal models of schizophrenia. *British Journal of Pharmacology, 164*, 1162–1194.

Jones, H. N., Jansson, T., Powell, T. L. (2009). IL-6 stimulates system A amino acid transporter activity in trophoblast cells through STAT3 and increased expression of SNAT2. *American Journal of Physiology - Cell Physiology, 297,* 1228–1235.

Joosten, S. C., Smits, K. M., Aarts, M. J., Melotte, V., Koch, A., Tjan-Heijnen, V. C., van Engeland, M. (2018). Epigenetics in renal cell cancer: mechanisms and clinical applications. *Nature Reviews Urology, 15*, 430-451.

Jurga, A. M., Paleczna, M., Kuter, K. Z. (2020). Overview of general and discriminating markers of differential microglia phenotypes. *Frontiers in Cellular Neuroscience, 14*, 198.

Kaar, S. J., Angelescu, I., Marques, T. R., Howes, O. D. (2019). Pre-frontal parvalbumin interneurons in schizophrenia: a meta-analysis of post-mortem studies. *Journal of Neural Transmission*, *126,* 1637-1651.

Kaas, G. A., Zhong, C., Eason, D. E., Ross, D. L., Vachhani, R. V., Ming, G. I., King, J. R., Song, H. J., Sweatt, J. D. (2013). TET1 controls CNS 5-methylcytosine hydroxylation, active DNA demethylation, gene transcription and memory formation. *Neuron, 79,* 1086-1093.

Kadriu, B., Guidotti, A., Chen, Y., Grayson, D. R. (2012). DNA methyltransferases1 (DNMT1) and 3a (DNMT3a) colocalize with GAD67-positive neurons in the GAD67-GFP mouse brain. *Journal of Comparative Neurology, 520,* 1951-1964.

Kahn, R. S., Sommer, I. E., Murray, R. M., Meyer-Lindenberg, A., Weinberger, D. R., Cannon, T. D., O'Donovan, M., Correll, C. U., Kane, J. M., van Os, J., Insel, T. R. (2015). Schizophrenia. *Nature Reviews Disease Primers, 1*, 15067.

Kalisch-Smith, J. I., Simmons, D. G., Dickinson, H., Moritz, K. M. (2017). Review: sexual dimorphism in the formation, function and adaptation of the placenta. *Placenta, 54*, 10–16.

Kalmady, S. V., Shivakumar, V., Jose, D., Ravi, V., Keshavan, M. S., Gangadhar, B. N., Venkatasubramanian, G. (2018). Plasma cytokines in minimally treated schizophrenia. *Schizophrenia Research, 199,* 292-296.

Kamimura, K., Maeda, N. (2021). Glypicans and heparan sulfate in synaptic development, neural plasticity and neurological disorders. *Frontiers in Neural Circuits, 15*, 595596.

Kanahara, N., Yamanaka, H., Shiko, Y., Kawasaki, Y., Iyo, M. (2022). The effects of cumulative antipsychotic dose on brain structures in patients with schizophrenia: Observational study of multiple CT scans over a long-term clinical course. *Psychiatry Research - Neuroimaging, 319*, 111422.

Kandasamy, P., Gyimesi, G., Kanai, Y., Hediger, M. A. (2018). Amino acid transporters revisited: new views in health and disease. *Trends in Biochemical Sciences, 43*, 752-789.

Kang, Z. C., Wang, H. G., Yang, Y. L., Zhao, X. Y., Zhou, Q. M., Yang, Y. L., Yang, J. Y., Du, G. H. (2020). Pinocembrin ameliorates cognitive impairment induced by vascular dementia: contribution of reelin-dab1 signaling pathway. *Drug Design, Development and Therapy, 14*, 3577-3587.

Kapur, S., Remington, G. (1996). Serotonin-dopamine interaction and its relevance to schizophrenia. *American Journal of Psychiatry, 153,* 466-476.

Kaur, T., Cadenhead, K. S. (2010). Treatment implications of the schizophrenia prodrome. *Current Topics in Behavoural Neuroscience, 4,* 97-121.

Kawaguchi, Y., Kubota, Y. (1997). GABAergic cell subtypes and their synaptic connections in rat frontal cortex. *Cerebral Cortex, 7*, 476-486.

Kawai, T., Akira, S. (2007). Signaling to NF-kappaB by toll-like receptors. *Trends in Molecular Medicine, 13*, 460-469.

Kawamura, S., Yamazoe, H., Hosokawa, Y. (2020). Diurnal gain and nocturnal reduction of body weight in young adult rabbits: the reverse of the circadian rhythm observed in rats and mice. *Journal of Toxicology: Current Research, 4*, 16.

Keefe, R. S. E., Sweeney, J. A., Gu, H. B., Hamer, R. M., Perkins, D. O., McEvoy, J. P., Lieberman, J. A. (2007). Effects of olanzapine, quetiapine and risperidone on neurocognitive function in early psychosis: a randomized, double-blind 52-week comparison. *American Journal of Psychiatry, 164*, 1061-1071.

Keil, J. M., Qalieh, A., Kwan, K. Y. (2018). Brain transcriptome databases: a user's guide. *The Journal of Neuroscience, 38,* 2399-2412.

Kelly, S., Guimond, S., Pasternak, O., Lutz, O., Lizano, P., Cetin-Karayumak, S., Sweeney, J. A., Pearlson, G., Clementz, B. A., McDowell, J. E., Tamminga, C. A., Shenton, M. E., Keshavan, M. S. (2021). White matter microstructure across brain-based biotypes for psychosis - findings from the bipolar-schizophrenia network for intermediate phenotypes. *Psychiatry research - Neuroimaging, 308,* 111234.

Kempton, M. J., Stahl, D., Williams, S. C., DeLisi, L. E. (2010). Progressive lateral ventricular enlargement in schizophrenia: a meta-analysis of longitudinal MRI studies. *Schizophrenia Research, 120*, 54-62.

Kennard, J. T., Guévremont, D., Mason-Parker, S. E., Abraham, W. C., Williams, J. M. (2014). Redistribution of ionotropic glutamate receptors detected by laser microdissection of the rat dentate gyrus 48 h following LTP induction *in vivo*. *PLoS One, 9*, e92972.

Kentner, A. C., Bilbo, S. D., Brown, A. S., Hsiao, E. Y., McAllister, A. K., Meyer, U., Pearce, B. D., Pletnikov, M. V., Yolken, R. H., Bauman, M. D. (2019). Maternal immune activation: reporting guidelines to improve the rigor, reproducibility and transparency of the model. *Neuropsychopharmacology, 44*, 245–258.

Kern, R. S., Nuechterlein, K. H., Green, M. F., Baade, L. E., Fenton, W. S., Gold, J. M., Keefe, R. S., Mesholam-Gately, R., Mintz, J., Seidman, L. J., Stover, E., Marder, S. R. (2008). The MATRICS Consensus Cognitive Battery, part 2: co-norming and standardization. *American Journal of Psychiatry, 165*, 214-220.

Keshvara, L., Benhayon, D., Magdaleno, S., Curran, T. (2001). Identification of reelin-induced sites of tyrosyl phosphorylation on disabled 1. *Journal of Biological Chemistry, 276*, 16008-16014.

Khan, D., Fernando, P., Cicvaric, A., Berger, A., Pollak, A., Monje, F. J., Pollak, D. D. (2014). Long-term effects of maternal immune activation on depression-like behavior in the mouse. *Translational Psychiatry, 4,* e363.

Khandaker, G. M., Pearson, R. M., Zammit, S., Lewis, G., Jones, P. B. (2014). Association of serum interleukin 6 and C-reactive protein in childhood with depression and psychosis in young adult life: a population-based longitudinal study. *JAMA Psychiatry, 71*, 1121-1128.

Khandaker, G. M., Zimbron, J., Dalman, C., Lewis, G., Jones, P. B. (2012). Childhood infection and adult schizophrenia: a meta-analysis of population-based studies. *Schizophrenia Research, 139*, 161-168.

Khare, T., Pai, S., Koncevicius, K., Pal, M., Kriukiene, E., Liutkeviciute, Z., Irimia, M., Jia, P., Ptak, C., Xia, M., Tice, R., Tochigi, M., Moréra, S., Nazarians, A., Belsham, D., Wong, A. H., Blencowe, B. J., Wang, S. C., Kapranov, P., Kustra, R., … Petronis, A. (2012). 5-hmC in the brain is abundant in synaptic genes and shows differences at the exon-intron boundary. *Nature Structural and Molecular Biology, 19*, 1037–1043.

Kho, S. H., Yee, J. Y., Puang, S. J., Han, L., Chiang, C., Rapisarda, A., Goh, W. W. B., Lee, J., Sng, J. C. G. (2022). DNA methylation levels of RELN promoter region in ultra-high risk, first episode and chronic schizophrenia cohorts of schizophrenia. *Schizophrenia, 8*, 81.

Khokhar, J. Y., Dwiel, L. L., Henricks, A. M., Doucette, W. T., Green, A. I. (2018). The link between schizophrenia and substance use disorder: a unifying hypothesis. *Schizophrenia Research, 194*, 78–85.

Kilian, S., Asmal, L., Chiliza, B., Olivier, M. R., Phahladira, L., Scheffler, F., Seedat, S., Marder, S. R., Green, M. F., Emsley, R. (2018). Childhood adversity and cognitive function in schizophrenia spectrum disorders and healthy controls: evidence for an association between neglect and social cognition. *Psychological Medicine, 48*, 2186-2193.

Kilonzo, K., Strahnen, D., Prex, V., Gems, J., van der Veen, B., Kapanaiah, S. K. T., Murthy, B. K. B., Schulz, S., Sprengel, R., Bannerman, D., Kätzel, D. (2022). Distinct contributions of GluA1-containing AMPA receptors of different hippocampal subfields to salience processing, memory and impulse control. *Translational Psychiatry, 12*, 102.

Kim, M. S., Akhtar, M. W., Adachi, M., Mahgoub, M., Bassel-Duby, R., Kavalali, E. T., Olson, E. N., Monteggia, L. M. (2012). An essential role for histone deacetylase 4 in synaptic plasticity and memory formation. *Journal of Neuroscience, 32*, 10879-10886.

King, S., Holleran, L., Mothersill, D., Patlola, S., Rokita, K., McManus, R., Kenyon, M., McDonald, C., Hallahan, B., Corvin, A., Morris, D., Kelly, J., McKernan, D., Donohoe, G. (2021). Early life adversity, functional connectivity and cognitive performance in schizophrenia: the mediating role of IL-6. *Brain, Behavior and Immunity, 98,* 388–396.

Kinney, J. W., Davis, C. N., Tabarean, I., Conti, B., Bartfai, T., Behrens, M. M. (2006). A specific role for NR2A-containing NMDA receptors in the maintenance of parvalbumin and GAD67 immunoreactivity in cultured interneurons. *The Journal of Neuroscience, 26,* 1604–1615.

Kinoshita, M., Numata, S., Tajima, A., Shimodera, S., Imoto, I., Ohmori, T. (2013). Plasma total homocysteine is associated with DNA methylation in patients with schizophrenia. *Epigenetics, 8,* 584-590.

Kinsella, R. J., Kähäri, A., Haider, S., Zamora, J., Proctor, G., Spudich, G., Almeida-King, J., Staines, D., Derwent, P., Kerhornou, A., Kersey, P., Flicek, P. (2011). Ensembl BioMarts: a hub for data retrieval across taxonomic space. *Database (Oxford), 23*, bar030.

Kirov, G., Grozeva, D., Norton, N., Ivanov, D., Mantripragada, K. K., Holmans, P., Craddock, N., Owen, M. J., O'Donovan, M. C., Consortium, I. S., Wellcome Trust Case Control Consortium (2009). Support for the involvement of large copy number variants in the pathogenesis of schizophrenia. *Human Molecular Genetics, 18,* 1497-1503.

Kocsis B. (2012). Differential role of NR2A and NR2B subunits in N-methyl-D-aspartate receptor antagonist-induced aberrant cortical gamma oscillations. *Biological Psychiatry, 71,* 987–995.

Koek, W., Woods, J. H., Winger, G. D. (1988). MK-801, a proposed noncompetitive antagonist of excitatory amino acid neurotransmission, produces phencyclidine-like behavioral effects in pigeons, rats and rhesus monkeys. *The Journal of Pharmacology and Experimental Therapeutics, 245*, 969–974.

Kogan, S., Ospina, L. H., Kimhy, D. (2018). Inflammation in individuals with schizophrenia - implications for neurocognition and daily function. *Brain, Behaviour and Immunity, 74*, 296-299.

Kolaka, R., Chotwiwatthanakun, C., Chutabhakdikul, N. (2019). Foetal exposure to high levels of maternal glucocorticoids alters reelin signaling in the prefrontal cortex of rat pups. *International Journal of Developmental Neuroscience, 78*, 185-190.

Kolk, S. M., Rakic, P. (2022). Development of prefrontal cortex. *Neuropsychopharmacology, 47,* 41-57.

Komanda, M., Nishimura, Y. (2022). Epigenetics and neuroinflammation associated with neurodevelopmental disorders: a microglial perspective. *Frontiers in Cell Development and Biology, 10*, e852752.

Kongsui, R., Beynon, S. B., Johnson, S. J., Walker, F. R. (2014). Quantitative assessment of microglial morphology and density reveals remarkable consistency in the distribution and morphology of cells within the healthy prefrontal cortex of the rat. *Journal of Neuroinflammation, 11*, 182.

Könnecke, H., Bechmann, I. (2013). The role of microglia and matrix metalloproteinases involvement in neuroinflammation and gliomas. *Clinical and Developmental Immunology, 2013*, 914104.

Konopka, A., Grajkowska, W., Ziemiańska, K., Roszkowski, M., Daszkiewicz, P., Rysz, A., Marchel, A., Koperski, L., Wilczyński, G. M., Dzwonek, J. (2013). Matrix metalloproteinase-9 (MMP-9) in human intractable epilepsy caused by focal cortical dysplasia. *Epilepsy Research, 104*, 45-58.

Kool, M. J., Proietti Onori, M., Borgesius, N. Z., van de Bree, J. E., Elgersma-Hooisma, M., Nio, E., Bezstarosti, K., Buitendijk, G. H. S., Aghadavoud Jolfaei, M., Demmers, J. A. A., Elgersma, Y., van Woerden, G. M. (2019). CAMK2-dependent signaling in neurons is essential for survival. *The Journal of Neuroscience, 39,* 5424–5439.

Kornau, H. C., Schenker, L. T., Kennedy, M. B., Seeburg, P. H. (1995). Domain interaction between NMDA receptor subunits and the postsynaptic density protein PSD-95. *Science, 269*, 1737–1740.

Koshiyama, D., Fukunaga, M., Okada, N., Morita, K., Nemoto, K., Usui, K., Yamamori, H., Yasuda, Y., Fujimoto, M., Kudo, N., Azechi, H., Watanabe, Y., Hashimoto, N., Narita, H., Kusumi, I., Ohi, K., Shimada, T., Kataoka, Y., Yamamoto, M., Ozaki, N., … COCORO (2020). White matter microstructural alterations across four major psychiatric disorders: mega-analysis study in 2937 individuals. *Molecular Psychiatry, 25,* 883–895.

Koskinen, M. K., van Mourik, Y., Smit, A. B., Riga, D., Spijker, S. (2021). From stress to depression: development of extracellular matrix-dependent cognitive impairment following social stress. *Science Reports, 10*, 17308.

Koszła, O., Targowska-Duda, K. M., Kędzierska, E., Kaczor, A. A. (2020). *In vitro* and *in vivo* models for the investigation of potential drugs against schizophrenia. *Biomolecules, 10,* 160.

Kowash, H. M. (2019). The effect of poly(I:C)-mediated maternal immune activation on foetal, placental and yolk sac outcomes in a rat model. PhD thesis, University of Manchester.

Kowash, H. M., Potter, H. G., Edye, M. E., Prinssen, E. P., Bandinelli, S., Neill, J. C., Hager, R., Glazier, J. D. (2019). Poly(I:C) source, molecular weight and endotoxin contamination affect dam and prenatal outcomes, implications for models of maternal immune activation. *Brain, Behavior and Immunity, 82*, 160–166.

Kowash, H. M., Potter, H. G., Woods, R. M., Ashton, N., Hager, R., Neill, J. C., Glazier, J. D. (2022). Maternal immune activation in rats induces dysfunction of placental leucine transport and alters foetal brain growth. *Clinical Science, 136*, 1117-1137.

Kozlenkov, A., Li, J. H., Apontes, P., Hurd, Y. L., Byne, W. M., Koonin, E. V., Wegner, M., Mukamel, E. A., Dracheva, S. (2018). A unique role for DNA (hydroxy) methylation in epigenetic regulation of human inhibitory neurons. *Science Advances, 4*, e6190.

Kozlenkov, A., Roussos, P., Timashpolsky, A., Barbu, M., Rudchenko, S., Bibikova, M., Klotzle, B., Byne, W., Lyddon, R., Di Narzo, A. F., Hurd, Y. L., Koonin, E. V., Dracheva, S. (2014). Differences in DNA methylation between human neuronal and glial cells are concentrated in enhancers and non-CpG sites. *Nucleic Acids Research, 42,* 109-127.

Krek, A., Grun, D., Poy, M. N., Wolf, R., Rosenberg, L., Epstein, E. J., MacMenamin, P., da Piedade, I., Gunsalus, K. C., Stoffel, M., Rajewsky, N. (2005). Combinatorial microRNA target predictions. *Nature Genetics, 37,* 495-500.

Kriaucionis, S., Heintz, N. (2009). The nuclear DNA base 5-hydroxymethylcytosine is present in purkinje neurons and the brain. *Science, 324,* 929-930.

Krichevsky, A. M., King, K. S., Donahue, C. P., Khrapko, K., Kosik, K. S. (2003). A microRNA array reveals extensive regulation of microRNAs during brain development. *RNA, 9,* 1274-1281.

Kriener, B., Hu, H., Vervaeke, K. (2022). Parvalbumin interneuron dendrites enhance gamma oscillations. *Cell Reports, 39*, 110948.

Krueger, D. D., Howell, J. L., Hebert, B. F., Olausson, P., Taylor, J. R., Nairn, A. C. (2006). Assessment of cognitive function in the heterozygous reeler mouse. *Psychopharmacology, 189*, 95–104.

Krueger, F. (2012). Trim Galore! Available at: https://www.bioinformatics.babraham.ac.uk/projects/trim_galore/

Krueger, F. Andrews, S. (2011). Bismark: a flexible aligner and methylation caller for BisulfiteSeq applications. *Bioinformatics, 27*, 1571–1572.

Kruger, G. M., Diemel, L. T., Copelman, C. A., Cuzner, M. L. (1999). Myelin basic protein isoforms in myelinating and remyelinating rat brain aggregate cultures. *Journal of Neuroscience Research, 56*, 241-247.

Krystal, J. H., Karper, L. P., Seibyl, J. P., Freeman, G. K., Delaney, R., Bremner, J. D., Heninger, G. R., Bowers, M. B., Charney, D. S. (1994). Subanesthetic effects of the noncompetitive NMDA antagonist, ketamine, in humans - psychotomimetic, perceptual, cognitive and neuroendocrine responses. *Archives of General Psychiatry, 51*, 199-214.

Kubicki, M., Westin, C. F., Nestor, P. G., Wible, C. G., Frumin, M., Maier, S. E., Kikinis, R., Jolesz, F. A., McCarley, R. W., Shenton, M. E. (2003). Cingulate fasciculus integrity disruption in schizophrenia: a magnetic resonance diffusion tensor imaging study. *Biological Psychiatry, 54*, 1171–1180.

Kuhn, S., Gritti, L., Crooks, D., Dombrowski, Y. (2019). Oligodendrocytes in development, myelin generation and beyond. *Cells, 8*, 1424.

Kuleshov, M. V., Jones, M. R., Rouillard, A. D., Fernandez, N. F., Duan, Q., Wang, Z., Koplev, S., Jenkins, S. L., Jagodnik, K. M., Lachmann, A., McDermott, M. G., Monteiro, C. D., Gundersen, G. W., Ma'ayan, A. (2016). Enrichr: a comprehensive gene set enrichment analysis web server 2016 update. *Nucleic Acids Research, 44*, 90-97.

Kulhara, P., Banerjee, A., Dutt, A. (2008). Early intervention in schizophrenia. *Indian Journal of Psychiatry, 50,* 128-134.

Kumari, E., Velloso, F. J., Nasuhidehnavi, A., Somasundaram, A., Savanur, V. H., Buono, K. D., Levison, S. W. (2020). Developmental IL-6 exposure favors production of PDGF-responsive multipotential progenitors at the expense of neural stem cells and other progenitors. *Stem Cell Reports, 14*, 861-875.

Kundakovic, M., Chen, Y., Guidotti, A., Grayson, D. R. (2009). The Reelin and GAD67 promoters are activated by epigenetic drugs that facilitate the disruption of local repressor complexes. *Molecular Pharmacology, 75*, 342-354.

Kunugi, H., Nanko, S., Murray, R. M. (2001). Obstetric complications and schizophrenia: prenatal underdevelopment and subsequent neurodevelopmental impairment. *British Journal of Psychiatry, 178*, 25-29.

Kuo, S. S., Pogue-Geile, M. F. (2019). Variation in fourteen brain structure volumes in schizophrenia: A comprehensive meta-analysis of 246 studies. *Neuroscience and Biobehavioral Reviews, 98*, 85–94.

Kurdyukov, S., Bullock, M. (2016). DNA methylation analysis: choosing the right method. *Biology, 5*, 3.

Labouesse, M.A., Dong, E., Grayson, D. R., Guidotti, A., Meyer, U. (2015a). Maternal immune activation induces GAD1 and GAD2 promoter remodeling in the offspring prefrontal cortex. *Epigenetics, 10*, 1143-1155.

Labouesse, M. A., Langhans, W., Meyer, U. (2015b). Long-term pathological consequences of prenatal infection: beyond brain disorders. *American Journal of Physiology – Regulatory, Integrative and Comparative Physiology, 309*, 1-12.

Labouesse, M. A., Lassalle, O., Richetto, J., Iafrati, J., Weber-Stadlbauer, U., Notter, T., Gschwind, T., Pujadas, L., Soriano, E., Reichelt, A.C., Meyer, U. (2017). Hypervulnerability of the adolescent prefrontal cortex to nutritional stress via reelin deficiency. *Molecular Psychiatry, 22*, 961-971.

Laighneach, A., Desbonnet, L., Kelly, J. P., Donohoe, G., Morris, D. W. (2021). Meta-analysis of brain gene expression data from mouse model studies of maternal immune activation using poly(I:C). *Genes, 12*, 1363.

Lam, D., Enright, H. A., Cadena, J., Peters, S. K., Sales, A. P., Osburn, J. J., Soscia, D. A., Kulp, K. S., Wheeler, E. K., Fischer, N. O. (2019). Tissue-specific extracellular matrix accelerates the formation of neural networks and communities in a neuron-glia co-culture on a multi-electrode array. *Science Reports, 9*, 4159.

Lang, F., Artunc, F., Vallon, V. (2009). The physiological impact of the serum and glucocorticoid-inducible kinase SGK1. *Current Opinion in Nephrology and Hypertension, 18,* 439-448.

Lange, C., Deutschenbaur, L., Borgwardt, S., Lang, U. E., Walter, M., Huber, C. G. (2017). Experimentally induced psychosocial stress in schizophrenia spectrum disorders: a systematic review. *Schizophrenia Research, 182,* 4–12.

Larsen, B., Luna, B. (2018). Adolescence as a neurobiological critical period for the development of higher-order cognition. *Neuroscience and Biobehavioral Reviews, 94,* 179-195.

Larson, J., Hoffman, J.S., Guidotti, A. Costa, E. (2003). Olfactory discrimination learning deficit in heterozygous reeler mice. *Brain Research, 971*, 40–46.

Laskaris, L. E., Di Biase, M. A., Everall, I., Chana, G., Christopoulos, A., Skafidas, E., Cropley, V. L., Pantelis, C. (2016). Microglial activation and progressive brain changes in schizophrenia. *British Journal of Pharmacology, 173*, 666-680.

Lauriat, T. L., Shiue, L., Haroutunian, V., Verbitsky, M., Ares, M. Jr., Ospina, L., McInnes, L. A. (2008). Developmental expression profile of quaking, a candidate gene for schizophrenia and its target genes in human prefrontal cortex and hippocampus shows regional specificity. *Journal of Neuroscience Research, 86,* 785-796.

Laursen, T. M., Nordentoft, M., Mortensen, P. B. (2014). Excess early mortality in schizophrenia. *Annual Reviews in Clinical Psychology, 10*, 425-448.

Laursen, T. M., Wahlbeck, K., Hallgren, J., Westman, J., Osby, U., Alinaghizadeh, H., Gissler, M., Nordentoft, M. (2013). Life expectancy and death by diseases of the circulatory system in patients with bipolar disorder or schizophrenia in the Nordic countries. *PLoS One, 8*, e67133.

Lawrence, M., Daujat, S., Schneider, R. (2016). Lateral thinking: how histone modifications regulate gene expression. *Trends in Genetics, 32*, 42–56.

Lawrie, S. M., Abukmeil, S. S. (1998). Brain abnormality in schizophrenia. A systematic and quantitative review of volumetric magnetic resonance imaging studies. *British Journal of Psychiatry, 172*, 110-120.

Lee, B. T., Barber, G. P., Benet-Pagès, A., Casper, J., Clawson, H., Diekhans, M., Fischer, C., Gonzalez, J. N., Hinrichs, A. S., Lee, C. M., Muthuraman, P., Nassar, L. R., Nguy, B., Pereira, T., Perez, G., Raney, B. J., Rosenbloom, K. R., Schmelter, D., Speir, M. L., Wick, B. D., Zweig, A. S., Haussler, D., Kuhn, R. M., Haeussler, M., Kent, W. J. (2022). The UCSC genome browser database: 2022 update. *Nucleic Acids Research, 50,* 1115-1122.

Lee, C. H., Liu, C. M., Wen, C. C., Chang, S. M., Hwu, H. G. (2010). Genetic copy number variants in sib pairs both affected with schizophrenia. *Journal of Biomedical Science, 17*, e2.

Lee, G., Zhou, Y. (2019). NMDAR hypofunction animal models of schizophrenia. *Frontiers in Molecular Neuroscience, 12,* 185.

Lee, G. A., Lin, Y. K., Lai, J. H., Lo, Y. C., Yang, Y. S. H., Ye, S. Y., Lee, C. J., Wang, C. C., Chiang, Y. H., Tseng, S. H. (2021). Maternal immune activation causes social behavior deficits and hypomyelination in male rat offspring with an autism-like microbiota profile. *Brain Sciences, 11*, 1085.

Lee, G. H., D'Arcangelo, G. (2016). New insights into Reelin-mediated signaling pathways. *Frontiers in Cellular Neuroscience, 10*, 122.

Lee, R. H., Grames, M. S., Wu, C. Y., Lien, C., Silva, A. C., Possoit, H. E., Clemons, G. A., Citadin, C. T., Neumann, J. T., Pastore, D., Lauro, D., Della-Morte, D., Lin, H. (2020). Upregulation of serum and glucocorticoid-regulated kinase 1 exacerbates brain injury and neurological deficits after cardiac arrest. *American Journal of Physiology-Heart and Circulatory Physiology, 319*, 1044-1050.

Lehmann, J., Pryce, C. R., Bettschen, D., Feldon, J. (1999). The maternal separation paradigm and adult emotionality and cognition in male and female Wistar rats. *Pharmacology, Biochemistry and Behavior, 64,* 705-715.

Lei, Q., Huang, X., Li, T., Zhong, Q., Chen, Q., Pan, R., Long, J., Su, L. (2023). Effects of PM2.5 pollution and single nucleotide polymorphisms of neurotrophin signaling pathway genes acting together on schizophrenia relapse. *International archives of occupational and environmental health*, *96,* 629–637.

Leonard, J. N., Ghirlando, R., Askins, J., Bell, J. K., Margulies, D. H., Davies, D. R., Segal, D. M. (2008). The TLR3 signaling complex forms by cooperative receptor dimerization. *Proceedings of the National Academy of Sciences of the United States of America, 105*, 258-263.

Leussis, M. P., Madison, J. M., Petryshen, T. L. (2012). Ankyrin 3: genetic association with bipolar disorder and relevance to disease pathophysiology. *Biology of Mood and Anxiety Disorders, 2*, 18.

Levav-Rabkin, T., Blumkin, E., Galron, D., Golan, H. M. (2011). Sex-dependent behavioral effects of Mthfr deficiency and neonatal GABA potentiation in mice. *Behavioral Brain Research, 216,* 505-513.

Levenson, J. M., Roth, T. L., Lubin, F. D., Miller, C. A., Huang, I. C., Desai, P., Malone, L. M., Sweatt, J. D. (2006). Evidence that DNA (cytosine-5) methyltransferase regulates synaptic plasticity in the hippocampus. *Journal of Biological Chemistry, 281*, 15763-15773.

Levine, J., Stahl, Z., Sela, B. A., Gavendo, S., Ruderman, V., Belmaker, R. H. (2002). Elevated homocysteine levels in young male patients with schizophrenia. *American Journal of Psychiatry, 159*, 1790-1792.

Levine, J. M., Reynolds, R., Fawcett, J. W. (2001). The oligodendrocyte precursor cell in health and disease. *Trends in Neuroscience, 24*, 39–47.

Levinson, J. N., Chéry, N., Huang, K., Wong, T. P., Gerrow, K., Kang, R., Prange, O., Wang, Y. T., El-Husseini, A. (2005). Neuroligins mediate excitatory and inhibitory synapse formation: involvement of PSD-95 and neurexin-1beta in neuroligin-induced synaptic specificity. *The Journal of Biological Chemistry, 280,* 17312–17319.

Levison. S. W., Jiang. F.J., Stoltzfus, O.K., Ducceschi, M. H. (2000). IL-6-type cytokines enhance epidermal growth factor-stimulated astrocyte proliferation. *Glia, 32*, 328–337.

Lewis, D. A., Curley, A. A., Glausier, J. R., Volk, D. W. (2012). Cortical parvalbumin interneurons and cognitive dysfunction in schizophrenia. *Trends in Neuroscience, 35*, 57–67.

Lewis, D. A., Hashimoto, T., Volk, D. W. (2005). Cortical inhibitory neurons and schizophrenia. *Nature Reviews Neuroscience, 6,* 312-324.

Lezak, K. R., Missig, G., Carlezon, W. A., Jr. (2017). Behavioral methods to study anxiety in rodents. *Dialogues in Clinical Neuroscience, 19,* 181–191.

Li, J., Barrero, C., Gupta, S., Kruger, W. D., Merali, S., Praticò, D. (2016). Homocysteine modulates 5-lipoxygenase expression level via DNA methylation. *Aging Cell, 16*, 273-280.

Li, M., Xiao, L., Chen, X. (2022). Histone acetylation and methylation underlie oligodendroglial and myelin susceptibility in schizophrenia. *Frontiers in Cellular Neuroscience, 16*, e823708.

Li, S., Yang, Q., Hou, Y., Jiang, T., Zong, L., Wang, Z., Luo, X., Liang, W., Zhao, H., Ning, Y., Zhao, C. (2018a). Hypomethylation of LINE-1 elements in schizophrenia and bipolar disorder. *Journal of Psychiatric Research, 107*, 68-72.

Li, S., Zhang, J., Huang, S., He, X. (2018b). Genome-wide analysis reveals that exon methylation facilitates its selective usage in the human transcriptome. *Briefings in Bioinformatics, 19*, 754–764.

Li, Y., Deuring, J., Peppelenbosch, M. P., Kuipers, E. J., Haar, C., van der Woude, C. J. (2012). IL-6-induced DNMT1 activity mediates SOCS3 promoter hypermethylation in ulcerative colitis-related colorectal cancer. *Carcinogenesis, 33*, 1889-1896.

Li, Y., Qiu, S., Shi, J., Guo, Y., Li, Z., Cheng, Y., Liu, Y. (2020a). Association between MTHFR C677T/A1298C and susceptibility to autism spectrum disorders: a meta-analysis. *BMC Paediatrics, 20*, 449.

Li, Y., Wang, K., Zhang, P., Huang, J., Liu, Y., Wang, Z., Lu, Y., Tan, S., Yang, F., Tan, Y. (2020b). Pyrosequencing analysis of IRS1 methylation levels in schizophrenia with tardive dyskinesia. *Molecular Medicine Reports, 21*, 1702-1708.

Licznerski, P., Duric, V., Banasr, M., Alavian, K. N., Ota, K. T., Kang, H. J., Jonas, E. A., Ursano, R., Krystal, J. H., Duman, R. S. (2015). Decreased SGK1 expression and function contributes to behavioral deficits induced by traumatic stress. *PLoS Biology, 13*, e1002282.

Lieberman, J. A. (1999). Is schizophrenia a neurodegenerative disorder? A clinical and neurobiological perspective. *Biological Psychiatry, 46*, 729-739.

Lieberman, J. A., Stroup, T. S., McEvoy, J. P., Swartz, M. S., Rosenheck, R. A., Perkins, D. O., Keefe, R. S. E., Davis, S. M., Davis, C. E., Lebowitz, B. D., Severe, J., Hsiao, J. K., Investigators, C. (2005). Effectiveness of antipsychotic drugs in patients with chronic schizophrenia. *New England Journal of Medicine, 353*, 1209-1223.

Liloia, D., Brasso, C., Cauda, F., Mancuso, L., Nani, A., Manuello, J., Costa, T., Duca, S., Rocca, P. (2021). Updating and characterizing neuroanatomical markers in high-risk subjects, recently diagnosed and chronic patients with schizophrenia: a revised coordinate-based meta-analysis. *Neuroscience and Biobehavioral Reviews, 123*, 83–103.

Lin, D., Chen, J., Duan, K., Perrone-Bizzozero, N., Sui, J., Calhoun, V., Liu, J. (2021). Network modules linking expression and methylation in prefrontal cortex of schizophrenia. *Epigenetics, 16,* 876-893.

Lin, L., Desai, R., Wang, X., Lo, E. H., Xing, C. (2017). Characteristics of primary rat microglia isolated from mixed cultures using two different methods. *Journal of Neuroinflammation, 14*, 101.

Lin, P. Y., Chen, L. Y., Jiang, M., Trotter, J. H., Seigneur, E., Südhof, T. C. (2023). Neurexin-2: an inhibitory neurexin that restricts excitatory synapse formation in the hippocampus. *Science Advances, 9*, eadd8856.

Lister, R., Ecker, J. R. (2009). Finding the fifth base: genome-wide sequencing of cytosine methylation. *Genome Research, 19*, 959-966.

Lister, R., Mukamel, E. A., Nery, J. R., Urich, M., Puddifoot, C. A., Johnson, N. D., Lucero, J., Huang, Y., Dwork, A. J., Schultz, M. D., Yu, M., Tonti-Filippini, J., Heyn, H., Hu, S., Wu, J. C., Rao, A., Esteller, M., He, C., Haghighi, F. G., Sejnowski, T. J., Behrens, M. M., Ecker, J. R. (2013). Global epigenomic reconfiguration during mammalian brain development. *Science, 341*, e1237905.

Liu, D., Diorio, J., Day, J. C., Francis, D. D., Meaney, M. J. (2000). Maternal care, hippocampal synaptogenesis and cognitive development in rats. *Nature Neuroscience, 3*, 799-806.

Liu, D., Diorio, J., Tannenbaum, B., Caldji, C., Francis, D., Freedman, A., Sharma, S., Pearson, D., Plotsky, P. M., Meaney, M. J. (1997). Maternal care, hippocampal glucocorticoid receptors and hypothalamic-pituitary-adrenal responses to stress. *Science, 277*, 1659-1662.

Liu, D., Zinski, A., Mishra, A., Noh, H., Park, G. H., Qin, Y., Olorife, O., Park, J. M., Abani, C. P., Park, J. S., Fung, J., Sawaqed, F., Coyle, J. T., Stahl, E., Bendl, J., Fullard, J. F., Roussos, P., Zhang, X., Stanton, P. K., Yin, C., … Chung, S. (2022). Impact of schizophrenia GWAS loci converge onto distinct pathways in cortical interneurons vs glutamatergic neurons during development. *Molecular Psychiatry, 27*, 4218–4233.

Liu, J., Pickford, R., Meagher, A. P., Ward, R. L. (2011). Quantitative analysis of tissue folate using ultra high-performance liquid chromatography tandem mass spectrometry. *Analytical Biochemistry, 411*, 210-217.

Liu, L., Wu, J., Qing, L., Li, J., Yang, H., Ji, A., Yan, M., Hu, L., Nie, S. (2020a). DNA methylation analysis of the NR3C1 gene in patients with schizophrenia. *Journal of Molecular Neuroscience, 70,* 1177-1185.

Liu, L., Wu, Q., Li, X., Song, R., Wei, N., Liu, J., Yuan, J., Yan, S., Sun, X., Liang, Y., Li, Y., Jin, X., Wu, Y., Mei, L., Song, J., Yi, W., Pan, R., Cheng, J., Su, H. (2023). Sunshine duration and risks of schizophrenia hospitalizations in main urban area: do built environments modify the association? *The Science of the Total Environment, 871,* 162057.

Liu, Y., Ouyang, P., Zheng, Y., Mi, L., Zhao, J., Ning, Y., Guo, W. (2021). A selective review of the excitatory-inhibitory imbalance in schizophrenia: underlying biology, genetics, microcircuits and symptoms. *Frontiers in Cell and Developmental Biology, 9,* 664535.

Liu, Y., Tang, Y., Li, C., Tao, H., Yang, X., Zhang, X., Wang, X. (2020b). Altered expression of glucocorticoid receptor and neuron-specific enolase mRNA in peripheral blood in first-episode schizophrenia and chronic schizophrenia. *Frontiers in Psychiatry, 11*, 760.

Liu, Z., Osipovitch, M., Benraiss, A., Huynh, N. P. T., Foti, R., Bates, J., Chandler-Militello, D., Findling, R. L., Tesar, P. J., Nedergaard, M., Windrem, M. S., Goldman, S. A. (2019). Dysregulated glial differentiation in schizophrenia may be relieved by duppression of SMAD4- and REST-dependent signaling. *Cell Reports, 27,* 3832-3843.

Lleó, A. (2021). Biomarkers in neurological disorders: a fast-growing market. *Brain Communications, 3,* fcab086.

Llorca, A., Deogracias, R. (2022). Origin, development and synaptogenesis of cortical interneurons. *Frontiers in Neuroscience, 16*, 929469.

Loewy, R. L., Pearson, R., Stuart, B. K., Mathalon, D. H., Vinogradov, S. (2011). Childhood trauma and stress responsivity in adolescents and young adults at clinical high risk for psychosis. *Schizophrenia Bulletin, 37,* 5-6.

Lorusso, J. M., Woods, R. M., McEwan, F., Glazier, J. D., Neill, J. C., Harte, M., Hager, R. (2022). Clustering of cognitive phenotypes identifies susceptible and resilient offspring in a rat model of maternal immune activation and early-life stress. *Brain, Behavior and Immunity - Health, 25*, 100514.

Lourenço. T., Grãos, M. (2016). Modulation of oligodendrocyte differentiation by mechanotransduction. *Frontiers in Cellular Neuroscience, 10*, 277.

Lovic, V., Fleming, A. S. (2004). Artificially-reared female rats show reduced prepulse inhibition and deficits in the attentional set shifting task - reversal of effects with maternal-like licking stimulation. *Behavioural Brain Research, 148*, 209-219.

Low, N. C., Hardy, J. (2007). What is a schizophrenic mouse? *Neuron, 54,* e1011.

Lu, A. K., Lin, J. J., Tseng, H. H., Wang, X. Y., Jang, F. L., Chen, P. S., Huang, C. C., Hsieh, S., Lin, S. H. (2023). DNA methylation signature aberration as potential biomarkers in treatment-resistant schizophrenia: Constructing a methylation risk score using a machine learning method. *Journal of Psychiatric Research, 157,* 57–65.

Lubin, F. D., Roth, T. L., Sweatt, J. D. (2008). Epigenetic regulation of BDNF gene transcription in the consolidation of fear memory. *Journal of Neuroscience, 28,* 10576-10586.

Luckett-Chastain, L. R., Gallucci, R. M. (2009). Interleukin (IL)-6 modulates transforming growth factor-beta expression in skin and dermal fibroblasts from IL-6-deficient mice. *British Journal of Dermatology, 161*, 237-248.

Luoni, A., Massart, R., Nieratschker, V., Nemoda, Z., Blasi, G., Gilles, M., Witt, S. H., Suderman, M. J., Suomi, S. J., Porcelli, A., Rizzo, G., Fazio, L., Torretta, S., Rampino, A., Berry, A., Gass, P., Cirulli, F., Rietschel, M., Bertolino, A., Deuschle, M., Szyf, M., Riva, M. A. (2016). Ankyrin-3 as a molecular marker of early-life stress and vulnerability to psychiatric disorders. *Translational Psychiatry, 6*, e943

Lussier, A. L., Weeber, E. J., Rebeck, G. W. (2016). Reelin proteolysis affects signaling related to normal synapse function and neurodegeneration. *Frontiers in Cellular Neuroscience, 10*, 75.

Lynch, M. A. (2004). Long-term potentiation and memory. *Physiological Reviews, 84*, 87-136.

Ma, K., Xing, S., Luan, Y., Zhang, C., Liu, Y., Fei, Y., Zhang, Z., Liu, Y., Chen, X. (2021). Glypican 4 regulates Aβ internalization in neural stem cells partly via Low-Density Lipoprotein Receptor-Related Protein 1. *Frontiers in Cellular Neuroscience, 15*, 732429.

Mably, A. J., Colgin, L. L (2018). Gamma oscillations in cognitive disorders. *Current Opinions in Neurobiology, 52*, 182-187.

MacArthur, I. C., Dawlaty, M. M. (2021). TET enzymes and 5-hydroxymethylcytosine in neural progenitor cell biology and neurodevelopment. *Developmental Biology, 9,* 645335.

MacDowell, K. S., Munarriz-Cuezva, E., Meana, J. J., Leza, J. C., Ortega, J. E. (2021). Paliperidone reversion of maternal immune activation-induced changes on brain serotonin and kynurenine pathways. *Frontiers in Pharmacology, 12,* 682602.

Mackenzie, B., Schäfer, M. K., Erickson, J. D., Hediger, M. A., Weihe, E., Varoqui, H. (2003). Functional properties and cellular distribution of the system A glutamine transporter SNAT1 support specialized roles in central neurons. *Journal of Biological Chemistry, 278*, 23720-23730.

Maes, M., Sirivichayakul, S., Matsumoto, A. K., Maes, A., Michelin, A. P., de Oliveira Semeão, L., de Lima Pedrão, J. V., Moreira, E. G., Barbosa, D. S., Geffard, M., Carvalho, A. F., Kanchanatawan, B. (2020). Increased levels of plasma Tumor Necrosis Factor-α mediate schizophrenia symptom dimensions and neurocognitive impairments and are inversely associated with natural IgM directed to Malondialdehyde and Paraoxonase 1 activity. *Molecular Neurobiology, 57,* 2333–2345.

Mafi, A. M., Hofer, L. N., Russ, M. G., Young, J. W., Mellott, J. G. (2020). The density of perineuronal nets increases with age in the inferior colliculus in the Fischer Brown Norway rat. *Frontiers in Aging Neuroscience, 12*, 27.

Makinodan, M., Tatsumi, K., Manabe, T., Yamauchi, T., Makinodan, E., Matsuyoshi, H., Shimoda, S., Noriyama, Y., Kishimoto, T., Wanaka, A. (2008). Maternal immune activation in mice delays myelination and axonal development in the hippocampus of the offspring. *Journal of Neuroscience Research, 86*, 2190-2200.

Malda, A., Boonstra, N., Barf, H., de Jong, S., Aleman, A., Addington, J., Pruessner, M., Nieman, D., de Haan, L., Morrison, A., Riecher-Rössler, A., Studerus, E., Ruhrmann, S., Schultze-Lutter, F., An, S. K., Koike, S., Kasai, K., Nelson, B., McGorry, P., Wood, S., … Pijnenborg, G. H. M. (2019). Individualized prediction of transition to psychosis in 1,676 individuals at clinical high risk: development and validation of a multivariable prediction model based on individual patient data meta-analysis. *Frontiers in Psychiatry, 10,* 345.

Mangnier, L., Joly-Beauparlant, C., Droit, A., Bilodeau, S., Bureau, A. (2022). Cis-regulatory hubs: a new 3D model of complex disease genetics with an application to schizophrenia. *Life Science Alliance, 5*, e202101156.

Mao, M. J., Yu, H. L., Wen, Y. Z., Sun, X. Y., Xu, C. Y., Gao, Y. Z., Jiang, M., Yuan, H. M., Feng, S. W. (2022). Deficit of perineuronal net induced by maternal immune activation mediates the cognitive impairment in offspring during adolescence. *Behavioural Brain Research, 434*, 114027.

Maor, G. L., Yearim, A., Ast, G. (2015). The alternative role of DNA methylation in splicing regulation. *Trends in Genetics, 31*, 274-280.

Maramis, M. M., Mahajudin, M. S., Khotib, J. (2021). Impaired cognitive flexibility and working memory precedes depression: a rat model to study depression. *Neuropsychobiology, 80*, 225–233.

Marin, O., Valiente, M., Ge, X., Tsai, L. H. (2010). Guiding neuronal cell migrations. *Cold Spring Harbour Perspectives in Biology, 2*, e001834.

Marshall, C. R., Howrigan, D. P., Merico, D., Thiruvahindrapuram, B., Wu, W., Greer, D. S., Antaki, D., Shetty, A., Holmans, P. A., Pinto, D., Gujral, M., Brandler, W. M., Malhotra, D., Wang, Z., Fajarado, K. V. F., Maile, M. S., Ripke, S., Agartz, I., Albus, M., Alexander, M., … CNV and Schizophrenia Working Groups of the Psychiatric Genomics Consortium (2017). Contribution of copy number variants to schizophrenia from a genome-wide study of 41,321 subjects. *Nature Genetics, 49,* 27–35.

Martins-Ferreira, R., Leal, B., Costa, P. P., Ballestar, E. (2021). Microglial innate memory and epigenetic reprogramming in neurological disorders. *Progress in Neurobiology, 200*, 101971.

Martinsen, V., Kursula, P. (2022). Multiple sclerosis and myelin basic protein: insights into protein disorder and disease. *Amino Acids, 54*, 99-109.

Mascio, G., Notartomaso, S., Martinello, K., Liberatore, F., Bucci, D., Imbriglio, T., Cannella, M., Antenucci, N., Scarselli, P., Lattanzi, R., Bruno, V., Nicoletti, F., Fucile, S., Battaglia, G. (2022). A progressive build-up of perineuronal nets in the somatosensory cortex is associated with the development of chronic pain in mice. *The Journal of Neuroscience, 42*, 3037–3048.

Mashayekhi, F., Ronaghi, M. (2007). Analysis of read length limiting factors in pyrosequencing chemistry. *Analytical Biochemistry, 363*, 275-287.

Massrali, A., Adhya, D., Srivastava, D. P., Baron-Cohen, S., Kotter, M. R. (2022). Virus-induced maternal immune activation as an environmental factor in the etiology of autism and schizophrenia. *Frontiers in Neuroscience, 16*, 834058.

Matsumoto, M., Oshiumi, H., Seya, T. (2011). Antiviral responses induced by the TLR3 pathway. *Reviews in Medical Virology, 21*, 67-77.

Matsumoto, M., Seya, T. (2008). TLR3: Interferon induction by double-stranded RNA including poly(I : C). *Advanced Drug Delivery Reviews, 60*, 805-812.

Mattei, D., Schweibold, R., Wolf, S. A. (2015). Brain in flames - animal models of psychosis: utility and limitations. *Neuropsychiatric Disease Treatment, 11*, 1313-1329.

Mauney, S. A., Athanas, K. M., Pantazopoulos, H., Shaskan, N., Passeri, E., Berretta, S., Woo, T. U. (2013). Developmental pattern of perineuronal nets in the human prefrontal cortex and their deficit in schizophrenia. *Biological Psychiatry, 74,* 427–435.

Maynard, S. A., Triller, A. (2019). Inhibitory receptor diffusion dynamics. *Frontiers in Molecular Neuroscience, 12,* 313.

McCarthy, M. M., Arnold, A. P., Ball, G. F., Blaustein, J. D., De Vries, G. J. (2012). Sex differences in the brain: the not so inconvenient truth. *The Journal of Neuroscience, 32*, 2241-2247.

McCarthy. M. M., Auger, A. P., Bale, T. L., De Vries, G. J., Dunn, G. A., Forger, N. G., Murray, E. K., Nugent, B. M., Schwarz, J. M., Wilson, M. E. (2009). The epigenetics of sex differences in the brain. *The Journal of Neuroscience, 29*, 12815-12823.

McColl, E. R., Hurtarte, M., Piquette-Miller, M. (2022). Impact of inflammation and infection on the expression of amino acid transporters in the placenta: a minireview. *Drug Metabolism and Disposition, 5*, online ahead of print.

McColl, E. R., Piquette-Miller, M. (2019). Poly(I:C) alters placental and foetal brain amino acid transport in a rat model of maternal immune activation. *American Journal of Reproductive Immunology, 29*, e13115.

McEwen, B. S., Milner, T. A. (2017). Understanding the broad influence of sex hormones and sex differences in the brain. *The Journal of Neuroscience Research, 95*, 24-39.

McEwan, F., Glazier, J. D., Hager, R. (2023). The impact of maternal immune activation on embryonic brain development. *Frontiers in Neuroscience, 17*, 1146710.

McFarland, R. (2012). Cerebral folate deficiency—mishaps and misdirection. *Brain, 135*, 2002-2003.

McGarel, C., Pentieva, K., Strain, J. J., McNulty, H. (2015). Emerging roles for folate and related B-vitamins in brain health across the lifecycle. *The Proceedings of the Nutritional Society, 74*, 46-55.

McGee, A. W., Yang, Y., Fischer, Q. S., Daw, N. W., Strittmatter, S. M. (2005). Experience-driven plasticity of visual cortex limited by myelin and Nogo receptor. *Science, 309*, 2222-2226.

McGrath, J., Saha, S., Welham, J., El Saadi, O., MacCauley, C., Chant, D. (2004). A systematic review of the incidence of schizophrenia: the distribution of rates and the influence of sex, urbanicity, migrant status and methodology. *BMC Medicine, 2,* e13.

McKerracher, L., David, S., Jackson, D. L., Kottis, V., Dunn, R. J., Braun, P. E. (1994). Identification of myelin-associated glycoprotein as a major myelin-derived inhibitor of neurite growth. *Neuron, 13*, 805–811.

McRae, P. A., Rocco, M. M., Kelly, G., Brumberg, J. C., Matthews, R. T. (2007). Sensory deprivation alters aggrecan and perineuronal net expression in the mouse barrel cortex. *The Journal of Neuroscience, 27*, 5405–5413.

Meaney, M. J. (2001). Maternal care, gene expression and the transmission of individual differences in stress reactivity across generations. *Annual Review of Neuroscience, 24*, 1161-1192.

Mednick, S. A., Machon, R. A., Huttunen, M. O., Bonett, D. (1988). Adult schizophrenia following prenatal exposure to an influenza epidemic. *Archives of General Psychiatry, 45*, 189-192.

Mehler, M. F., Kessler, J. A. (1997). Hematolymphopoietic and inflammatory cytokines in neural development. *Trends in Neuroscience, 20*, 357-365.

Meier, J., Vannier, C., Sergé, A., Triller, A., Choquet, D. (2001). Fast and reversible trapping of surface glycine receptors by gephyrin. *Nature Neuroscience, 4,* 253–260.

Meissner, A., Mikkelsen, T. S., Gu, H., Wernig, M., Hanna, J., Sivachenko, A., Zhang, X., Bernstein, B. E., Nusbaum, C., Jaffe, D. B., Gnirke, A., Jaenisch, R., Lander, E. S. (2008). Genome-scale DNA methylation maps of pluripotent and differentiated cells. *Nature, 454,* 766-770.

Mellen, M., Ayata, P., Dewell, S., Kriaucionis, S., Heintz, N. (2012). MeCP2 binds to 5hmC enriched within active genes and accessible chromatin in the nervous system. *Cell, 151*, 1417-1430.

Meltzer, H. Y., Li, Z., Kaneda, Y., Ichikawa, J. (2003). Serotonin receptors: their key role in drugs to treat schizophrenia. *Progress in Neuro-psychopharmacology and Biological Psychiatry, 27*, 1159–1172.

Meltzer, H. Y., Matsubara, S., Lee, J. C. (1989). Classification of typical and atypical antipsychotic drugs on the basis of dopamine D-1, D-2 and serotonin2 pKi values. *The Journal of Pharmacology and Experimental Therapeutics, 251*, 238–246.

Meltzer, H. Y., Rajagopal, L., Huang, M., Oyamada, Y., Kwon, S., Horiguchi, M. (2013). Translating the N-methyl-D-aspartate receptor antagonist model of schizophrenia to treatments for cognitive impairment in schizophrenia. *The International Journal of Neuropsychopharmacology, 16*, 2181–2194.

Menassa, D. A., Gomez-Nicola, D. (2018). Microglial dynamics during human brain development. *Frontiers in Immunology, 9*, e1014.

Mendizabal, I., Berto, S., Usui, N., Toriumi, K., Chatterjee, P., Douglas, C., Huh, I., Jeong, H., Layman, T., Tamminga, C. A., Preuss, T. M., Konopka, G., Yi, S. V. (2019). Cell type-specific epigenetic links to schizophrenia risk in the brain. *Genome Biology, 20*, 135.

Mendonca, A., Chang, E. H., Liu, W., Yuan, C. (2014). Hydroxymethylation of DNA influences nucleosomal conformation and stability *in vitro*. *Biochimica et Biophysica Acta, 1839*, 1323-1329.

Mentch, S. J., Locasale, J. W. (2016). One carbon metabolism and epigenetics: understanding the specificity. *Annals of the New York Academy of Sciences, 1363*, 91-98.

Messerschmidt, D. M., Knowles, B. B., Solter, D. (2014). DNA methylation dynamics during epigenetic reprogramming in the germline and preimplantation embryos. *Genes and Development, 28*, 812-828.

Mevorach, T., Taler, M., Dar, S., Lebow, M., Sapir, I. S., Rotkopf, R., Apter, A., Fennig, S., Chen, A., Weizman, A., Amitai, M. (2021). The relationship between the plasma proinflammatory cytokine levels of depressed/anxious children and their parents. *Science Reports, 11*, 11798.

Meyer, U. (2013). Developmental neuroinflammation and schizophrenia. *Progress in Neuropsychopharmacology and Biological Psychiatry, 42*, 20-34.

Meyer, U. (2014). Prenatal Poly(I:C) exposure and other developmental immune activation models in rodent systems. *Biological Psychiatry, 75,* 307-315.

Meyer, U., Feldon, J. (2010). Epidemiology-driven neurodevelopmental animal models of schizophrenia. *Progress in Neurobiology, 90*, 285-326.

Meyer, U., Feldon, J. (2012). To poly(I:C) or not to poly(I:C): advancing preclinical schizophrenia research through the use of prenatal immune activation models. *Neuropharmacology, 62,* 1308-1321.

Meyer, U., Feldon, J., Fatemi, S. H. (2009a). *In-vivo* rodent models for the experimental investigation of prenatal immune activation effects in neurodevelopmental brain disorders. *Neuroscience and Biobehavioral Reviews, 33*, 1061-1079.

Meyer, U., Feldon, J., Schedlowski, M., Yee, B. K. (2005). Towards an immuno-precipitated neurodevelopmental animal model of schizophrenia. *Neuroscience and Biobehavioral Reviews, 29*, 913-947.

Meyer, U., Feldon, J., Schedlowski, M., Yee, B. K. (2006a). Immunological stress at the maternal-foetal interface: a link between neurodevelopment and adult psychopathology. *Brain, Behavior and Immunity, 20,* 378-388.

Meyer, U., Feldon, J., Yee, B. K. (2009b). A review of the foetal brain cytokine imbalance hypothesis of schizophrenia. *Schizophrenia Bulletin, 35*, 959-972.

Meyer, U., Nyffeler, M., Engler, A., Urwyler, A., Schedlowski, M., Knuesel, I., Yee, B. K., Feldon, J. (2006b). The time of prenatal immune challenge determines the specificity of inflammation-mediated brain and behavioral pathology. *The Journal of Neuroscience, 26*, 4752-4762.

Meyer, U., Nyffeler, M., Schwendener, S., Knuesel, I., Yee, B. K., Feldon, J. (2008a). Relative prenatal and postnatal maternal contributions to schizophrenia-related neurochemical dysfunction after *in utero* immune challenge. *Neuropsychopharmacology, 33*, 441-456.

Meyer, U., Nyffeler, M., Yee, B. K., Knuesel, I., Feldon, J. (2008b). Adult brain and behavioral pathological markers of prenatal immune challenge during early/middle and late foetal development in mice. *Brain, Behavior and Immunity, 22*, 469-486.

Meyer, U., Spoerri, E., Yee, B. K., Schwarz, M. J., Feldon, J. (2010). Evaluating early preventive antipsychotic and antidepressant drug treatment in an infection-based neurodevelopmental mouse model of schizophrenia. *Schizophrenia Bulletin, 36,* 607-623.

Meyer, U., Yee, B. K., Feldon, J. (2007). The neurodevelopmental impact of prenatal infections at different times of pregnancy: the earlier the worse? *Neuroscientist, 13,* 241-256.

Michaluk, P., Mikasova, L., Groc, L., Frischknecht, R., Choquet, D., Kaczmarek, L. (2009). Matrix metalloproteinase-9 controls NMDA receptor surface diffusion through integrin beta1 signaling. *Journal of Neuroscience, 29,* 6007–6012.

Mielnik, C. A., Binko, M. A., Chen, Y., Funk, A. J., Johansson, E. M., Intson, K., Sivananthan, N., Islam, R., Milenkovic, M., Horsfall, W., Ross, R. A., Groc, L., Salahpour, A., McCullumsmith, R. E., Tripathy, S., Lambe, E. K., Ramsey, A. J. (2021). Consequences of NMDA receptor deficiency can be rescued in the adult brain. *Molecular Psychiatry, 26*, 2929–2942.

Migale, R., Herbert, B. R., Lee, Y. S., Sykes, L., Waddington, S. N., Peebles, D., Hagberg, H., Johnson, M. R., Bennett, P. R., MacIntyre, D. A. (2015). Specific lipopolysaccharide serotypes induce differential maternal and neonatal inflammatory responses in a murine model of preterm labor. *The American Journal of Pathology, 185*, 2390–2401.

Mihaljević-Peleš, A., Bajs Janović, M., Šagud, M., Živković, M., Janović, Š., Jevtović, S. (2019). Cognitive deficit in schizophrenia: an overview. *Psychiatria Danubina, 31,* 139-142.

Mill, J., Tang, T., Kaminsky, Z., Khare, T., Yazdanpanah, S., Bouchard, L., Jia, P., Assadzadeh, A., Flanagan, J., Schumacher, A., Wang, S. C., Petronis, A. (2008). Epigenomic profiling reveals DNA-methylation changes associated with major psychosis. *American Journal of Human Genetics, 82*, 696–711.

Miller, B. J., Buckley, P., Seabolt, W., Mellor, A., Kirkpatrick, B. (2011). Meta-analysis of cytokine alterations in schizophrenia: clinical status and antipsychotic effects. *Biological Psychiatry, 70*, 663-671.

Miller, B. J., Goldsmith, D. R. (2020). Evaluating the hypothesis that schizophrenia is an inflammatory disorder. *Focus, 18,* 391-401.

Miller, C. A., Gavin, C. F., White, J. A., Parrish, R. R., Honasoge, A., Yancey, C. R., Rivera, I. M., Rubio, M. D., Rumbaugh, G., Sweatt, J. D. (2010). Cortical DNA methylation maintains remote memory. *Nature Neuroscience, 13*, 664-666.

Miller, E. K. (2000). The prefrontal cortex and cognitive control. *Nature Reviews Neuroscience, 1*, 59-65.

Miller, F. D., Gauthier, A. (2007). Timing is everything: making neurons versus glia in the developing cortex. *Neuron, 54*, 357-369.

Moccia, L., Kotzalidis, G. D., Bartolucci, G., Ruggiero, S., Monti, L., Biscosi, M., Terenzi, B., Ferrara, O. M., Mazza, M., Di Nicola, M., Janiri, D., Simonetti, A., Caroppo, E., Janiri, L., Sani, G. (2023). COVID-19 and new-onset psychosis: a comprehensive review. *Journal of Personalized Medicine, 13*, 104.

Moghadam, K. K., Pizza, F., La Morgia, C., Franceschini, C., Tonon, C., Lodi, R., Barboni, P., Seri, M., Ferrari, S., Liguori, R., Donadio, V., Parchi, P., Cornelio, F., Inzitari, D., Mignarri, A., Capocchi, G., Dotti, M. T., Winkelmann, J., Lin, L., Mignot, E., Carelli, V., Plazzi, G. (2014). Narcolepsy is a common phenotype in HSAN IE and ADCA-DN. *Brain, 137,* 1643–1655.

Mohn, F., Weber, M., Rebhan, M., Roloff, T. C., Richter, J., Stadler, M. B., Bibel, M., Schubeler, D. (2008). Lineage-specific polycomb targets and *de novo* DNA methylation define restriction and potential of neuronal progenitors. *Molecular Cell, 30*, 755-766.

Monaco, S. A., Gulchina, Y., Gao, W. J. (2015). NR2B subunit in the prefrontal cortex: a double-edged sword for working memory function and psychiatric disorders. *Neuroscience and Biobehavioral Reviews, 56,* 127–138.

Monk, M., Adams, R. L., Rinaldi, A. (1991). Decrease in DNA methylase activity during preimplantation development in the mouse. *Development, 112,* 189-192.

Monk, M., Boubelik, M., Lehnert, S. (1987). Temporal and regional changes in DNA methylation in the embryonic, extraembryonic and germ-cell lineages during mouse embryo development. *Development, 99,* 371-382.

Montgomery, S. E., Sepehry, A. A., Wangsgaard, J. D., Koenig, J. E. (2014). The effect of S-adenosylmethionine on cognitive performance in mice: an animal model meta-analysis. *PLoS One, 9*, e107756.

Moore, L. D., Le, T., Fan, G. (2013). DNA methylation and its basic function. *Neuropsychopharmacology, 38,* 23-38.

Morais, L. H., Felice, D., Golubeva, A. V., Moloney, G., Dinan, T. G., Cryan, J. F. (2018). Strain differences in the susceptibility to the gut-brain axis and neurobehavioural alterations induced by maternal immune activation in mice. *Behavioral Pharmacology, 29*,181-198.

Morgan, H. D., Santos, F., Green, K., Dean, W., Reik, W. (2005). Epigenetic reprogramming in mammals. *Human Molecular Genetics, 14*, 47-58.

Morisawa, S., Yasuda, H., Kamiya, T., Hara, H., Adachi, T. (2017). Tumor necrosis factor-α decreases EC-SOD expression through DNA methylation. *Journal of Clinical Biochemistry and Nutrition, 60,* 169-175

Morishita, H., Kundakovic, M., Bicks, L., Mitchell, A., Akbarian, S. (2015). Interneuron epigenomes during the critical period of cortical plasticity: implications for schizophrenia. *Neurobiology of Learning and Memory, 124,* 104-110.

Moritz, S., Klein, J. P., Lysaker, P. H., Mehl, S. (2019). Metacognitive and cognitive-behavioral interventions for psychosis: new developments. *Dialogues in Clinical Neuroscience, 21,* 309–317.

Morris, M. J., Karra, A. S., Monteggia, L. M. (2010). Histone deacetylases govern cellular mechanisms underlying behavioral and synaptic plasticity in the developing and adult brain. *Behavioural Pharmacology, 21,* 409-419.

Morris, M. J., Mahgoub, M., Na, E. S., Pranav, H., Monteggia, L. M. (2013). Loss of histone deacetylase 2 improves working memory and accelerates extinction learning. *Journal of Neuroscience, 33*, 6401-6411.

Morris, M. J., Na, E. S., Autry, A. E., Monteggia, L. M. (2016). Impact of DNMT1 and DNMT3a forebrain knockout on depressive- and anxiety like behavior in mice. *Neurobiology of Learning and Memory, 135*, 139–145.

Morrison, H., Young, K., Qureshi, M., Rowe, R. K., Lifshitz, J. (2017). Quantitative microglia analyses reveal diverse morphologic responses in the rat cortex after diffuse brain injury. *Scientific Reports, 7*, 13211.

Mossa, A., Manzini, M. C. (2021). Molecular causes of sex-specific deficits in rodent models of neurodevelopmental disorders. *Journal of Neuroscience Research, 99*, 37-56.

Mouihate, A., Al-Hashash, H., Rakhshani-Moghadam, S., Kalakh, S. (2017). Impact of prenatal immune challenge on the demyelination injury during adulthood. *CNS Neuroscience and Therapeutics, 23*, 724-735.

Mourtzi, N., Sertedaki, A., Charmandari, E. (2021). Glucocorticoid signaling and epigenetic alterations in stress-related disorders. *International Journal of Molecular Science, 22*, 5964.

Mousa, A., Seiger, A., Kjaeldgaard, A., Bakhiet, M. (1999). Human first trimester forebrain cells express genes for inflammatory and anti-inflammatory cytokines. *Cytokine, 11*, 55-60.

Moustafa, A. A., Hewedi, D. H., Eissa, A. M., Frydecka, D., Misiak, B. (2014). Homocysteine levels in schizophrenia and affective disorders-focus on cognition. *Frontiers in Behavioral Neuroscience, 8*, e343.

Moyon, S., Huynh, J. L., Dutta, D., Zhang, F., Ma, D., Yoo, S., Lawrence, R., Wegner, M., John, G. R., Emery, B., Lubetzki, C., Franklin, R. J. M., Fan, G., Zhu, J., Dupree, J. L., Casaccia, P. (2016). Functional characterization of DNA methylation in the oligodendrocyte lineage. *Cell Reports, 15*, 748-760.

Mueller, B. R., Bale, T. L. (2008). Sex-specific programming of offspring emotionality after stress early in pregnancy. *The Journal of Neuroscience, 28*, 9055–9065.

Mueller D. R. (2023). Editorial: Integrated therapy approaches in schizophrenia: evidence and limitations. *Frontiers in Psychiatry, 14,* 1142493.

Mueller, F. S., Polesel, M., Richetto, J., Meyer, U., Weber-Stadlbauer, U. (2018). Mouse models of maternal immune activation: mind your caging system! *Brain, Behavior and Immunity, 73*, 643-660.

Mueller, F. S., Richetto, J., Hayes, L. N., Zambon, A., Pollak, D. D., Sawa, A., Meyer, U., Weber-Stadlbauer, U. (2019). Influence of poly(I:C) variability on thermoregulation, immune responses and pregnancy outcomes in mouse models of maternal immune activation. *Brain, Behavior and Immunity, 80*, 406–418.

Mueller, F. S., Scarborough, J., Schalbetter, S. M., Richetto, J., Kim, E., Couch, A., Yee, Y., Lerch, J. P., Vernon, A. C., Weber-Stadlbauer, U., Meyer, U. (2021). Behavioral, neuroanatomical and molecular correlates of resilience and susceptibility to maternal immune activation. *Molecular Psychiatry, 26*, 396-410.

Muench, J., Hamer, A. M. (2010). Adverse effects of antipsychotic medications. *American Family Physician, 81,* 617-622.

Müller, N., Schwarz, M. J. (2010). Immune system and schizophrenia. *Current Immunology Reviews, 6*, 213–220.

Müller, N., Weidinger, E., Leitner, B., Schwarz, M. J. (2015). The role of inflammation in schizophrenia. *Frontiers in Neuroscience, 9*, 372.

Munzel, M., Globisch, D., Bruckl, T., Wagner, M., Welzmiller, V., Michalakis, S., Muller, M., Biel, M., Carell, T. (2010). Quantification of the sixth DNA base hydroxymethylcytosine in the brain. *Angewandte Chemie - International Edition, 49*, 5375-5377.

Murgatroyd, C., Patchev, A. V., Wu, Y., Micale, V., Bockmühl, Y., Fischer, D., Holsboer, F., Wotjak, C. T., Almeida, O. F., Spengler, D. (2009). Dynamic DNA methylation programs persistent adverse effects of early-life stress. *Nature Neuroscience, 12*, 1559–1566.

Murphy, F. C., Michael, A., Sahakian, B. J. (2012). Emotion modulates cognitive flexibility in patients with major depression. *Psychological Medicine, 42*, 1373–1382.

Murray, A. J., Woloszynowska-Fraser, M. U., Ansel-Bollepalli, L., Cole, K. L., Foggetti, A., Crouch, B., Riedel, G., Wulff, P. (2015). Parvalbumin-positive interneurons of the prefrontal cortex support working memory and cognitive flexibility. *Scientific Reports, 5,* 16778.

Murray, K. M., Edye, M. E., Manca, M., Vernon, A. C., Oladipo, J. M., Fasolino, V., Harte, M. K., Mason, V., Grayson, B., McHugh, P. C., Prinssen, E. P., Hager, R., Neill, J. C. (2019). Evolution of a maternal immune activation (mIA) model in rats: early developmental effects. *Brain, Behavior and Immunity, 75*, 48-59.

Murray, R. (2003). The epidemiology of schizophrenia. Cambridge University Press. Cambridge, UK.

Murray, R. M., Lewis, S. W. (1988). Is schizophrenia a neurodevelopmental disorder. *British Medical Journal, 296*, e63.

Murtaj, V., Belloli, S., Di Grigoli, G., Pannese, M., Ballarini, E., Rodriguez-Menendez, V., Marmiroli, P., Cappelli, A., Masiello, V., Monterisi, C., Bellelli, G., Panina-Bordignon, P., Moresco, R. M. (2019). Age and sex influence the neuro-inflammatory response to a peripheral acute LPS challenge. *Frontiers in Aging Neuroscience, 11*, 299.

Muzio, L., Viotti, A., Martino, G. (2021). Microglia in neuroinflammation and neurodegeneration: from understanding to therapy. *Frontiers in Neuroscience, 15*, 742065.

Myatt, L. (2006) Placental adaptive responses and foetal programming. *Journal of Physiology, 572,* 25-30.

Naber, D., Lambert, M. (2009). The CATIE and CUtLASS studies in schizophrenia. *CNS Drugs, 23*, 649–659.

Nabil Fikri, R. M., Norlelawati, A. T., Nour El-Huda, A. R., Hanisah, M. N., Kartini, A., Norsidah, K., Nor Zamzila, A. (2017). Reelin (RELN) DNA methylation in the peripheral blood of schizophrenia. *Journal of Psychiatric Research, 88*, 28–37.

Nagy, V., Bozdagi, O., Matynia, A., Balcerzyk, M., Okulski, P., Dzwonek, J., Costa, R. M., Silva, A. J., Kaczmarek, L., Huntley, G. W. (2006). Matrix metalloproteinase-9 is required for hippocampal late-phase long-term potentiation and memory. *Journal of Neuroscience, 26*, 1923–1934.

Nahar, L., Delacroix, B. M., Nam, H. W. (2021). The role of parvalbumin interneurons in neurotransmitter balance and neurological disease. *Frontiers in Psychiatry, 12*, 679960.

Naik, A. A., Patro, N., Seth, P., Patro, I. K. (2017). Intra-generational protein malnutrition impairs temporal astrogenesis in rat brain. *Biology Open, 6,* 931-942.

Nakamura, J. P., Gillespie, B., Gibbons, A., Jaehne, E. J., Du, X., Chan, A., Schroeder, A., van den Buuse, M., Sundram, S., Hill, R. A. (2021). Maternal immune activation targeted to a window of parvalbumin interneuron development improves spatial working memory: Implications for autism. *Brain, Behavior and Immunity, 91*, 339–349.

Nakanishi, M., Niidome, T., Matsuda, S., Akaike, A., Kihara, T., Sugimoto, H. (2007). Microglia-derived interleukin-6 and leukaemia inhibitory factor promote astrocytic differentiation of neural stem/progenitor cells. *European Journal of Neuroscience, 25*, 649–658.

Nakazawa, K., Sapkota, K. (2020). The origin of NMDA receptor hypofunction in schizophrenia. *Pharmacology and Therapeutics, 205,* 107426.

Namvarpour, Z., Ranaei, E., Amini, A., Roudafshani, Z., Fahanik-Babaei, J. (2022). Effects of prenatal exposure to inflammation coupled with prepubertal stress on prefrontal white matter structure and related molecules in adult mouse offspring. *Metabolic Brain Disease, 37,* 1655-1668.

Naninck, E. F. G., Stijger, P. C., Brouwer-Brolsma, E. M. (2019). The importance of maternal folate status for brain development and function of offspring. *Advances in Nutrition, 10*, 502-519.

Nazzari, S., Fearon, P., Rice, F., Ciceri, F., Molteni, M., Frigerio, A. (2020). Neuroendocrine and immune markers of maternal stress during pregnancy and infant cognitive development. *Developmental Psychobiology, 62,* 1100-1110.

Neal, M., Richardson, J. R. (2018). Epigenetic regulation of astrocyte function in neuroinflammation and neurodegeneration. *Biochimica et Biophysica Acta - Molecular Basis of Disease, 1864*, 432-443.

Neill, J. C., Barnes, S., Cook, S., Grayson, B., Idris, N. F., McLean, S. L., Snigdha, S., Rajagopal, L., Harte, M. K. (2010). Animal models of cognitive dysfunction and negative symptoms of schizophrenia: focus on NMDA receptor antagonism. *Pharmacology and Therapeutics, 128*, 419–432.

Nelson, G. M., Guynn, J. M., Chorley, B. N. (2017). Procedure and key optimization strategies for an automated capillary electrophoretic-based immunoassay method. *Journal of Visualized Experiments, 10*, e55911.

Nelson, M. D., Saykin, A. J., Flashman, L. A., Riordan, H. J. (1998). Hippocampal volume reduction in schizophrenia as assessed by magnetic resonance imaging: a meta-analytic study. *Archives of General Psychiatry, 55*, 433-440.

Netser, S., Meyer, A., Magalnik, H., Zylbertal, A., de la Zerda, S. H., Briller, M., Bizer, A., Grinevich, V., Wagner, S. (2020). Distinct dynamics of social motivation drive differential social behavior in laboratory rat and mouse strains. *Nature Communications, 11*, 5908.

Newbury, J. B., Stewart, R., Fisher, H. L., Beevers, S., Dajnak, D., Broadbent, M., Pritchard, M., Shiode, N., Heslin, M., Hammoud, R., Hotopf, M., Hatch, S. L., Mudway, I. S., Bakolis, I. (2021). Association between air pollution exposure and mental health service use among individuals with first presentations of psychotic and mood disorders: retrospective cohort study. *The British Journal of Psychiatry, 219*, 678–685.

Newcomer, J. W. (2007). Antipsychotic medications: metabolic and cardiovascular risk. *Journal of Clinical Psychiatry, 68*, 8-13

Newman, A., Maddocks, O. (2017). One-carbon metabolism in cancer. *British Journal of Cancer, 116*, 1499–1504.

Newman, T. A., Woolley, S. T., Hughes, P. M., Sibson, N. R., Anthony, D. C., Perry, V. H. (2001). T-cell- and macrophage-mediated axon damage in the absence of a CNS-specific immune response: involvement of metalloproteinases. *Brain, 124*, 2203-2214.

Nicholson, C., Syková, E. (1998). Extracellular space structure revealed by diffusion analysis. *Trends in Neuroscience, 21*, 207-215.

Niciu, M. J., Kelmendi, B., Sanacora, G. (2012). Overview of glutamatergic neurotransmission in the nervous system. *Pharmacology Biochemistry and Behavior, 100*, 656-664.

Nicodemus, K. K., Marenco, S., Batten, A. J., Vakkalanka, R., Egan, M. F., Straub, R. E., Weinberger, D. R. (2008). Serious obstetric complications interact with hypoxia-regulated/vascular-expression genes to influence schizophrenia risk. *Molecular Psychiatry, 1*3, 873-877.

Nicole, O., Pacary, E. (2020). CaMKIIβ in neuronal development and plasticity: an emerging candidate in brain diseases. *International Journal of Molecular Science, 21*, 7272.

Niendam, T. A., Bearden, C. E., Johnson, J. K., McKinley, M., Loewy, R., O'Brien, M., Nuechterlein, K. H., Green, M. F., Cannon, T. D. (2006). Neurocognitive performance and functional disability in the psychosis prodrome. *Schizophrenia Research, 84*, 100-111.

Niethammer, M., Kim, E., Sheng, M. (1996). Interaction between the C terminus of NMDA receptor subunits and multiple members of the PSD-95 family of membrane-associated guanylate kinases. *The Journal of Neuroscience, 16*, 2157–2163.

Nishiyama, A., Shimizu, T., Sherafat, A., Richardson, W. D. (2021). Life-long oligodendrocyte development and plasticity. *Seminars in Cell Development and Biology, 116*, 25-37.

Novak, D. A., Beveridge, M. J. (1997). Glutamine transport in human and rat placenta. *Placenta, 18*, 379-386.

Numata, S., Ueno, S., Iga, J., Yamauchi, K., Hongwei, S., Hashimoto, R., Takeda, M., Kunugi, H., Itakura, M., Ohmori, T. (2008). TGFBR2 gene expression and genetic association with schizophrenia. *Journal of Psychiatric Research, 42*, 425-432.

Núñez-Estevez, K. J., Rondón-Ortiz, A. N., Nguyen, J. Q. T., Kentner, A. C. (2020). Environmental influences on placental programming and offspring outcomes following maternal immune activation. *Brain, Behaviour and Immunity, 83,* 44-55.

Oakley, R. H., Cidlowski, J. A. (2013). The biology of the glucocorticoid receptor: new signaling mechanisms in health and disease. *The Journal of Allergy and Clinical Immunology, 132*, 1033–1044.

Ohtsuki, S., Yamaguchi, H., Kang, Y. S., Hori, S., Terasaki, T. (2010). Reduction of L-type amino acid transporter 1 mRNA expression in brain capillaries in a mouse model of Parkinson's disease. *Biological and Pharmaceutical Bulletin, 33,* 1250-1252.

Olney, J. W., Farber, N. B. (1995). Glutamate receptor dysfunction and schizophrenia. *Archives of General Psychiatry, 52*, 998-1007.

Onori, M. P., van Woerden, G. M. (2021). Role of calcium/calmodulin-dependent kinase 2 in neurodevelopmental disorders. *Brain Research Bulletin, 171*, 209-220.

Oohashi, T., Hirakawa, S., Bekku, Y., Rauch, U., Zimmermann, D. R., Su, W. D., Ohtsuka, A., Murakami, T., Ninomiya, Y. (2002). Bral1, a brain-specific link protein, colocalizing with the versican V2 isoform at the nodes of Ranvier in developing and adult mouse central nervous systems. *Molecular and Cellular Neuroscience, 19*, 43-57.

Orellana, G., Slachevsky, A. (2013). Executive functioning in schizophrenia. *Frontiers in Psychiatry, 4*, 35.

Orhan, F., Fatouros-Bergman, H., Goiny, M., Malmqvist, A., Piehl, F., Cervenka, S., Collste, K., Victorsson, P., Sellgren, C. M., Flyckt, L., Erhardt, S., Engberg, G., Project, K. S. (2018). CSF GABA is reduced in first-episode psychosis and associates to symptom severity. *Molecular Psychiatry, 23*, 1244-1250.

Osborne, A. L., Solowij, N., Babic, I., Huang, X. F., Weston-Green, K. (2017a). Improved social interaction, recognition and working memory with cannabidiol treatment in a prenatal infection (poly I:C) rat model. *Neuropsychopharmacology, 42*, 1447–1457.

Osborne, A. L., Solowij, N., Babic, I., Lum, J. S., Huang, X. F., Newell, K. A., Weston-Green, K. (2019). Cannabidiol improves behavioural and neurochemical deficits in adult female offspring of the maternal immune activation (poly I:C) model of neurodevelopmental disorders. *Brain, Behavior and Immunity, 81,* 574–587.

Osborne, A. L., Solowij, N., Weston-Green, K. (2017b). A systematic review of the effect of cannabidiol on cognitive function: relevance to schizophrenia. *Neuroscience and Biobehavioral Reviews, 72*, 310–324.

Oskvig, D. B., Elkahloun, A. G., Johnson, K. R., Phillips, T. M., Herkenham, M. (2012). Maternal immune activation by LPS selectively alters specific gene expression profiles of interneuron migration and oxidative stress in the foetus without triggering a foetal immune response. *Brain, Behavior and Immunity, 26,* 623-634.

Ouellet, L., de Villers-Sidani, E. (2014). Trajectory of the main GABAergic interneuron populations from early development to old age in the rat primary auditory cortex. *Frontiers in Neuroanatomy, 8*, 40.

Owen, M. J., O'Donovan, M. C., Thapar, A., Craddock, N. (2011). Neurodevelopmental hypothesis of schizophrenia. *The British Journal of Psychiatry, 198*, 173–175.

Ozawa, K., Hashimoto, K., Kishimoto, T., Shimizu, E., Ishikura, H., Iyo, M. (2006). Immune activation during pregnancy in mice leads to dopaminergic hyperfunction and cognitive impairment in the offspring: a neurodevelopmental animal model of schizophrenia. *Biological Psychiatry, 59*, 546-554.

Page, N. F., Gandal, M. J., Estes, M. L., Cameron, S., Buth, J., Parhami, S., Ramaswami, G., Murray, K., Amaral, D. G., Van de Water J. A., Schumann, C. M., Carter, C. S., Bauman, M. D., McAllister, A. K., Geschwind, D. H. (2021). Alterations in retrotransposition, synaptic connectivity and myelination implicated by transcriptomic changes following maternal immune activation in nonhuman primates. *Biological Psychiatry, 89*, 896-910.

Paintlia, M. K., Paintlia, A. S., Contreras, M. A., Singh, I. Singh, A. K. (2008). Lipopolysaccharide-induced peroxisomal dysfunction exacerbates cerebral white matter injury: attenuation by N-acetyl cysteine. *Experimental Neurology, 210*, 560-576.

Paksarian, D., Trabjerg, B. B., Merikangas, K. R., Mors, O., Børglum, A. D., Hougaard, D. M., McGrath, J. J., Pedersen, C. B., Mortensen, P. B., Agerbo, E. (2018). The role of genetic liability in the association of urbanicity at birth and during upbringing with schizophrenia in Denmark. *Psychological Medicine, 48*, 305–314.

Palmeira, P., Quinello, C., Silveira-Lessa, A. L., Zago, C. A., Carneiro-Sampaio, M. (2012). IgG placental transfer in healthy and pathological pregnancies. *Clinical & Developmental Immunology, 2012*, 985646.

Pan, S., Zhou, Y., Yan, L., Xuan, F., Tong, J., Li, Y., Huang, J., Feng, W., Chen, S., Cui, Y., Yang, F., Tan, S., Wang, Z., Tian, B., Hong, L. E., Tan, Y. L., Tian, L. (2022). TGF-β1 is associated with deficits in cognition and cerebral cortical thickness in first-episode schizophrenia. *Journal of Psychiatry and Neuroscience, 47*, 86-98.

Pantazopoulos, H., Katsel, P., Haroutunian, V., Chelini, G., Klengel, T., Berretta, S. (2021). Molecular signature of extracellular matrix pathology in schizophrenia. *The European Journal of Neuroscience, 53*, 3960–3987.

Pantazopoulos, H., Woo, T. U., Lim, M. P., Lange, N., Berretta, S. (2010). Extracellular matrix-glial abnormalities in the amygdala and entorhinal cortex of subjects diagnosed with schizophrenia. *Archives of General Psychiatry, 67*, 155–166.

Pantelis, C., Velakoulis, D., McGorry, P. D., Wood, S. J., Suckling, J., Phillips, L. J., Yung, A. R., Bullmore, E. T., Brewer, W., Soulsby, B., Desmond, P., McGuire, P. K. (2003). Neuroanatomical abnormalities before and after onset of psychosis: a cross-sectional and longitudinal MRI comparison. *Lancet, 361*, 281-288.

Paoletti, P., Bellone, C., Zhou, Q. (2013). NMDA receptor subunit diversity: impact on receptor properties, synaptic plasticity and disease. *Nature Reviews Neuroscience, 14*, 383–400.

Pardiñas, A. F., Holmans, P., Pocklington, A. J., Escott-Price, V., Ripke, S., Carrera, N., Legge, S. E., Bishop, S., Cameron, D., Hamshere, M. L., Han, J., Hubbard, L., Lynham, A., Mantripragada, K., Rees, E., MacCabe, J. H., McCarroll, S. A., Baune, B. T., Breen, G., Byrne, E. M., … Walters, J. T. R. (2018). Common schizophrenia alleles are enriched in mutation-intolerant genes and in regions under strong background selection. *Nature Genetics, 50*, 381–389.

Park, J., Lee, K., Kim, K., Yi, S. J. (2022). The role of histone modifications: from neurodevelopment to neurodiseases. *Signal Transduction and Targeted Therapy, 7*, 217.

Park, M. (2018). AMPA receptor trafficking for postsynaptic potentiation. *Frontiers in Cellular Neuroscience, 12*, 361.

Park, S. Y., Kang, M. J., Han, J. S. (2018). Interleukin-1 beta promotes neuronal differentiation through the Wnt5a/RhoA/JNK pathway in cortical neural precursor cells. *Molecular Brain, 11*, 39.

Patterson, P. H. (2005). Maternal influenza infection leads to neuropathology and behavioral abnormalities in adult offspring. *Neuropsychopharmacology, 30,* e9.

Paxinos, G., Watson, C. (2007). The rat brain in stereotaxic coordinates, (6th Edition). Academic Press. London, UK.

Paylor, J. W., Lins, B. R., Greba, Q., Moen, N., de Moraes, R. S., Howland, J. G., Winship, I. R. (2016). Developmental disruption of perineuronal nets in the medial prefrontal cortex after maternal immune activation. *Science Reports, 6*, 37580.

Pedersen, S. F., Ho, Y. (2020). SARS-CoV-2: a storm is raging. *Journal of Clinical Investigation, 130,* 2202–2205.

Pekny, M., Pekna, M. (2014). Astrocyte reactivity and reactive astrogliosis: costs and benefits. *Physiology Reviews, 94,* 1077-1098.

Penn, A. C., Zhang, C. L., Georges, F., Royer, L., Breillat, C., Hosy, E., Petersen, J. D., Humeau, Y., Choquet, D. (2017). Hippocampal LTP and contextual learning require surface diffusion of AMPA receptors. *Nature, 549,* 384-388.

Penninck, L., Ibrahim, E. C., Artiges, E., Gorgievski, V., Desrivières, S., Farley, S., Filippi, I., de Macedo, C. E. A., Belzeaux, R., Banaschewski, T., Bokde, A. L. W., Quinlan, E. B., Flor, H., Grigis, A., Garavan, H., Gowland, P., Heinz, A., Brühl, R., Nees, F., Papadopoulos Orfanos, D., Paus, T., Poustka, L., Fröhner, J. H., Smolka, M. N., Walter, H., Whelan, R., Grenier, J., Schumann, G., Paillère Martinot, M. L., Tzavara, E. T., Martinot, J. L., IMAGEN Consortium (2021). Immune-related genetic overlap between regional gray matter reductions and psychiatric symptoms in adolescents and gene-set validation in a translational model. *Frontiers in Systems Neuroscience, 15*, 725413.

Permyakov, E. A., Uversky, V. N. (2022). What is parvalbumin for? *Biomolecules, 12*, 656.

Perry, B. I., Zammit, S., Jones, P. B., Khandaker, G. M. (2021). Childhood inflammatory markers and risks for psychosis and depression at age 24: examination of temporality and specificity of association in a population-based prospective birth cohort. *Schizophrenia Research, 230*, 69-76.

Perry, V. H. (2007). Stress primes microglia to the presence of systemic inflammation: implications for environmental influences on the brain. *Brain, Behavior and Immunity, 21*, 45-46.

Peschansky, V. J., Wahlestedt, C. (2014). Non-coding RNAs as direct and indirect modulators of epigenetic regulation. *Epigenetics, 9*, 3-12.

Pillai-Kastoori, L., Schutz-Geschwender, A. R., Harford, J. A. (2020). A systematic approach to quantitative Western blot analysis. *Analytical Biochemistry, 593*, 113608.

Pina-Camacho, L., Martinez, K., Diaz-Caneja, C. M., Mezquida, G., Cuesta, M. J., Moreno, C., Amoretti, S., González-Pinto, A., Arango, C., Vieta, E., Castro-Fornieles, J., Lobo, A., Fraguas, D., Bernardo, M., Janssen, J., Parellada, M., PEPs Group (2022). Cortical thinning over two years after first-episode psychosis depends on age of onset. *Schizophrenia, 8*, 20.

Pineda, M., Fernandez, E., Torrents, D., Estevez, R., Lopez, C., Camps, M., Lloberas, J., Zorzano, A., Palacin, M. (1999). Identification of a membrane protein, LAT-2, that co-expresses with 4F2 heavy chain, an L–type amino acid transport activity with broad specificity for small and large zwitterionic amino acids. *Journal of Biological Chemistry, 274*, 19738–19744.

Piontkewitz, Y., Arad, M., Weiner, I. (2012). Tracing the development of psychosis and its prevention: what can be learned from animal models. *Neuropharmacology, 62*, 1273-1289.

Piontkewitz, Y., Assaf, Y., Weiner, I. (2009). Clozapine administration in adolescence prevents postpubertal emergence of brain structural pathology in an animal model of schizophrenia. *Biological Psychiatry, 66*, 1038-1046.

Plotsky, P. M., Meaney, M. J. (1993). Early, postnatal experience alters hypothalamic corticotropin-releasing factor (CRF) mRNA, median eminence CRF content and stress-induced release in adult rats. *Molecular Brain Research, 18*, 195-200.

Plotsky, P. M., Thrivikraman, K. V., Nemeroff, C. B., Caldji, C., Sharma, S., Meaney, M. J. (2005). Long-term consequences of neonatal rearing on central corticotropin-releasing factor systems in adult male rat offspring. *Neuropsychopharmacology, 30,* 2192-2204.

Poggi, G., Albiez, J., Pryce, C. R. (2022). Effects of chronic social stress on oligodendrocyte proliferation-maturation and myelin status in prefrontal cortex and amygdala in adult mice. *Neurobiology of Stress, 18,* 100451.

Polese, D., Fornaro, M., Palermo, M., De Luca, V., de Bartolomeis, A. (2019). Treatment-resistant to antipsychotics: a resistance to everything? Psychotherapy in treatment-resistant schizophrenia and nonaffective psychosis: a 25-year systematic review and exploratory meta-analysis. *Frontiers in Psychiatry, 10*, 210.

Pons-Bennaceur, A., Lozovaya, N. (2017). Electrophysiological investigation of NMDA current properties in brain slices. *Methods in Molecular Biology, 1677*, 231–239.

Potter, H. G. (2021). Behavioural and developmental consequences of maternal immune activation in offspring. PhD Thesis, The University of Manchester.

Potter, H. G., Kowash, H. M., Woods, R. M., Revill, G., Grime, A., Deeney, B., Burgess, M. A., Aarons, T., Glazier, J. D., Neill, J. C., Hager, R. (2023). Maternal behaviours and adult offspring behavioural deficits are predicted by maternal TNFα concentration in a rat model of neurodevelopmental disorders. *Brain, Behavior and Immunity, 108*, 162-175.

Poutoglidou, F., Pourzitaki, C., Manthou, M. E., Saitis, A., Malliou, F., Kouvelas, D. (2021). Infliximab and tocilizumab reduce anxiety-like behavior, improve cognitive performance and reverse neuropathological alterations in juvenile rats with severe autoimmune arthritis. *International Immunopharmacology, 99*, 107917.

Prange, O., Wong, T. P., Gerrow, K., Wang, Y. T., El-Husseini, A. (2004). A balance between excitatory and inhibitory synapses is controlled by PSD-95 and neuroligin. *Proceedings of the National Academy of Sciences of the United States of America, 101*, 13915–13920.

Pries, L. K., Guloksuz, S., Kenis, G. (2017). DNA methylation in schizophrenia. *Neuroepigenomics in Aging and Disease, 978*, 211-236.

Proietti Onori, M., van Woerden, G. M. (2021). Role of calcium/calmodulin-dependent kinase 2 in neurodevelopmental disorders. *Brain Research Bulletin, 171*, 209-220.

Pujadas, L., Rossi, D. andrés, R., Teixeira, C. M., Serra-Vidal, B., Parcerisas, A., Maldonado, R., Giralt, E., Carulla, N., Soriano, E. (2014). Reelin delays amyloid-beta fibril formation and rescues cognitive deficits in a model of Alzheimer's disease. *Nature Communications, 5*, 3443.

Pujol Lopez, Y., Kenis, G., Stettinger, W., Neumeier, K., de Jonge, S., Steinbusch, H. W., Zill, P., van den Hove, D. L., Myint, A. M. (2016). Effects of prenatal Poly I:C exposure on global histone deacetylase (HDAC) and DNA methyltransferase (DNMT) activity in the mouse brain. *Molecular Biology Reports, 43,* 711–717.

Qu, G. J., Ma, J., Yu, Y. C., Fu, Y. (2016). Postnatal development of GABAergic interneurons in the neocortical subplate of mice. *Neuroscience, 322*, 78-93.

Quina, A. S., Buschbeck, M., Di Croce, L. (2006). Chromatin structure and epigenetics. *Biochemical Pharmacolology, 72*, 1563-1569.

Qureshi, I. A., Mehler, M. F. (2012). Emerging roles of non-coding RNAs in brain evolution, development, plasticity and disease. *Nature Reviews Neuroscience, 13*, 528-541.

Qureshi, T., Bjørkmo, M., Nordengen, K., Gundersen, V., Utheim, T. P., Watne, L. O., Storm-Mathisen, J., Hassel, B., Chaudhry, F. A. (2020). Slc38a1 conveys astroglia-derived glutamine into GABAergic interneurons for neurotransmitter GABA synthesis. *Cells, 9,* 1686.

Qureshi, T., Sørensen, C., Berghuis, P., Jensen, V., Dobszay, M. B., Farkas, T., Dalen, K. T., Guo, C., Hassel, B., Utheim, T. P., Hvalby, Ø., Hafting, T., Harkany, T., Fyhn, M., Chaudhry, F. A. (2019). The glutamine transporter Slc38a1 regulates GABAergic neurotransmission and synaptic plasticity. *Cerebal Cortex, 29,* 5166-5179.

Rafa-Zabłocka, K., Kreiner, G., Bagińska, M., Nalepa, I. (2019). The influence of CaMKII and ERK phosphorylation on BDNF changes observed in mice selectively devoid of CREB in serotonergic or noradrenergic neurons. *Pharmacological Reports, 71*, 753–761.

Rai, A., Cross, J. C. (2014). Development of the hemochorial maternal vascular spaces in the placenta through endothelial and vasculogenic mimicry. *Developmental Biology, 387,* 131-141.

Ramachandraiah, C. T., Subramaniam, N., Tancer, M. (2009). The story of antipsychotics: past and present. *Indian Journal of Psychiatry, 51*, 324–326.

Ramaekers, V. T., Quadros, E. V. (2022). Cerebral folate deficiency syndrome: early diagnosis, intervention and treatment strategies. *Nutrients, 14,* 3096.

Ramhøj, L., Axelstad, M., Svingen, T. (2019). Validation of endogenous reference genes in rat cerebral cortex for RT-qPCR analyses in developmental toxicity studies. *PeerJ, 7,* e7181.

Rapoport, J. C., Addington, A. M., Frangou, S. (2005). The neurodevelopmental model of schizophrenia: update 2005. *Molecular Psychiatry, 10*, e614.

Ratnayake, U., Quinn, T. A., Castillo-Melendez, M., Dickinson, H., Walker, D. W. (2012). Behaviour and hippocampus-specific changes in spiny mouse neonates after treatment of the mother with the viral-mimetic Poly I:C at mid-pregnancy. *Brain, Behavior and Immunity, 26*, 1288-1299.

Ravelli, G. P., Stein, Z. A., Susser, M. W. (1976). Obesity in young men after famine exposure *in utero* and early infancy. *New England Journal of Medicine, 295*, 349-353.

Read, J., Perry, B. D., Moskowitz, A., Connolly, J. (2001). The contribution of early traumatic events to schizophrenia in some patients: a traumagenic neurodevelopmental model. *Psychiatry - Interpersonal and Biological Processes, 64*, 319-345.

Reemst, K., Noctor, S. C., Lucassen, P. J., Hol, E. M. (2016). The indispensable roles of microglia and astrocytes during brain development. *Frontiers in Human Neuroscience, 10*, 566.

Rees, E., Walters, J. T., Georgieva, L., Isles, A. R., Chambert, K. D., Richards, A. L., Mahoney-Davies, G., Legge, S. E., Moran, J. L., McCarroll, S. A., O'Donovan, M. C., Owen, M. J., Kirov, G. (2014). Analysis of copy number variations at 15 schizophrenia-associated loci. *The British Journal of Psychiatry, 204*, 108–114.

Refsum, H. (2001). Folate, vitamin B12 and homocysteine in relation to birth defects and pregnancy outcome. *British Journal of Nutrition, 85,* 109-113.

Reichelt, A. C., Hare, D. J., Bussey, T. J., Saksida, L. M. (2019). Perineuronal nets: plasticity, protection and therapeutic potential. *Trends in Neuroscience, 42*, 458-470

Reik, W. (2007). Stability and flexibility of epigenetic gene regulation in mammalian development. *Nature, 447*, 425–432.

Reinhard, S. M., Razak, K., Ethell, I. M. (2015). A delicate balance: role of MMP-9 in brain development and pathophysiology of neurodevelopmental disorders. *Frontiers in Cellular Neuroscience, 9*, 280.

Reininghaus, U., Böhnke, J. R., Chavez-Baldini, U., Gibbons, R., Ivleva, E., Clementz, B. A., Pearlson, G. D., Keshavan, M. S., Sweeney, J. A., Tamminga, C. A. (2019). Transdiagnostic dimensions of psychosis in the Bipolar-Schizophrenia Network on Intermediate Phenotypes (B-SNIP). *World Psychiatry, 18*, 67–76.

Reisinger, S., Khan, D., Kong, E., Berger, A., Pollak, A., Pollak, D. D. (2015). The poly(I:C)-induced maternal immune activation model in preclinical neuropsychiatric drug discovery. *Pharmacology and Therapeutics, 149*, 213-226.

Reynolds, G. P., Neill, J. C. (2016). Modelling the cognitive and neuropathological features of schizophrenia with phencyclidine. *Journal of Psychopharmacology, 30,* 1141–1144.

Rice, J. C., Allis, C. D. (2001). Histone methylation versus histone acetylation: new insights into epigenetic regulation. *Current Opinion in Cell Biology, 13*, 263-273.

Richetto, J., Calabrese, F., Meyer, U., Riva, M. A. (2013). Prenatal versus postnatal maternal factors in the development of infection-induced working memory impairments in mice. *Brain, Behaviour and Immunity, 33*, 190-200.

Richetto, J., Chesters, R., Cattaneo, A., Labouesse, M. A., Gutierrez, A. M. C., Wood, T. C., Luoni, A., Meyer, U., Vernon, A., Riva, M. A. (2017a). Genome-wide transcriptional profiling and structural magnetic resonance imaging in the maternal immune activation model of neurodevelopmental disorders. *Cerebral Cortex, 27,* 3397-3413.

Richetto, J., Massart, R., Weber-Stadlbauer, U., Szyf, M., Riva, M. A., Meyer, U. (2017b). Genome-wide DNA methylation changes in a mouse model of infection-mediated neurodevelopmental disorders. *Biological Psychiatry, 81*, 265-276.

Riley, B. (2004). Linkage studies of schizophrenia. *Neurotoxicity Research, 6*, 17–34.

Ripke, S., Neale, B. M., Corvin, A., Walters, J. T. R., Farh, K. H., Holmans, P. A., Lee, P., Bulik-Sullivan, B., Collier, D. A., Huang, H. L., Pers, T. H., Agartz, I., Agerbo, E., Albus, M., Alexander, M., Amin, F., Bacanu, S. A., Begemann, M., Belliveau, R. A., Bene, J., … O'Donovan, M. C. (2014). Biological insights from 108 schizophrenia-associated genetic loci. *Nature, 511*, 421-427.

Ripke, S., O'Dushlaine, C., Chambert, K., Moran, J. L., Kähler, A. K., Akterin, S., Bergen, S. E., Collins, A. L., Crowley, J. J., Fromer, M., Kim, Y., Lee, S. H., Magnusson, P. K., Sanchez, N., Stahl, E. A., Williams, S., Wray, N. R., Xia, K., Bettella, F., Borglum, A. D., … Sullivan, P. F. (2013). Genome-wide association analysis identifies 13 new risk loci for schizophrenia. *Nature Genetics*, *45*, 1150–1159.

Ripke, S., Sanders, A. R., Kendler, K. S., Levinson, D. F., Sklar, P., Holmans, P. A., Lin, D. Y., Duan, J., Ophoff, R. A. andreassen, O. A., Scolnick, E., Cichon, S., Clair, D. S., Corvin, A., Gurling, H., Werge, T., Rujescu, D., Blackwood, D. H. R., Pato, C. N., Malhotra, A. K., … Gejman, P. V. (2011). Genome-wide association study identifies five new schizophrenia loci. *Nature Genetics, 43,* 969-976.

Roadmap Epigenomics Consortium, Kundaje, A., Meuleman, W., Ernst, J., Bilenky, M., Yen, A., Heravi-Moussavi, A., Kheradpour, P., Zhang, Z., Wang, J., Ziller, M. J., Amin, V., Whitaker, J. W., Schultz, M. D., Ward, L. D., Sarkar, A., Quon, G., Sandstrom, R. S., Eaton, M. L., Wu, Y. C., … Kellis, M. (2015). Integrative analysis of 111 reference human epigenomes. *Nature, 518,* 317–330.

Roderick, R. C., Kentner, A. C. (2019). Building a framework to optimize animal models of maternal immune activation: like your ongoing home improvements, it's a work in progress. *Brain, Behavior and Immunity, 75*, 6–7.

Rokita, K. I., Dauvermann, M. R., Donohoe, G. (2018). Early life experiences and social cognition in major psychiatric disorders: a systematic review. *European Psychiatry, 53*, 123-133.

Rolls, A., Shechter, R., London, A., Segev, Y., Jacob-Hirsch, J., Amariglio, N., Rechavi, G., Schwartz, M. (2008). Two faces of chondroitin sulfate proteoglycan in spinal cord repair: a role in microglia/macrophage activation. *PLoS Medicine, 5,* e171.

Romero, R., Avila, C., Santhanam, U., Sehgal, P. B. (1990). Amniotic-fluid interleukin-6 in preterm labor - association with infection. *Journal of Clinical Investigation, 85*, 1392-1400.

Romero, R., Manogue, K. R., Mitchell, M. D., Wu, Y. K., Oyarzun, E., Hobbins, J. C., Cerami, A. (1989). Infection and labor. IV. Cachectin-tumor necrosis factor in the amniotic fluid of women with intraamniotic infection and preterm labor. *American Journal of Obstetrics and Gynecology, 161,* 336-341.

Rose, D. R., Careaga, M., Van de Water, J., McAllister, K., Bauman, M. D., Ashwood, P. (2017). Long-term altered immune responses following foetal priming in a non-human primate model of maternal immune activation. *Brain, Behavior and Immunity, 63,* 60–70.

Roseboom, T., de Rooij, S., Painter, R. (2006). The Dutch famine and its long-term consequences for adult health. *Early Human Development, 82*, 485-491.

Rossier, G., Meier, C., Bauch, C., Summa, V., Sordat, B., Verrey, F., Kuhn, L. C. (1999). LAT2, a new basolateral 4F2hc/CD98-associated amino acid transporter of kidney and intestine. *Journal of Biological Chemistry, 274,* 34948–34954

Roussos, P., Haroutunian, V. (2014). Schizophrenia: susceptibility genes and oligodendroglial and myelin related abnormalities. *Frontiers in Cellular Neuroscience, 8*, 5.

Roy, P. H., Weissbach, A. (1975). DNA methylase from HeLa cell nuclei. *Nucleic Acids Research, 2,* 1669-1684.

Rubini, E., Baijens, I. M. M., Horánszky, A., Schoenmakers, S., Sinclair, K. D., Zana, M., Dinnyés, A., Steegers-Theunissen, R. P. M., Rousian, M. (2021). Maternal one-carbon metabolism during the periconceptional period and human foetal brain growth: a systematic review. *Genes, 12,* 1634.

Rubio, J. M., Taipale, H., Tanskanen, A., Correll, C. U., Kane, J. M., Tiihonen, J. (2021). Long-term continuity of antipsychotic treatment for schizophrenia: a nationwide study. *Schizophrenia Bulletin, 47,* 1611–1620.

Russell J. A. (1980). Milk yield, suckling behaviour and milk ejection in the lactating rat nursing litters of different sizes. *The Journal of Physiology, 303*, 403–415.

Saab, A. S., Nave, K. A. (2017). Myelin dynamics: protecting and shaping neuronal functions. *Current Opinion in Neurobiology, 47,* 104-112.

Saavedra, L. M., Hernández-Velázquez, M. G., Madrigal, S., Ochoa-Zarzosa, A., Torner, L. (2021). Long-term activation of hippocampal glial cells and altered emotional behavior in male and female adult rats after different neonatal stressors. *Psychoneuroendocrinology, 126,* 105164.

Sachar, E. J., Kanter, S. S., Buie, D., Engle, R., Mehlman, R. (1970). Psychoendocrinology of ego disintegration. *American Journal of Psychiatry, 126*, 1067-1078.

Saha, S., Chant, D., McGrath, J. (2007). A systematic review of mortality in schizophrenia: is the differential mortality gap worsening over time? *Archives of General Psychiatry, 64*, 1123-1131.

Saleem, S., Shaukat, F., Gul, A., Arooj, M., Malik, A. (2017). Potential role of amino acids in pathogenesis of schizophrenia. *International Journal of Health Science, 11*, 63-68.

Salgado-Pineda, P., Caclin, A., Baeza, I., Junqué, C., Bernardo, M., Blin, O., Fonlupt, P. (2007). Schizophrenia and frontal cortex: where does it fail? *Schizophrenia Research, 91,* 73-81.

Samuelsson, A. M., Jennische, E., Hansson, H. A., Holmang, A. (2006). Prenatal exposure to interleukin-6 results in inflammatory neurodegeneration in hippocampus with NMDA/GABA(A) dysregulation and impaired spatial learning. *American Journal of Physiology - Regulatory, Integrative and Comparative Physiology, 290,* 1345-1356.

Sánchez-Sarasúa, S., Meseguer-Beltrán, M., García-Díaz, C., Beltrán-Bretones, M. T., ElMlili, N., Sánchez-Pérez, A. M. (2022). IRS1 expression in hippocampus is age-dependent and is required for mature spine maintenance and neuritogenesis. *Molecular and Cellular Neuroscience, 118*, 103693.

Santos, F., Peters, A. H., Otte, A. P., Reik, W., Dean, W. (2005). Dynamic chromatin modifications characterise the first cell cycle in mouse embryos. *Developmental Biology, 280*, 225-236.

Sarieva, K., Kagermeier, T., Khakipoor, S., Atay, E., Yentür, Z., Becker, K., Mayer, S. (2023). Human brain organoid model of maternal immune activation identifies radial glia cells as selectively vulnerable. *Molecular Psychiatry, 6*, 1-13.

Sarkar, T., Patro, N., Patro, I. K. (2019). Cumulative multiple early life hits- a potent threat leading to neurological disorders. *Brain Research Bulletin, 147*, 58-68.

Sato, Y., Taoka, M., Sugiyama, N., Kubo, K., Fuchigami, T., Asada, A., Saito, T., Nakajima, K., Isobe, T., Hisanaga, S. (2007). Regulation of the interaction of Disabled-1 with CIN85 by phosphorylation with Cyclin-dependent kinase 5. *Genes to Cells, 12,* 1315-1327.

Saxonov, S., Berg, P., Brutlag, D. L. (2006). A genome-wide analysis of CpG dinucleotides in the human genome distinguishes two distinct classes of promoters. *Proceedings of the National Academy of Sciences of the United States of America, 103,* 1412-1417.

Schafer, M., Fruttiger, M., Montag, D., Schachner, M., Martini, R. (1996). Disruption of the gene for the myelin-associated glycoprotein improves axonal regrowth along myelin in C57BL/Wlds mice. *Neuron, 16,* 1107–1113.

Schalbetter, S. M., von Arx, A. S., Cruz-Ochoa, N., Dawson, K., Ivanov, A., Mueller, F. S., Lin, H. Y., Amport, R., Mildenberger, W., Mattei, D., Beule, D., Földy, C., Greter, M., Notter, T., Meyer, U. (2022). Adolescence is a sensitive period for prefrontal microglia to act on cognitive development. *Science Advances, 8,* eabi6672.

Schalinski, I., Teicher, M. H., Carolus, A. M., Rockstroh, B. (2018). Defining the impact of childhood adversities on cognitive deficits in psychosis: an exploratory analysis. *Schizophrenia Research, 192*, 351-356.

Schander, J. A., Marvaldi, C., Correa, F., Wolfson, M. L., Cella, M., Aisemberg, J., Jensen, F., Franchi, A. M. (2021). Maternal environmental enrichment modulates the immune response against an inflammatory challenge during gestation and protects the offspring. *Journal of Reproductive Immunology, 144*, 103273.

Scheiermann, C., Kunisaki, Y., Frenette, P. S. (2013). Circadian control of the immune system. *Nature Reviews Immunology, 13,* 190-198.

Schittmayer, M., Birner-Gruenberger, R., Zamboni, N. (2018). Quantification of cellular folate species by LC-MS after stabilization by derivatization. *Analytical Chemistry, 90*, 7349-7356.

Schmidt-Kastner, R., Guloksuz, S., Kietzmann, T., van Os, J., Rutten, B. P. F. (2020). Analysis of GWAS-derived schizophrenia genes for links to ischemia-hypoxia response of the brain. *Frontiers in Psychiatry, 11,* 393.

Schofield, C. M., Hsu, R., Barker, A. J., Gertz, C. C., Blelloch, R., Ullian, E. M. (2011). Monoallelic deletion of the microRNA biogenesis gene Dgcr8 produces deficits in the development of excitatory synaptic transmission in the prefrontal cortex. *Neural Development, 6,* e11.

Schoof, E., Girstl, M., Frobenius, W., Kirschbaum, M., Dorr, H. G., Rascher, W., Dotsch, J. (2001). Decreased gene expression of 11 beta-hydroxysteroid dehydrogenase type 2 and 15-hydroxyprostaglandin dehydrogenase in human placenta of patients with preeclampsia. *Journal of Clinical Endocrinology and Metabolism, 86,* 1313-1317.

Schwarz, J. M., Sholar, P. W., Bilbo, S. D. (2012). Sex differences in microglial colonization of the developing rat brain. *Journal of Neurochemistry, 120*, 948-963.

Schwartz, C. L., Christiansen, S., Vinggaard, A. M., Axelstad, M., Hass, U., Svingen, T. (2019a). Anogenital distance as a toxicological or clinical marker for foetal androgen action and risk for reproductive disorders. *Archives of Toxicology, 93,* 253-272.

Schwartz, E. K., Docherty, N. M., Najolia, G. M., Cohen, A. S. (2019b). Exploring the racial diagnostic bias of schizophrenia using behavioral and clinical-based measures. *Journal of Abnormal Psychology, 128*, 263–271.

Schwartz, R. C., Blankenship, D. M. (2014). Racial disparities in psychotic disorder diagnosis: a review of empirical literature. *World Journal of Psychiatry, 4*, 133–140.

Schweitzer, B., Singh, J., Fejtova, A., Groc, L., Heine, M., Frischknecht. (2017). Hyaluronic acid based extracellular matrix regulates surface expression of GluN2B containing NMDA receptors. *Science Reports, 7,* 10991.

Schwendener, S., Meyer, U., Feldon, J. (2009). Deficient maternal care resulting from immunological stress during pregnancy is associated with a sex-dependent enhancement of conditioned fear in the offspring. *Journal of Neurodevelopmental Disorders, 1*, 15-32.

Seeman, P., Chau-Wong, M., Tedesco, J., Wong, K. (1975). Brain receptors for antipsychotic drugs and dopamine: direct binding assays. *Proceedings of the National Academy of Sciences of the United States of America, 72,* 4376–4380.

Selemon, L. (2013). A role for synaptic plasticity in the adolescent development of executive function. *Translational Psychiatry, 3*, e238.

Sellgren, C. M., Gracias, J., Watmuff, B., Biag, J. D., Thanos, J. M., Whittredge, P. B., Fu, T., Worringer, K., Brown, H. E., Wang ,J., Kaykas, A., Karmacharya, R., Goold, C. P., Sheridan, S. D., Perlis, R. H. (2019). Increased synapse elimination by microglia in schizophrenia patient-derived models of synaptic pruning. *Nature Neuroscience, 22*, 374-385.

Semahegn, A., Torpey, K., Manu, A., Assefa, N., Tesfaye, G., Ankomah, A. (2018). Psychotropic medication non-adherence and associated factors among adult patients with major psychiatric disorders: a protocol for a systematic review. *Systematic Reviews, 7*, 10.

Sendžikaitė, G., Hanna, C.W., Stewart-Morgan, K.R., Ivanova, E., Kelsey, G. (2019). A DNMT3A PWWP mutation leads to methylation of bivalent chromatin and growth retardation in mice. *Nature Communications, 10*, 1884.

Sengupta, P. (2013). The laboratory rat: relating its age with human's. *International Journal of Preventative Medicine, 4*, 624-630.

Seutter, S., Winfield, J., Esbitt, A., Snyder, S., Magner, A., Kim, K., Carcuffe, C., Schmoyer, J., Kamrani, P., Mercando, J., Shamseddin, S. M., Green, K., Borghaei, R. C. (2020). Interleukin 1β and Prostaglandin E2 affect expression of DNA methylating and demethylating enzymes in human gingival fibroblasts. *International Immunopharmacology, 78,* 105920.

Sferruzzi-Perri, A. N., Camm, E. J. (2016) The programming power of the placenta. *Frontiers in Physiology, 7,* 33.

Shahidehpour, R. K., Higdon, R. E., Crawford, N. G., Neltner, J. H., Ighodaro, E. T., Patel, E., Price, D., Nelson, P. T., Bachstetter, A. D. (2021). Dystrophic microglia are associated with neurodegenerative disease and not healthy aging in the human brain. *Neurobiology of Aging, 99*, 19-27.

Shallie, P. D., Naicker, T. (2019). The placenta as a window to the brain: a review on the role of placental markers in prenatal programming of neurodevelopment. *International Journals of Developmental Neuroscience, 73*, 41-49.

Shams, M., Kilby, M. D., Somerset, D. A., Howie, A. J., Gupta, A., Wood, P. J., Afnan, M., Stewart, P. M. (1998). 11 beta-hydroxysteroid dehydrogenase type 2 in human pregnancy and reduced expression in intrauterine growth restriction. *Human Reproduction, 13*, 799-804.

Sharma, A. (2013). Cambridge Neuropsychological Test Automated Battery. In: Volkmar, F.R. (eds) Encyclopedia of Autism Spectrum Disorders. pp498-515. Springer. New York, USA.

Shayevitch, R., Askayo, D., Keydar, I., Ast, G. (2018). The importance of DNA methylation of exons on alternative splicing. *RNA, 24,* 1351-1362.

Shen, H. H. (2018). Core Concept: Perineuronal nets gain prominence for their role in learning, memory and plasticity. *Proceedings of the National Academy of Sciences of the United States of America, 115*, 9813-9815.

Shi, D. Q., Ali, I., Tang, J., Yang, W. C. (2017). New Insights into 5hmC DNA modification: generation, distribution and function. *Frontiers in Genetics, 8,* e100.

Shi, L., Fatemi, S. H., Sidwell, R. W., Patterson, P. H. (2003). Maternal influenza infection causes marked behavioral and pharmacological changes in the offspring. *Journal of Neuroscience, 23*, 297-302.

Shi, L., Zhang, Z., Su, B. (2016). Sex biased gene expression profiling of human brains at major developmental stages. *Science Reports, 6*, 21181.

Shivakumar, V., Sreeraj, V. S., Subbanna, M., Kalmady, S. V., Amaresha, A. C., Narayanaswamy, J. C., Debnath, M., Venkatasubramanian, G. (2020). Differential impact of interleukin-6 promoter gene polymorphism on hippocampal volume in antipsychotic-naïve schizophrenia patients. *Indian Journal of Psychiatry, 62*, 36-42.

Shirvani-Farsani, Z., Maloum, Z., Bagheri-Hosseinabadi, Z., Vilor-Tejedor, N., Sadeghi, I. (2021). DNA methylation signature as a biomarker of major neuropsychiatric disorders. *Journal of Psychiatric Research, 141*, 34-49.

Shook, L. L., Sullivan, E. L., Lo, J. O., Perlis, R. H., Edlow, A. G. (2022). COVID-19 in pregnancy: implications for foetal brain development. *Trends in Molecular Medicine, 28,* 319-330,

Short, S. J., Lubach, G. R., Karasin, A. I., Olsen, C. W., Styner, M., Knickmeyer, R. C., Gilmore, J. H., Coe, C. L., (2010). Maternal influenza infection during pregnancy impacts postnatal brain development in the rhesus monkey. *Biological Psychiatry, 67*, 965-973.

Shuffrey, L. C., Firestein, M. R., Kyle, M. H., Fields, A., Alcántara, C., Amso, D., Austin, J., Bain, J. M., Barbosa, J., Bence, M., Bianco, C., Fernández, C. R., Goldman, S., Gyamfi-Bannerman, C., Hott, V., Hu, Y., Hussain, M., Factor-Litvak, P., Lucchini, M., Mandel, A., … Dumitriu, D. (2022). Association of birth during the COVID-19 pandemic with neurodevelopmental status at 6 months in infants with and without *in utero* exposure to maternal SARS-CoV-2 infection. *JAMA Pediatrics, 176*, e215563.

Shukla, A., Choudhari, S. G., Gaidhane, A. M., Quazi Syed, Z. (2022). Role of art therapy in the promotion of mental health: a critical review. *Cureus, 14*, e28026.

Sigurdsson, T., Duvarci, S. (2016). Hippocampal-prefrontal interactions in cognition, behavior and psychiatric disease. *Frontiers in Systems Neuroscience, 9*, 190.

Sinagra, M., Verrier, D., Frankova, D., Korwek, K. M., Blahos, J., Weeber, E. J., Manzoni, O. J., Chavis, P. (2005). Reelin, very-low-density lipoprotein receptor and apolipoprotein E receptor 2 control somatic NMDA receptor composition during hippocampal maturation *in vitro*. *Journal of Neuroscience, 25*, 6127–6136.

Sinclair, D., Fillman, S. G., Webster, M. J., Weickert, C. S. (2013). Dysregulation of glucocorticoid receptor co-factors FKBP5, BAG1 and PTGES3 in prefrontal cortex in psychotic illness. *Scientific Reports, 3*, 3539.

Sinclair, D., Tsai, S. Y., Woon, H. G., Weickert, C. S. (2011). Abnormal glucocorticoid receptor mRNA and protein isoform expression in the prefrontal cortex in psychiatric illness. *Neuropsychopharmacology, 36*, 2698-2709.

Singer, B. D. (2019). A practical guide to the measurement and analysis of DNA methylation. *American Journal of Respiratory Cell and Molecular Biology, 61,* 417–428.

Singh, N., Ecker, G. F. (2018). Insights into the structure, function and ligand discovery of the large neutral amino acid transporter 1, LAT1. *International Journal of Molecular Science, 19,* 1278.

Sitko, K., Bewick,B. M., Owens, D., Masterson, C. (2020). Meta-analysis and meta-regression of cognitive behavioral therapy for psychosis (CBTp) across time: the effectiveness of CBTp has improved for delusions. *Schizophrenia Bulletin, 1*, sgaa023

Siu, C. R., Balsor, J. L., Jones, D. G., Murphy, K. M. (2015). Classic and Golli Myelin Basic Protein have distinct developmental trajectories in human visual cortex. *Frontiers in Neuroscience, 9*, 138.

Sizer, H., Brown, E., Geros, H., Yung, A., Nelson, B., McGorry, P., O'Donoghue, B. (2022). Outcomes for first-episode psychosis after entry via an at-risk mental state clinic compared to direct entry to a first episode of psychosis service: A systematic review and meta-analysis. *Schizophrenia Research, 240*, 214–219.

Sjöstedt, E., Zhong, W., Fagerberg, L., Karlsson, M., Mitsios, N., Adori, C., Oksvold, P., Edfors, F., Limiszewska, A., Hikmet, F., Huang, J., Du, Y., Lin, L., Dong, Z., Yang, L., Liu, X., Jiang, H., Xu, X., Wang, J., Yang, H., Bolund, L., Mardinoglu, A., Zhang, C., von Feilitzen, K., Lindskog, C., Pontén, F., Luo, Y., Hökfelt, T., Uhlén, M., Mulder, J. (2020). An atlas of the protein-coding genes in the human, pig and mouse brain. *Science, 367*, e5947.

Skaper, S. D. (2019). Oligodendrocyte precursor cells as a therapeutic target for demyelinating diseases. *Progress in Brain Research, 245*, 119-144.

Slob, A. K., Van der Werff Ten Bosch, J. J. (1975). Sex differences in body growth in the rat. *Physiology and Behavior, 14*, 353–361.

Smith, A, M., King, J. J., West, P. R., Ludwig, M. A., Donley, E. L. R., Burrier, R. E., Amaral, D. G. (2019). Amino acid dysregulation metabotypes: potential biomarkers for diagnosis and individualized treatment for subtypes of autism spectrum disorder. *Biological Psychiatry, 85*, 345-354.

Smith, K. R., Kopeikina, K. J., Fawcett-Patel, J. M., Leaderbrand, K., Gao, R., Schürmann, B., Myczek, K., Radulovic, J., Swanson, G. T., Penzes, P. (2014). Psychiatric risk factor ANK3/ankyrin-G nanodomains regulate the structure and function of glutamatergic synapses. *Neuron, 84,* 399–415.

Smith, S. E., Li, J., Garbett, K., Mirnics, K., Patterson, P. H. (2007). Maternal immune activation alters foetal brain development through interleukin-6. *The Journal of Neuroscience, 27*, 10695-10702.

Smith, S. M., Vale, W. W. (2006). The role of the hypothalamic-pituitary-adrenal axis in neuroendocrine responses to stress. *Dialogues in Clinical Neuroscience, 8*, 383-395.

Soares, M. J., Chakraborty, D., Karim Rumi, M. A., Konno, T., Renaud, S. J. (2012). Rat placentation: an experimental model for investigating the hemochorial maternal-foetal interface. *Placenta, 33*, 233-243.

Sofroniew, M, V. (2014). Astrogliosis. *Cold Spring Harbour Perspectives in Biology, 7,* e020420.

Solanky, N., Requena Jimenez, A., D'Souza, S. W., Sibley, C. P., Glazier, J. D. (2010). Expression of folate transporters in human placenta and implications for homocysteine metabolism. *Placenta, 31,* 134-143.

Sousa, N., Almeida, O. F., Wotjak, C. T. (2006). A hitchhiker's guide to behavioral analysis in laboratory rodents. *Genes, Brain and Behavior, 5,* 5–24.

Souza, D. G., Bellaver, B., Souza, D. O., Quincozes-Santos, A. (2013). Characterization of adult rat astrocyte cultures. *PLoS One, 8*, e60282.

Sozuguzel, M. D., Sazci, A., Yildiz, M. (2019). Female gender specific association of the Reelin (RELN) gene rs7341475 variant with schizophrenia. *Molecular Biology Reports, 46*, 3411–3416.

Spark, D. L., Fornito, A., Langmead, C. J., Stewart, G. D. (2022). Beyond antipsychotics: a twenty-first century update for preclinical development of schizophrenia therapeutics. *Translational Psychiatry, 12*, 147.

Spear, L. P. (2000). The adolescent brain and age-related behavioral manifestations. *Neuroscience and Biobehavioral Reviews, 24*, 417-463.

Spijker, S., Koskinen, M. K., Riga, D. (2020). Incubation of depression: ECM assembly and parvalbumin interneurons after stress. *Neuroscience and Biobehavioral Reviews, 118*, 65–79.

Spruijt, S. G., Gnerlich, F., Smits, A. H., Pfaffeneder, T., Jansen, P. W. T. C., Bauer, C., Münzel, M., Wagner, M., Müller, M., Khan, F., Eberl, H. C., Mensinga, A., Brinkman, A. B., Lephikov, K., Müller, U., Walter, J., Boelens, R., Ingen, H., Leonhardt, H., Carell, T., Vermeulen, M. (2013). Dynamic readers for 5-(hydroxy)methylcytosine and its oxidized derivatives. *Cell, 152,* 1146-1159.

Stadelmann, C., Timmler, S., Barrantes-Freer, A., Simons, M. (2019). Myelin in the central nervous system: structure, function and pathology. *Physiology Reviews, 99,* 1381-1431.

Steg, L. C., Shireby, G. L., Imm, J., Davies, J. P., Franklin, A., Flynn, R., Namboori, S. C., Bhinge, A., Jeffries, A. R., Burrage, J., Neilson, G. W. A., Walker, E. M., Perfect, L. W., Price, J., McAlonan, G., Srivastava, D. P., Bray, N. J., Cope, E. L., Jones, K. M., Allen, N. D., Pishva, E., Dempster, E. L., Lunnon, K., Mill, J., Hannon, E. (2021). Novel epigenetic clock for foetal brain development predicts prenatal age for cellular stem cell models and derived neurons. *Molecular Brain, 14,* 98.

Stegmayer, K., Horn, H., Federspiel, A., Razavi, N., Bracht, T., Laimbock, K., Strik, W., Dierks, T., Wiest, R., Muller, T. J., Walther, S. (2014). Ventral striatum gray matter density reduction in patients with schizophrenia and psychotic emotional dysregulation. *Neuroimage Clinical, 4,* 232-239.

Stephens, M. A. C., Wand, G. (2012). Stress and the HPA axis role of glucocorticoids in alcohol dependence. *Alcohol Research - Current Reviews, 34*, 468-483.

Stepniak, B., Papiol, S., Hammer, C., Ramin, A., Everts, S., Hennig, L., Begemann, M., Ehrenreich, H. (2014). Accumulated environmental risk determining age at schizophrenia onset: a deep phenotyping-based study. *The Lancet - Psychiatry, 1,* 444–453.

Stertz, L., Di Re, J., Pei, G., Fries, G. R., Mendez, E., Li, S., Smith-Callahan, L., Raventos, H., Tipo, J., Cherukuru, R., Zhao, Z., Liu, Y., Jia, P., Laezza, F., Walss-Bass, C. (2021). Convergent genomic and pharmacological evidence of PI3K/GSK3 signaling alterations in neurons from schizophrenia patients. *Neuropsychopharmacology, 46,* 673-682.

Steullet, P., Cabungcal, J. H., Coyle, J., Didriksen, M., Gill, K., Grace, A. A., Hensch, T. K., LaMantia, A. S., Lindemann, L., Maynard, T. M., Meyer, U., Morishita, H., O'Donnell, P., Puhl, M., Cuenod, M., Do, K. Q. (2017). Oxidative stress-driven parvalbumin interneuron impairment as a common mechanism in models of schizophrenia. *Molecular Psychiatry, 22*, 936–943.

Stevens, S. R., Longley, C. M., Ogawa, Y., Teliska, L. H., Arumanayagam, A. S., Nair, S., Oses-Prieto, J. A., Burlingame, A. L., Cykowski, M. D., Xue, M., Rasband, M. N. (2021). Ankyrin-R regulates fast-spiking interneuron excitability through perineuronal nets and Kv3.1b K+ channels. *eLife, 10,* e66491.

Stiles, J., Jernigan, T. L. (2010). The basics of brain development. *Neuropsychology Reviews, 20*, 327-348.

Straub, R. H., Cutolo, M. (2016). Glucocorticoids and chronic inflammation. *Rheumatology, 55*, 6-14.

Stroup, T. S., Gray, N. (2018). Management of common adverse effects of antipsychotic medications. *World Psychiatry, 17,* 341-356.

Su, J., Zhang, Y., Lv, J., Liu, H., Tang, X., Wang, F., Qi, Y., Feng, Y., Li, X. (2009). CpG_MI: a novel approach for identifying functional CpG islands in mammalian genomes. *Nucleic Acids Research, 38*, e6.

Su, M., Soomro, S. H., Jie, J., Fu, H. (2021). Effects of the extracellular matrix on myelin development and regeneration in the central nervous system. *Tissue and Cell, 69*, 101444.

Suderman, M., McGowan, P. O., Sasaki, A., Huang, T. C., Hallett, M. T., Meaney, M. J., Turecki, G., Szyf, M. (2012). Conserved epigenetic sensitivity to early life experience in the rat and human hippocampus. *Proceedings of the National Academy of Sciences of the United States of America, 109*, 17266–17272.

Sullivan, P. F., Kendler, K. S., Neale, M. C. (2003). Schizophrenia as a complex trait: evidence from a meta-analysis of twin studies. *Archives of General Psychiatry, 60,* 1187-1192.

Sun, Y., Koyama, Y., Shimada, S. (2022). Inflammation from peripheral organs to the brain: how does systemic inflammation cause neuroinflammation? *Frontiers in Aging Neuroscience,14*, e903455.

Susuki, K., Chang, K. J., Zollinger, D. R., Liu, Y., Ogawa, Y., Eshed-Eisenbach, Y., Dours-Zimmermann, M. T., Oses-Prieto, J. A., Burlingame, A. L., Seidenbecher, C. I., Zimmermann, D. R., Oohashi, T., Peles, E., Rasband, M. N. (2013). Three mechanisms assemble central nervous system nodes of Ranvier. *Neuron, 78,* 469-482.

Suvorov, A., Vandenberg, L. N. (2016). To cull or not to cull? Considerations for studies of endocrine-disrupting chemicals. *Endocrinology, 157,* 2586-2594.

Swartz, M. S., Perkins, D. O., Stroup, T. S., Davis, S. M., Capuano, G., Rosenheck, R. A., Reimherr, F., McGee, M. F., Keefe, R. S. E., McEvoy, J. P., Hsiao, J. K., Lieberman, J. A. (2007). Effects of antipsychotic medications on psychosocial functioning in patients with chronic schizophrenia: findings from the NIMH CATIE study. *American Journal of Psychiatry, 164*, 428-436

Szklarczyk, D., Gable, A. L., Nastou, K. C., Lyon, D., Kirsch, R., Pyysalo, S., Doncheva, N. T., Legeay, M., Fang, T., Bork, P., Jensen, L. J., von Mering, C. (2021). The STRING database in 2021: customizable protein–protein networks and functional characterization of user-uploaded gene/measurement sets. *Nucleic Acids Research, 49*, 605-612.

Szoke, A., Charpeaud, T., Galliot, A. M., Vilain, J., Richard, J. R., Leboyer, M., Llorca, P. M., Schurhoff, F. (2014). Rural-urban variation in incidence of psychosis in France: a prospective epidemiologic study in two contrasted catchment areas. *BMC Psychiatry, 14,* 78.

Szulwach, K. E., Li, X., Li, Y., Song, C. X., Wu, H., Dai, Q., Irier, H., Upadhyay, A. K., Gearing, M., Levey, A. I., Vasanthakumar, A., Godley, L. A., Chang, Q., Cheng, X., He, C., Jin, P. (2011). 5-hmC-mediated epigenetic dynamics during postnatal neurodevelopment and aging. *Nature Neuroscience, 14,* 1607-1616.

Szyf, M., Weaver, I., Meaney, M. (2007). Maternal care, the epigenome and phenotypic differences in behavior. *Reproductive Toxicology, 24*, 9–19.

Taber, K. H., Hurley, R. A., Yudofsky, S. C. (2010). Diagnosis and treatment of neuropsychiatric disorders. *Annual Review of Medicine, 61*, 121-133.

Tahiliani, M., Koh, K. P., Shen, Y. H., Pastor, W. A., Bandukwala, H., Brudno, Y., Agarwal, S., Iyer, L. M., Liu, D. R., Aravind, L., Rao, A. (2009). Conversion of 5-methylcytosine to 5-hydroxymethylcytosine in mammalian DNA by MLL partner TET1. *Science, 324*, 930-935.

Takizawa, T., Nakashima, K., Namihira, M., Ochiai, W., Uemura, A., Yanagisawa, M., Fujita, N., Nakao, M., Taga, T. (2001). DNA methylation is a critical cell-intrinsic determinant of astrocyte differentiation in the foetal brain. *Developmental Cell, 1*, 749-758.

Tamminga, C. (2008). Domains of dysfunction in schizophrenia: implications for diagnosis. *World Psychiatry, 7,* 34-35.

Tanila, H. (2018). Testing cognitive functions in rodent disease models: present pitfalls and future perspectives. *Behavioural Brain Research, 352*, 23-27.

Tanimizu, T., Kenney, J. W., Okano, E., Kadoma, K., Frankland, P. W., Kida, S. (2017). Functional connectivity of multiple brain regions required for the consolidation of social recognition memory. *The Journal of Neuroscience, 37,* 4103–4116.

Tannenbaum, J., Bennett, B. T. (2015). Russell and Burch's 3Rs then and now: the need for clarity in definition and purpose. *Journal of American Association for Laboratory Animal Science, 54*, 120-132.

Tanokashira, D., Fukuokaya, W., Taguchi, A. (2019). Involvement of insulin receptor substrates in cognitive impairment and Alzheimer's disease. *Neural Regeneration Research, 14*, 1330-1334.

Tarôco, G., Gaya, L., Resende, D., Santos, I., Madureira, A. (2015). Environmental and dam effects on cannibalism in Wistar rat litters. *Acta Scientiarum, 37,* 225.

Tatematsu, M., Seya, T., Matsumoto, M. (2014). Beyond dsRNA: toll-like receptor 3 signalling in RNA-induced immune responses. *Biochemical Journal, 458*, 195-201.

Tatton-Brown, K., Zachariou, A., Loveday, C., Renwick, A., Mahamdallie, S., Aksglaede, L., Baralle, D., Barge-Schaapveld, D., Blyth, M., Bouma, M., Breckpot, J., Crabb, B., Dabir, T., Cormier-Daire, V., Fauth, C., Fisher, R., Gener, B., Goudie, D., Homfray, T., Hunter, M., … Rahman, N. (2018). The Tatton-Brown-Rahman Syndrome: a clinical study of 55 individuals with de novo constitutive DNMT3A variants. *Wellcome Open Research, 3*, 46.

Tau, G. Z., Peterson, B. S. (2010). Normal development of brain circuits. *Neuropsychopharmacology, 35,* 147-168.

Taylor, D. L., Pirianov, G., Holland, S., McGinnity, C. J., Norman, A. L., Reali, C., Diemel, L. T., Gveric, D., Yeung, D., Mehmet, H. (2010). Attenuation of proliferation in oligodendrocyte precursor cells by activated microglia. *Journal of Neuroscience Research, 88,* 1632-1644.

Tazi, J., Bird, A. (1990). Alternative chromatin structure at CpG islands. *Cell, 60,* 909-920.

Teissier, A., Le Magueresse, C., Olusakin, J. andrade da Costa, B. L. S., De Stasi, A. M., Bacci, A., Imamura Kawasawa, Y., Vaidya, V. A., Gaspar, P. (2020). Early-life stress impairs postnatal oligodendrogenesis and adult emotional behaviour through activity-dependent mechanisms. *Molecular Psychiatry, 25,* 1159-1174.

Teixeira, C. M., Masachs, N., Muhaisen, A., Bosch, C., Pérez-Martínez, J., Howell, B., Soriano, E. (2014). Transient downregulation of Dab1 protein levels during development leads to behavioral and structural deficits: relevance for psychiatric disorders. *Neuropsychopharmacology, 39*, 556–568.

Tew, G. A., Bailey, L., Beeken, R. J., Cooper, C., Copeland, R., Brady, S., Heron, P., Hill, A., Lee, E., Spanakis, P., Stubbs, B., Traviss-Turner, G., Walker, L., Walters, S., Gilbody, S., Peckham, E. (2023). Physical activity in adults with schizophrenia and bipolar disorder: a large cross-sectional survey exploring patterns, preferences, barriers and motivating factors. *International Journal of Environmental Research and Public Health, 20,* 2548.

Tewari, B. P., Chaunsali, L., Prim, C. E., Sontheimer, H. (2022). A glial perspective on the extracellular matrix and perineuronal net remodeling in the central nervous system. *Frontiers in Cellular Neuroscience, 16*, 1022754.

Thapar, A., Cooper, M., Rutter, M. (2017). Neurodevelopmental disorders. *The Lancet, 4,* 339-346.

Thomas, P., Mortensen, M., Hosie, A. M., Smart, T. G. (2005). Dynamic mobility of functional GABAA receptors at inhibitory synapses. *Nature Neuroscience, 8*, 889–897.

Tisato, V., Silva, J. A., Longo, G., Gallo, I., Singh, A. V., Milani, D., Gemmati, D. (2021). Genetics and epigenetics of one-carbon metabolism pathway in autism spectrum disorder: a sex-specific brain epigenome? *Genes, 12*, 782.

Tojo, A., Bredt, D. S., Wilcox, C. S. (1999). Distribution of postsynaptic density proteins in rat kidney: relationship to neuronal nitric oxide synthase. *Kidney International, 55*, 1384-1394.

Toku, K., Tanaka, J., Fujikata, S., Hamamoto, Y., Horikawa, Y., Miyoshi, K., Tateishi, N., Suzuki, Y., Maeda, N. (1999). Distinctions between microglial cells and peripheral macrophages with regard to adhesive activities and morphology. *Journal of Neuroscience Research, 57*, 855-865.

Tong, C. K., Vidyadaran, S. (2016). Role of microglia in embryonic neurogenesis. *Experimental Biology and Medicine, 241,* 1669-1675.

Trabzuni, D., Ramasamy, A., Imran, S., Walker, R., Smith, C., Weale, M. E., Hardy, J., Ryten, M., North American Brain Expression Consortium (2013). Widespread sex differences in gene expression and splicing in the adult human brain. *Nature Communications, 4,* 2771.

Tristan, C., Shahani, N., Sedlak, T. W., Sawa, A. (2011). The diverse functions of GAPDH: views from different subcellular compartments. *Cell Signalling, 23,* 317-323.

Trolin, C. G., Löfberg, C., Trolin, G., Oreland, L. (1994). Brain ATP:l-methionine S-adenosyltransferase (MAT), S-adenosylmethionine (SAM) and S-adenosylhomocysteine (SAH): regional distribution and age-related changes. *European Neuropsychopharmacology, 4*, 469-477.

Trommsdorff, M., Gotthardt, M., Hiesberger, T., Shelton, J., Stockinger, W., Nimpf, J., Hammer, R. E., Richardson, J. A., Herz, J. (1999). Reeler/Disabled-like disruption of neuronal migration in knockout mice lacking the VLDL receptor and ApoE receptor 2. *Cell, 97*, 689–701.

Trotter, J., Lee, G. H., Kazdoba, T. M., Crowell, B., Domogauer, J., Mahoney, H. M., Franco, S. J., Müller, U., Weeber, E. J., D'Arcangelo, G. (2013). Dab1 is required for synaptic plasticity and associative learning. *The Journal of Neuroscience, 33*, 15652-15668.

Trubetskoy, V., Pardiñas, A. F., Qi, T., Panagiotaropoulou, G., Awasthi, S., Bigdeli, T. B., Bryois, J., Chen, C. Y., Dennison, C. A., Hall, L. S., Lam, M., Watanabe, K., Frei, O., Ge, T., Harwood, J. C., Koopmans, F., Magnusson, S., Richards, A. L., Sidorenko, J., Wu, Y., … Schizophrenia Working Group of the Psychiatric Genomics Consortium (2022). Mapping genomic loci implicates genes and synaptic biology in schizophrenia. *Nature, 604,* 502–508.

Trovão, N., Prata, J., VonDoellinger, O., Santos, S., Barbosa, M., Coelho, R. (2019). Peripheral biomarkers for first episode psychosis-opportunities from the neuroinflammatory hypothesis of schizophrenia. *Psychiatry Investigation, 16,* 177–184.

Tsitsiou, E., Sibley, C. P., D'Souza, S. W., Catanescu, O., Jacobsen, D. W., Glazier, J. D. (2009). Homocysteine transport by systems L, A and y+L across the microvillous plasma membrane of human placenta. *The Journal of Physiology, 587*, 4001–4013.

Tsivion-Visbord, H., Kopel, E., Feiglin, A., Sofer, T., Barzilay, R., Ben-Zur, T., Yaron, O., Offen D., Levanon, E. Y. (2020). Increased RNA editing in maternal immune activation model of neurodevelopmental disease. *Nature Communications, 11*, 5236.

Tsukada, T., Shimada, H., Sakata-Haga, H., Iizuka, H., Hatta, T. (2019). Molecular mechanisms underlying the models of neurodevelopmental disorders in maternal immune activation relevant to the placenta. *Congenital Anomalies, 59*, 81-87.

Ucok, A., Gaebel, W. (2008). Side effects of atypical antipsychotics: a brief overview. *World Psychiatry, 7,* 58-62.

Ueno, H., Takao, K., Suemitsu, S., Murakami, S., Kitamura, N., Wani, K., Okamoto, M., Aoki, S., Ishihara, T. (2018). Age-dependent and region-specific alteration of parvalbumin neurons and perineuronal nets in the mouse cerebral cortex. *Neurochemistry International, 112*, 59-70.

UK Research and Innovation (2023). Psychosis Immune Mechanism Stratified Medicine Study (PIMS). UK Research and Innovation Projects. Available from: https://gtr.ukri.org/projects?ref=MR%2FS037675%2F1#/tabOverview

Upthegrove, R., Manzanares-Teson, N., Barnes, N. M. (2014). Cytokine function in medication-naive first episode psychosis: a systematic review and meta-analysis. *Schizophrenia Research, 155*, 101-108.

Urakubo, A., Jarskog, L. F., Lieberman, J. A., Gilmore, J. H. (2001). Prenatal exposure to maternal infection alters cytokine expression in the placenta, amniotic fluid and foetal brain. *Schizophrenia Research, 47*, 27-36.

Ursini, G., Punzi, G., Chen, Q., Marenco, S., Jaffe, A., Straub, R., Berman, K., Hashimoto, R., Colantuoni, C., Blasi, G., Annamaria, P., Giancarlo, M., Joshua, R., Emily, H., Allessandro, B., Weinberger, D. (2017). Placental gene expression mediates the interaction between obstetrical history and genetic risk for schizophrenia. *Schizophrenia Bulletin, 43*, e60.

Valdés-Tovar, M., Rodríguez-Ramírez, A. M., Rodríguez-Cárdenas, L., Sotelo-Ramírez, C. E., Camarena, B., Sanabrais-Jiménez, M. A., Solís-Chagoyán, H., Argueta, J., López-Riquelme, G. O. (2022). Insights into myelin dysfunction in schizophrenia and bipolar disorder. *World Journal of Psychiatry, 12*, 264-285.

Valerio, A., Ferrario, M., Dreano, M., Garotta, G., Spano, P., Pizzi, M. (2002). Soluble interleukin-6 (IL-6) receptor/IL-6 fusion protein enhances *in vitro* differentiation of purified rat oligodendroglial lineage cells. *Molecular and Cellular Neuroscience, 21*, 602-615.

Valério-Gomes, B., Guimarães, D. M., Szczupak, D., Lent, R. (2018). The absolute number of oligodendrocytes in the adult mouse brain. *Frontiers in Neuroanatomy, 12*, 90.

Valinluck, V., Sowers, L. C. (2007). Endogenous cytosine damage products alter the site selectivity of human DNA maintenance methyltransferase DNMT1. *Cancer Research, 67*, 946-950.

van Bodegom, M., Homberg, J. R., Henckens, M. J. A. G. (2017). Modulation of the hypothalamic-pituitary-adrenal axis by early life stress exposure. *Frontiers in Cellular Neuroscience, 11*, 87.

van den Buuse, M. (2010). Modeling the positive symptoms of schizophrenia in genetically modified mice: pharmacology and methodology aspects. *Schizophrenia Bulletin, 36*, 246–270.

van Dongen, J., Boomsma, D. I. (2013). The evolutionary paradox and the missing heritability of schizophrenia. *American Journal of Medical Genetics Part B - Neuropsychiatric Genetics, 162*, 122-136.

van Esch, H. (2012). MECP2 duplication syndrome. *Molecular Syndromology, 2*, 128-136.

van Tilborg, E., de Theije, C. G. M., van Hal, M., Wagenaar, N., de Vries, L. S., Benders, M. J., H. Rowitch, D. H., Nijboer, C. H. (2017). Origin and dynamics of oligodendrocytes in the developing brain: implications for perinatal white matter injury. *Glia, 66*, 221-238.

Vandesompele, J., De preter, K., Pattyn, F., Poppe, B., Van Roy, N., De Paepe, A., Speleman, F. (2002). Accurate normalization of real-time quantitative RT-PCR data by geometric averaging of multiple internal control genes. *Genome Biology, 3,* e0034.

VanRyzin, J. W., Marquardt, A. E., Argue, K. J., Vecchiarelli, H. A., Ashton, S. E., Arambula, S. E., Hill, M. N., McCarthy, M. M. (2019). Microglial phagocytosis of newborn cells is induced by endocannabinoids and sculpts sex differences in juvenile rat social play. *Neuron, 102,* 435-449.

Varoqui, H., Zhu, H., Yao, D., Ming, H., Erickson, J. D. (2000). Cloning and functional identification of a neuronal glutamine transporter. *Journal of Biological Chemistry, 275*, 4049-4054.

Vasistha, N. A., Pardo-Navarro, M., Gasthaus, J., Weijers, D., Müller, M. K., García-González, D., Malwade, S., Korshunova, I., Pfisterer, U., von Engelhardt, J., Hougaard, K. S., Khodosevich, K. (2020). Maternal inflammation has a profound effect on cortical interneuron development in a stage and subtype-specific manner. *Molecular Psychiatry, 25*, 2313–2329.

Veillard, A. C., Datlinger, P., Laczik, M., Squazzo, S., Bock, C. (2016). Diagenode Premium RRBS technology: cost-effective DNA methylation mapping with superior coverage. *Nature Methods, 13*, application note i-ii.

Velakoulis, D., Pantelis, C., McGorry, P. D., Dudgeon, P., Brewer, W., Cook, M., Desmond, P., Bridle, N., Tierney, P., Murrie, V., Singh, B., Copolov, D. (1999). Hippocampal volume in first-episode psychoses and chronic schizophrenia: a high-resolution magnetic resonance imaging study. *Archives of General Psychiatry, 56*, 133-141.

Velazquez-Salinas, L., Verdugo-Rodriguez, A., Rodriguez, L. L., Borca, M. V. (2019). The role of interleukin 6 during viral infections. *Frontiers in Microbiology, 10*, 1057.

Veldic, M., Caruncho, H. J., Liu, W. S., Davis, J., Satta, R., Grayson, D. R., Guidotti, A., Costa, E. (2004). DNA-methyltransferase 1 mRNA is selectively overexpressed in telencephalic GABAergic interneurons of schizophrenia brains. *Proceedings of the National Academy of Sciences of the United States of America, 101*, 348-353.

Velloso, F. J., Wadhwa, A., Kumari, E., Carcea, I., Gunal, O., Levison, S. W. (2022). Modestly increasing systemic interleukin-6 perinatally disturbs secondary germinal zone neurogenesis and gliogenesis and produces sociability deficits. *Brain, Behavior and Immunity, 101,* 23-36.

Ventruti, A., Kazdoba, T. M., Niu, S., D'Arcangelo, G. (2011). Reelin deficiency causes specific defects in the molecular composition of the synapses in the adult brain. *Neuroscience, 189*, 32–42.

Verkhratsky, A., Zorec, R., Parpura, V. (2017). Stratification of astrocytes in healthy and diseased brain. *Brain Pathology, 27,* 629-644.

Verweij, K. J. H., Mosing, M. A., Zietsch, B. P., Medland, S. E. (2012). Estimating heritability from twin studies. In: Elston, R., Satagopan, J., Sun, S., (eds.), Statistical Human Genetics. Methods in Molecular Biology. pp151-170. Humana Press. New Jersey, USA.

Vicentic, A., Francis, D., Moffett, M., Lakatos, A., Rogge, G., Hubert, G. W., Harley, J., Kuhar, M. J. (2006). Maternal separation alters serotonergic transporter densities and serotonergic 1A receptors in rat brain. *Neuroscience, 140*, 355-365.

Vikhreva, O. V., Rakhmanova, V. I., Orlovskaya, D. D., Uranova, N. A. (2016). Ultrastructural alterations of oligodendrocytes in prefrontal white matter in schizophrenia: a post-mortem morphometric study. *Schizophrenia Research, 177*, 28–36.

Villicaña, S., Bell, J. T. (2021). Genetic impacts on DNA methylation: research findings and future perspectives. *BMC Genome Biology, 22*, 127.

Vinay, P., Balamurugan, K., Rajan, K. E. (2022). Reduced Reelin expression induces memory deficits through Dab-1/ NMDAR signaling pathway: Cronobacter sakazakii infection in a rat model of experimental meningitis. *Developmental Neuroscience*, *44*, 547-556.

Vincent, F. B., Nim, H. T., Lee, J. P. W., Morand, E. F., Harris, J. (2019). Effect of storage duration on cytokine stability in human serum and plasma. *Cytokine, 113,* 453-457.

Vita, A., De Peri, L., Deste, G., Sacchetti, E. (2012). Progressive loss of cortical gray matter in schizophrenia: a meta-analysis and meta-regression of longitudinal MRI studies. *Translational Psychiatry, 2,* e190.

Vlasova, R. M., Iosif, A. M., Ryan, A. M., Funk, L. H., Murai, T., Chen, S., Lesh, T. A., Rowland, D. J., Bennett, J., Hogrefe, C. E., Maddock, R. J., Gandal, M. J., Geschwind, D. H., Schumann, C. M., Van de Water, J., McAllister, A. K., Carter, C. S., Styner, M. A., Amaral, D. G., Bauman, M. D. (2021). Maternal immune activation during pregnancy alters postnatal brain growth and cognitive development in nonhuman primate offspring. *The Journal of Neuroscience, 41*, 9971–9987.

Vorhees, C. V., Graham, D. L., Braun, A. A., Schaefer, T. L., Skelton, M. R., Richtand, N. M., Williams, M. T. (2015). Prenatal immune challenge in rats: effects of polyinosinic-polycytidylic acid on spatial learning, prepulse inhibition, conditioned fear and responses to MK-801 and amphetamine. *Neurotoxicology and Teratology, 47*, 54-65.

Vuillermot, S., Feldon, J., Meyer, U. (2010). A longitudinal examination of the neurodevelopmental impact of prenatal immune activation in mice reveals primary defects in dopaminergic development relevant to schizophrenia. *Schizophrenia Research, 117*, e276.

Vyklicky, V., Stanley, C., Habrian, C., Isacoff, E. Y. (2021). Conformational rearrangement of the NMDA receptor amino-terminal domain during activation and allosteric modulation. *Nature Communications, 12*, 2694.

Waddington, C. H. (1956). Genetic assimilation of the bithorax phenotype. *Evolution, 10,* 1-13.

Waddington, C. H. (2012). The epigenotype. 1942. *International Journal of Epidemiology, 41,* 10-13.

Wakeling, E., McEntagart, M., Bruccoleri, M., Shaw-Smith, C., Stals, K. L., Wakeling, M., Barnicoat, A., Beesley, C., DDD Study, Hanson-Kahn, A. K., Kukolich, M., Stevenson, D. A., Campeau, P. M., Ellard, S., Elsea, S. H., Yang, X. J., Caswell, R. C. (2021). Missense substitutions at a conserved 14-3-3 binding site in HDAC4 cause a novel intellectual disability syndrome. *HGG Advances, 2*, 100015.

Walder, D. J., Walker, E. F., Lewine, R. J. (2000). Cognitive functioning, cortisol release and symptom severity in patients with schizophrenia. *Biological Psychiatry, 48*, 1121-1132.

Waller, R., Woodroofe, M. N., Wharton, S. B., Ince, P. G., Francese, S., Heath, P. R., Cudzich-Madry, A., Thomas, R. H., Rounding, N., Sharrack, B., Simpson, J. E. (2016). Gene expression profiling of the astrocyte transcriptome in multiple sclerosis normal appearing white matter reveals a neuroprotective role. *Journal of Neuroimmunology, 299*, 139-146.

Wan, L., Wei, J. (2021). Early-onset schizophrenia: a special phenotype of the disease characterized by increased MTHFR polymorphisms and aggravating symptoms. *Neuropsychiatric Disease and Treatment, 17*, 2511-2525.

Wan, L., Zhang, G., Liu, M., Wang, C., Li, Y., Li, Y. (2019). Sex-specific effects of methylenetetrahydrofolate reductase polymorphisms on schizophrenia with methylation changes. *Comprehensive Psychiatry, 94,* 152121.

Wang, K. C., Koprivica, V., Kim, J. A., Sivasankaran, R., Guo, Y., Neve, R. L., He, Z. (2002). Oligodendrocyte-myelin glycoprotein is a Nogo receptor ligand that inhibits neurite outgrowth. *Nature, 417*, 941-944.

Wang, L., Alachkar, A., Sanathara, N., Belluzzi, J. D., Wang, Z., Civelli, O. (2015). A methionine-induced animal model of schizophrenia: face and predictive validity. *International Journal of Neuropsychopharmacology, 18,* Epyv054.

Wang, M. J., Kuo, J. S., Lee, W. W., Huang, H. Y., Chen, W. F., Lin, S. Z. (2006). Translational event mediates differential production of tumor necrosis factor-alpha in hyaluronan-stimulated microglia and macrophages. *Journal of Neurochemistry, 97*, 857–871.

Wang, N., Gates, K. L., Trejo, H., Favoreto, S., Jr, Schleimer, R. P., Sznajder, J. I., Beitel, G. J., Sporn, P. H. (2010). Elevated CO2 selectively inhibits interleukin-6 and tumor necrosis factor expression and decreases phagocytosis in the macrophage. *FASEB Journal, 24*, 2178–2190.

Wang, X., Hu, Y., Liu, W., Ma, Y., Chen, X., Xue, T., Cui, D. (2021a). Molecular basis of GABA hypofunction in adolescent schizophrenia-like animals. *Neural Plasticity, 2021*, 9983438.

Wang, X., Li, Z., Zhu, Y., Yan, J., Liu, H., Huang, G., Li, W. (2021b). Maternal folic acid impacts DNA methylation profile in male rat offspring implicated in neurodevelopment and learning/memory abilities. *Genes and Nutrition, 16*, 1.

Wang, Y., Hannon, E., Grant, O. A., Gorrie-Stone, T. J., Kumari, M., Mill, J., Zhai, X., McDonald-Maier, K. D., Schalkwyk, L. C. (2021c). DNA methylation-based sex classifier to predict sex and identify sex chromosome aneuploidy. *BMC Genomics, 22*, 484.

Warre-Cornish, K., Perfect, L., Nagy, R., Duarte, R. R. R., Reid, M. J., Raval, P., Mueller, A., Evans, A. L., Couch, A., Ghevaert, C., McAlonan, G., Loth, E., Murphy, D., Powell, T. R., Vernon, A. C., Srivastava, D. P., Price, J. (2020). Interferon-γ signaling in human iPSC-derived neurons recapitulates neurodevelopmental disorder phenotypes. *Science Advances, 6*, eaay9506.

Wastnedge, E. A. N., Reynolds, R. M., van Boeckel, S. R., Stock, S. J., Denison, F. C., Maybin, J. A., Critchley, H. O. D. (2021). Pregnancy and COVID-19. *Physiological Reviews, 101*, 303–318.

Watanabe, D., Uchiyama, K., Hanaoka, K. (2006). Transition of mouse de novo methyltransferases expression from Dnmt3b to Dnmt3a during neural progenitor cell development. *Neuroscience, 142*, 727-737.

Watanabe, M., Maemura, K., Kanbara, K., Tamayama, T., Hayasaki, H. (2002). GABA and GABA receptors in the central nervous system and other organs. *International Review of Cytology - a Survey of Cell Biology, 213*, 1-47.

Weaver, I. C. G., Cervoni, N., Champagne, F. A., D'Alessio, A. C., Sharma, S., Jr, S., Dymov, S., Szyf, M., Meaney, M. J. (2004). Epigenetic programming by maternal behavior. *Nature Neuroscience, 7*, 847-854.

Weber-Stadlbauer, U., Richetto, J., Zwamborn, R. A. J., Slieker, R. C., Meyer, U. (2021). Transgenerational modification of dopaminergic dysfunctions induced by maternal immune activation. *Neuropsychopharmacology, 46*, 404–412.

Webster, M. J., Knable, M. B., O'Grady, J., Orthmann, J., Weickert, C. S. (2002). Regional specificity of brain glucocorticoid receptor mRNA alterations in subjects with schizophrenia and mood disorders. *Molecular Psychiatry, 7*, 985–924.

Weeber, E.J., Beffert, U., Jones, C., Christian, J.M., Forster, E., Sweatt, J.D., Herz, J. (2002). Reelin and ApoE receptors cooperate to enhance hippocampal synaptic plasticity and learning. *The Journal of Biological Chemistry, 277*, 39944–39952.

Wegrzyn, D., Manitz, M. P., Kostka, M., Freund, N., Juckel, G., Faissner, A. (2021). Poly I:C-induced maternal immune challenge reduces perineuronal net area and raises spontaneous network activity of hippocampal neurons *in vitro*. *The European Journal of Neuroscience, 53*, 3920–3941.

Wei, H., Zou, H., Sheikh, A. M., Malik, M., Dobkin, C., Brown, W. T., Li, X. (2011). IL-6 is increased in the cerebellum of autistic brain and alters neural cell adhesion, migration and synaptic formation. *Journal of Neuroinflammation*, *8*, 52.

Weinberger, D. R. (1987). Implications of normal brain-development for the pathogenesis of schizophrenia. *Archives of General Psychiatry, 44*, 660-669.

Weinstein-Fudim, L, Ergaz Z, Szyf M, Ornoy A. (2020). Prenatal S-adenosine methionine (SAMe) induces changes in gene expression in the brain of newborn mice that are prevented by co-administration of valproic acid (VPA). *International Journal of Molecular Science, 21*, 2834.

Weir, R. K., Forghany, R., Smith, S. E., Patterson, P. H., McAllister, A. K., Schumann, C. M., Bauman, M. D. (2015). Preliminary evidence of neuropathology in nonhuman primates prenatally exposed to maternal immune activation. *Brain, Behavior and Immunity, 48*, 139–146.

Weiss, M. D., Derazi, S., Rossignol, C., Varoqui, H., Erickson, J. D., Kilberg, M. S. anderson, K. J. (2003). Ontogeny of the neutral amino acid transporter SAT1/ATA1 in rat brain. *Brain Research, Developmental Brain Research, 143*, 151-159.

Wen, L., Li, X., Yan, L., Tan, Y., Li, R., Zhao, Y., Wang, Y., Xie, J., Zhang, Y., Song, C., Yu, M., Liu, X., Zhu, P., Li, X., Hou, Y., Guo, H., Wu, X., He, C., Li, R., Tang, F., Qiao, J. (2014). Whole-genome analysis of 5-hydroxymethylcytosine and 5-methylcytosine at base resolution in the human brain. *Genome Biology, 15,* 49.

Wen, T. H., Binder, D. K., Ethell, I. M., Razak, K. A. (2018). The perineuronal 'safety' net? Perineuronal net abnormalities in neurological disorders. *Frontiers in Molecular Neuroscience, 11*, 270.

Weng, Q., Wang, J., Wang, J., Tan, B., Wang, J., Wang, H., Zheng, T., Lu, Q. L., Yang, B., He, Q. (2017). Folate metabolism regulates oligodendrocyte survival and differentiation by modulating AMPKα activity. *Science Reports, 7*, 1-13.

Wenzel, A., Fritschy, J. M., Mohler, H., Benke, D. (1997). NMDA receptor heterogeneity during postnatal development of the rat brain: differential expression of the NR2A, NR2B and NR2C subunit proteins. *Journal of Neurochemistry, 68*, 469–478.

Wheelock, M. D., Hect, J. L., Hernandez-Andrade, E., Hassan, S. S., Romero, R., Eggebrecht, A. T., Thomason, M. E. (2019). Sex differences in functional connectivity during foetal brain development. *Developmental Cognitive Neuroscience, 36*, 100632.

Wiegand, A., Kreifelts, B., Munk, M. H. J., Geiselhart, N., Ramadori, K. E., MacIsaac, J. L., Fallgatter, A. J., Kobor, M. S., Nieratschker, V. (2021). DNA methylation differences associated with social anxiety disorder and early life adversity. *Translational Psychiatry, 11*, 104.

Williams, K., Christensen, J., Pedersen, M. T., Johansen, J. V., Cloos, P. A. C., Rappsilber, J., Helin, K. (2011). TET1 and hydroxymethylcytosine in transcription and DNA methylation fidelity. *Nature, 473,* 343.

Willner, P. (1986). Validation criteria for animal models of human mental disorders: learned helplessness as a paradigm case. *Progress in Neuropsychopharmacology and Biological Psychiatry, 10,* 677-690.

Wilson, E., Knudson, W., Newell-Litwa, K. (2020). Hyaluronan regulates synapse formation and function in developing neural networks. *Science Reports, 10*, 16459.

Wingert, J. C., Sorg, B. A. (2021). Impact of perineuronal nets on electrophysiology of parvalbumin interneurons, principal neurons and brain oscillations: a review. *Frontiers in Synaptic Neuroscience, 13*, 673210.

Winship, I. R., Dursun, S. M., Baker, G. B., Balista, P. A., Kandratavicius, L., Maia-de-Oliveira, J. P., Hallak, J., Howland, J. G. (2019). An overview of animal models related to schizophrenia. *Canadian journal of psychiatry. Revue Canadienne de Psychiatrie, 64*, 5–17.

Witham, K. L., Butcher, N. J., Sugamori, K. S., Brenneman, D., Grant, D. M., Minchin, R. F. (2013). 5-methyl-tetrahydrofolate and the S-adenosylmethionine cycle in C57BL/6J mouse tissues: gender differences and effects of arylamine N-acetyltransferase-1 deletion. *PLoS One, 8,* e77923.

Wong, C. C. Y., Caspi, A., Williams, B., Craig, I. W., Houts, R., Ambler, A., Moffitt, T. E., Mill, J. (2010). A longitudinal study of epigenetic variation in twins. *Epigenetics, 5*, 516-526.

Wood, T. C., Edye, M. E., Harte, M. K., Neill, J. C., Prinssen, E. P., Vernon, A. C. (2019). Mapping the impact of exposure to maternal immune activation on juvenile Wistar rat brain macro- and microstructure during early post-natal development. *Brain and Neuroscience Advances, 3*, 2398212819883086.

Woods, R. M., Lorusso, J. M., Harris, I., Kowash, H. M., Murgatroyd, C., Neill, J. C., Glazier, J. D., Harte, M., Hager, R. (2023). Maternal immune activation induces adolescent cognitive deficits preceded by developmental perturbations in cortical Reelin signalling. *Biomolecules, 13*, 489.

Woods, R. M., Lorusso, J. M., Potter, H. G., Neill, J. C., Glazier, J. D., Hager, R. (2021). Maternal immune activation in rodent models: a systematic review of neurodevelopmental changes in gene expression and epigenetic modulation in the offspring brain. *Neuroscience and Biobehavioural Reviews, 129*, 389-421.

World Health Organization (2019). International statistical classification of diseases and related health problems, (11th Edition). World Health Organization Publishing. Geneva.

Wreczycka, K., Gosdschan, A., Yusuf, D., Grüning, B., Assenov, Y., Akalin, A. (2017). Strategies for analyzing bisulfite sequencing data. *Journal of Biotechnology, 261*, 105–115.

Wright, B., Peters, E., Ettinger, U., Kuipers, E., Kumari, V. (2016). Effects of environmental noise on cognitive (dys)functions in schizophrenia: a pilot within-subjects experimental study. *Schizophrenia Research, 173*, 101–108.

Wu, C., Morris, J. R. (2001). Genes, genetics and epigenetics: a correspondence. *Science, 293*, 1103–1105.

Wu, J. I., Reed, R. B., Grabowski, P. J., Artzt, K. (2002). Function of quaking in myelination: regulation of alternative splicing. *Proceedings of the National Academy of Sciences of the United States of America, 99*, 4233-4238.

Wu, X., Reddy, D. S. (2012). Integrins as receptor targets for neurological disorders. *Pharmacology and Therapeutics, 134*, 68–81.

Wu, X., Ye, J., Wang, Z., Zhao, C. (2021). Epigenetic age acceleration was delayed in schizophrenia. *Schizophrenia Bulletin, 47*, 803-811.

Wu, Y., Li, X., Liu, J., Luo, X. J., Yao, Y. G. (2020). SZDB2.0: an updated comprehensive resource for schizophrenia research. *Human Genetics*, *139*, 1285-1297.

Wu, Y., Patchev, A. V., Daniel, G., Almeida, O. F., Spengler, D. (2014). Early-life stress reduces DNA methylation of the Pomc gene in male mice. *Endocrinology, 155*, 1751–1762.

Wyatt-Johnson, S. K., Herr, S. A., Brewster, A. L. (2017). Status epilepticus triggers time-dependent alterations in microglia abundance and morphological phenotypes in the hippocampus. *Frontiers in Neurology, 8*, 700.

Xia, Y., Zhang, Z., Lin, W., Yan, J., Zhu, C., Yin, D., He, S., Su, Y., Xu, N., Caldwell, R. W., Yao, L., Chen, Y. (2020). Modulating microglia activation prevents maternal immune activation induced schizophrenia-relevant behavior phenotypes via arginase 1 in the dentate gyrus. *Neuropsychopharmacology, 45*, 1896-1908.

Xie, X., Lu, J., Kulbokas, E. J., Golub, T. R., Mootha, V., Lindblad-Toh, K., Lander, E. S., Kellis, M. (2005). Systematic discovery of regulatory motifs in human promoters and 3' UTRs by comparison of several mammals. *Nature, 434,* 338-345.

Xiong, Y., Zhang, Y., Zheng, F., Yang, Y., Xu, X., Wang, W., Zhu, B., Wang, X. (2016). Expression of Glypican-4 in the brains of epileptic patients and epileptic animals and its effects on epileptic seizures. *Biochemical and Biophysical Research Communications, 478*, 241-246.

Xin, W., Chan, J. R. (2020). Myelin plasticity: sculpting circuits in learning and memory. *Nature Reviews Neuroscience, 21*, 682-694.

Xu, F., Li, X., Niu, W., Ma, G., Sun, Q., Bi, Y., Guo, Z., Ren, D., Hu, J., Yuan, F., Yuan, R., Shi, L., Li, X., Yu, T., Yang, F., He, L., Zhao, X., He, G. (2019). Metabolomic profiling on rat brain of prenatal malnutrition: implicated for oxidative stress and schizophrenia. *Metabolic Brain Disease, 34*, 1607–1613.

Xu, Y. J., Au, N. P. B., Ma, C. H. E. (2022). Functional and phenotypic diversity of microglia: implication for microglia-based therapies for Alzheimer's disease. *Frontiers in Aging Neuroscience, 14*, 896852.

Yang, A. C., Tsai, S. J. (2017). New targets for schizophrenia treatment beyond the dopamine hypothesis. *International Journal of Molecular Sciences, 18*, 1689.

Yang, B., Curran, B. M., Tymanskyj, S. R. (2017). A role for AnkyrinG in maturation and maintenance of the nodes of Ranvier. *The Journal of Neuroscience, 37*, 5796-5797.

Yashiro, K., Philpot, B. D. (2008). Regulation of NMDA receptor subunit expression and its implications for LTD, LTP and metaplasticity. *Neuropharmacology, 55*, 1081–1094.

Yasuda, S., Hasui, S., Yamamoto, C., Yoshioka, C., Kobayashi, M., Itagaki, S., Hirano, T., Iseki, K. (2008). Placental folate transport during pregnancy. *Bioscience, Biotechnology and Biochemistry, 72*, 2277-2284.

Yasui, N., Nogi, T., Takagi, J. (2010). Structural basis for specific recognition of reelin by its receptors. *Structure, 18,* 320–331.

Yildirim, O., Li, R. W., Hung, J. H., Chen, P. B., Dong, X. J., Ee, L. S., Weng, Z. P., Rando, O. J., Fazzio, T. G. (2011). Mbd3/NURD complex regulates expression of 5-hydroxymethylcytosine marked genes in embryonic stem cells. *Cell, 147*, 1498-1510.

Yin, Y., Qian, S., Chen, Y., Sun, Y., Li, Y., Yu, Y., Li, J., Wu, Z., Yu, X., Ge, R., Han, J., Sun, D., Wu, H., Liu, L., Xue, W., Wang, W. (2021). Latent sex differences in CaMKII-nNOS signaling that underlie antidepressant-like effects of Yueju-Ganmaidazao Decoction in the hippocampus. *Frontiers in Behavioral Neuroscience, 15*, 640258.

Yoo, K. S., Lee, K., Oh, J. Y., Lee, H., Park, H., Park, Y. S., Kim, H. K. (2019). Postsynaptic density protein 95 (PSD-95) is transported by KIF5 to dendritic regions. *Molecular Brain, 12*, 97.

Yoon, S., Piguel, N. H., Penzes, P. (2022). Roles and mechanisms of ankyrin-G in neuropsychiatric disorders. *Experimental Molecular Medicine, 54*, 867-877.

Young, J. W., Powell, S., Risbrough, V., Marston, H. M., Geyer, M. A. (2009). Using the MATRICS to guide development of a preclinical cognitive ibrahitest battery for research in schizophrenia. *Pharmacology and Therapeutics, 122*, 150-202.

Young, S. N., Shalchi, M. (2005). The effect of methionine and S-adenosylmethionine on S-adenosylmethionine levels in the rat brain. *Journal of Psychiatry and Neuroscience, 30*, 44-48.

Yu, G., He, Q. (2016). ReactomePA: an R/Bioconductor package for reactome pathway analysis and visualization. *Molecular BioSystems, 12*, 477-479.

Yudkoff, M. (1997). Brain metabolism of branched-chain amino acids. *Glia, 21,* 92-98.

Zaragozá, R. (2020). Transport of amino acids across the blood-brain barrier. *Frontiers in Physiology, 11*, 973.

Zaretsky, M. V., Alexander, J. M., Byrd, W., Bawdon, R. E. (2004). Transfer of inflammatory cytokines across the placenta. *Obstetrics and Gynecology, 103*, 546-550.

Zaric, M., Drakulic, D., Stojanovic, I. G., Mitrovic, N., Grkovic, I., Martinovic, J. (2018). Regional-specific effects of cerebral ischemia/reperfusion and dehydroepiandrosterone on synaptic NMDAR/PSD-95 complex in male Wistar rats. *Brain Research, 1688,* 73-80.

Zhang, J., Xu, Y., Li, D., Fu, L., Zhang, X., Bao, Y., Zheng, L. (2020a). Review of the correlation of LAT1 with diseases: mechanism and treatment. *Frontiers in Chemistry, 8*, 564809.

Zhang, S. Z., Wang, Q. Q., Yang, Q. Q., Gu, H. Y., Yin, Y. Q., Li, Y. D., Hou, J. C., Chen, R., Sun, Q. Q., Sun, Y. F., Hu, G., Zhou, J. W. (2019a). NG2 glia regulate brain innate immunity via TGF-β2/TGFBR2 axis. *BMC Medical, 17*, 204.

Zhang, X., Li, Y., Ma, L., Zhang, G., Liu, M., Wang, C., Zheng, Y., Li, R. (2020b). A new sex-specific underlying mechanism for female schizophrenia: accelerated skewed X chromosome inactivation. *Biology of Sex Differences, 11*, 39.

Zhang, Z., Ma, Z., Zou, W., Guo, H., Liu, M., Ma, Y., Zhang, L. (2019b). The appropriate marker for astrocytes: comparing the distribution and expression of three astrocytic markers in different mouse cerebral regions. *Biomedical Research International, 2019*, 9605265.

Zhao, D., Mokhtari, R., Pedrosa, E., Birnbaum, R., Zheng, D., Lachman, H. M. (2017). Transcriptome analysis of microglia in a mouse model of Rett syndrome: differential expression of genes associated with microglia/macrophage activation and cellular stress. *Molecular Autism, 8*, 17.

Zhao, M. G., Toyoda, H., Lee, Y. S., Wu, L. J., Ko, S. W., Zhang, X. H., Jia, Y., Shum, F., Xu, H., Li, B. M., Kaang, B. K., Zhuo, M. (2005). Roles of NMDA NR2B subtype receptor in prefrontal long-term potentiation and contextual fear memory. *Neuron, 47,* 859-872.

Zhao, R., Diop-Bove, N., Visentin, M., Goldman, I. D. (2011). Mechanisms of membrane transport of folates into cells and across epithelia. *Annual Review of Nutrition, 21*, 31.

Zhao, R., Matheryly, L. H., Goldman, I. D. (2009). Membrane transporters and folate homeostasis: intestinal absorption and transport into systemic compartments and tissues. *Expert Reviews in Molecular Medicine, 11,* e4.

Zhao, X., Mohammed, R., Tran, H., Erickson, M., Kentner, A. C. (2021). Poly (I:C)-induced maternal immune activation modifies ventral hippocampal regulation of stress reactivity: prevention by environmental enrichment. *Brain, Behavior and Immunity, 95*, 203-215.

Zheng, K., Huang, H., Yang, J., Qui, M. (2022). Origin, molecular specification and stemness of astrocytes. *Developmental Neurobiology, 82*, 149-159.

Zheng, S., Gray, E. E., Chawla, G., Porse, B. T., O'Dell, T. J., Black, D. L. (2012). PSD-95 is post-transcriptionally repressed during early neural development by PTBP1 and PTBP2. *Nature Neuroscience, 15*, 381.

Zhi, D., Aslibekyan, S., Irvin, M. R., Claas, S. A., Borecki, I. B., Ordovas, J. M., Absher, D. M., Arnett, D. K. (2013). SNPs located at CpG sites modulate genome-epigenome interaction. *Epigenetics, 8,* 802-806.

Zhou, X., Tian, B., Han, H. B. (2021). Serum interleukin-6 in schizophrenia: a system review and meta-analysis. *Cytokine, 141*, 155441.

Zhu, C., Kwok, N. T., Chan, T. C., Chan, G. H., So, S. H. (2021). Inflexibility in reasoning: comparisons of cognitive flexibility, explanatory flexibility and belief flexibility between schizophrenia and major depressive disorder. *Frontiers in Psychiatry, 11*, 609569.

Zhubi, A., Veldic, M., Puri, N. V., Kadriu, B., Caruncho, H., Loza, I., Sershen, H., Lajtha, A., Smith, R. C., Guidotti, A., Davis, J. M., Costa, E. (2009). An upregulation of DNA-methyltransferase 1 and 3a expressed in telencephalic GABAergic neurons of schizophrenia patients is also detected in peripheral blood lymphocytes. *Schizophrenia Research, 111*, 115-122.

Zöller, T., Schneider, A., Kleimeyer, C., Masuda, T., Potru, P. S., Pfeifer, D., Blank, T., Prinz, M., Spittau, B. (2018). Silencing of TGFβ signalling in microglia results in impaired homeostasis. *Nature Communications, 9*, 4011.

Zong, X., Zhang, Q., He, C., Huang, X., Zhang, J., Wang, G., Lv, L., Sang, D., Zou, X., Chen, H., Zheng, J., Hu, M. (2021). DNA methylation basis in the effect of white matter integrity deficits on cognitive impairments and psychopathological symptoms in drug-naive first-episode schizophrenia. *Fronters in Psychiatry, 12,* 777407.

Zuckerman, L., Rehavi, M., Nachman, R., Weiner, I. (2003). Immune activation during pregnancy in rats leads to a postpubertal emergence of disrupted latent inhibition, dopaminergic hyperfunction and altered limbic morphology in the offspring: a novel neurodevelopmental model of schizophrenia. *Neuropsychopharmacology, 28*, 1778-1789.

Zuckerman, L., Weiner, I. (2003). Post-pubertal emergence of disrupted latent inhibition following prenatal immune activation. *Psychopharmacology, 169,* 308-313.